



Journal of
*Marine Science
and Engineering*

Advances in Marine Engineering

Geological Environment and Hazards

Edited by

Xiaolei Liu, Thorsten Stoesser and Xingsen Guo

Printed Edition of the Special Issue Published in
Journal of Marine Science and Engineering

Advances in Marine Engineering: Geological Environment and Hazards

Advances in Marine Engineering: Geological Environment and Hazards

Editors

Xiaolei Liu

Thorsten Stoesser

Xingsen Guo

MDPI • Basel • Beijing • Wuhan • Barcelona • Belgrade • Manchester • Tokyo • Cluj • Tianjin



Editors

Xiaolei Liu
Ocean University of China
China

Thorsten Stoesser
University College London
UK

Xingsen Guo
University College London
UK

Editorial Office

MDPI
St. Alban-Anlage 66
4052 Basel, Switzerland

This is a reprint of articles from the Special Issue published online in the open access journal *Journal of Marine Science and Engineering* (ISSN 2077-1312) (available at: https://www.mdpi.com/journal/jmse/special_issues/Geological_Environment).

For citation purposes, cite each article independently as indicated on the article page online and as indicated below:

LastName, A.A.; LastName, B.B.; LastName, C.C. Article Title. <i>Journal Name</i> Year , <i>Volume Number</i> , Page Range.

ISBN 978-3-0365-7056-3 (Hbk)

ISBN 978-3-0365-7057-0 (PDF)

© 2023 by the authors. Articles in this book are Open Access and distributed under the Creative Commons Attribution (CC BY) license, which allows users to download, copy and build upon published articles, as long as the author and publisher are properly credited, which ensures maximum dissemination and a wider impact of our publications.

The book as a whole is distributed by MDPI under the terms and conditions of the Creative Commons license CC BY-NC-ND.

Contents

About the Editors vii

Kingsen Guo, Xiaolei Liu and Thorsten Stoesser

Advances in Marine Engineering: Geological Environment and Hazards
Reprinted from: *J. Mar. Sci. Eng.* **2023**, *11*, 475, doi:10.3390/jmse11030475 1

Zhigang Shan, Hao Wu, Weida Ni, Miaojun Sun, Kuanjun Wang, Liuyuan Zhao, et al.

Recent Technological and Methodological Advances for the Investigation of
Submarine Landslides
Reprinted from: *J. Mar. Sci. Eng.* **2022**, *10*, 1728, doi:10.3390/jmse10111728 7

Chenguang Liu, Qingxian Zhao, Zhen Liu, Yanhong Lian, Yanliang Pei, Baohua Liu, et al.

Development and Testing of a High-Resolution Three-Dimensional Seismic Detection System
for Gas Hydrate
Reprinted from: *J. Mar. Sci. Eng.* **2023**, *11*, 20, doi:10.3390/jmse11010020 23

**Qingfeng Hua, Guanbao Li, Qingjie Zhou, Shujiang Li, Tengfei Xu, Baohua Liu
and Hongxia Chen**

Sediment Waves on the Western Slope of the Chukchi Rise (Arctic Ocean) and Their
Implications for the Paleoenvironment
Reprinted from: *J. Mar. Sci. Eng.* **2022**, *10*, 1586, doi:10.3390/jmse10111586 37

Li Pang, Chong Jiang and Lujie Chen

Nonlinear Predictive Framework of the Undrained Clay Slope Effect on the Initial Stiffness of
p-y Curves of Laterally Loaded Piles by FEM
Reprinted from: *J. Mar. Sci. Eng.* **2022**, *10*, 1684, doi:10.3390/jmse10111684 49

Yujing Jiang, Meng Li, Hengjie Luan, Yichen Shi, Sunhao Zhang, Peng Yan and Baocheng Li

Discrete Element Simulation of the Macro-Meso Mechanical Behaviors of Gas-Hydrate-Bearing
Sediments under Dynamic Loading
Reprinted from: *J. Mar. Sci. Eng.* **2022**, *10*, 1042, doi:10.3390/jmse10081042 73

Qizhi Chen, Luju Liang, Baoping Zou, Changjie Xu, Bowen Kong and Jingyuan Ma

Analytical Solutions of Steady a Seepage Field for Deep-Buried Tunnel with Grouting Ring
Considering Anisotropic Flow
Reprinted from: *J. Mar. Sci. Eng.* **2022**, *10*, 1861, doi:10.3390/jmse10121861 97

**Mujun Chen, Xiangmei Meng, Guangming Kan, Jingqiang Wang, Guanbao Li,
Baohua Liu, et al.**

Predicting the Sound Speed of Seafloor Sediments in the East China Sea Based on an
XGBoost Algorithm
Reprinted from: *J. Mar. Sci. Eng.* **2022**, *10*, 1366, doi:10.3390/jmse10101366 115

Chenzhe Li, Tengfei Fu, Yushan Fu, Zhenyan Wang, Bin Li, Chen Qi, et al.

Origin and Implications of Pollution in Coastal Groundwater of the Guangdong Province
Reprinted from: *J. Mar. Sci. Eng.* **2022**, *10*, 1394, doi:10.3390/jmse10101394 131

Ziyu Wang and Lei Zhang

Experimental Study on Dynamic Parameters of Calcareous Sand Subgrade under Long-Term
Cyclic Loading
Reprinted from: *J. Mar. Sci. Eng.* **2022**, *10*, 1806, doi:10.3390/jmse10121806 151

Zhongde Gu, Xingsen Guo, Houbin Jiao, Yonggang Jia and Tingkai Nian Effect of Low Temperature on the Undrained Shear Strength of Deep-Sea Clay by Mini-Ball Penetration Tests Reprinted from: <i>J. Mar. Sci. Eng.</i> 2022 , <i>10</i> , 1424, doi:10.3390/jmse10101424	167
Jingqiang Wang, Zhengyu Hou, Guanbao Li, Guangming Kan, Baohua Liu, Xiangmei Meng, et al. High-Frequency Dependence of Acoustic Properties of Three Typical Sediments in the South China Sea Reprinted from: <i>J. Mar. Sci. Eng.</i> 2022 , <i>10</i> , 1295, doi:10.3390/jmse10091295	183
Ying Yang, Hailei Kou, Zhenghui Li, Yonggang Jia and Chaoqi Zhu Normalized Stress–Strain Behavior of Deep-Sea Soft Soils in the Northern South China Sea Reprinted from: <i>J. Mar. Sci. Eng.</i> 2022 , <i>10</i> , 1142, doi:10.3390/jmse10081142	195
Peng Yu, Jie Dong, Haisong Liu, Rui Xu, Rujie Wang, Meijun Xu and Hongjun Liu Analysis of Cyclic Shear Stress–Displacement Mechanical Properties of Silt–Steel Interface in the Yellow River Delta Reprinted from: <i>J. Mar. Sci. Eng.</i> 2022 , <i>10</i> , 1704, doi:10.3390/jmse10111704	211
Wei qi Fu, Wei Wei, Hao Wang, Bingxiang Huang and Zhiyuan Wang Study on the Rheology of CO ₂ Hydrate Slurry by Using the Capillary Method Reprinted from: <i>J. Mar. Sci. Eng.</i> 2022 , <i>10</i> , 1224, doi:10.3390/jmse10091224	229

About the Editors

Xiaolei Liu

He works as a professor and doctoral supervisor in Ocean University of China (OUC). He is the director of the institute of marine engineering geology and the environment at OUC, and the deputy director of Shandong Provincial Key Laboratory of Marine Environment and Geological Engineering. Also, he is the chairman of Committee on Marine Geo-disaster and Geo-environment (TC-4) in International Consortium on Geo-disaster Reduction (ICGdR). His research interests are focused on marine engineering geological environment and related disasters. He has obtained the first prize of Hainan Province Science and Technology Progress Award, the first prize of Science and Technology Award for Higher Education Institutions of Shandong Province and the first prize of Technological Invention Award by China Association of Oceanic Engineering. Besides, he was awarded the Outstanding Young Scientist Award of ICGdR and the 3rd Gu Dezhen Young Engineering Geologist Technology Award of the Engineering Geology Professional Committee of the Geological Society of China. He has undertaken more than 10 national scientific research projects and published more than 100 academic papers, including more than 50 SCI papers in mainstream journals within the international marine engineering geology field such as *Engineering Geology*, *Marine Geology*, *Ocean Engineering*, etc. At the same time, he has published 3 monographs and authorized more than 40 invention patents (including 5 international patents).

Thorsten Stoesser

The Leader of the Fluid Mechanics Research Group in the Department of Civil, Environmental and Geomatic Engineering at the University College London. His research interest is in developing advanced Computational Fluid Dynamics (CFD) tools and their application to solve environmental fluid mechanics problems. Thorsten has published over 100 peer-reviewed journal papers on developing, testing and applying advanced CFD methods to predict the hydrodynamics and transport processes in rivers, estuaries and coastal waters, fluid-structure interaction of marine turbines, and the nearfield dynamics of jets and plumes. For his research Prof. Stoesser received twice the American Society of Civil Engineers (ASCE) Karl Emil Hilgard Hydraulic Prize (2012 and 2016), in 2015 he won the International Association of Hydro-environmental Research (IAHR) Harold Shoemaker Award and in 2016 he won the Institution of Civil Engineers' George Stephenson medal. He has received over £5M in funding from industry, government institutions and research councils including the DFG (Germany), NSF (USA) and EPSRC (UK).

Xingsen Guo

A Research Fellow in the Department of Civil, Environmental and Geomatic Engineering at University College London (UCL) and a member of the Fluid Mechanics Research Group at UCL since 2020. His research mainly concerns marine engineering geology (e.g., surficial sediment and hydrodynamic environment) and geotechnical engineering (e.g., pipeline and pile), marine geological hazards (e.g., seabed stability and submarine landslide), and computational fluid dynamics into turbidity currents and plumes. He obtained his PhD at the Dalian University of Technology (DUT) for his work on the Susceptibility of Submarine Seismic Landslide and Landslide-pipeline Interaction in 2021. Xingsen has published over 40 peer-reviewed journal papers. For his research, Dr. Guo was honored with the Excellent Doctoral Dissertation Award of the International Consortium on Geo-disaster Reduction (ICGdR) in 2022, the Excellent Doctoral Dissertation Award of the Chinese

Society for Rock Mechanics & Engineering (CSRME) in 2021, the Liaoning Province Excellent Doctoral Dissertation Award in 2023, the DUT Excellent Doctoral Dissertation Award in 2022, the BGA (British Geotechnical Association) Fund Award in 2022, and the Liu Huixian Earthquake Engineering Scholarship Award awarded by the Huixian Earthquake Engineering Foundation (China) and the US-China Earthquake Engineering Foundation (USA) in 2020.

Editorial

Advances in Marine Engineering: Geological Environment and Hazards

Xingsen Guo ^{1,2}, Xiaolei Liu ^{1,3,*} and Thorsten Stoesser ²

¹ Shandong Provincial Key Laboratory of Marine Environment and Geological Engineering, Ocean University of China, Qingdao 266100, China

² Department of Civil, Environmental, Geomatic Engineering, University College London, London WC1E 6BT, UK

³ Laboratory for Marine Geology, Qingdao National Laboratory for Marine Science and Technology, Qingdao 266061, China

* Correspondence: xiaolei@ouc.edu.cn

1. Introduction

With the continuous advancement of coastal, offshore, and deep-sea engineering construction (e.g., marine oil, gas, and mineral resource development, offshore wind power projects), associated studies on marine geological environments and hazards have also advanced in parallel. This Special Issue (SI) was organized by Prof. Xiaolei Liu from the Ocean University of China, Prof. Thorsten Stoesser from University College London, and Dr. Xingsen Guo from University College London to document research advances in specific topics of marine engineering. The objective of this SI “Advances in Marine Engineering: Geological Environment and Hazards” is to collect high-quality papers in this field, including marine geological environments, marine geological hazards, marine engineering geology, marine hydrodynamics, marine fluid mechanics, and marine geotechnical engineering.

The SI includes 1 review paper [1] and 13 research papers [2–14] that cover different aspects related to the subject. A total of 95 scholars from universities, research institutions, and industries have contributed to this SI. The high-quality papers collected in this SI involve many classic and innovative methodologies in this research field, including, but not limited to, analytical and statistical analyses, numerical simulations, laboratory testing, and marine surveys. Specifically, some researchers carried out in situ marine surveys and monitoring [2,3], some implemented discrete element and finite element numerical simulations [4–6], some conducted indoor unit tests [7–12], some developed laboratory model tests [13,14], and others applied analytical and statistical methods [1,6–8]. These papers represent the state-of-the-art in the latest research concepts, advanced methods, and data that will contribute greatly to the development of the field of marine geological environments and hazards. The highlights of each paper in this SI are synthesized in the following section.

2. Papers Details

Shan et al. [1] systematically reviewed the past literature related to submarine landslides and proposed three stages of submarine landslide disaster evolution, namely, the submarine slope instability evolution stage, the large deformation landslide movement stage, and the stage of submarine landslide deposition. Based on these, they revealed the conversion mechanism of the submarine landslide disaster chain from the perspectives of in situ investigation techniques, physical simulation methods, and numerical simulation methods, respectively. Their study provides a useful reference for future research in the field of submarine landslides.

Liu et al. [2] developed a high-resolution three-dimensional seismic detection system for detecting gas hydrates. This system consists of a 50 kJ ultrahigh-energy plasma source,

Citation: Guo, X.; Liu, X.; Stoesser, T. Advances in Marine Engineering: Geological Environment and Hazards. *J. Mar. Sci. Eng.* **2023**, *11*, 475. <https://doi.org/10.3390/jmse11030475>

Received: 25 January 2023

Revised: 13 February 2023

Accepted: 20 February 2023

Published: 22 February 2023



Copyright: © 2023 by the authors. Licensee MDPI, Basel, Switzerland. This article is an open access article distributed under the terms and conditions of the Creative Commons Attribution (CC BY) license (<https://creativecommons.org/licenses/by/4.0/>).

two high-resolution digital seismic streamers with a group interval of 3.125 m, and a seismic acquisition system, which can detect anomalies such as bottom simulating reflection, the blanking zone, velocity anomaly, and the polarity reversal of gas hydrates. Their acquisition tests carried out in the northeastern part of the South China Sea show that the system has obvious advantages in terms of the frequency band range and minimum acquisition binning, which can provide technical support for highly targeted gas hydrate exploration and development and a fine description of the ore bodies.

Hua et al. [3] found a sediment wave field on the western slope of the Chukchi Rise in the Arctic Ocean using multibeam bathymetric data and high-resolution shallow sub-bottom profiles acquired during China's 10th Arctic Scientific Expedition Cruise in 2019. They conclude that these sediment waves are formed by contour currents and result from the interaction between continental slope bottom currents and the seabed; the sediment waves are still active, and their formation seems to date back to the Middle Pleistocene; and the sediment waves are formed by a bottom current, which may be genetically related to the Arctic Circumpolar Boundary Current flowing through the study area, aiding our understanding of the characteristics of the bottom current, thereby providing useful information on the Arctic Ocean environment.

Pang et al. [4] proposed nonlinear prediction methods for the slope effect on the initial stiffness of p - y curves of the undrained laterally loaded pile. They analyzed the slope effect on the initial stiffness of a laterally loaded pile based on the pile-slope position relationship, conducted a series of finite-element analysis simulations to calculate the slope effect, and calibrated parameters in the models using the results of the finite-element analysis. The results show that the methods they proposed are in a reasonable range and can predict more cases.

Jiang et al. [5] studied the mechanical properties of natural gas hydrate sediments under dynamic loading. They carried out triaxial compression tests on the discrete element specimens of hydrate sediments under static loading by using a particle flow code, verified the numerical method by some comparison, and determined the reasonable simulation parameters. Subsequently, multiple triaxial compression tests on hydrate sediment specimens under cyclic loading with different frequencies and amplitudes were carried out, revealing the influence of dynamic loading on their macro-meso mechanical properties. The results of their study are useful for the understanding of the dynamics of hydrate sediments and the prevention and control of submarine geohazards.

Chen et al. [6] derived the analytical solutions of a steady seepage field for a deep-buried tunnel with grouting ring considering anisotropic flow, and the analytical solutions are validated by numerical simulations. Subsequently, they carried out parameter analysis and the results show that (1) the seepage field of surrounding rocks around the deeply buried circular tunnel is no longer uniformly distributed and presented an elliptical distribution, (2) the difference between the permeability coefficient of the lining structure and the surrounding rock is small, (3) the change in the permeability coefficient of the lining structure has a significant influence on the hydraulic head, and (4) the size of the grouting ring has a more significant influence on the grouting effect.

Chen et al. [7] used the extreme gradient boosting (XGBoost) algorithm to predict the sound speed of the seafloor sediments based on the acoustic and physical data of the typical seafloor sediment samples from the East China Sea. They conducted the super parameter selection and contribution of the characteristic factors and established an XGBoost model based on five physical parameters. Moreover, they compared the machine learning prediction method with the traditional prediction method, demonstrated that the XGBoost prediction method for the sound speed of seafloor sediments was superior to the traditional single- and two-parameter regression equation prediction methods in the study area, and provided the accuracy, R^2 , mean absolute error, and mean absolute percent error under the optimal model.

Li et al. [8] proposed a novel approach to hydrochemical analysis combined with the health risk model and the water quality index to explain the hydrochemistry characteristics

and risks to human health of groundwater in the Guangdong coastal areas, and determined the average concentration of the total dissolved solids, the quality of water, the dominant hydrochemical types, and the main influencing factor of the hydrochemical composition. Using principal component analysis, they found that seawater intrusion and anthropogenic inputs also have an effect on the water quality. They evaluated the drinking quality of the water in the Guangdong coastal cities, and the result shows that most of the groundwater samples were acceptable for drinking except for samples of Maoming, Zhanjiang, and Shantou, and also found that children in the study area are at more danger to health risks than adults.

Wang and Zhang [9] used a dynamic triaxial apparatus to conduct long-term drainage cyclic loading tests for the unsaturated calcareous sand subgrade, and studied the cumulative strain development law of calcareous sand under different confining pressures, dynamic stress amplitudes, consolidation stress ratios, subgrade soil compactness, load frequencies, and moisture contents. They proposed a prediction formula combined with a hyperbolic model for the permanent deformation of calcareous sand under aircraft loading, providing a theoretical basis for the construction of a calcareous sand subgrade in the Nanhai island and reef project.

Gu et al. [10] investigated the low-temperature effect on the undrained shear strength of undisturbed marine clay samples from the South China Sea using a full-flow penetrometer. They found that the undrained shear strength at an in situ temperature (4 °C) is bigger than at room temperature (20 °C), which is valuable for offshore geotechnical engineers. In addition, they explained the effect of a low temperature on the undrained shear strength of marine clay samples under the framework of microscopic soil mechanics, which also provides a good insight for explaining some phenomena that microscopically changes the effect of the macroscopic physical and mechanical properties of marine sediments.

Wang et al. [11] investigated the acoustic properties of three fine-grained sediment types in the high-frequency range of 27–247 kHz in the South China Sea and established the relationship between the sound speed and attenuation dispersion of fine-grained sediment. Their study showed that the sound speed dispersion is a positive linear relation at the measured frequency range, and the attenuation follows nonlinear frequency dependence. In addition, they demonstrated that the Biot–Stoll model has a good applicability to different types of sediments in a high-frequency range.

Yang et al. [12] investigated the physical and mechanical properties of samples taken from the Shenhu sea area in the South China Sea (SCS), particularly normalized stress–strain behavior and microstructural and mineralogical characterization, using a series of basic geotechnical tests, triaxial compression tests, scanning electron microscopy (SEM), and X-ray diffraction (XRD). They discussed the factors and conditions for normalizing the stress–strain relationship in soft soil based on the hyperbolic equation of the stress–strain relationship proposed by Konder, applied the normalization factors to the consolidation undrained test of soft soil in the SCS, and established normalized models to predict the stress–strain relationship.

Yu et al. [13] investigated the cyclic shear stress–strain mechanical properties of the silt–steel interface in the Yellow River Delta, China. Their study carried out the constant normal load cyclic shear test (CNL) with a large interface shear apparatus and focused on the effects of normal stress, shear amplitude, roughness, and water content on the profiles of the shear–strain relationship and volumetric deformation characteristics. Based on the modified hyperbolic model, they also built a mathematical model that can describe the stress–strain relationship of the silt–steel interface in the Yellow River Delta.

Fu et al. [14] developed a novel experiment flow loop and presented the rheological experiments of CO₂ hydrate slurries. Their experiments verified that CO₂ hydrate slurry is a power-law fluid that exhibits a strong shear-thickening behavior and revealed the effects of a hydrate concentration and shear rate on the rheological properties of CO₂ hydrate slurry. By correlating with the experimental data, they developed a new Herschel–

Bulkley-type model to describe the rheological properties of CO₂ hydrate slurry with a high accuracy.

Author Contributions: Conceptualization, X.G., X.L., and T.S.; investigation, X.G.; resources, X.L. and T.S.; writing—original draft preparation, X.G.; writing—review and editing, X.L. and T.S. All authors have read and agreed to the published version of the manuscript.

Funding: Financial support for this work is provided by the National Natural Science Foundation of China (42022052 and 42277138), the Shandong Provincial Natural Science Foundation (ZR2020YQ29), UCL's Department of Civil, Environmental and Geomatic Engineering, and Ocean University of China.

Acknowledgments: We want to express our sincere thankfulness to all the authors, the Academic Editors, and the reviewers. We would also like to thank the Editorial Board for their support.

Conflicts of Interest: The authors declare no conflict of interest.

References

1. Shan, Z.; Wu, H.; Ni, W.; Sun, M.; Wang, K.; Zhao, L.; Lou, Y.; Liu, A.; Xie, W.; Zheng, X.; et al. Recent technological and methodological advances for the investigation of submarine landslides. *J. Mar. Sci. Eng.* **2022**, *10*, 1728. [[CrossRef](#)]
2. Liu, C.; Zhao, Q.; Liu, Z.; Lian, Y.; Pei, Y.; Liu, B.; Li, X.; Zhou, Q.; Yan, K.; Chen, Z. Development and Testing of a High-Resolution Three-Dimensional Seismic Detection System for Gas Hydrate. *J. Mar. Sci. Eng.* **2023**, *11*, 20. [[CrossRef](#)]
3. Hua, Q.; Li, G.; Zhou, Q.; Li, S.; Xu, T.; Liu, B.; Chen, H. Sediment Waves on the Western Slope of the Chukchi Rise (Arctic Ocean) and Their Implications for the Paleoenvironment. *J. Mar. Sci. Eng.* **2022**, *10*, 1586. [[CrossRef](#)]
4. Pang, L.; Jiang, C.; Chen, L. Nonlinear Predictive Framework of the Undrained Clay Slope Effect on the Initial Stiffness of py Curves of Laterally Loaded Piles by FEM. *J. Mar. Sci. Eng.* **2022**, *10*, 1684. [[CrossRef](#)]
5. Jiang, Y.; Li, M.; Luan, H.; Shi, Y.; Zhang, S.; Yan, P.; Li, B. Discrete Element Simulation of the Macro-Meso Mechanical Behaviors of Gas-Hydrate-Bearing Sediments under Dynamic Loading. *J. Mar. Sci. Eng.* **2022**, *10*, 1042. [[CrossRef](#)]
6. Chen, Q.; Liang, L.; Zou, B.; Xu, C.; Kong, B.; Ma, J. Analytical Solutions of Steady a Seepage Field for Deep-Buried Tunnel with Grouting Ring Considering Anisotropic Flow. *J. Mar. Sci. Eng.* **2022**, *10*, 1861. [[CrossRef](#)]
7. Chen, M.; Meng, X.; Kan, G.; Wang, J.; Li, G.; Liu, B.; Liu, C.; Liu, Y.; Liu, Y.; Lu, J. Predicting the Sound Speed of Seafloor Sediments in the East China Sea Based on an XGBoost Algorithm. *J. Mar. Sci. Eng.* **2022**, *10*, 1366. [[CrossRef](#)]
8. Li, C.; Fu, T.; Fu, Y.; Wang, Z.; Li, B.; Qi, C.; Chen, G.; Xu, X.; Yu, H. Origin and Implications of Pollution in Coastal Groundwater of the Guangdong Province. *J. Mar. Sci. Eng.* **2022**, *10*, 1394. [[CrossRef](#)]
9. Wang, Z.; Zhang, L. Experimental Study on Dynamic Parameters of Calcareous Sand Subgrade under Long-Term Cyclic Loading. *J. Mar. Sci. Eng.* **2022**, *10*, 1806. [[CrossRef](#)]
10. Gu, Z.; Guo, X.; Jiao, H.; Jia, Y.; Nian, T. Effect of Low Temperature on the Undrained Shear Strength of Deep-Sea Clay by Mini-Ball Penetration Tests. *J. Mar. Sci. Eng.* **2022**, *10*, 1424. [[CrossRef](#)]
11. Wang, J.; Hou, Z.; Li, G.; Kan, G.; Liu, B.; Meng, X.; Hua, Q.; Sun, L. High-Frequency Dependence of Acoustic Properties of Three Typical Sediments in the South China Sea. *J. Mar. Sci. Eng.* **2022**, *10*, 1295. [[CrossRef](#)]
12. Yang, Y.; Kou, H.; Li, Z.; Jia, Y.; Zhu, C. Normalized Stress–Strain Behavior of Deep-Sea Soft Soils in the Northern South China Sea. *J. Mar. Sci. Eng.* **2022**, *10*, 1142. [[CrossRef](#)]
13. Yu, P.; Dong, J.; Liu, H.; Xu, R.; Wang, R.; Xu, M.; Liu, H. Analysis of Cyclic Shear Stress–Displacement Mechanical Properties of Silt–Steel Interface in the Yellow River Delta. *J. Mar. Sci. Eng.* **2022**, *10*, 1704. [[CrossRef](#)]
14. Fu, W.; Wei, W.; Wang, H.; Huang, B.; Wang, Z. Study on the rheology of CO₂ hydrate slurry by using the capillary method. *J. Mar. Sci. Eng.* **2022**, *10*, 1224. [[CrossRef](#)]

Short Biography of the Authors

Xingsen Guo is a Research Fellow in the Department of Civil, Environmental and Geomatic Engineering at University College London (UCL) and a member of the Fluid Mechanics Research Group at UCL since 2020. His research mainly concerns marine engineering geology (e.g., surficial sediment and hydrodynamic environment) and geotechnical engineering (e.g., pipeline and pile), marine geological hazards (e.g., seabed stability and submarine landslide), and computational fluid dynamics into turbidity currents and plumes. He obtained his PhD at the Dalian University of Technology (DUT) for his work on the Susceptibility of Submarine Seismic Landslide and Landslide-pipeline Interaction in 2021. Xingsen has published over 40 peer-reviewed journal papers. For his research, Dr. Guo was honored with the Excellent Doctoral Dissertation Award of the International Consortium on Geo-disaster Reduction (ICGdR) in 2022, the Excellent Doctoral Dissertation Award of the Chinese Society for Rock Mechanics & Engineering (CSRME) in 2021, the DUT Excellent Doctoral Dissertation Award in 2022, the BGA (British Geotechnical Association) Fund Award in

2022, and the Liu Huixian Earthquake Engineering Scholarship Award awarded by the Huixian Earthquake Engineering Foundation (China) and the US-China Earthquake Engineering Foundation (USA) in 2020.

Xiaolei Liu works as a professor and doctoral supervisor in Ocean University of China (OUC). He is the director of the institute of marine engineering geology and the environment at OUC, and the deputy director of Shandong Provincial Key Laboratory of Marine Environment and Geological Engineering. Also, he is the chairman of Committee on Marine Geo-disaster and Geo-environment (TC-4) in International Consortium on Geo-disaster Reduction (ICGdR). His research interests are focused on marine engineering geological environment and related disasters. He has obtained the first prize of Hainan Province Science and Technology Progress Award, the first prize of Science and Technology Award for Higher Education Institutions of Shandong Province and the first prize of Technological Invention Award by China Association of Oceanic Engineering. Besides, he was awarded the Outstanding Young Scientist Award of ICGdR and the 3rd Gu Dezhen Young Engineering Geologist Technology Award of the Engineering Geology Professional Committee of the Geological Society of China. He has undertaken more than 10 national scientific research projects and published more than 100 academic papers, including more than 50 SCI papers in mainstream journals within the international marine engineering geology field such as *Engineering Geology*, *Marine Geology*, *Ocean Engineering*, etc. At the same time, he has published 3 monographs and authorized more than 40 invention patents (including 5 international patents).

Thorsten Stoesser is the Leader of the Fluid Mechanics Research Group in the Department of Civil, Environmental and Geomatic Engineering at the University College London. His research interest is in developing advanced Computational Fluid Dynamics (CFD) tools and their application to solve environmental fluid mechanics problems. Thorsten has published over 100 peer-reviewed journal papers on developing, testing and applying advanced CFD methods to predict the hydrodynamics and transport processes in rivers, estuaries and coastal waters, fluid-structure interaction of marine turbines, and the nearfield dynamics of jets and plumes. For his research Prof. Stoesser received twice the American Society of Civil Engineers (ASCE) Karl Emil Hilgard Hydraulic Prize (2012 and 2016), in 2015 he won the International Association of Hydro-environmental Research (IAHR) Harold Shoemaker Award and in 2016 he won the Institution of Civil Engineers' George Stephenson medal. He has received over £5M in funding from industry, government institutions and research councils including the DFG (Germany), NSF (USA) and EPSRC (UK).

Disclaimer/Publisher's Note: The statements, opinions and data contained in all publications are solely those of the individual author(s) and contributor(s) and not of MDPI and/or the editor(s). MDPI and/or the editor(s) disclaim responsibility for any injury to people or property resulting from any ideas, methods, instructions or products referred to in the content.

Review

Recent Technological and Methodological Advances for the Investigation of Submarine Landslides

Zhigang Shan ^{1,2}, Hao Wu ^{1,2,3,*}, Weida Ni ^{1,2}, Miaojun Sun ^{1,2}, Kuanjun Wang ^{1,2,*}, Liuyuan Zhao ^{1,2}, Yihuai Lou ⁴, An Liu ^{1,2}, Wei Xie ^{1,2}, Xing Zheng ^{1,2} and Xingsen Guo ⁵

- ¹ POWERCHINA Huadong Engineering Corporation Limited, Hangzhou 310014, China
² Zhejiang Engineering Research Center of Marine Geotechnical Investigation Technology and Equipment, Zhejiang Huadong Construction Engineering Corporation Limited, Hangzhou 311122, China
³ Institute of Mountain Hazards and Environment, Chinese Academy of Sciences, Chengdu 610299, China
⁴ College of Civil Engineering and Architecture, Zhejiang University, Hangzhou 310058, China
⁵ Department of Civil, Environmental, Geomatic Engineering, University College London, London WC1E 6BT, UK
* Correspondence: wuhao@imde.ac.cn (H.W.); wang_kj@hdec.com (K.W.)

Abstract: Submarine landslides have attracted widespread attention, with the continuous development of ocean engineering. Due to the recent developments of in-situ investigation and modelling techniques of submarine landslides, significant improvements were achieved in the evolution studies on submarine landslides. The general characteristics of typical submarine landslides in the world are analyzed. Based on this, three stages of submarine landslide disaster evolution are proposed, namely, the submarine slope instability evolution stage, the large deformation landslide movement stage, and the stage of submarine landslide deposition. Given these three stages, the evolution process of submarine landslide disaster is revealed from the perspectives of in-situ investigation techniques, physical simulation, and numerical simulation methods, respectively. For long-term investigation of submarine landslides, an in-situ monitoring system with long-term service and multi-parameter collaborative observation deserves to be developed. The mechanism of submarine landslide evolution and the early warning factors need to be further studied by physical modelling experiments. The whole process of the numerical simulation of submarine landslides, from seabed instability to large deformation sliding to the impact on marine structures, and economizing the computational costs of models by advanced techniques such as parallel processing and GPU-accelerators, are the key development directions in numerical simulation. The current research deficiencies and future development directions in the subject of submarine landslides are proposed to provide a useful reference for the prediction and early warning of submarine landslide disasters.

Keywords: submarine landslide; in-situ investigation; physical modelling; numerical simulation

Citation: Shan, Z.; Wu, H.; Ni, W.; Sun, M.; Wang, K.; Zhao, L.; Lou, Y.; Liu, A.; Xie, W.; Zheng, X.; et al. Recent Technological and Methodological Advances for the Investigation of Submarine Landslides. *J. Mar. Sci. Eng.* **2022**, *10*, 1728. <https://doi.org/10.3390/jmse10111728>

Academic Editor:
Eugenio Fraile-Nuez

Received: 15 October 2022
Accepted: 9 November 2022
Published: 11 November 2022

Publisher's Note: MDPI stays neutral with regard to jurisdictional claims in published maps and institutional affiliations.



Copyright: © 2022 by the authors. Licensee MDPI, Basel, Switzerland. This article is an open access article distributed under the terms and conditions of the Creative Commons Attribution (CC BY) license (<https://creativecommons.org/licenses/by/4.0/>).

1. Introduction

Submarine landslides are gravity-driven mass movements that occur in a variety of underwater slope environments around the world [1]. Thousands of cubic kilometers of sediment can be involved in submarine landslides, many times larger than land-based landslides [1,2]. A submarine landslide and its sediment density flow are thus important process for moving sediment from the continental slope to the deep ocean. Submarine landslides can damage important marine infrastructure such as telecommunication cables and gas and oil production equipment, and generate destructive tsunamis, with great harm to people's safety and economic development [3]. In 1929, for example, the Grand Banks submarine landslide in Canada reached a maximum velocity of 20 m/s and slipped for approximately 850 km, damaging 12 submarine pipelines between North America and Europe [4]. In 2006, 2009, and 2010, submarine landslides destroyed the underwater cables in the Luzon Strait multiple times, disrupting communications between Southeast Asian

countries and China for up to 12 h [5]. In 2004, a tsunami induced by a submarine landslide and earthquake occurred in Sumatra, Indonesia, which killed more than 200,000 people [6].

As coastal populations and development continue to grow, and as subsea energy and communication transfer become more common, submarine landslides have become an increasingly important research subject over the past decades. At present, many scholars have summarized the research on submarine landslides, which are listed in Table 1. Locat and Lee [7] summarized the causes, classification, characterization, geotechnical investigation methods, and mechanics of submarine landslides. Harbitz et al. [8] discussed the effect of submarine landslide volume, initial acceleration, maximum velocity, and possible retrogressive behavior on the characteristics of the tsunamis induced by submarine landslides. De Mol et al. [9] reviewed the relationship between cold-water coral bank development and submarine landslides. Zhu et al. [10] summarized the classification of submarine landslide types. Yavari-Ramshe and Ataie-Ashtiani [11] reviewed numerical studies on submarine landslide-generated waves and proposed further attention aspects for numerical methods. Jia et al. [12] introduced the characteristics and triggering mechanism of submarine landslides, and briefly described the typical cases of the in-situ investigation of submarine landslides and the progress of in-situ observation methods, and analyzed the advantages and limitations of various methods. Huhn et al. [13] provided a short review of submarine landslide studies, with some emphasis on the emerging needs in future landslide research, including the geohazard potential and long-term monitoring of submarine landslides. Nian et al. [14] summarized the current research deficiencies and future development directions of the chain disasters of submarine landslides and emphasized the importance of numerical simulation in the study of the evolution mechanism of submarine landslides.

Table 1. Summary of existing reviews regarding submarine landslides in recent years.

References	Research Content	Key Conclusions	Highlights of the Review
Locat and Lee [7]	Summarized the causes, classification, characterization, geotechnical investigation methods, and mechanics of submarine landslides.	A major challenge is the integration of submarine landslide movement mechanics in an appropriate evaluation of the hazard.	A comprehensive review of submarine landslides.
Harbitz et al. [8]	Analyzed the mechanisms of tsunami generation by submarine landslides.	Submarine landslide volume, initial acceleration, maximum velocity, and possible retrogressive behavior are important to the characteristics of the resulting tsunami.	The focus is on tsunamis induced by submarine landslides.
De Mol et al. [9]	Analyzed the relation between cold-water coral bank development and submarine landslides.	No general and direct relationship exists between submarine landslides and cold-water coral banks	This paper focuses on the trigger factors of submarine landslides.
Zhu et al. [10]	Summarized the classification of submarine landslide types	The classifications of submarine landslides are becoming more and more deep, detailed, and generalized.	This paper focuses on the classification of submarine landslide types.
Yavari-Ramshe and Ataie-Ashtiani [11]	Reviewed numerical studies on submarine landslide-generated waves.	The conceptual, mathematical, and numerical structures of submarine landslide-generated waves are comprehensive analyses.	The focus is on the numerical methods for simulation the tsunamis induced by submarine landslides.
Jia et al. [12]	Reviewed the in-situ observation methods of submarine landslides.	The research on in-situ testing method of submarine landslide is still in its early stage and needs to be further studied.	This paper focuses on field investigation and in-situ observation methods for submarine landslides.
Huhn et al. [13]	Reviewed triggering mechanisms, monitoring methods, and hazards and risks of submarine landslides.	In-depth study of submarine landslides requires more interdisciplinary approaches.	This paper’s emphasis is on the emerging needs in future landslide research.
Nian et al. [14]	Reviewed the advances in the chain disasters of submarine landslides.	The physical and numerical simulation techniques of submarine landslide movement evolution still need further study.	This paper focuses on the simulation methods of chain disasters of submarine landslides.

In recent years, the studies of submarine landslides have become a hot spot with the continuous development of ocean engineering, such as safe the exploitation of offshore oil and gas resources and safe construction of offshore wind power projects. However, there is a lack of systematic reviews of in-situ investigation techniques, physical simulation, and numerical simulation methods of submarine landslides. The present review of submarine landslides mainly focuses on analyzing the trigger factors, characteristics, and mechanisms of submarine landslides from field investigations. However, there are few reviews on the comprehensive analysis of submarine landslide evolution from the perspective of research methodology. In view of this, we present the technological and methodological advances that have occurred in submarine landslide research in recent years. On the basis of previous studies, this paper summarizes the research status of the evolution process of submarine landslides and its disaster effect from three different perspectives: in-situ investigation methods, physical experiment methods, and numerical simulation methods. Meanwhile, the current research deficiencies and future development directions on the subject of submarine landslides are proposed to provide a useful reference for the prediction and early warning of submarine landslide disasters.

2. Characteristics of Submarine Landslides

2.1. General Characteristics

There are submarine landslides on virtually all ocean slopes throughout the world [15], such as the Norwegian sea, the Mediterranean sea, the Gulf sea, the Japan sea, and the South China sea. There is a wide variety of locations where submarine landslides can occur, from passive to active continental margins, river-fed pro-deltas, submarine fans, on volcanic island flanks, and glaciated areas and sediment-starved margins (as shown in Figure 1). Submarine landslides may cover more than 10,000 km² of seafloor and involve more than 1 million cubic meters of sediment. Examples of extremely large and well-known slides include the Storegga Slide [16], the Trænadjupet Slide [17], the Hinlopen Slide [18], and the Sahara Slide Complex [19].

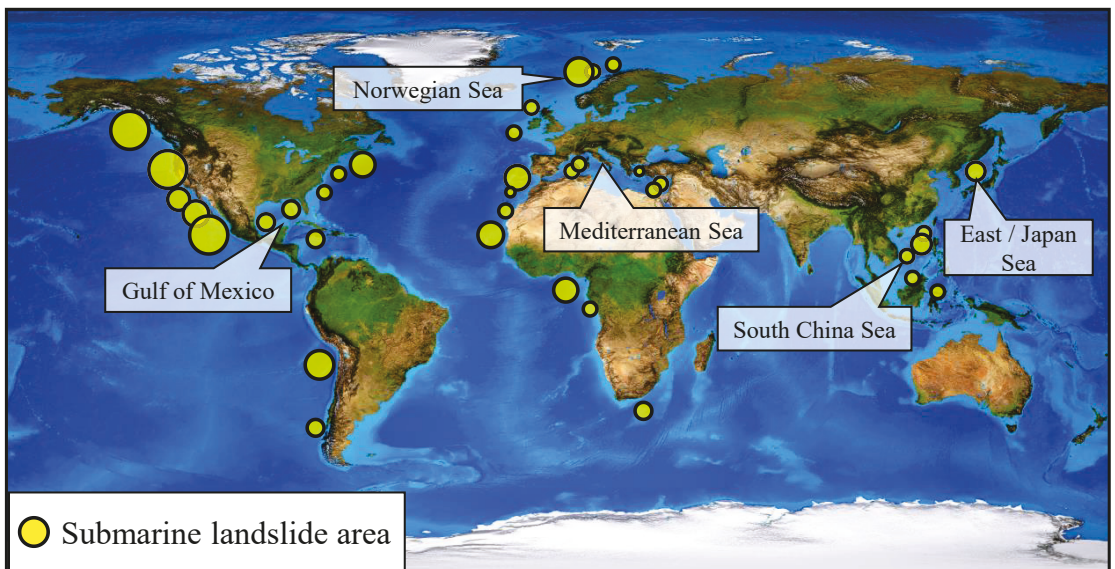


Figure 1. Regional distribution of main areas for submarine landslides. Modified from [15].

Turbidity currents derived from submarine landslides can travel even further distances, and their deposits can cover large areas within ocean basins. Consequently, submarine landslides are capable of moving hundreds of kilometers downslope. Even more curiously, submarine landslides may occur on slopes as low as 1°, which on land are almost always stable [13]. The U.S. Atlantic continental slope shows examples of submarine landslides with increasing slope angles; as shown in Figure 2a, more than 50% of submarine landslides have slope angles of less than 4°.

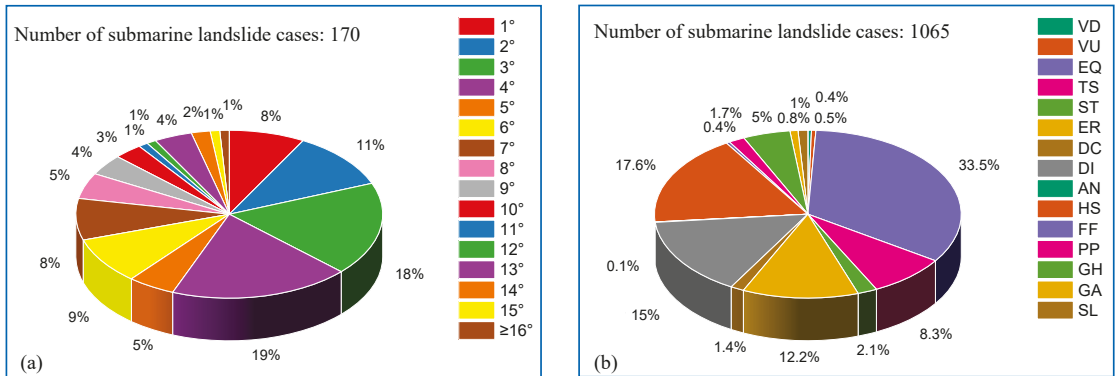


Figure 2. Characteristics of submarine landslides. (a) Slope angles of submarine landslides; (b) Trigger factors of submarine landslides.

According to the statistics and inducing mechanism analysis of 1065 submarine landslide cases worldwide, the trigger factors of submarine landslides can be classified into 15 factors (as shown in Figure 2b). The trigger factors include anthropic (AN), differential compaction (DC), diapirism (DI), earthquake (EQ), erosion (ER), fluid flow (FF), gas (GA), gas hydrates (GH), high sedimentation rates (HS), pore pressure (PP), steepening (ST), sea level (SL), tectonic steepening (TS), volcano development (VD), volcano uplift (VU). Among the above trigger factors, EQ, HS, and DI are the most common triggers for submarine landslides, accounting for 33.5%, 17.6%, and 12.1%, of the total, respectively.

2.2. Submarine Landslide Classification

Submarine landslides have been classified by many researchers, with many fruitful achievements. The various types of submarine landslides that can be involved are summarized by Locat and Lee [7]. They [7] classified the submarine landslides into five categories, including slides, topples, spreads, falls, and flows. Weimert et al. [20] used mass transport complexes (MTCs) to describe the deep-water sediment transport mechanism. Moscardelli and Wood [21] classified MTCs into plate transport complex and turbidity current, and further divided MTCs into slip, slump, and debris flow. Generally, submarine landslides evolve in three stages, as shown in Figure 3. In the initial stages of a submarine landslide (Phase 1), the submarine slope is unstable, the seabed collapses, and the landslide slumps and slides. In the middle stage of a submarine landslide (Phase 2), due to complex water–soil exchanges and long-distance migration, landslides gradually evolve into homogeneous debris flows. In the later stage of a submarine landslide (Phase 3), the water content of the landslide continues to increase. Debris flows and mudflows become turbidity currents and, eventually, heavy water flows as a result of the increased water content.

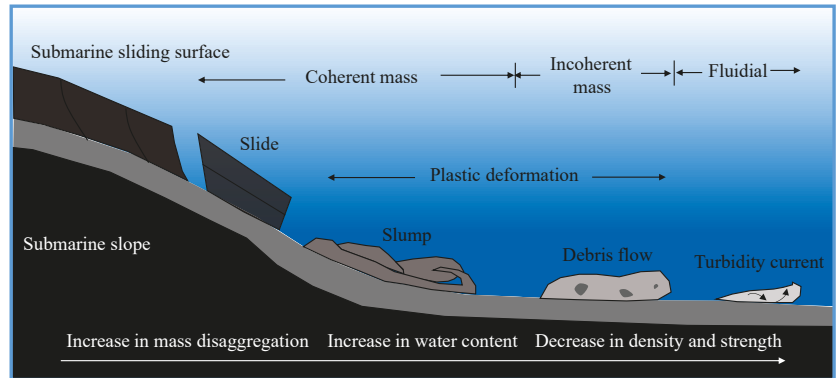


Figure 3. Overview of the stages in the evolution of a submarine landslide. Modified from [13,22].

3. Recent Advances in Submarine Landslide In-Situ Investigations

Compared with conventional land engineering monitoring, marine engineering geological environment monitoring has its unique features, mainly in that the seabed is covered by seawater, which cannot be directly observed, and that it can only be conducted through indirect technical means, which increases the difficulty of research. The dynamic action of seawater is continuous and strong, and the strong action of waves, currents, tides and storm surges brings about various engineering geological problems. The weak sediment makes sampling and observation difficult. Therefore, the offshore engineering geological survey is highly dependent on marine geophysical exploration methods, especially the combination of multiple detection techniques. The submarine landslide in-situ investigation methods include geotechnical monitoring, repeated seafloor surveys, water column imaging, acoustic doppler current profilers (ADCP), mobile sensors, sub-surface timelapse, seismological networks, cabled systems, etc. (as shown in Figure 4).

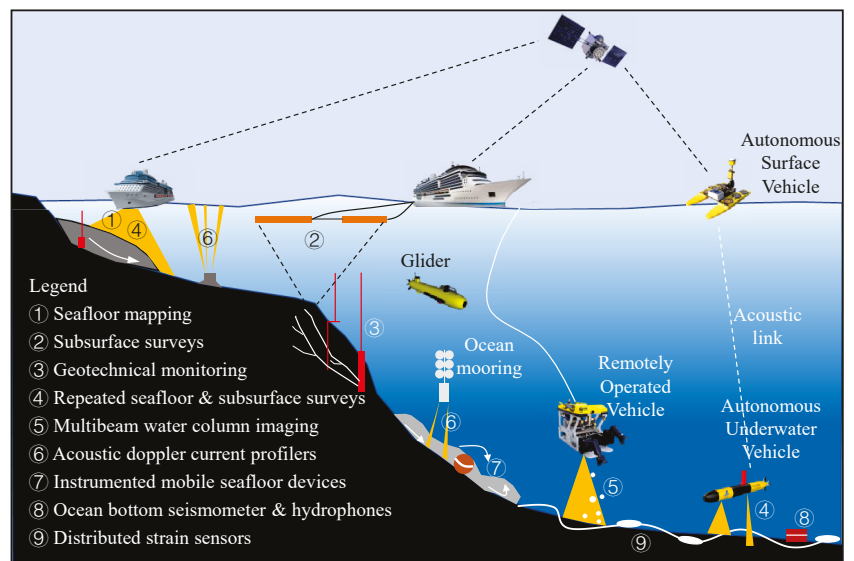


Figure 4. Conventional and emerging geophysical tools for submarine landslide in-situ investigations. Modified from [23].

The deformation monitoring of the sloping seabed is the most direct indicator to reflect the seabed instability. On the one hand, it can provide a reliable basis for the study of the early instability process of landslides (such as sliding velocity, sliding mode, sliding distance, etc.). On the other hand, it can provide an effective early warning for seabed instability caused by offshore oil and gas exploitation. Therefore, geotechnical engineering monitoring of offshore sites is becoming more and more common, such as using in-situ pressure gauges and inclinometers to understand in-situ-specific slope stability issues [23]. In addition, multi-session seafloor surveys using high-resolution multibeam systems reveal the magnitude and frequency of seafloor landslides in multiple systems around the world, such as in deep-water (200–300 m) submarine canyons [23–26], at active pro-deltas [27,28], in areas with shallow water, and in large displacement conditions [29].

In addition to using the above-mentioned equipment to measure changes in seabed topography, instruments such as ocean bottom seismometers (OBS) can also be used for monitoring, providing information on the timing and nature of slope failure. Mayotte Island, north of the Mozambique Channel, and the Indian Ocean, OBS, were used to monitor the submarine earthquakes [30]. The attenuation of the light waves and electromagnetic waves is serious, and the propagation distance is very limited. Therefore, it is difficult to meet the needs of ocean exploration. In contrast, the propagation performance of sound waves in water is much higher. The acoustic detection equipment developed based on marine acoustic technology has become the “ear” of human beings to detect the underwater world and has become the mainstream of marine detection equipment. For example, multiple moored hydrophones were tried to monitor earthquakes, volcanic activities, various types of tremors, signals related to lava extrusion, and landslides on the seafloor [31]. Shore-based monitoring can provide insight into submarine landslide activity as well. For example, Lin et al. [32] used terrestrial broadband seismic networks to detect offshore landslides in the Kaoping Canyon, offshore Taiwan.

Other major recent advances have been made by the direct measurement of turbidity currents [33,34]. However, monitoring turbidity flows remains somewhat challenging to date because of the logistical challenges of deploying instruments on the deep seafloor, the fact that flows may occur infrequently, and the powerful nature of flows that can damage instruments used for measurements. These challenges mean that turbidity currents have only been measured in a few relatively shallow waters (<2 km) in the world.

Designing a stable monitoring platform and improving the anti-interference ability of sensors will be the problems to solve in the next step of the turbidity flow monitoring of deeper sea areas [35]. However, monitoring large submarine landslides can be more challenging than monitoring turbidity currents because it is not clear where the next landslide will occur, and some landslides have recurrence intervals (>100–1000 s years) [23], which are difficult for most study projects (<5 years). Therefore, even though submarine landslide investigations still face many problems, such as environments and remote settings, positioning accuracy, data resolution, communications, frequency and accuracy of measurement equipment, and measurement equipment recyclability, the most difficult problem to solve is knowing where the next submarine landslide will occur.

4. Recent Advances in Physical Simulation Methods of Submarine Landslides

Submarine landslides occur in complex geological environments. It is almost impossible to capture the whole process of slope failure, slide, slump, debris flow, turbidity current, and the accompanying redeposition of the turbidity current through in-situ investigation. Therefore, laboratory-scale physical simulation experiments are used to discover characteristic physical phenomena and provide valuable experimental data for numerical simulations [36,37].

Flume experiments were conducted to determine the force exerted by a clay-rich submarine landslide on two pipelines by Zakeri et al. [38]. Their experimental results led them to propose a method to estimate drag forces normally directed at a pipeline axis. In order to investigate mudflow flow-front structures, Haza et al. [39] prepared mud models

derived from mixtures of 10–35% kaolin and water. Yamada et al. [40] performed a series of sandbox experiments to investigate the mechanical processes involved in the development of submarine landslides. Two types of submarine landslide failure modes were classified in their study, namely, small but frequent slides, and large but less frequent failures of the entire slope. Wang et al. [41] developed a system for simulating a submarine landslide and the relative motion between the submarine landslide and undersea cable. The main part of the test device is a ring water tank made of iron and steel material. The outer diameter of the water tank is 0.9 m, the inner diameter is 0.6 m, and the width is 0.4 m. The impact of the mixture of sediment and water on the cable during the rotation of the tank can be observed through the front transparent plexiglass. Based on the rotating flume test, Deng et al. [42] reproduced the low friction angle motion of underwater debris flow and further analysis revealed that the hydrodynamic pressure generated by the submarine sliding mass impacting the seabed may be the reason for the low friction angle motion of the submarine sliding mass. Based on physical simulations, Liu et al. [43] evaluated the stability of a hydrated seabed and discussed how different geological conditions affect it. By applying pressurized gas to the low-permeability silt layer, they simulated the excess pore pressure caused by the decomposition of hydrate and the physical appearance process of the overlying seabed damage. A study by Wang et al. [44] investigates the impact of submarine telecommunications cables shifting on the seabed. To investigate submarine slope failure caused by overpressure fluid due to gas hydrate dissociation, Nian et al. [45] designed a laboratory-scale device, as shown in Figure 5a. The influences of the thickness of the clay layer and sand layer, undrained strength of clay and injection rate on the submarine landslide failure models are discussed in their study. Based on this, the method of calculating the safety factor of submarine slopes under hydrate decomposition conditions was established, as shown in Figure 5b. Fan et al. [46] designed a flume testing system to simulate the mass transfer process at soil–water interfaces during submarine landslide motions at different velocities. The results show that soil–water interface mass transfer is primarily dependent on soil properties (shear strength, apparent viscosity) and velocity. The influence of sand/clay content on the depositional mechanism of submarine debris flows was investigated by Liu et al. [47] using a submersed flume model. According to the results, swirled-wedge front heads generate high-viscosity slurry flows with greater aspect ratios and rotation radii.

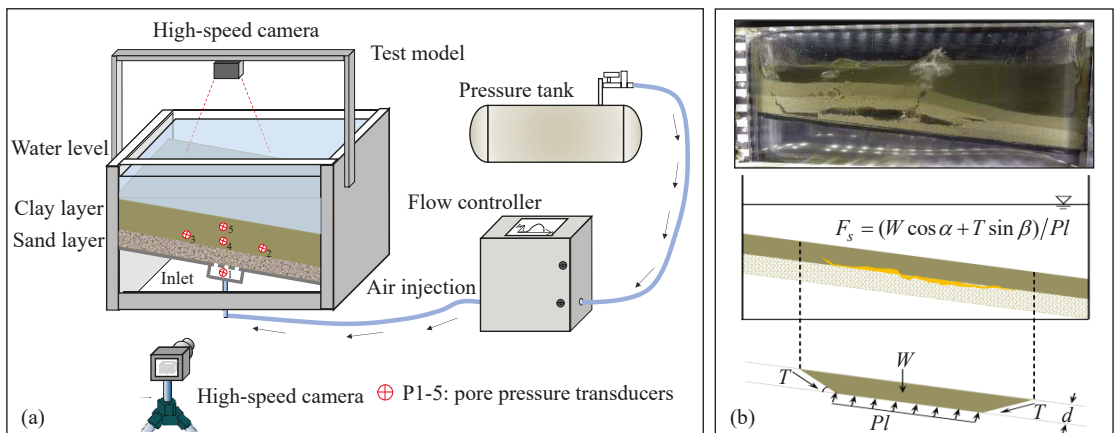


Figure 5. Investigation of submarine landslide induced by hydrate dissociation. (a) Schematic diagram of the experimental device; (b) Mode of submarine landslide induced by hydrate dissociation. Modified from [45].

The above experiments were carried out under conventional gravity conditions. The model is often a reduced-scale version of the prototype; as a result, the experimental model has some scaling effects and cannot reflect the real stress environment of the research object [48,49]. As centrifuge models and prototypes have equal stresses, centrifuge modeling is useful for gravitational effects and large-scale modeling in geotechnical materials [50,51]. Boylan et al. [52] carried out geotechnical centrifuge experiments to investigate submarine landslide runout. For observing submarine landslide movement in geotechnical centrifuge model experiments, Gaudin et al. [53] developed a wireless high-speed data-acquisition system. Zakeri et al. [54] investigated the impact forces of submarine landslides on pipelines with uniform velocities by carrying out centrifuge experiments with a centrifugal force of 30 times the Earth's gravity. Zhang et al. [55] conducted a series of centrifuge experiments to study the evolution of submarine landslides induced by hydrate dissociation. Through their centrifuge experiments, the expansion of cracks, settling zone and the slippage between the over layer and hydrate layer were observed, and the mechanism of submarine landslides induced by hydrate dissociation was revealed. Zhang et al. [56] analyzed the triggering mechanism of submarine landslides using centrifuge modeling experiments. They proposed two mechanisms: accumulation of high pore pressure and associated tensile failure and fracturing in clay and associated shear failure. Zhang et al. [57] developed a newly static liquefaction-triggering actuator to be used in enhanced gravity conditions in a geotechnical centrifuge, investigating the tilting rate effects on submarine landslide processes at various slope steepening rates. They found that as a result of local shear deformations, pore pressure builds up, causing submarine slope instabilities to occur. Among the most important issues in submarine landslide investigation is scaling for the centrifuge modeling of static liquefaction initiation and propagation. Zhang et al. [58] discussed this issue and suggested that an $N^{0.5}$ -fluid should be applied for simulating the onset of static liquefaction of underwater slopes triggered by monotonic loads and that a pore fluid, with a viscosity N times that of water, is required to simulate flow-slide dynamic behavior in a centrifuge, where N is the geometrical scaling factor in centrifuge modelling. Takahashi et al. [59] examined the submarine landslide of sand and silty sand induced by earthquake and liquefaction. They concluded that the debris induced by submarine landslides flowed not with a simple shear but as a clod of soil similar to a fluid, which encouraged high-speed flow.

There has been no model experiment able to simulate and clarify the conditions required for submarine landslides, their gravity flow transition, and sedimentation. Further large-scale flume experiments or drum centrifugal model experiments for simulating submarine landslides are very necessary.

5. Recent Advances in Numerical Simulation Methods of Submarine Landslides

In recent years, numerical simulation methods of submarine landslides have made many advances in the stability analysis of submarine slopes, based on random-field, large-deformation finite-element modelling techniques in submarine landslides, fluid–solid coupling analysis, and marine disaster analysis induced by submarine landslides. Figure 6 shows the current numerical simulation methods for the investigation of the submarine landslide disaster chain.

The uncertainty in input values, such as seismic parameters, soil properties, and hydraulic conditions, may make traditional deterministic methods unreliable for assessing submarine slope stability. Therefore, the enhanced Newmark method [60], Gaussian process regression [61], the Monte Carlo simulation [62] were used to analyze the submarine slope stability. According to Zhu et al. [63], a 3D stochastic finite element model was developed to study the random wave-induced response in a spatially heterogeneous seabed. Based on linear wave theory and Biot's theory, Zhu et al. [64] analyzed the response of the poroelastic sloping seabed by considering changes in wave length and height when propagated from relatively shallower to deep sea conditions. The above research is mainly aimed at analyzing the stability of submarine slope rather than the evolution process after instability. Dey

et al. [65] presented a large-deformation finite-element (LDFE) modelling technique, which incorporated a strain-softening model for the undrained shear strength of marine clay, to model submarine landslides. This technique simulates the development of plastic shear bands and their propagation with displacements of soil mass. Zhang et al. [66] simulated the complete evolution of a submarine landslide from shear band initiation, propagation, and slab failure, and the arrest of shear band propagation is observed through LDFE modelling. To overcome the large computational costs of the LDFE modelling technique, Buss et al. [67] established the energy-balance kinematic method of plasticity theory.

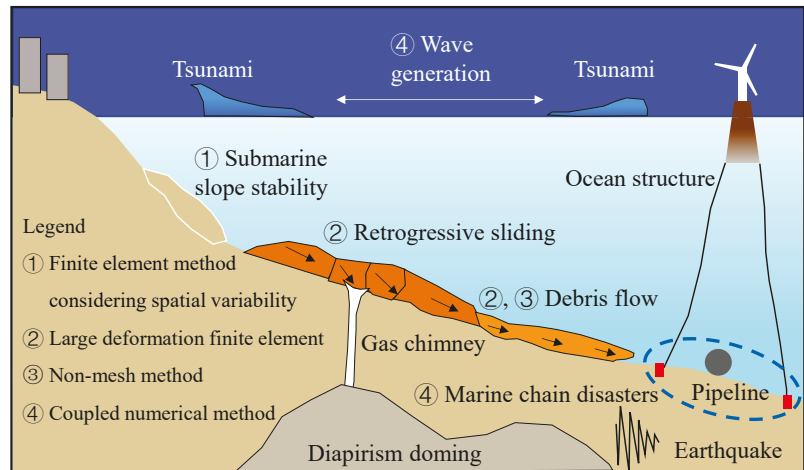


Figure 6. Current numerical simulation methods for investigation of submarine landslide disaster chain.

Although the LDFE modelling technique can simulate the large deformation of a submarine landslide, it cannot reflect the motion-evolution process of a submarine landslide [68]. Some numerical studies have focused mainly on replicating run-out characteristics, such as travel distance and velocity. For example, Gauer et al. [69] used the Bingham model to reproduce one of the world’s largest well-known submarine landslides, the Storegga slide. Dong et al. [70] investigated a real case history of a submarine landslide, reproducing the runout of the slides from steep slopes to moderate bases, by using the material point method (MPM). Dong et al. [71] enhanced the conventional depth-averaged method (DAM) algorithm, which is specialized for no-slip bases, to reproduce the phenomenon of block sliding on frictional bases. They assessed the feasibility of the DAM for slides with different sliding modes in terms of runout distances and morphologies. Zhang and Randolph [72] simulated submarine landslides using the smoothed-particle hydrodynamics (SPH) method. Jiang et al. [73] simulated a submarine landslide induced by seismic loading in a methane hydrate-rich zone using coupled computational fluid dynamics (CFD) and the discrete element method (DEM). However, the study only simulated the trigger initiation phase of the submarine landslide. However, almost all the above numerical methods need input information regarding the initial velocity and volume of the failed submarine landslide mass. To overcome this problem, Zhang and Puzrin [74] established a numerical scheme in consideration of the drag force from the ambient water for time-efficient modelling of the entire submarine landslide evolution, covering the pre-failure shear band propagation, slab failure, and post-failure dynamics.

As one of the most destructive marine geological disasters, a submarine landslide often causes the destruction of underwater infrastructures and even catastrophic tsunamis. In recent years, the numerical simulation of submarine landslide impact on underwater pipe and cable systems has achieved rich research results. Dong et al. [75] employed the material point method (MPM) with an enhanced contact algorithm to simulate the submarine

landslide impact of a fixed partially embedded pipeline for the first time. Zhang et al. [76] investigated the impact forces exerted by a submarine landslide on laid-on or suspended pipelines at various impact angles θ , based on the Herschel–Bulkley model, using the CFD approach. Nian et al. [77] considered the effect of the low-temperature environment of the seabed on the behavior of marine clay and then investigated the impact of the marine clay on suspended pipelines. According to their findings, 26.0% and 70.3% more force is applied to pipelines at 0.5 °C than at 22 °C when a mudflow impacts them. Li et al. [78] analyzed the interaction between monopile and submarine landslides at different flow heights using a three-dimensional biphasic numerical model. Two modes of interactional forces acting on the monopile (namely, interaction) force with peak value and interaction force without peak value were proposed by their study. Fan et al. [79] designed pipelines with a streamlined contour and investigated the interaction between submarine landslides and streamlined pipelines. Compared with a conventional circular pipeline, streamlined pipelines can reduce the lift and drag force of landslide–pipeline interaction with a maximum lessening percentage of 40% and 66%, respectively. Dutta and Hawlader [80] simulated the lateral penetration of a pipe in a clay block by a CFD approach by incorporating strain-rate and strain-softening dependent models for the undrained shear strength of clay sediment. Guo et al. systematically studied the impact of submarine landslides on pipelines, including the effect of opening and wall boundaries on CFD modeling [81], the effect of pipeline surface roughness on the interaction between pipelines and submarine mudflows [82–84], the instantaneous impact of submarine slumps with the shear rate effect on fixed suspended pipelines [85], and the influence of pipeline suspension height on the impact force of submarine landslides on pipelines [86,87]. Tsunamis induced by submarine landslides are also among the marine hazards that have stimulated the attention and concern of researchers during the past decades. However, related research mainly focuses on the evolution of tsunamis, and the simulation of submarine landslides is often simplified. More than 85% of numerical models apply depth-averaged equations to predict the submarine flow behavior through its motion [11]. The influence of more submarine landslide models on surges deserves further study.

6. Discussions on Future Research Directions

The evolution process of submarine landslides has achieved many results. From the perspectives of in-situ investigation techniques, physical simulation, and numerical simulation methods, future research directions of submarine landslides are proposed. Figure 7 summarizes the main points, and the details are discussed in this section.

Due to the uncertainty of the occurrence time of submarine landslides and the high cost of underwater monitoring, the current research on the movement process of submarine landslide is still focused on the tracking of the movement traces and accumulation characteristics after submarine landslides using geophysical exploration technology, while the real-time monitoring of the movement evolution process of submarine landslides is still blank. Therefore, it is urgent to develop an in-situ monitoring system for submarine landslides with long-term service and multi-parameter collaborative observation, so as to realize the long-term observation of various indicators of seabed sediments. In particular, the technique of space-sky-earth-sea can be used to establish a regional network for submarine landslide monitoring and early warning [88]. In addition, advanced methods such as machine learning and big data fusion technology can be fully utilized to conduct an in-depth analysis of the acquired multi-source heterogeneous data [89], which provides technical support for monitoring the kinematic and morphological characteristics of submarine landslides as well as accurate prediction and early warning. As the results obtained by geophysical methods are often multi-solution, while using various acoustic detection methods to identify the geological hazards, the methods of high-quality geological sampling and drilling should be combined to achieve the purpose of correctly identifying the submarine landslide hazards. The comprehensive analysis of geophysical survey data and soil drilling data can greatly enhance the accuracy of engineering geological evaluation.

Under ideal conditions, geophysical survey data can provide the extension and thickness of the sedimentary layer, and borehole sampling can provide the physical and mechanical properties of the sediment.

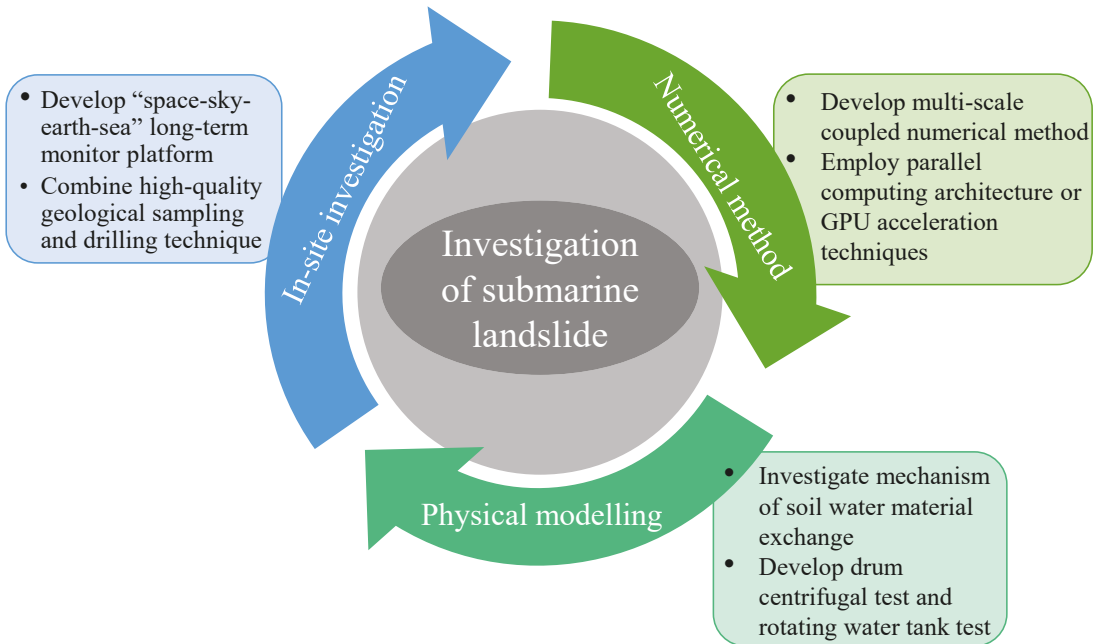


Figure 7. Future research directions of submarine landslides.

The small-scale flume test is a common method to simulate the evolution of submarine landslides. Although it can simulate the motion of submarine landslides, it is limited by the test situation and cannot reproduce long-distance motion-evolution scenarios, which is far from the real submarine landslide motion. Compared with the flume test, the drum centrifugal test and the rotating water tank test can eliminate the limitations of the test situation and can be used as an important means to study the evolution process of large-scale submarine landslides [90]. However, the water–soil coupling mechanism in the evolution of submarine landslide movement is extremely complex and changeable [91], and the current test method has not quantified the deformation and rupture behavior of the landslide mass caused by the intrusion of environmental water. It is suggested to develop soil–water interface monitoring technology to achieve a quantitative analysis of material exchange and front-end hydroplaning at the water–soil interface during the evolution of submarine landslides. In addition, in view of the lack of in-situ monitoring technology for submarine landslides, it is recommended to reveal the early warning factors of disasters in the evolution of submarine landslides through experiments, such as vibration response, soil pore pressure, and ocean water turbidity.

In terms of numerical simulation methods, the computational fluid dynamics method can be used to simulate large-scale submarine landslide motions. However, this method regards the landslide motion as a single fluid state motion, and it is difficult to consider the microscopic evolution in the process of submarine landslide motion [14,92]. Compared with the CFD method, LDFE, MPM, SPH, and other methods that consider the soil mechanical properties of a submarine landslide, can reproduce the evolution process of a submarine slope from instability to progressive sliding failure [93]. However, the methods are mainly used in the early instability deformation simulation of

small-scale submarine landslides due to their high calculation cost. It is worth noting that the above numerical methods are mainly employed in the motion simulation of submarine landslides at the macro level, and they ignore the deformation characteristics of particles inside a submarine landslide mass at the micro level. Therefore, in future numerical simulation research, the macro–micro interconnection effect in the evolution process of submarine landslide motion should be considered, and multi-scale coupled numerical calculation methods, such as CFD-DEM, should be developed to realize the fine simulation of the evolution process of submarine landslide motion. Meanwhile, in order to improve the computational efficiency of multi-scale coupling algorithms, parallel computing architecture or GPU acceleration techniques can be employed to solve this large-scale computational problem [94].

7. Conclusions

We present the technological and methodological advances that have occurred in submarine landslide research in recent years. The following conclusions could be drawn from this study:

According to the in-situ investigation, more than 50% of submarine landslides have slope angles of less than 4°. Earthquakes, high sedimentation rates, and diapirism are the most common triggers for submarine landslides, accounting for 33.5%, 17.6%, and 12.1% of the total, respectively.

It is urgent to develop an in-situ monitoring system and integrated space-sky-earth-sea technique for submarine landslides, with long-term service and multi-parameter collaborative observation, so as to realize the long-term observation of various indicators of seabed sediments. High-quality geological sampling and drilling should be developed to achieve the purpose of correctly identifying the submarine landslide hazards.

The mechanism of submarine landslide evolution, especially in the water–soil coupling mechanism, needs to be further studied by physical modelling experiments. We recommend revealing the early warning factors of disasters in the evolution of submarine landslides, such as vibration response, soil pore pressure, and ocean water turbidity, through experiments.

Multi-scale coupled numerical calculation methods should be integrated with parallel computing architecture or GPU acceleration techniques to realize the fine simulation of the whole evolution process of a submarine landslide motion.

Author Contributions: Conceptualization, Z.S.; formal analysis, W.N. and X.G.; investigation, M.S., Y.L., A.L., W.X. and X.Z.; writing—original draft preparation, H.W.; writing—review and editing, Z.S., K.W. and L.Z.; project administration, Z.S.; funding acquisition, H.W., K.W. and L.Z. All authors have read and agreed to the published version of the manuscript.

Funding: This research was supported by the National Natural Science Foundation of China under Grant 42207228, 42102313, and 52108356; the Zhejiang Provincial Natural Science Foundation of China under Grant LQ20E090001 and LQ22E090008; the Sichuan Science and Technology Program under Grant 2022NSFSC1060.

Institutional Review Board Statement: Not applicable.

Informed Consent Statement: Not applicable.

Data Availability Statement: Not applicable.

Acknowledgments: The authors gratefully acknowledge the support from the funding listed above. We also appreciate anonymous reviewers who gave comments to revise the paper.

Conflicts of Interest: The authors declare that they have no known competing financial interests with POWERCHINA Huadong Engineering Corporation Limited and Zhejiang Huadong Construction Engineering Corporation Limited, and no known competing financial interests or personal relationships that could have appeared to influence the work reported in this paper.

References

1. Hampton, M.A.; Lee, H.J.; Locat, J. Submarine landslides. *Rev. Geophys.* **1996**, *34*, 33–59. [[CrossRef](#)]
2. Masson, D.; Harbitz, C.; Wynn, R.; Pedersen, G.; Løvholt, F. Submarine landslides: Processes, triggers and hazard prediction. *Philos. Trans. R. Soc. A* **2006**, *364*, 2009–2039. [[CrossRef](#)] [[PubMed](#)]
3. Vanneste, M.; Sultan, N.; Garziglia, S.; Forsberg, C.F.; L'Heureux, J.S. Seafloor instabilities and sediment deformation processes: The need for integrated, multi-disciplinary investigations. *Mar. Geol.* **2014**, *352*, 183–214. [[CrossRef](#)]
4. Hance, J.J. Submarine Slope Stability. Master's Thesis, The University of Texas at Austin, Austin, TX, USA, 2003.
5. Hsu, S.K.; Kuo, J.; Chung-Liang, L.; Ching-Hui, T.; Doo, W.B.; Ku, C.Y.; Sibuet, J.C. Turbidity currents, submarine landslides and the 2006 Pingtung earthquake off SW Taiwan. *TAO Terr. Atmos. Ocean. Sci.* **2008**, *19*, 7. [[CrossRef](#)]
6. Brune, S.; Ladage, S.; Babeyko, A.Y.; Müller, C.; Kopp, H.; Sobolev, S.V. Submarine landslides at the eastern Sunda margin: Observations and tsunami impact assessment. *Nat. Hazards* **2010**, *54*, 547–562. [[CrossRef](#)]
7. Locat, J.; Lee, H. Submarine landslides: Advances and challenges. *Can. Geotech. J.* **2002**, *39*, 193–212. [[CrossRef](#)]
8. Harbitz, C.B.; Løvholt, F.; Pedersen, G.; Masson, D.G. Mechanisms of tsunami generation by submarine landslides: A short review. *Norw. J. Geol.* **2006**, *86*, 255–264.
9. De Mol, B.; Huvenne, V.; Canals, M. Cold-water coral banks and submarine landslides: A review. *Int. J. Earth Sci.* **2009**, *98*, 885–899. [[CrossRef](#)]
10. Zhu, C.Q.; Jia, Y.G.; Liu, X.L.; Zhang, H.; Wen, Z.M.; Huang, M.; Shan, H.X. Classification and genetic mechanism of submarine landslide: A review. *Mar. Geol. Quat. Geol.* **2015**, *35*, 153–163. (In Chinese)
11. Yavari-Ramshe, S.; Ataie-Ashtiani, B. Numerical modeling of subaerial and submarine landslide-generated tsunami waves—Recent advances and future challenges. *Landslides* **2016**, *13*, 1325–1368. [[CrossRef](#)]
12. Jia, Y.G.; Wang, Z.H.; Liu, X.L.; Yang, Z.N.; Zhu, C.Q.; Wang, X.L.; Shan, H.X. The research progress of field investigation and in-situ observation methods for submarine landslide. *Period. Ocean. Univ. China* **2017**, *10*, 61–72. (In Chinese)
13. Huhn, K.; Arroyo, M.; Cattaneo, A.; Clare, M.A.; Gràcia, E.; Harbitz, C.B.; Krastel, S.; Kopf, A.; Løvholt, F.; Rovere, M.; et al. Modern submarine landslide complexes: A short review. In *Submarine Landslides: Subaqueous Mass Transport Deposits from Outcrops to Seismic Profiles, Geophysical Monograph*, 1st ed.; Kei, O., Andrea, F., Gian, A.P., Eds.; John Wiley & Sons, Inc.: Hoboken, NJ, USA, 2019; pp. 181–200.
14. Nian, T.K.; Shen, Y.Q.; Zheng, D.F.; Lei, D.Y. Research advances on the chain disasters of submarine landslides (in Chinese). *J. Eng. Geol.* **2021**, *29*, 1657–1675.
15. Zhu, B.; Pei, H.; Yang, Q. Probability analysis of submarine landslides based on the Response Surface Method: A case study from the South China Sea. *Appl. Ocean Res.* **2018**, *78*, 167–179. [[CrossRef](#)]
16. Bryn, P.; Berg, K.; Forsberg, C.F.; Solheim, A.; Kvalstad, T.J. Explaining the Storegga slide. *Mar. Pet. Geol.* **2005**, *22*, 11–19. [[CrossRef](#)]
17. Laberg, J.; Vorren, T. The Trænadjupet Slide, offshore Norway—Morphology, evacuation and triggering mechanisms. *Mar. Geol.* **2000**, *171*, 95–114. [[CrossRef](#)]
18. Vanneste, M.; Mienert, J.; Büinz, S.J.E. The Hinlopen Slide: A giant, submarine slope failure on the northern Svalbard margin, Arctic Ocean. *Earth Planet. Sci. Lett.* **2006**, *245*, 373–388. [[CrossRef](#)]
19. Li, W.; Alves, T.M.; Urlaub, M.; Georgiopolou, A.; Klauke, I.; Wynn, R.B.; Gross, F.; Meyer, M.; Repschläger, J.; Berndt, C.; et al. Morphology, age and sediment dynamics of the upper headwall of the Sahara Slide Complex, Northwest Africa: Evidence for a large Late Holocene failure. *Mar. Geol.* **2017**, *393*, 109–123. [[CrossRef](#)]
20. Weimer, P.; Slatt, R.M.; Bouroulec, R. *Introduction to the Petroleum Geology of Deepwater Setting*; AAPG/Datapages: Tulsa, OK, USA, 2007.
21. Moscardelli, L.; Wood, L. New classification system for mass transport complexes in offshore Trinidad. *Basin Res.* **2008**, *20*, 73–98. [[CrossRef](#)]
22. Guo, X.S.; Nian, T.K.; Gu, Z.D.; Li, D.Y.; Fan, N.; Zheng, D.F. Evaluation Methodology of Laminar-Turbulent Flow State for Fluidized Material with Special Reference to Submarine Landslide. *J. Waterw. Port Coast. Ocean Eng.* **2021**, *147*, 04020048. [[CrossRef](#)]
23. Clare, M.A.; Vardy, M.E.; Cartigny, M.J.; Talling, P.J.; Himsforth, M.D.; Dix, J.K.; Harris, J.M.; Whitehouse, R.J.; Belal, M. Direct monitoring of active geohazards: Emerging geophysical tools for deep-water assessments. *Near Surf. Geophys.* **2017**, *15*, 427–444. [[CrossRef](#)]
24. Hughes Clarke, J.E. First wide-angle view of channelized turbidity currents links migrating cyclic steps to flow characteristics. *Nat. Commun.* **2016**, *7*, 11896. [[CrossRef](#)] [[PubMed](#)]
25. Kelner, M.; Migeon, S.; Tric, E.; Couboulex, F.; Dano, A.; Lebourg, T.; Taboada, A. Frequency and triggering of small-scale submarine landslides on decadal timescales: Analysis of 4D bathymetric data from the continental slope offshore Nice (France). *Mar. Geol.* **2016**, *379*, 281–297. [[CrossRef](#)]
26. Mountjoy, J.J.; Howarth, J.D.; Orpin, A.R.; Barnes, P.M.; Bowden, D.A.; Rowden, A.A.; Schimel, A.C.; Holden, C.; Horgan, H.J.; Nodder, S.D. Earthquakes drive large-scale submarine canyon development and sediment supply to deep-ocean basins. *Sci. Adv.* **2018**, *4*, 3748. [[CrossRef](#)] [[PubMed](#)]
27. Obelcz, J.; Xu, K.; Georgiou, I.Y.; Maloney, J.; Bentley, S.J.; Miner, M.D. Sub-decadal submarine landslides are important drivers of deltaic sediment flux: Insights from the Mississippi River Delta Front. *Geology* **2017**, *45*, 703–706. [[CrossRef](#)]

28. Maloney, J.M.; Bentley, S.J.; Xu, K.; Obelcz, J.; Georgiou, I.Y.; Miner, M.D. Mississippi River subaqueous delta is entering a stage of retrogradation. *Mar. Geol.* **2018**, *400*, 12–23. [[CrossRef](#)]
29. Syahnur, Y.; Jaya, K.A.; Ariseputra, I.P. Geomatics best practices in Saka Indonesia Pangkah Limited (Case Study: Ujung Pangkah Pipeline Integrity). In Proceedings of the 2015 Indonesian Petroleum Association Convention, Jakarta, Indonesia, 16–17 May 2015.
30. Saurel, J.-M.; Jacques, E.; Aiken, C.; Lemoine, A.; Retailleau, L.; Lavayssière, A.; Foix, O.; Dofal, A.; Laurent, A.; Mercury, N.; et al. Mayotte seismic crisis: Building knowledge in near real-time by combining land and ocean-bottom seismometers, first results. *Geophys. J. Int.* **2022**, *228*, 1281–1293. [[CrossRef](#)]
31. Tepp, G.; Dziak, R.P. The Seismo-Acoustics of Submarine Volcanic Eruptions. *J. Geophys. Res. Solid Earth* **2021**, *126*, 2020JB020912. [[CrossRef](#)]
32. Lin, C.; Kumagai, H.; Ando, M.; Shin, T. Detection of landslides and submarine slumps using broadband seismic networks. *Geophys. Res. Lett.* **2010**, *37*, L22309. [[CrossRef](#)]
33. Simmons, S.M.; Azpiroz-Zabala, M.; Cartigny, M.J.B.; Clare, M.A.; Cooper, C.; Parsons, D.R.; Pope, E.L.; Sumner, E.J.; Talling, P.J. Novel Acoustic Method Provides First Detailed Measurements of Sediment Concentration Structure Within Submarine Turbidity Currents. *J. Geophys. Res. Oceans* **2020**, *125*, e2019JC015904. [[CrossRef](#)]
34. Maier, K.L.; Gales, J.A.; Paull, C.K.; Rosenberger, K.; Talling, P.J.; Simmons, S.M.; Gwiazda, R.; McGann, M.; Cartigny, M.J.; Lundsten, E. Linking direct measurements of turbidity currents to submarine canyon-floor deposits. *Front. Earth Sci.* **2019**, *7*, 144. [[CrossRef](#)]
35. Clare, M.; Lintern, D.G.; Rosenberger, K.; Hughes Clarke, J.E.; Paull, C.; Gwiazda, R.; Cartigny, M.J.; Talling, P.J.; Perara, D.; Xu, J. Lessons learned from the monitoring of turbidity currents and guidance for future platform designs. *Geol. Soc.* **2020**, *500*, 605–634. [[CrossRef](#)]
36. Wu, H.; Zheng, D.F.; Zhang, Y.J.; Li, D.Y.; Nian, T.K. A photogrammetric method for laboratory-scale investigation on 3D landslide dam topography. *Bull. Eng. Geol. Environ.* **2020**, *79*, 4717–4732. [[CrossRef](#)]
37. Nian, T.K.; Wu, H.; Li, D.Y.; Zhao, W.; Takara, K.; Zheng, D.F. Experimental investigation on the formation process of landslide dams and a criterion of river blockage. *Landslides* **2020**, *17*, 2547–2562. [[CrossRef](#)]
38. Zakeri, A.; Høeg, K.; Nadim, F. Submarine debris flow impact on pipelines—Part I: Experimental investigation. *Coast. Eng.* **2008**, *55*, 1209–1218. [[CrossRef](#)]
39. Haza, Z.F.; Harahap, I.S.H.; Dakssa, L.M. Experimental studies of the flow-front and drag forces exerted by subaqueous mudflow on inclined base. *Nat. Hazards* **2013**, *68*, 587–611. [[CrossRef](#)]
40. Yamada, Y.; Yamashita, Y.; Yamamoto, Y. Submarine landslides at subduction margins: Insights from physical models. *Tectonophysics* **2010**, *484*, 156–167. [[CrossRef](#)]
41. Wang, F.; Dai, Z.; Nakahara, Y.; Sonoyama, T. Experimental study on impact behavior of submarine landslides on undersea communication cables. *Ocean Eng.* **2018**, *148*, 530–537. [[CrossRef](#)]
42. Deng, J.; Zhang, X.; Shen, S.; Koseki, J. Low friction coefficient (approximately $\tan 1^\circ$) of subaqueous debris flow in rotating flume tests and its mechanism. *Bull. Eng. Geol. Environ.* **2018**, *77*, 931–939. [[CrossRef](#)]
43. Liu, T.; Lu, Y.; Zhou, L.; Yang, X.; Guo, L. Experiment and Analysis of Submarine Landslide Model Caused by Elevated Pore Pressure. *J. Mar. Sci. Eng.* **2019**, *7*, 146. [[CrossRef](#)]
44. Wang, Y.; Fu, C.; Qin, X. Numerical and physical modeling of submarine telecommunication cables subjected to abrupt lateral seabed movements. *Mar. Georesour. Geotechnol.* **2021**, *39*, 1307–1319. [[CrossRef](#)]
45. Nian, T.K.; Song, X.L.; Nian, T.K.; Zhao, W.; Jiao, H.B.; Guo, X.S. Submarine slope failure due to overpressure fluid associated with gas hydrate dissociation. *Environ. Geotech. J.* **2020**, *9*, 108–123. [[CrossRef](#)]
46. Fan, N.; Nian, T.K.; Jiao, H.B.; Guo, X.S.; Zheng, D.F. Evaluation of the mass transfer flux at interfaces between submarine sliding soils and ambient water. *Ocean Eng.* **2020**, *216*, 108069. [[CrossRef](#)]
47. Liu, D.; Cui, Y.; Guo, J.; Yu, Z.; Chan, D.; Lei, M. Investigating the effects of clay/sand content on depositional mechanisms of submarine debris flows through physical and numerical modeling. *Landslides* **2020**, *17*, 1863–1880. [[CrossRef](#)]
48. Wu, H.; Nian, T.K.; Chen, G.Q.; Zhao, W.; Li, D.Y. Laboratory-scale investigation of the 3-D geometry of landslide dams in a U-shaped valley. *Eng. Geol.* **2020**, *265*, 105428. [[CrossRef](#)]
49. Guo, X.S.; Nian, T.K.; Wang, D.; Gu, Z.D. Evaluation of undrained shear strength of surficial marine clays using ball penetration-based CFD modelling. *Acta Geotech.* **2022**, *17*, 1627–1643. [[CrossRef](#)]
50. Wu, H.; Zhao, W.; Nian, T.K.; Song, H.B.; Zhang, Y.J. Study on the anti-dip layered rock slope topping failure based on centrifuge model test. *Shuili Xuebao* **2018**, *49*, 223–231. (In Chinese)
51. Guo, X.S.; Nian, T.K.; Zhao, W.; Gu, Z.D.; Liu, C.P.; Liu, X.L.; Jia, Y.G. Centrifuge experiment on the penetration test for evaluating undrained strength of deep-sea surface soils. *Int. J. Min. Sci. Technol.* **2022**, *32*, 363–373. [[CrossRef](#)]
52. Boylan, N.; Gaudin, C.; White, D.; Randolph, M.; Schneider, J. Geotechnical centrifuge modelling techniques for submarine slides. In Proceedings of the ASME 28th International Conference on Offshore Mechanics and Arctic Engineering, Honolulu, HI, USA, 31 May–5 June 2009.
53. Gaudin, C.; White, D.J.; Boylan, N.; Breen, J.; Brown, T.; De Catania, S.; Hortin, P. A wireless high-speed data acquisition system for geotechnical centrifuge model testing. *Meas. Sci. Technol.* **2009**, *20*, 095709. [[CrossRef](#)]
54. Zakeri, A.; Hawlader, B.; Chi, K. Drag forces caused by submarine glide block or out-runner block impact on suspended (free-span) pipelines. *Ocean Eng.* **2012**, *47*, 50–57. [[CrossRef](#)]

55. Zhang, X.H.; Lu, X.B.; Shi, Y.H.; Xia, Z.; Liu, W.T. Centrifuge experimental study on instability of seabed stratum caused by gas hydrate dissociation. *Ocean Eng.* **2015**, *105*, 1–9. [[CrossRef](#)]
56. Zhang, J.H.; Lin, H.L.; Wang, K.Z. Centrifuge modeling and analysis of submarine landslides triggered by elevated pore pressure. *Ocean Eng.* **2015**, *109*, 419–429. [[CrossRef](#)]
57. Zhang, W.; Askarinejad, A. Centrifuge modelling of submarine landslides due to static liquefaction. *Landslides* **2019**, *16*, 1921–1938. [[CrossRef](#)]
58. Zhang, W.; Askarinejad, A. Centrifuge modelling of static liquefaction in submarine slopes: Scaling law dilemma. *Can. Geotech. J.* **2021**, *58*, 200–209. [[CrossRef](#)]
59. Takahashi, H.; Fujii, N.; Sassa, S. Centrifuge model tests of earthquake-induced submarine landslide. *Int. J. Phys. Model. Geotech.* **2020**, *20*, 254–266. [[CrossRef](#)]
60. Yang, Q.; Zhu, B.; Hiraishi, T. Probabilistic evaluation of the seismic stability of infinite submarine slopes integrating the enhanced Newmark method and random field. *Bull. Eng. Geol. Environ.* **2021**, *80*, 2025–2043. [[CrossRef](#)]
61. Zhu, B.; Pei, H.; Yang, Q. An intelligent response surface method for analyzing slope reliability based on Gaussian process regression. *Int. J. Numer. Anal. Methods Geomech.* **2019**, *43*, 2431–2448. [[CrossRef](#)]
62. Zhu, B.; Hiraishi, T.; Pei, H.; Yang, Q. Efficient reliability analysis of slopes integrating the random field method and a Gaussian process regression-based surrogate model. *Int. J. Numer. Anal. Methods Geomech.* **2021**, *45*, 478–501. [[CrossRef](#)]
63. Zhu, B.; Hiraishi, T.; Mase, H.; Baba, Y.; Pei, H.; Yang, Q. A 3-D numerical study of the random wave-induced response in a spatially heterogeneous seabed. *Comput. Geotech.* **2021**, *135*, 104159. [[CrossRef](#)]
64. Zhu, B.; Hiraishi, T.; Mase, H.; Pei, H.; Yang, Q. Probabilistic analysis of wave-induced dynamic response in a poroelastic sloping seabed using random finite element method. *Ocean Eng.* **2022**, *252*, 111231. [[CrossRef](#)]
65. Dey, R.; Hawlader, B.C.; Phillips, R.; Soga, K. Numerical modelling of submarine landslides with sensitive clay layers. *Geotechnique* **2016**, *66*, 454–468. [[CrossRef](#)]
66. Zhang, W.; Randolph, M.F.; Puzrin, A.M.; Wang, D. Transition from shear band propagation to global slab failure in submarine landslides. *Can. Geotech. J.* **2019**, *56*, 554–569. [[CrossRef](#)]
67. Buss, C.; Friedli, B.; Puzrin, A.M. Kinematic energy balance approach to submarine landslide evolution. *Can. Geotech. J.* **2019**, *56*, 1351–1365. [[CrossRef](#)]
68. Guo, X.S.; Stoesser, T.; Zheng, D.F.; Luo, Q.; Liu, X.; Nian, T.K. A methodology to predict the run-out distance of submarine landslides. *Comput. Geotech.* **2023**, *153*, 105073. [[CrossRef](#)]
69. Gauer, P.; Kvalstad, T.J.; Forsberg, C.F.; Bryn, P.; Berg, K. The last phase of the Storegga Slide: Simulation of retrogressive slide dynamics and comparison with slide-scar morphology. *Mar. Pet. Geol.* **2005**, *22*, 171–178. [[CrossRef](#)]
70. Dong, Y.; Wang, D.; Randolph, M.F. Runout of submarine landslide simulated with material point method. *J. Hydrodyn.* **2017**, *29*, 438–444. [[CrossRef](#)]
71. Dong, Y.; Wang, D.; Cui, L. Assessment of depth-averaged method in analysing runout of submarine landslide. *Landslides* **2020**, *17*, 543–555. [[CrossRef](#)]
72. Zhang, W.; Randolph, M.F. A smoothed particle hydrodynamics modelling of soil–water mixing and resulting changes in average strength. *Int. J. Numer. Anal. Methods Geomech.* **2020**, *44*, 1548–1569. [[CrossRef](#)]
73. Jiang, M.; Shen, Z.; Wu, D. CFD-DEM simulation of submarine landslide triggered by seismic loading in methane hydrate rich zone. *Landslides* **2018**, *15*, 2227–2241. [[CrossRef](#)]
74. Zhang, W.; Puzrin, A.M. Depth integrated modelling of submarine landslide evolution. *Landslides* **2021**, *18*, 3063–3084. [[CrossRef](#)]
75. Dong, Y.; Wang, D.; Randolph, M.F. Investigation of impact forces on pipeline by submarine landslide using material point method. *Ocean Eng.* **2017**, *146*, 21–28. [[CrossRef](#)]
76. Zhang, Y.; Wang, Z.; Yang, Q.; Wang, H. Numerical analysis of the impact forces exerted by submarine landslides on pipelines. *Appl. Ocean Res.* **2019**, *92*, 101936. [[CrossRef](#)]
77. Nian, T.K.; Guo, X.S.; Fan, N.; Jiao, H.B.; Li, D.Y. Impact forces of submarine landslides on suspended pipelines considering the low-temperature environment. *Appl. Ocean Res.* **2018**, *81*, 116–125. [[CrossRef](#)]
78. Li, R.Y.; Chen, J.J.; Liao, C.C. Numerical Study on Interaction between Submarine Landslides and a Monopile Using CFD Techniques. *J. Mar. Sci. Eng.* **2021**, *9*, 736. [[CrossRef](#)]
79. Fan, N.; Nian, T.K.; Jiao, H.B.; Jia, Y.G. Interaction between submarine landslides and suspended pipelines with a streamlined contour. *Mar. Georesour. Geotechnol.* **2018**, *36*, 652–662. [[CrossRef](#)]
80. Dutta, S.; Hawlader, B. Pipeline–soil–water interaction modelling for submarine landslide impact on suspended offshore pipelines. *Geotechnique* **2019**, *69*, 29–41. [[CrossRef](#)]
81. Guo, X.; Stoesser, T.; Zhang, C.; Fu, C.; Nian, T. Effect of opening and wall boundaries on CFD modeling for submarine landslide–ambient water–pipeline interaction. *Appl. Ocean Res.* **2022**, *126*, 103266. [[CrossRef](#)]
82. Guo, X.; Stoesser, T.; Nian, T.; Jia, Y.; Liu, X. Effect of pipeline surface roughness on peak impact forces caused by hydrodynamic submarine mudflow. *Ocean Eng.* **2022**, *243*, 110184. [[CrossRef](#)]
83. Guo, X.; Nian, T.; Stoesser, T. Using dimpled-pipe surface to reduce submarine landslide impact forces on pipelines at different span heights. *Ocean Eng.* **2022**, *244*, 110343. [[CrossRef](#)]
84. Guo, X.S.; Nian, T.K.; Fan, N.; Jia, Y.G. Optimization design of a honeycomb-hole submarine pipeline under a hydrodynamic landslide impact. *Mar. Georesour. Geotechnol.* **2021**, *39*, 1055–1070. [[CrossRef](#)]

85. Guo, X.; Liu, X.; Zhang, H.; Li, M.; Luo, Q. Evaluation of instantaneous impact forces on fixed pipelines from submarine slumps. *Landslides* **2022**, *19*, 2889–2903. [[CrossRef](#)]
86. Guo, X.S.; Zheng, D.F.; Zhao, L.; Fu, C.W.; Nian, T.K. Quantitative composition of drag forces on suspended pipelines from submarine landslides. *J. Waterw. Port Coast. Ocean Eng.* **2022**, *148*, 04021050. [[CrossRef](#)]
87. Guo, X.S.; Zheng, D.F.; Nian, T.K.; Yin, P. Effect of different span heights on the pipeline impact forces induced by deep-sea landslides. *Appl. Ocean Res.* **2019**, *87*, 38–46. [[CrossRef](#)]
88. Wang, Z.; Jia, Y.; Liu, X.; Wang, D.; Shan, H.; Guo, L.; Wei, W. In situ observation of storm-wave-induced seabed deformation with a submarine landslide monitoring system. *Bull. Eng. Geol. Environ.* **2018**, *77*, 1091–1102. [[CrossRef](#)]
89. Lizama, E.; Morales, B.; Somos-Valenzuela, M.; Chen, N.; Liu, M. Understanding landslide susceptibility in Northern Chilean Patagonia: A basin-scale study using machine learning and field data. *Remote Sens.* **2022**, *14*, 907. [[CrossRef](#)]
90. Hotta, M.M.; Almeida, M.S.S.; Pelissaro, D.T.; de Oliveira, J.R.M.D.S.; Tibana, S.; Borges, R.G. Centrifuge tests for evaluation of submarine-mudflow hydroplaning and turbidity currents. *Int. J. Phys. Model. Geotech.* **2020**, *20*, 239–253. [[CrossRef](#)]
91. Shi, C.; An, Y.; Wu, Q.; Liu, Q.; Cao, Z. Numerical simulation of landslide-generated waves using a soil–water coupling smoothed particle hydrodynamics model. *Adv. Water Resour.* **2016**, *92*, 130–141. [[CrossRef](#)]
92. Nian, T.K.; Wu, H.; Takara, K.; Li, D.Y.; Zhang, Y.J. Numerical investigation on the evolution of landslide-induced river blocking using coupled DEM-CFD. *Comput. Geotech.* **2021**, *134*, 104101. [[CrossRef](#)]
93. Zhang, W.; Puzrin, A.M. How small slip surfaces evolve into large submarine landslides—Insight from 3D numerical modeling. *J. Geophys. Res. Earth Surf.* **2022**, *127*, e2022JF006640. [[CrossRef](#)]
94. Dong, Y.; Grabe, J. Large scale parallelisation of the material point method with multiple GPUs. *Comput. Geotech.* **2018**, *101*, 149–158. [[CrossRef](#)]

Article

Development and Testing of a High-Resolution Three-Dimensional Seismic Detection System for Gas Hydrate

Chenguang Liu ^{1,2,*}, Qingxian Zhao ^{3,*}, Zhen Liu ³, Yanhong Lian ⁴, Yanliang Pei ^{1,2}, Baohua Liu ², Xishuang Li ¹, Qingjie Zhou ¹, Keping Yan ⁴ and Zili Chen ⁵

- ¹ Key Laboratory of Marine Geology and Metallogeny, The First Institute of Oceanography, Ministry of Natural Resources, Qingdao 266061, China
² Laboratory for Marine Geology, Pilot National Laboratory for Marine Science and Technology (Qingdao), Qingdao 266237, China
³ Guangzhou Marine Geological Survey, China Geological Survey, Guangzhou 510075, China
⁴ Institute of Industrial Ecology and Environment, Zhejiang University, Hangzhou 310028, China
⁵ Xi'an Hong Lu Yang Electrical Equipment Co., Ltd., Xi'an 710199, China
* Correspondence: lcg@fio.org.cn (C.L.); zhqx@hyd.z.cn (Q.Z.)

Abstract: As a novel type of mineral resource, gas hydrate has received a considerable amount of attention worldwide. This seismic detection method can detect abnormal phenomena such as the BSR, blank zones, velocity anomalies and polarity inversion of gas hydrate and become an important method of gas hydrate detection. The occurrence area of gas hydrate in the South China Sea is usually buried deep beneath the seabed. The current method cannot meet the needs of the shape and structure detection of gas hydrate deposits. With the support of the National Key R&D Program of China, some key technologies have led to developmental breakthroughs, such as ultra-high-energy plasma sources, small-group-interval high-resolution seismic streamers, and distributed three-dimensional seismic acquisition. The seismic profile obtained north of the South China Sea shows that the stratum penetration depth reaches nearly 1000 m at a depth of 1500 m, and the vertical resolution is better than 1.5 m. This system can serve the needs of high-resolution exploration of gas hydrate resources.

Keywords: gas hydrate; high-resolution seismic; ultra-high-energy plasma source

Citation: Liu, C.; Zhao, Q.; Liu, Z.; Lian, Y.; Pei, Y.; Liu, B.; Li, X.; Zhou, Q.; Yan, K.; Chen, Z. Development and Testing of a High-Resolution Three-Dimensional Seismic Detection System for Gas Hydrate. *J. Mar. Sci. Eng.* **2023**, *11*, 20. <https://doi.org/10.3390/jmse11010020>

Academic Editors: Timothy S. Collett and Dmitry A. Ruban

Received: 29 September 2022

Revised: 7 December 2022

Accepted: 14 December 2022

Published: 23 December 2022



Copyright: © 2022 by the authors. Licensee MDPI, Basel, Switzerland. This article is an open access article distributed under the terms and conditions of the Creative Commons Attribution (CC BY) license (<https://creativecommons.org/licenses/by/4.0/>).

1. Introduction

Gas hydrate is considered as a strategic alternative energy source for sustainable human development for the 21st century. At present, more than 30 countries and regions are engaging in the research, investigation and exploration of gas hydrate. More than 230 sites globally have been found recovered or inferred to contain gas hydrates, and 97% of them are distributed in the continental margin of the oceans, with only a few distributed in the continental permafrost regions (Figure 1).

It is difficult to quantify the number of gas hydrate reservoirs in permafrost sediments via conventional seismic techniques due to the almost identical acoustic properties of hydrates and ice. A coupled geophysical-geothermal scheme is developed to predict hydrate saturation in gas-hydrate-bearing permafrost sediments by utilizing their geophysical and geothermal responses [1,2].

On the other hand, owing to its advantages of high efficiency and high precision, marine seismic exploration technology is commonly used in the field of gas hydrate exploration and has great application potential. The United States first discovered the phenomenon of bottom simulating reflection (BSR) through seismic investigation at the Black Submarine Platform in the Gulf of Mexico. Subsequent ocean drilling confirmed the presence of submarine gas hydrate in this area and proved that the seismic investigation method is an effective means to determine the existence of gas hydrate [3–7]. Since then, Canada, Japan, Germany, India, Belgium, Russia and other countries have successively carried out investigations of and

research on gas hydrate on the continental margin of Cascadia, Nankai Trough of Japan, the continental margin of India, the Black Sea, Lake Baikal, the Caspian Sea and various other places. Without exception, seismic investigation methods were used in these works, and remarkable results were subsequently obtained [3–24].

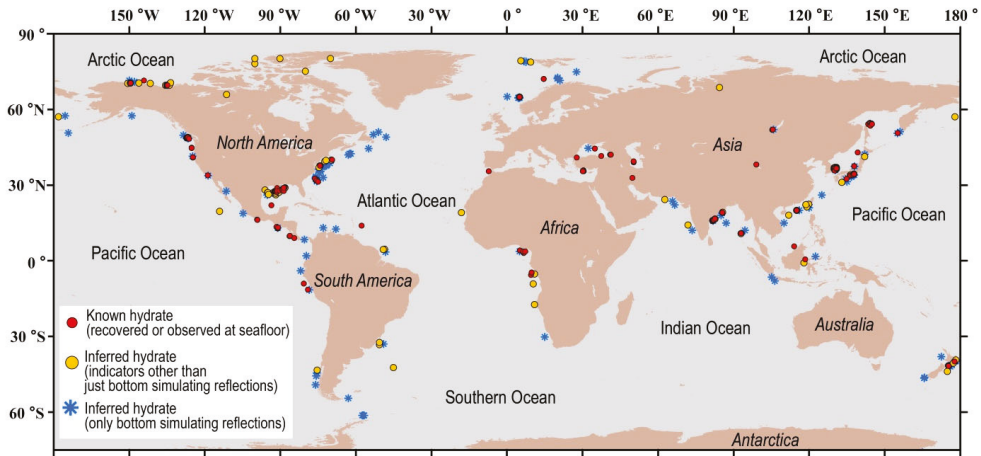


Figure 1. Global map of recovered and inferred gas hydrates (from the Woods Hole Coastal and Marine Science Center, 2020).

In the early exploration of gas hydrates, the four major seismic anomalies of gas hydrate (i.e., BSR, blank zone, velocity anomaly and polarity reversal) were mainly discovered through two-dimensional seismic detection [25]. With the deepening of exploration, seismic technology has been gradually developed to detect the occurrence and internal structure of gas hydrate ore bodies by 3D exploration to accurately delineate natural gas hydrate ore bodies, estimate their reserves and optimize drilling targets. Therefore, high-resolution 3D seismic exploration has become the main technical means of gas hydrate exploration. In Japan, the Ministry of Finance and the Ministry of Economy, Trade and Industry presided over the exploration and development of gas hydrate in Japan’s sea areas and conducted a large number of high-resolution 3D seismic exploration efforts in the Sea of Japan and Nankai Trough [26–28]. The adopted detection system included a pair of tuned air gun arrays; the capacity of a single gun array was 1158 in³, and eight 192-channel seismic streamers were used, with a channel spacing of 12.5 m and a streamer spacing of 100 m. In 2004, the University of Tromsø in Norway, the National Marine Science Center in Southampton in the UK and Kiel University in Germany jointly developed the P-Cable system [29,30]. In 2008, Bangs et al., (2011) carried out high-resolution 3D seismic data acquisition in the Gulf of Mexico using the P-Cable system. In total, ten 30-m long seismic streamers were used for the operation, with a distance of 12.5 m between the streamers, a combination of two Sercel GI guns as the source, and a total capacity of 150 in³. Singhroha et al., (2016) and Kunath et al., (2020) applied the P-Cable system to investigate gas hydrate in the Arctic region and the southwest sea area off Taiwan Island of China. The results show that the P-Cable system has a good bandwidth (20–300 Hz) and can detect gas hydrate and free gas through the seismic quality factor Q. [31–33].

Since 1999, China has conducted gas hydrate investigations and research in the Xisha Trough in the South China Sea and the Dongsha Islands, the Shenhu and Qiongdongnan areas, and the Okinawa Trough in the East China Sea. Using seismic detection technology, the China Geological Survey carried out a preliminary experimental investigation of natural gas hydrate in the Xisha Trough area of the South China Sea, made a breakthrough, and found the BSR seismic marker of natural gas hydrate in the China Sea. From 2005 to 2009,

the R/V FENDOUSIHAO carried out numerous multichannel seismic acquisitions in the northern South China Sea [34–36]. A series of abnormal signs of natural gas hydrate were found in many regions, which preliminarily confirmed the existence of gas hydrate in the China Seas. Its resource prospect is promising [25,37–42]. In May 2007, the China Geological Survey drilled physical samples of natural gas hydrate at three stations in the Shenhu area of the South China Sea. In 2017 and 2020, China successfully carried out two rounds of trial production of gas hydrate in the Shenhu area of the South China Sea.

In the early 21st century, China’s gas hydrate seismic survey mainly adopted high-resolution two-dimensional seismic exploration or quasi-3D seismic exploration collected by a single-source and single cable or double-source and single cable. The multichannel seismic system adopted was a single streamer with a trace spacing of 12.5 m and a record number of 192~240 channels. The excitation source was provided from a gun array composed of BOLT or GI guns, with a peak energy bandwidth between 50–120 Hz, and the total capacity of the gun array ranged from hundreds to thousands of cubic inches [43–47].

In 2018, the Shanghai Offshore Petroleum Bureau carried out a high-resolution and high-density 3D seismic survey of three sources and twelve cables in the South China Sea [48,49]. Adopting 12 seismic cables with a length of 5100 m and a distance of 12.5 m and a working mode of alternating excitation of three sources, the acquisition binning reached 6.25×12.5 m. Subsequently, the Guangzhou Marine Geological Survey conducted a successful “rake cable” acquisition test with the R/V HAIYANGDIZHIBAHAO in the northern waters of the South China Sea in 2020. Using acquisition methods such as multisource acquisition, the combination of one long cable and multiple short cables, and continuous recording, the seismic acquisition of a 6.25×1.5625 m ultrasmall area with a 100 Hz main frequency has been achieved [50].

Equipment and acquisition parameters are summarized in Table 1 for several 3D seismic explorations mentioned previously. Without exception, all seismic explorations used air guns as sources. In this paper, we introduce a new technology for gas hydrate detection by using ultra-high-energy plasma as the source.

Table 1. Main institutions engaged in the seismic detection of gas hydrate and the technical characteristics of their methods.

Serial Number	Institution	Main Acquisition Parameters	Test Area	Technical Features
1	Ministry of Economy, Trade and Industry	Eight multichannel seismic cables with 192 channels, 12.5 m group interval and a total length of 2400 m are used. The cable distance is 100 m. Two 1158 in ³ tuned gun arrays are used to create the source.	South China Sea Trough (Otsuka et al., 2015) [28].	Acquisition binning: 12.5 × 12.5 m Main frequency is 50 Hz.
2	University of Tromsø, Norway	The P-Cable 3D seismic detection system adopts 14 seismic cables with 8 channels each, the group interval is 3.125 m, the cable spacing is 12.5 m, and a Mini-GI gun is used as the seismic source.	Arctic waters (Singhroha et al., 2016) [32].	Acquisition binning: 6.25 × 6.25 m Frequency band range is 20–300 Hz.
3	Indian Oil and Gas Board	Five cables of 200 channels are used, the group interval is 25 m, the distance between the cables is 200 m, and 2 skid-type gun arrays with a total capacity of 2750 in ³ are used as the seismic source.	Bay of Bengal (Mishra et al., 2019) [23].	Acquisition binning: 12.5 × 50 m. Main frequency of approximately 30 Hz.

Table 1. *Cont.*

Serial Number	Institution	Main Acquisition Parameters	Test Area	Technical Features
4	Guangzhou Marine Geological Survey	The “rake cable” acquisition method adopts multiple seismic sources, a combination of a long cable and many short cables, and continuous recording.	Northern area of the South China Sea (Wen et al., 2020) [50].	Acquisition binning: 6.25×1.5625 m Main frequency of approximately 100 Hz.
5	Sinopec Shanghai Offshore Oil and Gas Branch	Using 12 cables of 408 channels, the group interval is 12.5 m, and the cable and cable spacing is 75 m. Three hypocenters with a capacity of 1160 in^3 are used for alternate excitation, and the distance between the cables is 25 m.	South China Sea (Li et al., 2021) [49].	Acquisition binning: 6.25×12.5 m Frequency band range is 7–118 Hz.

2. Methods

With the support of the National 863 Program, Chinese institutes have successively carried out research and development of a series of high-resolution multichannel seismic detection technologies for oil, gas, and gas hydrate detection. Great progress has been made in the evaluation of plasma sources, digital seismic acquisition streamers and multichannel seismic data recording systems. Related instruments and equipment have been successfully developed, and a high-resolution multichannel seismic detection system for shallow strata in shallow water to deep water has been established [51–57].

The gas hydrate occurrence areas in China are usually in water deeper than 1000 m and deeply buried below the seafloor [37–40,58]. With the development of more refined gas hydrate exploration, the existing seismic detection methods and means cannot meet the needs of the high-resolution exploration of hydrates and fine descriptions of ore bodies. We developed a set of high-resolution 3D seismic detection equipment, include an ultrahigh-energy plasma source with two transmitting array, two small-group-interval digital seismic streamers and 3D seismic acquisition system. The results showed that it can penetrate the stratum deeper than 500 m with vertical resolutions better than 1.5 m.

2.1. Ultrahigh-Energy Plasma Source

Bubbles generated by a pulsed discharge in water can emit extensive pulsed acoustic waves, which have applications in oceanic high-resolution seismic exploration. However, with the increase in discharge energy, a single electrode will produce a bubble effect. In order to achieve ultra-high-energy discharge, multi-electrode combination is usually used [59–63].

The ultra-high-energy plasma source system adopts a dual-output structure (Figure 2). The system includes two energy modules. Each module has a maximum output of 25,000 J, and bear the same structure. The main circuit adopts the mode of rectification-inverting-boosting-rectification-storage-discharging. Each module is equipped with a set of pulse transmission cables and transmitting electrodes, and the two modules communicate with the source upper controller through optical fibers. The upper controller of the source controls the start–stop and energy level of each module and controls the trigger output of each module through the external trigger input.

The source-transmitting array comprises two sets of independent arrays, each of which has 2080 electrodes. Bipolar electrode discharge technology is adopted to increase the circuit impedance, which can improve the energy efficiency and effectively reduce the loss of the transmitting electrode. To ensure that the quantum shocks can maintain a constant distance during offshore operations, the twin arrays are fixed with a link frame, which can keep the distance between the two subquakes at 3.2 m during operation; a relative GPS (RGPS) device and a battery module are installed above the link frame (Figure 3).

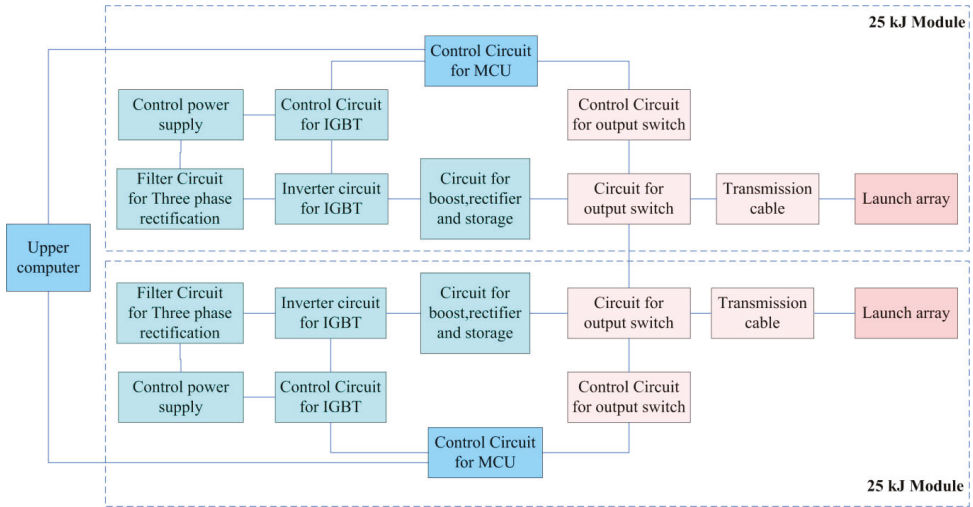


Figure 2. Structure diagram of the ultra-high-energy plasma source.

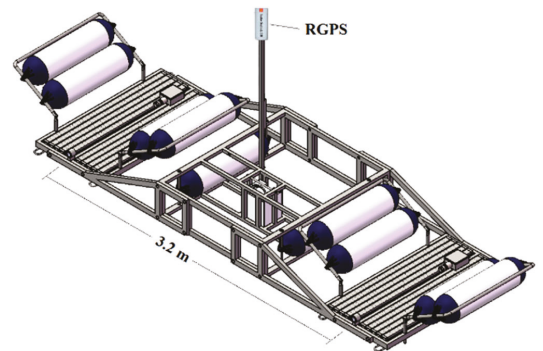


Figure 3. Plasma source array.

The verified standard hydrophone is used to measure the source wavelet at different sinking depths and different emission energies and calculate the sound source level of the source. The results show that under an emission energy of 25,000 J, the sound source level of the source can reach 240 dB. The frequency is approximately 380 Hz (Figure 4).

2.2. High-Resolution Seismic Streamer

A small-group-interval high-resolution seismic streamer consists of a leading section, a photoelectric conversion unit, a front elastic section, a data transmission unit, a working section, a rear elastic section, and a trailing transition section.

The leading section is an armored photoelectric composite cable, which transmits commands and signals through optical fibers and supplies power to each part of the cable through electrical wires; the photoelectric conversion unit converts the optical signal commands of the multichannel seismic data acquisition unit into electrical signals and transmits them to the working section. The collected electrical signals are converted into optical signals and transmitted to the streamer controller and the multichannel seismic data acquisition unit.

sition unit; the front elastic section connects the leading section and the working section to reduce the influence of ship vibration on the working section; the data transmission unit is located in the elastic section before the connection segment and between two work sections. The data transmission unit is used to collect the artificial reflection seismic signals collected in the working section and send them to the photoelectric conversion unit; the working section consists of multiple sets of hydrophone combinations and digital acquisition units, each digital acquisition unit controls 4 acquisition channels, and each acquisition channel consists of 4–6 hydrophones connected in series or in parallel. The digital acquisition unit digitizes the artificial reflection seismic signal collected by the hydrophone and sends it to the data transmission unit; the rear elastic section is used to connect the working section and the tail mark. The function is to reduce the influence of tail mark drag vibration and noise on the working section; the front end of the tail mark adapter section is connected with the rear elastic section through a swivel ring, and the rear end is connected with the tail mark. The swivel ring is used to eliminate the influence of the torque generated by the tail mark vibration on the working section.

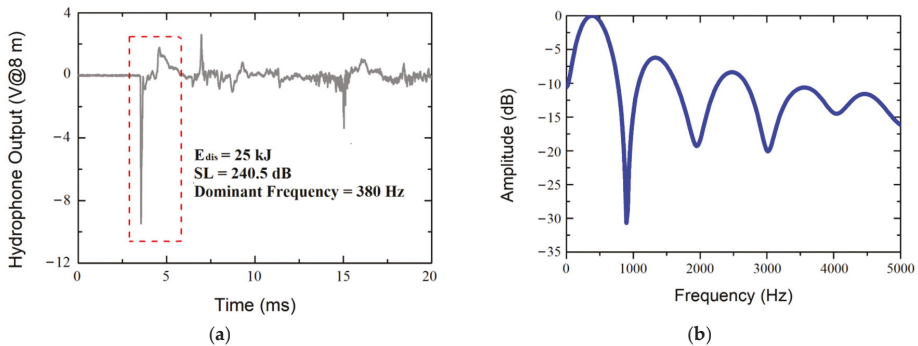


Figure 4. Results of the source wavelet test. (a) oscillogram of source wavelet; (b) frequency spectrum of source wavelet.

2.3. Seismic Acquisition System

The seismic acquisition system takes the network switch as the center, including a multichannel data acquisition unit, streamer controller, acquisition control server, quality monitoring server, disk array, plotter and client, to achieve the requirements of massive data transmission, storage, arrangement, real-time monitoring and control, linear hydrophone array geometry and data acquisition.

3. Data Acquisition and Analysis

In 2020, an acquisition experiment was carried out in the northern South China Sea using an ultrahigh-energy plasma source, a small-group-interval high-resolution seismic streamer, and a 3D seismic acquisition system. The test adopted the observation system of dual-source and dual-cable configuration for acquisition (Figure 5). Two 240-channel seismic streamers were used, with a cable spacing of 12.8 m at the depth of 5 m. The two pulse transmitting arrays were alternately excited with 25 kJ of emission energy, the shot interval was 12.5 m, at the depth was 0.5 m. The acquisition binning is 1.6×1.5625 m. Table 2 summarizes the acquisition parameters of 3D seismic acquisition experiment.

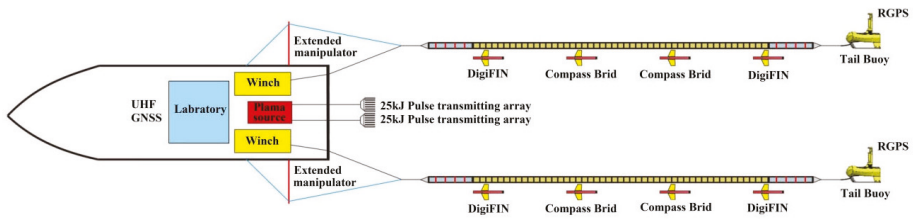


Figure 5. Design of the high-resolution 3D seismic detection system.

Table 2. Acquisition parameters for high-resolution seismic acquisition experiment.

Group interval	3.125 m	Recording Duration	4 s
Cable Spacing	12.8 m	Number of Streamer	2
Cable Length	240 channels/per cable	Cable Sinking	5 m
Number of Sources	2	Shot Interval	12.5 m
Source Spacing	3.2 m	Source Sinking	0.5 m
Sampling Rate	0.25 ms	Source Energy	25,000 J
Acquisition Binning	1.6×1.5625 m	Trigger Mode	Alternating

3.1. Detection Depth Analysis

Figure 6 shows the two-way reflection profile obtained in the shallow water area studied. The bottom reflection time $T1 = 0.2710$ s and the deepest stratum reflection time $T2 = 1.55$ s are read from Figure 6a. From the velocity map shown in Figure 6b, the seawater velocity at $T1$ is approximately 1500 m/s, and the average velocity at $T2$ is 1550 m/s. When the seabed depth is 205 m, the stratum penetration depth is approximately 1347 m.

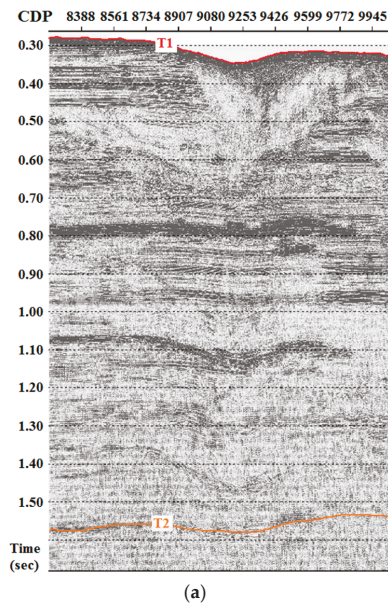


Figure 6. Cont.

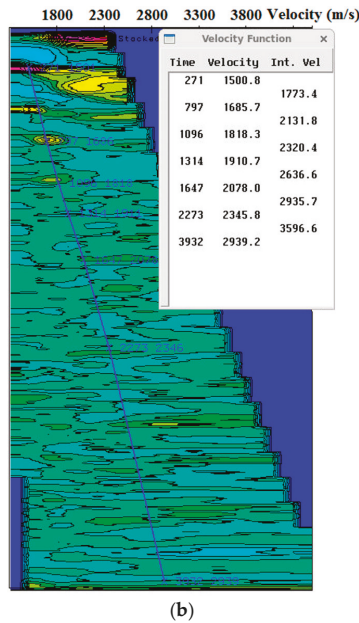


Figure 6. Seismic profiles obtained in shallow water north of the South China Sea. (a) Seismic profile; (b) Velocity spectrum.

Figure 7 shows the two-way reflection profile obtained in the deep water area studied. The seabed reflection time $T_1 = 2.0$ s and the deepest stratigraphic reflection time $T_2 = 2.950$ s are read from Figure 7a. From the velocity map shown in Figure 7b, the seawater velocity at T_1 is approximately 1495 m/s, and the average velocity at T_2 is 1666 m/s. The penetration depth when the bottom depth is 1495 m was calculated to be approximately 962 m.

3.2. Vertical Resolution Analysis

The spectrum scanning analysis was carried out on the seismic profile obtained in the deep water area of the South China Sea. From the spectrum scanning diagram of a single shot (Figure 8), there is almost no effective reflection signal at 0–80 Hz, and there are mainly interference and few reflection signals above 700 Hz. The frequency band of the reflection signal is 80–700 Hz. From the spectrogram of the reflection profile (Figure 9), it can be seen that the effective frequency band is 70–650 Hz and that the main frequency is 100–500 Hz. Taking the center frequency of 300 Hz and the speed of 1600–1800 m/s for calculation, the highest resolution obtained is 1.3–1.5 m.

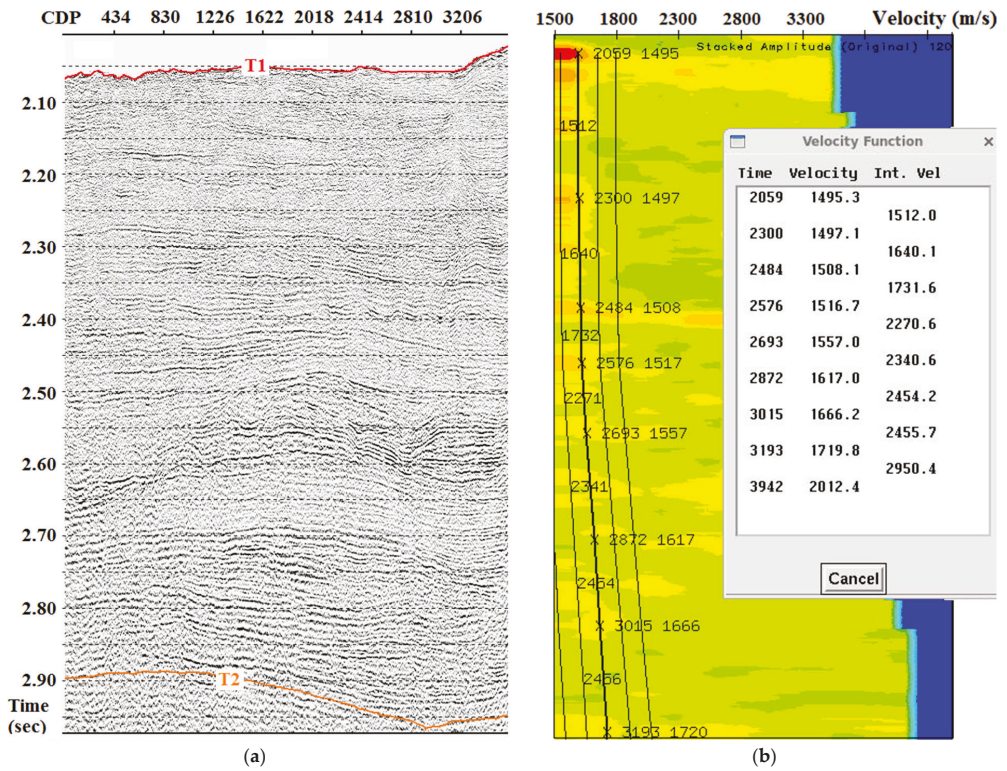


Figure 7. Seismic profiles obtained in deep water north of the South China Sea (a) Seismic profile; (b) Velocity spectrum.

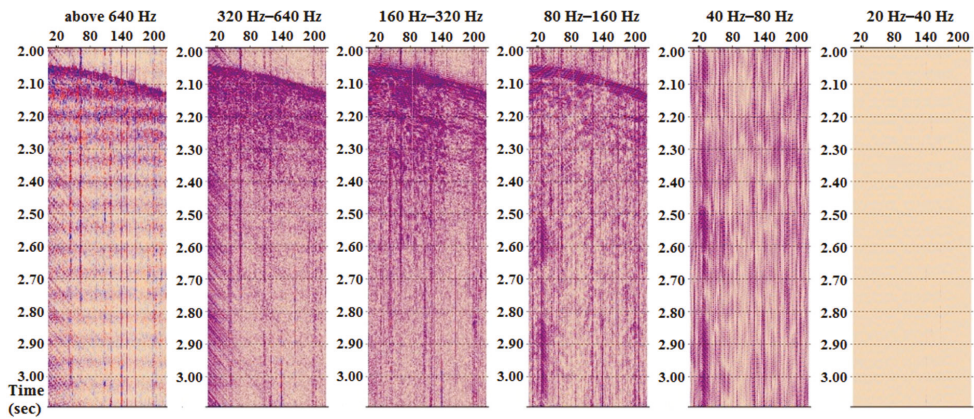


Figure 8. Spectrum scanning diagram of a single shot.

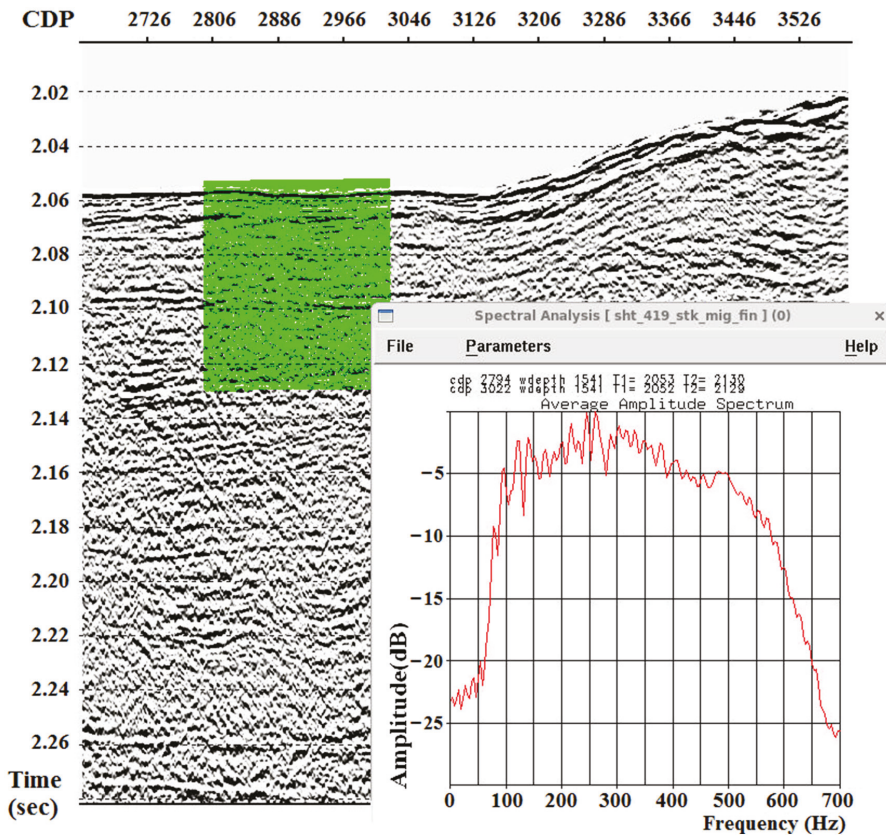


Figure 9. Reflection profile in deep water and spectrum diagram of shallow strata.

4. Results

After years of accumulative technical improvements, a high-precision 3D seismic detection system for gas hydrate was successfully developed, which includes a 50 kJ ultrahigh-energy plasma source, two high-resolution digital seismic streamers with a group interval of 3.125 m, and a seismic acquisition system. The acquisition test carried out in the northeastern part of the South China Sea shows that this system has obvious advantages in terms of the frequency band range and the minimum acquisition binning. The seismic profile obtained at a water depth of 205 m has a stratum penetration depth approximately 1347 m. The seismic profile obtained at a water depth of 1495 m and has a stratum penetration depth of approximately 962 m. The main frequency of profile is 100–500 Hz and the vertical resolution is better than 1.5 m. The acquisition binning is 1.6×1.5625 m.

5. Discussions

Compared with an air gun source, ultrahigh-energy plasma source can provide higher dominant frequency and stratigraphic resolution. If discharged with small energy, the shooting interval of plasma source can measure less than 1 s. Thus, the plasma source can provide higher folds than the air gun source. Furthermore, this approach can provide technical support for the highly targeted exploration and development of gas hydrates and a fine description of ore bodies.

Author Contributions: Conceptualization, B.L. and K.Y.; methodology, C.L. and Q.Z. (Qingxian Zhao); software, X.L. and Z.L.; validation, Y.L., Z.C. and Y.P.; formal analysis, X.L.; investigation and resources, Q.Z. (Qingxian Zhao) and X.L.; writing—original draft preparation, C.L.; writing—review and editing, C.L.; visualization, Q.Z. (Qingjie Zhou). All authors have read and agreed to the published version of the manuscript.

Funding: This work was supported by the Major Scientific and Technological Innovation Project of Shandong Province (No. 2019JZZY010803), the Basic Scientific Fund for National Public Research Institutes of China (2021Q03) and the National Key R&D Program of China (2017YFC0307400).

Institutional Review Board Statement: Not applicable.

Informed Consent Statement: Not applicable.

Data Availability Statement: Not applicable.

Acknowledgments: Data acquisition was supported by cruises R/V “XiangYangHong 01” and R/V “HaiYangDiZhiBaHao”, funded by the National Key R&D Program of China.

Conflicts of Interest: The authors declare no conflict of interest.

References

1. Farahani, M.V.; Hassanpouryouzband, A.; Yang, J.; Tohidi, B. Development of a coupled geophysical-geothermal scheme for quantification of hydrates in gas hydrate-bearing permafrost sediments. *Phys. Chem. Chem. Phys. PCCP* **2021**, *23*, 24249–24264. [[CrossRef](#)] [[PubMed](#)]
2. Farahani, M.V.; Hassanpouryouzband, A.; Yang, J.; Tohidi, B. Insights into the climate-driven evolution of gas hydrate-bearing permafrost sediments: Implications for prediction of environmental impacts and security of energy in cold regions. *RSC Adv.* **2021**, *11*, 14334–14346. [[CrossRef](#)] [[PubMed](#)]
3. Markl, R.G.; Bryan, G.M.; Ewing, J.I. Structure of the Blake-Bahama outer ridge. *J. Geophys. Res. Atmos.* **1970**, *75*, 4539–4555. [[CrossRef](#)]
4. Shipley, T.H.; Houston, M.H.; Buffler, R.T.; Shaub, F.J.; Mcmillen, K.J.; Laod, J.W.; Worzel, J.L. Seismic evidence for widespread possible gas hydrate horizons on continental slopes and rises. *AAPG Bull.* **1979**, *63*, 2204–2213. [[CrossRef](#)]
5. Holbrook, W.S.; Hoskins, H.; Wood, W.T.; Stephen, R.A.; Lizarralde, D. Methane hydrate and free gas on the Blake ridge from vertical seismic profiling. *Science* **1996**, *273*, 1840–1843. [[CrossRef](#)]
6. Hornbach, M.J.; Saffer, D.M.; Holbrook, W.S.; Van Avendonk, H.J.; Gorman, A.R. Three-dimensional seismic imaging of the Blake Ridge methane hydrate province: Evidence for large, concentrated zones of gas hydrate and morphologically driven advection. *J. Geophys. Res.* **2008**, *113*, B07101. [[CrossRef](#)]
7. Collett, T.S.; Johnson, A.H.; Knapp, C.C.; Boswell, R. Natural gas hydrates—A review. *Brows. Collect.* **2009**, *89*, 146–219. [[CrossRef](#)]
8. Hyndman, R.D.; Spence, G.D. A seismic study of methane hydrate marine bottom simulating reflectors. *J. Geophys. Res.* **1992**, *97*, 6683–6698. [[CrossRef](#)]
9. Hobro, J.W.; Minshull, T.A.; Singh, S.C. Tomographic seismic studies of the methane hydrate stability zone in the Cascadia Margin. *Geol. Soc. Lond. Spec. Publ.* **1998**, *137*, 133–140. [[CrossRef](#)]
10. Riedel, M. Three-Dimensional Seismic Investigations of Northern Cascadia Marine Gas Hydrates. Ph.D. Thesis, School of Earth and Ocean Science, University of Kiel, Kiel, Germany, 1998.
11. Kvenvolden, K.A.; Lorenson, T.D. The global occurrence of natural gas hydrate: Natural gas hydrates: Occurrence, distribution, and detection. *Am. Geophys. Union* **2001**, *124*, 3–18. [[CrossRef](#)]
12. Riedel, M.; Spence, G.D.; Chapman, N.R.; Hyndman, R.D. Deep-sea gas hydrates on the northern Cascadia margin. *Lead. Edge* **2001**, *20*, 87–109. [[CrossRef](#)]
13. Vanneste, M.; De Batist, M.; Golmshtok, A.; Kremlev, A.; Versteeg, W. Multi-frequency seismic study of gas hydrate-bearing sediments in Lake Baikal, Siberia. *Mar. Geol.* **2001**, *172*, 1–21. [[CrossRef](#)]
14. Ashi, J.; Tokuyama, H.; Taira, A. Distribution of methane hydrate BSRs and its implication for the prism growth in the Nankai Trough. *Mar. Geol.* **2002**, *187*, 177–191. [[CrossRef](#)]
15. Van Rensbergen, P.; De Batist, M.; Klerkx, J.; Hus, R.; Poort, J.; Vanneste, M.; Granin, N.; Khlystov, O.; Krinitsky, P. Sublacustrine mud volcanoes and methane seeps caused by dissociation of gas hydrates in Lake Baikal. *Geology* **2002**, *30*, 631–634. [[CrossRef](#)]
16. Zillmer, M.; Flueh, E.R.; Petersen, J. Seismic investigation of a bottom simulating reflector and quantification of gas hydrate in the Black Sea. *Geophys. J. R. Astron. Soc.* **2005**, *161*, 662–678. [[CrossRef](#)]
17. Popescu, I.; Lericolais, G.; Panin, N.; De Batist, M.; Gillet, H. Seismic expression of gas and gas hydrates across the western Black Sea. *Geo-Mar. Lett.* **2007**, *27*, 173–183. [[CrossRef](#)]
18. Petersen, C.J.; Bünz, S.; Hustoft, S.; Mienert, J.; Klaeschen, D. High-resolution P-Cable 3D seismic imaging of gas chimney structures in gas hydrated sediments of an Arctic sediment drift. *Mar. Pet. Geol.* **2010**, *27*, 1981–1994. [[CrossRef](#)]
19. Riedel, M.; Collett, T.S.; Kumar, P.; Sathe, A.V.; Cook, A. Seismic imaging of a fractured gas hydrate system in the Krishna-Godavari Basin offshore India. *Mar. Pet. Geol.* **2010**, *27*, 1476–1493. [[CrossRef](#)]

20. Giavarini, C.; Hester, K. *Gas Hydrates: Immense Energy Potential and Environmental Challenges*; Springer: London, UK, 2011.
21. Matsumoto, R.; Ryu, B.J.; Lee, S.R.; Lin, S.; Wu, S.; Sain, K.; Pecher, I.; Riedel, M. Occurrence and exploration of gas hydrate in the marginal seas and continental margin of the Asia and Oceania region. *Mar. Pet. Geol.* **2011**, *28*, 1751–1767. [[CrossRef](#)]
22. Sain, K.; Gupta, H. Gas hydrates in India: Potential and development. *Gondwana Res.* **2012**, *22*, 645–657. [[CrossRef](#)]
23. Mishra, C.K.; Dewangan, P.; Sriram, G.; Kumar, A.; Dakara, G. Spatial distribution of gas hydrate deposits in Krishna-Godavari offshore basin, Bay of Bengal. *Mar. Pet. Geol.* **2019**, *112*, 104037. [[CrossRef](#)]
24. Gerivani, H.; Putans, V.A.; Merklin, L.R.; Modarres, M.H. Characteristics of features formed by gas hydrate and free gas in the continental slope and abyssal plain of the Middle Caspian Sea. *Mar. Georesour. Geotechnol.* **2020**, *39*, 419–430. [[CrossRef](#)]
25. Zhang, G.; Huang, Y.; Chen, B. *Seismology of Gas Hydrate in the Sea*; Ocean Press: Beijing, China, 2003.
26. Nagakubo, S.; Kobayashi, T.; Fujii, T.; Inamori, T. Fusion of 3D seismic exploration and seafloor geochemical survey for methane hydrate exploration. *Explor. Geophys.* **2007**, *38*, 37–43. [[CrossRef](#)]
27. Saeki, T.; Hayashi, M.; Furukawa, T.; Inamori, T.; Asakawa, E. 3D seismic velocity structure below mounds and pockmarks in the deep water southwest of the Sado Island. *J. Geogr.* **2009**, *118*, 93–110. (In Japanese) [[CrossRef](#)]
28. Otsuka, H.; Morita, S.; Tanahashi, M.; Ashi, J. Foldback reflectors near methane hydrate bottom-simulating reflectors: Indicators of gas distribution from 3D seismic images in the eastern Nankai Trough. *Isl. Arc* **2015**, *24*, 145–158. [[CrossRef](#)]
29. Planke, S.; Berndt, C. Apparatus for Seismic Measurements. US7221620, 22 May 2007.
30. Planke, S.; Eriksen, F.N.; Berndt, C.; Mienert, J.; Masson, D.G. P-cable high-resolution seismic. *Oceanography* **2009**, *22*, 85. [[CrossRef](#)]
31. Bangs, N.L.; Hornbach, M.J.; Berndt, C. The mechanics of intermittent methane venting at South Hydrate Ridge inferred from 4D seismic surveying. *Earth Planet. Sci. Lett.* **2011**, *310*, 105–112. [[CrossRef](#)]
32. Singhroha, S.; Bünz, S.; Plaza-Faverola, A.; Chand, S. Gas hydrate and free gas detection using seismic quality factor estimates from high-resolution P-cable 3D seismic data. *Interpretation* **2016**, *4*, SA39–SA54. [[CrossRef](#)]
33. Kunath, P.; Chi, W.C.; Berndt, C.; Chen, L.; Liu, C.S.; Kläschen, D.; Muff, S. A shallow seabed dynamic gas hydrate system off SW Taiwan: Results from 3-D seismic, thermal, and fluid migration analyses. *J. Geophys. Res. Solid Earth* **2020**, *125*, e2019JB019245. [[CrossRef](#)]
34. Wu, Z. Study of source in 3-D seismic and OBS exploration of marine gas hydrate. *J. Trop. Oceanogr.* **2011**, *30*, 49–60. [[CrossRef](#)]
35. Sun, Y. Time-frequency signature extraction and recognition of unconsolidated sediments containing gas hydrate and free gas in Shenhu area, northern South China Sea. *Prog. Geophys.* **2013**, *28*, 2155–2163. [[CrossRef](#)]
36. Zhang, G.; Xu, H.; Liu, X.; Zhang, M.; Wu, Z.; Liang, J.; Wang, H.; Sha, Z. The acoustic velocity characteristics of sediment with gas hydrate revealed by integrated exploration of 3D seismic and OBS data in Shenhu area. *Chin. J. Geophys.* **2014**, *57*, 1169–1176. [[CrossRef](#)]
37. Fu, X.; Yang, M.Z.; Wen, P.F.; Xu, H.N. Seismic data processing and characteristics for gas hydrates in South China Sea. *Geol. Sci. Technol. Inf.* **2001**, *20*, 33–36.
38. Yao, B. The forming condition and distribution characteristics of the gas hydrate in the South China Sea. *Mar. Geol. Quat. Geol.* **2005**, *25*, 81–90. [[CrossRef](#)]
39. Wu, B.; Zhang, G.; Zhu, Y.; Lu, Z.; Chen, B. Progress of gas hydrate investigation in China offshore. *Earth Sci. Front.* **2003**, *10*, 177–189. [[CrossRef](#)]
40. Wu, S.; Zhang, G.; Huang, Y.; Liang, J.; Wong, H.K. Gas hydrate occurrence on the continental slope of the northern South China Sea. *Mar. Pet. Geol.* **2005**, *22*, 403–412. [[CrossRef](#)]
41. Zhang, H.; Zhang, H.; Xu, Z. Gas hydrates in China. *Geol. Surv. China* **2014**, *1*, 1–6. [[CrossRef](#)]
42. Liang, J.; Zhang, W.; Lu, J.; Wei, J.; Kuang, Z.; He, Y. Geological occurrence and accumulation mechanism of natural gas hydrates in the eastern Qiongdongnan Basin of the South China Sea: Insights from site GMGS5-W9-2018. *Mar. Geol.* **2019**, *418*, 106042. [[CrossRef](#)]
43. Zhao, Q. *The Investigation of Exploration Technology about Gas-Hydrate Semi-Three Dimension Datum*; Jilin University: Changchun, China, 2009.
44. Xu, H.; Shu, H.; Li, L.; Zhang, M.; Zhang, G. 3-D seismic data processing technique for gas hydrate by single-source and single-cable acquisition method. *Prog. Geophys.* **2009**, *24*, 1801–1806. [[CrossRef](#)]
45. Zhang, X.; Wen, P.; Xu, Y.; Zhang, B. Footprint analysis and suppress processing of dual-source and single cable 3D seismic data for gas hydrate. *Mar. Geol. Front.* **2015**, *31*, 55–61. [[CrossRef](#)]
46. Li, L.; Liu, H.; Zhang, X.; Lei, X.; Sha, Z. BSRs, estimated heat flow, hydrate-related gas volume and their implications for methane seepage and gas hydrate in the Dongsha region, northern South China Sea. *Mar. Pet. Geol.* **2015**, *67*, 785–794. [[CrossRef](#)]
47. Zhang, W.; Liang, J.; Wei, J.; Lu, J.; Su, P.; Lin, L.; Huang, W.; Guo, Y.; Deng, W.; Yang, X.; et al. Geological and geophysical features of and controls on occurrence and accumulation of gas hydrates in the first offshore gas-hydrate production test region in the shenhu area, northern south china sea. *Mar. Pet. Geol.* **2020**, *114*, 104191. [[CrossRef](#)]
48. Li, B.; Gu, Y.; Huang, F.; Feng, Q. Application of three-source and Multi-cable high-density seismic acquisition for gas hydrate in offshore China. *Offshore Oil.* **2021**, *41*, 1–7. [[CrossRef](#)]
49. Yang, P.; Li, B.; Shao, W.; Gu, Y.; Huang, F.; Wang, W. The key technique of 3D seismic processing for gas hydrate. *Offshore Oil* **2021**, *41*, 1–7. [[CrossRef](#)]

50. Wen, P.; Liu, B.; Xu, Y.; Xue, H.; Yang, Z.; Li, Y.; Meng, D.; Lu, Y. A novel seismic exploration technique targeting fine characterization of marine gas hydrates: Rake-like seismic exploration. *Prog. Geophys.* **2020**, *36*, 2215–2221. [[CrossRef](#)]
51. Pei, Y.; Wang, K.; Yan, K. Study of deep-sea high-resolution multi-channel seismic exploring system. *Adv. Mar. Sci.* **2010**, *28*, 244–249. [[CrossRef](#)]
52. Wang, K.; Huang, Y.; Lian, Y.; Zhang, X. *Technology and Application of High-Resolution Multi-Channel Seismic Detection in Shallow Water*; Ocean Press: Beijing, China, 2011.
53. Yan, H.; Huang, Y.; Pei, Y.; Liu, Z.; Wang, K.; Liu, B.; Yan, K. Plasma seismic source and its application in oceanic seismic exploration. *High Volt. Eng.* **2012**, *38*, 1711–1718. [[CrossRef](#)]
54. Lei, X. *Study of Key Technologies of High-Precision Marine Multichannel Seismic Survey*; Ocean University of China: Qingdao, China, 2012.
55. Pei, Y.; Liu, B.; Lian, Y.; Liu, C.; Xie, Q. Marine high resolution multi-channel digital seismic streamer and its application in the ocean engineering. *Prog. Geophys.* **2013**, *28*, 3280–3286. [[CrossRef](#)]
56. Hao, X.; Zhao, Q.; Pei, Y. Large-energy plasma source for gas hydrate exploration. *J. Trop. Oceanogr.* **2017**, *36*, 35–40. [[CrossRef](#)]
57. Liu, Z.; Guan, X.; Zhang, L.; Zhang, Y.; Pei, Y.; Liu, C.; Zhou, H.; Liu, B.; Yan, K. Investigations of dynamics of a single spark-induced bubble in saline water. *J. Phys. D Appl. Phys.* **2021**, *54*, 075203. [[CrossRef](#)]
58. Xu, H.; Yang, S.; Zheng, X.; Wang, M.; Wang, J. Seismic identification of gas hydrate and its distribution in Shenhu area, South China Sea. *Chin. J. Geophys.* **2010**, *53*, 1691–1698. [[CrossRef](#)]
59. Parkinson, R. *High Resolution Site Surveys*; CRC Press: London, UK, 2000.
60. Huang, Y.; Zhang, L.; Zhang, X.; Liu, Z.; Yan, K. The plasma-containing bubble behavior under pulsed discharge of different polarities. *IEEE Trans. Plasma Sci.* **2014**, *43*, 567–571. [[CrossRef](#)]
61. Huang, Y.; Zhang, L.; Yan, H.; Zhu, X.; Liu, Z.; Yan, K. Experimental study of the electric pulse-width effect on the acoustic pulse of a plasma sparker. *IEEE J. Ocean. Eng.* **2016**, *41*, 724–730. [[CrossRef](#)]
62. Pei, Y.; Zhang, L.; Huang, Y.; Yan, H.; Zhu, X.; Liu, Z.; Yan, K.P. Discharge electrode configuration effects on the performance of a plasma sparker. *Plasma Sci. Technol.* **2017**, *19*, 095401. [[CrossRef](#)]
63. Pei, Y.; Kan, G.; Zhang, L.; Huang, Y.; Liu, Z.; Liu, B.; Yan, K. Characteristics of source wavelets generated by two sparkers. *J. Appl. Geophys.* **2019**, *170*, 103819. [[CrossRef](#)]

Disclaimer/Publisher's Note: The statements, opinions and data contained in all publications are solely those of the individual author(s) and contributor(s) and not of MDPI and/or the editor(s). MDPI and/or the editor(s) disclaim responsibility for any injury to people or property resulting from any ideas, methods, instructions or products referred to in the content.

Article

Sediment Waves on the Western Slope of the Chukchi Rise (Arctic Ocean) and Their Implications for the Paleoenvironment

Qingfeng Hua ¹, Guanbao Li ^{1,2,*}, Qingjie Zhou ¹, Shujiang Li ³, Tengfei Xu ³, Baohua Liu ^{2,4} and Hongxia Chen ³

¹ Key Laboratory of Marine Geology and Metallogeny, First Institute of Oceanography, Ministry of Natural Resources, Qingdao 266061, China

² Qingdao National Laboratory for Marine Science and Technology, No. 1 Wenhai Road, Jimo City, Qingdao 266237, China

³ Key Laboratory of Marine Science and Numerical Modeling, First Institute of Oceanography, Ministry of Natural Resources, Qingdao 266061, China

⁴ National Deep Sea Center, Ministry of Natural Resources, No. 1 Weiyang Road, Jimo City, Qingdao 266237, China

* Correspondence: gbli@fio.org.cn

Abstract: Based on multibeam bathymetric data and high-resolution shallow sub-bottom profiles acquired during China's 10th Arctic Scientific Expedition Cruise in 2019, a sediment wave field was found on the western slope of the Chukchi Rise, in the Arctic Ocean. This sediment wave field developed on the lower slope with water depths of between 1200 m and 1800 m and stretched 15 km in the downslope direction. It comprised several parallel sediment waves, with wavelengths ranging from 700 m to 3400 m and wave heights from 12 m to 70 m. In the vertical direction, well-stratified deposits, tens of meters thick, were affected by sediment waves, which exhibit asymmetric waveforms and upslope migration trends. The morphological and seismostratigraphic characteristics of the sediment waves suggested their genesis as a result of the interaction between the bottom current and seafloor morphology, which was also supported by hydrographical data adjacent to the sediment wave field. It was inferred that this bottom current was related to the Arctic Circumpolar Boundary Current, which many researchers suggest flows through the study area.

Keywords: seafloor bedform; multibeam bathymetry; sub-bottom profile; bottom current

Citation: Hua, Q.; Li, G.; Zhou, Q.; Li, S.; Xu, T.; Liu, B.; Chen, H. Sediment Waves on the Western Slope of the Chukchi Rise (Arctic Ocean) and Their Implications for the Paleoenvironment. *J. Mar. Sci. Eng.* **2022**, *10*, 1586. <https://doi.org/10.3390/jmse10111586>

Academic Editor: George Kontakiotis

Received: 7 September 2022

Accepted: 19 October 2022

Published: 26 October 2022

Publisher's Note: MDPI stays neutral with regard to jurisdictional claims in published maps and institutional affiliations.



Copyright: © 2022 by the authors. Licensee MDPI, Basel, Switzerland. This article is an open access article distributed under the terms and conditions of the Creative Commons Attribution (CC BY) license (<https://creativecommons.org/licenses/by/4.0/>).

1. Introduction

A sediment wave is defined as a large-scale (generally between tens of meters and a few kilometers long and several meters high), undulating, depositional bedform that is generated beneath a current flowing at, or close to, the seafloor [1]. The wave-forming current can either be a contour current or a turbidity current in the deep ocean [1–3]. Sediment wave formation, which often takes hundreds to thousands of years, represents the long-term response of sedimentation processes to environmental conditions [4], thereby influencing thick strata below the seabed [5]. As such, sediment waves are often clearly displayed on the seabed topography and on shallow strata, and they can be effectively identified using modern technology, such as multibeam bathymetry, sub-bottom profiles, and side-scan sonar. Based on the features of sediment waves in plain view and of vertical stacking patterns, in combination with regional settings, the characteristics of the wave-forming bottom current can be determined [1,6,7] and important information on the modern and palaeoceanographic environment and dynamic processes can be obtained [3]. Most sediment waves are found in deep-sea areas in middle and low latitudes [2,3,7], where research investment is greatest; in higher-latitude sea areas, the sediment waves are mainly found around Antarctica [8–10]. In recent years, sediment waves have also been found in some regions around the Arctic, such as the Nordic Seas [11], the Faroe Islands [12,13], off the coast of Greenland [14], and in the Canadian Basin [15].

Multibeam bathymetry and sub-bottom profile data obtained from China’s 10th Arctic Scientific Expedition in 2019 at the protrusion of the western continental slope of the Chukchi Rise (Figure 1b) revealed a sediment wave field [16]. In the same period, scholars from Korea also found evidence of the presence of sediment waves in this area [17], but they did not conduct an in-depth analysis of their characteristics. Considering the unique position of the Chukchi Borderland in the Arctic flow field [18–20], studying these sediment waves should aid our understanding of the characteristics of the bottom current, thereby providing useful information on the Arctic Ocean environment.

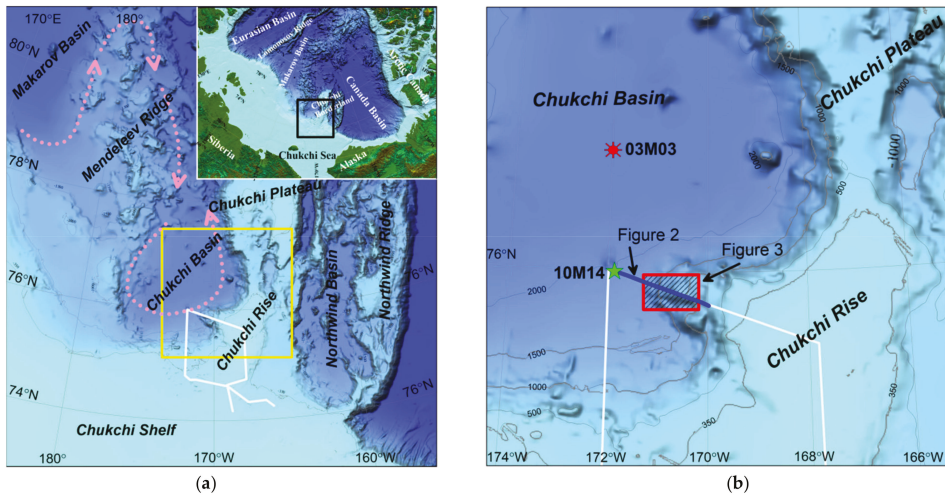


Figure 1. Bathymetric chart of the Chukchi Borderland and its neighboring areas (a) and a zoomed-in image of the study area (within the yellow box in Figure 1a) (b). The inset indicates the location (black box) of Figure 1a in the Arctic region. Pink dotted lines with arrows represent the speculated pathway of the Arctic Circumpolar Boundary Current (according to [19,20]). White solid lines mark the research vessel’s track during China’s 10th Arctic Scientific Expedition in 2019. The blue solid line indicates the location of Figure 2, and the red shaded area identifies the location of Figure 3a, where the sediment waves were found. The green star (10M14) and red point (03M03) mark the locations of the lowered ADCP site and gravity sediment core, respectively, which are mentioned below.

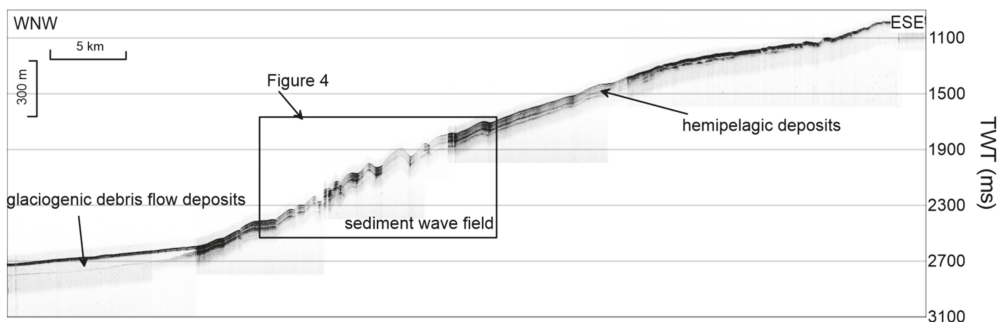


Figure 2. Sub-bottom profile across the western slope of the Chukchi Rise (see Figure 1b for its location). The vertical axis is the two-way travel time (TWT) in milliseconds, and the depth scale in meters is estimated at a sound speed of 1500 m/s. The location of Figure 4 is also shown.

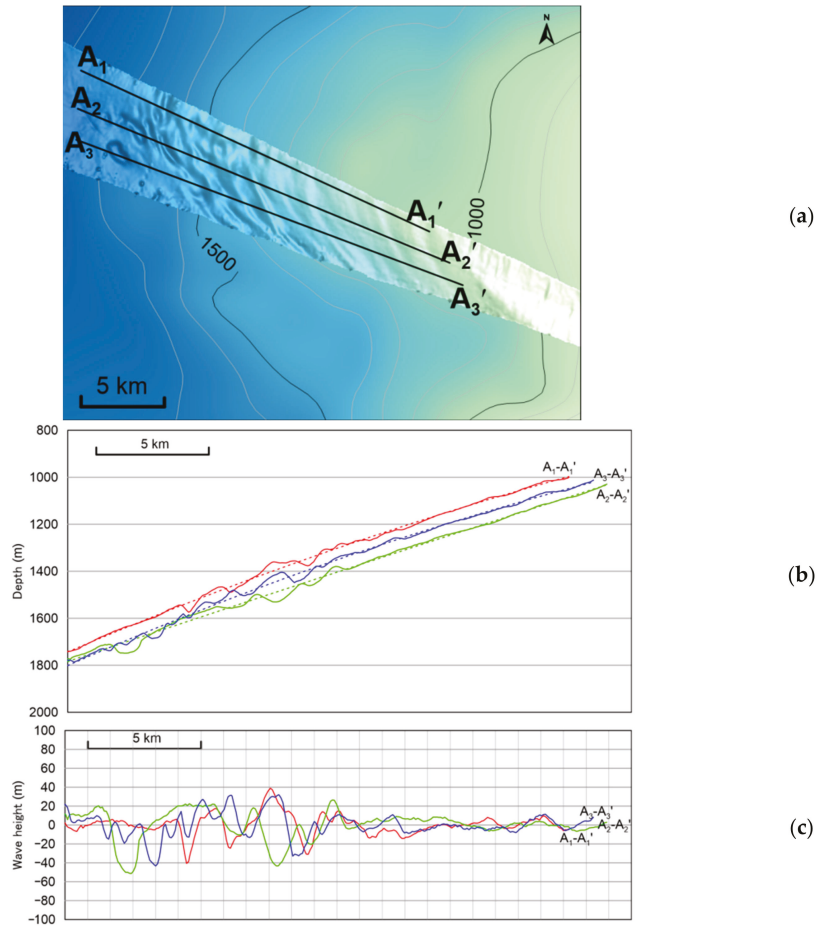


Figure 3. Sediment waves on the multibeam bathymetric map and the locations of the water depth sections used to measure the wavelengths and the wave heights (a). Water depth changes (solid lines) along the three sections identified in (a); the dotted lines represent water depths obtained by polynomial fitting, which indicate the trend of the water depth changes along the continental slope (b). The real undulations of the sediment waves along the sections, i.e., the differences between water depths and their fitting values (c).

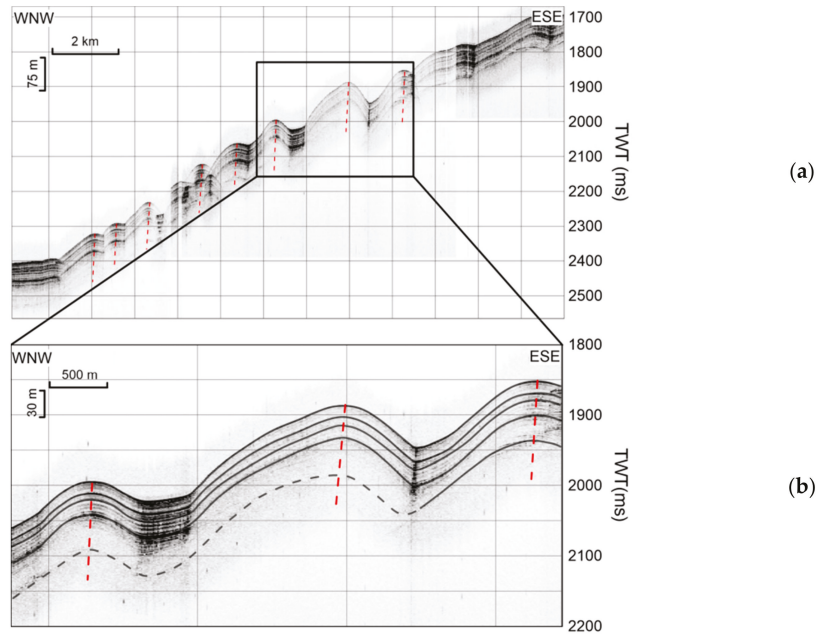


Figure 4. Sediment wave field shown on the sub-bottom profile (a) and a zoomed-in image of the rectangular area (b). The location is shown in Figure 2. The red dashed lines show the connecting lines of the wave crest for each internal reflector. The vertical axis is the two-way travel time (TWT) in milliseconds, and the depth scale in meters is estimated at 1500 m/s sound speed.

2. Regional Settings

The study area is located at the junction of the Chukchi Borderland and the Chukchi Shelf, in the western Arctic Ocean. The Chukchi Borderland is a large underwater platform extending northward from the Chukchi Shelf into the Amerasian Basin and comprises four geomorphological units: the Chukchi Rise, the Chukchi Plateau, the Northwind Ridge, and the Northwind Basin (Figure 1a). The water depth here changes drastically, ranging from less than 300 m in the Chukchi Rise and the Chukchi Plateau to nearly 3000 m in the Northwind Basin [21]. The Chukchi Rise is adjacent to two deep-water basins, the Northwind Basin in the east and the Chukchi Basin in the west, and is connected in the north to the Chukchi Plateau through a narrow, saddle-shaped underwater depression. The rise is roughly triangular, but, in the middle, a spur-like protrusion extends westward into the Chukchi Basin, forming “W”-shaped contour lines on the continental slope between the Chukchi Rise and the Chukchi Basin (Figure 1b).

The Chukchi Rise developed the Cenozoic strata which is several-hundred-meters-thick and multiple sets of progradational sequences formed from the Oligocene to the Pliocene [22,23]. Glacial sedimentation became dominant in this area during some period of the Quaternary. Many plow marks and mega-scale glacial lineations caused by ice-grounding developed across the shelf breaks. Multistage glaciogenic debris-flow deposits formed on the continental slope and the bottom of the slope, buried by tens of meters of thick hemipelagic deposits [24–29].

The oceanographic environment in the study area is heavily influenced by the anti-cyclonic Beaufort Gyre circulation at the surface, while Pacific and Atlantic water inputs contribute to the intermediate and deep-water masses [18–20]. The Atlantic water, which constitutes the bottom current of the Arctic Circumpolar Boundary Current, may reach

the Chukchi Borderland after crossing the Mendeleev Ridge and the southern slope of the Chukchi Basin, extending to 1000 m and below, as proposed by Woodgate et al. [30].

3. Methods

In China's 10th Arctic Scientific Expedition, the research vessel "Xiangyanghong 01" was used to conduct geophysical, geological and hydrological surveys on the southwestern Chukchi Rise and the adjacent Chukchi Basin and Chukchi Shelf (Figure 1a). A hull-mounted multibeam bathymetry system and a sub-bottom profiling system were used to obtain more than 700 km of high-resolution data, revealing the seabed topography and shallow seismostratigraphic structure along the route.

3.1. Multibeam Bathymetry

Seabed topography was measured using a Wärsilä ELAC SeaBeam 3012 full-ocean-deep multibeam echo-sounder system. The water depth of the working area ranged from 80 to 2500 m, of which the beam coverage width was approximately 3–3.5 times the water depth when the water depth was shallower than 1000 m and approximately 3.5–4 times the water depth when the water depth exceeded 1000 m. During the voyage, an AML Minos series sound velocity profiler was used to acquire the vertical variation in the seawater sound velocity. Caris software was used to perform multibeam data processing and corrections according to the standard workflow, which included parameter correction, navigation data editing, water-depth point-noise editing, tide level correction, and sound speed correction. Then, a built-in combined uncertainty and bathymetry estimator (CUBE) multibeam automatic processing tool was used to construct the CUBE surface and multibeam grid data with a grid spacing of 20 m.

3.2. Sub-Bottom Profiling

A hull-mounted Kongsberg TOPAS PS18 parametric sub-bottom profiler system, which has a high spatial resolution in water depths between less than 20 m and full ocean depth, was used for shallow stratum detection. This system transmits frequency modulation (FM) signals with a frequency band of 2–6 kHz and acquires the returned signals with a sampling rate of 36 kHz and record length of 800 ms. The seabed was tracked automatically according to the water depth input from the multibeam system, and the acquisition delay was adjusted accordingly. Then, the SEG Y format record was processed by TRITON software for filtering, automatic gain, reflection interface tracking, and digitization. Because of the lack of sound velocity data on the seabed strata in the study area, a sound velocity of 1500 m/s was used for travel time–depth conversion of the sub-bottom profile, as proposed previously by other authors [24,28]. The penetration depth of the sub-bottom profile ranged from 10 to 80 m, depending mainly on the regional seabed undulation and sediment type. At the top of the Chukchi Rise and the upper part of the neighboring continental slope, the penetration depth was less than 20 m, while on the lower continental slope, where the sediment wave field was located, the penetration depth exceeded 50 m (Figure 2).

3.3. Hydrological Measurement

The hydrographical data (Figure 5) were collected at site 10M14 (171°57.37' W, 70°01.89' N, see Figure 1b for location), including lowered acoustic Doppler current profiling (LADCP) and conductivity–temperature–depth (CTD) measurement. The full-depth current profile was obtained by Teledyne RDI Workhorse Sentinel self-contained 300 kHz LADCP. The seawater pressure, in situ temperature, and salinity were measured using a Seabird SBE 911 Plus CTD. The LADCP was bound on the frame of the CTD system, and was lowered down to a depth near the seabed. The "LDEO Implementation" of the velocity-inversion method [31] was used for processing the LADCP data, and the CTD time-series data were included as input parameters; then, the eastward and northward components of the horizontal velocity of the current could be figured out.

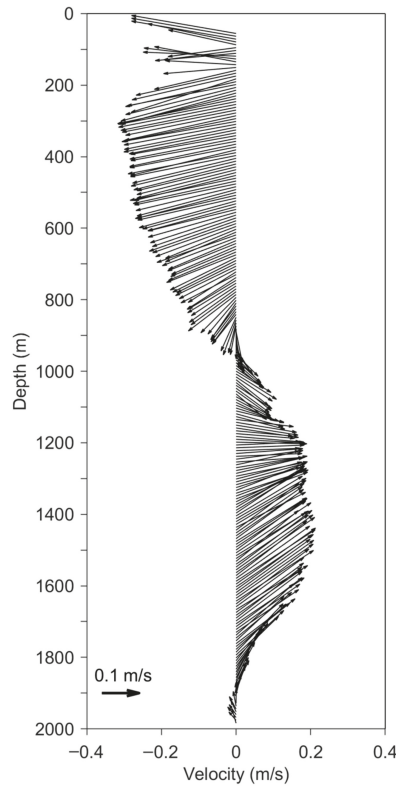


Figure 5. The vertical profile of sea water velocity measured by LADCP at site 10M14 (see Figure 1b for its location). The upward and rightward vectors indicate northward and eastward currents, respectively. The length of each vector gives the magnitude of the current.

4. Results

4.1. Echo Character Type and Distribution along the Slope

In Figure 2, the sub-bottom profiling data show the stratal geometries, internal structure, stacking patterns, and sequence relationships of the uppermost tens of meters of thick deposits on the middle–lower slope of the Chukchi Rise within a water depth range of approximately 700–2000 m. Along this profile, the slope break occurs at a water depth of approximately 450 m, according to multibeam bathymetry data [16]. Downward from the slope break, until approximately 900 m depth (TWT 1200 ms), deposits less than 30 m-thick were captured by a sub-bottom profiler. The acoustically stratified reflection, with strong, continuous, and subparallel internal reflectors, became increasingly thin toward the slope break and finally pinched out. Below a 900 m depth, a thicker acoustically stratified reflection was shown. The internal reflectors became weaker, and severe undulation was found at the lower slope. At the bottom of the slope, a transparent reflection was observed. It wedges into the stratified reflection at the slope and then away from the slope, and its thickness becomes gradually constant, to approximately 50 m.

4.2. Location, Morphology, and Acoustic Structure of Sediment Waves

4.2.1. Geomorphic Features

The wavy bedforms are located on the middle and lower parts of the continental slope at a water depth of 1200–1800 m; the largest one occurs at about 1500 m (Figure 3a,b). The incline of the slope is approximately 1.8–1.9°. On the bathymetric map, the sediment

wave field is shown as a series of alternating ridges and gullies, or some locally closed depressions. In addition, the wave field span exceeds 15 km in range; the single sediment wave crest forms a linear or crescent shape on the plane, which is generally oblique to the contour at a small angle (Figure 3a). The wavelength and wave height parameters of the sediment waves were calculated along three water depth sections, as shown in Figure 3a. To eliminate the influence of the slope incline, the average water depth along the continental slope was calculated using a polynomial fitting method and subtracted from the measured water depth (Figure 3b). The results indicate that the wavelength is between 700 m and 3400 m, and the wave height is between 12 m and 70 m (Figure 3c); therefore, it is a so-called large-scale sediment wave [1,7]. The wave in the middle of the field has the largest wavelength and height in the direction perpendicular to the continental slope, which gradually decreases toward both sides (Figure 3c). Moreover, the wavelength and wave height vary along the direction of the sediment wave. The wave crest length exceeds the beam width of the multibeam echo sounder, which measures about 5 km in the wave field.

4.2.2. Seismostratigraphic Features

The wavy bedforms correspond to continuous wave-like bending of the well-stratified seismic reflector below the seabed within the thickness visible in the sub-bottom profile (Figure 4a). The sedimentary layer affected by these waves maintains the original good stratification, with moderate–weak internal reflectors and nearly transparent, constant-thickness layers within them. Most of the reflectors can be continuously traced along the adjacent waves. The wave shape is laterally variable but mostly shows asymmetrical waveforms, of which the upslope wing has a larger inclination and thickness than the downslope wing (Figure 4b). The line connecting the wave crests of each reflection interface of the waves is slightly inclined downslope, indicating a characteristic of upslope migration (Figure 4a,b). For the whole wave field, the waveform asymmetry on both sides of the field is higher than that at the center, whereas the wave height is larger at the center than on both sides.

4.3. Current Velocity Profile at Site 10M14

Figure 5 shows the horizontal velocity profile observed by the LADCP at 10M14, a site near the bottom of the continental slope, approximately 15 km away from the wave field. Strikingly, different current direction was observed in the upper and lower parts of the seawater. There are westward currents in the upper 800 m, with a maximum velocity speed of approximately 0.33 m/s, whereas eastward and northeastward currents in the intermediate (800–1300 m) and deep (1300–2000 m) layers have maximum velocity speeds of approximately 0.22 and 0.26 m/s, respectively.

5. Discussion

5.1. Sediment Wave Formation

The wavy bedforms observed in the spur-like protrusion of the continental slope were interpreted as sediment waves, according to its planar and vertical characteristics in multibeam bathymetry and the sub-bottom profile [1,7]. The more widely distributed multibeam survey lines revealed that sediment waves spread all over the slope of the protrusion, and their wave crest lengths mostly exceeded 5 km [17].

Sediment waves can be formed by contour currents flowing laterally along the slope or turbidity currents flowing down the slope. To distinguish between the sediment waves formed by these two processes, five criteria, including wave regularity, wave crest alignment, sequence thickness, sediment type, and regional setting, were proposed by Wynn and Stow [1].

In terms of wave regularity, each sediment wave under consideration has an asymmetrical waveform, the wave height and length decrease from the middle of the wave field to both sides, and the waves show a trend of upslope migration, which are all typical features

of sediment waves due to contour currents. In contrast, the dimensions of sediment waves with turbidity current origins tend to decrease gradually downward along the slope. In terms of the wave crest shape and alignment, the crest of the sediment waves in question is slightly crescent-shaped and aligned obliquely to the contour at a small angle, while the crest of turbidity current sediment waves is relatively straight in most cases, and the direction is mostly parallel to the contour. For the sequence thickness, sediment waves with turbidity current origins generally decrease progressively downslope as they move from the provenance area, with the reduction range reaching 40–60% [1]. In contrast, the sequence thickness affected by the sediment wave here is almost unchanged down the continental slope, showing a key feature of contour current sediment waves.

For the sediment type, although no sediment samples were collected on the sediment wave field in this cruise, some lithostratigraphic and seismostratigraphic studies in the Chukchi–East Siberian margin seem to support the idea that the well-stratified deposits forming sediment waves are mainly composed of fine-grained or sandy mud [17,32–34]. Similar acoustical characteristics to the study area were observed on the Chukchi–East Siberian margin and the Chukchi Basin [17,24,25,28]. The acoustically stratified reflection with subparallel internal reflectors might be correlated with the fine-grained–sandy muds revealed by lithostratigraphic studies [32–34]. The internal weak reflectors were interpreted as poorly sorted sandy muds with lower concentrations of iceberg-rafted debris, and the outermost constant thickness layers within internal reflectors were interpreted through fine-grained muds deposited in a hemipelagic environment [17,24]. The acoustically transparent reflection at the slope bottom indicates homogeneous sediments without internal bedding, which was interpreted thanks to the fast sedimentation of glaciogenic debris flow [17,28].

Regarding the regional setting, sediment waves formed by turbidity currents are mostly located in some confined environments, such as the levees of submarine canyons or on channel mouths. In contrast, sediment waves formed by contour currents, especially large-scale sediment waves, mostly develop in the lower part of the unconfined slope, as revealed by the multibeam bathymetric data discussed here and that of Kim et al. [17].

The above analysis indicates that the sediment waves in the study area may have been formed by contour currents as a result of the interaction between the seabed and bottom currents flowing laterally along the continental slope. The hydrological data (Figure 5) collected at site 10M14 adjacent to the wave field (Figure 1b) also support the contour current genesis. The strong and stable bottom current at water depths between 1200 m and 1800 m would subsequently contribute to the wavy bottom topography observed in the study area.

The source and route of this bottom current are still unknown. The LADCP observed currents in the deep layer are in agreement with the previously identified boundary current that transports Atlantic waters into the Arctic [35]. According to hydrographical and tracer studies, Woodgate et al. [20,30,36] proposed that the Atlantic water that constitutes the bottom current of the Arctic Circumpolar Boundary Current may flow along the southern slope of the Chukchi Basin after crossing the Mendeleev Ridge and then flow eastward to the Chukchi Borderland. This point is also supported by numerical simulation results [19,37]. The Arctic Circumpolar Boundary Current is roughly distributed along the continental slope in the Chukchi Basin, and the center of the current is located between 1000 and 2000 m in depth [30,36], which is essentially consistent with the depth range of the sediment waves observed in our study. Therefore, seemingly reasonable inference is that the formation of these sediment waves is related to the occurrence of the Arctic Circumpolar Boundary Current. However, this hypothesis is still far from being confirmed, and more hydrological observations will be necessary.

5.2. Implication for the Palaeoceanographic Environment

Sediment waves are often formed by long-term interactions between the bottom current and the seabed [4]. Kim et al. [17] interpreted the sediment waves on the slope of the western spur as “buried”, meaning that they formed before the hemipelagic drape was

deposited. The sediment waves developed in the study area are obvious on the seabed topography map and affect the distribution of surficial deposits, which might indicate that they are still active. A statistical analysis of modern sediment waves reveals that the two parameters of wavelength and wave height offer a good reflection on the formation environment of sediment waves [7]. A logarithmic plot of the wavelength versus the wave height of the sediment waves in the study area (Figure 6) reveals that they belong to the nominal large-scale sediment waves with mixed relief, corresponding to the unconfined continental slope environment and fine-grained sediment formed by the weak contour current with linear stratification [7]. According to the bedform–velocity matrix [6], these mud waves correspond to a flow rate of approximately 0.1–0.2 m/s, a little lower than the sea water velocity at site 10M14 within same depth range measured by LADCP (Figure 5). The reason might be that the wave field is located more than 15 km away from site 10M14, and that the bottom current velocity is variable laterally.

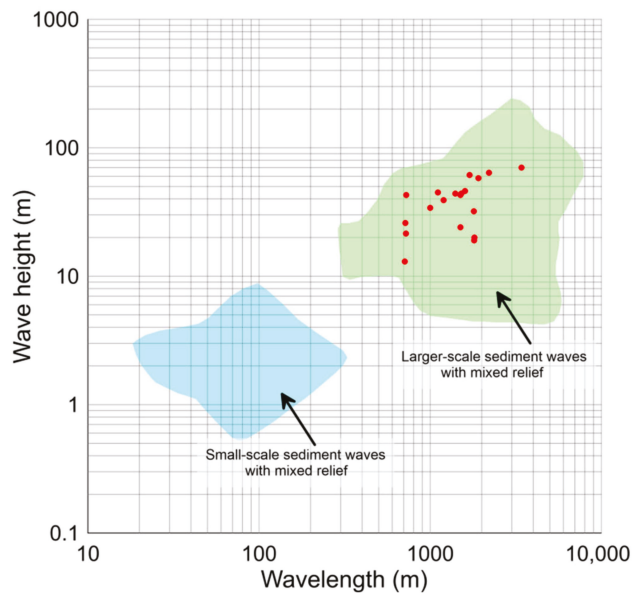


Figure 6. Logarithmic plot of wavelength versus wave height for the bedforms in Figure 3a. The red dots represent the waves used for statistics in Figure 3c. The two areas indicating the sediment wave types were obtained from [7].

Because of the limited penetration of sub-bottom profiling, the maximum strata thickness affected by sediment waves cannot be captured. Within the discernible depth of the sub-bottom profile, the sedimentary layers show continuous wave-like curvature from top to bottom, indicating that the bottom currents forming the sediment wave field have long-term effects on the sedimentary environment of the continental slope. The subparallel characteristics of internal reflectors also imply that the velocity and direction of the bottom current have been relatively stable for many years. The thickness of the strata affected by the sediment wave is over 50 m on the sub-bottom profile (Figure 4). The existing drilling cores in the adjacent Chukchi Basin (such as core 03M03 [31] in Figure 1b) reveal that the sedimentation rate is approximately several centimeters per thousand years since marine oxygen isotope stage 5 (MIS5) [27,29,32,34]. Therefore, we can infer that this set of sedimentary layers was formed over hundreds of thousands of years, indicating that sediment wave formation seems to date back to the Middle Pleistocene, when the glaciation began on the edge of the East Siberian Shelf as proposed by Niessen et al. [24].

6. Conclusions

A sediment wave field that developed on the western slope of the Chukchi Rise was identified using high-resolution multibeam bathymetry and shallow sub-bottom profile data obtained during China's 10th Arctic Scientific Expedition. By analyzing the planar and sectional characteristics of the sediment wave field, the following conclusions were drawn:

- (1) These sediment waves are formed by contour currents and result from the interaction between continental slope bottom currents and the seabed;
- (2) The sediment waves are still active, and their formation seems to date back to the Middle Pleistocene;
- (3) Sediment waves are formed by a bottom current, which may be genetically related to the Arctic Circumpolar Boundary Current flowing through the study area.

Author Contributions: Conceptualization, G.L. and B.L.; methodology, Q.Z. and Q.H.; validation, G.L., Q.H. and T.X.; formal analysis, S.L.; investigation, G.L., Q.Z., T.X. and H.C.; resources, T.X.; data curation, H.C.; writing—original draft preparation, Q.H.; writing—review and editing, G.L., S.L. and B.L.; visualization, Q.Z. and T.X.; supervision, B.L.; project administration, B.L.; funding acquisition, G.L. All authors have read and agreed to the published version of the manuscript.

Funding: This study was supported by the Wenhai Program of the S&T Fund of Shandong Province for Pilot National Laboratory for Marine Science and Technology (Qingdao) (No. 2021 WHZZB0702), the National Natural Science Foundation of China under contract Nos. 42076082 and 42176191, National Key R&D Program of China (2021YFF0501200 and 2021YFF05012001), and the Taishan Scholar Project Funding under contract No. tspd20161007.

Institutional Review Board Statement: Not applicable.

Informed Consent Statement: Not applicable.

Data Availability Statement: Not applicable.

Acknowledgments: Data acquisition was supported by the China's 10th Arctic Scientific Expedition Cruise. The authors thank Zexun Wei and crew of R/V Xiangyanghong 01 for their assistance in field data acquisition. The authors also thank three anonymous reviewers, whose comments greatly improved this manuscript.

Conflicts of Interest: The authors declare no conflict of interest.

References

1. Wynn, R.B.; Stow, D.A.V. Classification and characterisation of deep-water sediment waves. *Mar. Geol.* **2002**, *192*, 7–22. [[CrossRef](#)]
2. Wynn, R.B.; Weaver, P.P.E.; Ercilla, G.; Stow, D.A.V.; Masson, D.G. Sedimentary processes in the Selvage sediment-wave field, NE Atlantic: New insights into the formation of sediment waves by turbidity currents. *Sedimentology* **2000**, *47*, 1181–1197. [[CrossRef](#)]
3. Rebesco, M.; Hernández-Molina, F.J.; Rooij, D.V.; Wåhlin, A. Contourites and associated sediments controlled by deep-water circulation processes: State-of-the-art and future considerations. *Mar. Geol.* **2014**, *352*, 111–154. [[CrossRef](#)]
4. Flood, R.; Shor, A. Mud waves in the argentine basin and their relationship to regional bottom circulation patterns. *Deep Sea Res. Part A Oceanogr. Res. Pap.* **1988**, *35*, 943–971. [[CrossRef](#)]
5. Gong, C.; Wang, Y.; Peng, X.; Li, W.; Qiu, Y.; Xu, S. Sediment waves on the South China Sea Slope off southwestern Taiwan: Implications for the intrusion of the Northern Pacific deep water into the South China Sea. *Mar. Pet. Geol.* **2012**, *32*, 95–109. [[CrossRef](#)]
6. Stow, D.A.V.; Hernández-Molina, F.J.; Llave, E.; Sayago-Gil, M.; Diaz-del Rio, V.; Branson, A. Bedform-velocity matrix: The estimation of bottom current velocity from bedform observations. *Geology* **2009**, *37*, 327–330. [[CrossRef](#)]
7. Symons, W.O.; Sumner, E.J.; Talling, P.J.; Cartigny, M.J.B.; Clare, M.A. Large-scale sediment waves and scours on the modern seafloor and their implications for the prevalence of supercritical flows. *Mar. Geol.* **2016**, *371*, 130–148. [[CrossRef](#)]
8. Maldonado, A.; Barnolas, A.; Bohoyo, F.; Galindo-Zaldivar, A.; Hernandez-Molina, F.J.; Lobo, F.; Rodriguez-Fernandez, J.; Somoza, L.; Vazquez, J.T. Contourite deposits in the central Scotia Sea: The importance of the Antarctic Circumpolar Current and the Weddell Gyre flows. *Palaeogeogr. Palaeoclimatol. Palaeoecol.* **2003**, *198*, 187–221. [[CrossRef](#)]
9. Maldonado, A.; Bohoyo, F.; Galindo-Zaldivar, J.; Hernández-Molina, F.J.; Jabaloy, A.; Lobo, F.J.; Rodríguez-Fernández, J.; Suriñach, E.; Vázquez, J.T. Ocean basins near the Scotia-Antarctic plate boundary: Influence of tectonics and paleoceanography on the Cenozoic deposits. *Mar. Geophys. Res.* **2006**, *27*, 83–107. [[CrossRef](#)]
10. Koenitz, D.; White, N.; McCave, I.N.; Hobbs, R. Internal structure of a contourite drift generated by the Antarctic Circumpolar Current. *Geochem. Geophys. Geosy.* **2008**, *9*, Q06012. [[CrossRef](#)]

11. Laberg, J.S.; Baeten, N.J.; Forwick, M.; Wiberg, D.H. Ocean-current controlled sedimentation: The Lofoten Contourite Drift, Norwegian Sea. In *Atlas of Submarine Glacial Landforms: Modern, Quaternary and Ancient*; Dowdeswell, J.A., Canals, M., Jakobsson, M., Todd, B.J., Dowdeswell, E.K., Hogan, K.A., Eds.; Geological Society: London, UK, 2016; Volume 46, pp. 395–396.
12. Masson, D.G.; Plets, R.M.K.; Huvenne, V.A.L.; Wynn, R.B.; Bett, B.J. Sedimentology and depositional history of Holocene sandy contourites on the lower slope of the Faroe-Shetland Channel, northwest of the UK. *Mar. Geol.* **2010**, *268*, 85–96. [[CrossRef](#)]
13. Masson, D.G.; Howe, J.A.; Stoker, M.S. Bottom current sediment waves, sediment drifts and contourites in the northern Rockall Trough. *Mar. Geol.* **2002**, *192*, 215–237. [[CrossRef](#)]
14. García, M.; Batchelor, C.L.; Dowdeswell, J.A.; Hogan, K.A.; Cofaigh, C.Ó. A glacier-influenced turbidite system and associated landform assemblage in the Greenland Basin and adjacent continental slope. In *Atlas of Submarine Glacial Landforms: Modern, Quaternary and Ancient*; Dowdeswell, J.A., Canals, M., Jakobsson, M., Todd, B.J., Dowdeswell, E.K., Hogan, K.A., Eds.; Geological Society: London, UK, 2016; Volume 46, pp. 461–468.
15. Mosher, D.C.; Boggild, K. Impact of bottom currents on deep water sedimentary processes of Canada Basin, Arctic Ocean. *Earth Planet. Sci. Lett.* **2021**, *569*, 117067. [[CrossRef](#)]
16. Li, G.B.; Zhou, Q.J.; Hua, Q.F.; Wang, J.Q.; Liu, C.G.; Liu, B.H. Characteristics of the shallow strata structure on the northern margin of the Chukchi Sea and its significance on palaeo-glaciation. *Adv. Mar. Sci.* **2021**, *39*, 393–402. (In Chinese)
17. Kim, S.; Polyak, L.; Joe, Y.J.; Niessen, F.; Kim, H.J.; Choi, Y.; Kang, S.-G.; Hong, J.K.; Nam, S.-I.; Jin, Y.K. Seismostratigraphic and geomorphic evidence for the glacial history of the northwestern Chukchi margin, Arctic Ocean. *J. Geophys. Res. Earth Surf.* **2021**, *126*, e2020JF006030. [[CrossRef](#)]
18. Rudels, B.; Friedrich, H.J.; Quadfasel, D. The Arctic circumpolar boundary current. *Deep-Sea Res. II Top. Stud. Oceanogr.* **1999**, *46*, 1023–1062. [[CrossRef](#)]
19. Aksenov, Y.; Ivanov, V.V.; Nurser, A.J.G.; Bacon, S.; Polyakov, I.V.; Coward, A.C.; Naveira-Garabato, A.C.; Beszczynska-Moeller, A. The Arctic circumpolar boundary current. *J. Geophys. Res. Oceans.* **2011**, *116*, C09017. [[CrossRef](#)]
20. Woodgate, R.A. Arctic Ocean circulation: Going around at the top of the world. *Nat. Educ. Knowl.* **2013**, *4*, 1–15.
21. Jakobsson, M.; Mayer, L.; Coakley, B.; Dowdeswell, J.A.; Forbes, S.; Fridman, B.; Hodnesdal, H.; Noormets, R.; Pedersen, R.; Rebecco, M.; et al. The International Bathymetric Chart of the Arctic Ocean Version 4.0. *Sci. Data* **2020**, *7*, 176. [[CrossRef](#)]
22. Hegewald, A.; Jokat, W. Tectonic and sedimentary structures in the northern Chukchi region, Arctic Ocean. *J. Geophys. Res. Solid Earth* **2013**, *118*, 3285–3296. [[CrossRef](#)]
23. Hegewald, A.; Jokat, W. Relative sea level variations in the Chukchi region—Arctic Ocean—Since the late Eocene. *Geophys. Res. Lett.* **2013**, *40*, 803–807. [[CrossRef](#)]
24. Niessen, F.; Hong, J.K.; Hegewald, A.; Matthiessen, J.; Stein, R.; Kim, H.; Kim, S.; Jensen, L.; Jokat, W.; Nam, S.-I.; et al. Repeated Pleistocene glaciation of the East Siberian continental margin. *Nat. Geosci.* **2013**, *6*, 842–846. [[CrossRef](#)]
25. Dove, D.; Polyak, L.; Coakley, B. Widespread, multi-source glacial erosion on the Chukchi margin, Arctic Ocean. *Quat. Sci. Rev.* **2014**, *92*, 112–122. [[CrossRef](#)]
26. Jakobsson, M.; Andreassen, K.; Bjarnadóttir, L.R.; Dove, D.; Dowdeswell, J.A.; England, J.H.; Funder, S.; Hogan, K.; Ingólfsson, Ó.; Jennings, A.; et al. Arctic Ocean glacial history. *Quat. Sci. Rev.* **2014**, *92*, 40–67. [[CrossRef](#)]
27. Schreck, M.; Nam, S.-I.; Polyak, L.; Vogt, C.; Kong, G.-S.; Stein, R.; Matthiessen, J.; Niessen, F. Improved Pleistocene sediment stratigraphy and paleoenvironmental implications for the western Arctic Ocean off the East Siberian and Chukchi margins. *Arktos* **2018**, *4*, 1–20. [[CrossRef](#)]
28. O'Regan, M.; Backman, J.; Barrientos, N.; Cronin, T.M.; Gemery, L.; Kirchner, N.; Mayer, L.A.; Nilsson, J.; Noormets, R.; Pearce, C.; et al. The De Long Trough: A newly discovered glacial trough on the East Siberian continental margin. *Clim. Past* **2017**, *13*, 1269–1284. [[CrossRef](#)]
29. Stein, R.; Matthiessen, J.; Niessen, F.; Krylov, R.; Nam, S.; Bazhenova, E. Towards a better (Litho-) stratigraphy and reconstruction of Quaternary Paleoenvironment in the Amerasian Basin (Arctic Ocean). *Polarforschung* **2010**, *79*, 97–121.
30. Woodgate, R.A.; Aagaard, K.; Swift, J.H.; Smethie, W.M., Jr.; Falkner, K.K. Atlantic water circulation over the Mendeleev Ridge and Chukchi Borderland from thermohaline intrusions and water mass properties. *J. Geophys. Res.* **2007**, *112*, C02005. [[CrossRef](#)]
31. Visbeck, M. Deep velocity profiling using lowered acoustic Doppler current profilers: Bottom track and inverse solutions. *J. Atmos. Ocean. Tech.* **2002**, *19*, 794–807. [[CrossRef](#)]
32. Wang, R.; Xiao, W.; März, C.; Li, Q. Late Quaternary paleoenvironmental changes revealed by multi-proxy records from the Chukchi Abyssal Plain, western Arctic Ocean. *Glob. Planet. Chang.* **2013**, *108*, 100–118. [[CrossRef](#)]
33. Joe, Y.J.; Polyak, L.; Schreck, M.; Niessen, F.; Yoon, S.H.; Kong, G.S.; Nam, S.-I. Late Quaternary depositional and glacial history of the Arliss Plateau off the East Siberian margin in the western Arctic Ocean. *Quaternary. Sci. Rev.* **2020**, *228*, 106099. [[CrossRef](#)]
34. Zhang, W.; Yu, X.; Liu, Y.; Jin, L.; Ye, L.; Xu, D.; Bian, Y.; Zhang, D.; Yao, X.; Zhang, F. Paleoenvironmental record of core M04 in the Chukchi Sea Basin during Late Pleistocene. *Acta Oceanol. Sin.* **2015**, *37*, 85–96. (In Chinese)
35. Corlett, W.B.; Pickart, R.S. The Chukchi slope current. *Prog. Oceanogr.* **2017**, *153*, 50–65. [[CrossRef](#)]
36. Woodgate, R.A.; Aagaard, K.; Muench, R.D.; Gunn, J.; Bjork, G.; Rudels, B.; Roach, A.T.; Schauer, U. The Arctic Ocean Boundary Current along the Eurasian slope and the adjacent Lomonosov Ridge: Water mass properties, transports and transformations from moored instruments. *Deep Sea Res. Part I Oceanogr. Res. Pap.* **2001**, *48*, 1757–1792. [[CrossRef](#)]
37. Mauldin, A.; Schlosser, P.; Newton, R.; Smethie, W.M.; Bayer, R., Jr.; Rhein, M.; Jones, E.P. The velocity and mixing time scale of the Arctic Ocean Boundary Current estimated with transient tracers. *J. Geophys. Res. Oceans* **2010**, *115*, C08002. [[CrossRef](#)]

Article

Nonlinear Predictive Framework of the Undrained Clay Slope Effect on the Initial Stiffness of p - y Curves of Laterally Loaded Piles by FEM

Li Pang¹, Chong Jiang^{1,2,*} and Lujie Chen¹¹ School of Resources and Safety Engineering, Central South University, Changsha 410083, China² Hunan Provincial Key Laboratory of Hydropower Development Key Technology, Changsha 410014, China

* Correspondence: jiangchong@csu.edu.cn

Abstract: The hyperbolic p - y curve method is commonly used to design laterally loaded piles, in which the initial stiffness is one of the two key parameters that need to be determined. In this paper, the effect of an undrained clay slope on the initial stiffness of p - y curves of laterally loaded piles was explored, and nonlinear models of the reduction factor (μ) were proposed. A series of finite-element analyses was performed for different pile–slope geometric relationships according to whether the slope geometry had influence on pile–soil interaction, in which the geometrical parameters were varied. Based on simulation results, a semi-empirical method was mainly used to derive nonlinear formulations for the undrained clay slope effect on the initial stiffness of hyperbolic p - y curves. The wedge failure theory was also used to analyze the effect of the dimensionless slope height on the initial stiffness. Comparing with other researchers' reduction factor models, the results of the present model are in the reasonable range and can predict more cases. Test cases were used to validate the proposed model, and the results show that theoretical results are in better agreement with test results using the present model.

Citation: Pang, L.; Jiang, C.; Chen, L. Nonlinear Predictive Framework of the Undrained Clay Slope Effect on the Initial Stiffness of p - y Curves of Laterally Loaded Piles by FEM. *J. Mar. Sci. Eng.* **2022**, *10*, 1684. <https://doi.org/10.3390/jmse10111684>

Academic Editor: Barbara Zanuttigh

Received: 20 September 2022

Accepted: 28 October 2022

Published: 7 November 2022

Publisher's Note: MDPI stays neutral with regard to jurisdictional claims in published maps and institutional affiliations.



Copyright: © 2022 by the authors. Licensee MDPI, Basel, Switzerland. This article is an open access article distributed under the terms and conditions of the Creative Commons Attribution (CC BY) license (<https://creativecommons.org/licenses/by/4.0/>).

Keywords: laterally loaded piles; initial stiffness; undrained clay slope; nonlinear formulations; finite-element analysis

1. Introduction

Piles have been widely used in marine geotechnical engineering to support axial and lateral loads for different structures, such as offshore wind turbines, bridges, and offshore drilling platforms constructed at or near the slope [1–4]. There are several methods to analyze the load–displacement characteristics of laterally loaded piles. The p - y curves method is known to be a relatively accurate and effective method [5,6]. Many investigators have developed p - y curves for sand [7–9], clay [10–12], and rock masses, [13,14] mainly based on laboratory tests [15,16], field tests [17], and numerical simulation [18–20]. A popular hyperbolic p - y curves method is commonly used to predict the load–displacement characteristics of the soil–pile system under lateral load. There are two key parameters in p - y curves, which are initial stiffness (K_i) and ultimate resistance of the soil (p_u) [13,21,22]. The ultimate resistance of the soil (p_u) determines the ultimate state, and the initial stiffness (K_i) determines the initial state for a pile under lateral load. Accurately calculating p_u and K_i is a crucial step to establish p - y curves, and it is meaningful in the design of laterally loaded piles.

In clayey soils, the ultimate soil resistance (p_u) is found to increase nonlinearly with depth, and a consensus regarding how this term is evaluated is evident in the literature [18,23–25]. However, different formulas of the initial stiffness (K_i) have been proposed based on the results of laboratory tests, in-situ tests, and finite-element methods. Vesic [26] proposed an elastic solution model which was deduced from the theory of a beam on an elastic Winkler foundation. Rajashree and Sitharam [5] suggested that the

value of initial stiffness could be taken as twice that of Vesic's model to account for real soil resistance around the circumference of the pile, a suggestion which was widely used by researchers. Then the model was modified to take into account the effect of diameter or depth [13,27–29]. These models considered the effect of different soil–pile parameters and resulted in distinct engineering performances [30]. However, these models just focus on the case of piles on level ground. When the pile is embedded in or near the slopes, the initial stiffness is decreased because of the weakening of the soil in front of the pile [22], which is rather different from that of level ground.

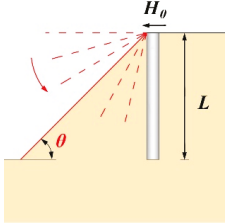
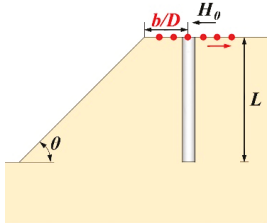
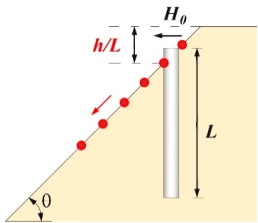
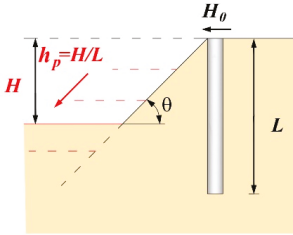
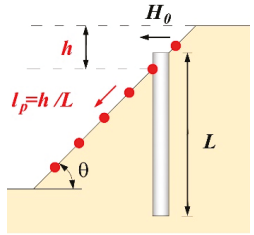
The slope effect on the pile–soil response often refers to the weakening effect of the slope parameters (e.g., slope angle, slope height, near-slope distance and so on) on the pile lateral load capacity. Available information concerning the clay slope effect on the initial stiffness of p - y curves is rather limited and mainly refers to linear analysis. Several investigations have considered the equivalent problem of initial stiffness of p - y curves for the case of piles in or near clay slope. Georgiadis and Georgiadis [18] performed a series of FEA simulations of piles at relatively gentle slopes, and provided a reduction factor (μ) which represented the linear weakening effect of the slope angle. Then Georgiadis and Georgiadis [22] provided a smooth transition from a pile at the slope crest to a pile near the slope crest. However, the equation proved to be relatively accurate only for slope angles lower than 30°. Yang et al. [16,31] performed laboratory tests and FEA simulations for a pile at the slope crest or in the slope. The results indicated that the critical depth (the depth with the initial stiffness equal to one) increased with the slope angle. A linear model of the reduction factor (μ) was then provided. Jiang et al. [9] provided an elastic stress solution of the soil in a slope under the self-weight, which proved to be accurate only for a narrow range of the slope angle. Considering that the current researches for the undrained clay slope effect on the initial stiffness are insufficient and have some weaknesses, systematical and comprehensive studies should be performed to explore the real slope effect on the initial stiffness of the pile–soil system.

To analyze the undrained clay slope effect on the initial stiffness, this paper established a series of 3D undrained finite-element models. Different pile–slope position relationships were considered according to whether the slope geometry had influence on pile–soil interaction. Based on simulation results, a semi-empirical method was mainly used to derive nonlinear formulations for the slope effect on the initial stiffness of hyperbolic p - y curves. The wedge failure theory was used to analyze the effect of the dimensionless slope height. Then the model performance of the present study was compared with those of other researchers' models. Moreover, the pile head load–displacement curves and p - y curves deduced with the proposed model were validated with other test results. The new model proved to be more appropriate and reasonable to fit real cases and could predict more cases.

2. Basic Assumptions

Based on the length relationship between the pile length and the slope height, two cases are considered in this paper: the case of “no slope geometry effect” and the case of “existence of the slope geometry effect”. The case of “no slope geometry effect” refers to the slope geometry having no influence on the shape of the affected area with load increase. The case of “existence of slope geometry effect” refers to the slope geometry having influence on the shape of the affected area with load increase. The detail of the concept will be discussed in Section 4.2.1. Based on these two cases, considering the distance between the pile and slope crest, pile–slope geometry relationships can be divided into five detailed cases, as in Table 1.

Table 1. Pile-slope geometry relationships.

Pile-Slope Geometry Relationships	Variables		
	(a) Slope Angle θ	(b) Dimensionless Near-Slope Distance b/D	(c) Dimensionless Pile Head-Crest Distance h/L
No slope geometry effect			
Pile-Slope Geometry Relationships	Variables		
	(d) Dimensionless Slope Height h_p	(e) Pile Location in the Slope l_p	
Existence of the slope geometry effect			

Three parameters are focused on in the “no slope geometry effect” case, which are slope angle (θ), dimensionless near-slope distance (b/D) and dimensionless pile head-crest distance (h/L), as seen in Table 1(a–c). Two parameters are focused on in the “existence of the slope geometry effect” case, which are dimensionless slope height (h_p) and pile location in the slope (l_p), as seen in Table 1(d,e).

The basic assumptions in this paper are described as follows:

- (1) The slope is stable and flat without a sliding surface, and the pile head is free.
- (2) The pile bends because of the pile head lateral load. Based on the discussions on p - y curves by Reese et al. [21] and Terzaghi [32], the soil resistance is assumed to be nonlinear with pile displacement. The popular hyperbolic p - y curve method is adopted to reflect the nonlinear response of laterally loaded piles as the following:

$$p = y / (y / p_u + 1 / K_i) \tag{1}$$

where p_u is the ultimate lateral load per unit length, and K_i is the initial stiffness.

- (3) The ultimate soil resistance (p_u) in front of and behind the pile varies nonlinearly with depth [18,23–25]. The initial stiffness (K_i) of undrained clayey soil in the level ground case is independent on depth [26,28,29].
- (4) Based on the study of Georgiadis and Georgiadis [18], a reduction factor (μ) is adopted to reflect the undrained clay slope effect on the initial stiffness:

$$\mu = K_{i\theta} / K_{i0} \tag{2}$$

where $K_{i\theta}$ is the initial stiffness in the slope condition, and K_{i0} is the initial stiffness in the level ground condition. For the convenience of readers, this paper provides the description of some used symbols, as shown in Table 2.

- (5) Poulos’ relative stiffness (K_R) method is used to judge whether a pile is flexible or rigid, as follows [33]:

$$K_R = \frac{E_p I_p}{E_s L^4} \begin{cases} > 0.208 & \text{Rigid pile} \\ < 0.0025 & \text{Flexible pile} \end{cases} \quad (3)$$

where $E_p I_p$ is the bending stiffness, E_s is the soil Young’s modulus, and L is the pile length. When $0.0025 \leq K_R \leq 0.208$, the pile is not rigid or flexible, which is named elastic pile.

Table 2. The description of some used symbols.

Symbols	Description
K_i	Initial stiffness
K_{i0}	Initial stiffness in the level ground condition
$K_{i\theta}$	Initial stiffness in the slope condition
K_{ii}	Initial stiffness at the ground surface
μ	Reduction factor
μ_θ	Reduction factor in the “no slope geometry effect” case with varying (θ)
$\mu_{b/D}$	Reduction factor in the “no slope geometry effect” case with varying (b/D)
$\mu_{h/D}$	Reduction factor in the “no slope geometry effect” case with varying (h/D)
μ_{h_p}	Reduction factor in the “existence of the slope geometry effect” case with varying (h_p)
μ_{l_p}	Reduction factor in the “existence of the slope geometry effect” case with varying (l_p)

3. Finite-Element Analysis

The finite-element analysis program ABAQUS was used to perform analyses in which the geometrical characteristics of the problem (slope angle θ , dimensionless near-slope distance b/D , dimensionless pile head-crest distance h/L , dimensionless slope height h_p , pile location in slope l_p , pile length L) were varied. Material properties were the same as Georgiadis and Georgiadis’ numerical simulation data [18], as shown in Table 3, and variable values are shown in Table 4.

Table 3. Soil and pile properties.

Properties	Value
<i>Soil</i>	
Young’s module E_s (MPa)	14
Undrained shear strength c_u (kPa)	70
Bulk unit weight γ_s (kN/m ³)	18
Poisson’s ratio ν_s	0.49
Adhesion factor α_s	0.5
<i>Pile</i>	
Young’s module E_p (MPa)	2.9×10^4
Bulk unit weight γ_p (kN/m ³)	25
Poisson’s ratio ν_p	0.1
Pile length L (m)	4, 12, 20
Pile diameter D (m)	1

Table 4. Variables values.

Variables	Conditions	Values
<i>“no slope geometry effect” case</i>		
Slope angle θ	$L = 4, 12, 20$ m; pile at crest	0, 15, 30, 45, 60, 75, 90
Dimensionless near-slope distance b/D	$L = 20$ m; $\theta = 30^\circ, 60^\circ, 90^\circ$	1, 2, 3, 4, 5, 6
Dimensionless pile head-crest distance h/L	$L = 4, 12, 20$ m; $\theta = 45^\circ$; pile in slope	0.5, 1, 1.5, 2
<i>“existence of the slope geometry effect” case</i>		
Dimensionless slope height $h_p = h/L$	$L = 4, 12, 20$ m; $\theta = 45^\circ$; pile in slope	$h_p = 0.5, 1, 1.5, 2$
Pile location in slope $l_p = h/L$	$L = 4, 12, 20$ m; $\theta = 45^\circ$; pile in slope	$l_p = 0.25, 0.5, 0.75, 1$

The soil was modeled as a linear elastic–perfectly plastic Tresca material [34–36] with the undrained Young’s modulus $E_s = 14 \text{ MPa}$, the undrained shear strength $c_u = 70 \text{ kPa}$, Poisson ratio $\nu_u = 0.49$, and the bulk unit weight $\gamma_s = 18 \text{ kN/m}^3$. Since the loading was undrained, the limiting pile–soil adhesion $\tau = \alpha_s c_u$, where α_s is adhesion factor. Considering the lower bound of the relationship between α_s and c_u , α_s was calculated to be 0.5 for the contact between the pile and soil, according to Georgiadis and Georgiadis’ study [18]. The breadth and the bottom depth of the FE model were set to be ten times and six times the pile diameter, respectively, which is enough to eliminate the boundary effects [37,38].

All piles were modeled with a diameter (D) of 1 m. The piles were assumed to behave in a linear elastic manner [18,36], with Young’s modulus $E_p = 2.9 \times 10^7 \text{ kPa}$, Poisson’s ratio $\nu = 0.1$, and the bulk unit weight $\gamma_p = 25 \text{ kN/m}^3$. Piles were modeled with lengths of $L = 4 \text{ m}$, 12 m , and 20 m . The relative stiffness (K_R) of the three length piles are calculated in Equation (3) to be 0.3972, 0.0050, and 0.0006, respectively. Thus, the three piles can be regarded as rigid pile, elastic pile, and flexible pile, respectively.

More than 80 models were established in the present study. A typical 3D finite-element meshing of the 30° slope soil is shown in Figure 1. Eight-node quadrilateral (C3D8R) interface elements were used for the majority part of both the pile and the soil. There was more detailed meshing around the pile to allow effective pile–soil separating at the back of the pile. In this method, the total element number of models was around 8000 to 20,000. Each analysis step was performed referring to the construction process of drilled piles. The simulation could be divided into five construction parts. First of all, the bottom boundary of the mesh was fixed in all directions, and other boundaries were fixed only in the normal direction. Secondly, the geostatic equilibrium of soil domain under self-weight was considered without the pile. Thirdly, the soil elements located at pile positions were removed and the pile elements were activated. The normal and tangential contact between pile and soil were applied. Fourthly, self-weight was applied on the pile through gravity loading, and the overall model was balanced again. Finally, the lateral load was applied on the top of the pile and the response of the pile was analyzed. Note that each load increment was 100 kN for 12 m and 20 m piles and 20 kN for 4 m piles. For the case of $\theta = 90^\circ$, all boundary conditions would work at first to balance the crustal stress, and then the boundary near the pile-placed side would be removed to form a 90° slope. It is noted that large angles like 75° and 90° are rare in engineering, and are just used to explore the real slope effect on the initial stiffness in this paper.

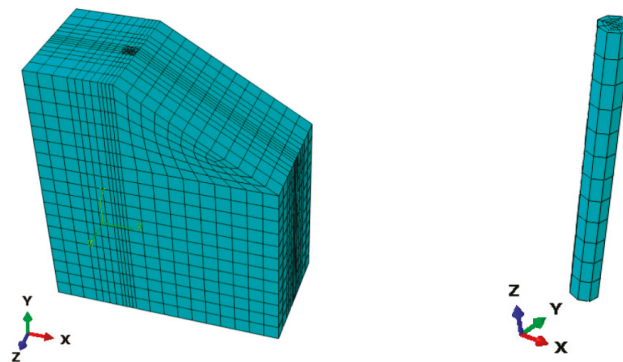


Figure 1. Typical 3D finite-element meshing in ABAQUS.

Figure 2 shows the comparison between FEA results and the theoretical method of Georgiadis and Georgiadis [18]. The pile length is 20 m, the slope angles are 15° , 45° , and 60° , and the other parameters are the same as shown in Table 1. The results prove that the FEA results are within the reasonable range. To derive p - y curves, the curves of shear

force (Q) versus depth (z) were exported from the nodes of the piles of FEA results. The Q - z curves were curve-fitted in a relatively accurate method of seven-order polynomial function. Then the polynomial functions were differentiated to give curves of lateral load per unit pile length (p) and depth (z) for each pile head lateral load. The obtained p - z curves were combined with y - z curves to produce p - y curves. Then, the initial slopes of these p - y curves could be obtained as the initial stiffness (K_i). Then, the reduction factors (μ) could be obtained using Equation (2). The whole procedure is shown in Appendix B. The total number of data on the initial stiffness was around 700.

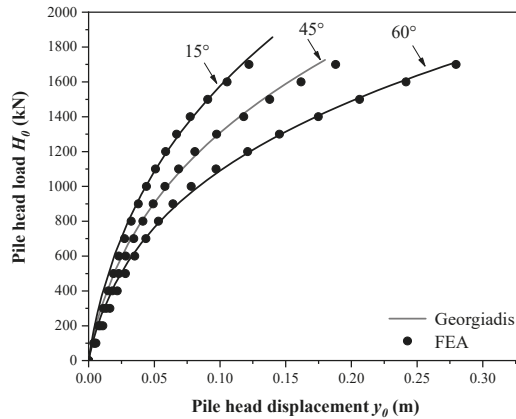


Figure 2. Comparison of FEA results with the theoretical method of the 20 m length pile and 15°, 45°, and 60° slope angles.

Note that the used polynomial method may have resulted in discontinuity at the ground surface and pile end. Thus, the data on fitting results at ground surface were invalid and not used in the present study. Moreover, the data of the nodes below the first turning point were not considered (e.g., as shown in Figure 3a, though the pile length is 20 m, only the data for the depths from 1 m to 7 m are used, because the pile first turns at around the depth of 8 m).

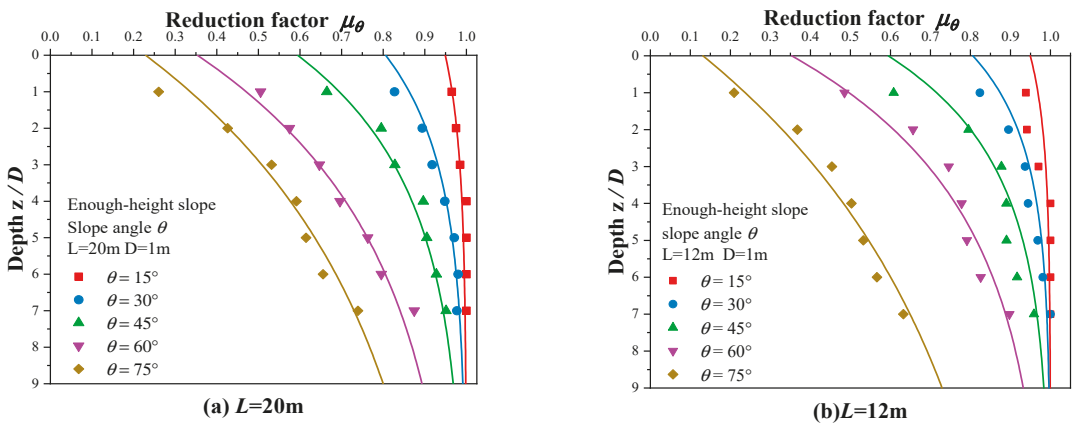


Figure 3. Cont.

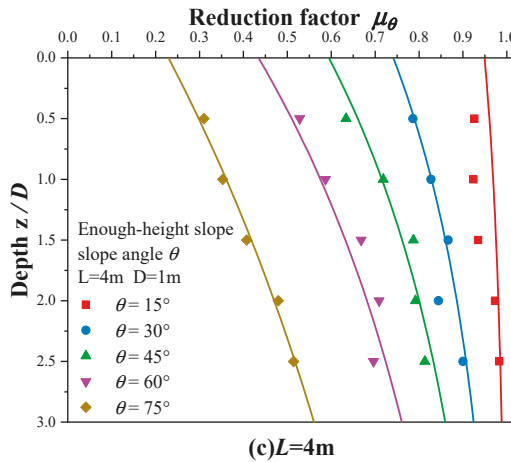


Figure 3. Effect of θ on μ_θ by FEA for (a) $L = 20$ m; (b) $L = 12$ m; (c) $L = 4$ m.

4. Theoretical Analysis for FEA Results

Based on cases with different slope heights, the pile–slope geometry relationships can be divided into two main cases, as Table 1 shows: (1) the “no slope geometry effect” case and (2) the “existence of the slope geometry effect” case. The following sub-sections will discuss the slope effect on the initial stiffness based on these two cases.

4.1. The “No Slope Geometry Effect” Case

In this case, three parameters are focused on, which are slope angle (θ), dimensionless near-slope distance (b/D), and dimensionless pile head-crest distance (h/L), as seen in Table 1(a–c). Theoretical analyses about the effect of these parameters are discussed in the following sub-sections, based on FEA simulation results.

4.1.1. Case 1: Variation of Slope Angle (θ)

In this case, the pile is installed at the crest, as seen in Table 1(a). The reduction factor (μ_θ) is calculated as shown in Figure 3. Different from the linear results of Georgiadis and Georgiadis [18] and Yang et al. [30], the reduction factor (μ_θ) increases nonlinearly with the depth in this paper. These nonlinear curves indicate that the value of the initial stiffness ($K_{i\theta}$) in slope conditions approaches K_{i0} with depth. The empirical exponential equation is provided as following:

$$\mu_\theta = \frac{K_{i\theta}}{K_{i0}} = \cos^\alpha \theta + \left(1 - e^{-\beta(z/D)\cos\theta}\right)(1 - \cos^\alpha \theta) \tag{4}$$

where α and β are non-dimensional coefficients, which are determined in Section 4.1.2. Equation (4) shows that the reduction factor (μ_θ) increases from $\cos^\alpha \theta$ at horizontal ground ($z = 0$) and nonlinearly approaches 1 with the depth ($z \rightarrow \infty$).

4.1.2. Case 2: Variation of Dimensionless Near-Slope Distance (b/D)

In this case, the pile is installed at a distance (b) from the slope crest, as seen in Table 1(b). Considering the effect of the near-slope distance, an idealization is illustrated in Figure 4, where K_{ii} is the value of the initial stiffness at depth $z = 0$ at horizontal ground. It provides a smooth translation from a pile at the slope crest to one near the slope. By replacing depth (z) in Equation (4) with $(z + z_1)$, where $z_1 = (b - D/2) \tan \theta$, it becomes:

$$\mu_{b/D} = \frac{K_{i\theta}}{K_{i0}} = \cos^\alpha \theta + \left(1 - e^{-\beta(z+(b-0.5D)\tan\theta)\cos\theta/D}\right)(1 - \cos^\alpha \theta) \tag{5}$$

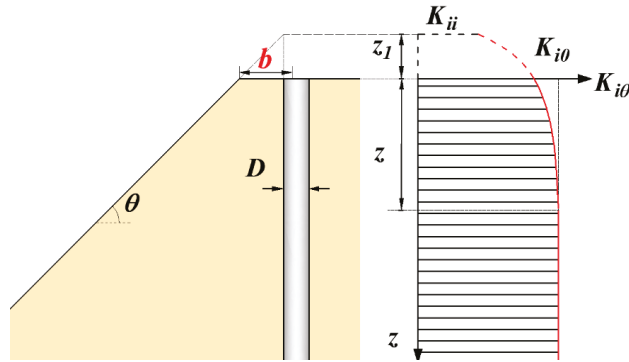


Figure 4. Transition from a pile at the slope crest to a pile near the slope crest.

Equation (5) can also be expressed as follows:

$$\mu_{b/D} = \frac{K_{i\theta}}{K_{i0}} = \cos^a \theta + (1 - e^{-\beta(z \cos \theta + (b-0.5D) \sin \theta)/D})(1 - \cos^a \theta) \quad (6)$$

In the ideal case of $\theta = 90^\circ$ at the slope crest, there is no Winkler spring in the outside part of the pile, so $K_{i\theta} = 0$ and $\mu_{b/D} = 0$. When a pile is not installed at the slope crest, there is still soil constraining the outside of the pile. In this case, Equation (6) becomes:

$$\mu_{b/D} = 1 - e^{-\beta(b/D-0.5)} \quad (7)$$

Equation (7) demonstrates that for the ideal case of $\theta = 90^\circ$, the slope has the same effect on $K_{i\theta}$ at any depth, and $K_{i\theta}$ just changes with the distance (b). Then, the parameter β in Equation (7) can be determined through a series of b/D effect simulations in the case of $\theta = 90^\circ$.

Figure 5 shows results of the slope angle (θ) effect on $\mu_{b/D}$ by deriving the results from FEA. Averaging the results to obtain the ratio of slope case to level ground case, $\mu_{b/D}$ becomes 0.32, 0.46, 0.62, 0.74, 0.81, and 0.88, respectively. Then, substituting $\mu_{b/D}$ values into Equation (7), β is obtained as 0.39, 0.42, 0.39, 0.38, 0.37, and 0.38, respectively. Thus, $\beta = 0.4$ is suggested to be reasonable for use in this study.

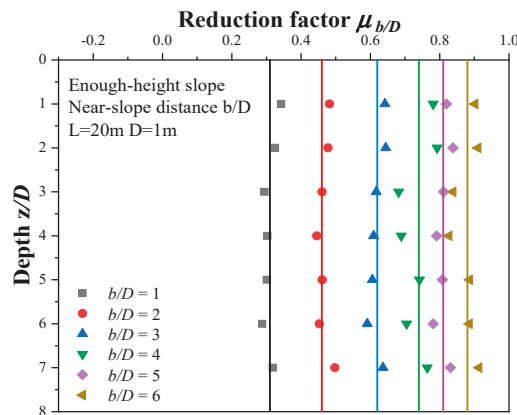


Figure 5. Effect of b/D on $\mu_{b/D}$ by deriving the results of FEA for $\theta = 90^\circ$.

Since β is determined, α can be determined in Equation (6) by fitting curves in Figure 3. Figure 6 shows the distribution of α for a total of 95 data from piles. Then, a recommended value of $\alpha = 1.2$. is able to represent the most cases precisely.

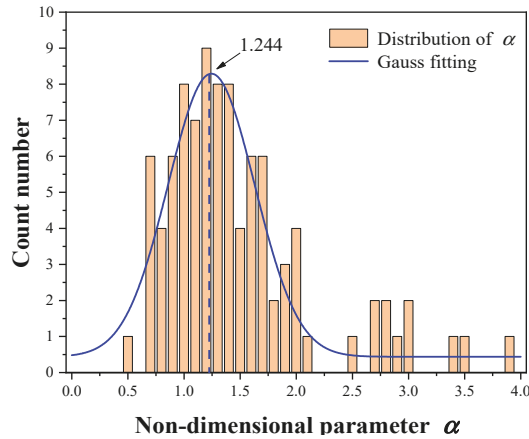


Figure 6. Distribution of non-dimensional parameter α .

Finally, now that $\alpha = 1.2$ and $\beta = 0.4$ have been obtained, Equation (6) can be provided as:

$$\mu_{b/D} = \frac{K_{i\theta}}{K_{i0}} = \left[\cos^{1.2} \theta + \left(1 - e^{-0.4(z \cos \theta + (b-0.5D) \sin \theta)/D} \right) \left(1 - \cos^{1.2} \theta \right) \right] \quad (8)$$

Additional cases of both the dimensionless near-slope distance (b/D) and the slope angle (θ) effects are conducted using FEA, and the results of μ are plotted in Figure 7, together with curves of Equation (8), which shows good agreement between predictions and simulation results.

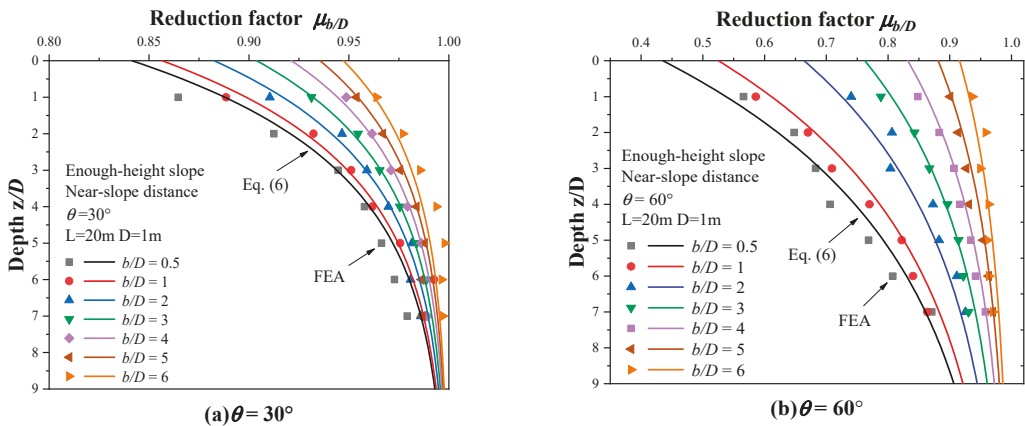


Figure 7. Effect of b/D on μ for (a) $\theta = 30^\circ$; (b) $\theta = 60^\circ$.

4.1.3. Case 3: Variation of Dimensionless Pile Head-Crest Distance (h/L)

In this case, the pile is installed on the slope, at a distance h away from the slope crest, as seen in Table 1(c). As shown in Figure 8, the lateral bearing capacity is almost independent of the pile head-crest distance (h). This phenomenon indicates that the soil

behind the pile hardly participates in the soil–pile response for undrained clay slopes, which is similar to the results of Sivapriya et al.’s laboratory test [39]. This can be explained by the theory of Coulomb earth pressure, which considers that the active earth pressure is dependent on the soil properties and the height of the structure. Thus, the case of the variation of dimensionless pile head-crest distance (h/L) is nearly the same as that of the pile at the slope crest. The slope effect on the initial stiffness in this case can be expressed as:

$$\mu_{h/L} = \mu_{\theta} \tag{9}$$

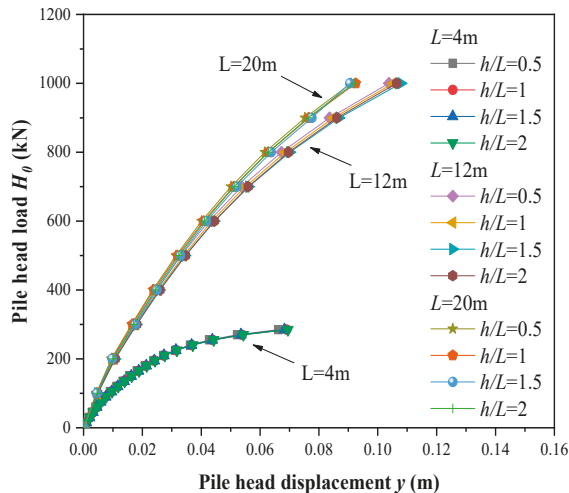


Figure 8. Effect of the slope height on pile head displacement of piles.

4.2. The “Existence of the Slope Geometry Effect” Case

In this case, two parameters are focused on, which are dimensionless slope height (h_p) and pile location in slope (l_p), as seen in Table 1(d,e). Theoretical analyses about these parameters are discussed in the following sub-sections, based on simulation results.

4.2.1. Case 4: Variation of Dimensionless Slope Height (h_p)

In this case, the pile is installed at the crest and dimensionless slope height (h_p) varies, as seen in Table 1(d). Figure 9 shows that the lateral bearing capacity decreases with the increase of h_p from 0 to 1 for slope angle $\theta = 45^\circ$. It is obvious that h_p hardly affects the soil–pile response when h_p is beyond a certain height (e.g., the curves in Figure 9a when $h_p \geq 0.30$). This indicates that the dimensionless slope height (h_p) affects the soil–pile response in a nonlinear way.

The phenomenon can be explained by a wedge failure theory first proposed by Reese and Welch and Reese et al. [40,41]. The wedge failure model considers that the soil–pile response relates to the lowest value of two possible failure mechanisms: a wedge failure mechanism at shallow depths and a flow failure around the pile at greater depths. Moreover, the passive wedge develops along the depth as the load increases to form a larger wedge failure body, as shown in Figure 10, where ϕ is the angle between the sliding surface and the vertical plane. Under undrained conditions, the angle (ϕ) is suggested to be 45° by Reese et al. [41].

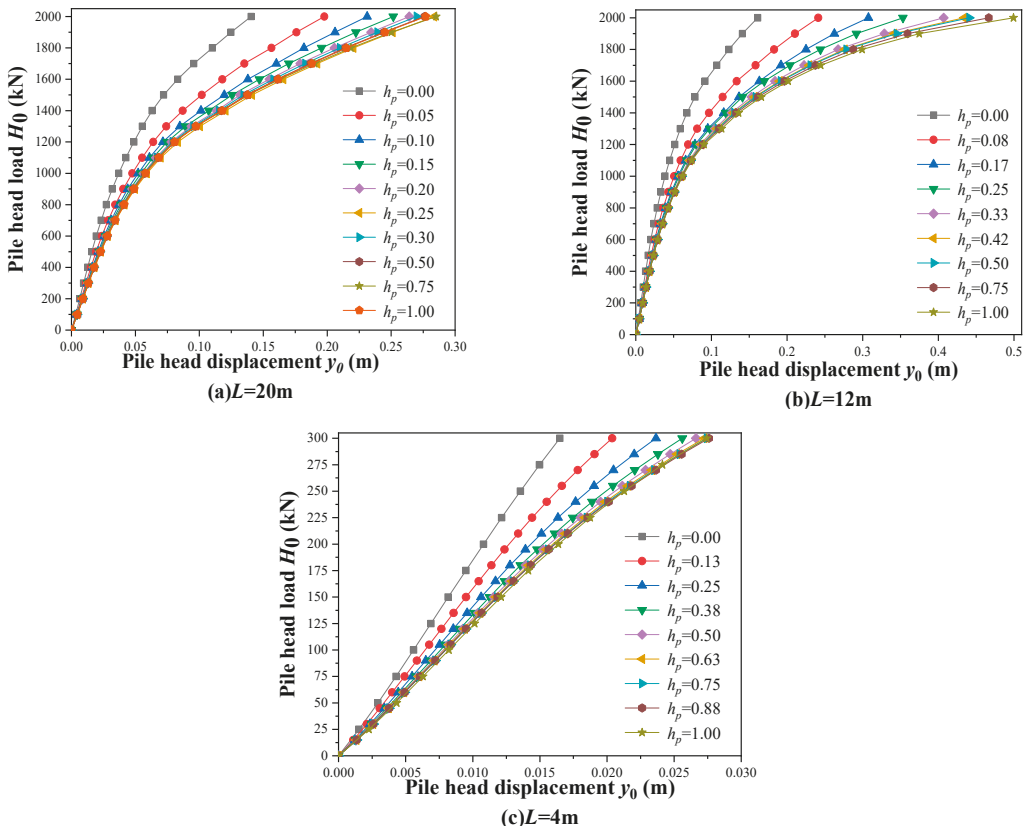


Figure 9. Effect of the dimensionless slope height (h_p) on pile-head displacement y_0 for slope angle $\theta = 45^\circ$. Piles of (a) 20 m, (b) 12 m, and (c) 4 m lengths.

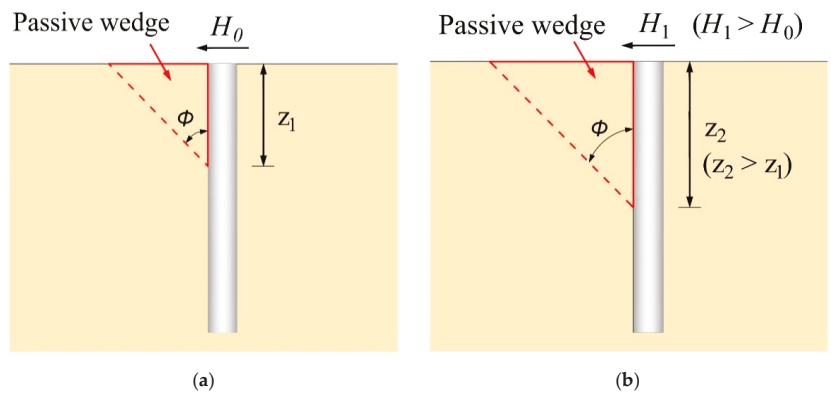


Figure 10. The wedge failure model at shallow depth for level ground. (a) H_0 and (b) H_1 .

Yang et al. analyzed the near-slope failure wedge for three “existence of the slope geometry effect” cases. The study considered that as the load increased, the passive wedge expanded, and the passive wedge shape changed from a triangle to a concave quadrilateral [31]. However, a theoretical largest passive wedge exists because the depth of

the bottom of the wedge will not exceed the first bending point of the pile. Similarly, for the changing h_p case in this paper, the shape of the largest passive failure wedge changes from a concave quadrilateral for a small h_p value to a triangle for a larger h_p value, as shown in Figure 11, where z_t is the depth of the first turning point, and z_{cr} is the depth of the intersection of the bottom plane of the largest passive wedge and the slope surface.

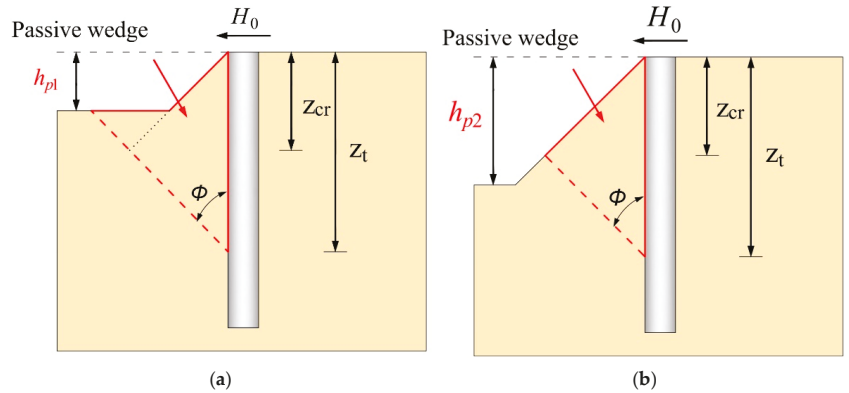


Figure 11. The theoretical largest passive wedge for (a) h_{p1} and (b) h_{p2} .

For “existence of the slope geometry effect” cases, when the slope angle remains constant, the shape of the theoretical largest passive wedge changes with h_p when $h_p < z_{cr}/L$, but remains constant when $h_p \geq z_{cr}/L$, as shown in Figure 11. This indicates that “existence of the slope geometry effect” cases are the same as “no slope geometry effect” cases when $h_p \geq z_{cr}/L$. The reduction factor (μ_{h_p}) can be calculated for the dimensionless slope height (h_p) variation case as follows:

$$\mu_{h_p} = \begin{cases} f(h_p, \mu_\theta), & h_p < z_{cr}/L \\ \mu_\theta, & h_p \geq z_{cr}/L \end{cases} \quad (10)$$

where z_{cr} is related to the slope angle, as shown in Figure 12, and can be calculated in geometry as follows:

$$z_{cr} = z_t / (1 + \frac{1}{\tan \theta}) \quad (11)$$

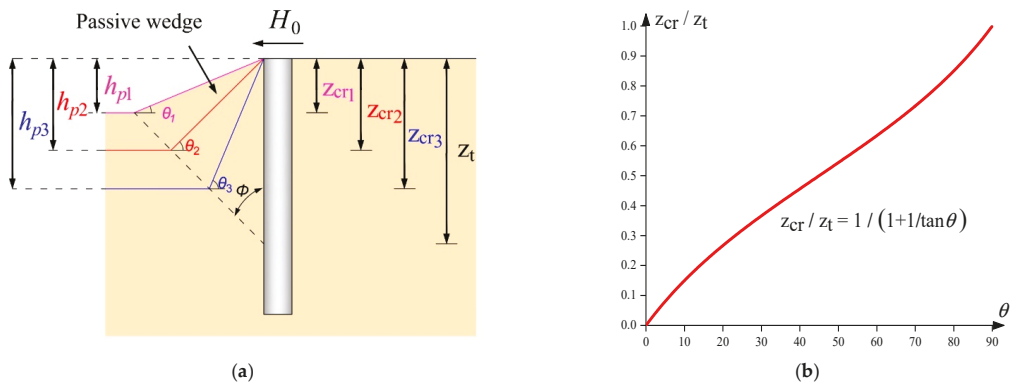


Figure 12. (a) Different passive wedges with slope angle (θ) and (b) variation of z_{cr} with slope angle (θ).

Calculation Method of z_t

Actually, the depth of the first turning point (z_t) of the pile is dependent on soil and pile properties, loading conditions, and so on (e.g., for a certain pile, the value of z_t approaches 0 when the soil stiffness is extremely large, but approaches the value of L when the soil stiffness is extremely small). Sun et al. [36] also indicated this, providing a range of $0.62 \sim 0.73L$ for z_t of a large-diameter monopile on sandy level ground. In this paper, the variation of z_t is considered to be related to the relative stiffness (K_R). It is obvious that the relative stiffness (K_R) is influenced by the pile length because of the fourth order of the pile length (L) in Equation (3). Recording the depths of the first turning point (z_t) of piles derived from FEA results, as shown in Figure 13, the ratio (z_t/L) results of the depth of the first turning point and the pile length are shown in Figure 14. The figure indicates that z_t/L decreases as the pile length increases. For each length of the undrained, laterally loaded pile, z_t/L remains almost the same value.

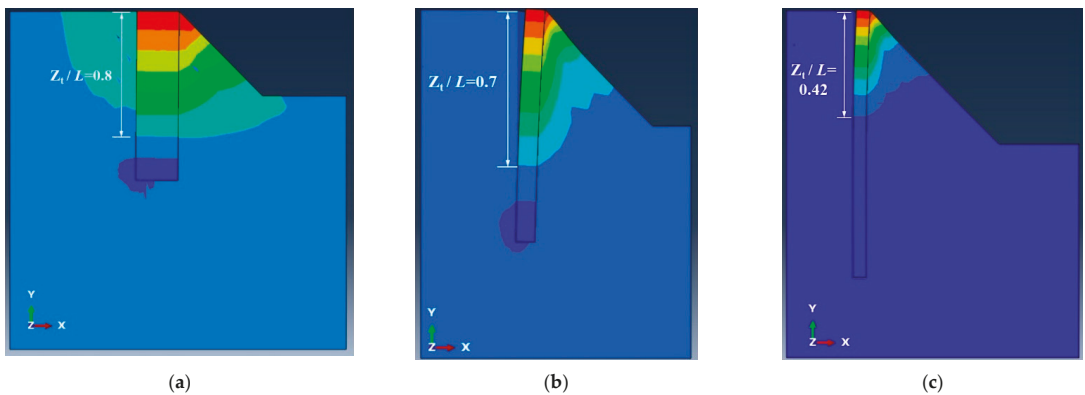


Figure 13. The value of z_t/L derived by FEA. (a) 4 m length pile, (b) 12 m length pile, and (c) 20 m length pile.

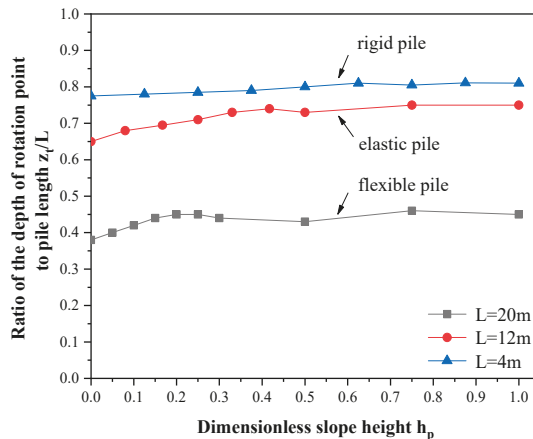


Figure 14. The variation of the z_t/L with h_p derived by FEA.

However, when the pile is flexible, the lower part of the pile hardly bears the load. As a result, z_t does not increase with the pile length. Thus, the value of z_t/L is around 0.7 for 4 m and 12 m length piles, but is as small as 0.4 for 20 m length piles, as shown in

Figure 14. To solve the problem, a minimum flexible pile length (L_{flex}) is proposed in this paper, which can be calculated with Equation (3) when $K_R = 0.0025$, as follows:

$$L_{flex} = \sqrt[4]{\frac{E_p I_p}{0.0025 E_s}} \tag{12}$$

The minimum flexible pile length (L_{flex}) for the pile and soil in this paper is calculated to be 14.28 m ($0.71L$). This means that when the pile is longer than 14.28 m, the lower part of the pile will not bear the load, and z_t will not increase with depth. Thus, in this case, L_{flex} and z_t are considered to be unchanged for the flexible pile. Then, for the flexible pile with a length of 20 m in this paper, $z_t = 0.4L (0.56L_{flex})$ is finally obtained. The variation of z_t can be regarded as $0.8L \sim 0.6L_{flex}$ for a pile varied from rigidity to flexibility, as shown in Figure 15.

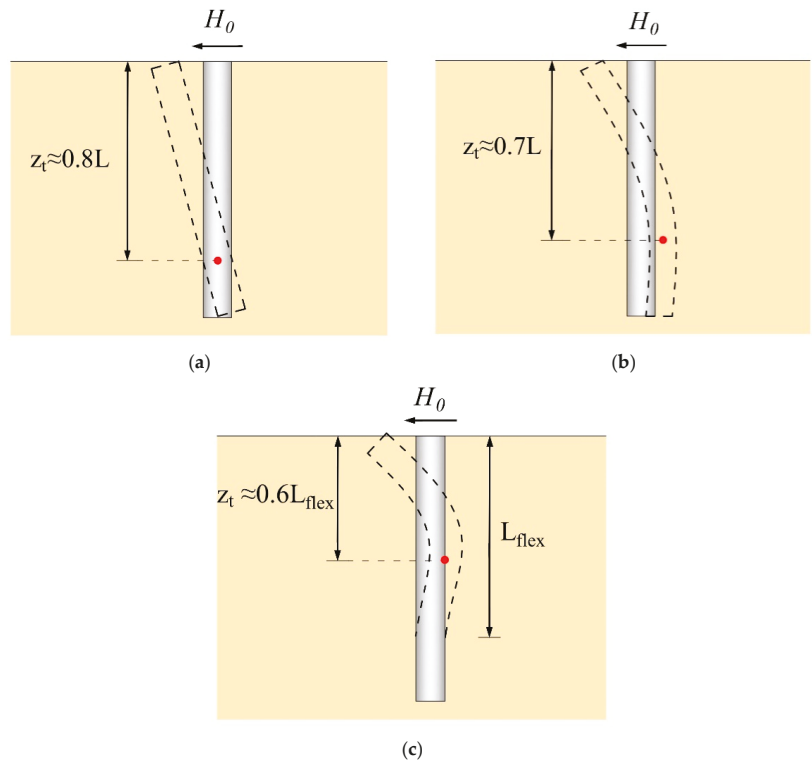


Figure 15. The depth (z_t) of the first turning point of pile for (a) a rigid pile, (b) a elastic pile and (c) a flexible pile.

A simple calculation method of z_t is provided in this paper, as seen in Equation (13). Further discussions of z_t can be studied by researchers in the future.

$$z_t = \begin{cases} 0.8L & \text{Rigid pile} \\ 0.7L & \text{Elastic pile} \\ 0.6L_{flex} & \text{Flexible pile} \end{cases} \tag{13}$$

Calculation Method of $f(h_p, \mu_\theta)$

As shown in Figure 11, the shape of the passive wedge is a triangle and does not change when $h_p \geq z_{cr}/L$. At this time, the reduction factor (μ_{h_p}) remains the same as μ_θ .

Furthermore, the soil–pile system is not affected by the slope for cases with level ground ($h_p = 0$) and $\mu_{hp} = 1$. Thus, a conclusion can be drawn that μ_{hp} decreases from 1 to μ_θ as h_p increases from 0 to z_{cr} . To figure out the problem of how μ_{hp} varies, a normalized reduction factor λ_{norm} is proposed in this paper that can be calculated as follows:

$$\lambda_{norm} = (\mu_{hp} - \mu_\theta) / (1 - \mu_\theta) \tag{14}$$

Equation (14) uses the normalized method to reflect the weight of μ_{hp} for different values of μ_θ . Figure 16 shows the nonlinear variation of λ_{norm} with h_p for different depths of piles. At deep depths, though curves show differences to shallow-depth curves, these curves are not considered because the μ_{hp} of these curves is close to 1. Thus, the relationship between λ_{norm} and h_p is provided in a nonlinear form as follows:

$$\lambda_{norm} = \frac{\mu_{hp} - \mu_\theta}{1 - \mu_\theta} = e^{\left[\frac{kh_p}{h_p - z_{cr}/L} \right]} \tag{15}$$

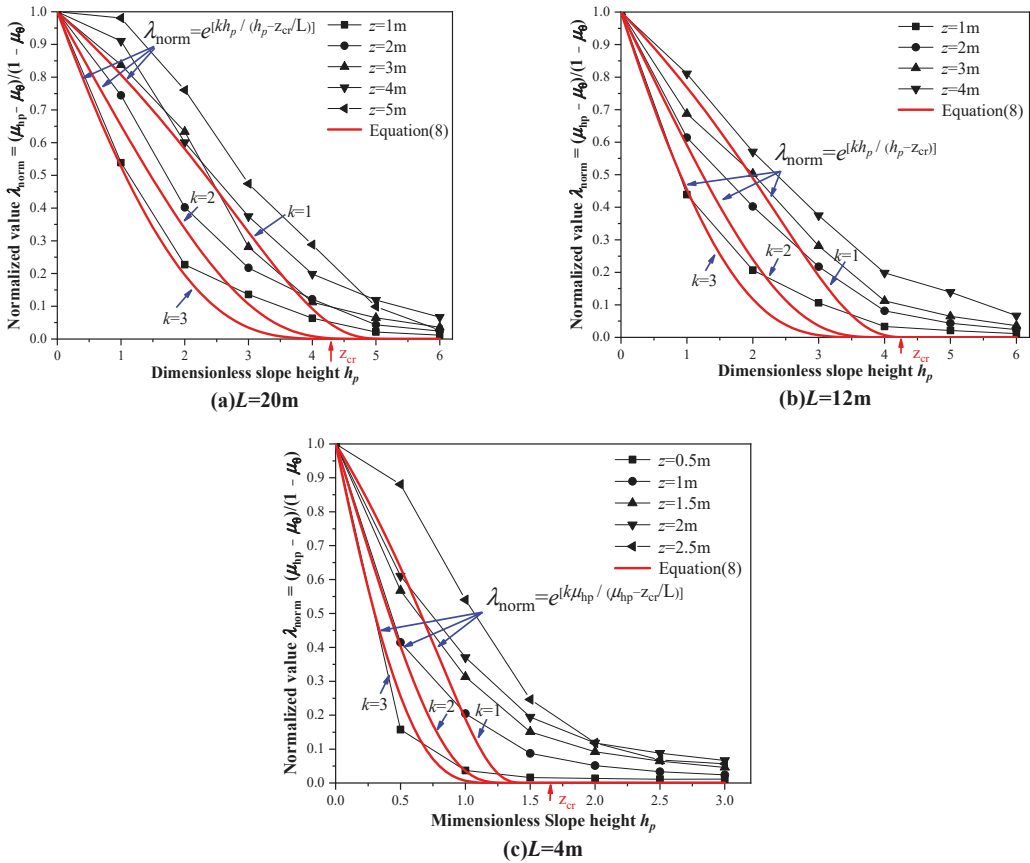


Figure 16. The variation of λ_{norm} with h_p for (a) $L = 20$ m, (b) $L = 12$ m, and (c) $L = 4$ m.

Rearranging Equation (15), μ_{hp} can be calculated as the following when $h_p < z_{cr}/L$:

$$\mu_{hp} = f(h_p, \mu_\theta) = \mu_\theta + (1 - \mu_\theta) e^{\left(\frac{kh_p}{h_p - z_{cr}/L} \right)} \quad (h_p < z_{cr}/L) \tag{16}$$

where z_{cr} is calculated to be 1.6 m, 4.2 m, and 4.26 m with Equations (11) and (13), for pile lengths of 4 m, 12 m, and 20 m, respectively; k is a parameter that controls the shape of the curve, as shown in Figure 16. Equation (16) reflects more characteristics of shallow depths with the increase of k . To fit more cases of depths, $k = 2$ is considered to be suitable and reasonable. Additionally, the numbers “1” and “ μ_θ ” in Equation (16) can be regarded as the reduction factor of the slope bottom (level ground) and that of the slope, respectively.

Finally, Equation (10) can be expressed as:

$$\mu_{h_p} = \begin{cases} \mu_\theta + (1 - \mu_\theta)e^{\left(\frac{2h_p}{h_p - z_{cr}/L}\right)}, & h_p < z_{cr}/L \\ \mu_\theta, & h_p \geq z_{cr}/L \end{cases} \quad (17)$$

Figure 17 shows the curves derived using Equation (17) and the data from FEA, which show good agreement between the prediction and the simulation results.

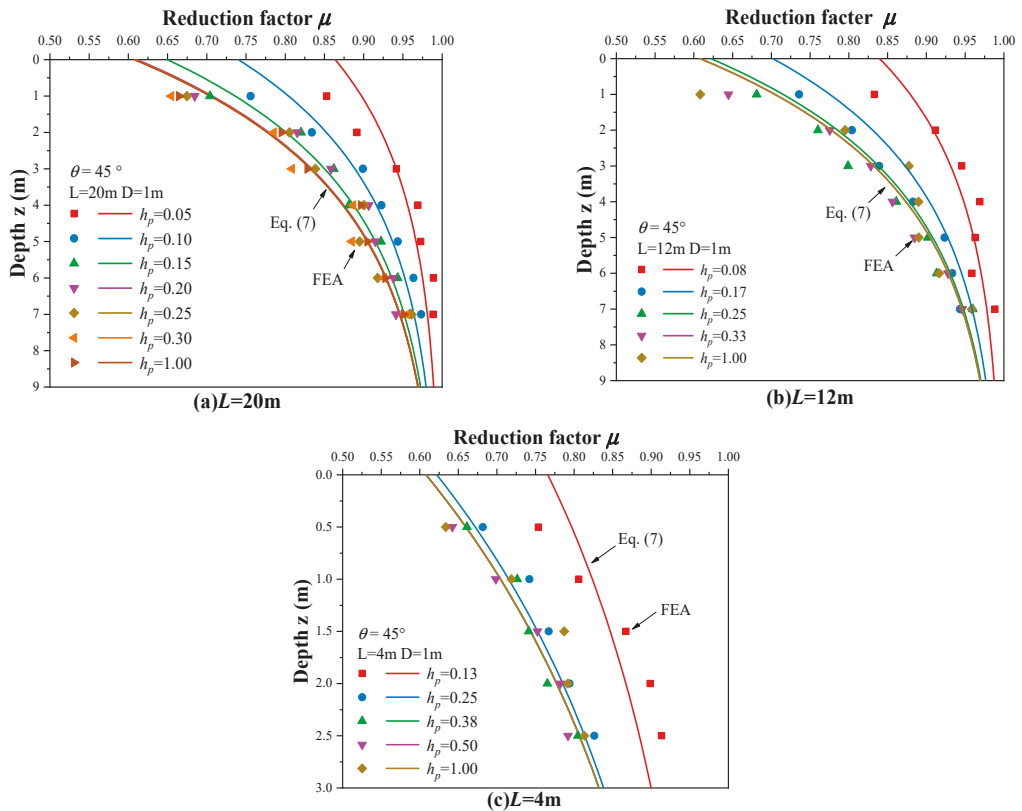


Figure 17. Effect of h_p on μ for pile length of (a) 20 m, (b) 12 m, and (c) 4 m.

4.2.2. Case 5: Variation of Pile Location on Slope (l_p)

In this case, the pile is installed on the slope, at a distance (l_p) away from the crest, as shown in Table 1(e), where $l_p = h/L$. Figure 18 shows that the lateral bearing capacity increases with l_p , increasing from zero to one for cases where the slope angle $\theta = 45^\circ$. It is obvious that, although l_p increases in a linear way, the lateral bearing capacity increases nonlinearly. Considering that the soil–pile response is independent of the soil behind the pile, as Case 3 shows, the case of variation of pile location on slope (l_p) (case 5) can be

regarded as the combination of Case 3 and Case 4. Replacing h_p in Equation (17) with $(H/L - l_p)$, the reduction factor (μ_{l_p}) can be calculated using the following equation:

$$\mu_{l_p} = \begin{cases} \mu_\theta + (1 - \mu_\theta)e^{\left[\frac{k(H/L-l_p)}{(H/L-l_p)-z_{cr}/L}\right]}, & l_p > (H - z_{cr})/L \\ \mu_\theta, & l_p \leq (H - z_{cr})/L \end{cases} \quad (18)$$

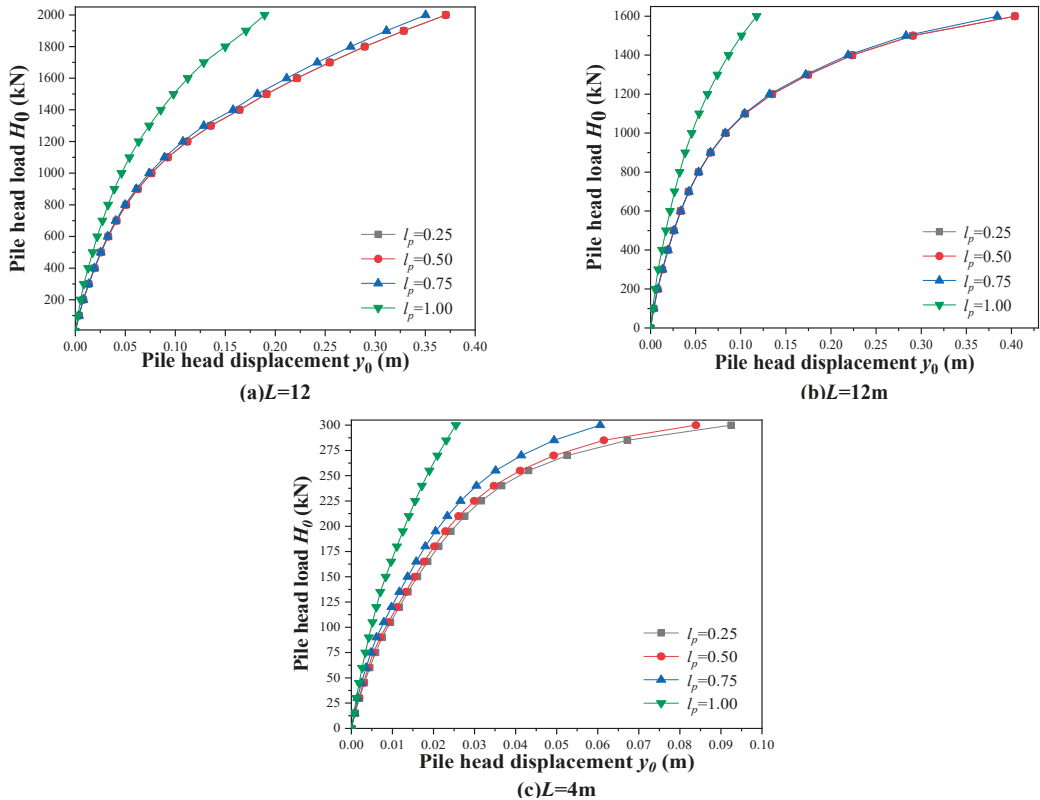


Figure 18. Effect of pile location on slope (l_p) on pile head displacement from the data of FEA, for slope angle $\theta = 45^\circ$. Piles of (a) 20 m, (b) 12 m, and (c) 4 m lengths.

5. Comparison and Validation

5.1. Comparison with Other Methods

Since Georgiadis and Georgiadis [18] proposed the concept of the reduction factor (μ) of the initial stiffness for soil–pile response in undrained clay slopes, some researchers have developed the method. Figures 19 and 20 show the comparison of μ from the present study with the methods of Georgiadis and Georgiadis [18,22] and Yang et al. [16]. Figure 19a shows that μ approaches one with depth for both the present study and the method of Yang et al., but equals one below $z = 6D$ for the method of Georgiadis and Georgiadis. Moreover, the present study shows a relatively smaller value of μ , which is more conservative for the engineering design. Figure 19b shows that the value of μ in the present study is similar to the μ value of the method of Georgiadis and Georgiadis, and the μ value of the method of Yang et al. is larger.

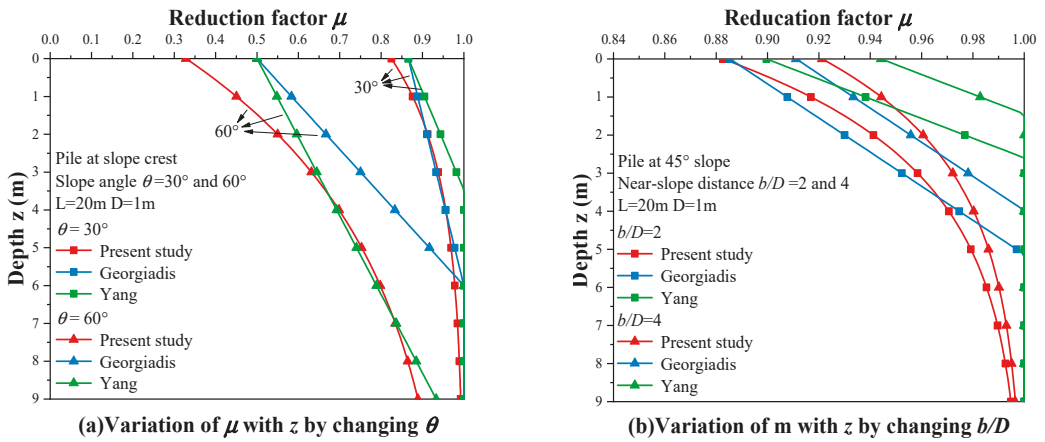


Figure 19. Comparison of the variation of μ with z by changing (a) θ and (b) b/D [16,18].

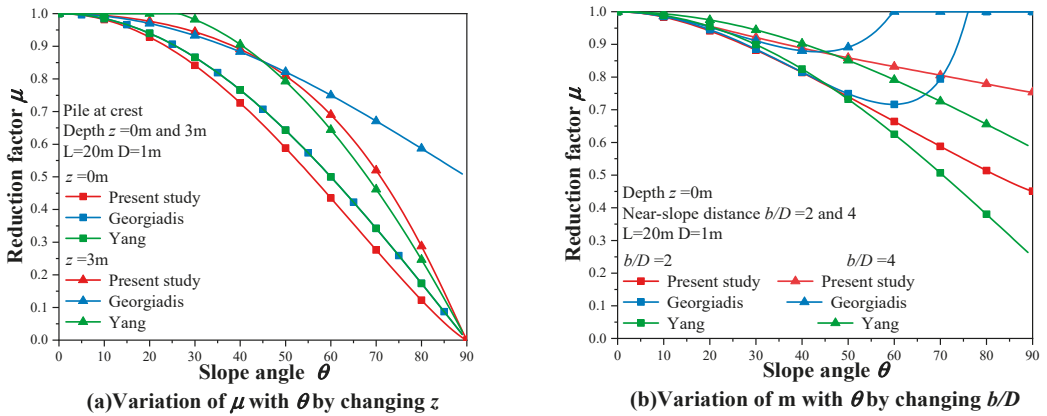


Figure 20. Comparison of the variation of μ with θ by changing (a) z and (b) b/D [16,18].

Figure 20a shows that all the μ values of the three methods are nearly the same for small angle slopes. As the slope angle increases, the trend of μ in the present study is similar to Yang et al.'s method. However, Georgiadis and Georgiadis' method only shows good agreement with real cases for small slope angles, which is also indicated in Georgiadis and Georgiadis' study [18]. Figure 20b shows the similar trend of μ for both the present study and Yang et al.'s method, and the μ value of Yang et al.'s method is smaller for large slope angles. In the same way, the μ value of Georgiadis and Georgiadis' method only shows good agreement for small slope angles, and the μ value of the present study is better predicted for large slope angles. Additionally, note that both Georgiadis and Georgiadis' method and Yang et al.'s method cannot predict the ideal case of the slope angle $\theta = 90^\circ$, but it can be obtained by using the method of the present study.

5.2. Application to Test Cases

The present study is validated by two pile tests in this section. Usually, the soil–pile response is reflected by monitoring the pile head load (H_0) and displacement (y_0), which is

known to be a $H_0 - y_0$ curve. The hyperbolic $p-y$ curves in Equation (1) and the deflection differential equation are used to derive $H_0 - y_0$ curves as follows:

$$E_p I_p \frac{d^4 y}{dz^4} + p = 0 \tag{19}$$

The finite difference method is used to transform differential equations into difference equations. The displacement of the laterally loaded pile can be obtained by solving these difference equations. Then the pile head load–displacement curve ($H_0 - y_0$) can also be obtained.

The values of the parameters used to calculate $H_0 - y_0$ curves are as shown in Table 5, where e is the height of the load applied above the ground level; c_u is undrained shear strength; and E_s is Young’s modulus of the soil.

Table 5. Summary of pile load tests.

Pile Test	Geometrical Characteristics				Soil Properties		
	L (m)	D (m)	$E_p I_p$ (kN m ²)	e (m)	θ	c_u (kPa)	E_s (kPa)
Bhushan	5.185	1.22	2.25×10^6	0.23	20	220	24,440
Yang	1	0.025	0.1	0.15	0, 30, 60	53.2	30,120

5.2.1. Case 1: Bhushan’s Pile Test

A laterally loaded rigid pile test at a stiff clay slope crest by Bhushan et al. [42] was used to validate the present study, together with the theoretical results of Reese and Welch [40], Bhushan et al. [42], and Georgiadis and Georgiadis [18]. The case is the same as the case in Section 4.1.1 where $\theta = 20^\circ$, and the parameter values are shown in Table 5. The calculation method of p_u and K_i is the same as the method of Georgiadis and Georgiadis [18], as seen in Appendix A, and the method of the present study is used to calculate $\mu_\theta = K_{i\theta} / K_i$. The $H_0 - y_0$ curves are shown in Figure 21, which shows better agreement with the pile test when using the method of μ in the present study.

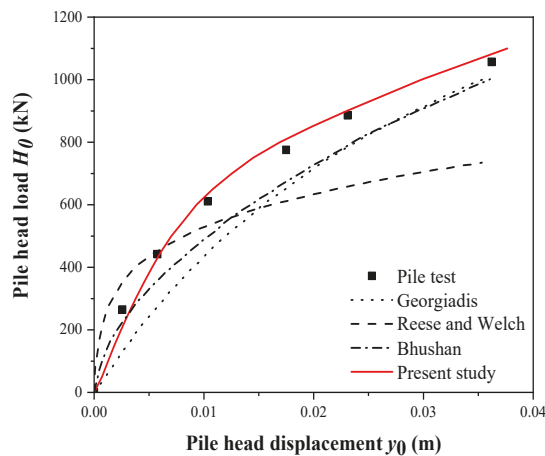


Figure 21. Validation with rigid pile test at the stiffness clay slope crest [18,40,42].

5.2.2. Case 2: Yang’s Pile Test

A lateral flexible pile test in the middle of the clay slope by Yang et al. [16] was used to validate the present study. The case is the same as the case in Section 4.2.1 where $h_p / L = 0.5$, and the parameter values are shown in Table 5. The calculation method of p_u

and K_i is the same as the method of Yang et al. [16], as seen in Appendix A, and the method of the present study is used to calculate $\mu_{hp} = K_{ihp}/K_i$. Note that z_t is calculated to be 0.19 m in the case of the pile test. The $H_0 - y_0$ curves and $p - y$ curves at $z = 0$ m depth are shown in Figure 22. Compared with Yang et al.'s method, the result of the present study proves to have good agreement with the pile test for the large load when the slope angle is small. Moreover, when the slope angle is large, the results of the present study are similar to the result of Yang et al.'s method. Additionally, the lateral load per unit (p) is calculated to be larger than the results of Yang et al.

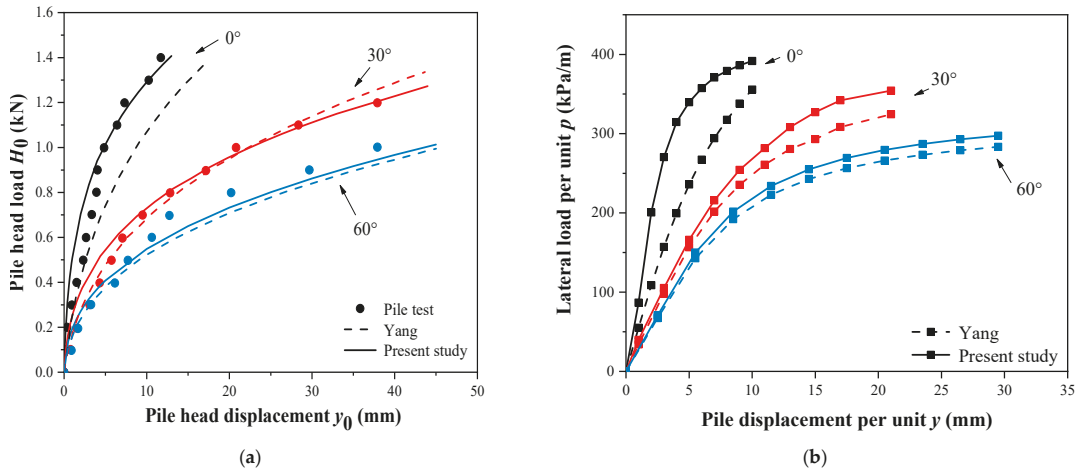


Figure 22. Validation with the flexible pile test in the middle of the clay slope.(a) $H_0 - y_0$ curves and (b) $p - y$ curves at depth of $z = 0$ m [16].

6. Conclusions

The paper proposes nonlinear prediction methods for the slope effect (μ) on the initial stiffness (K_i) of $p - y$ curves of the undrained laterally loaded pile. Five cases are classified to analyze the slope effect (μ) on the initial stiffness (K_i) of a laterally loaded pile, based on the pile–slope position relationship. A series of FEA simulations were conducted, and the data were derived to calculate μ . Nonlinear models of μ were established for these five cases, and parameters in the models were calibrated using the results of FEA. The nonlinear models showed good agreement with FEA results. Compared with other researchers' μ models, the method in this paper is in a reasonable range and can predict more cases. The test cases were used to validate the proposed model, which shows that the $p - y$ curves are in better agreement with test results when using the model of the present study. Additionally, some other conclusions were also obtained:

- (1) The pile–soil response in undrained clay conditions was nearly independent of the dimensionless pile head-crest distance (h/L) for the “no slope geometry effect” case, which can be explained by the theory of Coulomb earth pressure.
- (2) The depth of the first turning point of the pile under undrained loading was explored as $0.8L$ for the flexible pile, $0.7L$ for the elastic pile, and $0.6L_{flex}$ for the flexible pile. The soil–pile response for the case of $h_p \geq z_{cr}/L$ was found to be the same as the case of $h_p \geq 1$ (“no slope geometry effect” case).
- (3) Compared with the available initial stiffness (μ) calculation methods, the results are more reasonable for large slope angle cases, and can predict some ideal cases, such as the case of $\theta = 90^\circ$, by using the method of the present study.

Author Contributions: Conceptualization, L.P. and C.J.; Funding acquisition, C.J.; Methodology, L.P.; Resources, C.J.; Software, L.C.; Supervision, L.C.; Validation, L.C.; Visualization, L.C.; Writing—original draft, L.P.; Writing—review and editing, C.J. All authors have read and agreed to the published version of the manuscript.

Funding: This research was funded by the National Natural Science Foundation of China, grant number 51978665.

Institutional Review Board Statement: Not applicable.

Informed Consent Statement: Not applicable.

Data Availability Statement: The data presented in this study are available on request from the corresponding author.

Conflicts of Interest: The authors declare no conflict of interest.

Appendix A. Theoretical Method of Georgiadis and Georgiadis [18] and Yang et al. [16]

For undrained laterally loaded piles, the ultimate lateral load per unit pile length (p_u) in Equation (1) is calculated by:

$$p_u = N_p c_u D \tag{A1}$$

where N_p was calculated by Georgiadis and Georgiadis [18] for piles at the slope crest:

$$N_p = N_{pu} - (N_{pu} - N_{p0} \cos \theta) e^{-\lambda(z/D)/(1+\tan \theta)} \tag{A2}$$

and calculated by Yang et al. [16] for piles in the middle of the slope, as following:

$$N_p = N_{pu} - (N_{pu} - N_{p0} \alpha_1^2 \alpha_2^2) e^{-\lambda(z/D) \alpha_1^2} \tag{A3}$$

where $\alpha_1 = 1/(1 + \tan \theta)$, $\alpha_2 = 1 - \sin \theta(1 + \sin \theta)/2$; and N_{pu} , N_{p0} , and λ can be calculated as follows:

$$N_{pu} = \pi + 2\Delta + 2 \cos \Delta + 4(\cos \frac{\Delta}{2} + \sin \frac{\Delta}{2}) \tag{A4}$$

$$N_{p0} = 2 + 1.5\alpha \tag{A5}$$

$$\lambda = 0.55 - 0.15\alpha \tag{A6}$$

where $\Delta = 1/\sin \alpha$ and α is the adhesion factor, which is related to c_u and can be determined by figuring out α versus c_u relationships from Georgiadis and Georgiadis' [18] study.

The initial stiffness K_i in Equation (1) is calculated by:

$$K_i = 3E_s \left(\frac{E_s D^4}{E_p I_p} \right)^{1/12} \tag{A7}$$

The linear reduction factor proposed by Georgiadis and Georgiadis [18] is given as:

$$\mu = \frac{K_{i\theta}}{K_{i0}} = \cos \theta + \frac{1 - \cos \theta}{6D} \left[\frac{z}{D} + \left(\frac{b}{D} - 0.5 \right) \tan \theta \right] \leq 1 \tag{A8}$$

It is given by Yang et al. [31] as:

$$\mu = \frac{K_{i\theta}}{K_{i0}} = \cos \theta + \frac{z}{6D \tan \theta} (1 - \cos \theta) \tag{A9}$$

Appendix B. The Process of Deriving the $K_{i\theta}$ from Simulation Results

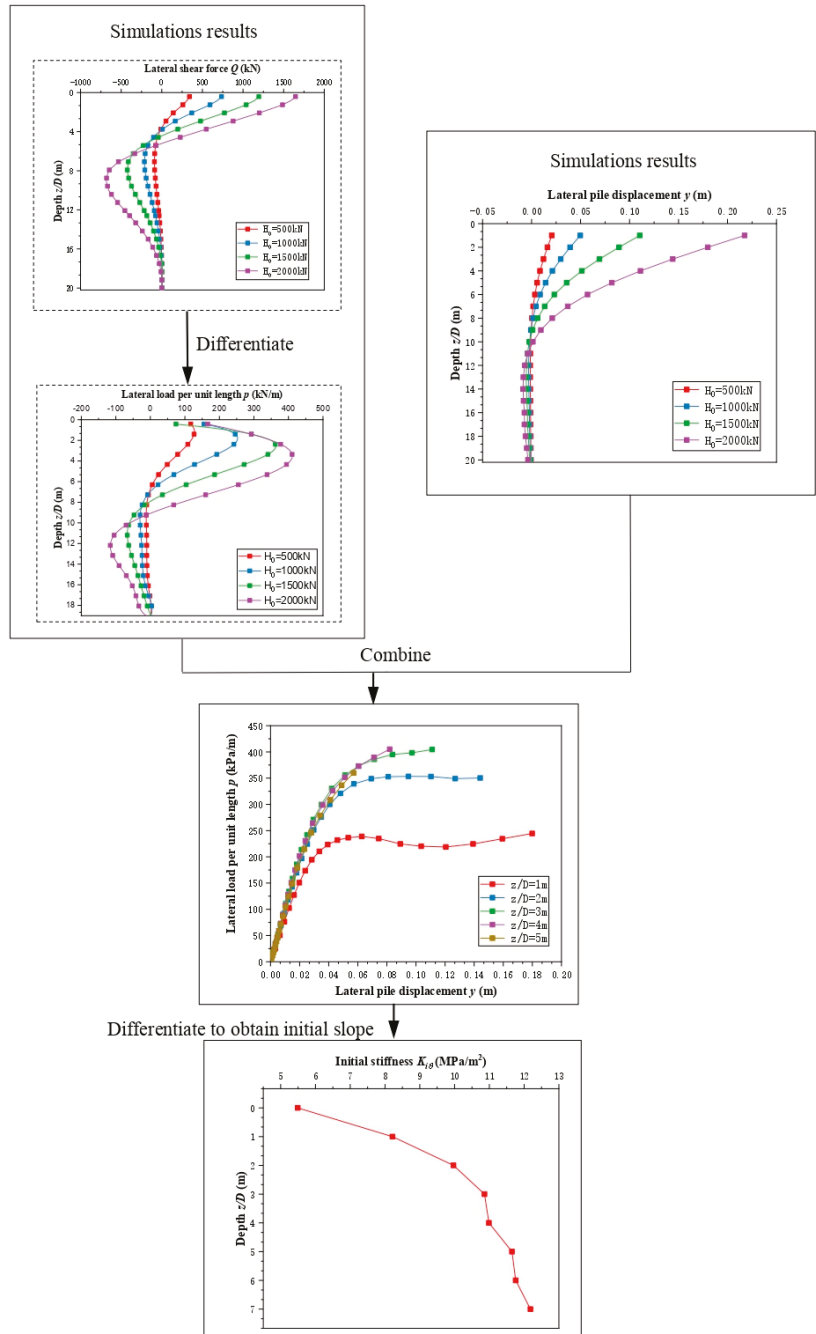


Figure A1. Process of deriving $K_{i\theta}$ from simulation results.

References

1. Wang, S.; Wang, P.; Zhai, H.; Zhang, Q.; Chen, L.; Duan, L.; Liu, Y.; Jeng, D. Experimental study for wave-induced pore-water pressures in a porous seabed around a mono-pile. *J. Mar. Sci. Eng.* **2019**, *7*, 237–255.
2. Wan, Z.; Dai, G.; Gong, W. Field study on post-grouting effects of cast-in-place bored piles in extra-thick fine sand layers. *Acta Geotech.* **2019**, *14*, 1357–1377.
3. Liu, X.; Lu, Y.; Yu, H.; Ma, L.; Ma, L.; Li, X.; Li, W.; Zhang, H.; Bian, C. In-situ observation of storm-induced wave-supported fluid mud occurrence in the subaqueous Yellow River delta. *J. Geophys. Res. Ocean.* **2022**, *127*, e2021JC018190. [[CrossRef](#)]
4. Liu, X.; Yang, Q.; Wang, Y.; Jeng, D.; Sturm, H. New advances in marine engineering geology. *J. Mar. Sci. Eng.* **2021**, *9*, 66.
5. Rajashree, S.; Sitharam, T. Nonlinear finite-element modeling of batter piles under lateral load. *J. Geotech. Geoenviron. Eng.* **2001**, *127*, 604–612.
6. Kim, B.; Kim, N.; Jin, L.; Kim, Y. Experimental load–transfer curves of laterally loaded piles in Nak-Dong river sand. *J. Geotech. Geoenviron. Eng.* **2004**, *130*, 416–425.
7. Sawant, V.; Shukla, S. Effect of edge distance from the slope crest on the response of a laterally loaded pile in sloping ground. *Geotech. Geol. Eng.* **2014**, *32*, 197–204. [[CrossRef](#)]
8. Yin, P.; He, W.; Yang, Z. A Simplified Nonlinear Method for a Laterally Loaded Pile in Sloping Ground. *Adv. Civ. Eng.* **2018**, *2018*, 5438618. [[CrossRef](#)]
9. Jiang, C.; Zhang, Z.; He, J. Nonlinear analysis of combined loaded rigid piles in cohesionless soil slope. *Comput. Geotech.* **2020**, *117*, 117. [[CrossRef](#)]
10. Matlock, H. Correlation for design of laterally loaded piles in soft clay. In Proceedings of the 2nd Offshore Technology Conference, Houston, TX, USA, 22–24 April 1970; pp. 577–594.
11. O’Neill, M.W.; Gazizoglu, S.M. *An Evaluation of P-y Relationships in Clays*; University of Houston, Department of Civil Engineering: Houston, TX, USA, 1984.
12. Sharafi, H.; Maleki, Y.; Karimpour-Fard, M. Three-dimensional finite difference modeling of static soil-pile interactions to calculate p-y curves in pile-supported slopes. *Arab. J. Geosci.* **2015**, *9*, 5. [[CrossRef](#)]
13. Yin, J.; Li, S.; Sun, L.; Li, T. Pile installation assessment of offshore wind jacket foundation in completely weathered rock: A case study of the South China Sea. *J. Mar. Sci. Eng.* **2022**, *10*, 900. [[CrossRef](#)]
14. Sun, W. A p-y model for predicting the lateral nonlinear interaction between pile and soil-rock mixture material based on discrete element modeling. *Simul. Model. Pract. Theory* **2020**, *100*, 102060. [[CrossRef](#)]
15. Rathod, D.; Muthukkumaran, K.; Thallak, S. Experimental investigation on behavior of a laterally loaded single pile located on sloping ground. *Int. J. Geomech.* **2019**, *19*, 04019021. [[CrossRef](#)]
16. Yang, M.; Deng, B.; Zhao, M. Experimental and theoretical studies of laterally loaded single piles in slopes. *J. Zhejiang Univ. Sci. A* **2019**, *20*, 838–851. [[CrossRef](#)]
17. Nimityongskul, N.; Kawamata, Y.; Rayamajhi, D.; Scott, A. Full-scale tests on effects of slope on lateral capacity of piles installed in cohesive soils. *J. Geotech. Geoenviron. Eng.* **2018**, *144*, 04017103. [[CrossRef](#)]
18. Georgiadis, K.; Georgiadis, M. Development of p-y curves for undrained response of piles near slopes. *Comput. Geotech.* **2012**, *40*, 53–61. [[CrossRef](#)]
19. Peng, W.; Zhao, M.; Yao, X.; Yang, C.; Zhao, H. Analysis of laterally loaded piles in sloping ground using a modified strain wedge model. *Comput. Geotech.* **2018**, *107*, 163–175. [[CrossRef](#)]
20. Liu, J.; Guo, Z.; Han, B. Load transfer of offshore open-ended piles considering the effect of soil plugging. *J. Mar. Sci. Eng.* **2019**, *7*, 313. [[CrossRef](#)]
21. Reese, L.; Cox, W.; Koop, F. Analysis of laterally loaded piles in sand. In *Offshore Technology in Civil Engineering: Hall of Fame Papers from the Early Years*; American Society of Civil Engineers: Reston, VA, USA, 1974; pp. 95–105.
22. Georgiadis, K.; Georgiadis, M. Undrained lateral pile response in sloping ground. *J. Geotech. Geoenviron. Eng.* **2010**, *136*, 1489–1500. [[CrossRef](#)]
23. Brown, D.; Shie, C. Some numerical experiments with a three dimensional finite element model of a laterally loaded pile. *Comput. Geotech.* **1991**, *12*, 149–162. [[CrossRef](#)]
24. Murff, J.; Hamilton, J. P-ultimate for undrained analysis of laterally loaded piles. *J. Geotech. Eng.* **1993**, *119*, 91–107. [[CrossRef](#)]
25. Pedram, B. Effects of pile shape in improving the performance of monopiles embedded in onshore clays. *Can. Geotech. J.* **2015**, *52*, 1144–1158. [[CrossRef](#)]
26. Vesic, A. Bending of beams resting on isotropic elastic solid. *J. Eng. Mech. Div.* **1961**, *87*, 35–54. [[CrossRef](#)]
27. Carter, D.P. A Non-Linear Soil Model for Predicting Lateral Pile Response. Ph.D. Thesis, Department of Civil and Environmental Engineering, University of Auckland, Auckland, New Zealand, 1984.
28. Kim, Y.; Jeong, S.; Lee, S. Wedge failure analysis of soil resistance on laterally loaded piles in clay. *J. Geotech. Geoenviron. Eng.* **2011**, *137*, 678–694. [[CrossRef](#)]
29. Jeong, S.; Kim, Y.; Kim, J. Influence on lateral rigidity of offshore piles using proposed p–y curves. *Ocean Eng.* **2011**, *38*, 397–408. [[CrossRef](#)]
30. Yang, Y.; Shen, M.; Juang, C. Assessing initial stiffness models for laterally loaded piles in undrained clay: Robust design perspective. *J. Geotech. Geoenviron. Eng.* **2019**, *145*, 04019073.

31. Yang, M.; Zhu, L.; Luo, H.; Feng, C. Experiment and numerical simulation of p-y curve method for laterally loaded single pile in sloping ground. *Journal Highw. Transp. Res. Dev.* **2017**, *24*, 83–90.
32. Terzaghi, K. Evaluation of coefficient of subgrade reaction. *Geotechnique* **1955**, *5*, 297–326. [[CrossRef](#)]
33. Poulos, H. Single pile response to cyclic lateral load. *J. Geotech. Geoenviron. Eng.* **1982**, *108*, 355–375. [[CrossRef](#)]
34. Zhou, J.; Gong, X.; Wang, K.; Zhang, R.; Yan, J. A simplified nonlinear calculation method to describe the settlement of pre-bored grouting planted nodular piles. *J. Zhejiang Univ. Sci. A* **2007**, *18*, 895–909. [[CrossRef](#)]
35. Wang, A.; Zhang, D.; Deng, Y. Lateral response of single piles in cement-improved soil: Numerical and theoretical investigation. *Comput. Geotech.* **2018**, *102*, 164–178. [[CrossRef](#)]
36. Sun, Y.; Xu, C.; Du, X.; Naggar, M.; Jia, J. Nonlinear lateral response of offshore large-diameter monopile in sand. *Ocean. Eng.* **2020**, *216*, 108013. [[CrossRef](#)]
37. Yang, X.; Zhang, C.; Huang, M.; Yuan, H. Lateral loading of a pile using strain wedge model and its application under scouring. *Mar. Georesour. Geotechnol.* **2018**, *36*, 340–350. [[CrossRef](#)]
38. Chen, L.; Jiang, C.; Pang, L.; Liu, P. Lateral soil resistance of rigid pile in cohesionless soil on slope. *Comput. Geotech.* **2021**, *135*, 104163. [[CrossRef](#)]
39. Sivapriya, S.; Gandhi, S. Soil–Structure Interaction of Pile in a Sloping Ground Under Different Loading Conditions. *Geotech. Geol. Eng.* **2019**, *38*, 1185–1194. [[CrossRef](#)]
40. Reese, L.; Wlech, R. Lateral loading of deep foundations in stiff clay. *J. Geotech. Eng. Div.* **1975**, *101*, 633–649. [[CrossRef](#)]
41. Reese, L.; Isenhower, W.; Wang, S. *Analysis of Design of Shallow and Deep Foundations*; John Wiley and Sons: Hoboken, NJ, USA, 2006.
42. Bhushan, K.; Haley, S.; Fong, P. Lateral load tests on drilled piers in stiff clays. *J. Geotech. Eng. Div.* **1979**, *105*, 969–985. [[CrossRef](#)]

Article

Discrete Element Simulation of the Macro-Meso Mechanical Behaviors of Gas-Hydrate-Bearing Sediments under Dynamic Loading

Yujing Jiang ^{1,2,3}, Meng Li ^{1,2}, Hengjie Luan ^{1,2,*}, Yichen Shi ¹, Sunhao Zhang ^{1,2}, Peng Yan ^{1,2} and Baocheng Li ^{1,2}

¹ College of Energy and Mining Engineering, Shandong University of Science and Technology, Qingdao 266590, China; jiang@nagasaki-u.ac.jp (Y.J.); 202082010012@sdust.edu.cn (M.L.); 202001010612@sdust.edu.cn (Y.S.); skzsh@sdust.edu.cn (S.Z.); 201882010009@sdust.edu.cn (P.Y.); 202082010008@sdust.edu.cn (B.L.)

² State Key Laboratory of Mining Disaster Prevention and Control Co-Founded by Shandong Province and the Ministry of Science and Technology, Shandong University of Science and Technology, Qingdao 266590, China

³ Graduate School of Engineering, Nagasaki University, Nagasaki 852-8521, Japan

* Correspondence: luanjie0330@126.com; Tel.: +86-0532-86058052

Abstract: Under the action of dynamic loadings such as earthquakes and volcanic activities, the mechanical properties of gas-hydrate-bearing sediments will deteriorate, leading to a decrease in the stability of hydrate reservoirs and even inducing geological disasters such as submarine landslides. In order to study the effect of dynamic loading on the mechanical properties of hydrate sediments, triaxial compression tests of numerical specimens were carried out by using particle flow code (PFC2D), and the macro-meso mechanical behaviors of specimens were investigated. The results show that the loading frequency has a small effect on the stiffness of the hydrate sediment, while it has a large effect on the peak strength. The peak strength increases and then decreases with the increase in loading frequency. Under the same loading frequency, the peak strength of the hydrate sediment increases with the increase in loading amplitude, and the stiffness of the specimen decreases with the increase in loading amplitude. The maximum shear expansion of the specimen changes with the movement of the phase change point and the rearrangement of the particles. The maximum shear expansion of the specimen changes with the movement of the phase change point and the change of the bearing capacity of the particles after the rearrangement, and the more forward the phase change point is, the stronger the bearing capacity of the specimen in the plastic stage. The shear dilatancy angle and the shear dilatancy amount both increase linearly with the increase in loading amplitude. The influence of loading frequency and amplitude on the contact force chain, displacement, crack expansion, and the number of cementation damage inside the sediment is mainly related to the average axial stress to which the specimen is subjected, and the number of cracks and cementation damage of the sediment specimen increases with the increase in the average axial stress to which the sediment specimen is subjected. As the rate of cementation damage increases, the distribution of shear zones becomes more obvious.

Keywords: gas-hydrate-bearing sediments; mechanical behavior; dynamic loading; discrete element simulation; macro-meso

Citation: Jiang, Y.; Li, M.; Luan, H.; Shi, Y.; Zhang, S.; Yan, P.; Li, B. Discrete Element Simulation of the Macro-Meso Mechanical Behaviors of Gas-Hydrate-Bearing Sediments under Dynamic Loading. *J. Mar. Sci. Eng.* **2022**, *10*, 1042. <https://doi.org/10.3390/jmse10081042>

Academic Editor: Timothy S. Collett

Received: 24 June 2022

Accepted: 26 July 2022

Published: 29 July 2022

Publisher's Note: MDPI stays neutral with regard to jurisdictional claims in published maps and institutional affiliations.



Copyright: © 2022 by the authors. Licensee MDPI, Basel, Switzerland. This article is an open access article distributed under the terms and conditions of the Creative Commons Attribution (CC BY) license (<https://creativecommons.org/licenses/by/4.0/>).

1. Introduction

Natural gas hydrate is a crystalline cage-shaped solid complex produced by methane and water molecules under a low temperature and high pressure, which is widely distributed in deep-sea sediments or onshore permafrost areas and is considered to be one of the most promising new clean alternative energy sources in the future [1]. The dynamic loads caused by earthquakes, submarine landslides, and hydrate mining activities can lead to the decomposition of hydrates, resulting in the deterioration of the mechanical properties of

hydrate sediments, which can lead to a series of geotechnical disasters, such as wellbore instability, submarine subsidence, submarine landslides, etc. [2,3]. Therefore, the study of the dynamic properties of hydrate sediments is important for hydrate mining design and hydrate reservoir stability evaluation, etc.

At present, many researchers have conducted many experimental studies on the mechanical properties of hydrate sediments. For example, Masui et al. [4] and Hyodo et al. [5] studied the mechanical properties of hydrate sediments and showed that the increase in saturation greatly increases the strength of the sediments. Song et al. [6] studied the mechanical response of methane hydrate sediments before and during natural gas production, and the results indicated that the dissociation of hydrate due to thermal decomposition led to the proportional loss of strength. Wu et al. [7] conducted triaxial compression experiments on hydrate sediments and showed that the shear and deformation properties of hydrate sediments are closely related to hydrate saturation and net peritectic pressure. Kajiyama et al. [8] conducted triaxial shear tests on hydrate sediments with different fines content and found that both shear strength and shear dilatancy of hydrate sediments significantly increased with increasing fines content. Li et al. [9] investigated the effect of hydrate distribution patterns on the mechanical parameters and damage mechanisms of hydrate sediments. The above studies have provided a preliminary understanding of the hydrostatic properties of hydrate sediments. However, due to the harsh conditions of hydrate sediment in sandy soils, it is still difficult to conduct an in-depth and systematic study on the dynamic properties of hydrate sediments due to the current development level of relevant test equipment and technology.

With the development of computer technology, the discrete element numerical simulation method has provided a new way to solve this problem [10–15]. As one of the discrete element simulation methods, the calculation principle of the particle flow program (PFC) is based on Newton's second law of motion to establish the equation of motion of the cell, and then use the explicit central difference method to solve the equation of motion, while the deformation or rupture process of the material is described by the rigid cell and its mutual position. It is based on the basic contact mechanics relationship between particles, which can easily construct and observe the microstructure of natural gas hydrate sediments and their evolution, and can also accurately evaluate the mechanical properties of geotechnical bodies under dynamic loading [16]. Brugada et al. [17] conducted a series of triaxial compression simulations by particle flow code (PFC) to study the effects of methane hydrate saturation on stress–strain relationship, volume strain, and macroscopic geomechanical properties (e.g., friction and expansion angle). Jiang et al. [18–22] developed a microscopic cementation model for hydrate mechanical properties to reflect the contact mechanical response of hydrate cementation between hydrate sediment grains, and a series of related discrete element simulations were conducted. Jung et al. [23] also considered the cementation effect of hydrate and performed three-dimensional discrete element simulations for sediments having two hydrate forms. Yang et al. [24] used the “radius expansion method” to generate hydrate sediment specimens and compared the simulation results with the existing indoor triaxial tests in terms of stress–strain relationship, bulk strain properties, elastic modulus, and peak strength, and studied the effect of different cementation radii and other microscopic cementation properties on the mechanical properties. He et al. [25] used the discrete element method to simulate the effect of different intermediate principal stresses on the mechanical behavior of methane-hydrate-filled sandy sediments. The above studies investigated the mechanical properties of hydrate sediments from different perspectives such as surrounding pressure and saturation. However, numerical simulations of the mechanical behavior of hydrate under dynamic loading have rarely been studied.

In view of the above understanding, in order to study the mechanical properties of natural gas hydrate sediments under dynamic loading, this paper firstly carried out triaxial compression tests on discrete element specimens of hydrate sediments under static loading and verified them by comparison, and determined reasonable simulation parameters; then, triaxial compression tests on hydrate sediment specimens under cyclic loading with

different frequencies and amplitudes were carried out to reveal the influence of dynamic loading on their macro-meso mechanical properties. The research results of this paper are useful for the understanding of the dynamics of hydrate sediments and the prevention and control of submarine geohazards.

2. Discrete Element Simulation of Gas-Hydrate-Bearing Sediments

2.1. Model Building

In order to establish a realistic numerical model of hydrate sediment specimens, the particle gradation selected in the model is similar to that of Toyoura sand [26], and the diameter of soil particles is 0.1–0.4 mm. Hydrate particles are generated in the pores of the sediment, and their particle radii are small, while too small a particle radius will inevitably lead to an increase in the number of particles and thus slow down the calculation efficiency. Combining the above factors, the radius of hydrate particles is taken as 0.06 mm. The modeling process is carried out with reference to the modeling method of Cheng [27]. The specific steps are as follows.

(1) Hydrate sediment specimen generation. Firstly, for generating the cylindrical specimen and subsequent loading, three walls were established at the specimen boundary, and then the initial sediment cylindrical specimen with soil particles of 2 mm in diameter and 4 mm in height was generated according to the Toyoura sand grading curve shown in Figure 1, at which time the internal pore ratio of the specimen was 0.42; then, according to the set value range of hydrate particles and soil particles, saturation, and initial porosity, the new porosity and particle size gradation curves were calculated. After that, the sediment cylindrical specimens containing soil particles and hydrate particles were generated according to the particle size gradation curves meeting the requirements of saturation and porosity.

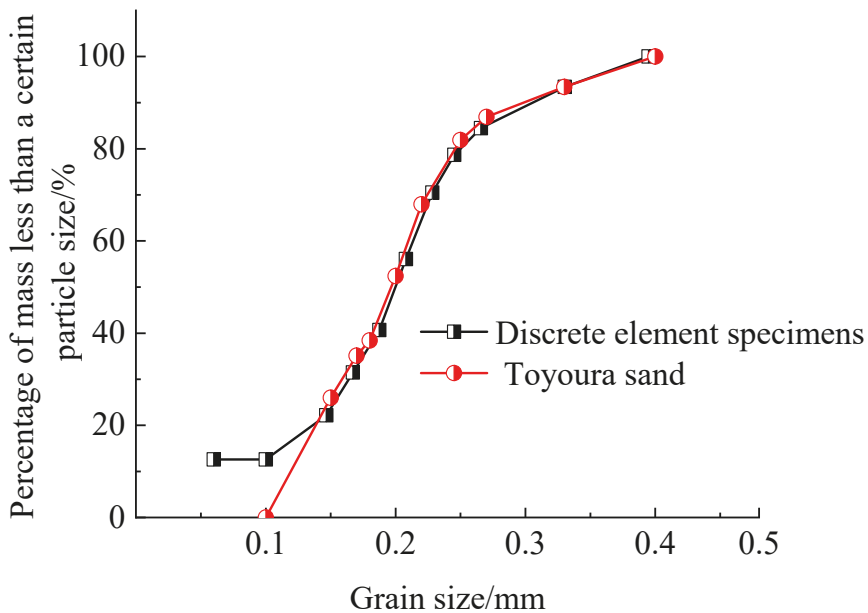


Figure 1. Gradation curves of discrete element samples and Toyoura sand (Adapted with permission from Ref. [26]. 2022, Xie, Y.; Feng, J.; Hu, W).

(2) A consolidation pressure F_c was applied to the specimens. A consolidation pressure of 1.0 MPa was applied to the generated specimens so that the particles in the specimens

were in contact with each other under this consolidation pressure until the calculation reached equilibrium.

(3) The saturation of specimens was made to reach the desired level. By “cmat” command, a parallel bond model was added between hydrate particles and between hydrate particles and sand particles, and a linear model was added between sand particles to generate a discrete hydrate sediment with 30% saturation, as shown in Figure 2.

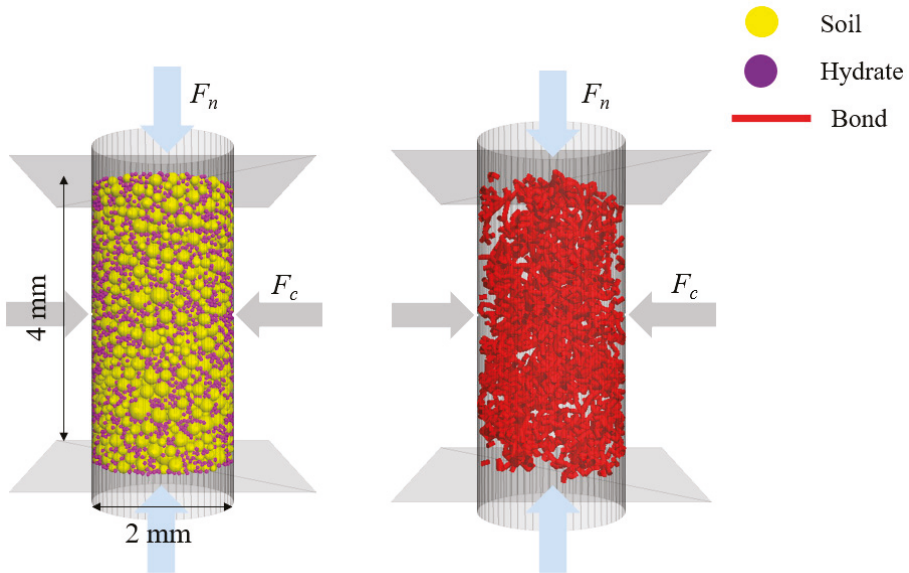


Figure 2. Saturation and formation of hydrate bond of discrete element specimens of hydrate sediments.

(4) Apply loads to the model. The axial load F_n was applied to the model by updating the velocity of the top and bottom walls to ensure that the confining stresses reached the desired stress state [28]. The specimens were tested at a constant loading rate of 1×10^{-6} m/s under an effective enclosing pressure of 1.0 MPa, and the test was stopped when the axial strain ϵ reached 25%.

Among them, since the load cannot be applied directly to the wall in the PFC numerical simulation software, servo loading was required according to the difference between the given target load and the actual load applied to the specimen, as shown in Figure 3. The PFC wall velocity conversion equation is [29]:

$$v^w = G(\sigma^{measured} - \sigma^{required}) = G\Delta\sigma, \tag{1}$$

where $\Delta\sigma$ is the difference between the target stress $\sigma^{required}$ and the actual monitored stress $\sigma^{measured}$, and G is the servo parameter whose value is calculated using Equation (2) [29]:

$$G = \frac{\alpha A}{k_n^{(w)} N_c \Delta t}, \tag{2}$$

where α is the stress release factor, taken as 0.5; A is the area of the boundary wall, $k_n^{(w)}$ is the average contact stiffness, N_c is the number of contacts between the boundary wall and the particles, and Δt is the unit time step.

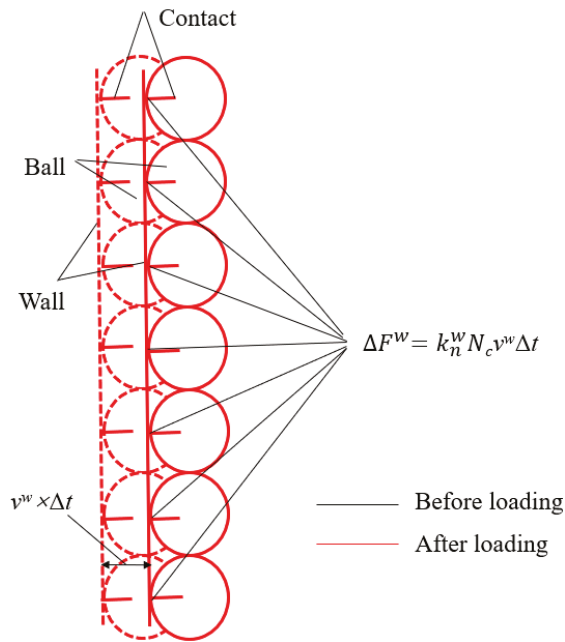


Figure 3. Realization method of dynamic load loading.

The amount of contact force change caused by the boundary wall motion in the unit time step is [29]:

$$\Delta F^w = k_n^{(w)} N_c v^w \Delta t, \tag{3}$$

2.2. Contact Models and Parameters

The mechanical properties of hydrate sediments are governed by the hydrate distribution in addition to factors such as net confining pressure, saturation, and mid-major stress coefficient [30]. Hydrate in hydrate sediments exists in three main forms [31], as shown in Figure 3: (i) pore-filling (Figure 4a); (ii) acting as a sediment soil skeleton (Figure 4b), and (iii) cemented between soil particles in the form of colloidal material (Figure 4c). Among them, the results of Waite et al. [32] and Brugada et al. [17] both showed that the pore-filling type has less influence on the mechanical properties of hydrate sediments, and the influence of hydrate distribution factors on the simulation results can be excluded to the maximum extent. Therefore, the pore-filling-type structure is used in the modeling in this paper.

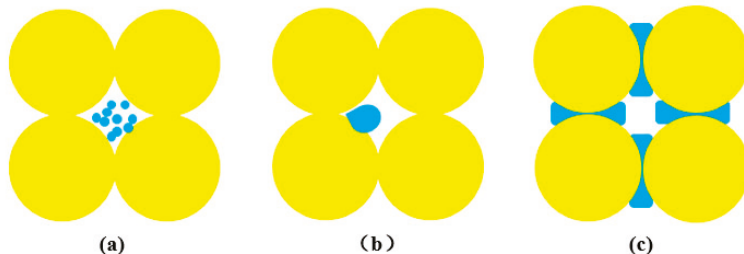


Figure 4. This type of hydrate sediment bond (Adapted with permission from Ref. [32]. 2009, the American Geophysical Union); (a) Pore-filling; (b) Soil skeleton; (c) Bond.

In this paper, the parallel bonding model is chosen to calculate the contact state between particles according to the model of cemented clustered hydrate sediment distribution proposed by Li et al. [31], i.e., there is bonding not only between hydrate and hydrate particles, but also between hydrate and soil particles, as shown in Figure 5. Figure 6a shows the forces and moments transmitted by the cementation, respectively, which decompose into normal and tangential components along the contact surface [29] (see Equations (4) and (5)). R is the radius of the short cylindrical cementation, and its value is calculated using Equation (6) [33,34]. $R^{(1)}$, and $R^{(2)}$ are the radii of the two spheres at contact. λ is a dimensionless parameter, and if λ is 1, the cemented material will fill the particles in contact with each other as much as possible.

$$F_i = F_i^n + F_i^s, \tag{4}$$

$$M_i = M_i^n + M_i^s, \tag{5}$$

$$R = \lambda \min(R^{(1)}, R^{(2)}), \tag{6}$$



Figure 5. Schematic diagram of hydrate sediment contact model: (a) cemented cluster hydrate sediments; (b) schematic diagram of 3D cementation model.

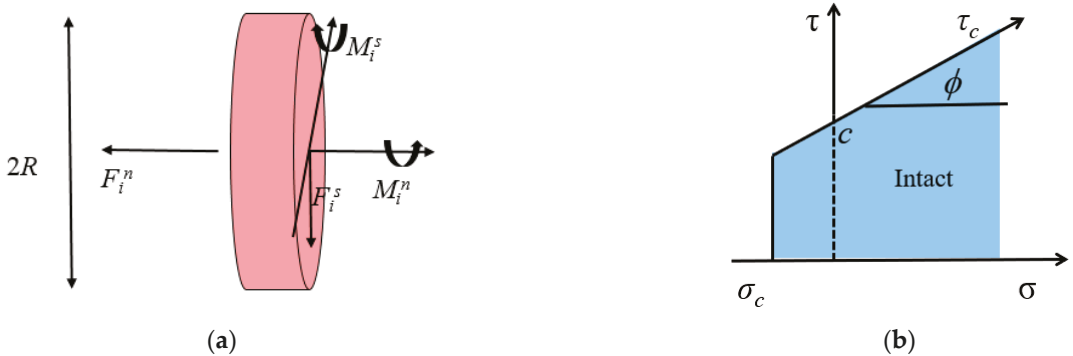


Figure 6. Schematic diagram of 3D parallel bonding model: (a) forces and moments transmitted by the bond (Adapted with permission from Ref. [32]. 2009, the American Geophysical Union); (b) failure criterion of classical parallel bonding model (Adapted with permission from Ref. [30]. 2022, Wei, R.; Jia, C.; Liu, L).

The parallel bonding model is defined by five parameters: normal stiffness k_n , tangential stiffness k_s , normal strength tangential strength τ_c , and short cylindrical radius R of the

cementation. The maximum normal σ^{max} and tangential stresses τ^{max} can be expressed as [35]:

$$\sigma^{max} = \frac{-F^n}{A} + \frac{|M^s| R}{I}, \tag{7}$$

$$\tau^{max} = \frac{|F^s|}{A} + \frac{|M^n| R}{I}, \tag{8}$$

where A , I , and J are cross-sectional area, cross-sectional moments of inertia, and cross-sectional polar moments of inertia, respectively, using the following calculation formulas: $A = \pi R^2$, $I = 0.5\pi R^4$ and $J = 0.25\pi R^4$.

As shown in Figure 6b, if the maximum normal stress exceeds its tensile strength limit ($\sigma^{max} \geq \sigma_c$), or the maximum tangential stress exceeds the shear strength limit ($\tau^{max} \geq \tau_c$), the parallel bonding model will be destroyed.

2.3. Model Validation

In order to determine the meso parameters of the numerical model in this paper, the simulation results of Brugada et al. [17] were used as the basis for calibration, and the trial and error method was used to continuously and dynamically adjust the meso parameters until the curves in this paper basically matched with the curve of Brugada et al. The final calibration results are shown in Figure 7, and the meso parameters determined after calibration are shown in Table 1. It can be seen that the trends of the two sets of curves are generally consistent and can be roughly divided into three stages. The first stage is the linear elastic stage, where the bias stress of the sediment specimen increases approximately linearly with the increase in axial strain; the second stage is the yield stage, where the bias stress reaches its peak. The peak strength of the bias stress simulated in this paper is 1.52 MPa, and that of Brugada et al. is 1.54 MPa, with an error of only 1.3% between them; the third stage is the residual stage, where both sets of simulations show strain softening and the bias stress rapidly decreases and tends to a stable value, and the specimen is damaged. The second half of the curve derived in this paper has a certain degree of jitter, which is because, in the compression process, a small displacement or misalignment of the particles will cause a relatively obvious change in the stress monitored on the monitoring wall with the increase in particle density. In general, the numerical simulation curve results in this paper have good accuracy.

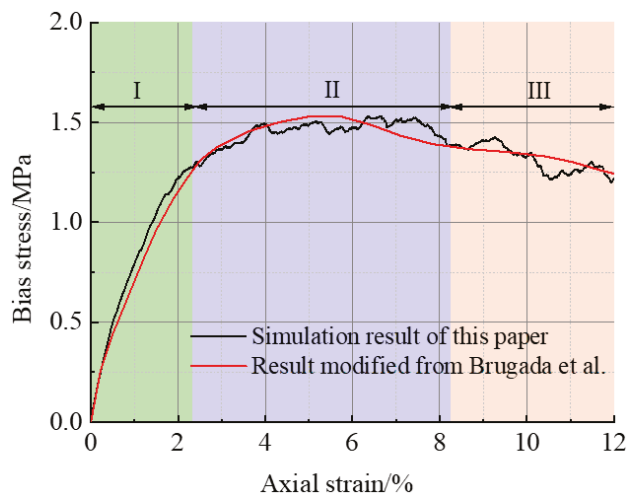


Figure 7. Comparison of discrete element simulation results [17].

Table 1. Material parameters in discrete element simulation.

Type	Density/(g/cm ³)	Friction Coefficient	Linear Model		Gluing Model				
			Effective Modulus/(MPa)	Stiffness Ratio	Effective Modulus/(MPa)	Stiffness Ratio	Tensile Strength/(MPa)	Bond Strength/(MPa)	Friction Angle/(°)
Soil particles	2.3	0.75	286	1.43					
Hydrate particles									
Between hydrate particles	0.9	0.75	28.6	1.43	24	1.5	5	5	40
Between hydrate particles and soil particles					24.6	1.5	5	5	40

2.4. Simulation Scheme

At present, displacement-controlled loading is commonly used in tests or simulations to equate the vibrational loading of earthquakes, i.e., the velocity magnitude is kept constant during the loading process, and the loading and unloading are added and removed back and forth within a certain displacement range [35–37], but this is not consistent with reality, and the velocity of real seismic waves changes continuously with time. Therefore, in order to reveal the macro-meso structural evolution of hydrate sediments under dynamic loading and its mechanical properties, this paper simulates dynamic loading by varying the axial loading velocity. In general, a seismic wave is a kind of random wave, and the random wave can be described by its amplitude, period, and phase. Although discrete elements can simulate random waveforms, the interpretation of the dynamic response mechanism of hydrate sediments under the action of random waveforms is very complicated. For this reason, the regular sinusoidal wave loading velocity will be introduced for analysis in this paper, and its expression is

$$v^w = A \sin(2\pi f * t), \tag{9}$$

where A is the loading amplitude, f is the loading frequency, and t is the time.

Since the frequency of seismic waves is generally less than 10 Hz, four frequencies of $f = 1, 2, 3,$ and 4 Hz were selected in this paper. Three amplitudes of $A = 1.2 \times 10^{-1}, 1.5 \times 10^{-1},$ and $1.8 \times 10^{-1} \text{ m}\cdot\text{s}^{-1}$ were selected based on the peak wave velocity recorded in Hachinohe, Japan [38], according to which different cyclic loading schemes were composed, as shown in Table 2. The adopted cyclic velocity curves are shown in Figure 8.

Table 2. Simulation scheme.

Title	Frequency/Hz	Peak/m·s ⁻¹
Sine wave	1, 2, 3, 4	1.2×10^{-1}
Sine wave	1.0	$1.2 \times 10^{-1}, 1.5 \times 10^{-1}, 1.8 \times 10^{-1}$

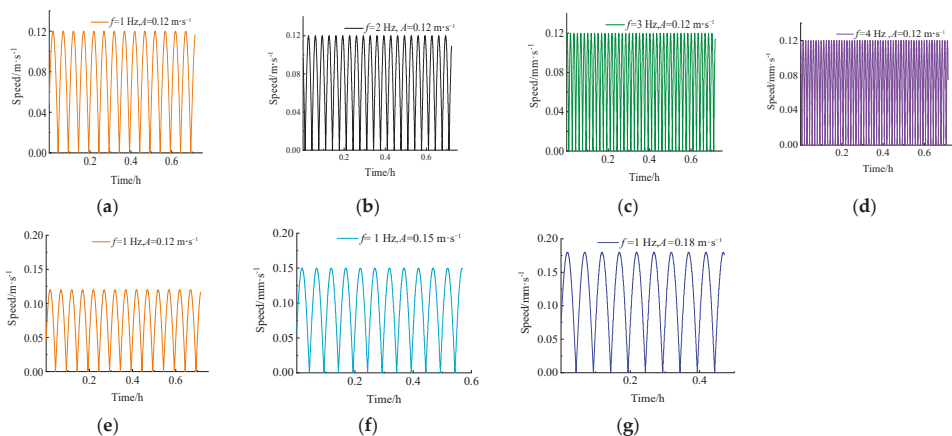


Figure 8. (a–g) the loading speed of each group of simulations.

3. Results and Analysis

3.1. Stress–Strain Curves

Unlike quasi-static loading, the mechanical characteristics of hydrate sediments under dynamic loading conditions change continuously with the cyclic change of loading velocity. To analyze the mechanical characteristics of hydrate sediment under dynamic loading, the stress–strain of hydrate sediment under dynamic loading of $f = 2 \text{ Hz}$ and $A = 0.12 \text{ m s}^{-1}$ as shown in Figure 9 was analyzed as an example. It can be seen that the stress–strain curves of hydrate sediment under dynamic loading can be roughly divided into four stages. The first stage is the elastic stage, which obeys Hooke’s law and shows the elastic characteristics, and the stress–strain curve is a straight line with a fixed slope. With the increase in axial strain, the slope of the curve slowly decreases, and the specimen enters the second stage (yield stage), in which the slope decreases continuously before the curve reaches the peak point, and the stress increases nonlinearly with strain and increases slowly. During this stage, the sediment specimen is compressed, the skeleton and cementation are destroyed, and the particles are rearranged. At the same time, the pores within the sediment specimen are squeezed under pressure, which makes the volume of the specimen decrease, at which time the bearing capacity of the specimen decreases, and thus the elastic modulus of the specimen gradually decreases. The third stage is the strain softening stage. After the peak point of the stress–strain curve, the partial stress decreases with the increase in the axial strain. The strength of the hydrate sediment specimen starts to decline slowly, and the stress–strain curve shows a strain softening trend. The fourth stage is the strain strengthening stage. In this stage, the partial stress increases with the increase in axial strain, which is because the hydrate particles in the sediment specimen still have a certain cementing effect on them, which can resist part of the stress. At the same time, the interaction between the particles caused by the presence of the surrounding pressure increases the contact area and frictional resistance, which inhibits the increase in cracks and prevents the slip or rearrangement between the particles, making the specimen more resistant to the damage caused by the axial load. As the loading proceeds, the particles inside the specimen are rearranged, the specimen is slowly and fully stressed, and its load-bearing capacity is gradually stabilized so that the sample also maintains a certain strength.

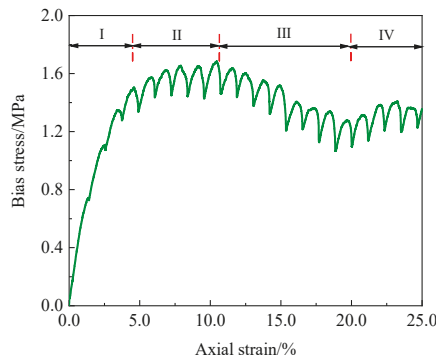


Figure 9. Stress–strain curve of hydrate sediments under dynamic loading ($f = 2 \text{ Hz}$, $A = 0.12 \text{ m}\cdot\text{s}^{-1}$).

The stress–strain curves of hydrate sediment under different loading frequencies and different loading amplitudes are shown in Figure 10. As can be seen from the figure, the stress–strain curve of the velocity cyclic loading mode is different from the force cyclic loading mode, and its stress–strain curve does not form a closed hysteresis loop curve, which is because even though the loading speed decreases, the axial displacement in the simulation keeps increasing downward, i.e., the hydrate sediment specimen keeps loading state without the process of unloading in the force cyclic loading mode.

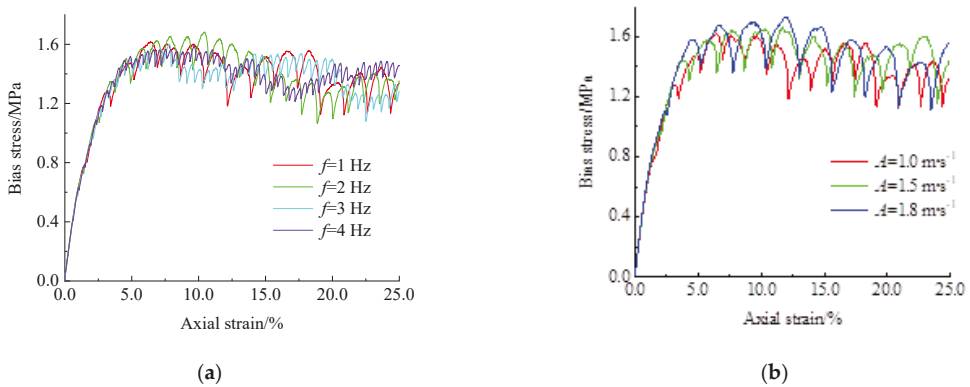


Figure 10. Stress–strain curves of sediment under different dynamic loads: (a) different loading frequencies; (b) different loading amplitudes.

It can also be seen from the figure that the change in the frequency and amplitude of the loading rate will have some effect on the characteristics of the stress–strain curve of the hydrate sediment. For this reason, the relationship between the axial strain interval L of the sediment and the loading conditions (Stages I and II) was counted, as shown in Figure 11. As can be seen from the figure, the axial strain corresponding to Stage I under all loading frequency conditions is 3.2%, which means that the loading frequency does not affect the distribution range of hydrate sediment specimens in Stage I. However, with the increase in the loading amplitude, the L corresponding to the first stage also increases, and when the loading amplitude increases from 0.12 m s^{-1} to 0.18 m s^{-1} , the L corresponding to the first stage is, respectively, 3.2%, 4.7%, and 5.6%. It shows that as the loading amplitude increases, the L corresponding to the elastic phase of the specimen becomes shorter, which is since the strength limit of the specimen is certain, and the greater the dynamic loading action, the faster it reaches its elastic limit.

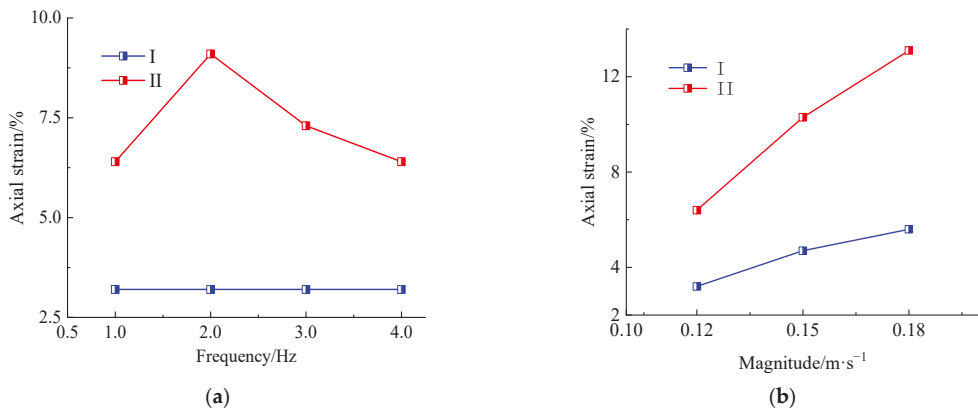


Figure 11. Relationship between sediment strain interval L and loading conditions (Stage I, Stage II): (a) different loading frequencies; (b) different loading amplitudes.

In Stage II, as the loading frequency increases, the L corresponding to the yielding stage of the specimen first increases and then decreases; when the loading frequency increases from 1 Hz to 2 Hz, the L corresponding to Stage II are, respectively, 6.4% and 9.1%. This is because the higher the loading frequency, the shorter the loading cycle, i.e., the shorter the

action time of each cycle, the less the cementation damage inside the specimen. However, as the loading frequency continues to increase from 2 Hz to 4 Hz, the L corresponding to phase II is 9.1%, 7.3%, and 6.4%, respectively. This is due to the fact that the more the number of cycles of cyclic loading at the same time, the collision damage inside the specimen increases, making the time experienced in the yielding phase of the specimen decrease with the change in frequency. As the loading amplitude increases, the L corresponding to the yielding stage of the specimen also increases. When the loading amplitude increases from $0.12 \text{ m}\cdot\text{s}^{-1}$ to $0.18 \text{ m}\cdot\text{s}^{-1}$, the L corresponding to the second stage is, respectively, 6.4%, 10.3%, and 13.1%. This is because the larger loading amplitude indicates that the specimen is loaded at a larger rate in the same cycle, i.e., the larger the axial force on the specimen in each cycle, the larger the load carrying capacity of the specimen, which is also in accordance with the characteristics of the hydrate sediment as a frictional material.

Figure 12 shows the strain–time curves of hydrate sediments under different dynamic loads. It can be seen that the strain–time curves vary basically the same for different loading frequencies, but the strain rate increases with the increase in loading amplitude. It shows that the loading amplitude has a greater effect on the strain of hydrate specimens. This is due to the fact that the larger the loading amplitude is at the same loading frequency, the greater the stress on the specimen in each cycle, the greater the number of cementation damage, the easier the specimen is to deform and destroy, and the greater the strain rate.

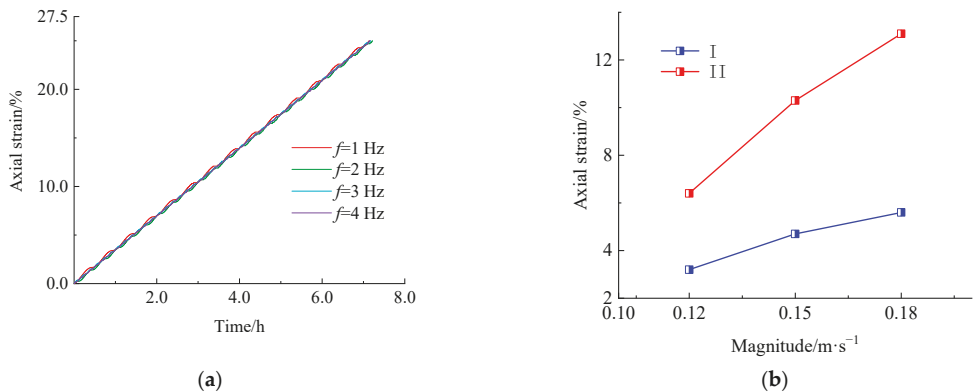


Figure 12. Strain–time curves of sediment under different dynamic loads: (a) different loading frequencies; (b) different loading amplitudes.

3.2. Strength Characteristics

3.2.1. The Effect of Loading Frequency

Figure 13 shows the relationship between the peak sediment strength, the sediment E_{50} , and the loading frequency. From the figure, it can be seen that the peak sediment strength increases and then decreases as the loading frequency increases. When the loading frequency increases from 1 Hz to 2 Hz, the peak sediment strength increases from 1.62 MPa to 1.68 MPa, and its peak strength increases by 3.7% compared to 1 Hz. When the loading frequency continues to increase to 3 Hz and 4 Hz, the peak sediment strength decreases to 1.6 MPa and 1.59 MPa, respectively, and decreases by 5% and 5.2% compared to 2 Hz, respectively. It shows that the effect of loading frequency on the peak strength is not monotonic, and there exists a critical value, less than which the peak strength increases with increasing loading frequency, and greater than which the peak strength decreases with increasing loading frequency. This is due to the loading frequency being small, as the loading cycle becomes shorter with the increase in loading frequency. That is, the shorter the time of the action of each cycle with the same number of cycles, the specimen’s internal cementation damage is less, and the bearing capacity of the specimen is greater. However,

as the loading frequency continues to increase beyond its critical value, the number of cyclic loading at the same time increases, and the cementation damage inside the specimen increases. Comparing the length of the action time of each cycle, the influence of the number of cyclic loading within the same time on the cementation damage dominates, which makes the bearing capacity of the specimen decrease. At the same time, when the loading frequency exceeds the critical value, the particles inside the sediment specimen frequently adjust the arrangement, which leads to the instability of the internal mechanical structure of the sediment and makes the internal force uneven, and even generates the stress concentration phenomenon, and finally leads to a certain degree of reduction in the yield strength of the sediment specimen.

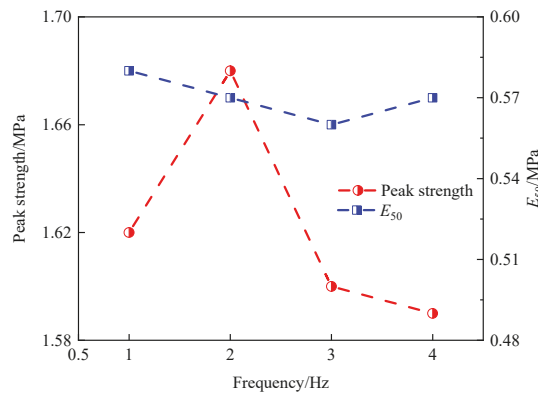


Figure 13. The relationship between the peak strength of sediment, E_{50} , and the loading amplitude.

Hydrate sediments are inelastic materials, so it is difficult to obtain the initial modulus E_0 . In this test, the cut-line modulus E_{50} was used to describe the stiffness of the specimen. E_{50} is defined as the slope of the line connecting the point half the value of the breaking strength in the stress–strain curve to the origin. From the relationship between the sediment E_{50} and the loading frequency in Figure 13, it can be seen that the E_{50} of the sediment specimen is 0.58 MPa at a loading frequency of 1 Hz, 0.57 MPa when the loading frequency increases to 2 Hz, 0.56 MPa when the loading frequency continues to increase to 3 Hz, and 0.57 MPa when the loading frequency continues to increase to 4 Hz. With the increase in loading frequency, the E_{50} of hydrate specimens changed less, only 0.01 MPa, which means that the effect of loading frequency on the stiffness of hydrate specimens is small.

3.2.2. The Effect of Loading Amplitude

Figure 14 shows the curve of peak sediment strength, sediment E_{50} , and loading amplitude. When the loading amplitude was increased from 0.12 m s^{-1} to 0.18 m s^{-1} , the peak sediment strengths were 1.62 MPa, 1.66 MPa, and 1.73 MPa, respectively, which were 2.4% and 6.7% higher compared to the peak strengths at loading frequencies of 0.15 m s^{-1} and 0.18 m s^{-1} for a loading amplitude of 0.12 m s^{-1} , respectively. Under the action of loading, the particles in the sediment specimen will first overcome the interparticle interaction forces before the relative misalignment occurs, mainly including interparticle friction and cohesion. When the amplitude of the loading rate increases, due to the inertia of the sediment particles, particle-to-particle squeezing begins to occur, resulting in an increase in the positive stress between the sediment particles, which in turn increases the inter-particle friction and the strength of the sediment. Combined with Figure 12b, the strain rate of the specimen increases with the increase in loading amplitude under dynamic loading, and the time required for the specimen to respond to strain decreases with the increase in strain rate. This makes the strain more localized, and then makes the specimen

all strained and will require more stress so the peak strength of the specimen will increase as the cyclic loading amplitude increases.

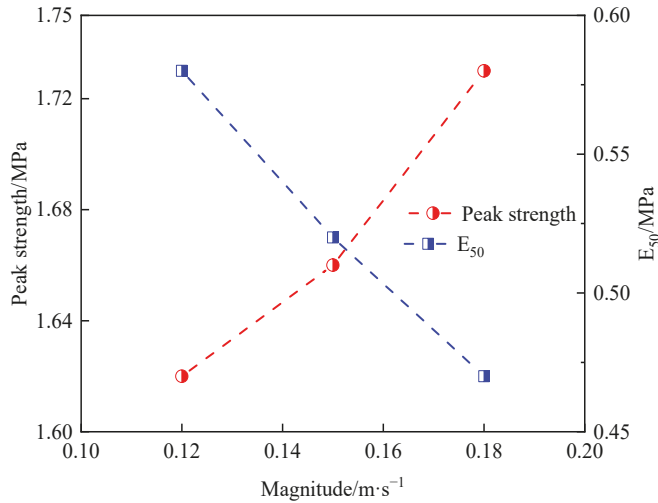


Figure 14. The relationship between the peak strength of sediment, E_{50} , and the loading amplitude.

The relationship between the E_{50} loading amplitude of the sediment in Figure 14 shows that the E_{50} of the hydrate specimen decreases with the increase in the loading amplitude. The E_{50} of the sediment specimen was 0.58 MPa at a loading amplitude of 0.12 m s^{-1} ; when the loading amplitude increased to 0.15 m s^{-1} , the E_{50} decreased to 0.52 MPa with a decrease of 10.3%; when the loading amplitude continued to increase to 0.18 m s^{-1} , the E_{50} decreased again to 0.47 MPa with a decrease of 9.6%. This is due to the fact that the cementation between soil and hydrate particles in the sediment specimen will be destroyed under the action of loading, and the rearrangement between the particles will occur; the greater the loading amplitude, the greater the stress on the specimen in each cycle, and the greater the number of cementation failures, which makes the sediment specimen less able to resist deformation and reduces the stiffness of the specimen.

3.3. Volumetric Strain Characteristics

3.3.1. Comparison of Volume Strain Curves

Dilatancy is one of the most important properties of sandy soils. This is because most of the accidents under load are due to shear swell or shear shrinkage damage of the soil, which leads to the loss of bearing capacity. Hydrate sediments have a similar structure to sandy soils, so their dilatancy is important to study [39]. The results of volume strain simulations of hydrate sediments under different dynamic loads are shown in Figure 15. It can be seen that the simulation results of each group show the bulk strain law of shear shrinkage followed by shear dilatancy. Firstly, as the loading proceeds, the pore ratio between the specimen particles decreases with the increase in consolidation pressure, which makes the specimen appear to have obvious shear shrinkage. Then, as the loading continues, the cementation in the specimen gradually breaks down, and because the soil particles are closely arranged, the soil particles at the shear zone must rotate around the adjacent particles in order to produce larger movement, which causes the expansion of the specimen. It can also be seen from the figure that the correlation between the shear shrinkage of hydrate sediment and the loading frequency and amplitude is small. However, the maximum shear dilatancy is influenced by the loading frequency and loading amplitude.

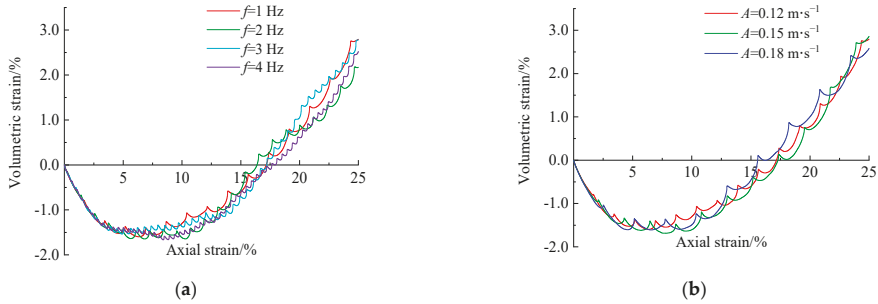


Figure 15. Volumetric strain-axial strain curves of sediment under different dynamic loads: (a) different loading frequencies; (b) different loading amplitudes.

3.3.2. Frequency, Amplitude–Dilation Relationship

To quantify the effects of loading frequency and loading amplitude on shear dilatancy, the maximum shear dilatancy under different loading frequencies and loading amplitude conditions were counted separately, as shown in Figure 16. It is obvious from the figure that the maximum shear expansion of sediment specimens at loading frequencies of 1, 2, 3, and 4 Hz are 2.793%, 2.17%, 2.780%, and 2.52%, respectively, which means that the shear dilatancy decreases and then increases and finally decreases again with the increase in frequency. At the loading amplitudes of 0.12, 0.15, and 0.18 m s^{-1} , the maximum shear dilatancy was 2.79%, 2.858%, and 2.52%, respectively, which also increased and then decreased with increasing amplitude. As Figure 15 shows, it can be seen that there is a critical point between shear shrinkage and shear dilatancy of the specimen, called the phase change point. The more forward the phase change point is, the shorter the shear shrinkage process is and the more obvious the shear expansion of the specimen is. At a frequency of 2 Hz, the phase change point is the most forward compared to the other three groups, and the maximum shear dilatancy of the specimen is the smallest at 2.17%. This is because the specimen with an axial strain of about 25% at a frequency of 2 Hz is exactly in the process of a certain increase in the load-bearing capacity after the rearrangement of the particles, resulting in a consequent decrease in its maximum shear expansion.

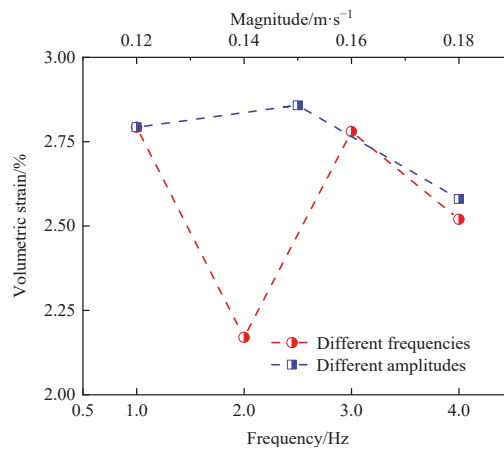


Figure 16. Relationship between maximum shear dilatation of sediment, loading frequency, and loading amplitude.

As can be seen from Figure 16, the effect of loading amplitude on shear dilatancy amount is not monotonic as the loading amplitude increases. The maximum shear dilatancy of the sediment specimens increased with increasing amplitude at the loading amplitude of 0.12, 0.15 m s⁻¹, 2.79%, and 2.858%, respectively. At the amplitude of 0.18 m s⁻¹, the phase change point was the most forward compared to the other three groups, while the maximum shear dilatancy of the specimens was the smallest at 2.52% for the same reason as described in the previous paper.

The variation of the shear dilatancy angle with different loading frequencies and amplitudes are given in Figure 17. The formula for the shear dilatancy angle ψ proposed by Roscoe [40] is as follows.

$$\psi = \arcsin - \frac{\varepsilon_1 + \varepsilon_2}{\varepsilon_1 - \varepsilon_2}, \tag{10}$$

where ε_1 and ε_2 are the axial and lateral strain increments, respectively.

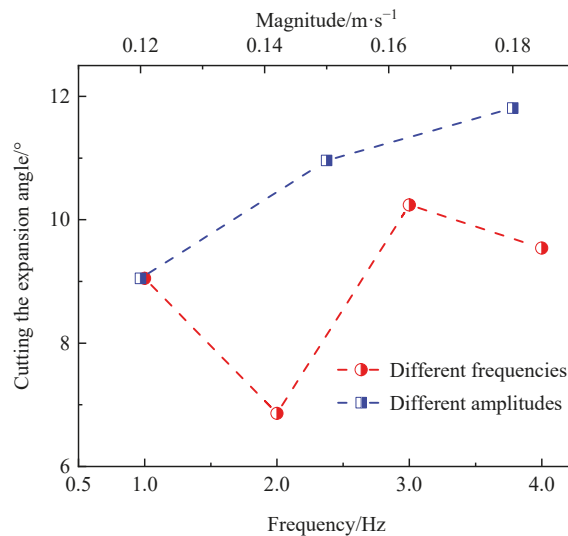


Figure 17. Relationship between sediment dilatancy angle, loading frequency, and loading amplitude.

As can be seen from Figure 17, the variation law of shear dilatancy angle of sediment specimens with loading frequency under the action of the same loading amplitude is similar to the variation law of shear dilatancy amount with loading frequency, and the shear dilatancy angle of specimens under the action of the same loading frequency tends to increase linearly with the increase in loading amplitude. It was shown [41] that when the shear dilatancy angle was higher, the sediment specimens obtained larger lateral deformation, and the precursors of instability damage of the specimens were more obvious. That means that the higher the loading frequency of the test conditions, the more likely the sediment specimens are to have destabilization damage.

3.4. Volumetric Strain Characteristics

Under a triaxial stress state, hydrate sediments exhibit their deformation damage process in terms of stress-strain and bulk strain development changes at the macroscopic level and shear zone generation and development at the fine level [42]. The effect of loading frequency and amplitude on the deformation damage of hydrate sediment specimens can be studied by particle displacement, contact force chain distribution, and microcrack extension evolution law.

3.4.1. Evolution of Deformation and Failure Characteristics

Taking the deformation damage law of hydrate sediment under $f = 1.0 \text{ Hz}$, $A = 0.12 \text{ m}\cdot\text{s}^{-1}$ dynamic load as an example, the particle displacement, contact force chain distribution, and microcrack expansion simulation results are shown in Figure 18. From the particle displacement cloud shown in Figure 18a, it can be seen that with the increase in axial strain, the particles in the upper and lower parts of the model are compressed and move toward the middle, and the pores inside the model are gradually compressed and form a shear zone, as shown in the area marked by the black wire frame in the figure. From the contact force chain cloud shown in Figure 18b, it can be seen that a weak force chain (green part) is formed at the center of the shear zone, the strong force chain (red part) gradually expands toward the ends of the shear zone of the specimen, and the contact force near the shear zone is roughly perpendicular to the particle displacement direction, which corresponds to the displacement cloud atlas of the particles. This is due to the frictional forces generated by the misalignment of the particles in the specimen, which are composed of unbalanced forces between the particles when relative sliding is generated by the particles inside the specimen [43].

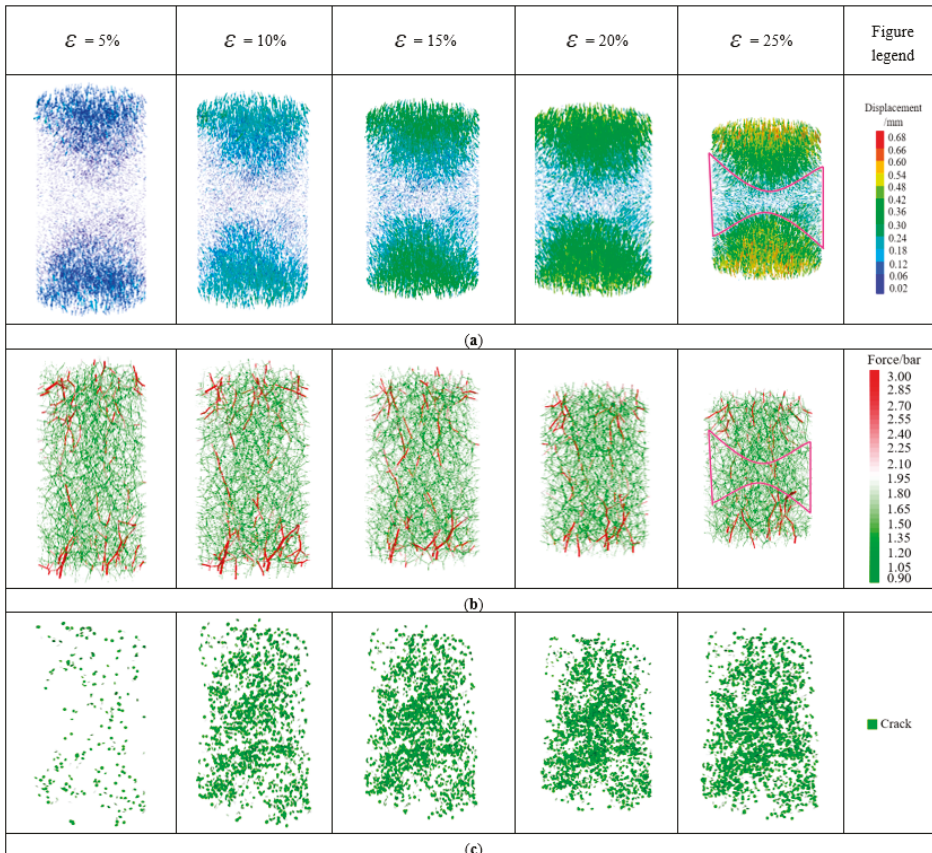


Figure 18. Typical failure law of hydrate sediments under the dynamic load of $f = 1.0 \text{ Hz}$ and $A = 0.12 \text{ m}\cdot\text{s}^{-1}$: (a) cloud diagram of sample particle displacement, (b) contact force chain diagram, and (c) microcrack expansion diagram.

From the microcrack expansion diagram shown in Figure 18c, it can be seen that the number of cracks at 5% of axial strain (before the peak strength) is small and mainly concentrated at the two ends of the specimen, and there is no obvious cementation damage in the hydrate sediment specimen. The number of cracks increases significantly at 10% and 15% of the axial strain (after the peak strength). At this time, the cementation between the hydrate particles and the cementation between the hydrate particles and the soil particles are destroyed in large quantities, but the cracks are randomly distributed in an irregular manner. The number of cracks in the specimen tends to be stable at 20% and 25% of the axial strain (after shear expansion), so it can be seen that the change law of the number of cracks in the specimen with the axial strain is similar to the change law of the stress–strain relationship. The number of cracks in the middle of the specimen is significantly larger than the number of cracks at the two ends of the specimen, which indicates that the number of collision damage near the shear zone continues to increase with the further increase in the axial strain and is concentrated near the shear zone.

A similar conclusion can be drawn from the damage–strain relationship curve of stress–cementation in Figure 19. The degree of stress is low in the initial stage of specimen loading, the cementation damage is less, and the rate of cementation damage is slow. With the development of strain reaching the peak strength, the rate of cementation damage increases significantly, and the cementation damage increases by a large amount; thus, the development of cementation damage can explain to some extent the process of change in the macroscopic mechanical behavior of the specimen during the test.

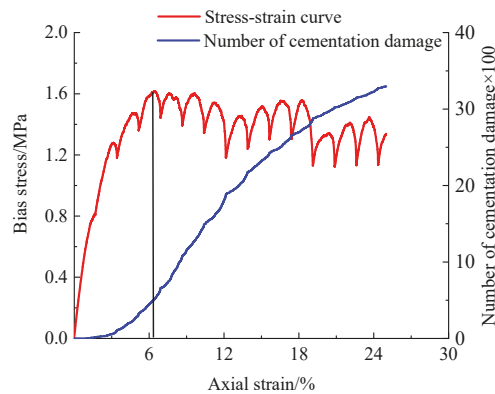


Figure 19. The stress–cementation failure–strain curve of hydrate sediments under dynamic load of $f = 1.0 \text{ Hz}$ and $A = 0.12 \text{ m}\cdot\text{s}^{-1}$.

3.4.2. Effect of Loading Frequency

The simulation results under different frequency loading conditions at an amplitude of $0.12 \text{ m}\cdot\text{s}^{-1}$ and an axial strain of 25% are shown in Figure 20. From the displacement cloud atlas in Figure 20a, it can be seen that when the loading frequency is less than γ ($2 \text{ Hz} < \gamma < 3 \text{ Hz}$), with the increase in loading frequency, the displacement of the middle particles within the model increases, and the distribution of the shear zone becomes less and less obvious. When the loading frequency is greater than γ , with the increase in loading frequency, the displacement of the middle particles within the model decreases, and the distribution of the shear zone becomes more and more obvious. By calculation, it can be obtained that the average stresses of the specimen are 1.334, 1.319, 1.323, and 1.344 MPa when f is 1, 2, 3, and 4 Hz, respectively. The lateral pressure and constraint provided by the wall on the particles are all the same under the same circumferential pressure, so with the axial stress getting smaller, the distribution of the shear zone is also becoming less and less obvious. On the contrary, the distribution of the shear zone is becoming more and more obvious. As shown in the Figure 20c microcrack expansion diagram, the less obvious the shear zone is, the less

the number of cracks near the shear zone of the corresponding specimen. At the same time, in Figure 21, the curves of cementation damage–time step curves show the same trend for each loading frequency condition, and the number of cementation damage with time step for loading frequency conditions with similar average axial stresses has approximately the same law. The smaller the average axial stress is, the smaller the rate of cementation damage is. It can be seen that the damage to the cementation of specimens is closely related to the average axial stress to which they are subjected. As shown in the contact force chain cloud atlas in Figure 20b, when the loading frequency is less than β ($2 \text{ Hz} < \beta < 3 \text{ Hz}$), the color of the contact force chain between the particles in the shear zone becomes lighter, and the contact force decreases significantly with the increase in the loading frequency; when the loading frequency is greater than β , the contact force chain between the particles near the shear zone becomes more obvious, and the contact force increases significantly with the increase in the loading frequency. In the displacement cloud atlas, the greater the displacement of the particles, the more obvious the contact force chain, i.e., the greater the frictional resistance caused by particle dislocation, and on the contrary, the contact force chain is obviously reduced.

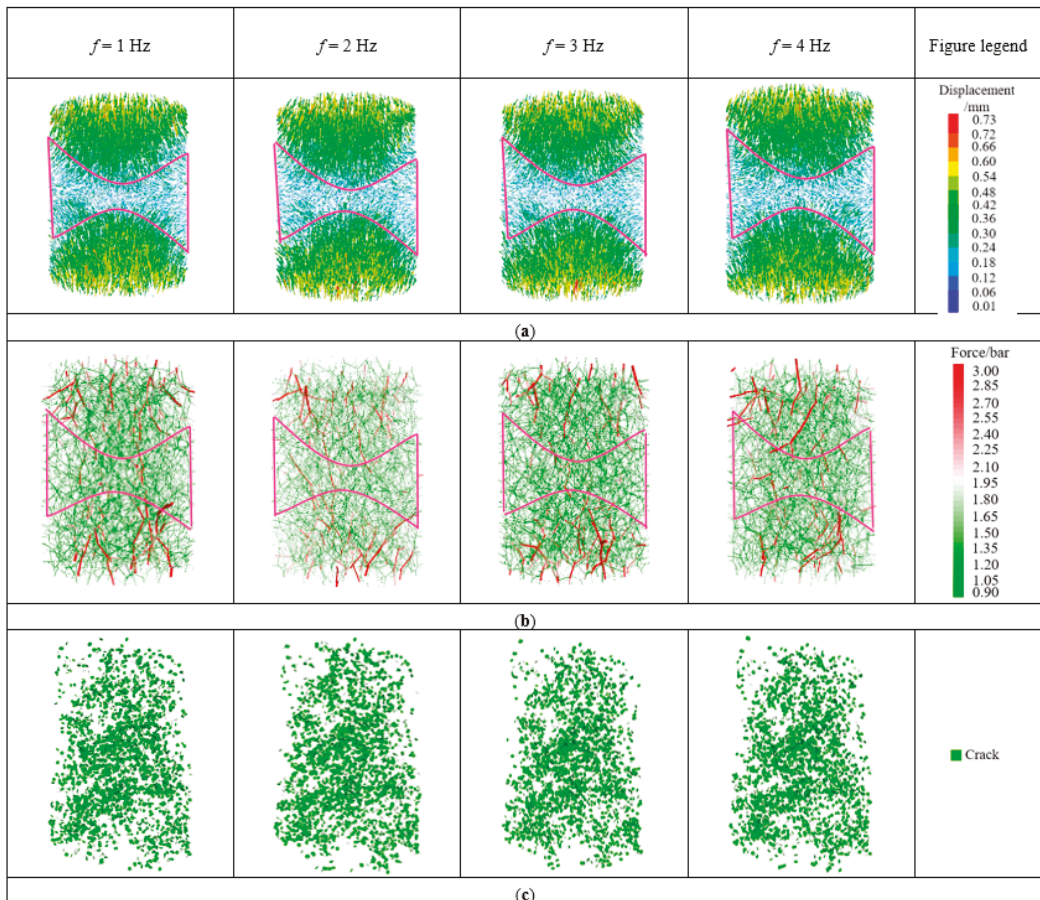


Figure 20. Typical failure law of hydrate sediments with an axial strain of 25% under dynamic loads of different frequencies: (a) cloud atlas of sample particle displacement, (b) contact force chain atlas, and (c) microcrack expansion diagram.

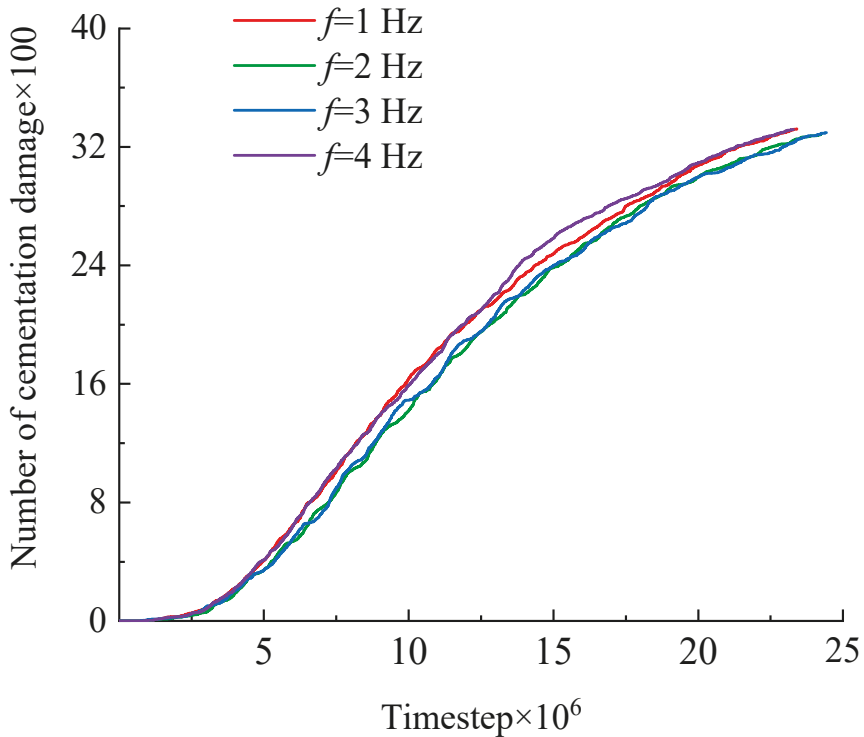


Figure 21. Failure–time step relationship of hydrate sediments cementation under different frequencies of dynamic loads.

3.4.3. Effect of Loading Amplitude

The simulation results for different amplitude loading conditions at a frequency of 1 Hz and an axial strain of 25% are shown in Figure 22. The average stresses in the specimens were calculated to be 1.334, 1.387, and 1.394 MPa for loading amplitudes of 0.12, 0.15, and 0.18 $\text{m}\cdot\text{s}^{-1}$, respectively. Combined with the displacement cloud in Figure 22a and the microcrack extension in Figure 22c, it can be seen that the average axial stress on the specimen increases with the increase in the loading amplitude. At this time, the displacement of the middle particles within the model decreases, the number of cracks increases, and the distribution of shear zones becomes more and more obvious. The reason is the same as the mechanism described in the previous section, so the larger the loading amplitude, the greater the axial stress, and the more obvious the distribution of the shear zone. As seen from the cementation damage–time step curve in Figure 23, with the increase in loading amplitude, both the number of cementation damage of the specimen and the damage rate increase. From the contact force chain atlas in Figure 22b, it can be seen that the contact force chain near the shear zone increases significantly with the increase in the loading amplitude, and the contact force chain between the particles is more obvious and increases significantly. Corresponding to the displacement cloud atlas, the greater the displacement of the particles, the more obvious the contact force chain, which means the greater the frictional resistance caused by the misalignment of the particles.

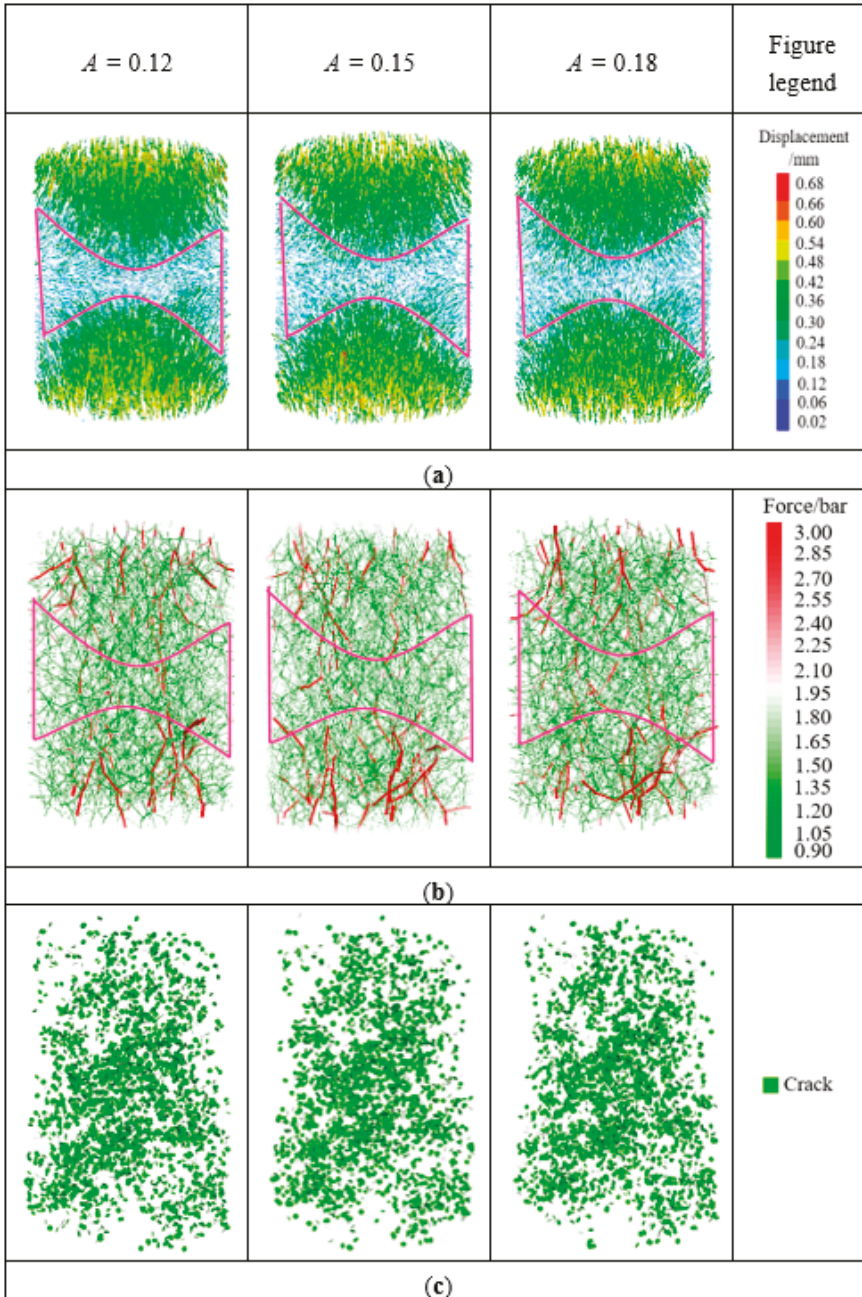


Figure 22. Typical failure laws of hydrate sediments with an axial strain of 25% under dynamic loads of different amplitudes: (a) cloud atlas of sample particle displacement, (b) contact force chain atlas, and (c) microcrack expansion diagram.

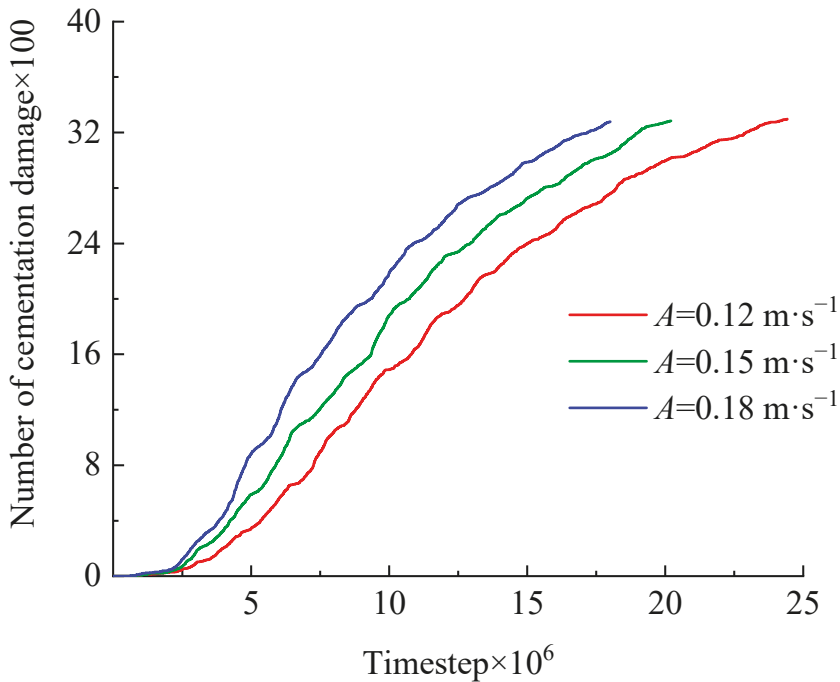


Figure 23. Failure–time step relationship of hydrate sediments cementation under different frequencies of dynamic loads.

4. Conclusions

In this paper, numerical simulations of triaxial compression of hydrate sediment specimens under cyclic loading with different frequencies (1.2×10^{-1} , 1.5×10^{-1} , and $1.8 \times 10^{-1} \text{ m}\cdot\text{s}^{-1}$) and amplitudes (1, 2, 3, and 4 Hz) were carried out to study the macroscopic mechanical properties of hydrate sediments under dynamic loading, revealing the effects of loading frequency and loading amplitude. The following main conclusions were obtained.

(1) The effect of loading frequency on the stiffness of hydrate sediment is small, but the effect on the peak strength is large and not monotonic. There is a critical value. When it is less than this value, the peak strength increases with the increase in loading rate, and when it is greater than this value, the peak strength decreases to a certain extent.

(2) The effect of loading amplitude on the peak strength and stiffness of hydrate sediments is monotonic. As the loading amplitude increases, the strength of the hydrate sediment specimens increases significantly, while the stiffness decreases.

(3) The loading frequency and amplitude have a large effect on the maximum shear dilatancy of sediment specimens, mainly due to the difference in the bearing capacity of the specimens because of the phase change point and particle rearrangement.

(4) The variation law of shear dilatancy angle with loading frequency for the sediment specimens is similar to that of shear dilatancy with loading frequency, which tends to increase linearly with the increase in loading amplitude.

(5) The effect of loading frequency and amplitude on the contact force chain, displacement, crack extension, and number of cementation damage inside the sediment is mainly related to the average axial stress to which the specimen is subjected. The higher the axial stress, the higher the rate of cementation damage, the more obvious the distribution of the shear zone of the specimen, and the more the number of cracks and cementation damage.

Author Contributions: Conceptualization, formal analysis, funding acquisition, writing and editing, Y.J., methodology, formal analysis, data curation, writing and editing, M.L., conceptualization, methodology, writing-review and editing, H.L., data curation, review and editing, Y.S. and B.L., methodology, validation, S.Z. and P.Y. All authors have read and agreed to the published version of the manuscript.

Funding: This research was funded by Shandong Provincial Natural Science Foundation, China (No. ZR2019ZD14) and the National Natural Science Foundation of China (No. 520095077).

Institutional Review Board Statement: Not applicable.

Informed Consent Statement: Not applicable.

Data Availability Statement: Data associated with this research are available and can be obtained by contacting the corresponding author upon reasonable request.

Conflicts of Interest: The authors declare no conflict of interest.

References

1. Guo, X.S.; Nian, T.K.; Zhao, W.; Gu, Z.D.; Liu, C.P.; Liu, X.L.; Jia, Y.G. Centrifuge experiment on the penetration test for evaluating undrained strength of deep-sea surface soils. *Int. J. Min. Sci. Technol.* **2022**, *32*, 363–373. [CrossRef]
2. Li, S.; Xu, X.; Zheng, R. Experimental investigation on dissociation driving force of methane hydrate in porous media. *Fuel* **2015**, *160*, 117–122. [CrossRef]
3. Guo, X.S.; Stoesser, T.; Nian, T.K.; Jia, Y.G.; Liu, X.L. Effect of pipeline surface roughness on peak impact forces caused by submarine mudflow. *Ocean. Eng.* **2021**, *243*, 110184. [CrossRef]
4. Masui, A.; Haneda, H.; Ogata, Y. Effects of methane hydrate formation on shear strength of synthetic methane hydrate sediments. *Int. Soc. Offshore Polar Eng.* **2005**, 364–369. Available online: <https://onepetro.org/ISOPEIOPEC/proceedings-abstract/ISOPE05/All-ISOPE05/ISOPE-I-05-056/9186> (accessed on 25 July 2022).
5. Hyodo, M.; Yoneda, J.; Yoshimoto, N. Mechanical and dissociation properties of methane hydrate-bearing sand in deep seabed. *Soils Found.* **2013**, *53*, 299–314. [CrossRef]
6. Song, Y.; Luo, T.; Madhusudhan, B.N. Strength behaviors of CH₄ hydrate-bearing silty sediments during thermal decomposition. *J. Nat. Gas Sci. Eng.* **2019**, *72*, 103031. [CrossRef]
7. Wu, Q.; Lu, J.S.; Li, D.L. Mechanical characterization of hydrate-bearing sediments during decompression mining. *Rock Soil Mech.* **2018**, *39*, 4508–4516.
8. Kajiyama, S.; Hyodo, M.; Nakata, Y. Shear behavior of methane hydrate bearing sand with various particle characteristics and fines. *Soils Found.* **2017**, *57*, 176–193. [CrossRef]
9. Li, Y.; Dong, L.; Wu, N. Influences of hydrate layered distribution patterns on triaxial shearing characteristics of hydrate-bearing sediments. *Eng. Geol.* **2021**, *294*, 106375. [CrossRef]
10. Hao, L.K.; Shi, C.; Shan, Z.G. Numerical simulation of dynamic properties of marine soft soil under cyclic loading. *J. China Three Gorges Univ. (Nat. Sci.)* **2021**, *43*, 7.
11. Guo, X.S.; Nian, T.K.; Wang, D.; Gu, Z.D. Evaluation of undrained shear strength of surficial marine clays using ball penetration-based CFD modelling. *Acta Geotech.* **2022**, *17*, 1627–1643. [CrossRef]
12. Shen, Z.; Jiang, M.; Thornton, C. DEM simulation of bonded granular material. Part I: Contact model and application to cemented sand. *Comput. Geotech.* **2016**, *75*, 192–209. [CrossRef]
13. Cundall, P.A.; Strack, O.D.L. discrete numerical model for granular assemblies. *Comput. Geotech.* **1979**, *29*, 47–65. [CrossRef]
14. Dai, S.; Santamarina, J.C.; Waite, W.F. Hydrate morphology: Physical properties of sands with patchy hydrate saturation. *J. Geophys. Res.* **2012**, *117*, B11205. [CrossRef]
15. Bai, Q.; Konietzky, H.; Dang, W. Microscopic modeling of frictional response of smooth joint under normal cyclic loading. *Rock Mech. Rock Eng.* **2022**, *55*, 169–186. [CrossRef]
16. Li, X.; Zou, Y.; Zhou, Z. Numerical simulation of the rock shpb test with a special shape striker based on the discrete element method. *Rock Mech. Rock Eng.* **2014**, *47*, 1693–1709. [CrossRef]
17. Brugada, J.; Cheng, Y.P.; Soga, K. Discrete element modelling of geomechanical behavior of methane hydrate soils with pore-filling hydrate distribution. *Granul. Matter* **2010**, *12*, 517–525. [CrossRef]
18. Jiang, M.J.; Sun, Y.G.; Yang, Q.J. A simple distinct element modeling of the mechanical behavior of methane hydrate-bearing sediments in deep seabed. *Granul. Matter* **2013**, *15*, 209–220. [CrossRef]
19. Jiang, M.J.; Yu, H.S.; Harris, D. Bond rolling resistance and its effect on yielding of bonded granulates by DEM analyses. *Int. J. Numer. Anal. Methods Geomech.* **2006**, *30*, 723–761. [CrossRef]
20. Jiang, M.J.; Peng, D.; Ooi, J.Y. DEM investigation of mechanical behavior and strain localization of methane hydrate bearing sediments with different temperatures and water pressures. *Eng. Geol.* **2017**, *223*, 92–109. [CrossRef]
21. Jiang, M.J.; Liu, J.; Kwok, C.Y. Exploring the undrained cyclic behavior of methane-hydrate-bearing sediments using CFD-DEM. *Comptes Rendus Mécanique* **2018**, *346*, 815–832. [CrossRef]

22. Jiang, M.J.; Xiao, Y.; Zhu, F.Y. Study on micromechanical cementation model and parameters of deep-sea energy soil. *Chin. J. Geotech. Eng.* **2012**, *34*, 1574–1583.
23. Jung, J.W.; Santamarina, J.C.; Soga, K. Stress-strain response of hydrate-bearing sands: Numerical study using discrete element method simulations. *J. Geophys. Res. Solid Earth* **2012**, *117*, B04202. [[CrossRef](#)]
24. Yang, Q.J.; Zhao, C.F. Three-dimensional discrete element analysis of the mechanical properties of hydrate sediments. *Rock Soil Mech.* **2014**, *35*, 255–262.
25. He, J.; Blumenfeld, R.; Zhu, H. Mechanical behaviors of sandy sediments bearing pore-filling methane hydrate under different intermediate principal stress. *Int. J. Geomech.* **2021**, *21*, 04021043. [[CrossRef](#)]
26. Xie, Y.; Feng, J.; Hu, W. Deep-sea sediment and water simulator for investigation of methane seeping and hydrate formation. *J. Mar. Sci. Eng.* **2022**, *10*, 514. [[CrossRef](#)]
27. Cheng, Y.T. Triaxial compression mechanical behavior of the hydrate sediments based on particles arranged model. *Model. Simul.* **2018**, *07*, 199–208. [[CrossRef](#)]
28. Deng, B.Q. *Discrete Element Triaxial Numerical Simulation Study of Irregular Gravelly Soil with Irregular Particles*; Tianjin University Hydraulic Engineering: Tianjin, China, 2019.
29. Li, T.; Li, L.; Liu, J. Influence of hydrate participation on the mechanical behavior of fine-grained sediments under one-dimensional compression: A DEM study. *Granul. Matter* **2022**, *24*, 1–7. [[CrossRef](#)]
30. Wei, R.; Jia, C.; Liu, L. Analysis of the characteristics of pore pressure coefficient for two different hydrate-bearing sediments under triaxial shear. *J. Mar. Sci. Eng.* **2022**, *10*, 509. [[CrossRef](#)]
31. Liu, L.; Zhang, X.; Ji, Y. Acoustic wave propagation in a borehole with a gas hydrate-bearing sediment. *J. Mar. Sci. Eng.* **2022**, *10*, 235. [[CrossRef](#)]
32. Waite, W.F. Physical properties of hydrate-bearing sediments. *Rev. Geophys.* **2009**, *47*, 1–38. [[CrossRef](#)]
33. Potyondy, D.; Cundall, P. A bonded-particle model for rock. *Int. J. Rock Mech. Min. Sci.* **2004**, *41*, 1329. [[CrossRef](#)]
34. He, J.; Jiang, M.J. New method of discrete element formation and macromechanical properties of pore-filled deep-sea energy soils. *J. Tongji Univ. (Nat. Sci.)* **2016**, *44*, 709–717.
35. Ke, W. *Study on Fatigue Damage Characteristics of Sandstone and Dynamic Influencing Factors of Slope Stability under Cyclic Dynamic Loading*; Chongqing University Civil Engineering: Chongqing, China, 2018.
36. Guo, Z.W. Analysis of seismic wave modulus of asphalt pavement under accelerated loading. *J. Highw. Transp. Res. Dev.* **2014**, *31*, 6.
37. Lu, Z.H.; Qi, C.Z.; Jiang, K. Experimental study of shear swelling characteristics of sandy soils. *Res. Explor. Lab.* **2020**, *39*, 19–24.
38. Summary of Commonly Used Seismic Wave Data (72448 Seismic Wave-Hach.txt). Available online: https://download.csdn.net/download/weixin_44423448/14021977 (accessed on 15 April 2022).
39. Roscoe, K.H. The influence of strain in soil mechanics. *Geotechnique* **1970**, *20*, 129–170. [[CrossRef](#)]
40. He, J.; Jiang, M.J. Discrete element analysis of true triaxial test of macro and micro mechanical properties of pore-filled energy soils. *Rock Soil Mech.* **2016**, *37*, 3026–3034.
41. Wang, E.H. *PFC3D Particle Flow Simulation of Mechanical Properties of Saturated Densified Muddy Sand*; Nanchang University: Nanchang, China, 2019.
42. Zhang, Z.H. *Meso-Scale Numerical Simulation of Triaxial Test of Coarse-Grained Soil Based on PFC3D*; Sanxia University: Yichang, China, 2015.
43. Zhao, J.; Liu, C.; Li, C. Pore-scale investigation of the electrical property and saturation exponent of archive's law in hydrate-bearing sediments. *J. Mar. Sci. Eng.* **2022**, *10*, 111. [[CrossRef](#)]

Article

Analytical Solutions of Steady a Seepage Field for Deep-Buried Tunnel with Grouting Ring Considering Anisotropic Flow

Qizhi Chen ¹, Luju Liang ², Baoping Zou ^{1,*}, Changjie Xu ^{3,4}, Bowen Kong ¹ and Jingyuan Ma ¹

¹ School of Civil Engineering and Architecture, Zhejiang University of Science & Technology, Hangzhou 310023, China

² School of Engineering, Zhejiang University City College, Hangzhou 310015, China

³ Engineering Research & Development Centre for Underground Technology of Jiangxi Province, East China Jiaotong University, Nanchang 330013, China

⁴ Research Centre of Coastal and Urban Geotechnical Engineering, Zhejiang University, Hangzhou 310058, China

* Correspondence: zoubp@zust.edu.cn

Abstract: Difficulties related to seepage are frequently encountered in tunnel design and construction, especially in deep-buried tunnels. Nowadays, analytical solutions of steady seepage fields for deep-buried tunnel usually assume that the surrounding rock mass is homogeneous. In this study, analytical solutions of a steady seepage field for a deep-buried tunnel with grouting ring considering anisotropic flow are proposed. The proposed analytical solutions are verified by numerical simulations and parameter analysis are carried out. Results show that the seepage field of surrounding rocks around the deep buried circular tunnel is no longer uniformly distributed and presents elliptical distribution. The change of permeability coefficient of the lining structure has a great influence on the hydraulic head when the difference between permeability coefficient of lining structure and surrounding rock is not very large. The results show that the size of the grouting ring has more significant influence on the grouting effect.

Keywords: deep-buried tunnel; analytical solution; anisotropic flow; conformal mapping; seepage field

Citation: Chen, Q.; Liang, L.; Zou, B.; Xu, C.; Kong, B.; Ma, J. Analytical Solutions of Steady a Seepage Field for Deep-Buried Tunnel with Grouting Ring Considering Anisotropic Flow. *J. Mar. Sci. Eng.* **2022**, *10*, 1861. <https://doi.org/10.3390/jmse10121861>

Academic Editor: Kamal Djidjeli

Received: 31 October 2022

Accepted: 20 November 2022

Published: 2 December 2022

Publisher's Note: MDPI stays neutral with regard to jurisdictional claims in published maps and institutional affiliations.



Copyright: © 2022 by the authors. Licensee MDPI, Basel, Switzerland. This article is an open access article distributed under the terms and conditions of the Creative Commons Attribution (CC BY) license (<https://creativecommons.org/licenses/by/4.0/>).

1. Introduction

With the development of China's economy and society, tunnels play an important role in the national economy and people's daily life and travel. However, there are still many difficulties in tunnel design and construction, especially in tunnels in water-rich strata, mountain tunnels with high water level and sub-sea tunnels. The existence of a seepage field makes the working conditions faced by tunnel construction and operation more complex, and the existence of seepage field increases the potential safety hazards during construction and operation [1]. Therefore, studying the distribution law of a tunnel seepage field can provide necessary reference for design and construction.

The research on the seepage field of an underwater tunnel has always been a hot topic. Based on some assumptions and simplified models, the seepage field can be quickly obtained by an analytical solution, in which the key parameters can be analyzed. The mirror image method [2–5] and conformal mapping in the complex variable method [6,7] were mainly employed analytical studies for the seepage field of underwater tunnels. Lei [8] derived an analytical solution for calculating the seepage field and water inflow of a circular tunnel based on the mirror image method. Tani [9] obtained the seepage field around an underwater shallow tunnel using the conformal mapping method for a circular tunnel. Wu et al. [10] established a combined analytical–numerical method to estimate the groundwater inflow into circular tunnels in drained conditions. Guo et al. [11] proposed an exact analytical solution of a seepage field for underwater multiple tunnel problems

using the Schwartz alternating method combined with conformal mapping. Luo et al. [12] established a simplified steady-state seepage model for a deep buried tunnel and parallel adit, and the model was solved iteratively using the complex variable method and the Schwartz alternating method. Ying et al. [13] presented an analytical solution for the hydraulic head that considers the effects of the seabed thickness and lining layers using conformal mapping and the principle of superposition.

The above studies have laid an important theoretical foundation for the design and construction of underwater tunnels. Because of the complexity when solving the seepage field of a tunnel, most existing analytical studies simplified the soil layer into saturated homogeneous and isotropic porous material. However, due to the different arrangement of soil particles in the process of natural deposition, the seepage in natural soil often presents anisotropy in engineering [14]. Zienkiewicz et al. [15] studied the orthotropic anisotropic seepage problem in a two-dimensional inhomogeneous medium using numerical approaches. Hu et al. [16] presents a general solution for active earth pressure acting on a vertical retaining wall with a drainage system along the soil–structure interface considering an anisotropic seepage effect. Xu et al. [17] proposed analytical solutions on a steady seepage field of deep buried circular tunnel considering anisotropic flow. Tang et al. [18] proposed an analytical solution for groundwater flow through a circular tunnel in anisotropic soils based on conformal mapping. Luo et al. [19] proposed an analytical solution of external water pressure on a deep tunnel lining in two types of horizontally layered hydrogeological structures. It can be seen that some existing research approaches are numerical simulations, and the influence of a grouting ring has not been considered in the existing tunnel anisotropic seepage field research.

This study proposes analytical solutions of a steady seepage field for a deep-buried tunnel with grouting ring considering anisotropic flow. The seepage field of surrounding rocks is solved by coordinate transformation and conformal mapping methods. The seepage fields of the grouting ring and lining structure are solved by boundary conditions and continuous flow conditions between them. The analytical solution for the seepage field is verified with numerical simulation results. Additionally, the effects of total hydraulic head, permeability coefficient of lining structure and grouting ring, and grouting influence factors are discussed.

2. Analytical Solutions of Steady Seepage Field

2.1. Theoretical Calculation Model and Hypothesis

Based on the anisotropic seepage field calculation model proposed by Xu et al. [17], the tunnel seepage field calculation model is shown in Figure 1 considering the existence of a lining and grouting ring. The z -plane contains the area of surrounding rock (Area I), grouting ring (Area II) and lining structure (Area III). r_0 is the inner radius of the lining structure, r_L is the outer radius of the lining structure, r_G is the radius of the grouting ring and ρ is the distance from any point to the center of the tunnel. θ is the angle between any point and the x -axis. It is assumed that anisotropic seepage flow exists in surrounding rocks. The permeability coefficients of surrounding rock in horizontal direction (x direction) and vertical direction (y direction) are k_x and k_y , respectively. The lining structure and the grouting ring are continuous homogeneous and isotropic media with permeability coefficients of k_L and k_G , respectively.

In order to derive the analytical solution, the following assumptions are made:

(1) Anisotropic seepage flow exists in surrounding rocks; the permeability coefficients k_x and k_y in x and y directions has the following relationship $n = \sqrt{k_y/k_x}$, where n defined as permeability coefficient ratio. The lining structure and the grouting ring are homogeneous, continuous and isotropic (Xu et al. [17]).

(2) Surrounding rocks and water are incompressible and have adequate groundwater recharge. The seepage is steady state and complies with Darcy’s law (Xu et al. [17]).

(3) The radius of a tunnel is much smaller than its buried depth. Therefore, a uniform distribution of total hydraulic head on the boundary between the grouting ring and surrounding rock (Atkinson and Mair [20]; Wang et al. [21]; Li et al. [22]).

(4) Only radial seepage is considered in the grouting ring and the lining structure (Pan et al. [23]).

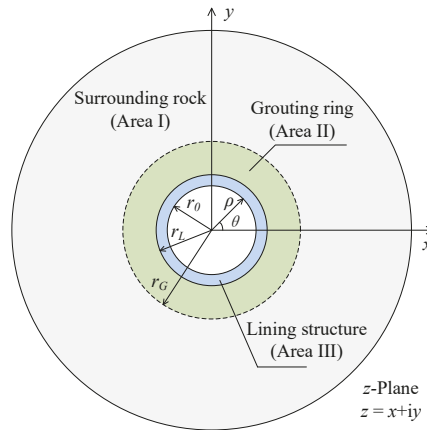


Figure 1. Calculation model of steady seepage field for deep-buried tunnel.

2.2. Governing Equations and Boundary Conditions

The two-dimensional steady seepage field around the tunnel in the calculation model conforms to Laplace equation. Therefore, in the z-plane, the seepage differential equation in area I in the Cartesian coordinate can be obtained as [2]:

$$k_x \frac{\partial^2 \varphi_S}{\partial x^2} + k_y \frac{\partial^2 \varphi_S}{\partial y^2} = 0 \tag{1}$$

where φ_S is the total hydraulic head of surrounding rock.

The seepage differential equation in area II and III in the polar coordinate can be obtained as:

$$\frac{\partial^2 \varphi_G}{\partial \rho^2} + \frac{1}{\rho} \frac{\partial \varphi_G}{\partial \rho} + \frac{1}{\rho^2} \frac{\partial^2 \varphi_G}{\partial \theta^2} = 0 \tag{2}$$

$$\frac{\partial^2 \varphi_L}{\partial \rho^2} + \frac{1}{\rho} \frac{\partial \varphi_L}{\partial \rho} + \frac{1}{\rho^2} \frac{\partial^2 \varphi_L}{\partial \theta^2} = 0 \tag{3}$$

where φ_G is the total hydraulic head of the grouting ring and φ_L is the total hydraulic head of the lining structure. ρ is the polar diameter in polar coordinate and θ is the polar angle in polar coordinates as shown in Figure 1.

The deep buried tunnel and its corresponding lining structure and grouting ring are in area I, so the boundary conditions are as follows:

$$\varphi_S|_{\rho=\rho_a(\rho_a \rightarrow \infty)} = H_a \tag{4}$$

$$\varphi_S|_{\rho=r_G} = \varphi_G|_{\rho=r_G} = H_G \tag{5}$$

$$\varphi_G|_{\rho=r_L} = \varphi_L|_{\rho=r_L} = H_L \tag{6}$$

$$\varphi_L|_{\rho=r_0} = H_0 \tag{7}$$

where H_a is the total hydraulic head at great distance, H_0 is the inner hydraulic head of the lining structure, H_L is the hydraulic head between the lining structure and the grouting ring, and H_G is the hydraulic head between the grouting ring and surrounding rock.

2.3. Analytical Solutions of Steady Seepage Field in Surrounding Rock

It is assumed that anisotropic seepage exists in the surrounding rock; the following coordinate transformation can be obtained:

$$\begin{cases} x' = nx \\ y' = y \end{cases} \tag{8}$$

So the governing Equation (1) can be transformed into:

$$\frac{\partial^2 \varphi_S}{\partial x'^2} + \frac{\partial^2 \varphi_S}{\partial y'^2} = 0 \tag{9}$$

Therefore, the circular tunnel in the z -plane becomes an elliptical tunnel in the z' -plane, which is shown in Figure 2a. The equation for the elliptical tunnel is as follows:

$$\frac{x'^2}{(nr_G)^2} + \frac{y'^2}{r_G^2} = 1 \tag{10}$$

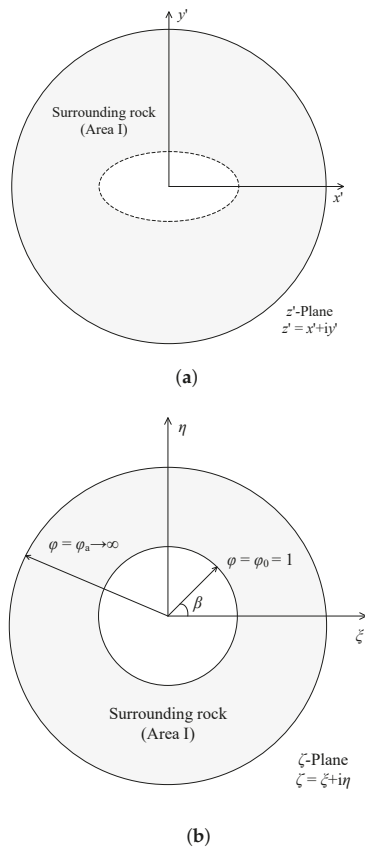


Figure 2. Calculation model after coordinate transformation and conformal mapping. (a) Plane of coordinate transformation. (b) Plane of conformal mapping.

By conformal mapping, the area containing an elliptical tunnel in z' -plane is projected to the area containing a circular tunnel with a radius of $\varphi = 1$ in ζ -plane (Zhou et al. [24]). The conformal mapping function is shown as follows:

$$z = \omega(\zeta) = R \left(\zeta + \frac{m}{\zeta} \right) \tag{11}$$

in which:

$$z = x + iy \tag{12}$$

$$\zeta = \xi + i\eta = \varphi e^{i\beta} \tag{13}$$

$$R = \frac{(n+1)r_G}{2} \tag{14}$$

$$m = \frac{n-1}{n+1} \tag{15}$$

(ξ, η) and (φ, β) are the Cartesian and polar coordinates in the ζ -plane. Therefore, the coordinates of any point in the z -plane can be expressed by φ and β as follows:

$$\begin{cases} x = \frac{R}{n} \left(\varphi + \frac{m}{\varphi} \right) \cos \beta \\ y = R \left(\varphi - \frac{m}{\varphi} \right) \sin \beta \end{cases} \tag{16}$$

The seepage differential equation in ζ -plane also satisfies the Laplace equation. Equation (9) in the Cartesian coordinate of ζ -plane can be written as:

$$\frac{\partial^2 \varphi_S}{\partial \xi^2} + \frac{\partial^2 \varphi_S}{\partial \eta^2} = 0 \tag{17}$$

Equation (17) can be converted to polar coordinates as follows:

$$\frac{d}{d\varphi} \left(\varphi \frac{d\varphi_S}{d\varphi} \right) = 0 \tag{18}$$

The general solution of this Equation (18) is:

$$\varphi_S = C_1 + C_2 \ln \varphi \tag{19}$$

where C_1 and C_2 are undetermined constants, which are determined by boundary conditions. Boundary condition Equations (4) and (5) in ζ -plane can be written as:

$$\varphi_S|_{\varphi=\varphi_a(\varphi_a \rightarrow \infty)} = H_a \tag{20}$$

$$\varphi_S|_{\varphi=\varphi_0=1} = H_G \tag{21}$$

Substituting Equations (20) and (21) into Equation (19) can obtain:

$$C_1 = H_G \tag{22}$$

$$C_2 = \frac{H_a - H_G}{\ln \varphi_a} \tag{23}$$

Therefore, Equation (19) can be rewritten as:

$$\varphi_S = H_G + \frac{H_a - H_G}{\ln \varphi_a} \ln \varphi \tag{24}$$

The seepage discharge between area I and area II can be obtained by integrating Equation (24) as follows:

$$Q_S = k_x \int_0^{2\pi} \frac{\partial \varphi_S}{\partial \varphi} \varphi d\beta = \frac{2\pi k_x}{\ln \varphi_a} (H_a - H_G) \tag{25}$$

where Q_S is the seepage discharge between area I and area II.

2.4. Analytical Solutions of Steady Seepage Field in Lining Structure and Grouting Ring

It is assumed that only radial seepage is considered in the grouting ring and the lining structure, the seepage in the grouting ring and the lining structure can be simplified as an axisymmetric steady seepage problem. Therefore, the governing Equations (2) and (3) can be simplified as:

$$\frac{\partial^2 \varphi_G}{\partial \rho^2} + \frac{1}{\rho} \frac{\partial \varphi_G}{\partial \rho} = 0 \tag{26}$$

$$\frac{\partial^2 \varphi_L}{\partial \rho^2} + \frac{1}{\rho} \frac{\partial \varphi_L}{\partial \rho} = 0 \tag{27}$$

According to boundary condition Equations (5)–(7), Equations (26) and (27) can be solved as:

$$\varphi_G = \frac{H_L \ln r_G - H_G \ln r_L}{\ln(r_G/r_L)} + \frac{H_G - H_L}{\ln(r_G/r_L)} \ln \rho \tag{28}$$

$$\varphi_L = \frac{H_0 \ln r_L - H_L \ln r_0}{\ln(r_L/r_0)} + \frac{H_L - H_0}{\ln(r_L/r_0)} \ln \rho \tag{29}$$

The seepage discharge can be obtained by integrating Equations (28) and (29) respectively as follows:

$$Q_G = k_G \int_0^{2\pi} \frac{\partial \varphi_G}{\partial \rho} \rho d\theta = \frac{2\pi k_G}{\ln(r_G/r_L)} (H_G - H_L) \tag{30}$$

$$Q_L = k_L \int_0^{2\pi} \frac{\partial \varphi_L}{\partial \rho} \rho d\theta = \frac{2\pi k_L}{\ln(r_L/r_0)} (H_L - H_0) \tag{31}$$

where Q_G is the seepage discharge between area II and area III, and Q_L is the seepage discharge inside area III.

2.5. Combined Analytical Solutions of Steady Seepage Field

According to continuous condition of seepage discharge, the seepage discharge between areas is equal as follows:

$$Q = Q_S = Q_G = Q_L \tag{32}$$

According to Equations (25) and (30), it can be obtained:

$$H_L = \frac{B + E - F}{B} H_G + \frac{F - E}{B} H_a \tag{33}$$

where $B = \frac{k_G}{k_x}$, $E = \frac{\ln r_G}{\ln \varphi_a}$, and $F = \frac{\ln r_L}{\ln \varphi_a}$.

According to Equations (25) and (31), it can be obtained:

$$(F - G)(H_a - H_G) = D(H_L - H_0) \tag{34}$$

where $D = \frac{k_L}{k_x}$, and $G = \frac{\ln r_0}{\ln \varphi_a}$.

Substituting Equation (33) into (34) yields:

$$H_G = \frac{(BF + DE - BG - DF)H_a + BDH_0}{BD + DE + BF - DF - BG} \tag{35}$$

Substituting Equation (35) into (33) yields:

$$H_L = \frac{B^2(F - G) + DF(F - E)}{B(BD + DE + BF - DF - BG)} H_a + \frac{D(B + E - F)}{(BD + DE + BF - DF - BG)} H_0 \tag{36}$$

By substituting (35) into (24), the seepage field of surrounding rock in ζ -plane can be obtained as follows:

$$\varphi_S = \frac{\ln \varphi}{\ln \varphi_a} H_a + \left(1 - \frac{\ln \varphi}{\ln \varphi_a} \right) \frac{(BF + DE - BG - DF)H_a + BDH_0}{BD + DE + BF - DF - BG} \tag{37}$$

The seepage field of surrounding rock in z -plane can be obtained by transforming the seepage field in ζ -plane through Equation (16). However, Equation (16) is a transcendental equation, so the explicit solution can be obtained only on the x and y coordinate axes in the z -plane. For another arbitrary point (x, y) , it can be calculated by MATLAB.

For any point on the x coordinate axis, it can be obtained according to Equation (16):

$$\varphi = \frac{|x|n + \sqrt{x^2n^2 - (n^2 - 1)r_G^2}}{(n + 1)r_G} \tag{38}$$

For any point on the y coordinate axis, it can be obtained according to Equation (16):

$$\varphi = \frac{|y| + \sqrt{y^2 - (n^2 - 1)r_G^2}}{(n + 1)r_G} \tag{39}$$

Subscribing Equations (38) and (39) into Equation (37), the analytical expression of total hydraulic head on the x and y coordinate axes in the z -plane can be obtained as follows, respectively:

$$\begin{aligned} \varphi_{Sx} &= \frac{(BF + DE - BG - DF)H_a + BDH_0}{BD + DE + BF - DF - BG} \\ &+ \frac{1}{\ln \varphi_a} \frac{BD(H_a - H_0)}{BD + DE + BF - DF - BG} \ln \left(\frac{|x|n + \sqrt{x^2n^2 - (n^2 - 1)r_G^2}}{(n + 1)r_G} \right) \end{aligned} \tag{40}$$

$$\begin{aligned} \varphi_{Sy} &= \frac{(BF + DE - BG - DF)H_a + BDH_0}{BD + DE + BF - DF - BG} \\ &+ \frac{1}{\ln \varphi_a} \frac{BD(H_a - H_0)}{BD + DE + BF - DF - BG} \ln \left(\frac{|y| + \sqrt{y^2 - (n^2 - 1)r_G^2}}{(n + 1)r_G} \right) \end{aligned} \tag{41}$$

In addition, it can be obtained from Equation (24):

$$\varphi = (\varphi_a)^{\frac{\varphi_S - H_G}{H_a - H_G}} \tag{42}$$

Substituting (42) into (16) shows that a circle with radius φ in the ζ -plane corresponds to an ellipse in the z -plane. Therefore, the hydraulic head contour line in the z -plane is an ellipse and its semi minor axis and semi major axis are as follows:

$$\begin{cases} a_\varphi = \frac{R}{n} \left((\varphi_a)^{\frac{\varphi_S - H_G}{H_a - H_G}} + m(\varphi_a)^{\frac{H_a - H_G}{\varphi_S - H_G}} \right) \\ b_\varphi = R \left((\varphi_a)^{\frac{\varphi_S - H_G}{H_a - H_G}} - m(\varphi_a)^{\frac{H_a - H_G}{\varphi_S - H_G}} \right) \end{cases} \tag{43}$$

where a_φ and a_β are the semi minor axis and semi major axis.

3. Verification of Analytical Solution of Seepage Field

Li et al. [25] proposed an analytical solution for the isotropic seepage field of a deep buried circular tunnel without lining structure and grouting ring as follows:

$$\varphi_S = H_0 + \frac{H_a - H_0}{\ln \frac{r_a}{r_0}} \ln \frac{r}{r_0} \tag{44}$$

Corresponding to the solution in this paper, when there is no lining structure and grouting ring, there is:

$$\begin{cases} r_G = r_L = r_0 \\ H_G = H_L = H_0 \end{cases} \tag{45}$$

Because the seepage field is simplified as isotropic, there is $n = 1$. Equation (16) can be simplified as follows:

$$\begin{cases} x = r_0 \varphi \cos \beta \\ y = r_0 \varphi \sin \beta \end{cases} \tag{46}$$

Substituting Equation (46) into Equation (24) yields:

$$\varphi_S = H_G + \frac{H_a - H_G}{\ln \varphi_a} \ln \frac{\sqrt{x^2 + y^2}}{r_0} \tag{47}$$

r_a is assumed as the semi major axis length of the ellipse in z -plane, which the circle $\varphi = \varphi_a$ corresponded in the ζ -plane. According to Equation (16), the semi major axis of the ellipse in z -plane is as follows:

$$r_a = \frac{(n + 1)r_0}{2} \left(\varphi_a - \frac{m}{\varphi_a} \right) \tag{48}$$

Substituting $n = 1$ and $m = 0$ into Equation (48) yields:

$$r_a = \varphi_a r_0 \tag{49}$$

Substituting Equations (45) and (49) into the Equation (47), it can be found that the simplified proposed solution is identical with that proposed by Li et al. [25], which proves the correctness of the solution to some extent.

In order to further verify the correctness of the solution, an example comparison with numerical method is carried out. Finite element limit analysis software OptumG2 (Krabbenhoft et al. [26]) is used for numerical calculation of seepage field. Considering the symmetry of the calculation model, a quarter model is used to simulate the seepage field as shown in Figure 3a. The left and lower surrounding rock boundaries of the calculation model are set as impermeable boundaries with normal restraint. As it is a deep buried tunnel, uniform distributed total hydraulic heads are set along the outer boundary of the surrounding rock and the inner lining structure of the tunnel. The parameters used in numerical simulation are shown in Table 1. OptumG2 uses adaptive meshing method in the calculation, and the meshing is shown in Figure 3b.

From the derivation process of the solution in this paper, a specific value of φ_a which meet the accuracy of general engineering is needed to obtain the seepage field. Li et al. [25] took $\varphi_a = 30r_0$ and Li et al. [27] took $\varphi_a = 20r_0$ in their research respectively. In the following calculation in this paper, $\varphi_a = 30r_0$ is adopted for calculation.

The results of the total hydraulic head by numerical simulation under different permeability coefficient ratio are shown in Figure 4. It can be seen from Figure 4a that the total hydraulic head contour of surrounding rock is circular when the permeability coefficients of surrounding rock in horizontal and vertical direction are the same, which means the seepage of surrounding rock is isotropic. When anisotropic seepage flow happens in surrounding rock around the deep buried tunnel, the total hydraulic head contour of surrounding rock is no longer uniformly circular distribution but elliptical distribution as

shown in Figure 4b,c. The hydraulic gradient along y -axis which have a higher permeability coefficient is relatively smaller than that along the x -axis.

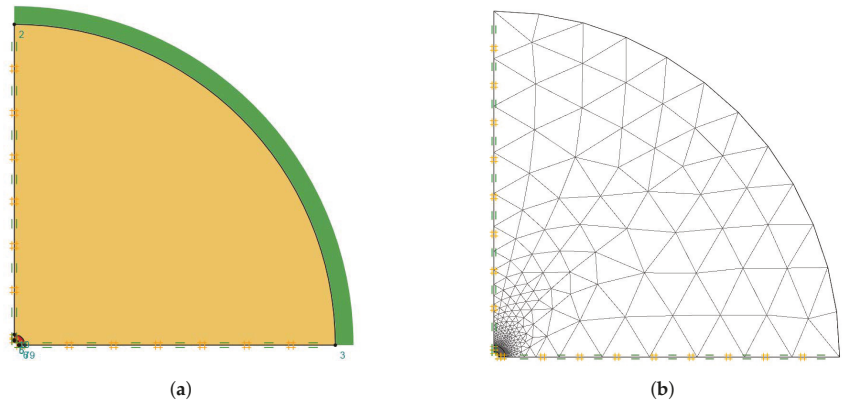


Figure 3. Finite element limit analysis model and meshing. (a) Calculation model. (b) Adaptive meshing.

Table 1. Calculation parameters in numerical simulation.

r_0/m	r_l/m	r_G/m	$k_L/m \cdot s^{-1}$	$k_G/m \cdot s^{-1}$	$k_x/m \cdot s^{-1}$	n	H_0/m	H_a/m
2.4	3	6	1×10^{-6}	1×10^{-6}	1×10^{-5}	1 to 3	0	500

The results of total hydraulic head along coordinate axis calculated by numerical simulation and the proposed analytical solution are shown in Figure 5. It can be seen from Figure 5 that the results calculated by the proposed analytical solution are in agreement with those calculated by numerical simulation, which can verify the correctness of the proposed analytical solution in this paper.

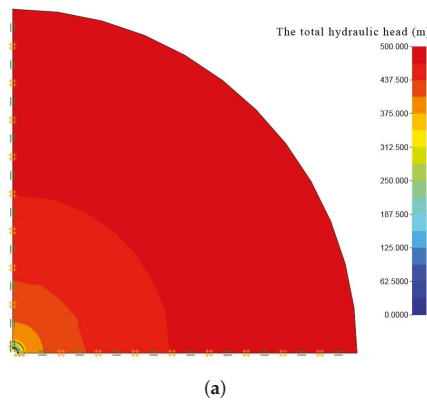
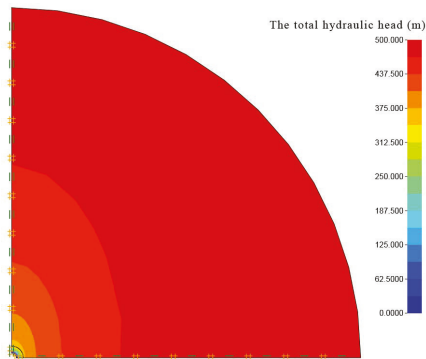
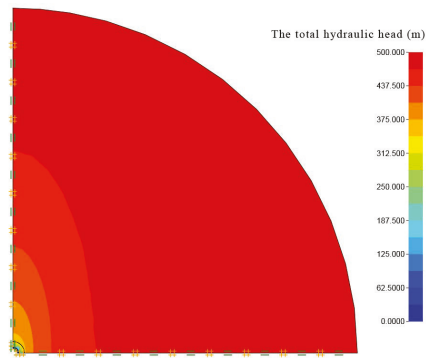


Figure 4. Cont.

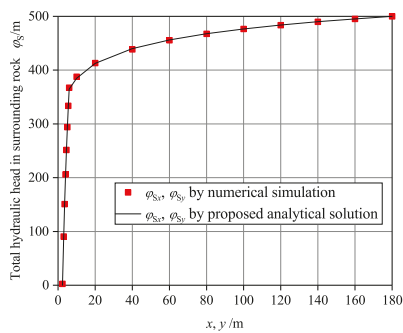


(b)



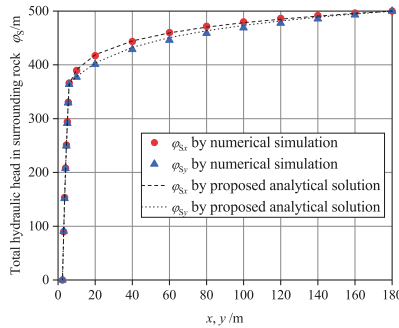
(c)

Figure 4. Total hydraulic head of lining structure, grouting ring and surrounding rock by numerical simulation. (a) $n = 1$. (b) $n = 2$. (c) $n = 3$.

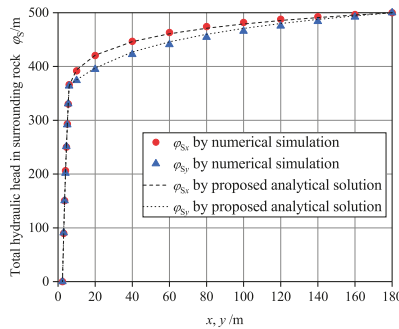


(a)

Figure 5. Cont.



(b)



(c)

Figure 5. Total hydraulic head along coordinate axis. (a) $n = 1$. (b) $n = 2$. (c) $n = 3$.

4. Parameter Analysis of Analytical Solution of Seepage Field

In order to further reveal the influence of anisotropy of permeability coefficient on seepage field of deep buried circular tunnel, the hydraulic head contour in surrounding rocks is calculated by proposed analytical solution. The parameters in Table 1 are used for the calculation, and a quarter of the calculation area is taken. The results are shown in Figure 6. Anisotropic seepage occurs when the permeability coefficient is anisotropic. The seepage field of surrounding rock around the buried circular tunnel is no longer uniformly distributed and presents elliptical distribution. Different head contour shapes occur with different permeability ratios of surrounding rocks. The hydraulic gradient is larger in the direction with smaller permeability coefficient, which is about n times of the direction with larger permeability coefficient.

The hydraulic head and seepage discharge between grouting ring and lining structure, and between grouting ring and surrounding rock are analyzed in following examples. The calculation parameters in examples are shown in Table 2.

Figure 7 shows the hydraulic head between grouting ring and lining structure, and between grouting ring and surrounding rock under different total hydraulic head at infinite distance. The permeability coefficient of lining structure in this example is $1 \times 10^{-8} \text{ m}\cdot\text{s}^{-1}$. Figure 8 shows the seepage discharge under different total hydraulic head at infinite distance. It can be seen from the results that the hydraulic head of grouting ring and lining structure and the seepage discharge increase linearly with the increase of the total hydraulic head at infinite distance. Obviously, it can also be seen from Equations (30), (35) and (36) that the hydraulic head and seepage discharge have a linear relationship with the total hydraulic head at a very far distance when other parameters remain the same.

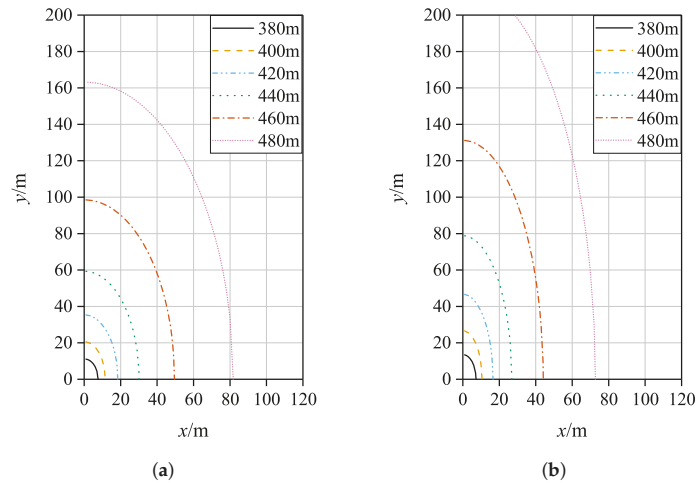


Figure 6. Total hydraulic head along coordinate axis. (a) $n = 2$. (b) $n = 3$.

Table 2. Calculation parameters in parameter analysis.

r_0/m	r_L/m	r_G/m	$k_L/m \cdot s^{-1}$	$k_G/m \cdot sy^{-1}$	$k_x/m \cdot s^{-1}$	n	H_0/m	H_a/m
2.4	3	6	1×10^{-5} to 1×10^{-8}	1×10^{-6}	1×10^{-5}	2	0	20 to 220

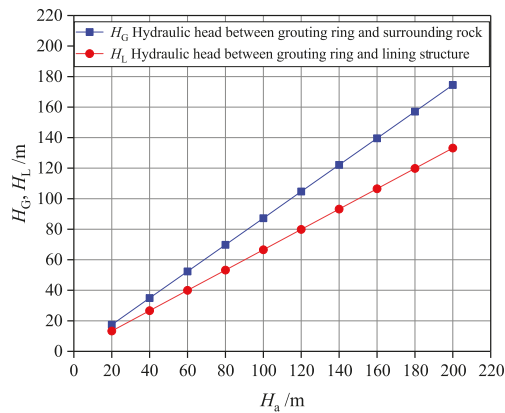


Figure 7. Hydraulic head of grouting ring and lining structure under different total hydraulic head at infinite distance.

The following example will analyze the influence of the permeability coefficient of the lining structure on the hydraulic head and seepage discharge. The total hydraulic head at a large distance in this example is 100 m, and other calculation parameters are shown in Table 2. Figure 9 shows the hydraulic head of grouting ring and lining structure under a different permeability coefficient of lining structure. It can be found that with the decrease of the permeability coefficient of the lining structure, the hydraulic heads of the lining structure and the grouting ring are increased. When the difference between the permeability

coefficient of the lining structure and surrounding rock is not large (e.g., $k_x/k_L \leq 100$), the change of the permeability coefficient of the lining structure has a great impact on the hydraulic head. However, when the permeability coefficient of lining structure differs greatly from that of surrounding rock (e.g., $k_x/k_L > 100$), the influence of the permeability coefficient of lining structure on hydraulic head is no longer significant. Because when the permeability coefficient differs greatly, the lining structure can be considered as impermeable, so the hydraulic head of lining structure will be close to the total hydraulic head at infinity. Figure 10 shows the seepage discharge under different permeability coefficient of lining structure. It can also be seen that when the difference of permeability coefficient is small (e.g., $k_x/k_L \leq 100$), the decrease of lining structure permeability coefficient greatly reduces the seepage discharge. However, when the difference of permeability coefficient is large (e.g., $k_x/k_L > 100$), the decrease of lining permeability coefficient has little impact on the seepage discharge, and the seepage discharge tends to be zero.

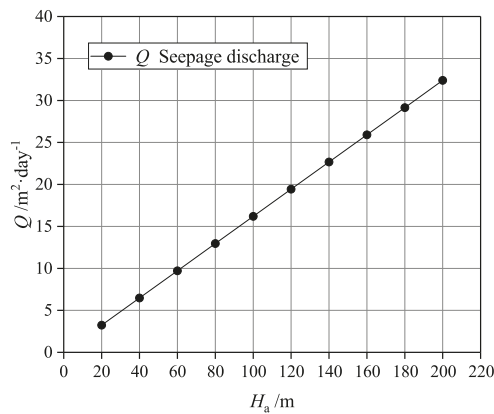


Figure 8. Seepage discharge under different total hydraulic head at infinite distance.

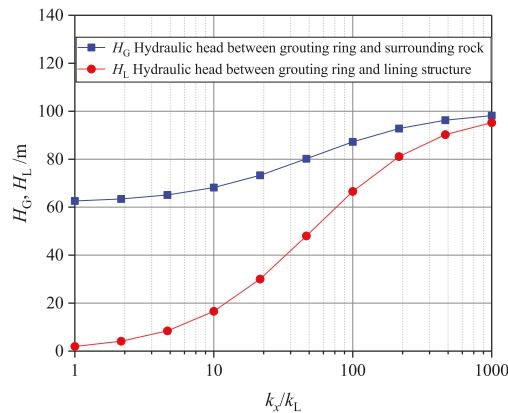


Figure 9. Hydraulic head of grouting ring and lining structure under different permeability coefficient of lining structure.

Wang [28] and Liu et al. [29] pointed out that the water shall be blocked by grouting ring for deep buried tunnels with hydraulic head greater than 60 m. Wang et al. [21] studied water pressure distribution on tunnel lining and the results indicated that the grouting

ring effectively reduced the water pressure on tunnel lining. Seikan tunnel in Japan and Yuanliangshan tunnel in China both adopt this method (Zhang [30]).

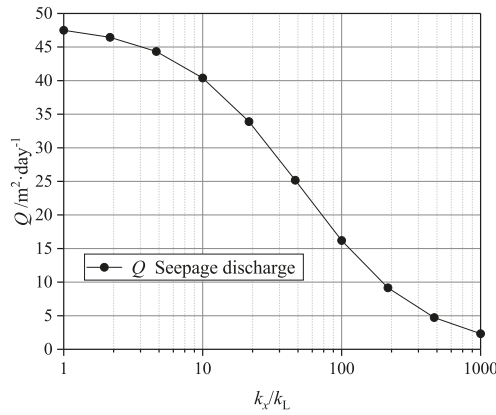


Figure 10. Seepage discharge under different permeability coefficient of lining structure.

Grouting ring is widely used as water plugging method in subsea tunnel. It is important to determine the influence of grouting ring parameters on hydraulic head and seepage discharge for the design of subsea tunnel. According to Equation (7), the internal hydraulic head of lining structure is 0, Equations (31) and (36) can be written as follows:

$$H_L = \frac{\frac{k_x}{k_L} \ln \frac{r_L}{r_0}}{\ln \varphi_a + \frac{k_x}{k_L} \ln \frac{r_L}{r_0} + \frac{k_x}{k_G} \ln \frac{r_G}{r_L}} H_a \tag{50}$$

$$Q = \frac{2\pi k_x}{\ln \varphi_a + \frac{k_x}{k_L} \ln \frac{r_L}{r_0} + \frac{k_x}{k_G} \ln \frac{r_G}{r_L}} H_a \tag{51}$$

Pan et al. [23] proposed an influence factor for grouting parameters. With reference to this influence factor, the grouting influence factor is defined as follows:

$$F_G = \frac{k_x}{k_G} \ln \frac{r_G}{r_L} \tag{52}$$

where is k_x/k_G the ratio of permeability coefficient between surrounding rock and grouting ring, which reflects the impermeability of the grouting ring. r_G/r_L is the ratio of the grouting circle radius to the tunnel outer diameter, reflecting the size of the grouting ring.

According to Equations (50) and (51), when other parameters are determined, the hydraulic head of the lining structure and seepage discharge will be determined by the grouting influence factor. The larger the grouting influence factor is, the smaller the hydraulic head of lining structure is, and the smaller the seepage discharge is.

The variation of grouting influence factor with k_x/k_G and r_G/r_L is shown in Figure 11. It can be seen from the results in the diagram that the grouting influence factor shows a linear growth trend with the increase of k_x/k_G and a logarithmic growth trend with the increase of r_G/r_L . The size of the grouting ring has a more significant effect on the grouting influence factor. In practical engineering, the adjustment range of grouting ring permeability is larger than that of grouting ring size for economic reasons. Therefore, in engineering design, the minimum value of permeability of grouting ring, i.e., the maximum value of k_x/k_G can be determined first, and then the grouting ring size can be determined on this basis.

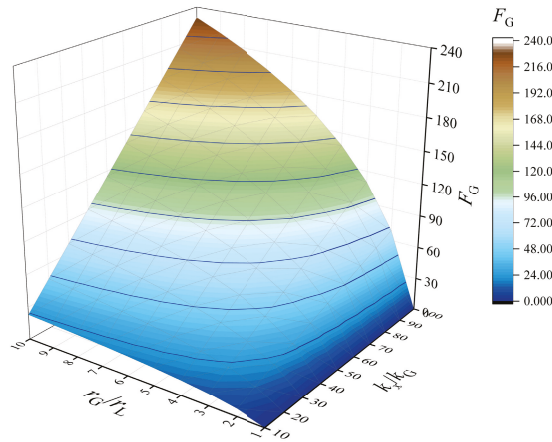


Figure 11. Grouting influence factors under different grouting ring parameters.

5. Conclusions

Based on the existing theoretical research of the tunnel seepage flow field for a deep-buried tunnel, analytical solutions of the steady seepage field for a deep-buried tunnel with grouting ring are proposed considering different permeability coefficients of surrounding rocks in horizontal and vertical directions i.e., the anisotropic seepage flow and considering the influence of tunnel lining structure and grouting ring. Through coordinate transformation and conformal mapping, the seepage field of surrounding rock is solved. Then the seepage fields of surrounding rock, grouting ring and lining structure are solved by boundary conditions and continuous flow conditions between them. Verification analysis and parameter analysis are carried out, several conclusions can be drawn as follows:

(1) The analytical solution of the anisotropic seepage field of surrounding rock proposed in this paper is completely consistent with the analytical solution of isotropic seepage field in the case of simplification, which proves the correctness of the solution in this paper to some extent.

(2) For the anisotropic seepage field of a deep buried tunnel with grouting ring, the calculation results of the analytical solution in this paper are completely consistent with the calculation results of the finite element limit analysis software OptumG2, which can verify the correctness of the solution in this paper.

(3) The seepage field of surrounding rocks around a deep buried circular tunnel is no longer uniformly distributed and presents elliptical distribution, after considering anisotropic seepage flow. Under different permeability coefficient ratios of surrounding rocks, different results of the hydraulic head contour are presented. In the direction of a smaller permeability coefficient, the hydraulic gradient is larger.

(4) As the permeability coefficient of a lining structure decreases, the hydraulic head of the lining structure and grouting ring are increased. When the difference between permeability coefficient of lining structure and surrounding rock is not very large, the change of permeability coefficient of lining structure has a great influence on the hydraulic head. However, when the permeability coefficient of the lining structure differs greatly from that of the surrounding rock, the change of the permeability coefficient of lining structure has no significant effect on the hydraulic head.

(5) The parameters of grouting ring are analyzed by using the grouting influence factors. The results show that the size of grouting ring has more significant influence on the grouting effect.

Author Contributions: Conceptualization, Q.C.; Project administration, Q.C.; Software, B.Z. and L.L.; Validation, C.X. and J.M.; Writing—original draft, L.L. and Q.C.; Writing—review & editing, Q.C. and B.K. All authors have read and agreed to the published version of the manuscript.

Funding: The financial supports from National Natural Science Foundation of China (NSFC Grant No. 52008373) and Natural Science Foundation of Zhejiang Province of China (No. LQ22E080009) are greatly acknowledged.

Institutional Review Board Statement: Not applicable.

Informed Consent Statement: Not applicable.

Data Availability Statement: Not applicable.

Conflicts of Interest: The authors declare no conflict of interest.

References

1. Ahmad, S.; Naji, A.M.; Hussain, I.; Rehman, H.; Yoo, H. Ground saturation response during first filling of lined pressure tunnels: A case study. *Rock Mech. Rock Eng.* **2021**, *54*, 513–535. [[CrossRef](#)]
2. Harr, M.E. *Groundwater and Seepage*; McGraw-Hill: New York, NY, USA, 1962.
3. Fernández, G.; Alvarez, T.A., Jr. Seepage-induced effective stresses and water pressures around pressure tunnels. *J. Geotech. Eng.* **1994**, *120*, 108–128. [[CrossRef](#)]
4. Qin, Z.; Wang, Y.; Song, Y.; Dong, Q. The analysis on seepage field of grouted and shotcrete lined underwater tunnel. *Math. Probl. Eng.* **2020**, *2020*, 7319054. [[CrossRef](#)]
5. Li, Z.; He, C.; Chen, Z.; Yang, S.; Ding, J.; Pen, Y. Study of seepage field distribution and its influence on urban tunnels in water-rich regions. *Bull. Eng. Geol. Environ.* **2019**, *78*, 4035–4045. [[CrossRef](#)]
6. Park, K.H.; Owatsiriwong, A.; Lee, J.G. Analytical solution for steady-state groundwater inflow into a drained circular tunnel in a semi-infinite aquifer: A revisit. *Tunn. Undergr. Space Technol.* **2008**, *23*, 206–209. [[CrossRef](#)]
7. Kolymbas, D.; Wagner, P. Groundwater ingress to tunnels—the exact analytical solution. *Tunn. Undergr. Space Technol.* **2007**, *22*, 23–27. [[CrossRef](#)]
8. Lei, S. An analytical solution for steady flow into a Ttonnel. *Groundwater* **1999**, *37*, 23–26. [[CrossRef](#)]
9. El Tani, M. Circular tunnel in a semi-infinite aquifer. *Tunn. Undergr. Space Technol.* **2003**, *18*, 49–55. [[CrossRef](#)]
10. Wu, J.; Zhou, Z.; Zhuang, C. A combined analytical-numerical method for groundwater inflow into circular tunnels in drained conditions. *Hydrogeol. J.* **2021**, *29*, 2529–2543. [[CrossRef](#)]
11. Guo, Y.; Wang, H.; Jiang, M. Efficient Iterative Analytical Model for Underground Seepage around Multiple Tunnels in Semi-Infinite Saturated Media. *J. Eng. Mech.* **2021**, *147*, 04021101. [[CrossRef](#)]
12. Luo, X.; Xiang, Y.; Yu, C. A Semi-Analytical Model and Parameter Analysis of a Collaborative Drainage Scheme for a Deeply Buried Tunnel and Parallel Adit in Water-Rich Ground. *Appl. Sci.* **2022**, *12*, 3759. [[CrossRef](#)]
13. Ying, H.W.; Zhu, C.W.; Gong, X.N.; Wang, X. Analytical solutions for the steady-state seepage field in a finite seabed with a lined tunnel. *Mar. Georesour. Geotechnol.* **2019**, *37*, 972–978. [[CrossRef](#)]
14. Mitchell, J.K.; Soga, K. *Fundamentals of Soil Behavior*; John Wiley & Sons: New York, NY, USA, 2005; Volume 3.
15. Zienkiewicz, O.; Mayer, P.; Cheung, Y.K. Solution of anisotropic seepage by finite elements. *J. Eng. Mech. Div.* **1966**, *92*, 111–120. [[CrossRef](#)]
16. Hu, Z.; Yang, Z.X.; Wilkinson, S.P. Active earth pressure acting on retaining wall considering anisotropic seepage effect. *J. Mt. Sci.* **2017**, *14*, 1202–1211. [[CrossRef](#)]
17. Xu, C.; Liang, L.; Ding, W. Analytical Solutions on Steady Seepage Field of Deep Buried Circular Tunnel After Considering Anisotropic Flow. *J. Shanghai Jiaotong Univ.* **2018**, *52*, 1565.
18. Tang, Y.; Chan, D.H.; Zhu, D.Z. Analytical solution for steady-state groundwater inflow into a circular tunnel in anisotropic soils. *J. Eng. Mech.* **2018**, *144*, 06018003. [[CrossRef](#)]
19. Luo, S.; Xu, M.; Kang, X.; Li, X.; Rao, L. Analytical solution of external water pressure on deep tunnel lining in horizontally layered hydrogeological structures. *Bull. Eng. Geol. Environ.* **2022**, *81*, 1–13. [[CrossRef](#)]
20. Atkinson, J.; Mair, R. Loads on leaking and watertight tunnel linings, sewers and buried pipes due to groundwater. *Geotechnique* **1983**, *33*, 341–344. [[CrossRef](#)]
21. Wang, X.; Tan, z.; Wang, M.; Zhang, M.; Ming, H. Theoretical and experimental study of external water pressure on tunnel lining in controlled drainage under high water level. *Tunn. Undergr. Space Technol.* **2008**, *23*, 552–560. [[CrossRef](#)]
22. Li, P.; Zhang, D.; Zhao, Y.; Zhang, C. Study of distribution law of water pressure acting on composite lining and reasonable parameters of grouting circle for subsea tunnel. *Chin. J. Rock Mech. Eng.* **2012**, *31*, 280–288.
23. Pan, Y.; Luo, Q.; Zhou, B.; Chen, J. Analytical study on seepage field of deep tunnel with grouting circle in half plane. *J. Zhejiang Univ. Eng. Sci.* **2018**, *52*, 1114–1122.
24. Zhou, H.; Liu, H.; Kong, G.; Cao, Z. Analytical solution for pressure-controlled elliptical cavity expansion in elastic–perfectly plastic soil. *Geotech. Lett.* **2014**, *4*, 72–78. [[CrossRef](#)]

25. Li, Z.; Ren, Q.; Wang, Y. Elasto-plastic analytical solution of deep-buried circle tunnel considering fluid flow field. *Chin. J. Rock Mech. Eng.* **2004**, *23*, 1291–1295.
26. Krabbenhoft, K.; Lyamin, A.; Krabbenhoft, J. Optum computational engineering (OptumG2). *Comput. Softw.* **2015**.
27. Li, P.; Fang, Q.; Zhang, D. Analytical solutions of stresses and displacements for deep circular tunnels with liners in saturated ground. *J. Zhejiang Univ. Sci. A* **2014**, *15*, 395–404. [[CrossRef](#)]
28. Wang, M.; Huang, F. Key problems on subsea tunnel construction. *J. Archit. Civ. Eng.* **2005**, *22*, 1–4.
29. Liu, Z.W.; Zhang, D.L.; Zhang, M.Q. Grouting technique for high-pressure and water-rich area in Maoba syncline at Yuanliangshan tunnel. *Chin. J. Rock Mech. Eng.* **2005**, *24*, 1728–1734.
30. Zhang, C.; Zhang, D.L.; Wang, M.S.; Xiang, Y.Y. Study on appropriate parameters of grouting circle for tunnels with limiting discharge lining in high water pressure and water-enriched region. *Chin. J. Rock Mech. Eng.* **2007**, *26*, 2270–2276.

Article

Predicting the Sound Speed of Seafloor Sediments in the East China Sea Based on an XGBoost Algorithm

Mujun Chen ^{1,2}, Xiangmei Meng ^{1,2}, Guangming Kan ^{1,2,*}, Jingqiang Wang ^{1,2}, Guanbao Li ^{1,2}, Baohua Liu ²,
Chenguang Liu ^{1,2}, Yanguang Liu ^{1,2}, Yuanxu Liu ^{1,3} and Junjie Lu ^{1,2}

¹ Key Laboratory of Marine Geology and Metallogeny, First Institute of Oceanography, Ministry of Natural Resources, Qingdao 266061, China

² Laboratory for Marine Geology, Pilot National Laboratory for Marine Science and Technology (Qingdao), Qingdao 266237, China

³ College of Underwater Acoustic Engineering, Harbin Engineering University (Harbin), Harbin 150001, China

* Correspondence: kgming135@fio.org.cn

Abstract: Based on the acoustic and physical data of typical seafloor sediment samples collected in the East China Sea, this study on the super parameter selection and contribution of the characteristic factors of the machine learning model for predicting the sound speed of seafloor sediments was conducted using the eXtreme gradient boosting (XGBoost) algorithm. An XGBoost model for predicting the sound speed of seafloor sediments was established based on five physical parameters: density (ρ), water content (w), void ratio (e), sand content (S), and average grain size (M_z). The results demonstrated that the model had the highest accuracy when $n_estimator$ was 75 and max_depth was 5. The model training goodness of fit (R^2) was as high as 0.92, and the mean absolute error and mean absolute percent error of the model prediction were 7.99 m/s and 0.51%, respectively. The results demonstrated that, in the study area, the XGBoost prediction method for the sound speed of seafloor sediments was superior to the traditional single- and two-parameter regression equation prediction methods, with higher prediction accuracy, thus providing a new approach to predict the sound speed of seafloor sediments.

Keywords: sound speed; seafloor sediments; XGBoost; the East China Sea

Citation: Chen, M.; Meng, X.; Kan, G.; Wang, J.; Li, G.; Liu, B.; Liu, C.; Liu, Y.; Liu, Y.; Lu, J. Predicting the Sound Speed of Seafloor Sediments in the East China Sea Based on an XGBoost Algorithm. *J. Mar. Sci. Eng.* **2022**, *10*, 1366. <https://doi.org/10.3390/jmse10101366>

Academic Editor: George Kontakiotis

Received: 7 August 2022

Accepted: 19 September 2022

Published: 24 September 2022

Publisher's Note: MDPI stays neutral with regard to jurisdictional claims in published maps and institutional affiliations.



Copyright: © 2022 by the authors. Licensee MDPI, Basel, Switzerland. This article is an open access article distributed under the terms and conditions of the Creative Commons Attribution (CC BY) license (<https://creativecommons.org/licenses/by/4.0/>).

1. Introduction

The shallow sediments of the seafloor exhibit unique acoustic properties that provide the necessary basic data for seafloor acoustic field research, seafloor engineering geology, and marine petroleum geology and are important factors in determining the marine acoustic field environment [1]. They have important research value in the fields of seafloor sediment investigation, marine resource exploration and development, and marine environmental monitoring [2,3]. Seafloor sediments are generally considered a two-phase medium consisting of solid and liquid phases [4], and their acoustic properties are closely related to the physical properties of seafloor sediments.

As the basic element of seafloor acoustics research, the measuring methods of the sound speed of seafloor sediments primarily include in situ measurements, laboratory measurements, and the geoacoustic inversion method. In addition, prediction based on geoacoustic models is an important method for obtaining the sound speed of seafloor sediments. Therefore, it is extremely important to establish an accurate geoacoustic model to describe the relationship between the sediment sound speed and physical parameters. Many studies established theoretical models for predicting sound speed in seafloor sediments [5–11]. However, because of the complex and diverse marine sedimentary environment and sedimentary disturbance error in the determination process, the several input parameters of the theoretical model are difficult to measure. Concomitantly, many studies have established regression equations of sound speed prediction in different sea areas by

examining the correlation between the sound speed and physical parameters of seafloor sediments [12–22]. However, the physical properties of sediments frequently require multiple parameters for accurate characterization. The empirical equation only establishes the correlation between the sediment sound speed and one or two physical parameters to an extent, and there are limitations and reduced accuracy in the sound speed prediction.

To supplement the existing literature, this study proposes a machine learning prediction method for the sound speed of seafloor sediments based on the eXtreme gradient boosting (XGBoost) algorithm, which can fuse multiple sediment physical parameters as well as effectively improve the problem of the previous empirical equations tending to overfit or underfit the measured sound speed of seafloor sediment. Here, data preprocessing was performed on the data measured at laboratory of sediment samples from the East China Sea. The physical parameters with high correlation were then extracted using the Pearson correlation coefficient matrix, and the model was trained and verified. Then, using the test samples and traditional single- and two-parameter regression equations to comprehensively evaluate the model, we analyzed the contribution of each physical parameter. The results demonstrated that the prediction model of the seafloor sediment sound speed based on the XGBoost algorithm was superior to the traditional prediction equation methods with higher prediction accuracy.

2. Study Area and Data Source

2.1. Location of the Study Area

The study area is located on the continental shelf of the East China Sea at a water depth of 26–107 m. The water depth of the western-inland region is shallow and gradually increases to the east. As one of the widest continental shelves worldwide, it has considerable terrigenous input and is an important area for studying land–ocean interactions and source–sink processes [23]. The deposition of terrigenous sediments in this area is primarily controlled by the coastal upwelling and downwelling of the southern continental shelf of the East China Sea [24]. Owing to the inflow of small coastal rivers such as the Yangtze River and the influence of the Yellow River, the continental shelf of the East China Sea has received a high input of terrigenous materials [25]. In the interaction between the Zhejiang–Fujian coastal current and Taiwan warm current, most sediments diffused from the north to the south were confined in the continental shelf, thus forming an intrashelf mud wedge [26]; however, most of the sediments in the study area were confined in the continental shelf and covered by sand [27]. The coastal sediments in the study area are parallel to the coast and distributed in a band, and the nearshore is mostly silty clay, whereas the outward is clay. The sediment then quickly changes to coarse-grained silt or fine sand.

2.2. Data Sources

Seafloor sediment samples were collected at 45 sites on the East China Sea shelf using box and gravity samplers during the open research cruise of the East China Sea supported by the National Science Foundation of China (NSFC) Shiptime Shearing Project in 2021. Among these samples, those that were ~400 cm in length were obtained from 16 stations in the East China Sea’s silty clay and clayey silt areas, while most obtained from the sandy bottom in the study area were 20–200 cm in length. The sound speed and physical parameters were measured in the laboratory. First, the sample was cut and divided as per the actual requirements, generally cut into 30 cm long sections and placed on a cylindrical sample measurement platform. The laboratory measurement system of the acoustic property of seafloor sediment cores was used to measure the sound speed of the sediment samples using the transmission method. After the 30 cm long sediment measurement was completed, a length of 10 cm was cut off, and the sound speed of the remaining 20 cm long sediment was measured again to obtain as much data as possible. The sound speed was calculated as follows:

$$V_P = L / (10^3 (t - t_0)) \tag{1}$$

where V_p is the sound speed of the seafloor sediment sample (m/s), L is the column length of the sample (mm), t is the sound wave penetration time (μ s), and t_0 is the correction value of zero sound time (μ s).

After measuring the sound speed of the sample, the physical and mechanical properties of the sediment were measured [28]. The properties included density, water content, void ratio, sand content, silt content, clay content, and average grain size. During the laboratory measurements, two-frequency (25 and 100 kHz) acoustic transducers were used to measure the acoustic properties and physical parameters of each section of the sample. Because the acoustic data with a frequency of 100 kHz were of good quality and the covered physical parameters were more representative, although the sound speed values at different frequencies differed, the relationship between them and the physical properties of the sediments was the same. Thus, this study selected sound speed data of 100 kHz (292 groups). Table 1 lists the maximum, minimum, and average of the physical parameters and sound speeds.

Table 1. Statistics of sound speed and physical parameters of sediments in the study area.

	$\rho/$ (g/cm ³)	$w/$ %	e	$S/$ %	$T/$ %	$Y/$ %	$M_z/$ Φ	$V_p/$ (m/s)
Max	2.00	74.85	2.04	76.30	79.30	73.10	8.78	1695.38
Min	1.56	24.25	0.68	0.10	10.70	34.50	6.71	1492.86
Ave	1.72	52.07	1.43	10.34	55.15	7.60	5.9	1540.96

3. Methods

3.1. Data Preprocessing

3.1.1. Data Noise Removal

The experimental data were collected from a real scene and contained a lot of data noise; therefore, they could not be directly used for model training. The primary task of data noise removal is to remove incomplete or wrong data. Here, data cleaning was divided into outlier and missing value removal. Data points significantly far from the fitted curve are marked as outliers using a regression fit between the sound speed and each physical parameter. The missing sound speed values and physical parameters of each sample were simultaneously removed to improve the data quality and integrity.

3.1.2. Normalization Processing

The numerical units of different physical parameters differ; therefore, the data required normalization. The parameters were uniformly set to a value between 0 and 1. Normalizing the input data can prevent neuron saturation and increase the accuracy and generalization ability of the model prediction. The formula of normalization is as follows:

$$\bar{X} = \frac{X - X_{\min}}{X_{\max} - X_{\min}} \tag{2}$$

where \bar{X} is the normalized data, X is the original data, and X_{\min} and X_{\max} are the maximum and minimum values of the original data, respectively.

3.1.3. Physical Parameter Extraction

In order to reduce the complexity of the model and improve the generalization ability of the model, some but not all parameters with relatively strong correlation were selected while ensuring accuracy during the data processing. Here, the data collected included the sound speed, basic information of the following sampling stations, and physical parameters of the sediments:

1. Geospatial information of the seafloor sediment sampling stations—longitude (Log), latitude (Lat), and depth (D);
2. Basic physical parameters—density (ρ), water content (w), and void ratio (e);

3. Grain composition—sand (S), silt (T), clay contents (Y);
4. Grain size coefficient—average grain size (M_z).

Among the acoustic parameters and physical and mechanical parameters of seafloor sediments, the sound speed exhibits a good correlation with the density, water content, and porosity [18]. The Pearson correlation coefficient can measure the degree of correlation and whether there is a linear correlation between two features [29]. Thus, the Pearson correlation coefficient was used to measure the correlation between the sound speed and other physical parameters and plot the correlation coefficient matrix (Figure 1). Using two variables— X and Y —the Pearson correlation coefficient between the variables is as follows:

$$f_{X,Y} = \frac{E(XY) - E(X)E(Y)}{\sqrt{E(X^2) + E^2(X)}\sqrt{E(Y^2) + E^2(Y)}} \quad (3)$$

where $f_{X,Y}$ is the correlation coefficient. A positive value indicates a positive correlation between the physical parameters and sound speed, and a negative value indicates a negative correlation.

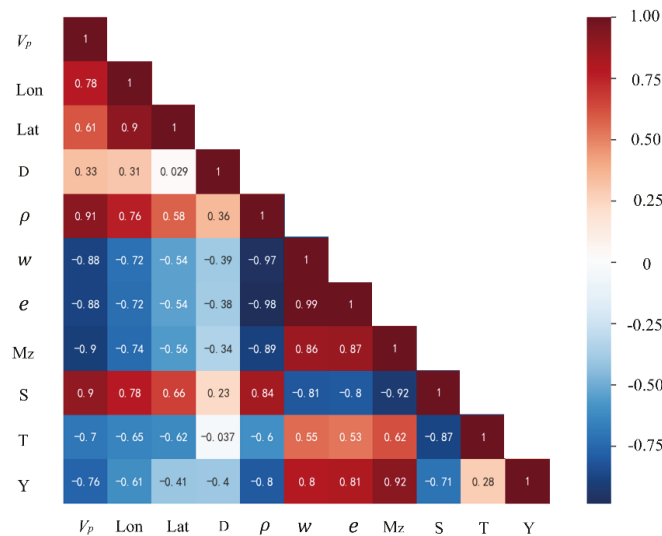


Figure 1. Half-matrix plot of Wilson's correlation coefficients between the sediment sound speed and physical parameters. The first column of the matrix is the distribution of the correlation coefficient between the sound speed and each physical parameter. The redder the matrix unit, the more evident the positive correlation, and the bluer the unit, the more evident the negative correlation.

As per the first column of the matrix diagram of the correlation coefficient between the sound speed and each physical parameter (Figure 1), it was concluded that the correlation coefficient between the sound speed and density, water content, void ratio, sand content, and average particle size of the seafloor sediments reached ~ 0.90 , exhibiting strong or extremely strong correlation. The correlation coefficient with other parameters was below 0.80. During the training of the XGBoost algorithm model, the highest correlation between the input feature factor and target parameter was selected such that the predicted result was closer to the expected value. Similarly, the dimension of the model was reduced as much as possible while ensuring the accuracy of the model to reduce the complexity of the model. Therefore, the factors selected for training in this study were the density, water content, void ratio, sand content, and average grain size. Among these factors, the density and sand content positively correlated with the sound speed, indicating that the higher the density and sand content, the higher the sound speed. The water content, void ratio,

and average grain size negatively correlated with the sound speed, indicating that with an increase in each parameter, the sound speed decreased.

3.1.4. Data Division

After data preprocessing, 280 data sample groups were collected, and the samples were randomly divided into 200 training, 40 validation, and 40 test sample groups. After the training, validation, and test sets were determined, only then were the parameters of the learning algorithm adjusted to explore suitable parameters, screen suitable features, rapidly detect the algorithm performance, and guide the most important changes to the machine learning model. The training samples were used to train the sound speed prediction model, and the final model was trained by setting the parameters of the fitter. After training multiple models via the training set, the model with the best effect was selected from the validation set. The corresponding parameters can then be used to control the occurrence of model over-fitting. To measure the performance of the optimized model, the test samples were considered as a nonexistent data set—a data sample that did not participate in the entire model building process and was used to measure the performance of the optimized model. Figure 2 shows the training, validation, and test samples in the sediment triangulation. There were multiple types of sediments in the data samples, which improved the generalization ability of the model.

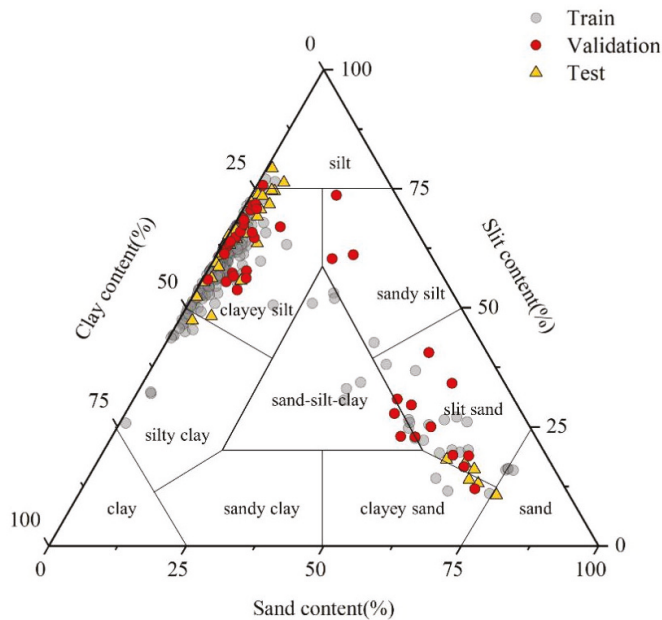


Figure 2. Triangular sediment classification diagram. Most of the sediment in the data samples included clay silt, followed by silt sand, a small amount of silt, silty clay, and clay sand. The grey dots, red dots, and yellow triangles indicate training, validation, and test samples, respectively.

3.2. XGBoost Algorithm

XGBoost is a boosted tree model that integrates multiple weak learners to build a strong learner [30,31]. The idea of the algorithm is to fit the negative gradient of the loss function in repeated iterations after optimizing the empirical loss function, select sample features to generate a basic learner, and continuously fit the previous residuals to minimize the objective function. We repeated this process to build hundreds of basic learners and integrated them in a comprehensive model (Figure 3).

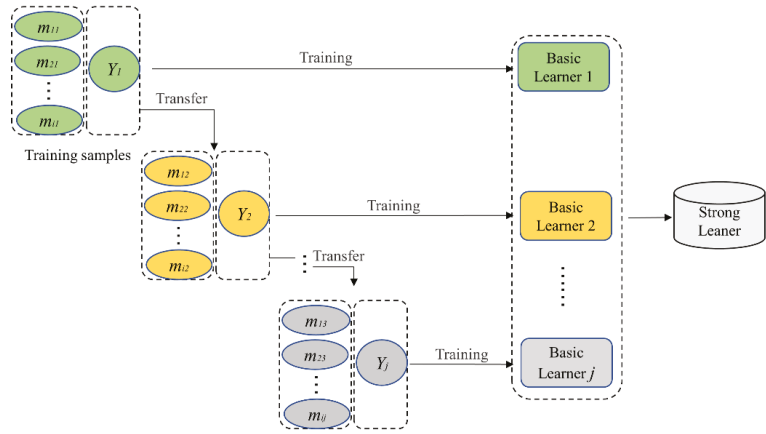


Figure 3. The boosting algorithm principle, where m is the characteristic factor of the training sample in the model, which is each physical parameter; m_{ij} is the i -th characteristic factor of the j -th base learner; and Y represents the target value of the training sample in the model, which is the sound speed of the seafloor sediment in this study.

The objective function of XGBoost comprises a loss function, regularization term, and constant term. The equation is as follows:

$$\text{Obj}(\theta) = L(\theta) + \Omega(\theta) + C \tag{4}$$

The loss function was used to measure the quality of the model prediction, and the regularization term was used to control the complexity of the model and avoid overfitting.

3.2.1. Loss Function

The XGBoost algorithm can be considered as an additive model comprising K trees, as shown in Equation (5). The tree model used in this study is a regression tree:

$$\hat{y}_i = \sum_{k=1}^K f_k(x_i), f_k \in F \tag{5}$$

where \hat{y}_i is the sample prediction result, x_i , i is the i -th sample input, k is the sum of trees, f_k is each regression tree, and F is the set space with the regression tree.

The improvement of XGBoost over the Gradient Boosting Decision Tree (GBDT) is that it uses the first- and second-order derivatives and the Taylor expansion for approximation. If g_i is the first derivative and h_i is the second derivative:

$$g_i = \partial_{y^{(t-1)}} l(y_i, \hat{y}_i^{(t-1)}) \tag{6}$$

$$h_i = \partial_{\hat{y}_i^{(t-1)}}^2 l(y_i, \hat{y}_i^{(t-1)}) \tag{7}$$

3.2.2. Regularization

The complexity of the regression tree can effectively control the overfitting of the model. It comprises two parts: the number and weight of leaf nodes. It was defined by the equation as:

$$\Omega(f_t) = \gamma T + \frac{1}{2} \lambda \sum_{j=1}^T w_j^2 \tag{8}$$

where γ and λ are the normalization coefficients. Combining the two aforementioned parts, the objective function was rewritten as the following equation:

$$\text{Obj}(\theta) \approx \sum_{j=1}^T \left[\left(\sum_{i \in I_j} g_i \right) w_j + \frac{1}{2} \left(\sum_{i \in I_j} h_i + \lambda \right) w_j^2 \right] + \gamma T \tag{9}$$

where I_j is the sample on the j -th leaf node, and w_j is the weight of the j -th leaf node. The optimal objective function was then obtained:

$$\text{Obj}(\theta) = -\frac{1}{2} \sum_{j=1}^T \frac{G_j}{H_j + \lambda} + \gamma T \tag{10}$$

The smaller the objective function, the smaller the prediction error, and the better the model effect.

4. Results

4.1. Training and Validation of Seafloor Sediment Prediction Model

This study was based on the XGBoost algorithm with the CART (Classification and Regression Tree) as the base learner. The 200 sets of training data obtained in the laboratory were used for model training, and the 40 sets of validation samples were used to assist the model training to obtain optimal parameters such that the model performance could reach the highest level. The selected training target parameter was the sediment sound speed; the characteristic factors were the density, water content, void ratio, average grain size, and clay content. During the model training process, the XGBoost algorithm had multiple hyperparameters, and it was impossible to adjust all the parameters. Therefore, this study optimized two parameters—`n_estimator` and `max_depth`, which were important to the model training accuracy—and the parameter adjustment and optimization followed the principle of “first importantly then weak, first coarse then fine.” Here, the mean absolute error (MAE) and mean absolute percentage error (MAPE) were selected to compare the performance of different models. The equations of the two indicators are as follows:

$$\text{MAE} = \frac{\sum_{i=1}^n |\hat{y}_i - y_i|}{n} \tag{11}$$

$$\text{MAPE} = \frac{100\%}{n} \sum_{i=1}^n \left| \frac{\hat{y}_i - y_i}{y_i} \right| \tag{12}$$

where y_i is the true value, \hat{y}_i is the predicted value, and n is the number of predicted samples.

The `n_estimator` in the XGBoost hyperparameters, i.e., the maximum number of trees, can be considered as the number of iterations that determines the learning ability of the model. The greater the number of trees, the stronger the learning ability of the model. When the number of trees in the XGBoost was low, the impact on the model was relatively high; when the number of trees was already high, the impact on the model was relatively low. The smaller the trees, the easier it was to cause the model to under-fit, and excess trees easily caused the model to over-fit. Therefore, selecting the appropriate `n_estimator` can impact the training accuracy of the model. Here, the optimal selection of the `n_estimator` was made within the range of [20, 200]. As shown in Figure 4, when the `n_estimator` exceeded 75, the training error of the model continually decreased, and the error of the validation sample gradually increased. Therefore, it was determined that when the `n_estimator` exceeded 75, the model was in the overfitting state, and so the `n_estimator` of the research model was 75, and the model effect was the best. At this time, the goodness of fit (R^2) of the model training was 0.917, the real value of the MAE of the training result was 8.15 m/s, and that of the validation result was 9.11 m/s.

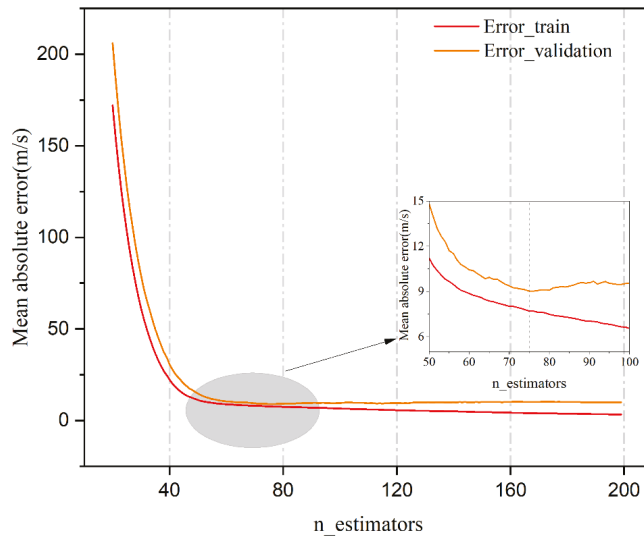


Figure 4. The training process of the XGBoost model is based on the hyperparameter—*n_estimators*. The red and orange solid lines indicate the iterative changes in the model training error and validation result, respectively.

The *max_depth* is the maximum depth of the tree in the model, which is used to control the model fitting state. The larger the *max_depth*, the more specific the model learns; however, if the *max_depth* is excessively large, the model overfits. Based on the premise that *A* in the model was 75, this study set the *max_depth* to perform optimal model training in [1,20]. As shown in Figure 5, when the *max_depth* was 5, the model had the highest validation accuracy. At this time, the R^2 of the model training was 0.923, the real value of the MAE of the training result was 7.79 m/s, and that of the validation result was 8.96 m/s.

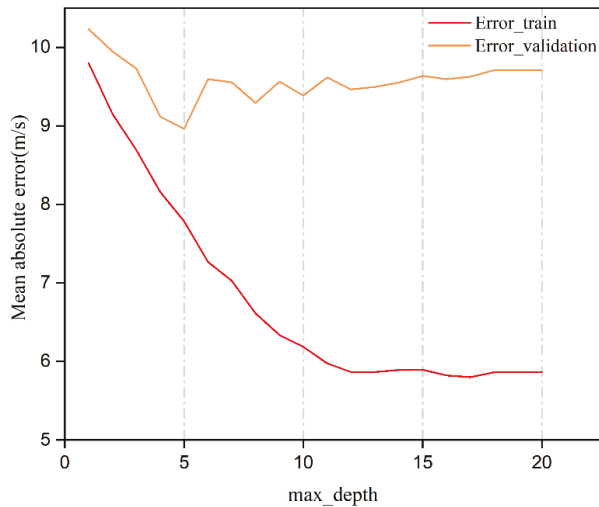


Figure 5. The training process of the XGBoost model was based on the hyperparameter—*max_depth*. The red and orange solid lines indicate the iterative changes in the model training and validation result errors, respectively.

After the continuous optimization of the model, along with the error performance of the training and validation results, the optimal model had an `n_estimator` and `max_depth` of 75 and 5, respectively. Figure 6 shows that the training results of the 200 training sample groups and validation results of 40 validation sample groups had a high degree of fit with the real values.

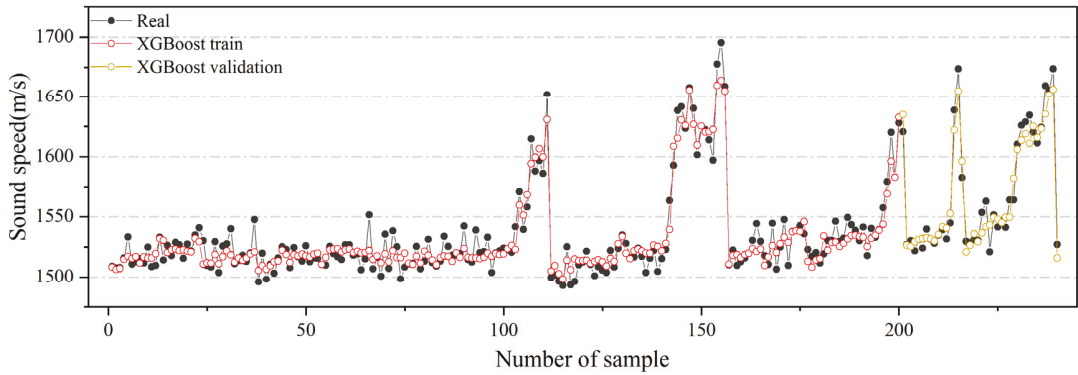


Figure 6. Training and validation results of the final model. The black line is the actual measured value, the red line is the training result of 200 sets of training samples, and the brown line is the validation result of 40 sets of validation samples.

4.2. Model Interpretation

SHapley Additive exPlanations (SHAP) can be used to explain the output of the machine learning model and build an additive explanation model, and all features are regarded as “contributors.” For each predicted sample, the model produced a predicted value, and the SHAP value was the value assigned to each feature in that sample. If the i -th sample was x_i , the j -th feature of the i -th sample was x_{ij} , the predicted value of the model for the sample is y_i , the baseline of the entire model (usually the mean of the target variable of the samples) is y_{base} , and then the SHAP value obeyed the following equation:

$$y_i = y_{base} + f(x_{i1}) + f(x_{i2}) + \dots + f(x_{ij}) \tag{13}$$

where $f(x_{ij})$ is the SHAP value of x_{ij} . Intuitively, it was the contribution value of the first feature in the i -th sample to the final predicted value. When $f(x_{i1}) > 0$, it implied that the feature improved the predicted value, showing a positive effect; otherwise, it showed that the feature reduced the predicted value, showing a negative effect.

The characteristic factors of the prediction model of the seafloor sediment sound speed in this study were the density, water content, void ratio, sand content, and average particle size. Figure 7 shows the characteristic factors arranged from top to bottom, and the successive decrease in their contribution to the model, i.e., the contribution of the physical parameters to the sound speed in this model. The degree of influence is arranged in terms of the water content, density, sand content, average particle size, and void ratio. Moreover, Figure 7 shows that the sound speed increased with an increase in the density and sand content and decreased with an increase in the water content, void ratio, and average grain size.

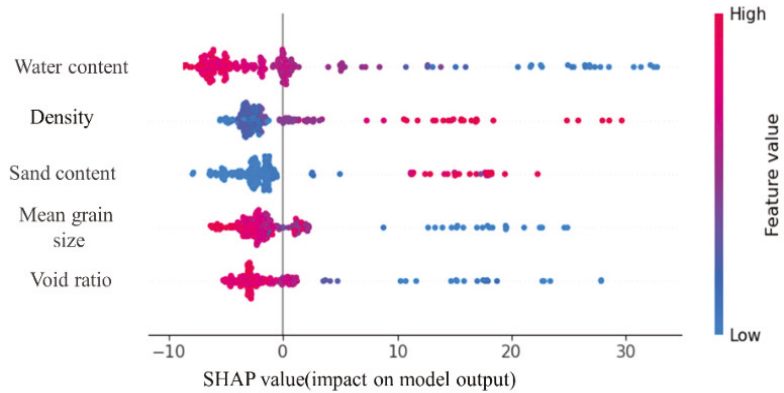


Figure 7. SHAP value distribution of characteristic factors in the model, which shows the contribution of the sample point of each characteristic factor to the model.

5. Discussion

5.1. Single-Parameter Prediction Equation

Based on the 200 training sample groups, a regression analysis was performed between the sound speed and each parameter—density, water content, void ratio, sand content, and average grain size. In previous relevant studies, the traditional single parameter method for sediment sound speed is basically dominated by the unary quadratic equation [16,18,19], and in our single parameter regression analysis and comparison, the fitting effect of the single parameter using the quadratic equation is the best. For example, it is found that the fitting degree of the cubic equation established by water content and average grain size is lower than that of the quadratic equation, and the fitting degree of the cubic equation of other parameters is not improved too. So, the unary quadratic regression method was employed to obtain the single parameter equation of the sound speed prediction (Table 2). The results demonstrated that the correlation coefficient between the physical parameters and sound speed was high ($R^2 \geq 0.76$); the density and void ratio had the highest correlation coefficient of 0.86, followed by the water content ($R^2 = 0.85$), sand content ($R^2 = 0.76$), and average grain size ($R^2 = 0.76$). Figure 8 shows the fitting curve of the sound speed and physical parameters.

Table 2. Expressions of the single-parameter equations and fitting correlation coefficients.

Related Parameters	Prediction Equation	R^2
ρ	$V_p = 1141.54\rho^2 - 3642.28\rho + 4419.83$	0.86
w	$V_p = 0.088w^2 - 11.74w + 1903.64$	0.85
e	$V_p = 123.96e^2 - 448.07e + 1916.74$	0.86
M_z	$V_p = 7.90M_z^2 - 136.04M_z + 2086.99$	0.76
S	$V_p = 2.97s - 0.015s^2 + 1515.95$	0.76

5.2. Two-Parameter Prediction Equation

Based on the 200 training sample groups, the bivariate quadratic regression prediction equation of the sound speed and two of the parameters among density, water content, void ratio, and average grain size was obtained using the principle of least square (Table 3). The results demonstrated that the correlation coefficient between the tow physical parameters and sound speed was high ($R^2 \geq 0.86$), the correlation coefficient of the equation obtained using the density and average grain size-based equation, density and void ratio-based equation, density and water content-based equation is 0.87, and water content and void ratio-based equation is 0.86. Figure 9 shows the 3D spatial distribution between the sound speed and parameters.

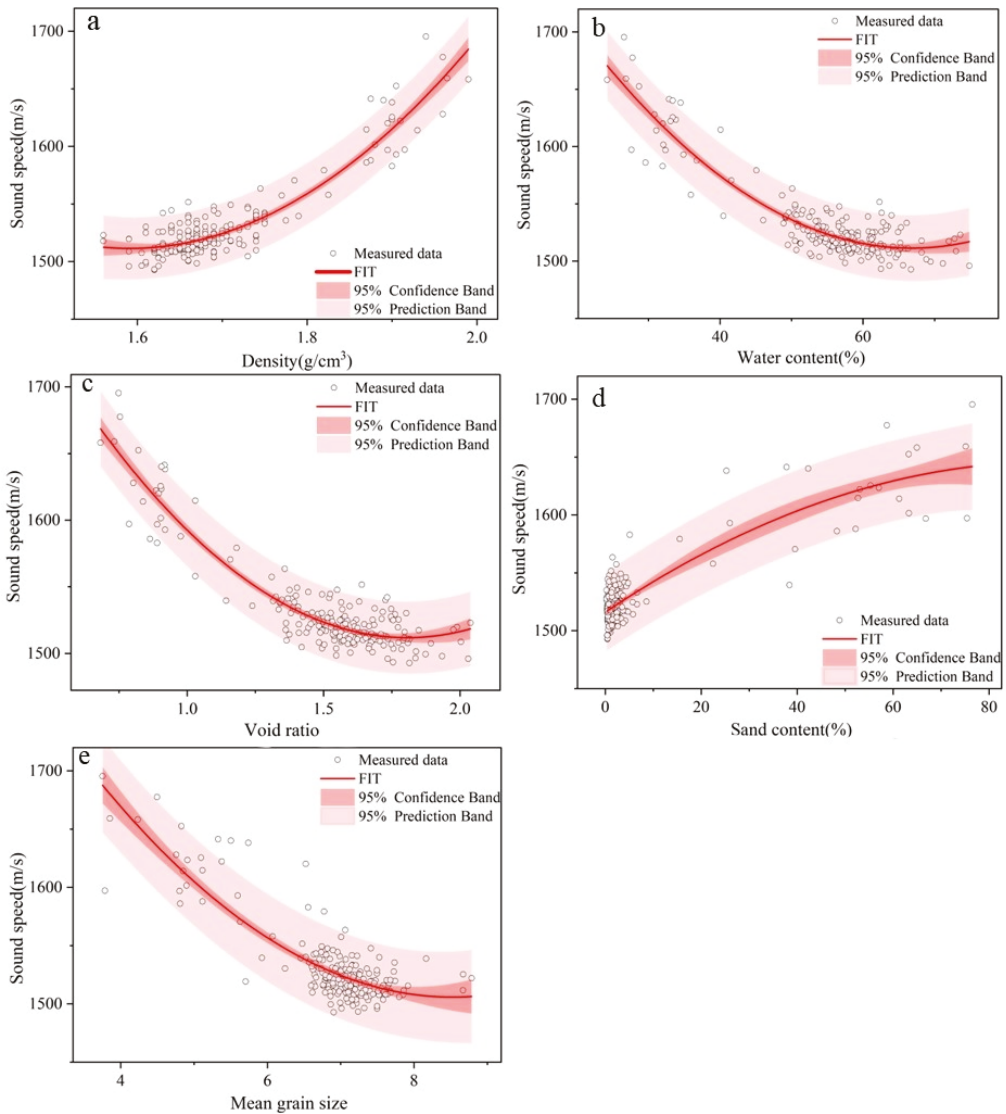


Figure 8. The single-parameter equation regression fitting of the sound speed and physical parameters: (a) density, (b) water content, (c) void ratio, (d) sand content, and (e) average grain size curves. The black hollow point, red solid line, red area, and pink area indicate the 200 training sample groups, fitted curve, confidence interval at 95%, and prediction interval at 95%, respectively.

Table 3. Expressions of double-parameter equations and fitting correlation coefficients.

Related Parameters	Prediction Equation	R ²
ρ, w	$V_p = 966.58\rho^2 + 0.012w^2 - 3123.61\rho - 1.95w + 4111.86$	0.87
ρ, e	$V_p = 852.79\rho^2 + 34.85e^2 - 2804.28\rho - 146.72e + 3968.22$	0.87
w, e	$V_p = 258.35e^2 - 0.099w^2 - 898.03e + 12.13w + 1921.24$	0.86
ρ, M_z	$V_p = 917.54\rho^2 + 1.3M_z^2 - 2904.8\rho - 18.79M_z + 3889.6$	0.87

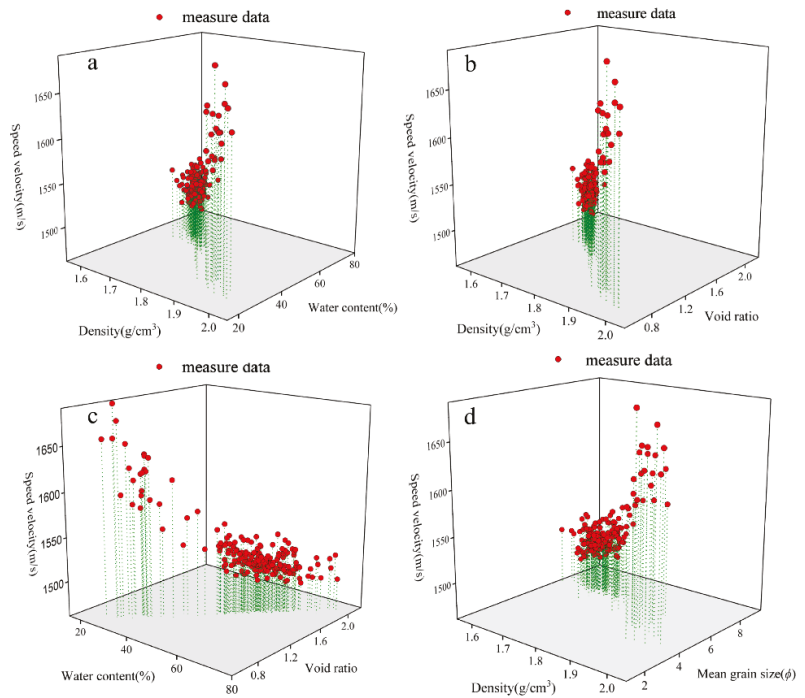


Figure 9. Three-dimensional scatter distribution of the sound speed and two parameters: (a) density and water content, (b) density and void ratio, (c) water content and void ratio, and (d) density and average grain size. The red dots indicate the 200 sets of training samples, and the green dotted lines indicate the projections of the dots on the coordinate plane formed by the parameters.

5.3. Comparison of XGBoost Prediction Models with Predictions of Single- and Two-Parameter Equations

Based on the trained XGBoost model, single-parameter prediction equations, and two-parameter prediction equations, the sound speed of the seafloor sediments was predicted for 40 groups of test samples to confirm the accuracy and superiority of the model (Figure 10). Table 4 shows the correlation error statistics between the prediction results and true values of each model. The results demonstrated that the XGBoost model exhibited the highest prediction accuracy, and the MAE, MAPE, and max absolute error are 7.99 m/s, 0.51%, and 29.27 m/s, respectively. This was followed by the density–void ratio, density, average grain size, void ratio, water content, density–water content, water content–void ratio, density–average grain size, and sand content equation. Compared with the prediction results of the traditional single- and two-parameter equations, the XGBoost model reduced the MAE and MAPE by 2.47–7.73 m/s and 0.16–0.49%, respectively. At the same time, it is found that the XGBoost model has a good performance in decreasing the max absolute error and max absolute percentage error. Compared with the traditional single- and two-parameter equation, the max absolute error and max absolute percentage error decreased by 6.54–19.56 m/s and 0.47–1.06%, respectively. Especially the max absolute error of specific density, water content, average grain size, density–water content, density–average grain size, and water content–void ratio equation decreased by more than 10 m/s. It is proven that the model has better performance in controlling errors and improving the prediction accuracy of the sediment sound speed.

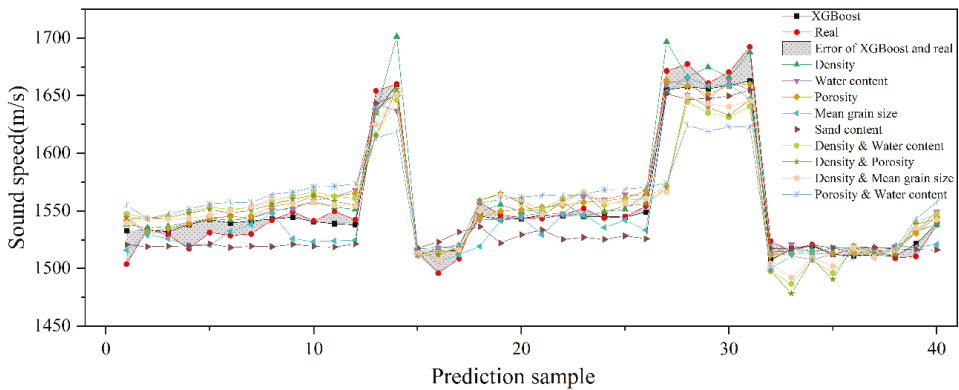


Figure 10. Comparison of prediction results of 40 groups of test samples of the sediment prediction model of the XGBoost algorithm and single- and two-parameter equations. The red dotted line indicates the real sound speed value, the black dotted line indicates the prediction result of the XGBoost model, the gray area indicates the error range between the XGBoost model and the real value, and the prediction results of the single- and two-parameter equations.

Table 4. The error analysis of the prediction results of the XGBoost model and single- and two-parameter equations.

Prediction Model	Max Absolute Error (m/s)	Max Absolute Percentage Error (%)	MAE (m/s)	MAPE (%)
ρ	41.29	2.49	10.53	0.67
w	42.03	2.79	12.30	0.79
e	37.88	2.52	11.97	0.77
M_z	48.83	2.65	10.57	0.67
S	37.24	2.20	15.72	1.00
ρ, w	39.36	2.38	13.89	0.89
ρ, e	35.81	2.37	10.46	0.67
w, e	39.39	2.62	14.36	0.93
ρ, M_z	41.42	2.75	14.77	0.95
XGBoost	29.27	1.73	7.99	0.51

6. Conclusions

Here, the sound speed prediction of seafloor sediments in the East China Sea was conducted based on the XGBoost algorithm. The optimal model super parameters were determined using 240 groups of samples from the East China Sea. Finally, the prediction accuracy of 40 groups of test samples was compared with the traditional single- and two-parameter regressional equations, and the contribution degree of the characteristic factors of the model was studied. The main conclusions of this study are as follows:

1. The XGBoost machine learning method exhibited high prediction accuracy and generalization ability when applied to the prediction of the sound speed of sediments in the East China Sea. When the $n_estimator$ of the model was 75 and the max_depth was 5, the performance of the model was excellent, the goodness of fit (R^2) was 0.923, the MAE of the training results and true values was 7.79 m/s, and the MAE of the validation results and true values was 8.96 m/s.
2. Compared with the traditional single- and two-parameter models, the seafloor sediment model exhibited a higher goodness-of-fit and prediction accuracy. The MAE, MAPE, max absolute error, and max absolute percentage error of the prediction results were 7.99 m/s, 0.51% and 29.27 m/s, 1.73%, respectively, which were 2.47–7.73 m/s, 0.16–0.49%, 6.54 m/s–19.56 m/s, and 0.47–1.06% lower than those of the traditional

single- and two-parameter equations. It is proven that the model has better performance in controlling error and the prediction accuracy of the sound speed of the seafloor sediment improved.

Author Contributions: Conceptualization, G.K.; methodology, M.C.; software, X.M.; validation, M.C.; formal analysis, M.C.; investigation, X.M. and G.K.; resources and data curation, J.W.; writing—original draft preparation, M.C., Y.L. (Yuanxu Liu) and J.L.; writing—review and editing, G.K., M.C. and B.L.; visualization, G.L.; supervision, C.L. and Y.L. (Yanguang Liu). All authors have read and agreed to the published version of the manuscript.

Funding: This study was supported by the National Natural Science Foundation of China under Grant [numbers 42049902, 41676055, 41706062]; the Central Public-Interest Scientific Institution Basal Research Fund under Grant [number GY0220Q09].

Institutional Review Board Statement: Not applicable.

Informed Consent Statement: Not applicable.

Data Availability Statement: Not applicable.

Acknowledgments: Data acquisition and sample collections were supported by the National Natural Science Foundation of China Open Research Cruise (Cruise No. NORC2021-02+NORC2021-301), funded by the Shiptime Sharing Project of the National Natural Science Foundation of China. This cruise was conducted onboard R/V “XiangYangHong 18” by The First Institute of Oceanography, Ministry of Natural Resources, China.

Conflicts of Interest: The authors declare no conflict of interest.

References

1. Pan, G. *Research on the Acoustic Characteristics of Seafloor Sediments in the Northern South. China Sea*; Tongji University: Shanghai, China, 2003.
2. Jin, X.L. The development of research in marine geophysics and acoustic technology for submarine exploration. *Prog. Geophys.* **2007**, *22*, 1243–1249.
3. Wen, D.D.; Wang, N.; Zhou, X.H. Interdisciplinary study of acoustics and marine sedimentology. *Adv. Mar. Sci.* **2006**, *24*, 392–396.
4. Zhu, Z.Y.; Wang, D.; Zhou, J.P.; Wang, X.M. Acoustic wave dispersion and attenuation in marine sediment based on partially gas-saturated Biot-Stoll model. *Chin. J. Geophys.* **2012**, *55*, 180–188.
5. Biot, M.A. Theory of propagation of elastic waves in a fluid-saturated porous solid: II. Higher frequency range. *J. Acoust. Soc. Am.* **1956**, *28*, 179–191. [[CrossRef](#)]
6. Buckingham, M.J. Wave propagation, stress relaxation, and grain-to-grain shearing in saturated, unconsolidated marine sediments. *J. Acoust. Soc. Am.* **2000**, *108*, 2796–2815. [[CrossRef](#)]
7. Buckingham, M.J. Theory of acoustic attenuation, dispersion, and pulse propagation in unconsolidated granular materials including marine sediments. *J. Acoust. Soc. Am.* **1997**, *102*, 2579–2596. [[CrossRef](#)]
8. Buckingham, M.J. Theory of compressional and shear waves in fluidlike marine sediments. *J. Acoust. Soc. Am.* **1998**, *103*, 288–299. [[CrossRef](#)]
9. Stoll, R.D. *Sediments Acoustics*; Springer: New York, NY, USA, 1989.
10. Stoll, R.D. Acoustic waves in ocean sediments. *Geophysics* **1977**, *42*, 715–725. [[CrossRef](#)]
11. Wood, A.B.; Lindsay, R.B. A Textbook of Sound. *Phys. Today* **1956**, *9*, 37. [[CrossRef](#)]
12. Fu, S.S.; Tao, C.H.; Prasad, M.; Wilkens, R.H.; Frazer, L.N. Acoustic properties of coral sands, Waikiki, Hawaii. *J. Acoust. Soc. Am.* **2004**, *115*, 2013–2020. [[CrossRef](#)]
13. Fu, S.S.; Wilkens, R.H.; Frazer, L.N. In situ velocity profiles in gassy sediments: Kiel Bay. *Geo-Mar. Lett.* **1996**, *16*, 249–253. [[CrossRef](#)]
14. Hamilton, E.L.; Bachman, R.T. Sound velocity and related properties of marine sediments. *J. Acoust. Soc. Am.* **1982**, *72*, 1891–1904. [[CrossRef](#)]
15. Hamilton, E.L. Prediction of in-situ acoustic and elastic properties of marine sediments. *Geophysics* **1971**, *36*, 266–284. [[CrossRef](#)]
16. Hamilton, E.L. Geoacoustic modeling of the sea floor. *J. Acoust. Soc. Am.* **1980**, *68*, 1313–1340. [[CrossRef](#)]
17. Guangming, K.; Yuexia, Z.; Guanbao, L.; Guozhong, H.; Xiangmei, M. Comparison on the sound speeds of seafloor sediments measured by in-situ and laboratorial technique in Southern Yellow Sea. *Ocean. Technol.* **2011**, *30*, 52–56.
18. Kan, G.; Su, Y.; Li, G.; Liu, B.; Meng, X. The correlations between in-situ sound speeds and physical parameters of seafloor sediments in the middle area of the southern Huanghai Sea. *Acta Oceanol. Sin.* **2013**, *35*, 166–171.
19. Dapeng, Z.; Baihai, W.; Bo, L. Analysis and study on the sound velocity empirical equations of seafloor sediments. *Acta Oceanol. Sin.* **2007**, *29*, 43–50.

20. Orsi, T.H.; Dunn, D.A. Sound velocity and related physical properties of fine grained abyssal sediments from the Brazil Basin (South Atlantic Ocean). *J. Acoust. Soc. Am.* **1990**, *88*, 1536–1542. [[CrossRef](#)]
21. Orsi, T.H.; Dunn, D.A. Correlations between sound velocity and related properties of glacio-marine sediments: Barents Sea. *Geo-Mar. Lett.* **1991**, *11*, 79–83. [[CrossRef](#)]
22. Richardson, M.D.; Briggs, K.B. In situ and laboratory geoacoustic measurements in soft mud and hard-packed sand sediments: Implications for high-frequency acoustic propagation and scattering. *Geo-Mar. Lett.* **1996**, *16*, 196–203. [[CrossRef](#)]
23. Liu, X.; Li, A.; Dong, J.; Lu, J.; Huang, J.; Wan, S. Provenance discrimination of sediments in the Zhejiang-Fujian mud belt, East China Sea: Implications for the development of the mud depocenter. *J. Asian Earth Sci.* **2018**, *151*, 1–15. [[CrossRef](#)]
24. Xu, F.J.; Li, A.C.; Huang, J.L. Research progress in the mud deposits along the Zhemin coast of the East China Sea continental shelf. *Mar. Sci. Bull.* **2021**, *31*, 97–104.
25. Liu, S.; Shi, X.; Fang, X.; Dou, Y.; Liu, Y.; Wang, X. Spatial and temporal distributions of clay minerals in mud deposits on the inner shelf of the East China Sea: Implications for paleoenvironmental changes in the Holocene. *Quat. Intern.* **2014**, *349*, 270–279. [[CrossRef](#)]
26. Zhang, K.; Li, A.; Huang, P.; Lu, J.; Liu, X.; Zhang, J. Sedimentary responses to the cross-shelf transport of terrigenous material on the East China Sea continental shelf. *Sediment. Geol.* **2019**, *384*, 50–59. [[CrossRef](#)]
27. Lim, D.I.; Choi, J.Y.; Jung, H.S.; Rho, K.C.; Ahn, K.S. Recent sediment accumulation and origin of shelf mud deposits in the Yellow and East China Seas. *Prog. Oceanogr.* **2007**, *73*, 145–159. [[CrossRef](#)]
28. Meng, X.M.; Liu, B.H.; Kan, G.M.; Li, G.B. An experimental study on acoustic properties and their influencing factors of marine sediment in the southern Huanghai Sea. *Acta Oceanol. Sin.* **2012**, *34*, 74–83.
29. Dong, Y.H.; Liu, L. An improved ID3 algorithm based on correlation coefficients. *Comput. Eng. Sci.* **2016**, *38*, 2342–2347.
30. Qian, N.; Wang, X.; Fu, Y.; Zhao, Z.; Xu, J.; Chen, J. Predicting heat transfer of oscillating heat pipes for machining processes based on extreme gradient boosting algorithm. *Appl. Therm. Eng.* **2020**, *164*, 114521. [[CrossRef](#)]
31. Shi, J.; Zhang, J. Load forecasting based on multi-model by stacking ensemble learning. *Proc. CSEE* **2019**, *39*, 4032–4042.

Article

Origin and Implications of Pollution in Coastal Groundwater of the Guangdong Province

Chenzhe Li ^{1,2}, Tengfei Fu ^{1,2,*}, Yushan Fu ^{1,2}, Zhenyan Wang ^{3,4}, Bin Li ⁵, Chen Qi ^{1,2,6}, Guangquan Chen ^{1,2}, Xingyong Xu ⁷ and Hongjun Yu ^{1,2}

- ¹ Key Laboratory of Coastal Science and Integrated Management, First Institute of Oceanography, Ministry of Natural Resources of the People's Republic of China, Qingdao 266061, China
 - ² Laboratory for Marine Geology, Qingdao National Laboratory for Marine Science and Technology, Qingdao 266061, China
 - ³ MOE Key Laboratory of Groundwater Circulation and Environment Evolution, School of Water Resources and Environment, China University of Geosciences (Beijing), Beijing 100083, China
 - ⁴ State Key Laboratory of Biogeology and Environmental Geology, China University of Geosciences (Beijing), Beijing 100083, China
 - ⁵ Marine Science Research Institute of Shandong Province, Qingdao 266071, China
 - ⁶ College of Earth Science and Engineering, Shandong University of Science and Technology, Qingdao 266590, China
 - ⁷ Fourth Institute of Oceanography, Ministry of Natural Resources of the People's Republic of China, Beihai 536000, China
- * Correspondence: futengfei@fio.org.cn

Abstract: The groundwater resource is crucial to the urbanization and industrialization in the Guangdong coastal area; the rapid development of Daya Bay has presented a challenge for the management of the groundwater quantity and quality. Therefore, a novel approach to hydrochemical analysis, which, combined with the health risk model and the water quality index (WQI), was used to explain the hydrochemistry characteristics and risks to human health of groundwater in the Guangdong coastal areas in addition to investigating the factors controlling groundwater quality. The results showed that the average concentration of total dissolved solids (TDS) in groundwater was 1935.26 mg/L and the quality of water was weakly alkaline. The dominant hydrochemical types of groundwater were identified to be Mg-HCO₃ and Na-Cl-HCO₃. The main factor influencing the hydrochemical composition was rock weathering, while the result of principal component analysis (PCA) shows seawater intrusion and anthropogenic inputs also have an effect on the water quality. The conclusions of the water quality assessment indicated that most of the groundwater samples were acceptable for drinking. However, both WQI and the non-carcinogenic hazard quotient (HQ) values indicated unacceptable risks in any area of Maoming, Zhanjiang and Shantou, and, according to the hazard index (HI) value, children in the study area are at more danger to health risks than adults. It is suggested that both groundwater salinization and nitrate pollution should be paid attention to when improving groundwater quality and exploring the sustainable utilization of groundwater resources.

Keywords: groundwater; hydrochemistry; Guangdong coastal zone; seawater intrusion; nitrate pollution

Citation: Li, C.; Fu, T.; Fu, Y.; Wang, Z.; Li, B.; Qi, C.; Chen, G.; Xu, X.; Yu, H. Origin and Implications of Pollution in Coastal Groundwater of the Guangdong Province. *J. Mar. Sci. Eng.* **2022**, *10*, 1394. <https://doi.org/10.3390/jmse10101394>

Academic Editors: Xiaolei Liu, Thorsten Stoesser and Xingsen Guo

Received: 9 September 2022

Accepted: 26 September 2022

Published: 29 September 2022

Publisher's Note: MDPI stays neutral with regard to jurisdictional claims in published maps and institutional affiliations.



Copyright: © 2022 by the authors. Licensee MDPI, Basel, Switzerland. This article is an open access article distributed under the terms and conditions of the Creative Commons Attribution (CC BY) license (<https://creativecommons.org/licenses/by/4.0/>).

1. Introduction

Groundwater is firmly connected to human society, such as in industrial, agricultural, and domestic activities [1]. Due to the benefits of wide distribution, convenient use, and good water quality, groundwater is always considered as an important drinking water source [2]. Nevertheless, the enormous expansion in population has driven the request for freshwater and has caused stress on groundwater resources; over-exploitation has recently led to the depletion of groundwater, which has been a worldwide problem [3]. According to WHO, roughly 780 million individuals all over the globe have no access to harmless drinking water [4]. The groundwater quality has been affected by urbanization,

population growth, industrialization, and many other anthropogenic activities, especially in developing countries [5,6].

As a developing country, China depends heavily on groundwater, and more than 70% of urban communities make use of groundwater for domestic and drinking purposes in China [7]. Due to the accelerated progress of the Guangdong-Hong Kong-Macao Greater Bay Area, more and more attention should be paid to developing and utilizing groundwater resources in the coastal zones. In Guangdong, the issue of the quality and quantity of groundwater is turning into a severe matter on account of the developing need. Nevertheless, a rising population followed by urbanization has increased the demand for groundwater supplies in Guangdong. Guangdong has undergone extensive urbanization and has been confronting various groundwater quality issues inferable from overpopulation and industrialization, similar to other urbanized regions [8–11]. The industrialization and urbanization have sped up the deterioration of groundwater quality in Guangdong over past three decades [12], as well as groundwater contamination [13]. Therefore, we should understand that the chemical characteristics of groundwater are of great importance for revealing the quality assessment and the hydrochemical process of groundwater. In recent years, studies on hydrochemistry in the Guangdong coastal zone have been focused on the Pearl River [14–18], while few investigations have been conducted in the other areas of Guangdong coastal area. The evolution of coastal groundwater resulting from the rapid industrial development over the past decade is not yet well understood. It is necessary to understand the specific ionic sources, which change the chemistry of groundwater and lead to groundwater contamination. Therefore, sustainable development and management of groundwater resources and their protection from pollution activities play a vital role in the Chinese economy.

Groundwater geochemistry, due to the impact of landfill and stormwater runoff from agricultural fields, is vulnerable to non-geogenous inputs [19]. Geochemical ratios can be used to understand the chemical processes that take place between the water and soils/rocks, as well as the water and anthropogenic activities that alter the chemical composition of groundwater [20]. A groundwater quality survey on the Prakasam district in India showed that rock-weathering, mineral dissolution, ion exchange, and evaporation were the dominant hydrochemical processes and the anthropogenic sources (waste waters and agricultural activities) were the secondary activities regulating the aquifer chemistry.

Generally, most of the groundwater chemistry is characterized by geogenic processes and non-geogenic sources, which can alter the chemistry of the groundwater [21]. A groundwater quality investigation was conducted in Visakhapatnam, Andhra Pradesh, India and it was found that the silicate weathering and dissolution, ion exchange and evaporation were the dominant geogenic processes. Domestic waste, septic-tank seepage, irrigation practices, and fertilizers were the artificial activities that control the groundwater chemistry [19–21].

In general, individual activities and nature have an impact on ground and surface water quality [22]. Numerous studies have presented that both hydrochemical and water quality are consequences of long-term associations between groundwater and the surrounding environment, which are affected by various factors, such as geology, hydrogeology, hydrodynamic conditions, precipitation, climate, and anthropogenic inputs [20–24]. Usually, freshwater in the coastal region is a vital resource for a few communities, as they are vulnerable to salinization, especially because of their proximity to the ocean and because coastal regions are vulnerable to over-exploration due to their high population density [25–29]. In addition, NO_3^- and heavy metal-contaminated groundwater is also a global environmental issue that has a long-term health influence. The elevated contamination of NO_3^- in drinking water instigates health diseases such as methemoglobinemia in infants, thyroid dysfunctions, and hypertension [30]. The nitrate contamination in groundwater caused by agricultural surface contamination started to appear during the 1990s [31,32]. At present, nitrate-contaminated groundwater has become a hazard in all nations [33]. With the rapid development of the economy, nitrate pollution in groundwater in China is

becoming more and more serious. In addition, the NO_3^- concentration in groundwater is significantly elevated due to the domestic sewage, industrial wastewater, septic tanks, and landfill leachate caused by urban expansion [34]. In the past few decades, urbanization has led to population concentration, economic growth, and expansion of construction land; around urban areas, the simultaneous existence of industrial, domestic, and agricultural pollution sources have made the pollution sources of “triple nitrogen” in groundwater very complex [35]. The recognizable proof of pollutants’ origin could assist in the understanding of geochemical processes, elucidate the circulation, and convey a model of the pollutants.

The water quality index (WQI) was usually used for drinking purposes [36,37]. In general, consumption of contaminated drinking water and groundwater can pose a serious risk to humans, primarily through two routes of exposure, the first being drunk water (or the oral route) and the second being a dermal or skin connection [38,39]. Comprehensive hazard quotients (HQ) and the hazard index (HI) are useful for health risk assessment [40–42]. This extensive model for human health risk evaluation was initially proposed by the United States Environmental Protection Agency [43]. At present, many investigations have likewise explored heavy metals, volatile organics, pesticides, polycyclic aromatic hydrocarbons, and the human health risk of nitrate pollution on a provincial or national level [44–47]. In spite of this, few researchers have explored the connection between human health risks and nitrate contamination in the coastal zone.

Therefore, it is of extraordinary importance to concentrate on the significant particle science and water quality assessment of groundwater in the Guangdong coastal zone. Research on groundwater hydrochemistry and water quality in Guangdong is outstandingly restricted. Therefore, the targets of this study are to (1) identify the hydrochemical characteristics of groundwater; (2) evaluate the controlling factors of the water chemistry; (3) assess the health risks due to contamination. This paper will be useful for understanding the hydrochemical composition and characteristics of groundwater in the Guangdong coastal area and will benefit sustainable development of groundwater environments, and will provide a valuable data set for the formulations of future mitigation strategies and policy updates.

2. Study Area

The Guangdong Province is located in the southeast of China (geographical coordinates: latitude: $20^\circ 13' \sim 25^\circ 31' \text{ N}$; longitude: $109^\circ 39' \sim 117^\circ 19' \text{ E}$) (Figure 1). The coastline of Guangdong is the longest one in the provinces of China, extending for 3368.10 km and including 1288 km of silt coastline and 27,778.30 km^2 of mangroves [48]. The study area has a southern subtropical monsoon climate. The southwest monsoon and southeast trade winds prevail in summer, which is humid and rainy, with many typhoons. In winter, northerly and northeasterly winds prevail, and rainfall is scarce. The average annual temperature in the area is 21.9°C , and the average annual temperature in the coastal area is higher than that in the northern inland zone. Influenced by the monsoon climate conditions, the province has strongly seasonal rainfall, rain days, rainfall, and uneven distribution, with an average annual rainfall of 1300–2500 mm.

Under the combined influence of crustal movement, magma movement, folding, and fracture tectonics, the territory has complex types of landforms, including mountains, hills, terraces, plains, and valleys. The mountains in the west, northeast, and north of the region are high, while the central and southern coastal areas are mostly hills, terraces or plains. In general, Guangdong Province is topographically high in the north and low in the south. In the investigation region, the river network area is, for the most part, covered by Quaternary sediments. At present, 80% of the water supply sources in the Zhanjiang, Lufeng, and Huiyang city areas come from groundwater. Due to the long-term, concentrated and massive exploitation of medium and deep pressurized water, the medium and deep pressure water has changed from the original one-way net flow to a runoff pattern of convergence from the funnel around to the center of the funnel, forming an artificially exploited flow field. This regional water-level landing funnel is gradually expanding in

the direction of the northwest and southeast recharge zone areas and the direction of the East China Sea drainage area. The rivers in Guangdong are located in the transition area between the low mountains of central Guangdong and the Pearl River Delta. The coastal area is mostly plain, interspersed with low hills and mountains, especially in Zhanjiang, Lufeng, and Huiyang. The terrain slopes from northeast to southwest and the stratified structure of the landscape is obvious. The northern part is dominated by mountains and hills, the central part by terraces, and the southern and western parts by plains. The river system in the territory is well developed, with many rivers of various sizes and a vast water area. The southern river network area is in a tidally influenced area, with high runoff and strong tidal action. Groundwater is essentially renewed by the precipitation of vertical penetration, and when it is in a flood period, the horizontal progression of waterways occurs. The groundwater resources in the coastal cities of Guangdong have been exploited for more than 50 years. Due to the massive exploitation of middle and deep groundwater over a long period, the groundwater level has fallen significantly, triggering a variety of hydrogeological and environmental issues such as water resource depletion, ground subsidence, and seawater intrusion [49].

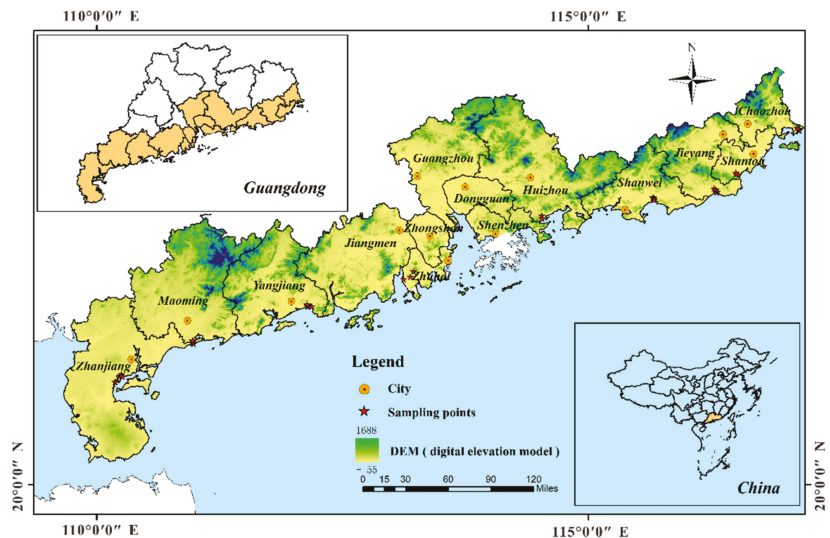


Figure 1. Sampling sites in Guangdong. The sampling points include all the cities along the coast of Guangdong: Zhanjiang, Maoming, Yangjiang, Jiangmen, Zhongshan, Guangzhou, Dongguan, Shenzhen, Huizhou, Shantou, Jieyang, Shantou, and Chaozhou. The top left image is a map of the coastal region of Guangdong Province, with the coastal cities highlighted. The bottom right image is a map of China, with the study area of Guangdong highlighted.

3. Materials and Methods

3.1. Sampling and Test

Thirty-nine groundwater and two seawater samples were collected from the shallow aquifer (<100 m) in eight cities Zhanjiang (ZJ), Maoming (MM), Yangjiang (YJ), Zhuhai (ZH), Huizhou (HZ), Shanwei (SW), Shantou (ST), and Jieyang (JY), along the Guangdong coastline in October 2019. Twenty-one water samples within 1 km of the coastline were considered to be near-sea samples (in the figures, the abbreviation “N” indicates near-sea samples and “F” indicates far-sea samples). The sampling locations are shown in Figure 1. EC, pH, TDS, and different parameters of the groundwater sample were measured in the field using YSI Professional Plus (YSI, USA). The groundwater samples were collected and stored in polyethylene bottles. To eliminate the effects of stagnant water, the wells

were pumped two to three times before being collected in 150 mL polyethylene bottles, which were rinsed 2–3 times with nitric acid, after which they were washed with deionized water and dried. The bottles were thoroughly washed three times with well water from the sampling site before collecting the groundwater samples, after which three separate bottles were collected at each sampling site. During sampling, we filled the entire bottle and sealed it with adhesive tape. One bottle was sealed directly for the major ions and halogenated elements, one bottle was filtered through a membrane and sealed for the hydroxide isotopes, and another bottle was filtered through a membrane and filtered with concentrated nitric acid to $\text{pH} < 2$ for the metal elements. The second group of water samples was used as a blank control after the hydroxide isotopes had been measured to allow the extent of contamination caused by improper sampling to be seen. They were labeled, stored, and transported to the laboratory for chemical analysis.

The indexes, such as Ca^{2+} , Mg^{2+} , Na^+ , K^+ , SO_4^{2-} , NO_3^- , F^- , Cl^- and Br^- were tested by ICS-6000 (Thermo Fisher, Waltham, MA, USA), and the detection limit was 0.01 mg/L. HCO_3^- was determined by acid-base indicator titration, and the detection limit was 1 mg/L. The oxygen and hydrogen stable isotope values were analyzed by LGR liquid water isotope laser spectroscopy (MAT 253 PLUS, Thermo Fisher, USA) from the Institute of Oceanology, Chinese Academy of Sciences, and calculated according to the Vienna Standard Mean Ocean Water (V-SMOW). The analytical accuracies of the long-term standard measurements of δD and $\delta^{18}\text{O}$ were $\pm 0.2\text{‰}$ and $\pm 0.6\text{‰}$, respectively. The descriptive statistics of the groundwater chemistry data use the criteria for evaluation indicators of groundwater utilizing their concentrations in mg/L.

3.2. Multivariate Statistical Analysis

Multivariate statistical methods can provide inferred information of cause-and-effect relationships. The method of correlation analysis has been effectively applied to extract variables and the results obtained show that the factors controlling the chemical processes in groundwater are anthropogenic or natural influences [50–52]. Descriptive analyses of hydrogeochemical data and graphical representations were used in this paper to investigate hydrogeochemical characteristics, ionic generators, and associated major mechanisms influencing hydrogeochemical processes by using the SPSS software version 26.0 (SPSS, 2019).

Concentrations of some indicators in groundwater above the allowable values probably lead to poor-quality groundwater. We need to know which ones are the main impact indicators. It is known that PCA is a useful tool for data reduction, and parameters on the same PC with positive loadings mean the same origin or similar geochemical behaviors [53,54]. Thus, in this study, PCA was used to reduce the indicators and extract the main impact indicators (in the same PC with results of the groundwater quality assessment) which are responsible for the poor-quality groundwater. In the PCA, the rotation of principal components (PCs) was carried out using the varimax method, and only PCs with eigenvalues that exceed one were retained for analyses. This study selected the maximum absolute PC loading of one index to evaluate the relationships between the PCs and indicators.

The principal components (PCs) issued from different exploratory data analyses can be automatically described by quantitative or categorical variables [55–60]. For the purposes of this study, TDS (a measure of groundwater salinity) was entered as a quantitative supplementary variable. In addition to the PCA, ion ratios were used to find the inter-relationships of the chemical parameters for samples in each cluster.

3.3. Analytical Method

Multivariate statistical methods can provide inferred information on cause-and-effect relationships. The method of correlation analysis has been effectively applied to extract variables and the results obtained show that factors controlling the chemical processes in groundwater are anthropogenic or natural influences [50–52]. Descriptive analyses of hydrogeochemical data and graphical representations were used in the paper to investigate hydrogeochemical

characteristics, ionic generators, and associated major mechanisms influencing hydrogeochemical processes by using the SPSS software version 26.0 (SPSS, 2019).

WQI is a significant parameter for establishing groundwater quality and its suitability for the purpose of consumption. WQI is an approach of rating that provides the composite influence of individual parameters on the comprehensive quality of water for human utilization. The standards for drinking purposes are as recommended by the WHO [4]. The calculation of WQI is in three steps.

Firstly, each of the nine parameters was weighted by their relative significance in the overall water quality for consumption. A maximum weight of 5 was assigned to the parameters, including the nitrate, fluoride, chloride, and total dissolved solids, because of their importance in evaluating water quality. Bicarbonate with a minimum weight of 1 is a negligible factor in the evaluation of water quality. Other items such as sodium, calcium, potassium, and magnesium were assigned weights ranging from 1 to 5 depending on their importance in the determination of water quality.

Secondly, the relative weight (W_i) was calculated in the present study as:

$$W_i = w_i / \sum_{i=1}^n w_i \tag{1}$$

The relative weight is W_i . The weight of each parameter is w_i . The number of parameters is n . Table 1 shows calculated relative weight (W_i) values of each parameter.

Table 1. Relative weights of chemical parameters.

Parameters (mg/L)	WHO Standards (2022)	w_i	Relative Weight $W_i = w_i / \sum_{i=1}^n w_i$
TDS	500	5	0.128
Bicarbonate	500	1	0.0256
Chloride	250	5	0.128
Sulphate	200	5	0.128
Nitrate	45	5	0.128
Calcium	75	3	0.0769
Magnesium	30	3	0.0769
Sodium	200	5	0.128
Potassium	12	2	0.0523
Fluoride	1.5	5	0.128

Furthermore, by dividing the concentration in each water sample by its own criteria according to the guidelines outlined in WHO [4], a quality rating scale (q_i) is assigned for each parameter, and the result is multiplied by 100:

$$q_i = (C_i / S_i) \times 100 \tag{2}$$

The quality rating is " q_i ". The concentration of each chemical parameter in each water sample in milligrams per liter is " C_i ". " S_i " is the China drinking water standard based on the recommendations of the WHO [4] (Table 1), the units of which chemical parameter are mg/L.

When calculating the WQI, first determined for each chemical parameter is the " SI ", which is then used to determine the WQI according to the following equation:

$$SI_i = W_i \times q_i \tag{3}$$

$$WQI = \sum SI_i \tag{4}$$

The sub-index of the i th parameter is SI_i . According to WQI values, five classifications can be allocated: undrinkable ($WQI \geq 300$), very poor ($200 \leq WQI < 300$), poor ($100 \leq WQI < 200$), good ($50 \leq WQI < 100$), and excellent ($WQI < 50$) [53].

The risk assessment investigation of the toxic contaminant of drinking water in terms of a non-carcinogenic health hazard is based on the risk level [26]. In general, the oral

pathway of exposure covers a great threat to health and other routes of dermal and oral contact. Taking this into consideration, a health risk assessment of non-carcinogenic contaminants were selected [30–35]. According to the research, the health hazard of dermal and oral connection was evaluated individually for children, females and males. The non-carcinogenic risk from dermal and oral connection was calculated and listed hereafter [12–14]:

For drinking water intake:

$$CDI = \frac{C \times IR \times ED \times EF}{ABW \times AET} \tag{5}$$

$$HQ_{Oral} = \frac{CDI}{RfD} \tag{6}$$

The chronic daily intake is “CDI” (mg/kg/day). The content of nitrate is “C” (mg/L). The daily ingestion rate of water is “IR” (L/day), the values of which are 1 L/day, 2.5 L/day and 2.5 L/day for children, males, and females, respectively. The exposure duration is “ED” (year), the values of which are 64 years for males, 67 years for females, and 12 years for children [38,58]. The exposure frequency is “EF” (days/year), the values of which are 365 days/year for everyone [43]. The average body weight is ABW, the values of which are 65 kg, 55 kg and 15 kg for males, females and children, respectively. The hazard quotient is demonstrated as HQ. The average exposure time is “AET” (days), the values of which are 23,360 days, 24,455 days, and 4380 days for males, females and children, respectively. The reference portion of pollutants is “RfD” (mg/kg/day) with 1.6 mg/kg/day for NO₃⁻ according to US EPA [43].

In the case of a non-carcinogenic hazard resulting from dermal contact, the calculation formula should be chosen as below [5,46]:

$$DAD = \frac{TC \times C \times Ki \times ED \times EV \times CF \times EF \times SSA}{AET \times ABW} \tag{7}$$

$$HQ_{Dermal} = \frac{DAD}{RfD} \tag{8}$$

$$HI_{total} = \sum_1^n (HQ_{Oral} + HQ_{Dermal}) \tag{9}$$

The dose of absorbed dermal is “DAD” (mg/kg × day). The time of contact is “TC” (h/day). The parameters of dermal adsorption are “Ki” (cm/h), and the conversion factor is “CF”. The values of “TC”, “Ki” and “CF” are regarded as 0.4 h/day, 0.001 cm/h, and 0.001, respectively [43]. The frequency of showering is “EV” (times/day) and its value is considered as 1 time in a day. The area of skin surface is “SSA” (cm²), the value of which is defined as 12,000 cm², 16,600 cm² and 16,600 cm² for children, males and females, respectively (USEPA, 2017). The value of HI can represent the non-carcinogenic health risk, which is a hazard index. A HI > 1 indicates that non-carcinogenic health risk is potential, while HI < 1 means that the health risk impersonated by non-carcinogenic substances is within a satisfactory level [43].

4. Results and Discussion

4.1. Hydrochemical Compositions

The statistical results of the main components of groundwater chemistry in the coastal zone of Guangdong are shown in Table 2. The mean value of Cl⁻ content in Guangdong was 1009.50 mg/L, indicating that the groundwater in the coastal zone of Guangdong is affected by salinization. The pH values of groundwater samples in the study area ranged from 5.15 to 8.20, with the mean pH value of 7.18 in Guangdong Province, which was weakly alkaline, whereas the average TDS concentration was 1935.26 mg/L (Table 2). The average concentrations of pH and TDS in groundwater exceeded China’s permissible

groundwater quality standards [4] of 7 and 1000 mg/L, respectively. In accordance with the classification, most of the groundwater was classified as alkaline-freshwater and alkaline-saline water. It is worth noting that the shallow groundwater in the Pearl River Delta is generally characterized by variational TDS and weak acidity, with Na⁺ and Ca²⁺ as the main cations and Cl⁻ and HCO₃⁻ as the main anions in the groundwater. The Pearl River Delta is prone to seawater intrusion, causing the salinization of water bodies. As the climate warms, the sea level rises and salty tides occur dramatically, resulting in acidification of groundwater bodies in the Pearl River Delta region.

Table 2. Statistical characteristics of the major chemical composition of groundwater in Guangdong.

Parameters	Units	Minimum	Maximum	Mean	SD	CV	DWQI
Na+	mg/L	14.03	1590	121.97	296.47	2.43	200
K+	mg/L	1.04	264.8	25.7	50.93	1.98	12
Ca+	mg/L	0.8	282.7	38.87	56.67	1.46	75–200
Mg2+	mg/L	0.46	275.6	20.7	57.77	2.79	30–100
HCO ₃ ⁻	mg/L	15.62	917.6	165.34	161.99	0.98	-
Cl ⁻	mg/L	3.64	18,441.76	1009.5	4076.78	4.04	250–1000
SO ₄ ²⁻	mg/L	0.74	2238.06	137.82	464.21	3.37	150–400
NO ₃ ⁻	mg/L	0.12	115.12	30.55	32.89	1.08	45
TDS	mg/L	27.95	31,245	1935.26	6808.76	3.52	500–2000
EC	µs/cm	0.04	48.16	2.98	10.48	3.52	-
ORP	mv	-132.6	-7.5	-75.23	30.76	-0.41	-
pH	/	5.51	8.2	7.18	0.58	0.08	6.5–8.5
δD	‰	-52.68	-27.99	-39.26	10.61	-0.27	-
δ18O	‰	-7.36	-4.33	-5.97	0.67	-0.11	-

4.2. Hydrochemical Type

The Piper diagram [54] can reflect the water chemistry characteristics and types of water bodies. From Figure 2, it can be observed that the main anions and cations in the groundwater of the Guangdong coastal zone are found in the bottom corner of the Piper diagram, and their distribution is relatively concentrated, indicating that the ionic composition of most groundwater has a high consistency. The hydrochemical characteristics in the coastal zone also indicate that the distance from the sea influences the chemical composition in the Guangdong coastal zone.

The main types of groundwater chemistry in the Guangdong coastal zone are Mg-HCO₃ and Na-Cl-HCO₃. From land to sea, the water chemistry of the study area progressively varies from Ca-HCO₃ to Na·Mg-Cl. The freshwater chemistry of the Guangdong coastal zone is Na-Ca-Cl and Ca·Mg-HCO₃, while the saline water chemistry is Na-Cl-SO₄. This is consistent with Huang Guan’s conclusion, who concluded that the main hydrochemical type of the Pearl River Delta was Ca-HCO₃ and Ca-Cl types.

4.3. Factors Controlling the Hydrochemical Characteristics of Groundwater of the Guangdong

Gibbs diagrams [55] were constructed by the comparability proportions of TDS divided by Na⁺/(Na⁺ + Ca²⁺) and Cl⁻/(Cl⁻ + HCO₃⁻). This methodology has been broadly used to recognize hydrogeochemical evolution processes, which include evaporation, mineral weathering, and precipitation.

As shown in the Gibbs diagram (Figure 3), the result shows that both the cation and anion drawn in the middle of the figure signify that mineral weathering is the main process that controls the groundwater characteristics. For the cation, more than half of the samples are out of the three-control-end membership zone, while for the Cl⁻/(Cl⁻ + HCO₃⁻), approximately 90–95% of the samples fall in the mineral weathering domain and 5–10% of samples fall between the mineral weathering and evaporation region. There is a mixed controlling mechanism here, and we should take into account the element of human activities affecting the area.

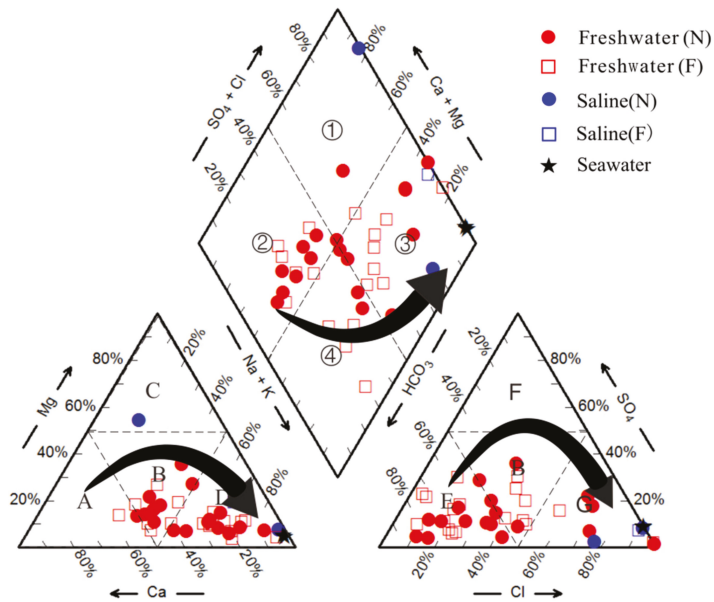


Figure 2. Piper diagram of water chemistry in the coastal zone of Guangdong province (① Ca-Mg-SO₄-Cl type; ② Ca-Mg-HCO₃ type; ③ Na-SO₄-Cl type; ④ Na-HCO₃ type; A. Calcium type; B. No dominant type; C. Magnesium type; D. Sodium type; E. Bicarbonate type; F. Sulfate type; G. Chloride type).

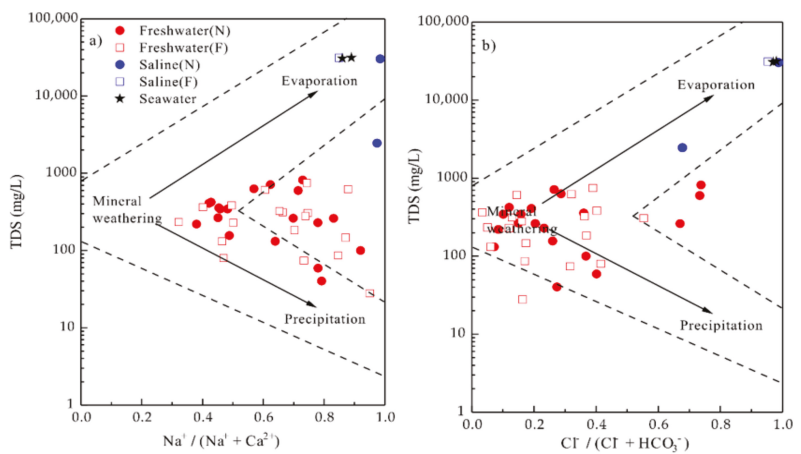


Figure 3. Gibbs chart of the coastal zone of Guangdong province. The dashed boxed areas represent the three control factors, the top for evaporation, the middle for Mineral weathering, and the bottom for Precipitation. (a) Cationic Gibbs figure: TDS versus $Na^+ / (Na^+ + Ca^{2+})$. (b) Anionic Gibbs figure: TDS versus $Cl^- / (Cl^- + HCO_3^-)$.

In general, atmospheric precipitation varies by altitude, latitude, temperature, and proximity to the coastline, and is generally less than -60% (SMOW). When atmospheric precipitation forms groundwater, unlike $\delta^{18}O$, the rocks contain few hydrogen minerals and have low δD values, so isotope exchange reactions have little effect on the δD values of the water. Since the δD difference between seawater and atmospheric precipitation

is large, δD and $\delta^{18}O$ is an important basis for determining the origin of formation of groundwater. The global meteoric water line (GMWL) is a linear correlation line between the hydrogen-oxygen stable isotopes of atmospheric precipitation on a global scale. The hydrogen-oxygen isotope ratio line, compared to the precipitation line, can indicate the origin of local water sources. The values of δD and $\delta^{18}O$ are shown in Table 2, while the saline water and seawater samples had relatively high δD and $\delta^{18}O$ values, as shown in Figure 4. From (Figure 4a), there is a large variation in hydrogen-oxygen isotope content of groundwater in Guangdong and the values are mainly distributed between the global meteoric water line (GMWL) and the local meteoric water line (LMWL), indicating that atmospheric precipitation is the major supplier of groundwater replenishment.

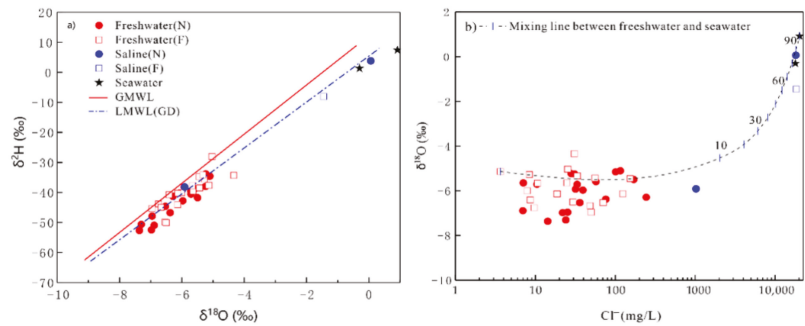


Figure 4. Relationship between (a) δD - $\delta^{18}O$ isotopes and (b) Cl^- - $\delta^{18}O$ of underground water in the coastal zone of Guangdong province. (a) The red line represents the global meteoric water line (GMWL), and the blue line represents the local meteoric water line (LMWL). (b) The black line represents freshwater-seawater mixing line. The starting point is the freshwater end element and the ending point is the seawater end element.

The relationship between $\delta^{18}O$ and Cl^- was also used to determine the mixing trajectory and proportions of different waters. Figure 4b demonstrates that the majority of the groundwater samples are distributed as the freshwater states. The water samples in Guangdong are firmly dispersed on the blending line among freshwater and seawater. Furthermore, the seawater blending proportion ranges from 0% to 10% and the saline mixing proportion is from 60% to 90%, which also demonstrates that part of the groundwater samples in this area have been affected by seawater intrusion.

As shown in Figure 5a, most of the water sample points were distributed near the $y = x$ relationship line, implying that the dissolution of halite is the primary hydrogeochemical process influencing the synthetic parts of groundwater [3]. Figure 5b shows that the water samples were mainly drawn in the upper side of the $y = x$ relationship line, indicating that silicate weathering was the main factor driving the hydrochemical characteristics of groundwater. Figure 5c shows that the water samples were mainly located on the upper side of the 1:1 line, indicating that other sources of Ca^{2+} may exist, such as cation exchange. As shown in Figure 5d, the water samples were mainly located around the $y = x$ relationship line, thereby indicating that Ca^{2+} and SO_4^{2-} in the groundwater of Guangdong mainly originated from the dissolution of gypsum. The ratio of Ca^{2+}/Mg^{2+} can be utilized to investigate the impact of carbonate (calcite) and silicate weathering on groundwater hydrochemical characteristics [39]. Most water samples fall below the $y = 0.5x$ relationship line, which is shown in Figure 5e, subsequently showing that a great deal of water samples are affected by silicate weathering. Cation exchange occurs widely between groundwater and rock minerals [56]. A remarkable influence of cation exchange on the chemical characteristics of groundwater would result in the relationship of $Na^+ + K^+ - Cl^-$ to $HCO_3^- + SO_4^{2-} - Ca^{2+} - Mg^{2+}$ being 1:1 [57,58]. As shown in Figure 5f, most of the water sample points fell on the left side of the 1:1 line, with a few points falling on the line, thereby showing that although

cation exchange had an influence on the groundwater of Guangdong, it was not the main dominant factor and seawater may be a process affecting the hydrochemical characteristics of groundwater in Guangdong. The ion contents of groundwater near the coast are higher, indicating that the source is influenced by seawater intrusion.

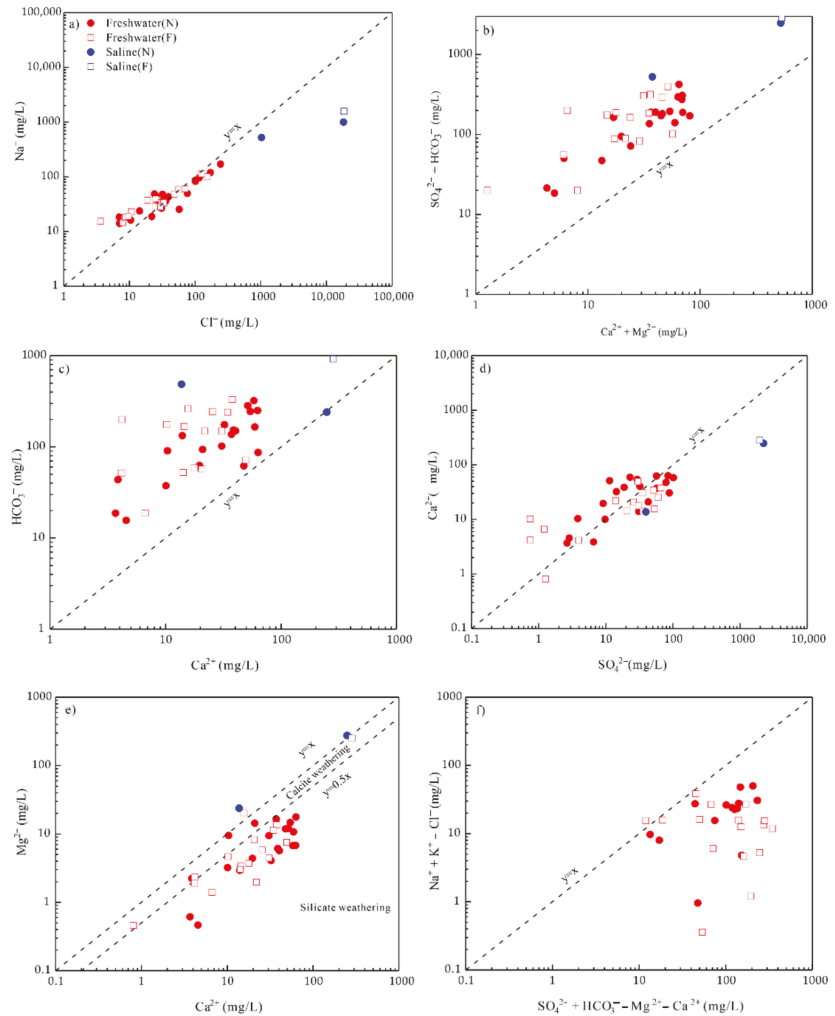


Figure 5. Plots of the relationships among significant ions in the groundwater of the coastal zone of Guangdong Province, China. (a) Na^+ versus Cl^- , (b) $\text{SO}_4^{2-} + \text{HCO}_3^-$ versus $\text{Ca}^{2+} + \text{Mg}^{2+}$, (c) HCO_3^- versus Ca^{2+} , (d) Ca^{2+} versus SO_4^{2-} , (e) Mg^{2+} versus Ca^{2+} , (f) $\text{Na}^+ + \text{K}^+ - \text{Cl}^-$ versus $\text{SO}_4^{2-} + \text{HCO}_3^- - \text{Mg}^{2+} - \text{Ca}^{2+}$. The dotted lines represent the function “ $y = x$ ”. Function “ $y = 0.5x$ ” has been added to e, and between functions “ $y = x$ ” and “ $y = 0.5x$ ” represent Calcite weathering and the below function “ $y = 0.5x$ ” represents silicate weathering.

4.4. Possible Sources of Chemical Composition

The regional hydrogeochemical characteristics are affected by many factors, while multivariate statistical methods can infer the main mechanisms affecting regional groundwater chemistry based on hydrochemical variables. As a quantitative and independent approach for groundwater classification, principal component analysis (PCA) was utilized

for grouping groundwater samples and explaining relationships between groundwater samples and chemical parameters. In this study, PCA was adopted to analyze 12 chemical variables (TDS, EC, ORP, pH, Na⁺, K⁺, Mg²⁺, Ca²⁺, HCO₃⁻, SO₄²⁻, Cl⁻, and NO₃⁻) in 39 samples in order to explore the main factors and mechanisms affecting the groundwater chemical characteristics and water quality in Guangdong.

As shown in Table 3, the two principal components were extracted. The eigenvalue of principal component 1 was 8.519 with a variance contribution of 70.993%, while the eigenvalue of principal component 2 was 2.000 with a variance contribution of 16.663%. The cumulative contribution of variance was as high as 87.656%. The hydrochemical composition of groundwater in the study area was mainly determined by principal components 1 and 2 (Table 3).

Principal component 1 was mainly TDS, Na⁺, K⁺, Ca²⁺, Mg²⁺, Cl⁻, SO₄²⁻, and HCO₃⁻, with load matrix of 0.990, 0.959, 0.956, 0.960, 0.989, 0.987, 0.981, and 0.696, respectively, which explained that they are similar in terms of causes, and as discussed above, it can be concluded that principal component 1 can be an explanation of silicate weathering and seawater intrusion. According to the classification results, only three samples in Shantou were saline water, which should be paid attention to.

Principal component 2 has a strong negative loading (>0.70) with NO₃⁻, ORP, and pH with a load matrix of 0.722, 0.822, and 0.854 mm, respectively. NO₃⁻ mainly explains pollution caused by industrial and agricultural activities, while ORP and pH mainly explain fertilizer pollution and chemical plant pollution from agricultural activities. Far less fertilizer is used in urbanized areas than in agricultural areas, and the dose of NO₃⁻ in urban fertilizers is commonly less than 20 mg/L, indicating that the contribution of fertilizers to NO₃⁻ in granular aquifers in urbanized areas is negligible. Therefore, fertilizer is not the main source of NO₃⁻ in granular aquifers, because most of the high- NO₃⁻ groundwater occurred in urbanized areas. Therefore, the principal component 2 explains the degree of pollution caused by anthropogenic activities.

Table 3. Principal component eigenvalues and variance contribution rates and principal component load matrix.

Component	Initial Eigenvalue			Extract the Sum of Load Squares			Component		
	Total	Variance Percentage	Cumulate %	Total	Variance Percentage	Cumulate %	1	2	
1	8.519	70.993	70.993	8.519	70.993	70.993	Cl	0.987	0.110
2	2.000	16.663	87.656	2.000	16.663	87.656	NO ₃	-	-0.722
3	0.684	5.698	93.354				SO ₄	0.981	0.103
4	0.613	5.111	98.465				HCO ₃	0.696	-
5	0.077	0.643	99.108				Na	0.959	-
6	0.057	0.473	99.581				K	0.956	-
7	0.029	0.244	99.825				Ca	0.960	-
8	0.015	0.128	99.953				Mg	0.989	-
9	0.004	0.035	99.988				TDS	0.990	0.107
10	0.001	0.012	100.000				EC	0.990	0.106
11	0	0	100.000				ORP	0.471	-0.822
12	0	0	100.000				PH	-0.430	0.854

Extraction method: principal component analysis method.

4.5. Anthropogenic Inputs

Based on the statistical results, nitrate pollution has occurred in Shantou, Maoming, and Zhanjiang due to urbanization and industrialization. In accordance with the National Standardization Administration of China (GB/T14848-2017), the safe concentration of nitrate in drinking water is under 20 mg/L. The average of the nitrate compounds is 29.77 mg/L, with a maximum value of 155.12 mg/L and minimum value of 0.01 mg/L in Guangdong. The average value is higher than the standard value of 20 mg/L, indicating the presence of slight pollution.

As Figure 6 shows, nitrate pollution in freshwater groundwater in the study area is more serious than in saline water. The proportion of groundwater samples exceeding the safety standard of nitrate in drinking water is 75.5% in Maoming (3 of 4 groundwater samples), 50% in Shantou (7 of 14 groundwater samples), 66.7% in Zhanjiang and Zhuhai, 33.3% in Yangjiang, 25% in Lufeng, and no pollution in Huiyang. Furthermore, the nitrate concentration in Maoming ranges from 8.67 to 111.56, with an average value of 51.60. The nitrate concentration in the groundwater of Shantou and Zhangjiang ranges from 0.19 to 115.12 with an average value of 34.38, and from 0.49 to 98.77 with an average value of 42.64, separately. NO_3^- contamination ($>20 \text{ mg/L}$) exists in nineteen samples of all the first ten of them were more than 50 mg/L . The level of nitrate contamination in Guangdong is indicated as below: Shantou < Zhanjiang < Maoming.

Increasing urbanization, industrialization, and growing human populations have resulted in progressively negative consequences on the groundwater environment. Contaminated groundwater commonly displays higher molar proportions of $\text{NO}_3^-/\text{Na}^+$ and Cl^-/Na^+ . According to Figure 7, it leads to the conclusion that groundwater NO_3^- in Guangdong coastal area mainly affected by agricultural activities and domestic sewage. The relatively higher NO_3^- concentration in Guangdong has been identified as caused by agricultural production, which is non-point-source water pollution. The potential non-point sources of nitrogen from agricultural production include manure and fertilizer. Consequently, it is suggested that control of groundwater contamination ought to be a significant point of groundwater management in the Guangdong coastal zone.

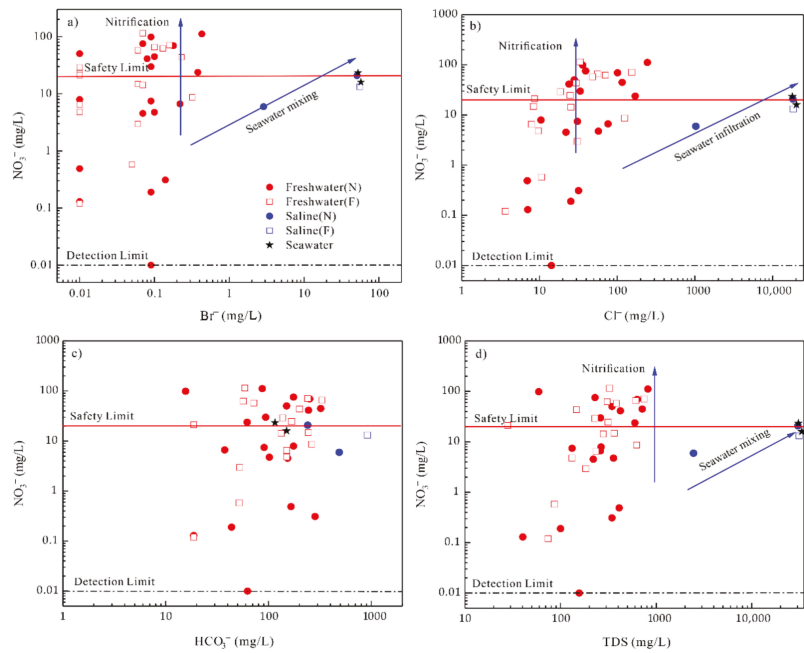


Figure 6. Plots of the source of NO_3^- among NO_3^- and HCO_3^- , Br^- , Cl^- , and TDS in groundwater. (a) NO_3^- versus Br^- , (b) NO_3^- versus Cl^- , (c) NO_3^- versus HCO_3^- , (d) NO_3^- versus TDS. The red lines represent the safety limit “ $y = 20$ ”, which means points above this line have nitrate contamination. The black lines represent the detection limit “ $y = 0.01$ ”, which means points below this line will not be detected for content of NO_3^- . The blue line represents the two trends, which are nitrification and seawater mixing).

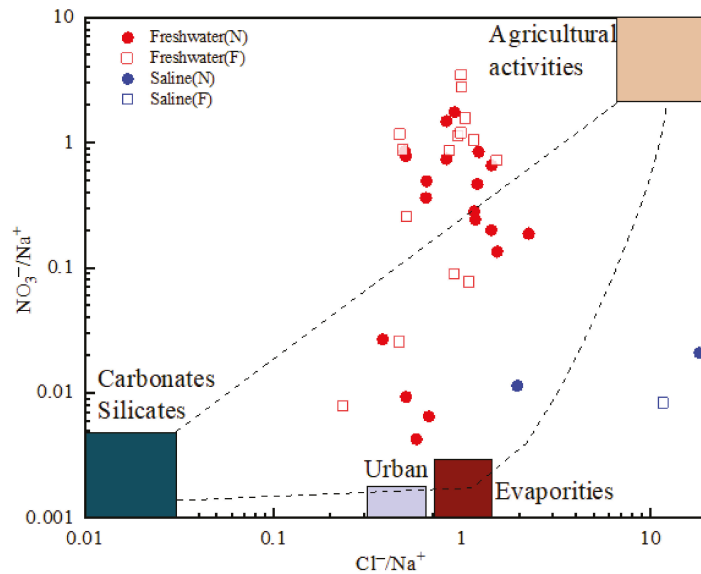


Figure 7. Plot of the source of NO_3^- among $\text{NO}_3^-/\text{Na}^+$ versus Cl^-/Na^+ in groundwater. The lower left square area represents carbonates silicates, the upper right square area represents the agricultural activities and the lower middle square area represents the urban and evaporities, respectively. Most groundwater is affected by agricultural activities.

4.6. Drinking Water Quality

In this paper, we used the criteria set out by the drinking water standards of WHO [4] to assess the drinking quality of water. The water quality evaluation used 39 Guangdong sample sites and classified the water quality into 5 classes according to the WQI value: Class I water ($\text{WQI} < 50$), Class II water ($50 \leq \text{WQI} < 100$), Class III water ($100 \leq \text{WQI} < 200$), Class IV water ($200 \leq \text{WQI} < 300$), and Class V water ($\text{WQI} \geq 300$). The results showed that 64.1% of the samples were ranked as Class I, these sampling sites were far away from the coastal zone and less affected by seawater; 28.2% of the samples were ranked as Class II, 3% of the samples were ranked as Class III, and 5.1% of the samples were ranked as Class V water. There are two sample sites (ST1-1 and ST3-4) in Shantou, Guangdong, with WQI values of 2132.57 and 2161.40, which have more serious seawater pollution, and an ST2-1 value of 175.01, which also indicates poor water quality not suitable for drinking (Figure 8). In addition, some of the samples in Maoming, Zhanjiang, and Maoming were not suitable for drinking. More attention should be paid, especially in Maoming, Zhanjiang, and Shantou, where both the salinity and nitrate contamination of some samples exceed the drinking water standards of WHO [4]. It is well-known that high concentrations of NO_3^- and Cl^- commonly occur in the groundwater of cultivated land due to the amount of application of chemical fertilizers, such as nitrogenous fertilizer and muriate of potash [19–21], especially in shallow groundwater with high permeability of the vadose zone. Further, groundwater with elevated NH_4^+ and NO_3^- was also reported in the PRD, and the natural source of groundwater containing NH_4^+ in granular aquifers and anthropogenic sources of groundwater containing NO_3^- have also been discussed. Therefore, the fissured aquifer should be protected and exploited for drinking and irrigation purposes.

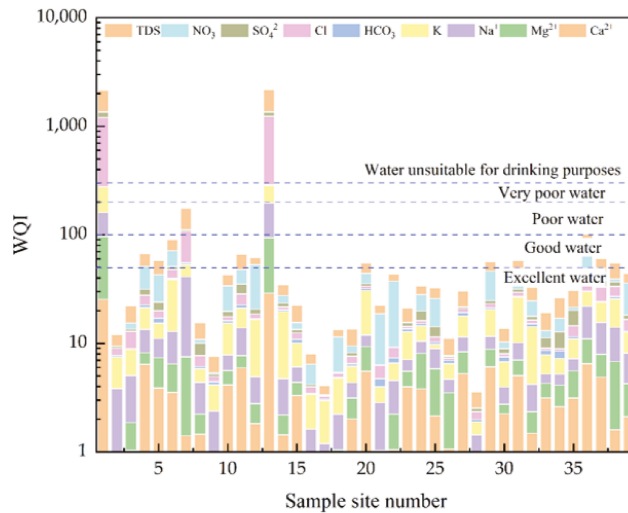


Figure 8. Bar graph of calculated WQI values in 39 groundwater samples (1–14: Shantou; 15–21: Yangjiang; 22–27: Zhujiang; 28–29: Huiyang; 30–31: Zhuhai; 32–35: Lufeng; 36–39: Maoming).

4.7. Human Health Risk Assessment

HQ analyzation was adopted for health risk assessment in the Guangdong coastal zone. Only when the values of HQ were less than 1, there were minor hazards to human health. In this study, health risk evaluation of nitrate pollution for children, males, and females was performed depending on USEPA [43] and the consequences are introduced in Table A1. We can notice that the HQ_{Dermal} results for NO_3^- were very low in three unique groups with some data below 0, while HQ_{Oral} of NO_3^- changes from 0.0004 to 4.7967 with its mean as 1.2404 for children, 0.0003 to 3.2705 with an average of 0.8457 for females, and 0.0002 to 2.7673 with a mean value of 0.7156 for males. This finding discloses that the request for non-carcinogenic hazard quotient (HQ) under dermal and oral radiation was definitely examined as $HQ_{Dermal} < HQ_{Oral}$ (Appendix A). We found a high quotient of nitrate occur in Shantou, Maoming and Zhanjiang, which was accorded with the result of WQI.

As noted above, under USEPA risk evaluation instructions, the limit of non-carcinogenic risk we can accept is ≤ 1 , which means $HI \leq 1$. Assuming that the worth of the HI is more noteworthy than 1, the likelihood of antagonistic human well-being risk due to openness is very high. For the non-carcinogenic risk, the HI_{Total} values of NO_3^- of groundwater in the investigated region ranged from 0.0004 to 4.8197 (mean of 1.2463), 0.0003 to 3.2791 (mean of 0.8479), and 0.0002 to 2.7747 (mean of 0.7175) for children, females and males, respectively (Figure 9). It should be noted that out of 39 groundwater samples, the nitrate exposure levels in drinking water in 16, 13 and 12 communities for children, females, and males expose these age groups to acute nitrate poisoning in the study area. All the more explicitly, the results demonstrate that the children in the study area have more risk to non-carcinogenic impacts because of the higher level of nitrate in drinking water. This was significantly to numerous different researchers [57–60] who have profoundly observed that children are more powerless to chronic non-carcinogenic risks on account of their more modest body weight. Excessive intake of nitrates can lead to harmful physiological reactions, even in small orders of magnitude, such as high blood pressure and poisoning [24,29,50]. What is more, unsatisfactory non-carcinogenic values were accounted for partial samples of Zhanjiang, Shantou, Maoming and Zhuhai, which indicated that the groundwater was unsuitable for direct drinking in these areas. Therefore, fundamental measures to limit nitrate pollution should be initiated by local government to ensure a safe drinking water supply.

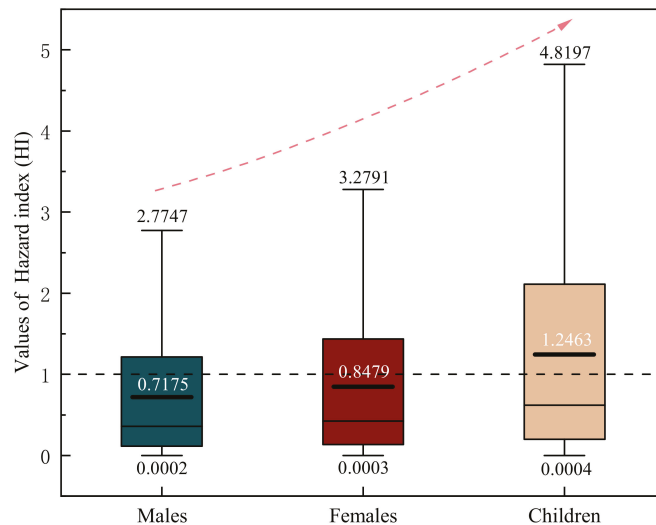


Figure 9. Diagram for non-carcinogenic risks for children, females and males. The red dashed line indicates the trend of increasing health risk Children > Females > Males. The thick black line in the middle of the box is the mean, and the 75th and 25th percentiles are shown on the square horizontal line and the horizontal line below the box, respectively.

5. Conclusions

The groundwater in the Guangdong coastal zone is weakly alkaline, with mean value concentrations of TDS of 1935.26 mg/L and Cl of 1009.5 mg/L. The hydrochemical categories of groundwater in the Guangdong coastal zone are Mg-HCO₃ and Na-Cl-HCO₃, and the trend of evolution from land to sea is Ca-HCO₃ → Na·Ca-Cl.

The Gibbs diagram shows that the groundwater composition was mainly responsible for mineral weathering, and the ratio of ions indicates that silicate weathering and the dissolution of gypsum were the dominant origins of salt of the groundwater. The result of PCA shows that rock weathering, groundwater salinization, and anthropogenic activities have affected the water quality. According to this investigation, the seawater intrusion occurs in Shantou, while the nitrate pollution mainly occurs in Maoming, Zhanjiang, and Shantou.

Based on water quality index (WQI) and hazard quotients (HQ), most of the samples were labelled as good water quality, except for some spots in Shantou, Maoming, and Zhanjiang. The HQ result exposed that the health risk of direct intake is more serious than that of dermal exposure, and compared with the adult, the HI value for children was much higher, with the average exceeding 1. This indicates that women and men are at a significantly lower health risk than children in the Guangdong coastal areas.

These results indicate that the pollution in the Guangdong coastal area caused by seawater intrusion as well as nitrate input should be taken seriously. More importantly, rational utilization of groundwater resources and the monitoring and evaluation of groundwater quality, in which the control and analysis of groundwater contamination are essential, should be taken seriously by local governments.

Author Contributions: Conceptualization, C.L. and Y.F.; methodology, C.L. and Z.W.; software, C.L. and C.Q.; validation, B.L., G.C. and X.X.; formal analysis, B.L.; investigation, H.Y.; resources, T.F.; data curation, T.F.; writing—original draft preparation, C.L. and X.X.; writing—review and editing, C.L. and T.F.; visualization, C.L.; supervision, T.F.; project administration, T.F.; funding acquisition, T.F. and X.X. All authors have read and agreed to the published version of the manuscript.

Funding: This research was funded by National Natural Science Foundation of China (U1806212, 42276226), Basic Scientific Fund for National Public Research Institutes of China (2019Q01), Key

Research and Development Program of Shandong Province (2021RZB07028), Shandong Academy of Chinese Engineering S&T Strategy for Development (202103SDYB15), National Key Research and Development Program of China (No. 2016YFC0402801) and Open Fund of the 801 Institute of Hydrogeology and Engineering Geology (801KF2021-6).

Institutional Review Board Statement: Authors have signed the statement.

Informed Consent Statement: Authors have signed the statement.

Data Availability Statement: Data is from the experiments we conducted in this work.

Acknowledgments: We give thanks to the support of “observation and research station of seawater intrusion and soil salinization, Laizhou Bay”. Meanwhile, we would like to thank the anonymous reviewers and the editor, who helped improve the manuscript.

Conflicts of Interest: The authors declare no conflict of interest.

Appendix A

Table A1. Nitrate results of non-carcinogenic risk through drinking water intake and dermal contact.

Samples	Non-Carcinogenic Risk								
	HQOral			HQDermal			HItotal		
	Males	Females	Children	Males	Females	Children	Males	Females	Children
HY 1-1	0.0075	0.0088	0.0129	0.0000	0.0000	0.0001	0.0075	0.0088	0.0130
HY 1-3	0.0031	0.0037	0.0054	0.0000	0.0000	0.0000	0.0031	0.0037	0.0054
LF1-1	0.5901	0.6974	1.0229	0.0016	0.0019	0.0049	0.5917	0.6993	1.0278
LF1-2	0.1563	0.1847	0.2708	0.0004	0.0005	0.0013	0.1567	0.1851	0.2721
LF1-3	0.3567	0.4216	0.6183	0.0009	0.0011	0.0030	0.3577	0.4227	0.6213
LF1-4	0.1142	0.1349	0.1979	0.0003	0.0004	0.0010	0.1145	0.1353	0.1989
MM 1-1	2.6817	3.1693	4.6483	0.0071	0.0084	0.0223	2.6889	3.1777	4.6706
MM 1-2	0.5724	0.6764	0.9921	0.0015	0.0018	0.0048	0.5739	0.6782	0.9968
MM 1-3	0.2084	0.2463	0.3613	0.0006	0.0007	0.0017	0.2090	0.2470	0.3630
MM 1-4	1.4993	1.7719	2.5988	0.0040	0.0047	0.0125	1.5033	1.7766	2.6112
ST1-1	0.5007	0.5918	0.8679	0.0013	0.0016	0.0042	0.5021	0.5933	0.8721
ST1-2	0.0046	0.0054	0.0079	0.0000	0.0000	0.0000	0.0046	0.0054	0.0080
ST1-3	0.1601	0.1892	0.2775	0.0004	0.0005	0.0013	0.1605	0.1897	0.2788
ST1-4	1.6700	1.9736	2.8946	0.0044	0.0052	0.0139	1.6744	1.9788	2.9085
ST1-5	1.5776	1.8645	2.7346	0.0042	0.0050	0.0131	1.5818	1.8694	2.7477
ST1-6	1.7130	2.0244	2.9692	0.0045	0.0054	0.0143	1.7175	2.0298	2.9834
ST2-1	0.1430	0.1690	0.2479	0.0004	0.0004	0.0012	0.1434	0.1695	0.2491
ST2-2	0.0712	0.0841	0.1233	0.0002	0.0002	0.0006	0.0713	0.0843	0.1239
ST2-3	0.0139	0.0165	0.0242	0.0000	0.0000	0.0001	0.0140	0.0165	0.0243
ST3-1	1.2113	1.4315	2.0996	0.0032	0.0038	0.0101	1.2145	1.4353	2.1097
ST3-2	1.0750	1.2705	1.8633	0.0029	0.0034	0.0089	1.0779	1.2738	1.8723
ST3-3	2.7673	3.2705	4.7967	0.0073	0.0087	0.0230	2.7747	3.2791	4.8197
ST3-4	0.3183	0.3761	0.5517	0.0008	0.0010	0.0026	0.3191	0.3771	0.5543
ST3-5	0.3425	0.4048	0.5938	0.0009	0.0011	0.0029	0.3435	0.4059	0.5966
YJ 1-4	0.5103	0.6031	0.8846	0.0014	0.0016	0.0042	0.5117	0.6047	0.8888
YJ 2-1	0.1089	0.1287	0.1888	0.0003	0.0003	0.0009	0.1092	0.1290	0.1897
YJ 2-2	0.7180	0.8486	1.2446	0.0019	0.0023	0.0060	0.7199	0.8508	1.2506
YJ1-1	0.1793	0.2119	0.3108	0.0005	0.0006	0.0015	0.1798	0.2125	0.3123
YJ1-2	0.1909	0.2256	0.3308	0.0005	0.0006	0.0016	0.1914	0.2262	0.3324
YJ1-3	0.0029	0.0034	0.0050	0.0000	0.0000	0.0000	0.0029	0.0034	0.0050
ZH 1-1	1.8115	2.1409	3.1400	0.0048	0.0057	0.0151	1.8163	2.1466	3.1551
ZH 1-2	0.1154	0.1364	0.2000	0.0003	0.0004	0.0010	0.1157	0.1367	0.2010
ZH 1-3	1.3877	1.6401	2.4054	0.0037	0.0044	0.0115	1.3914	1.6444	2.4170
ZJ 1-1	1.0505	1.2415	1.8208	0.0028	0.0033	0.0087	1.0533	1.2448	1.8296
ZJ 1-2	2.3743	2.8060	4.1154	0.0063	0.0075	0.0198	2.3806	2.8134	4.1352
ZJ 1-3	0.0002	0.0003	0.0004	0.0000	0.0000	0.0000	0.0002	0.0003	0.0004
ZJ 2-1	0.6988	0.8259	1.2113	0.0019	0.0022	0.0058	0.7007	0.8280	1.2171
ZJ 2-2	0.9894	1.1693	1.7150	0.0026	0.0031	0.0082	0.9921	1.1724	1.7232
ZJ 2-3	0.0118	0.0139	0.0204	0.0000	0.0000	0.0001	0.0118	0.0140	0.0205
Min	0.0002	0.0003	0.0004	0.0000	0.0000	0.0000	0.0002	0.0003	0.0004
Max	2.7673	3.2705	4.7967	0.0073	0.0087	0.0230	2.7747	3.2791	4.8197
Mean	0.7156	0.8457	1.2404	0.0019	0.0022	0.0060	0.7175	0.8479	1.2463

References

1. Wang, Z.; Su, Q.; Wang, S.; Gao, Z.; Liu, J. Spatial distribution and health risk assessment of dissolved heavy metals in groundwater of eastern China coastal zone. *Environ. Pollut.* **2021**, *290*, 118016. [[CrossRef](#)] [[PubMed](#)]
2. Zou, L.; Yao, X.; Yamaguchi, H.; Guo, X.; Gao, X.; Wang, K.; Sun, M. Seasonal and Spatial Variations of Macro Benthos in the Intertidal Mudflat of Southern Yellow River Delta, China in 2007/2008. *J. Ocean Univ. China* **2018**, *17*, 233–240. [[CrossRef](#)]
3. Wu, Z.; Wang, X.; Chen, Y.; Cai, Y.; Deng, J. Assessing river water quality using water quality index in Lake Taihu Basin, China. *Sci. Total Environ.* **2018**, *612*, 914–922. [[CrossRef](#)] [[PubMed](#)]
4. World Health Organization. *Guidelines for Drinking-Water Quality*, 4th ed.; WHO: Geneva, Switzerland, 2022.
5. Han, D.; Song, X.; Matthew, J.; Yang, J.; Xiao, G. Chemical and isotopic constraints on the evolution of groundwater salinization in the coastal plain aquifer of Laizhou Bay, China. *J. Hydrol.* **2014**, *508*, 12–27. [[CrossRef](#)]
6. Giri, A.; Bharti, V.; Kalia, S.; Kumar, K.; Khansu, M. Hydrochemical and quality assessment of irrigation water at the trans-himalayan high-altitude regions of Leh, Ladakh, India. *Appl. Water Sci.* **2022**, *12*, 197. [[CrossRef](#)]
7. Liu, J.; Gao, Z.; Wang, M.; Li, Y.; Ma, Y.; Shi, M.; Zhang, H. Study on the dynamic characteristics of groundwater in the valley plain of Lhasa City. *Environ. Earth Sci.* **2018**, *77*, 646. [[CrossRef](#)]
8. Zhang, T.; Cai, W.; Li, Y.; Geng, T.; Zhang, Z.; Lv, Y.; Miao, Z.; Liu, J. Ion chemistry of groundwater and the possible controls within Lhasa River Basin, SW Tibetan Plateau. *Arab. J. Geosci.* **2018**, *11*, 510. [[CrossRef](#)]
9. Xiao, J.; Jin, Z.; Ding, H.; Wang, J.; Zhang, F. Geochemistry and solute sources of surface waters of the Tarim River Basin in the extreme arid region, NW Tibetan Plateau. *J. Asian Earth Sci.* **2012**, *54*, 162–173. [[CrossRef](#)]
10. Yang, K.; Liu, W.; Xu, X.; Chen, G.; Liu, Y.; Fu, T.; Wang, C.; Fu, Y. Evaluation of seawater intrusion in typical coastal zones of Hainan Province. *Mar. Sci.* **2019**, *43*, 57–60.
11. Zereq, S.; Boudoukha, A.; Benaabidate, L. Impacts of natural conditions and anthropogenic activities on groundwater quality in Tebessa plain, Algeria. *Sustain. Environ. Res.* **2018**, *28*, 340–349. [[CrossRef](#)]
12. Huang, G.; Sun, J.; Zhang, Y.; Chen, Z.; Liu, F. Impact of anthropogenic and natural processes on the evolution of groundwater chemistry in a rapidly urbanized coastal area, South China. *Sci. Total Environ.* **2013**, *463*, 209–221. [[CrossRef](#)] [[PubMed](#)]
13. Huang, G.; Liu, C.; Li, L.; Zhang, F.; Chen, Z. Spatial distribution and origin of shallow groundwater iodide in a rapidly urbanized delta: A case study of the Pearl River Delta. *J. Hydrol.* **2020**, *585*, 124860. [[CrossRef](#)]
14. Tiwari, A.; Ghione, R.; Maio, M.; Lavy, M. Evaluation of hydrogeochemical processes and groundwater quality for suitability of drinking and irrigation purposes: A case study in the Aosta Valley region, Italy. *Arab. J. Geosci.* **2017**, *10*, 264. [[CrossRef](#)]
15. Han, Z.; Ma, H.; Shi, G.; He, L.; Wei, L.; Shi, Q. A review of groundwater contamination near municipal solid waste landfill sites in China. *Sci. Total Environ.* **2016**, *569*, 1255–1264. [[CrossRef](#)]
16. Hou, Q.; Zhang, Q.; Huang, G.; Liu, C.; Zhang, Y. Elevated manganese concentrations in shallow groundwater of various aquifers in a rapidly urbanized delta, south China. *Sci. Total Environ.* **2020**, *701*, 134777. [[CrossRef](#)]
17. Shi, G.; Chen, Z.; Bi, C.; Wang, L.; Teng, J.; Li, Y.; Xu, S. A comparative study of health risk of potentially toxic metals in urban and suburban road dust in the most populated city of China. *Atmos. Environ.* **2011**, *45*, 764–771. [[CrossRef](#)]
18. Li, J.; Zhou, H.; Qian, K.; Xie, X.; Xue, X.; Yang, Y.; Wang, Y. Fluoride and iodine enrichment in groundwater of North China Plain: Evidences from speciation analysis and geochemical modeling. *Sci. Total Environ.* **2017**, *598*, 239–248. [[CrossRef](#)]
19. Rao, N.; Dinakar, A.; Kumari, B. Appraisal of vulnerable zones of non-cancer-causing health risks associated with exposure of nitrate and fluoride in groundwater from a rural part of India. *Environ. Res.* **2021**, *202*, 111674. [[CrossRef](#)]
20. Rao, N.; Dinakar, A.; Sun, L. Estimation of groundwater pollution levels and specific ionic sources in the groundwater, using a comprehensive approach of geochemical ratios, pollution index of groundwater, unmix model and land use/land cover—A case study. *J. Contam. Hydrol.* **2022**, *248*, 103990.
21. Rao, N.; Sunitha, B.; Sun, L.; Spandana, B.; Chaudhary, M. Mechanisms controlling groundwater chemistry and assessment of potential health risk: A case study from South India. *Geochemistry* **2019**, *80*, 125568.
22. Wang, Y.; Jiao, J.; Cherry, J. Occurrence and geochemical behavior of arsenic in a coastal aquifer–aquitard system of the Pearl River Delta, China. *Sci. Total Environ.* **2012**, *427*, 286–297. [[CrossRef](#)] [[PubMed](#)]
23. Maharana, C.; Gautam, S.; Singh, A.; Tripathi, J. Major ion chemistry of the Son River, India: Weathering processes, dissolved fluxes and water quality assessment. *J. Earth Syst. Sci.* **2015**, *124*, 1293–1309. [[CrossRef](#)]
24. Marghade, D.; Malpe, D.; Rao, N. Identification of controlling processes of groundwater quality in a developing urban area using principal component analysis. *Environ. Earth Sci.* **2015**, *74*, 5919–5933. [[CrossRef](#)]
25. Xiao, J.; Jin, Z.; Wang, J.; Zhang, F. Hydrochemical characteristics, controlling factors and solute sources of groundwater within the Tarim River Basin in the extreme arid region, NW Tibetan Plateau. *Quat. Int.* **2020**, *380*, 237–246. [[CrossRef](#)]
26. Li, P.; Zhang, Y.; Yang, N.; Jing, L.; Yu, P. Major ion chemistry and quality assessment of groundwater in and around a mountainous tourist town of China. *Water Qual. Expo. Health* **2016**, *8*, 239–252. [[CrossRef](#)]
27. Xing, L.; Huang, L.; Hou, X.; Yang, L.; Chi, G.; Xu, J.; Zhu, H. Groundwater Hydrochemical Zoning in Inland Plains and its Genetic Mechanisms. *Water* **2018**, *10*, 752. [[CrossRef](#)]
28. Kamtchueng, B.; Antong, J.; Wirmvem, M.; Tiodjio, R.; Takounjou, A.; Ngoupayou, J.; Kusakabe, M.; Zhang, J.; Ohba, T.; Tanyileke, G.; et al. Hydrogeochemistry and quality of surface water and groundwater in the vicinity of Lake Monoun, West Cameroon: Approach from multivariate statistical analysis and stable isotopic characterization. *Environ. Monit. Assess.* **2016**, *188*, 524. [[CrossRef](#)]

29. Flexer, V.; Fernando, C.; Ines, C. Lithium recovery from brines: A vital raw material for green energies with a potential environmental impact in its mining and processing. *Sci. Total Environ.* **2018**, *639*, 1188–1204. [[CrossRef](#)]
30. Wang, G.; Zeng, C.; Zhang, F.; Zhang, Y.; Scott, C.; Yan, X. Traffic related trace elements in soils along six highway segments on the Tibetan Plateau: Influence factors and spatial variation. *Sci. Total Environ.* **2017**, *581*, 811–821. [[CrossRef](#)]
31. Tamasi, G.; Cini, R. Heavy metals in drinking waters from Mount Amiata (Tuscany, Italy). Possible risks from arsenic for public health in the Province of Siena. *Sci. Total Environ.* **2004**, *327*, 41–51. [[CrossRef](#)]
32. Krishna, K.; Hari, B.; Esvar, R.; Selvakumar, S.; Thivya, C.; Muralidharan, S.; Jeyabal, G. Evaluation of water quality and hydrogeochemistry of surface and groundwater, Tiruvallur District, Tamil Nadu, India. *Appl Water Sci.* **2016**, *7*, 2533–2544. [[CrossRef](#)]
33. Mgbenu, C.; Egbueri, J. The hydrogeochemical signatures, quality indices and health risk assessment of water resources in Umunya district, Southeast Nigeria. *Appl Water Sci.* **2019**, *9*, 22. [[CrossRef](#)]
34. Chen, J.; Qian, H.; Wu, H. Nitrogen contamination in groundwater in an agricultural region along the New Silk Road, northwest China: Distribution and factors controlling its fate. *Environ. Sci. Pollut. Res.* **2017**, *24*, 13154–13167. [[CrossRef](#)] [[PubMed](#)]
35. Rajas, A.; Pacheco, J.; Esteller, M.; Cabrera, S.; Camargo, M. Spatial distribution of nitrate health risk associated with groundwater use as drinking water in Merida, Mexico. *Appl. Geogr.* **2015**, *65*, 49–57. [[CrossRef](#)]
36. Singh, G.; Rishi, M.S.; Herojeet, R.; Kaur, L.; Sharma, K. Evaluation of groundwater quality and human health risks from fluoride and nitrate in the semi-arid region of northern India. *Environ. Geochem. Health* **2020**, *42*, 1833–1862. [[CrossRef](#)]
37. Liu, T.; Xu, S.; Lu, S.Y.; Qin, P.; Bi, B.; Ding, H.; Liu, Y.; Guo, X.; Liu, X. A review on removal of organophosphorus pesticides in constructed wetland: Performance, mechanism and influencing factors. *Sci. Total Environ.* **2019**, *651*, 2247–2268. [[CrossRef](#)]
38. Huang, G.; Liu, C.; Sun, J.; Zhang, M.; Jing, J.; Li, L. A regional scale investigation on factors controlling the groundwater chemistry of various aquifers in a rapidly urbanized area: A case study of the Pearl River Delta. *Sci. Total Environ.* **2018**, *625*, 510–518. [[CrossRef](#)]
39. Rao, N. Nitrate pollution and its distribution in the groundwater of Srikakulam district, Andhra Pradesh, India. *Environ. Geol.* **2006**, *51*, 631–645. [[CrossRef](#)]
40. Gou, L.; Jin, Z.; Galy, A.; Gong, Y.; Nan, X.; Jin, C.; Wang, X.; Bouchez, J.; Cai, H.; Chen, J.; et al. Seasonal riverine barium isotopic variation in the middle Yellow River: Sources and fractionation. *Earth Planet. Sci.* **2020**, *531*, 115990. [[CrossRef](#)]
41. Adimalla, N.; Qian, H. Groundwater quality evaluation using water quality index (WQI) for drinking purposes and human health risk (HHR) assessment in an agricultural region of Nanganur, south India. *Ecotoxicol. Environ. Saf.* **2019**, *176*, 153–161. [[CrossRef](#)]
42. Fan, B.; Zhao, Z.; Tao, F.; Liu, B.; Tao, Z.; Gao, S.; Zhang, L. Characteristics of carbonate, evaporite and silicate weathering in Huanghe River basin: A comparison among the upstream, midstream and downstream. *J. Asian Earth Sci.* **2014**, *96*, 17–26. [[CrossRef](#)]
43. Huan, H.; Zhang, B.; Kong, H.; Li, M.; Wang, W.; Xi, B.; Wang, G. Comprehensive assessment of groundwater pollution risk based on HVF model: A case study in Jilin City of northeast China. *Sci. Total Environ.* **2018**, *628*, 1518–1530. [[CrossRef](#)] [[PubMed](#)]
44. Ahmed, N.; Bodrud, M.; Islam, A.; Hossain, S.; Moniruzzaman, M.; Deb, N.; Bhuiyan, M. Appraising spatial variations of As, Fe, Mn and NO₃ contaminations associated health risks of drinking water from Surma basin, Bangladesh. *Chemosphere* **2019**, *218*, 726–740. [[CrossRef](#)] [[PubMed](#)]
45. Ustaoglu, F.; Tepe, Y.; Tas, B. Assessment of stream quality and health risk in a subtropical Turkey river system: A combined approach using statistical analysis and water quality index. *Ecol. Indic.* **2020**, *113*, 105815. [[CrossRef](#)]
46. US EPA. *Pesticide. United States Environmental Protection Agency, Integrated Risk Information System (IRIS)*; US EPA: Washington, DC, USA, 2017; pp. 200–300.
47. Zhai, Y.; Zheng, F.; Zhao, X.; Xia, X.; Teng, Y. Identification of hydrochemical genesis and screening of typical groundwater pollutants impacting human health: A case study in Northeast China. *Environ. Pollut.* **2019**, *252*, 1202–1205. [[CrossRef](#)]
48. Gao, Z.; Han, C.; Xu, Y.; Zhao, Z.; Luo, Z.; Liu, J. Assessment of the water quality of groundwater in Bohai Rim and the controlling factors—A case study of northern Shandong Peninsula, north China. *Environ. Pollut.* **2021**, *285*, 117482. [[CrossRef](#)]
49. Liu, G.; Wang, J.; Zhang, E.; Jing, H.; Liu, X. Heavy metal speciation and risk assessment in dry land and paddy soils near mining areas at Southern China. *Environ. Sci. Pollut. Res.* **2016**, *23*, 8709–8720. [[CrossRef](#)]
50. Xu, Y.; Dai, S.; Meng, K.; Wang, Y.; Ren, W.; Zhao, L.; Christie, P.; Teng, Y. Occurrence and risk assessment of potentially toxic elements and typical organic pollutants in contaminated rural soils. *Sci. Total Environ.* **2018**, *630*, 618–629. [[CrossRef](#)]
51. Yang, Q.; Li, Z.; Ma, H.; Wang, L.; Martin, J. Identification of the hydrogeochemical processes and assessment of groundwater quality using classic integrated geochemical methods in the Southeastern part of Ordos basin, China. *Environ. Pollut.* **2016**, *218*, 879–888. [[CrossRef](#)]
52. Yang, Y.; Meng, Z.; Jiao, W. Hydrological and pollution processes in mining area of Fenhe River Basin in China. *Environ. Pollut.* **2018**, *234*, 743–750. [[CrossRef](#)]
53. Aiuppa, A.; D’Alessandro, W.; Federico, C. The aquatic geochemistry of arsenic in volcanic groundwaters from southern Italy. *Appl. Geochem.* **2003**, *18*, 1283–1296. [[CrossRef](#)]
54. Güler, C.; Kurt, M.; Alpaslan, M.; Akbulut, C. Assessment of the impact of anthropogenic activities on the groundwater hydrology and chemistry in Tarsus coastal plain (Mersin, SE Turkey) using fuzzy clustering, multivariate statistics and GIS techniques. *J. Hydrol.* **2012**, *414*, 435–451. [[CrossRef](#)]

55. Gao, Y.; Qian, H.; Ren, W.; Wang, H.; Liu, F.; Yang, F. Hydrogeochemical characterization and quality assessment of groundwater based on integrated-weight water quality index in a concentrated urban area. *J. Clean. Prod.* **2020**, *260*, 121006. [[CrossRef](#)]
56. Piper, A. A graphic procedure in the geochemical interpretation of water analyses. *Eos Trans. Am. Geophys. Union* **1944**, *25*, 914–928. [[CrossRef](#)]
57. Gibbs, R. Mechanisms controlling world water chemistry. *Science* **1970**, *170*, 1088–1090. [[CrossRef](#)] [[PubMed](#)]
58. Gao, Y.; Qian, H.; Wang, H.; Chen, J.; Ren, W.; Yang, F. Assessment of background levels and pollution sources for arsenic and fluoride in the phreatic and confined groundwater of Xi'an city, Shaanxi, China. *Environ. Sci. Pollut. Res. Int.* **2020**, *27*, 34702–34714. [[CrossRef](#)] [[PubMed](#)]
59. Li, P.; Wu, J.; Qian, H. Hydrochemical appraisal of groundwater quality for drinking and irrigation purposes and the major influencing factors: A case study in and around Hua County, China. *Arab. J. Geosci.* **2015**, *9*, 15. [[CrossRef](#)]
60. Liu, J.; Gao, Z.; Wang, Z.; Xu, X.; Su, Q.; Wang, S.; Qu, W.; Xing, T. Hydrogeochemical processes and suitability assessment of groundwater in the Jiaodong Peninsula, China. *Environ. Monit. Assess.* **2020**, *192*, 384. [[CrossRef](#)]

Article

Experimental Study on Dynamic Parameters of Calcareous Sand Subgrade under Long-Term Cyclic Loading

Ziyu Wang ^{1,2,*} and Lei Zhang ³

¹ Yazhou Bay Innovation Institute, Hainan Tropical Ocean University, Sanya 572025, China

² College of Marine Science and Technology, Hainan Tropical Ocean University, Sanya 572022, China

³ College of Environmental Science and Engineering, Ocean University of China, Qingdao 266003, China

* Correspondence: zywang@hntou.edu.cn

Abstract: A long-term cyclic loading test of calcareous sand from an island reef in the South China Sea was conducted under conditions of unequal consolidation and drainage. The axial cumulative strain and dynamic characteristics of coral sand samples with different physical and mechanical properties were studied under different stress levels, yielding a model prediction formula. The results show that (1) the axial cumulative strain and dynamic elastic modulus increase with increasing vibration times of the cyclic load, whereas the dynamic damping ratio decreases with increasing cyclic vibration time; (2) the axial cumulative strain, elastic modulus, and damping ratio are affected by dynamic stress amplitude, load frequency, confining pressure, consolidation stress, compactness and moisture content; and (3) based on dynamic triaxial test results, the axial cumulative strain model of calcareous sand under cyclic loading and its permanent deformation prediction formula are established by introducing the cyclic stress ratio. Two parameters, the elastic modulus evolution parameter and the damping ratio evolution parameter, are introduced, and the axial cumulative strain is normalized. The results of this research have significance for understanding the long-term deformation and dynamic response of coral sand subgrade soil under cyclic vibration loads.

Keywords: calcareous sand; cyclic load; cumulative axial strain; stiffness; damping ratio

Citation: Wang, Z.; Zhang, L. Experimental Study on Dynamic Parameters of Calcareous Sand Subgrade under Long-Term Cyclic Loading. *J. Mar. Sci. Eng.* **2022**, *10*, 1806. <https://doi.org/10.3390/jmse10121806>

Academic Editor: Assimina Antonarakou

Received: 31 October 2022

Accepted: 18 November 2022

Published: 22 November 2022

Publisher's Note: MDPI stays neutral with regard to jurisdictional claims in published maps and institutional affiliations.



Copyright: © 2022 by the authors. Licensee MDPI, Basel, Switzerland. This article is an open access article distributed under the terms and conditions of the Creative Commons Attribution (CC BY) license (<https://creativecommons.org/licenses/by/4.0/>).

1. Introduction

Calcareous sand is a special soil medium of marine biogenesis and is distributed widely throughout the South China Sea. It is composed mainly of coral detritus and other marine biological detritus, with a calcium carbonate content above 90%. As a result of its biogenesis and sedimentary conditions, its physical and mechanical properties are notably different from those of general continental and coastal sedimentary soils, and particle breakage and deformation occur readily under long-term loading [1–4].

In recent years, the gradual development of the South China Sea and the implementation of island and reef engineering constructions have led to calcareous sand being used widely in the construction of airport runways, ports, subgrades, and other structures. In a marine environment, a calcareous sand foundation is not only vulnerable to waves, tides, earthquakes, and other cyclic loads [5–7], but also will lead to permanent deformation and uneven settlement under traffic load. Previous studies have investigated the dynamic characteristics and permanent deformation of calcareous sand foundations under long-term dynamic loads. Some researchers [8–10] conducted indoor triaxial cyclic loading tests on calcareous sand under different working conditions, showing that particle breakage caused by long-term loading increases the porosity of calcareous sand. Under cyclic compression, even when the cyclic load level is lower than the static strength, calcareous sand exhibits substantial permanent deformation. The residual strain depends on the average stress acting on the specimen and the cyclic stress in the limit state. Yu Haizhen and Wang Ren [11] discussed the influence of dynamic stress, confining pressure, consolidation stress

ratio, relative density, gradation, and vibration frequency on the dynamic characteristics of calcareous sand through a large number of dynamic triaxial tests. Li Jianguo [12,13] conducted experimental studies on the dynamic characteristics of saturated calcareous sand under wave loading, providing a preliminary comparison with the dynamic characteristics of quartz sand. The results show that under the action of wave load, the dynamic strength of saturated calcareous sand and quartz sand shows the same change rule with the direction angle of initial principal stress, and their dynamic strength gradually decreases with the increase of the direction angle of initial principal stress. Coop et al. [14] and Donohue et al. [15] studied particle breakage in calcareous sand and found that breakage increases with increasing cyclic loading time. Li Xue et al. [16] and Wang Gang et al. [17] conducted an in-depth study on particle breakage in calcareous sand, concluding that the degree of breakage increases with increasing cyclic shear time, whereas the growth rate gradually decreases. He Shaoheng et al. [18] conducted a series of long-term drained cyclic loading triaxial tests with different confining pressures and cyclic dynamic stress ratios and established a cyclic residual cumulative strain model of coral sand that can reflect the initial consolidation conditions and cyclic stress ratios. Studies simulating calcareous sand subgrades under vibration load have also been conducted: Zhou Sizhen [19] used node dynamic loading and surface dynamic loading to simulate aircraft loading, showing that under these two simplified dynamic loads, the vertical displacement value of node dynamic loading is larger and can maximize the safety of airport subgrade structures. Qin Lei [20] studied the characteristics of aircraft loading, simulating two simplified aircraft load forms with a moving constant load and moving sinusoidal load, and analyzing the dynamic response of airport subgrade under both kinds of action. Zhou Sujie [21] used repeated sinusoidal loading to simulate aircraft loading, considering the deformation and settlement of airport subgrade. The results of the abovementioned research are consistent with actual engineering settlement and monitoring values are also consistent with estimations.

In this paper, a dynamic triaxial apparatus was used to conduct long-term drainage cyclic loading tests for the unsaturated calcareous sand subgrade. The cumulative strain development law of calcareous sand under different confining pressures, dynamic stress amplitudes, consolidation stress ratios, subgrade soil compactness, load frequencies, and moisture contents is studied. Combined with a hyperbolic model, a prediction formula for the permanent deformation of calcareous sand under aircraft loading is presented. This formula provides a theoretical basis for the construction of a calcareous sand subgrade in the Nanhai island and reef project.

2. Materials and Methods

2.1. Experimental Materials and Instruments

The calcareous sand sample used in this test was obtained from a reef in the South China Sea. Calcareous sand contains inorganic elements Al, P, S, Cl, Sr, metalloid element Si, transition metal element Sc, and trace metal elements Fe, Co, Mg, and the content of Ca is 93.53%. The sand sample was washed using distilled water and dried, after which large pieces of gravel and impurities were removed. Calcareous sand particles with a particle size of less than 5 mm were selected for the dynamic triaxial loading test. The specific gravity of the sample was 2.75, its maximum void ratio was 1.27, and its minimum void ratio was 0.66. The particle grading curve is shown in Figure 1. The British GDS dynamic triaxial test system was adopted as the test equipment. The system comprises a confining pressure volume controller, back pressure volume controller, data acquisition instrument, and host and test loading platforms. The maximum axial load can reach 10 kN, the maximum loading frequency is 5 Hz, and the maximum confining pressure is 2000 kPa.

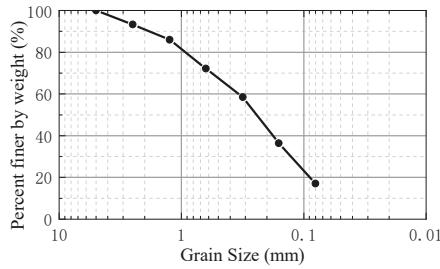


Figure 1. Grain size distribution curve of calcareous sand sample.

2.2. Test Method

The diameter and height of the sample were set at 50 mm and 100 mm, respectively. According to the requirements of compactness and moisture content, sand samples were prepared according to the grade shown in Figure 1, placed in a beaker, and sealed with a plastic film and plastic bag for 24 h such that moisture was evenly distributed throughout the sand; these uniform sand samples were then compacted to the specified height in three parts, and filter paper, permeable stone, and a top cap were placed in sequence for the consolidation loading test.

The stress control adopted in the test was divided into three parts: isotropic consolidation, eccentric consolidation, and cyclic loading, as shown in Figure 2. During the cyclic loading stage, a sinusoidal waveform was used to simulate the unidirectional pulse vibration of aircraft loading. To consider permanent deformation of subgrade soil under different degrees of compactness, the test was set to the drainage condition, the number of cyclic loading n was set to 10,000, and compactness K can be calculated according to Equation (1):

$$K = \rho / \rho_{max} \tag{1}$$

where ρ is the sample density and ρ_{max} is the maximum dry density of the sample. As airport runways are often subject to complex stress states, and as aircraft loading is accompanied by a large vertical dead load, airport runways are not in an isotropic consolidation state. Herein, the consolidation stress ratio $K_c = 1.5, 2, 2.5$ is proposed to simulate the real consolidation stress state of airport subgrade soil, where KC can be calculated according to Equation (2):

$$K_c = \sigma_1 / \sigma_3 \tag{2}$$

where σ_3 and σ_1 represent the confining pressure and axial pressure of the specimen, respectively, at the consolidation stage.

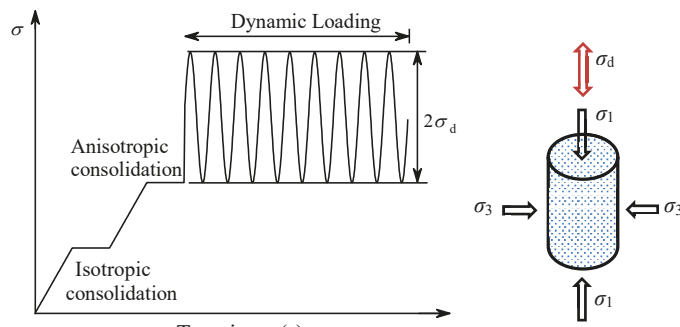


Figure 2. Schematic of the loading process.

Considering the above test parameters and actual working conditions, and referring to Zhou Sujie’s [21] effective simulation of loading due to an A320-200 aircraft, the test scheme was designed as shown in Table 1.

Table 1. Summary of cyclic triaxial test conditions.

Sample Number	Confining Pressure	Cyclic Loading	Consolidation Stress Ratio	Relative Density	Loading Frequency	Moisture Content
	σ_3/kPa	q_d/kPa	K_c	K	F/Hz	Ws/%
DT-1	25	100	1.5	95	1	16
DT-2	50	100	1.5	95	1	16
DT-3	100	100	1.5	95	1	16
DT-4	150	100	1.5	95	1	16
DT-5	200	100	1.5	95	1	16
DT-6	300	100	1.5	95	1	16
DT-7	100	50	1.5	95	1	16
DT-8	100	150	1.5	95	1	16
DT-9	100	200	1.5	95	1	16
DT-10	100	250	1.5	95	1	16
DT-11	100	100	2	95	1	16
DT-12	100	100	2.5	95	1	16
DT-13	100	100	1.5	85	1	16
DT-14	100	100	1.5	88	1	16
DT-15	100	100	1.5	90	1	16
DT-16	100	100	1.5	92	1	16
DT-17	100	100	1.5	95	2	16
DT-18	100	100	1.5	95	3	16
DT-19	100	100	1.5	95	1	12
DT-20	100	100	1.5	95	1	14
DT-21	100	100	1.5	95	1	18
DT-22	100	100	1.5	95	1	20

3. Results and Analyses

On the one hand, the effects of long-term dynamic loading on calcareous sand are reflected in its dynamic characteristics, for example, the dynamic elastic modulus and damping ratio; on the other hand, they are reflected in its cumulative deformation. As shown in Figure 3a, the irrecoverable residual strain caused by cyclic loading and unloading means that the loading and unloading curves cannot be closed. The closed area formed by the n-1 unloading curve and the nth loading curve is termed the hysteretic circle, whereas the closed ellipse surrounded by curve abcd is the hysteretic circle formed by cyclic loading. The slope of the line connecting vertices A ($\epsilon_{i,max}, q_{i,max}$) and C ($\epsilon_{i,min}, q_{i,min}$) of the major axis of ellipse abcd is the secant modulus of the corresponding hysteresis loop. The secant modulus of the nth hysteresis loop is defined as the dynamic elastic modulus $E_{c,N}$ of the sample under cyclic vibration. This is calculated as shown in Equation (3):

$$E_{c,N} = \frac{q_{i,max} - q_{i,min}}{\epsilon_{i,max} - \epsilon_{i,min}} \tag{3}$$

The damping ratio D of the sample can be calculated according to Equation (4):

$$D = \frac{S_{abcd}}{\pi * S_{ABC}} \tag{4}$$

where S_{abcd} is the area of the hysteresis loop abcd and S_{ABC} is the area of triangle abc.

Figure 3b shows the development pattern of the axial strain in coral sand under cyclic loading. The total axial strain of coral sand under the nth cyclic loading contains both recoverable elastic strain ϵ_e^n and unrecoverable cumulative axial strain $\epsilon_p^{acc,n}$.

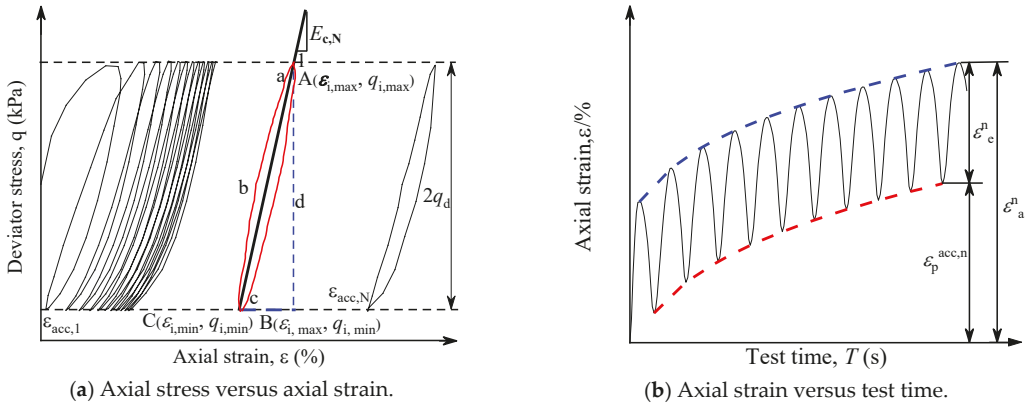


Figure 3. Schematic of axial stress–strain under cyclic loading.

3.1. Development Law of Axial Cumulative Strain

Figure 4 shows the relationship curve between the axial cumulative strain and vibration time in calcareous sand under different confining pressures, stress ratios, compactness, moisture contents, and load vibration frequencies and amplitudes. This shows that the relationship between the axial strain and vibration times of calcareous sand subgrade can be divided into two types: stable and failure. For the stable type, the cumulative axial strain slowly and nonlinearly increases, tending to be stable when the number of vibrations is greater than 1000; for the failure type, the cumulative axial strain rapidly increases with the increase of loading times until failure.

As shown in Figure 4a, at a confining pressure of 25 kPa, the axial cumulative strain of the sample is destructive, whereas confining pressures of 50, 100, 150, 200, 250, and 300 kPa are associated with an axial cumulative strain between 1% and 2%, which corresponds to a stable state. Figure 4b demonstrates that load amplitudes of 50, 100, 150, and 200 kPa are associated with an axial cumulative strain between 0.5% and 2%. When the vibration load amplitude reaches 250 kPa and the number of vibrations is 614, the axial cumulative strain reaches 15%, causing damage to the specimen. As shown in Figure 4c–e, the axial cumulative strain increases with the increasing consolidation stress ratio and decreases with the increasing vibration load frequency and compactness. Figure 4f shows that water contents between 14% and 20% cause the axial cumulative strain to increase and then decrease. When the water content reaches 16%, the axial cumulative strain is the largest, that is, 1.6%.

3.2. Development Law of Elastic Modulus

3.2.1. Influence of Confining Pressure

Figure 5 shows the relationship between the elastic modulus and the vibration times of calcareous sand under different confining pressures, stress ratios, compactness, moisture contents, and load vibration frequencies and amplitudes. As shown in Figure 5a, when the confining pressure is greater than 50 kPa, the elastic modulus of the sample linearly increases with increasing cyclic vibration time, exhibiting stable behavior; when the confining pressure is less than 50 kPa, the elastic modulus initially increases and then gradually decreases with increasing cyclic vibration time, showing destructive behavior. It can further be noted that when the confining pressure increases from 50 to 300 kPa, the initial elastic modulus of the sample increases from 750 to 2700 kPa; under the same cyclic vibration times, greater confining pressures and larger elastic modulus values are noted. This is because a greater confining pressure strengthens the deformation resistance of the sample.

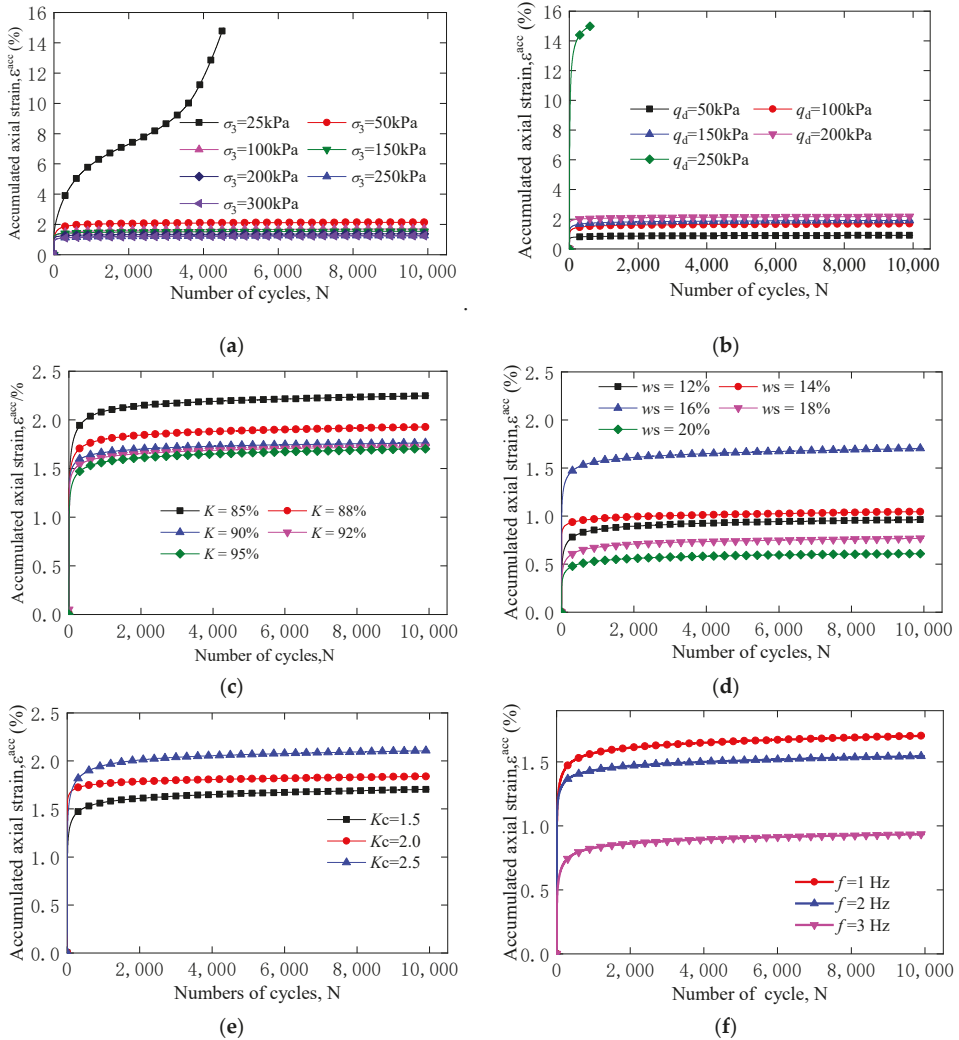


Figure 4. Accumulated axial strain under different test conditions. (a) Accumulated axial strain versus number of loading cycles under different confining pressures. (b) Accumulated axial strain versus number of loading cycles under different loading amplitudes. (c) Accumulated axial strain versus number of loading cycles under different K_c (d) Accumulated axial strain versus number of loading cycles under different loading frequencies. (e) Accumulated axial strain versus number of loading cycles under different densities, K . (f) Accumulated axial strain versus number of loading cycle under different moisture content.

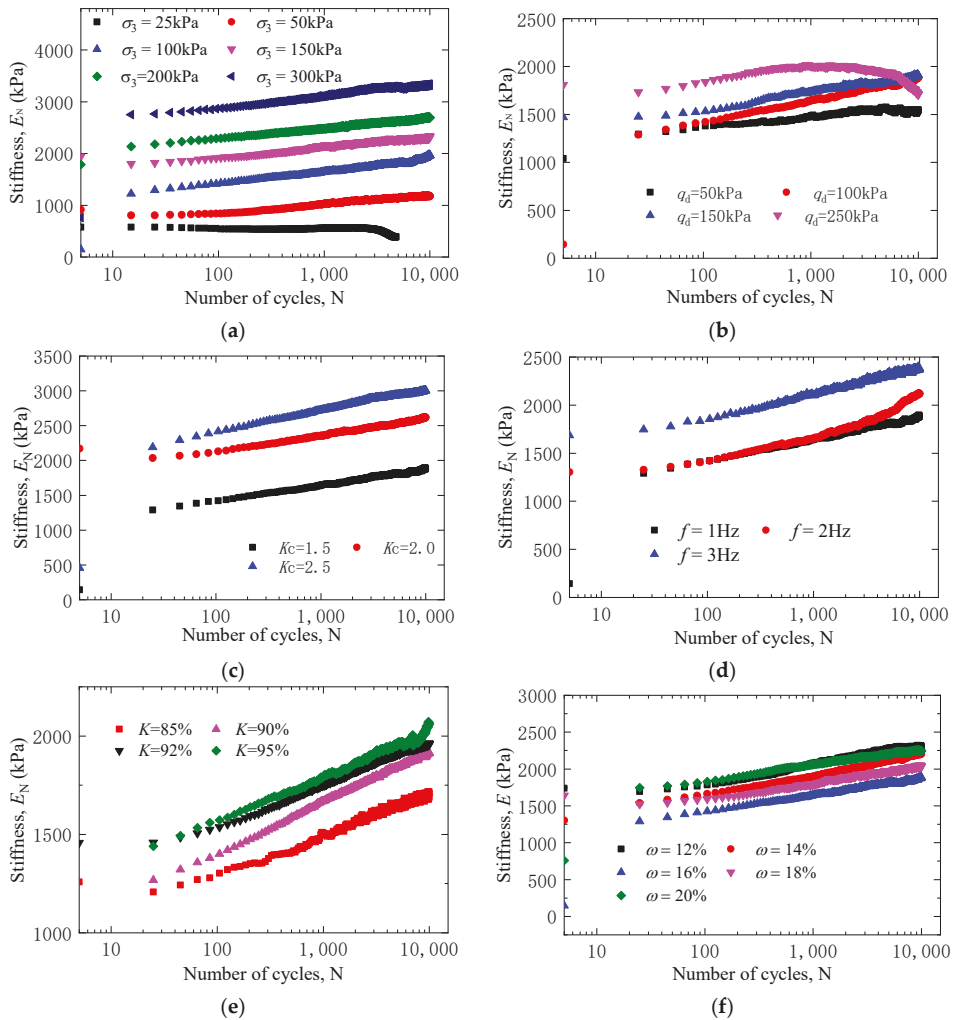


Figure 5. Stiffness under different testing conditions. (a) Stiffness versus number of cyclic loading under different confining pressures. (b) Stiffness versus number of cyclic loading under different loading amplitudes. (c) Stiffness versus number of cyclic loading under different K_c . (d) Stiffness versus number of cyclic loading under different loading frequencies. (e) Stiffness versus number of cyclic loading under different relative densities, K . (f) Stiffness versus number of cyclic loading under different moisture content.

3.2.2. Influence of Cyclic Load Amplitude

The cyclic load amplitude is an important index of dynamic load. As shown in Figure 5b, when the cyclic load amplitude reaches 50–200 kPa, the elastic modulus of the sample also increases. When the load amplitude is 250 kPa, the elastic modulus of the sample increases and then decreases with increasing amplitude until the sample fails. This occurs because low vibration amplitudes are associated with larger load amplitudes, increased density, and enhanced deformation resistance. When the vibration amplitude increases, the sample is initially compacted, and then gradually destroyed with increasing vibration time.

3.2.3. Influence of Consolidation Stress Ratio

The relationship curve of the elastic modulus of specimens with different consolidation stress ratios changes with the number of cycles, as shown in Figure 5c. As the consolidation stress ratio increases from 1.5 to 2.5, the initial elastic modulus increases from 1250 to 2100 kPa. Under the same cyclic vibration, a greater consolidation stress ratio is associated with a higher elastic modulus. This is because of the compaction effect of consolidation stress, the density of the soil, enhanced occlusion and friction between soil particles, and an improved ability to resist deformation.

3.2.4. Influence of Cyclic Load Frequency

The relationship curve of the elastic modulus of the specimen against the number of cycles under different cyclic loading frequencies is shown in Figure 5d; high-frequency loads under the same vibration frequency correspond to a higher elastic modulus because the load frequency directly reflects the vibration speed of the load. At higher load frequencies, the time of rearrangement and plastic flow of soil particles is shorter, and the deformation of the sample is smaller, such that the dynamic elastic modulus increases. On the contrary, the response time of particle rearrangement increases under low-frequency cyclic loads, while greater deformation occurs under similar stress levels and the elastic modulus is smaller.

3.2.5. Influence of Compaction Degree

The relationship curve of the elastic modulus of samples with different compactness versus the number of cycles is shown in Figure 5e. The elastic modulus increases as the number of cycles increases. When the compactness increases from $k = 85\%$ to 95% , the initial elastic modulus increases from 1200 to 1400 kPa, and the corresponding elastic modulus under the same vibration time also increases. This reflects the compactness of the sample: with increasing compactness, the elastic modulus also increases.

3.2.6. Influence of Water Content

Dynamic triaxial tests were carried out at five different moisture contents (12%, 14%, 16%, 18%, and 20%). The relationship curve of the elastic modulus versus the cycle time is shown in Figure 5f. This demonstrates that the elastic modulus of samples with different moisture contents increases with increasing cyclic vibration time. Under the same cyclic vibration time, when the optimal moisture content is 16%, the minimum elastic modulus of the sample is 1250 kPa. When the moisture content is below the optimal level, the elastic modulus decreases with the increasing moisture content, but when the moisture content is higher than the optimal level, the elastic modulus increases with increasing moisture content.

3.3. Development Law of Damping Ratio

3.3.1. Influence of Confining Pressure

The variations in the damping ratio of the confining pressure for specimens according to the cyclic loading time are shown in Figure 6a. In general, an increase in the number of loading cycles causes the damping ratio to gradually decrease. For the same number of vibrations, smaller confining pressures are associated with larger damping ratios and greater rates of damping ratio reduction. When the number of cycles increases to more than 5000, the damping ratio tends to be stable and less than 0.05. When the transverse restraint of the specimen is strong, soil particles more closely occlude, and lower energy dissipation is observed under the same dynamic load.

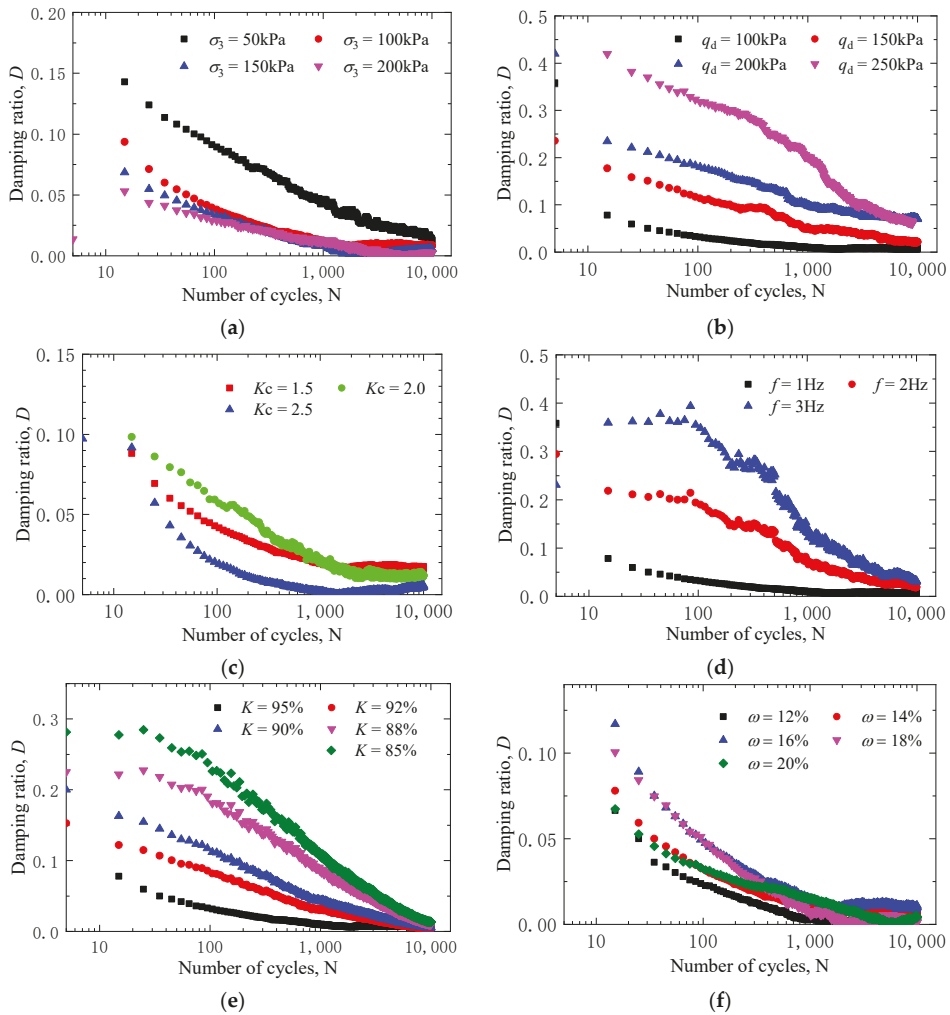


Figure 6. Damping ratio under different test conditions. (a) Damping ratio versus number of cyclic loading under different confining pressures. (b) Damping ratio versus number of cyclic loading under different loading amplitudes. (c) Damping ratio versus number of cyclic loading under different K_c . (d) Damping ratio versus number of cyclic loading under different loading frequencies. (e) Damping ratio versus number of cyclic loading under different densities, K . (f) Damping ratio versus number of cyclic loading under different moisture content.

3.3.2. Influence of Cyclic Load Amplitude

The cyclic load amplitude is an important index of dynamic load. As shown in Figure 6b, when the cyclic load amplitude reaches 50–200 kPa, the elastic modulus of the sample also increases. When the load amplitude is 250 kPa, the elastic modulus of the sample increases and then decreases with an increase in amplitude until failure occurs. This is because low vibration amplitudes are associated with larger load amplitudes, increased density, and enhanced deformation resistance. When the vibration amplitude increases, the sample is initially compacted and then gradually destroyed with an increase in vibration time.

3.3.3. Influence of Consolidation Stress Ratio

The relationship curve between the elastic modulus of specimens with different consolidation stress ratios changes with the number of cycles (Figure 6c). As the consolidation stress ratio increases from 1.5 to 2.5, the initial elastic modulus increases from 1250 to 2100 kPa. Under the same cyclic vibration, a greater consolidation stress ratio is associated with a higher elastic modulus. This is because of the compactness effect of consolidation stress, soil density, enhanced occlusion and friction between soil particles, and improved ability to resist deformation.

3.3.4. Influence of Cyclic Load Frequency

The variations in the damping ratio with the number of loading cycles under different frequency loadings are shown in Figure 6d. It can be seen that the load frequency has an obvious effect on the damping ratio of the sample. When the cyclic load frequency decreases from 3 to 1 Hz, the initial damping ratio of the sample decreases from 0.35 to 0.1. At the same cyclic vibration time, larger load frequencies correspond to larger damping ratios. However, increasing the cyclic vibration time causes the damping ratio of different samples to gradually decrease to a stable value. The frequency mainly reflects the speed of load action. Lower frequencies denote that the load is closer to a static load. Low-frequency loads can effectively transfer more energy and reduce energy dissipation, such that a low-frequency load corresponds to a low damping ratio.

3.3.5. Influence of Compaction Degree

The influence of the damping ratio of specimens with different compactness on the cyclic loading time is shown in Figure 6e. Dynamic triaxial tests were conducted for samples with compactness of 85%, 88%, 90%, 92%, and 95%. The results of these tests demonstrate that a decrease in compactness from 95% to 85% causes the initial damping ratio of the sample to decrease from 0.3 to 0.1. This shows that the damping ratio of a high-pressure compactness specimen is lower than that of a low-pressure compactness specimen, whereas the damping ratio decreases with increasing cyclic vibration time. This is because higher compactness causes denser soil particles to become occluded, and smaller residual deformation to occur under cyclic loads. As the cyclic vibration time of the load increases, the sample becomes gradually compacted, and the damping ratio decreases until the compactness of the sample becomes stable.

3.3.6. Influence of Water Content

The influence of the damping ratio of samples with different moisture contents on the cyclic loading time is shown in Figure 6f. In general, the damping ratio of the sample reaches its maximum at the optimal moisture content of 16%, at which time the initial damping ratio also reaches its maximum value of 0.12. When the moisture content is lower than the optimal moisture content, the damping ratio of the sample increases with increasing moisture content. When the moisture content is higher than the optimal moisture content, the damping ratio of the sample decreases with increasing moisture content. This is primarily because low moisture contents and relatively high density correspond to a large particle bite and small load energy dissipation under cyclic loading. The increasing moisture content results in soil particles becoming relatively prone to particle reorganization and plastic flow under pore water lubrication. This causes a gradual increase in the residual deformation and nonlinearity of the sample and an increased damping ratio; when the moisture content is high, the pore water pressure of the sample increases. The residual deformation of the soil skeleton under effective stress is small, whereas the damping ratio is relatively large.

4. Evolution Model

4.1. Normalized Model of Permanent Deformation

In practical engineering, the subgrade soil of an airport runway must be stable and resist deformation under long-term cyclic loading, such that its permanent deformation eventually tends to a smaller stable value. As shown in Equations (5) and (6), the hyperbolic model established by Zhang Feng et al. [22] can be used to describe the axial cumulative strain of the specimen as follows:

$$\epsilon^{acc,N} = \left(\frac{NC}{A + B * NC} \right)^{\frac{1}{C}} \tag{5}$$

where the loading number N tends to be positive infinity and the permanent deformation of the specimen under cyclic loading can be obtained according to Equation (2), as shown in Equation (3):

$$\epsilon^{acc,ult} = \left(\frac{1}{B} \right)^{\frac{1}{C}} \tag{6}$$

where $\epsilon^{acc,N}$ is the axial cumulative strain of the specimen under the nth vibration, and $\epsilon^{acc,ult}$ is the permanent strain of the specimen. A, B, and C are regression parameters obtained by linear regression, whose values are related to the stress conditions (such as confining pressure and cyclic load characteristics) and the physical and mechanical properties (such as density, moisture content, and pre-consolidation stress) of the specimen.

Figure 7 shows the permanent deformation of coral sand samples with different physical and mechanical properties under different load conditions. For the same stress level, the deformation of samples with different physical and mechanical properties exhibits good consistency, such that a permanent deformation of approximately 2% is observed. We therefore assume that the compactness, water content, consolidation stress ratio, and load frequency of samples are important parameters to consider when studying permanent deformation characteristics. The permanent deformation of coral sand subgrade soil depends on the amplitude of the cyclic load and the confining pressure. The cyclic stress ratio (CSR) parameter is introduced to analyze and predict permanent deformation. The CSR is defined as the ratio of cyclic stress amplitude to confining pressure, and can be calculated as follows:

$$CSR = q_d / \sigma_3 \tag{7}$$

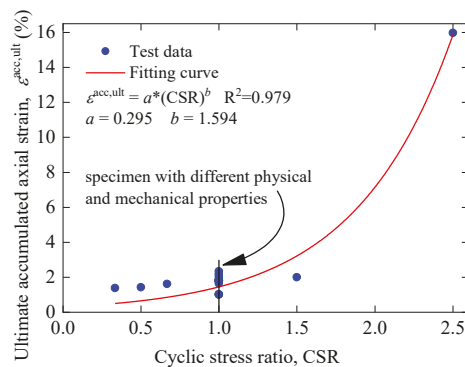


Figure 7. The ultimate accumulated axial strain versus the cyclic stress ratio.

As shown in Figure 7, the relationship between the ultimate axial cumulative strain and the CSR of coral sand can be accurately fitted using an exponential function, and the model is as follows (8):

$$\varepsilon^{acc,ult} = a * CSR^b \tag{8}$$

This prediction formula accurately reflects the deformation of calcareous sand sub-grade soil under cyclic loading. Under low stress, coral sand exhibits better resistance to deformation and smaller permanent deformation. When the stress level increases, the sample exhibits more significant permanent deformation under cyclic loading because of the fragility and low strength of coral sand particles.

4.2. Elastic Modulus Normalization Model

According to Idriss [23], the parameter $\delta_{E,N}$ was introduced to study the relationship between the elastic modulus and the axial cumulative strain ratio. $\delta_{E,N}$ is defined as the ratio of the elastic modulus to the initial elastic modulus under a certain cycle vibration and can be calculated according to the following Equation (9):

$$\delta_{E,N} = E_N / E_1 \tag{9}$$

where E_N and E_1 represent the elastic modulus and initial elastic modulus, respectively, of a specimen under a certain cyclic loading. Thus, samples with different physical and mechanical properties and cyclic loads can be normalized. Figure 8 shows the relationship between the axial cumulative strain ratio $\delta_{acc,N}$ and the elastic modulus growth ratio $\delta_{E,N}$ of different specimens. All data points occur within a specific range, and the best fit curve and the upper and lower envelope can be determined according to Equations (10)–(12):

Top bound curve:

$$\delta_{E,N} = 0.8 + 0.1901\delta_{acc,N} + 0.7127\delta_{acc,N}^2 \tag{10}$$

Fitting curve:

$$\delta_{E,N} = 0.8 + 0.1271\delta_{acc,N} + 0.5278\delta_{acc,N}^2 \tag{11}$$

Bottom bound curve:

$$\delta_{E,N} = 0.8 + 0.0693\delta_{acc,N} + 0.3016\delta_{acc,N}^2 \tag{12}$$

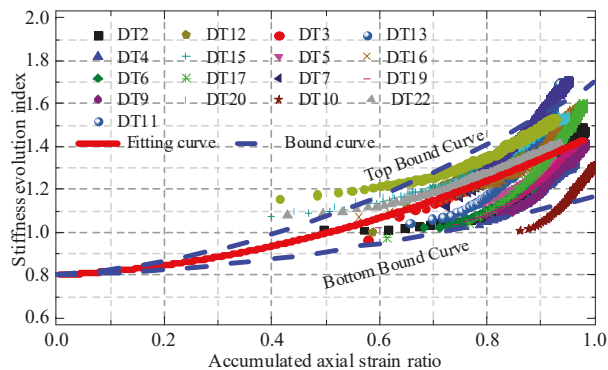


Figure 8. Relationship between the accumulated axial strain ratio and the stiffness evolution index.

4.3. Damping Ratio Normalization Model

According to research by Ling Xianzhang [24], the parameter $\delta_{D,N}$ was introduced to study the relationship between the elastic modulus and the axial cumulative strain ratio.

$\delta_{D,N}$ is defined as the ratio of the damping ratio to the initial damping ratio under a certain cycle vibration and can be calculated according to Equation (13):

$$\delta_{D,N} = \frac{D_N}{D_1} \tag{13}$$

where D_N and D_1 refer to the damping ratio and initial damping ratio, respectively, of a sample under a certain cyclic loading. The normalized analysis of specimens with different physical and mechanical properties and cyclic load is conducted as shown in Figure 9, where the relationship between the axial cumulative strain ratio $\delta_{acc,N}$ and the damping ratio evolution parameters $\delta_{D,N}$ of different specimens are shown. With increasing $\delta_{acc,N}$, $\delta_{D,N}$ gradually decreases and the test data points fall within a specific range, such that the best fit curve and the upper and lower envelope can be determined using the following Equations (14)–(16):

Top bound curve:

$$\delta_{E,N} = 1 - 0.0884\delta_{acc,N} - 0.5729\delta_{acc,N}^2 \tag{14}$$

Fitting curve:

$$\delta_{E,N} = 1 - 0.2473\delta_{acc,N} - 0.7268\delta_{acc,N}^2 \tag{15}$$

Bottom bound curve:

$$\delta_{E,N} = 1 - 0.4834\delta_{acc,N} - 0.8829\delta_{acc,N}^2 \tag{16}$$

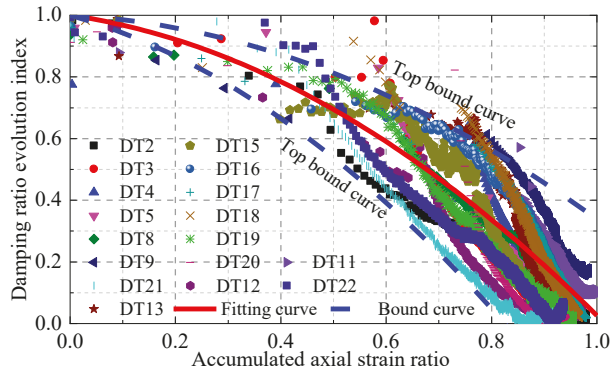


Figure 9. Relationship between the accumulated axial strain ratio and the damping ratio evolution index.

5. Conclusions

In this study, the evolution of the dynamic characteristics and deformation of coral sand samples with different confining pressure, compactness, water contents, and pre-consolidation stress under cyclic loading of different amplitudes and frequencies were studied using GDS dynamic triaxial apparatus. Based on the hyperbolic function, a model of the development of axial cumulative strain and the dynamic characteristics of coral sand subgrade soil has been established, and a relevant prediction formula has been given. The permanent deformation, elastic modulus, and damping ratio of coral sand subgrade soil under cyclic loading were predicted, and the following conclusions can be made:

- (1) The dynamic triaxial test shows that the stiffness of calcareous sand increases with increased cyclic loading, whereas the damping ratio decreases with increased cyclic loading. When cyclic loading approaches infinity, the stiffness of the sample tends to be stable, and the damping ratio becomes less than 0.05.
- (2) The initial value and rate of change of stiffness and damping ratio vary under different parameters. When the vibration number of the cyclic load is kept constant, the

dynamic stress amplitude is larger, the confining pressure is lower, water and salt contents are higher, and the change of stiffness and damping ratio from the initial to the given cycle increases.

- (3) At higher dynamic stress amplitudes, the frequency is higher, the confining pressure, consolidation stress, and compactness are lower, and the moisture content is closer to its optimal value. Furthermore, the axial cumulative strain is higher, the elastic modulus is lower, and the damping ratio is higher.
- (4) The permanent deformation of the calcareous sand subgrade can be calculated by inputting the cyclic load stress. Moreover, according to the field settlement deformation monitoring data, the dynamic elastic modulus and damping ratio evolution of the subgrade can be calculated, and then the long-term service performance of the subgrade can be reasonably predicted.

Author Contributions: Investigation, writing—original draft preparation and data curation, L.Z.; formal analysis, writing—review and editing, visualization, resources, investigation, data curation, project administration, and funding acquisition, Z.W. All authors have read and agreed to the published version of the manuscript.

Funding: This research was supported by the Hainan Provincial Natural Science Foundation of China (Grant No. 421RC592), and the National Natural Science Foundation of China (Grant No. 42162024).

Data Availability Statement: The data used during the study are available from the first author and corresponding author by request.

Conflicts of Interest: The authors declare no conflict of interest.

References

1. Shahnazari, H.; Rezvani, R. Effective parameters for the particle breakage of calcareous sands: An experimental study. *Eng. Geol.* **2013**, *159*, 98–105. [[CrossRef](#)]
2. Wang, X.Z.; Jiao, Y.-Y.; Wang, R.; Hu, M.; Meng, Q.; Tan, F. Engineering characteristics of the calcareous sand in Nansha Islands, South China Sea. *Eng. Geol.* **2011**, *120*, 40–47. [[CrossRef](#)]
3. Shahnazari, H.; Rezvani, R.; Tutunchian, M.A. Post-cyclic volumetric strain of calcareous sand using hollow cylindrical torsional shear tests. *Soil Dyn. Earthq. Eng.* **2019**, *124*, 162–171. [[CrossRef](#)]
4. Wang, X.; Weng, Y.; Wei, H.; Meng, Q.; Hu, M. Particle obstruction and crushing of dredged calcareous soil in the Nansha Islands, South China Sea. *Eng. Geol.* **2019**, *261*, 105274. [[CrossRef](#)]
5. Wang, X.; Zhu, C.-Q.; Wang, X.Z. Experimental study on the coefficient of lateral pressure at rest for calcareous soils. *Mar. Georesour. Geotechnol.* **2020**, *38*, 989–1001. [[CrossRef](#)]
6. Chen, W.; Jeng, D.; Chen, W.; Chen, G.; Zhao, H. Seismic-induced dynamic responses in a poro-elastic seabed: Solutions of different formulations. *Soil Dyn. Earthq. Eng.* **2020**, *131*, 106021. [[CrossRef](#)]
7. Yu, J.; Zhu, Y.; Yao, W.; Liu, X.; Ren, C.; Cai, Y.; Tang, X. Stress relaxation behaviour of marble under cyclic weak disturbance and confining pressures. *Measurement* **2021**, *182*, 109777. [[CrossRef](#)]
8. Datta, M.; Rao, G.V.; Gulhati, S. Development of pore water in a dense calcareous sand under repeated compressive stress cycles. In Proceedings of the International Symposium on Soils under Cyclic and Transient Loading, Swansea, Wales, UK, 7–11 January 1980; pp. 33–47.
9. Knight, K. Contribution to the performance of calcareous sands under cyclic loading. In Proceedings of the International Conference on Calcareous Sediments, Perth, WA, Australia, 15–18 March 1988; pp. 877–880.
10. Kaggwa, W.S.; Poulos, H.G.; Carter, J.P. Response of carbonate sediments under cyclic triaxial test conditions. In Proceedings of the 1st International Conference on Calcareous Sediments, Perth, WA, Australia, 15–18 March 1988; Volume 1, pp. 97–107.
11. Haizhen, Y.; Ren, W. The cyclic strength test research on calcareous sand. *Rock Soil Mech.* **1999**, *4*, 3–5. (In Chinese)
12. Jianguo, L.; Ren, W.; Haizhen, Y. Experimental research on effect of initial principal stress orientation on dynamic properties of calcareous sand. *Rock Soil Mech.* **2005**, *5*, 723–727. (In Chinese)
13. Jianguo, L. *Experimental Research on Dynamic Behavior of Saturated Calcareous Sand under Wave Loading*; Institute of Rock and Soil Mechanics, Chinese Academy of Sciences: Wuhan, China, 2005. (In Chinese)
14. Coop, M.R.; Sorensen, K.K.; Bodas Freitas, T.M.; Georgoutsos, G. Particle breakage during shearing of a carbonate sand. *Géotechnique* **2004**, *54*, 157–163. [[CrossRef](#)]
15. Donohue, S.; O'sullivan, C.; Long, M. Particle breakage during cyclic triaxial loading of a carbonate sand. *Géotechnique* **2009**, *59*, 477–482. [[CrossRef](#)]
16. Li, X.; Liu, J. One-dimensional compression feature and particle crushability behavior of dry calcareous sand considering fine-grained soil content and relative compaction. *Bull. Eng. Geol. Environ.* **2021**, *80*, 4049–4065. [[CrossRef](#)]

17. Gang, W.; Jingjing, Z.; Xing, W. Evolution of particle crushing of carbonate sands under cyclic triaxial stress path. *Chin. J. Geotech. Eng.* **2019**, *41*, 755–760. (In Chinese)
18. Shaoheng, H.; Zhi, D.; Tangdai, X. Long-term behaviour and degradation of calcareous sand under cyclic loading. *Eng. Geol.* **2020**, *276*, 105756. [[CrossRef](#)]
19. Sizhen, Z. Dynamic Analysis of Mining Tunnel and Airport Runway under Aircraft Moving Loads. Ph.D. Thesis, Beijing Jiaotong University, Beijing, China, 2012. (In Chinese).
20. Lei, Q. Study on Deformation of Airport Pavement Foundation under the Action of Airport Loads and Groundwater. Ph.D. Thesis, Zhengzhou University, Zhengzhou, China, 2017. (In Chinese).
21. Sujie, Z. Study on Dynamic Response and Deformation of Airport Pavement Foundation under the Action of Aircraft Loads. Ph.D. Thesis, Nanjing University of Aeronautics and Astronautics, Nanjing, China, 2018. (In Chinese).
22. Feng, Z. Heavy Track Induced Dynamic Response and Permanent Deformation of Subgrade in Deep Seasonally Frozen Region. Ph.D. Thesis, Harbin Institute of Technology, Harbin, China, 2012. (In Chinese).
23. Idriss, I.M.; Dobry, R.; Singh, R.D. Nonlinear behavior of soft clays during cyclic loading. *J. Geotech. Eng. Div. ASCE* **1978**, *104*, 1427–1447. [[CrossRef](#)]
24. Ling, X.; Li, Q.; Wang, L.; Zhang, F.; An, L.; Xu, P. Stiffness and damping ratio evolution of frozen clays under long-term low-level repeated cyclic loading: Experimental evidence and evolution model. *Cold Reg. Sci. Technol.* **2013**, *86*, 45–54. [[CrossRef](#)]

Article

Effect of Low Temperature on the Undrained Shear Strength of Deep-Sea Clay by Mini-Ball Penetration Tests

Zhongde Gu ¹, Xingsen Guo ^{2,3,*}, Houbin Jiao ¹, Yonggang Jia ² and Tingkai Nian ^{1,*}

¹ State Key Laboratory of Coastal and Offshore Engineering, Dalian University of Technology, Dalian 116024, China

² Shandong Provincial Key Laboratory of Marine Environment and Geological Engineering, Ocean University of China, Qingdao 266100, China

³ Department of Civil, Environmental, Geomatic Engineering, University College London, London WC1E 6BT, UK

* Correspondence: xingsen.guo@ucl.ac.uk (X.G.); tknian@dlut.edu.cn (T.N.)

Abstract: The technology for in situ testing of the undrained shear strength of deep-sea clay is underdeveloped. Indoor tests remain necessary, and there is a large temperature difference between in situ and laboratory tests. To analyse the effect of temperature on undrained shear strength, in this study the physical characteristics of marine clay samples from the South China Sea were determined, followed by penetration tests by the mini-ball method under low (4 °C) and room (20 °C) temperatures. The results indicated that the clay strength increased by 14.1–30.0% as the temperature decreased from 20 °C to 4 °C, and the strength of the bound water and the viscosity of the free water in the clay sample increased as the temperature decreased, which was the root cause of the increase in the clay strength. Based on the research, it is possible to correct the undrained shear strength values measured in laboratory tests and provide more reasonable parameters for ocean engineering.

Keywords: undrained shear strength; clay samples; mini-ball penetration test; low temperature; strength of bound water; viscosity of free water

Citation: Gu, Z.; Guo, X.; Jiao, H.; Jia, Y.; Nian, T. Effect of Low Temperature on the Undrained Shear Strength of Deep-Sea Clay by Mini-Ball Penetration Tests. *J. Mar. Sci. Eng.* **2022**, *10*, 1424. <https://doi.org/10.3390/jmse10101424>

Academic Editor: Antoni Calafat

Received: 15 July 2022

Accepted: 21 September 2022

Published: 3 October 2022

Publisher's Note: MDPI stays neutral with regard to jurisdictional claims in published maps and institutional affiliations.



Copyright: © 2022 by the authors. Licensee MDPI, Basel, Switzerland. This article is an open access article distributed under the terms and conditions of the Creative Commons Attribution (CC BY) license (<https://creativecommons.org/licenses/by/4.0/>).

1. Introduction

Marine engineering construction has moved to the deep sea, and researchers are paying more attention to the undrained shear strength of deep-sea clay [1], which is crucial for the design and installation of marine pipelines [2,3], development of marine mineral resources [4] and evaluation of marine geological hazards [5–11]. Nevertheless, the in situ technology for testing the undrained shear strength of deep-sea clay is not well developed, especially for seawater depths exceeding 4000 m [12]. Therefore, it is necessary to retrieve samples from the deep sea and conduct laboratory tests to comprehensively evaluate the deep-sea clay strength. In situ tests of deep-sea clay were conducted in a low-temperature environment, e.g., the continental shelf (6–14 °C), continental slope (2–6 °C), and deep-sea basin (2–3 °C) [13], while the clay samples were tested in the laboratory at 20–35 °C. To reasonably evaluate the deep-sea clay strength, the effect of low temperatures must be explored in the laboratory.

A series of experiments were conducted by researchers to investigate the effect of temperature on the undrained shear strength of marine clay. Mitchell et al. [14] tested the undrained shear strength of remoulded San Francisco Bay mud under isotropically consolidated undrained triaxial compression, which demonstrated a 9% increase as the temperature decreased from 20 °C to 4.7 °C. In the case of marine clay, Perkins and Sjrnsen [15] performed tests on intact specimens of Troll clay using consolidated anisotropic undrained compression (CAUC), and the results indicated that the undrained shear strength was 10–21% greater at low temperatures than at room temperature. Gue et al. [16] studied clay in the Norwegian Sea, including the preconsolidation stress, undrained shear strength,

rate effects, and anisotropy ratio, at different temperatures. The results showed that the undrained shear strength increased by 15–30% when tested at low temperatures by triaxial tests.

Measuring the undrained shear strength of deep-sea clay through a temperature-controlled triaxial instrument requires solving two problems: (1) it is difficult to test ultrasoft clay with very low strength in a triaxial apparatus; and (2) there is an unavoidable temperature effect on membrane stiffening for triaxial tests [16]. To address both issues, a full-flow penetrometer could be used to determine the effect of temperature on the undrained shear strength of deep-sea clay. Full-flow penetrometers have many advantages, which have been described by numerous researchers [17–23]. In particular, full-flow penetrometers are suitable for measuring low-strength clay and can achieve direct contact between the test instrument and clay. There are two main types of full-flow penetrometers, namely, the T-bar and the ball. The T-bar was first introduced in 1991 [24,25] and applied to in situ testing in 1998. However, due to its slender structure, a bending moment was produced during the testing that resulted in inaccurate results [26]. The ball-type penetrometer was subsequently invented and used in 2005 to avoid the bending moment [17]. Consequently, a mini-ball full-flow penetrometer was used in this study.

Above all, studies have indicated that the undrained shear strength differs between room and low temperatures. However, the mechanism of the temperature effect on the undrained shear strength of deep-sea clay has rarely been studied and discussed. In this paper, based on the same full-flow test principle in both the in situ and laboratory tests, mini-ball penetration tests were conducted to discover and quantify the effect of temperature on the undrained shear strength of deep-sea clay from the South China Sea. Then, the mechanism of temperature influence was analysed and explained in detail. The results will be useful to correct the undrained shear strength measured in the laboratory and provide more reasonable parameters for deep-sea development and disaster prevention.

2. Methodology

2.1. Sediment Samples

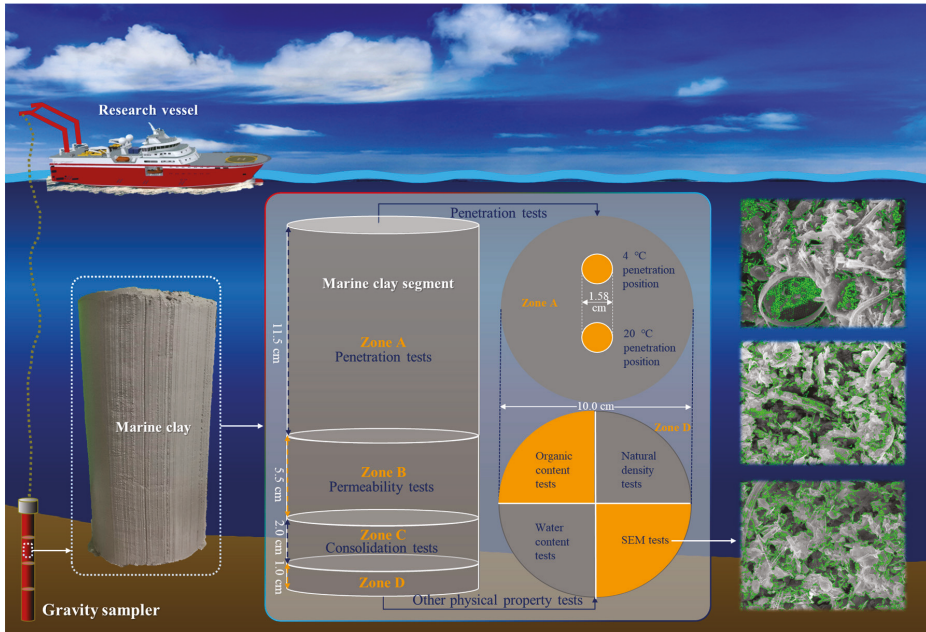
Deep-sea sediment samples were taken in the South China Sea at 21°23'30" N and 118°45'44.4" E. At the sampling position, the water depth was 2535 m, which was classified as deep sea, and the seabed surface temperature was approximately 4 °C. The sediment samples were collected from the deep sea by a gravity core sampler whose length and diameter are 7 m and 0.1 m, respectively, and stored in the geotechnical laboratory at 4 °C. Finally, these sediment samples were transported to the geotechnical laboratory of Dalian University of Technology for storage, where the temperature was maintained at 20 °C.

2.2. Physical Properties of Sediment Samples

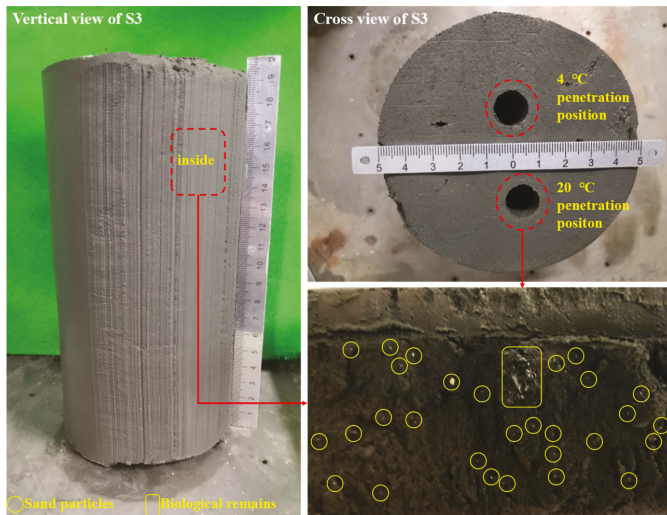
There were six sediment segments in total (i.e., from S1 to S6), each 20 cm long. Various tests were performed to provide a description of the six sediment segments, partly shown in Figure 1, including measurements of density, water content, plastic and liquid limits, specific gravity, organic content, compression factor, permeability factor, grain-size, and imaging by scanning electron microscopy (Figure 2). Table 1 summarizes the results of the physical properties of the sediment segments. From the grain size data (Figure 3) and using the China Standard for Engineering Classification of Soils (GB/T 50145-2007) and the USA Unified System of Soil Classification (ASTM D2487-00), the sediment has been classified as “clay” [27,28]. Note that the consolidation loads are 12.5, 25, 50, 100, 200, and 400 kPa. To determine the consolidation coefficients, first calculate the void ratio under consolidation pressures of 0.1 and 0.2 MPa and then calculate according to Equation (1) below. All the sediment segments belong to high liquid limit clay containing organic matter based on the Casagrande plasticity diagram:

$$a = \frac{e_1 - e_2}{P_2 - P_1} \tag{1}$$

where α is the compression coefficient; e_1 is the void ratio under 0.1 MPa consolidation pressure; e_2 is the void ratio under 0.2 MPa consolidation pressure; P_1 is 0.1 MPa consolidation pressure; and P_2 is 0.2 MPa consolidation pressure.



(a)



(b)

Figure 1. Diagram and physical map of the sediment segments: (a) Schematic diagram of the spatial layout of penetration and physical property tests of each sediment segment; (b) Physical map of a 100–150 cm sediment segment (S3).

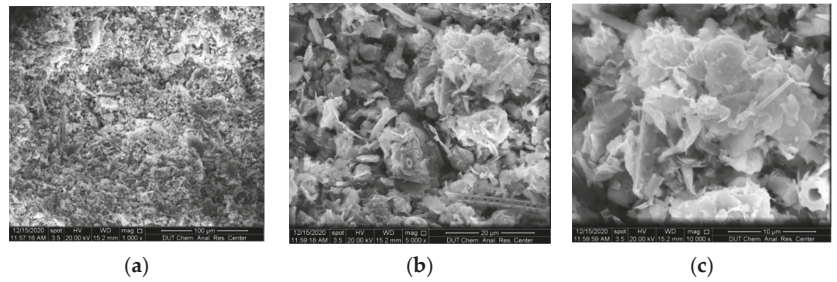


Figure 2. SEM images of the 0–20 cm sediment segment S1 at different magnifications: (a) 1000×; (b) 5000×; (c) 10000×.

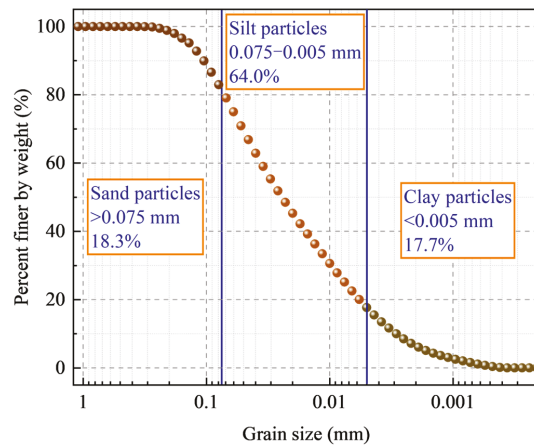


Figure 3. Average grain size distribution curve of the six sediment segments.

Table 1. Physical properties of the six sediment segments.

Clay Segments	Depth cm	Water Content (w)	Density (ρ) g/cm ³	Plastic Limit (w _p) %	Liquid Limit (w _L) %	Plastic Index (I _p) -	Liquid Index (I _L) -	Compression		Organic Content %	Mean Grain Size (D ₅₀) µm	Specific Gravity (G _s) -
								Coefficient (a) MPa ⁻¹	Permeability Coefficient (k) 10 ⁻⁷ cm/s			
S1	0–20	97.62	1.48	36.75	64.42	27.67	2.20	1.04	3.62	2.71	17.568	2.65
S2	50–70	93.85	1.60	33.40	56.64	23.24	2.60	1.26	2.83	2.24	28.777	2.78
S3	100–120	87.01	1.52	35.29	60.82	25.53	2.03	1.58	3.29	2.17	48.663	2.78
S4	150–170	90.73	1.50	35.72	58.91	23.19	2.37	1.20	3.54	2.04	23.456	2.74
S5	200–220	93.62	1.45	34.74	56.70	21.96	2.68	1.22	4.67	1.92	20.136	2.74
S6	250–270	109.33	1.49	35.73	57.82	22.09	3.33	1.00	4.76	2.07	23.827	2.74

3. Results

3.1. Temperature Calibration of the Load Cell

Figure 4 shows the mini-ball device used to measure the undrained shear strength of sediment segments, with a probe diameter of 1.58 cm, a shaft diameter of 0.6 cm, and a length of 28.5 cm. When the mini-ball is forced, the force is transmitted to the load cell through the dowel bar, which can then detect penetration resistance. As the load cell may be affected by temperature, it is necessary to calibrate it at various temperatures. Figure 5 shows that the sensor calibration factor was 0.200 at 4 °C and 0.197 at 20 °C.

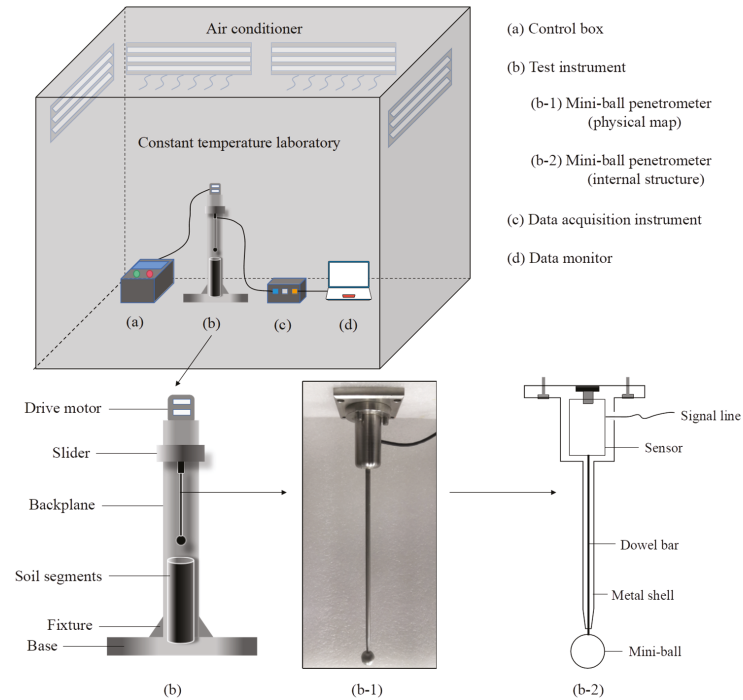


Figure 4. Mini-ball penetration tests in the constant temperature laboratory: (a) Control box; (b) Test instrument; (c) Data acquisition instrument; (d) Data monitor.

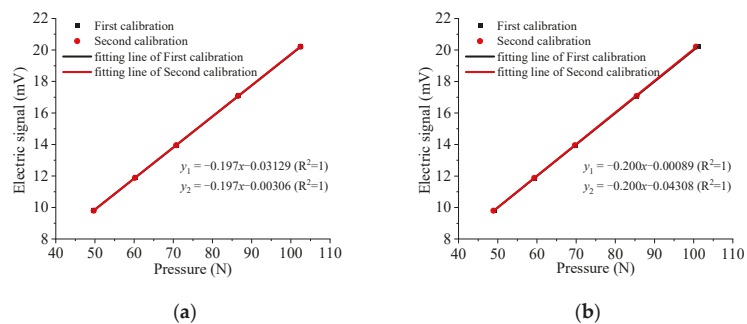


Figure 5. Temperature calibration of the load cell at 20 °C and 4 °C: (a) Pressure calibration at 20 °C; (b) Pressure calibration at 4 °C.

3.2. Penetration Tests at Room and Low Temperatures

Mini-ball penetration tests were conducted consecutively at room and low temperatures in the constant temperature laboratory (Figure 4). First, to control the test temperature, both the mini-ball and sediment segments were placed in a constant temperature laboratory for at least 24 h, where the temperature was set to 20 °C. To ensure that the sediment sample reached the desired temperature, the temperature was then tested with a thermometer. After that, the test was performed with a maximum penetration depth of approximately 12 cm and a penetration velocity of 0.2 cm/s. According to Lehane et al. [29], Equation (2) was used to determine whether the sediment was in an undrained condition, i.e., when the normalized velocity (V) exceeded the range of 11–17, it was deemed to be undrained. In Figure 6, the normalized velocities for all sediment segments were under undrained conditions, and thus the results of the penetration tests represented the undrained shear strength:

$$\begin{cases} V = \frac{vD}{c_v} \\ c_v = \frac{k(1+e)}{a \cdot \gamma_w} \end{cases} \quad (2)$$

where V is the normalized velocity; v is the penetration velocity (0.2 cm/s); D is the diameter of the mini-ball (1.58 cm); c_v is the vertical consolidation coefficient, cm²/s; k is the permeability coefficient, cm/s; e is the natural pore ratio; a is the compression coefficient, kPa⁻¹; and γ_w is the water weight, 10 kN/m³.

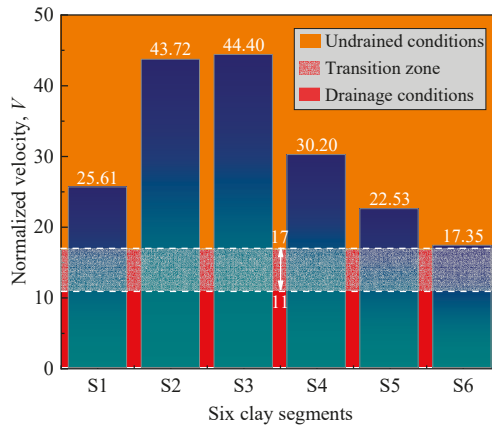


Figure 6. Normalized velocity for each sediment segment.

After room-temperature penetration tests were performed, the temperature was set to 4 °C for at least 24 h to ensure that the six sediment segments were fully at the low temperature. Next, low-temperature penetration tests were conducted using the same procedures as the room-temperature penetration tests.

4. Results and Analysis

4.1. Penetration Results at Room and Low Temperatures

A method for evaluating the undrained shear strength (s_u) was proposed by DeJong et al. [21] and Zhou et al. [30] as follows:

$$\begin{cases} q_{net} = \frac{q-F}{A} \\ F = f_b \times \gamma \times V_e \\ s_u = \frac{q_{net}}{N_{Ball}} \end{cases} \quad (3)$$

where q_{net} is the net penetration resistance, kPa; q is the penetration resistance, kN; A is the project area of the mini-ball, m^2 ; F is buoyancy, kN; f_b accounts for the effect of local heave (since there is little or no heave in the penetration process, as shown in Figure 1b, it is set as 1); γ is the gravity of sediment, kN/m^3 ; V_e is the volume of the embedded mini-ball below the mud line level, m^3 ; and N_{Ball} is the penetration resistance factor, which ranges from 11.21 to 15.19 and is related to surface roughness based on Equation (4) [31]:

$$N_{Ball-ideal} = 11.21 + 5.04\alpha - 1.06\alpha^2 \tag{4}$$

where $N_{Ball-ideal}$ is the penetration resistance factor in the ideal state and α is the surface roughness of the probe. Usually, the probe surface is sandblasted, so it is recommended that $\alpha = 0.4$. Although the surface of the mini-ball was polished smoothly, it still could not reach an ideal smooth state. According to Table 2, the penetration resistance factors were in the 12.0–12.5 range; therefore, N_{Ball} was adopted as 12.18 with $\alpha = 0.2$ based on Equation (4).

Table 2. Penetration resistance factors (N_{Ball}) from different studies.

Detail Information	N_{Ball}	Researchers
Soft massive clay and shelly massive clay. DIS-2 and DIS-5, located in the floodplain of the Nakdong River delta, west of Busan, Korea.	12.09–12.21	Nguyen and Chung [32]
Irish clay, located in Athlone, Belfast, Lough Erne	12.00	Long et al. [23]
Onshore sites: Onsøy (Norway), Burswood (Australia), Ariake (Japan)	12.00–12.38	Low et al. [19]
Offshore sites: West Africa, Norwegian Sea, Timor Sea, and offshore Egypt		
Kaolin clay, Laboratory tests (1 g)	12.50	Liu et al. [33]

In addition, this study focused on the temperature effect on s_u ; the changes in N_{Ball} with penetration depth were not considered. The s_u profiles at 4–6 times the diameter of the mini-ball (4–6 D) were used to assess the difference in s_u between 20 °C and 4 °C. According to Equation (3), s_u tested by the mini-ball penetration tests at 20 °C and 4 °C is shown in Figure 7, where s_u ranged from approximately 3.2 kPa to 7.7 kPa in the six sediment segments and was lower at 20 °C than 4 °C in all tests except for S3. For S3, s_u decreased from 6.8 kPa to 5.9 kPa at 20 °C, while it was nearly stable at 5.9 kPa at 4 °C.

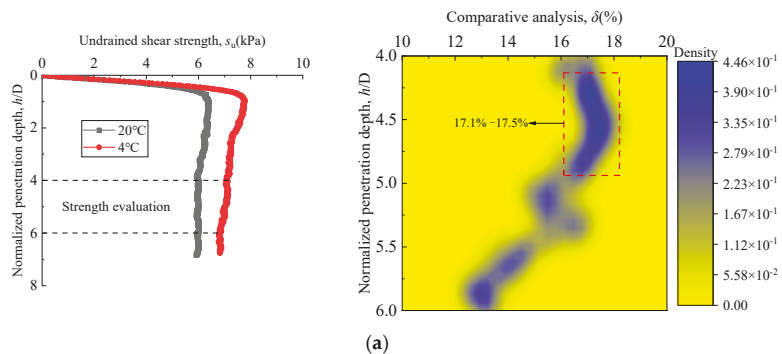


Figure 7. Cont.

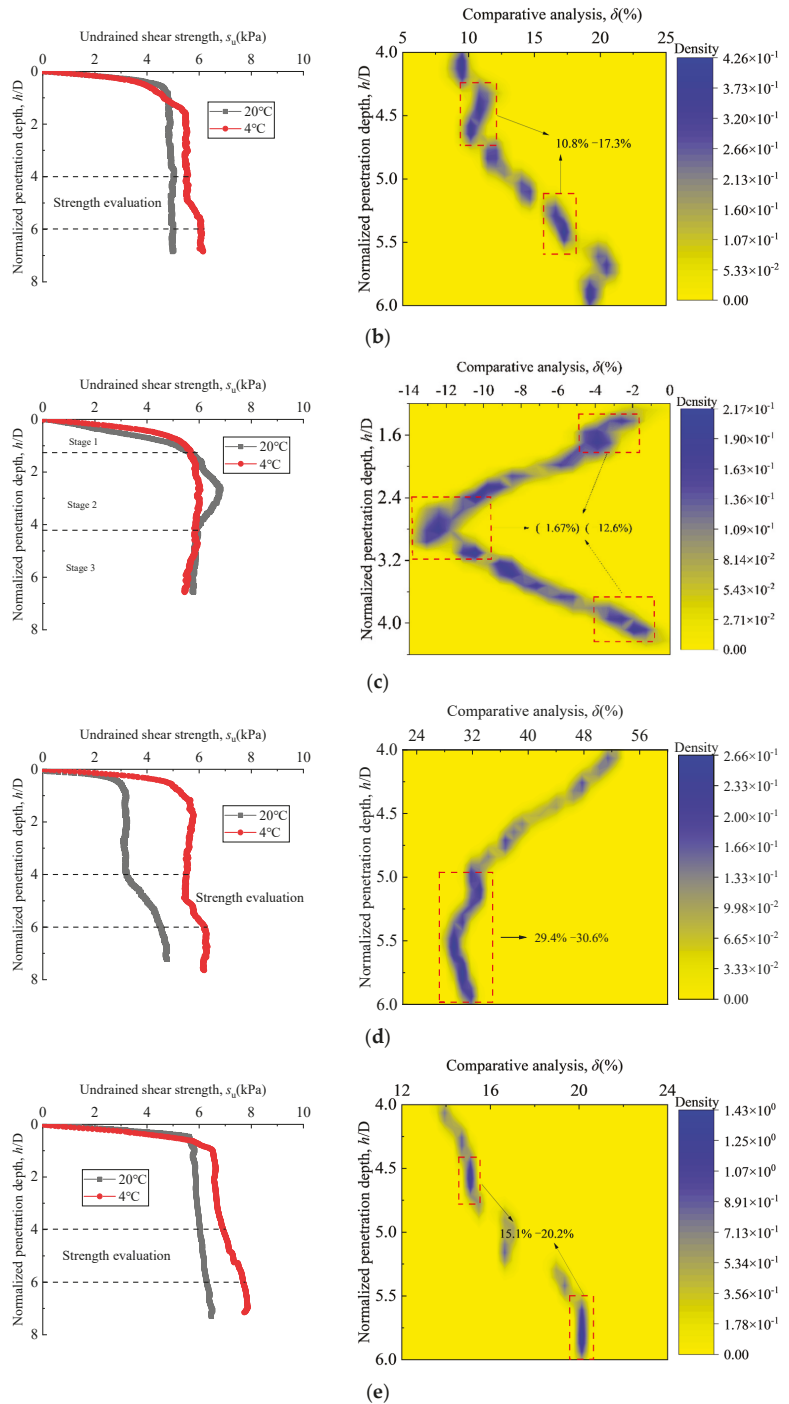


Figure 7. Cont.

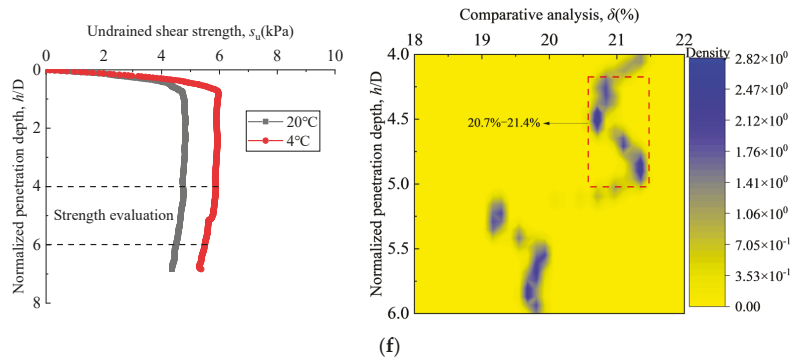


Figure 7. Undrained shear strength and difference in strength caused by temperature for six sediment segments at 20 °C and 4 °C: (a) 0–20 cm sediment segment S1; (b) 50–70 cm sediment segment S2; (c) 100–120 cm sediment segment S3; (d) 150–170 cm sediment segment S4; (e) 200–220 cm sediment segment S5; and (f) 250–270 cm sediment segment S6.

4.2. Strength Difference at Room and Low Temperatures

Figure 7 shows that the s_u values at 20 °C and 4 °C were different. To quantify these differences, two possible factors were analysed, namely, the inhomogeneity of sediment segments and temperature. The inhomogeneity is shown in Figure 7c. For S3, s_u profiles tested at 20 °C and 4 °C were crossed together and divided into three stages. For 0–1.3 D (Stage 1), s_u measured at 4 °C was greater, while for 1.3–4.2 D (Stage 2), it was higher at 20 °C. The values of s_u tested at 20 °C and 4 °C were very close for 4.2–6.6 D (Stage 3). After the penetration tests, this clay segment (i.e., S3) was cut near the 20 °C penetration position. Some sand particles and biological remains were found, as shown in Figure 1b, which caused s_u to be higher at 20 °C in Stage 2. Additionally, sand particles may have been carried into Stage 3, which caused s_u to be higher at 20 °C than at 4 °C in Stage 3. Due to the extreme nonuniformity of S3, the test data were not suitable for the analysis of the temperature effect. The other five sediment segments, S1, S2, S4, S5, and S6, however, were more uniform and suitable.

To quantify the temperature effect on s_u , the following comparative analysis equation was proposed:

$$\begin{cases} \delta = 2 \cdot \frac{s_{u-low} - s_{u-room}}{s_{u-low} + s_{u-room}} \times 100\% & (a) \\ \delta_T = \delta_{ave.} = \frac{\delta_{max} + \delta_{min.}}{2} & (b) \end{cases} \quad (5)$$

where δ is the normalized effect of temperature on s_u , %; s_{u-low} is the s_u measured at 4 °C, kPa; and s_{u-room} is the s_u measured at 20 °C, kPa. The $\delta_{max.}$ and $\delta_{min.}$ can be obtained from Figure 7. It is considered that $\delta_{ave.}$ (i.e., δ_T) is also the normalized effect of temperature on s_u , %, which could eliminate the effect caused by the inhomogeneity of the clay.

Table 3 shows that the result of temperature effect on s_u for the five sediment segments, where can be found that s_u was approximately 14.1–30.0% lower at 20 °C than at 4 °C. In addition, the result is consistent with Gue et al. [16] and Lunne et al. [34]. Note that Gue et al. proposed that s_u (the peak shear stress) would be increased by 15–30% with temperature decreasing from 20 °C to 5 °C, and Lunne et al. pointed out that s_u (the peak shear stress) in the laboratory at 20 °C is 10–20% lower than s_u at in-situ temperature (5 °C).

Table 3. Temperature effect on the undrained shear strength of deep-sea sediment segments.

Clay Segments	Depth (cm)	δ (%)		
		Max.	Min.	Ave. (δ_T)
S1	0–20	17.5	17.1	17.3
S2	50–70	17.3	10.8	14.1
S4	150–170	30.6	29.4	30.0
S5	200–220	20.2	15.1	17.7
S6	250–270	21.4	20.7	21.1

Notes: δ is the normalized effect of temperature on the undrained shear strength (%), which can be obtained by Equation (5a); δ_T is also the normalized effect of temperature on undrained shear strength (%), which could eliminate the effect caused by the inhomogeneity of the clay and can be obtained by Equation (5b).

5. Discussion

As illustrated in Figure 7, a decrease in temperature leads to an increase in the undrained shear strength of the sediment segments. Considering that the sediment segments consist of clay structure and free water, to analyse the mechanism of the influence of temperature on undrained shear strength, the effect of temperature on clay structure and free water are discussed.

5.1. Effect of Temperature on the Clay Sturcture

5.1.1. Effect of Temperature on Clay Particles

According to the principle of thermal expansion and cold contraction, the clay particles should become closer with decreasing temperatures, and the pores among the sediment segments should decrease. Thus, SEM tests [35] at room and low temperatures were conducted to verify this hypothesis. The green coils are drawn with the pores of the sediment samples. By observing the size and quantity of the green circle of the sediment samples under room temperature and low temperature, we can compare and analyse the pore size under room temperature and low temperature. Unfortunately, the changes in the pores of the sediment segments could not be clearly observed with changes in temperature, as shown in Figure 8, which demonstrated that: (1) the effect of temperature on clay particles was too small to be observed; or (2) the effect was not suitable to be observed at this scale. The shrinkage of clay particles caused by a temperature drop of only 16 °C should be very small, so the pore changes could not be clearly observed in the SEM images.

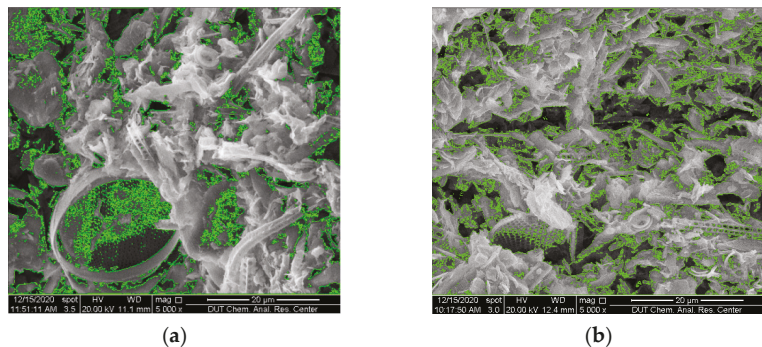


Figure 8. Cont.

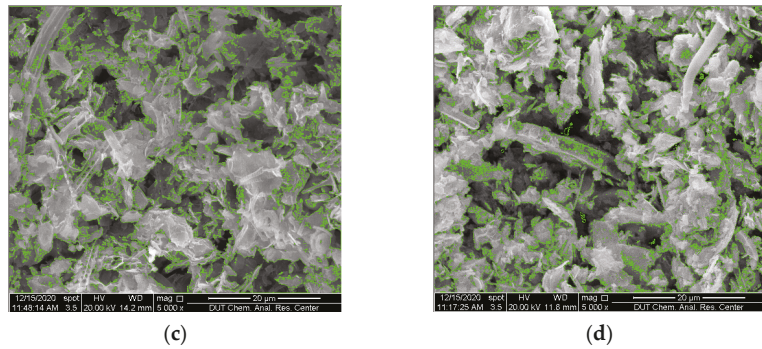


Figure 8. SEM images of the five sediment segments at 20 °C and 4 °C (pores of sediment segments represented by the green outlines): (a) S1 at 20 °C; (b) S1 at 4 °C; (c) S2 at 20 °C; and (d) S2 at 4 °C.

5.1.2. Effect of Temperature on Bound Water

The clay structure includes clay particles and bound water, as illustrated in Figure 9 [36], and the interaction forces between the two are displayed in Figure 10 [37,38]. Clay particles with a negative surface charge attract and collect cations and polar water molecules around them under the influence of electrostatic forces, upon interacting with the pore fluid. The cations and polar water molecules are subjected to three kinds of forces: (1) the electrostatic force, leading to being neatly and closely arranged on the surface of the clay particles; (2) the diffusion force of cations and polar water molecules caused by thermal movement, which leads them to diffuse to the free water layer; and (3) van der Waals forces, as illustrated in Figure 10a.

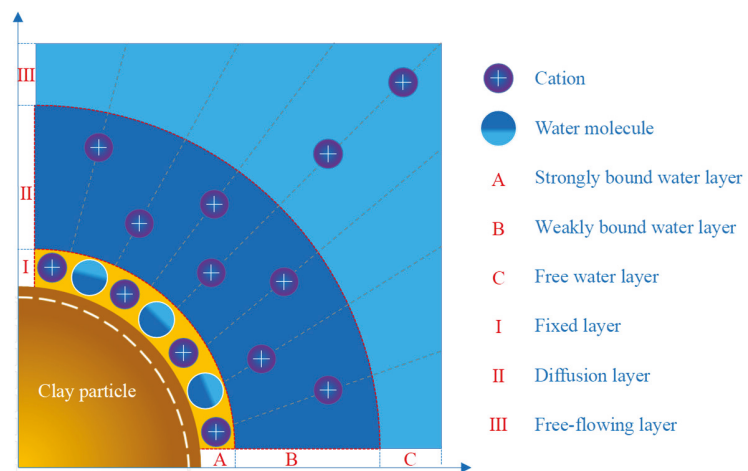


Figure 9. Bound water around a clay particle (reproduced with permission from from Kong et al., Soil Mechanics and Foundations; published by China Electric Power Press: Beijing, China, 2015 [36]).

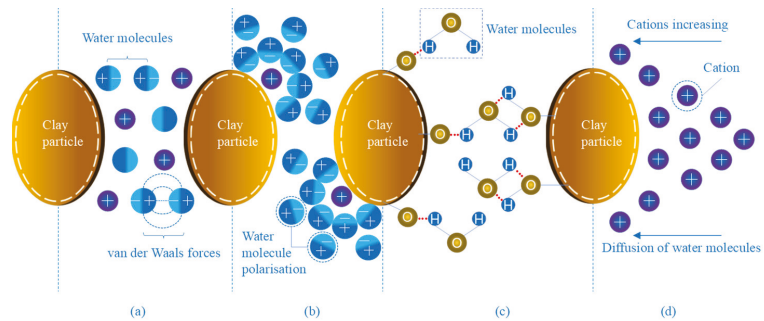


Figure 10. Interaction forces between clay particles and water (reproduced with permission from Li., *Advanced Soil Mechanics*; 2nd ed.; published by Tsinghua University Press: Beijing, China, 2016. [37], and Liu et al., published by *Geotechnics and Soil Mechanics*; published by Science Press: Beijing, China, 2009 [38]).

Likewise, cations can also attract polar water molecules by electrostatic attraction to form hydrated cations, which are capable of transporting water molecules to adsorb on clay particles, as shown in Figure 10b. Furthermore, clay mineral crystal cells are generally exposed to oxygen at the bottom of a silicon–oxygen tetrahedron or hydrogen–oxygen at the bottom of an octahedron, which attract the positive and negative ends of water molecules, respectively, to form hydrogen bonds. As a result, water molecules are attracted to the surfaces of clay particles, as shown in Figure 10c. In addition, as the concentration of cations on the surface of the clay particles increases, the water molecules continue to penetrate and diffuse towards its surface, as depicted in Figure 10d.

As shown in Figure 10, the electrostatic force is the most important force between clay particles and water molecules in the strongly bound layer, while penetration and van der Waals forces gradually become the main forces in the weakly bound water layer. In strongly bound water layers, as the temperature decreases from 20 °C to 4 °C, the thermal movement of cations and water molecules in the pore fluid decreases, which leads to a decrease in the diffusion tendency. Therefore, the distance between cations or water molecules and clay particles becomes shorter, which leads to an increase in electrostatic forces. Many scholars have already illustrated that the hydrogen bonds between water molecules and clay particles become stronger with decreasing temperature [39,40]. Similarly, in weakly bound water layers, lower temperatures increase the van der Waals force between polarized molecules [41]. Therefore, it can be inferred that the strength of bond water in the clay structure increases with decreasing temperature, which in turn represents an increase in the undrained shear strength of the sediment segments.

5.2. Effect of Temperature on Free Water

Free water is a typical Newtonian fluid whose viscosity increases rapidly as the temperature decreases. It shows a 54.5% increase in water viscosity as the temperature decreases from 20 °C to 4 °C according to Guo et al. [42]. Considering that the penetration tests in this study were performed under undrained conditions, it is reasonable to infer that the undrained shear strength of sediment segments increases with increasing viscosity of water, which explains the increase in undrained shear strength at low temperatures.

5.3. Summary of the Temperature Effect Mechanism

Through the above analysis, it can be determined that the clay structure and free water are affected when the temperature is reduced from 20 °C to 4 °C. In the clay structure, the volume change in clay particles is too small to be observed with the decrease in temperature, but the strength of bound water is improved due to the increases in electrostatic forces, van der Waals forces, and hydrogen bonds. In free water, the viscosity of water increases

rapidly with decreasing temperature. For these two reasons, the undrained shear strength of the sediment segments increases at low temperatures.

6. Conclusions

For the deep-sea clay samples from the South China Sea, the basic physical parameters of sediment segments were first determined, and then six penetration tests were performed by the mini-ball method at low (4 °C) and room (20 °C) temperatures. Finally, the mechanism of the influence of temperature on the undrained shear strength of the sediment segments was revealed. The main conclusions are as follows:

- (1) The undrained shear strength of the sediment segments tested by the mini-ball method showed a 14.1–30.0% increase with decreasing temperature from 20 °C to 4 °C, which was consistent with the research of Gue et al. and Lunne et al.;
- (2) In the clay structure, both the clay particles and the bound water were affected by temperature. As the temperature decreased from 20 °C to 4 °C, based on SEM tests, the clay particles were less affected by temperature. However, the increases in electrostatic forces, hydrogen bonds between the clay particles and water molecules, and van der Waals forces between the water molecules led to an increase in the strength of the bound water, which was manifested as an increase in the undrained shear strength of the clay;
- (3) The free water in sediment segments was also affected by temperature. As the temperature decreased from 20 °C to 4 °C, the viscosity of the free water increased by 54.5%, which increased the undrained shear strength of the sediment segments.

Author Contributions: Conceptualization, T.N. and Z.G.; formal analysis, Z.G., X.G. and T.N.; investigation, T.N. and X.G.; resources, Y.J. and T.N.; data curation, Z.G., X.G. and H.J.; writing—original draft preparation, Z.G., X.G. and H.J.; writing—review and editing, X.G. and H.J.; supervision, T.N. and Y.J.; funding acquisition, T.N. and Y.J. All authors have read and agreed to the published version of the manuscript.

Funding: This research was funded by the National Key Research and Development Program of China (No. 2018YFC0309200) and the National Natural Science Foundation of China (Nos. 41831280, 51879036, and 52079020).

Institutional Review Board Statement: Not applicable.

Informed Consent Statement: Not applicable.

Data Availability Statement: Not applicable.

Acknowledgments: We thank Wei Zhao provided the Mini-ball and the help of Hao Zhang, Xinchang Liao, and Guodong Wang in the experiments.

Conflicts of Interest: The authors declare no conflict of interest.

References

1. Guo, X.; Nian, T.; Wang, D.; Gu, Z. Evaluation of undrained shear strength of surficial marine clays using ball penetration-based CFD modelling. *Acta Geotech.* **2022**, *17*, 1627–1643. [[CrossRef](#)]
2. Fan, N.; Jiang, J.; Dong, Y.; Guo, L.; Song, L. Approach for evaluating instantaneous impact forces during submarine slide-pipeline interaction considering the inertial action. *Ocean Eng.* **2022**, *245*, 110466. [[CrossRef](#)]
3. Nian, T.; Guo, X.; Fan, N.; Jiao, H.; Li, D. Impact forces of submarine landslides on suspended pipelines considering the low-temperature environment. *Appl. Ocean Res.* **2018**, *81*, 116–125. [[CrossRef](#)]
4. Amon, D.; Gobin, J.; Van Dover, C.; Levin, L.; Marsh, L.; Raineault, N. Characterization of methane-seep communities in a deep-sea area designated for oil and natural gas exploitation off Trinidad and Tobago. *Front. Mar. Sci.* **2017**, *4*, 342. [[CrossRef](#)]
5. Guo, X.; Stoesser, T.; Nian, T.; Jia, Y.; Liu, X. Effect of pipeline surface roughness on peak impact forces caused by submarine mudflow. *Ocean Eng.* **2022**, *243*, 110184. [[CrossRef](#)]
6. Al-Umar, M.; Fall, M.; Daneshfar, B. GIS-based modelling of snowmelt-induced landslide susceptibility of sensitive marine clays. *Geoenviron. Disasters* **2020**, *7*, 9. [[CrossRef](#)]
7. Nian, T.; Shen, Y.; Zheng, D.; Lei, D. Research advances on the chain disasters of submarine landslides. *J. Eng. Geol.* **2021**, *29*, 1657–1675.

8. Nian, T.; Song, X.; Zhao, W.; Jiao, H.; Guo, X. Submarine slope failure due to overpressure fluid associated with gas hydrate dissociation. *Environ. Geotech.* **2020**, *9*, 108–123. [[CrossRef](#)]
9. Fu, C.; Nian, T.; Guo, X.; Gu, Z.; Zheng, D. Investigation on responses and capacity of offshore pipelines subjected to submarine landslides. *Appl. Ocean Res.* **2021**, *117*, 102904. [[CrossRef](#)]
10. Guo, X.; Nian, T.; Zhao, W.; Gu, Z.; Liu, C.; Liu, X.; Jia, Y. Centrifuge experiment on the penetration test for evaluating undrained strength of deep-sea surface soils. *Int. J. Min. Sci. Technol.* **2022**, *32*, 363–373. [[CrossRef](#)]
11. Coffin, S.; Weisberg, S.; Rochman, C.; Kooi, M.; Koelmans, A. Risk Characterization of Microplastics in San Francisco Bay, California. *Microplast. Nanoplast.* **2022**, *2*, 9. [[CrossRef](#)]
12. Lunne, T. The CPT in offshore soil investigations—a historic perspective. In Proceedings of the 2nd International Symposium on Cone Penetration Testing, Huntington Beach, CA, USA, 9–11 May 2010.
13. Jin, C.; Wang, J. A preliminary study of the gas hydrate stability zone in the South China Sea. *Acta Geol. Sin.-Engl. Ed.* **2002**, *76*, 423–428. [[CrossRef](#)]
14. Mitchell, J. Shearing resistance of soils as a rate process. *J. Soil Mech. Found. Div.* **1964**, *90*, 29–61. [[CrossRef](#)]
15. Perkins, S.; Sjørnsen, M. Effect of cold temperatures on properties of unfrozen Troll clay. *Can. Geotech. J.* **2009**, *46*, 1473–1481. [[CrossRef](#)]
16. Gue, C.; Lunne, T.; Perkins, S. Temperature effects on laboratory measured strength on deep water soft clays. In *Frontiers in Offshore Geotechnics III, Proceedings of the 3rd International Symposium on Frontiers in Offshore Geotechnics (ISFOG 2015)*; Taylor & Francis Books Ltd.: Abingdon, UK, 2015; Volume 1, pp. 1055–1060.
17. Kelleher, P.; Randolph, M. Seabed geotechnical characterization with a ball penetrometer deployed from the portable remotely operated drill. In Proceedings of the International Symposium on Frontiers in Offshore Geotechnics (ISFOG), Perth, WA, Australia, 19–21 August 2005; pp. 365–371.
18. Yafraate, N.; DeJong, J.; DeGroot, D.; Randolph, M. Evaluation of remoulded shear strength and sensitivity of soft clay using full-flow penetrometers. *J. Geotech. Geoenviron. Eng.* **2009**, *135*, 1179–1189. [[CrossRef](#)]
19. Low, H.; Randolph, M.; Lunne, T.; Andersen, K.; Sjørnsen, M. Effect of soil characteristics on relative values of piezocone, T-bar and ball penetration resistances. *Géotechnique* **2011**, *61*, 651–664. [[CrossRef](#)]
20. Lunne, T.; Andersen, K.; Low, H.; Randolph, M.; Sjørnsen, M. Guidelines for offshore in situ testing and interpretation in deepwater soft clays. *Can. Geotech. J.* **2011**, *48*, 543–556. [[CrossRef](#)]
21. DeJong, J.; Yafraate, N.; DeGroot, D.; Low, H.; Randolph, M. Recommended practice for full-flow penetrometer testing and analysis. *Geotech. Test. J.* **2010**, *33*, 137–149. [[CrossRef](#)]
22. DeJong, J.; Yafraate, N.; DeGroot, D. Evaluation of undrained shear strength using full-flow penetrometers. *J. Geotech. Geoenviron. Eng.* **2011**, *137*, 14–26. [[CrossRef](#)]
23. Long, M.; Colreavy, C.; Ward, D.; Quigley, P. Piezoball tests in soft Irish clays. In Proceedings of the 3rd International Symposium on Cone Penetration Testing, Las Vegas, NV, USA, 13–14 May 2014; Volume 14.
24. Stewart, D. A new site investigation tool for the centrifuge. In Proceedings of the International Conference Centrifuge 91, Boulder, Colorado, 13–14 January 1991.
25. Stewart, D.; Randolph, M. T-bar penetration testing in soft clay. *J. Geotech. Eng.-ASCE* **1994**, *120*, 2230–2235. [[CrossRef](#)]
26. Randolph, M.; Hefer, P.; Geise, J.; Watson, P. Improved seabed strength profiling using T-bar penetrometer. In *Offshore Site Investigation and Foundation Behaviour: New Frontiers, Proceedings of the International Conference, London, UK, 22–24 September 1998*; Society of Underwater Technology: London, UK, 1998.
27. *GB/T 50145-2007*; Standard for Engineering Classification of Soil. China National Standards: Beijing China, 2007.
28. *ASTM D2487-00*; Standard Practice for Classification of Soils for Engineering Purposes (Unified Soil Classification System). American Society for Testing and Materials (ASTM): West Conshohocken, PA, USA, 2000.
29. Lehane, B.; O’loughlin, C.; Gaudin, C.; Randolph, M. Rate effects on penetrometer resistance in kaolin. *Géotechnique* **2009**, *59*, 41–52. [[CrossRef](#)]
30. Zhou, M.; Hossain, M.; Hu, Y.; Liu, H. Behaviour of ball penetrometer in uniform single-and double-layer clays. *Géotechnique* **2013**, *63*, 682–694. [[CrossRef](#)]
31. Martin, C.; Randolph, M. Upper-bound analysis of lateral pile capacity in cohesive soil. *Géotechnique* **2006**, *56*, 141–145. [[CrossRef](#)]
32. Nguyen, T.; Chung, S. Ball penetration test for characterization of soft clays. *Proc. Inst. Civ. Eng.-Geotech. Eng.* **2018**, *171*, 133–146. [[CrossRef](#)]
33. Liu, J.; Chen, X.; Han, C.; Wang, X. Estimation of intact undrained shear strength of clay using full-flow penetrometers. *Comput. Geotech.* **2019**, *115*, 103161. [[CrossRef](#)]
34. Lunne, T.; Gue, C.; Perkins, S.; Selvig, M. Temperature effects on laboratory strength measured on soft clays sampled in deepwater and cold environments. In *Offshore Site Investigation and Geotechnics: Integrated Technologies—Present and Future*; Society of Underwater Technology: London, UK, 2012.
35. Nian, T.; Jiao, H.; Fan, N.; Guo, X. Microstructure analysis on the dynamic behavior of marine clay in the South China Sea. *Mar. Geores. Geotechnol.* **2020**, *38*, 349–362. [[CrossRef](#)]
36. Kong, J.; Gao, X.; Xiao, J.; Wei, H.; Tian, H.; Sun, J.; Lv, C. *Soil Mechanics and Foundations*; China Electric Power Press: Beijing, China, 2015.
37. Li, G. *Advanced Soil Mechanics*, 2nd ed.; Tsinghua University Press: Beijing, China, 2016.

38. Liu, G.; Liu, H.; Gong, X.; Zhang, J. *Geotechnics and Soil Mechanics*; Science Press: Beijing, China, 2009.
39. Muller, N.; Reiter, R. Temperature dependence of chemical shifts of protons in hydrogen bonds. *J. Chem. Phys.* **1965**, *42*, 3265–3269. [[CrossRef](#)]
40. Raiteri, P.; Laio, A.; Parrinello, M. Correlations among hydrogen bonds in liquid water. *Phys. Rev. Lett.* **2004**, *93*, 087801. [[CrossRef](#)]
41. Parsegian, V.; Ninham, B. Temperature-dependent van der Waals forces. *Biophys. J.* **1970**, *10*, 664–674. [[CrossRef](#)]
42. Guo, X.; Nian, T.; Wang, Z.; Zhao, W.; Fan, N.; Jiao, H. Low-temperature rheological behaviour of submarine mudflows. *J. Waterw. Port Coast. Ocean Eng.* **2020**, *146*, 04019043. [[CrossRef](#)]

Article

High-Frequency Dependence of Acoustic Properties of Three Typical Sediments in the South China Sea

Jingqiang Wang¹, Zhengyu Hou^{2,3,*}, Guanbao Li^{1,4}, Guangming Kan^{1,4}, Baohua Liu^{4,5}, Xiangmei Meng^{1,4}, Qingfeng Hua¹ and Lei Sun¹

- ¹ Key Laboratory of Marine Geology and Metallogeny, First Institute of Oceanography, MNR, No. 6 Xianxialing Road, Qingdao 266061, China
 - ² School of Ocean Engineering and Technology, Sun Yat-sen University, Zhuhai 519000, China
 - ³ Key Laboratory of Ocean and Marginal Sea Geology, Key Laboratory of Science and Technology on Operational Oceanography, South China Sea Institute of Oceanology, Chinese Academy of Sciences, Guangzhou 510301, China
 - ⁴ Laboratory for Marine Geology, Qingdao National Laboratory for Marine Science and Technology, No. 1 Wenhai Road, Jimo City, Qingdao 266237, China
 - ⁵ National Deep Sea Center, Ministry of Natural Resources (MNR), No. 1 Weiyang Road, Jimo City, Qingdao 266237, China
- * Correspondence: zyhou2022@163.com

Abstract: The acoustic characteristics of three fine-grained sediments (silty sand, silt, silty clay) in the South China Sea (SCS) were measured and analyzed at high frequency range of 27–247 kHz. The measurement results show that the sound speed dispersion is a positive linear relation at the measured frequency range, and the attenuation follows nonlinear frequency dependence, $\alpha = kj^n$, where n ranges from 0.59 to 0.85 for the three different sediments in the SCS. The frequency dependence of sound speed and attenuation were compared with the published literature. It was found that for silty clay, clayey silt, silt, and silty sand, the dispersion characteristics of these four sediments are basically consistent; in general, the dispersion of coarse particles is significant, and that of fine particles is weak, and permeability is the key parameter that determines the inflection point of high frequency to low frequency. By modeling these sediments with the Biot–Stoll model, it was found that the Biot–Stoll model can better predict the frequency-dependent characteristics of sound attenuation in a high-frequency band under the matching constraints of sound speed dispersion characteristics, indicating that the Biot–Stoll model has good applicability to different types of sediments in a high-frequency band.

Keywords: sediment acoustic; frequency dependence; sound speed; attenuation; Biot–Stoll model

Citation: Wang, J.; Hou, Z.; Li, G.; Kan, G.; Liu, B.; Meng, X.; Hua, Q.; Sun, L. High-Frequency Dependence of Acoustic Properties of Three Typical Sediments in the South China Sea. *J. Mar. Sci. Eng.* **2022**, *10*, 1295. <https://doi.org/10.3390/jmse10091295>

Academic Editor: Anabela Oliveira

Received: 7 July 2022

Accepted: 11 August 2022

Published: 14 September 2022

Publisher's Note: MDPI stays neutral with regard to jurisdictional claims in published maps and institutional affiliations.



Copyright: © 2022 by the authors. Licensee MDPI, Basel, Switzerland. This article is an open access article distributed under the terms and conditions of the Creative Commons Attribution (CC BY) license (<https://creativecommons.org/licenses/by/4.0/>).

1. Introduction

Seafloor sediment is a kind of solid-liquid two-phase medium, mainly composed of solid particles and pore fluid. The acoustic propagation characteristics of seafloor sediments have been an important research topic in hydro-acoustics, geophysics, and other disciplines [1,2].

As early as in the 1950s, Gassmann (1951) first proposed the Gassmann theory, which can quantitatively reflect the relationship between velocity and porosity [3]. In 1956, Biot described a three-variable model of porous solids and free and trapped fluids based on the theory with mass coupled terms [4]. Subsequently, Biot developed Gassmann's theory of a fluid-saturated porous two-phase medium based on the potential characteristics of moist soil and the absorption characteristics of acoustic waves, which laid the foundation of the wave theory of two-phase media. The Biot theory fully considers the dual-phase characteristics of porous media, discovers the second type of longitudinal waves (slow p-waves), and points out that the relative motion in pore fluid controlled by viscous force

is an important mechanism for the attenuation of elastic waves during the propagation of porous media.

The Biot theory indicates that the significant frequency band of sound speed dispersion in water-saturated sediments is 1–10 kHz. At low frequencies, attenuation is proportional to the square of frequency; at high frequencies, attenuation is proportional to the square root of the frequency. Hamilton gave an empirical formula for the sound speed and attenuation of seafloor sediments and sediment type and frequency, and he pointed out that the sound speed dispersion is very weak and can be ignored [5]; in the frequency range from a few hertz to megahertz, the attenuation is approximately proportional to the frequency. However, a large number of subsequent sampling measurements and in situ measurement experiments show that the sound speed also has a dispersion phenomenon.

Subsequently, Stoll applied the Biot theory to seafloor sediments and established the Biot–Stoll model [6], which considered that the solid particles in the sediment were attached to the pore water as an elastic “frame” and introduced the frame loss. Compared with the fluid model and the viscoelastic model, the model predicts the sound speed and attenuation coefficient in the sandy sediment more accurately and can better describe the characteristics of sound speed dispersion. Williams (2001) developed the effective density fluid model (EDFM) model, considering that the frame moduli are far smaller than the grain moduli and the fluid moduli [7], and if the frame moduli can be set to zero, the sediment is approximated as a fluid medium represented by an equivalent density, which reduces the 13 parameters involved in the Biot–Stoll model to 9; and in soft sediments, such as mud or fine sand, the reflection losses predicted by the EDFM model agree well with the Biot–Stoll model.

Considering the widespread attenuation, the Biot theory has received in the seafloor acoustics field, relatively little has been reported regarding conform of its validity [8]. Hovem and Ingram [9] used glass beads in their experiments and showed that in the frequency range 20–300 kHz the results are good agreement with the Biot theory. Simpson et al. [10] reported the field measurements of sandy sediments supporting the Biot theory over the 3–80 kHz frequency band. The measurements results appear consistent with the Biot model, but attenuation is essentially a linear frequency dependence in the measurement frequency band. In the SAX99 offshore experiment [1], the sound speed of sandy sediments in the 125–400 kHz frequency band and the attenuation of sandy sediments in the 2.6–400 kHz frequency band were obtained using an in-situ system, and the results showed that the sound speed dispersion in the frequency range from 25 to 100 kHz is weak, which is consistent with the Biot theory; the attenuation is approximately linear with the frequency, and the deviation above 50 kHz deviates from the Biot theory. Ragione et al. [11] reported a study based upon a micro-mechanics analysis to support the presence of both slow and fast compression waves in different materials. Buckingham [12] developed the viscous grain shearing model (VGS) based on grain-to-grain contacts in sediments. The VGS model has been used to compare with the Biot theory. The major feature of the Biot theory in the high-frequency band is to predict the frequency dependence of the sound speed and attenuation [13] (Bonomo and Isakson, 2018). Holmes et al. [14] reviewed a large number of attenuation data, arguing that the attenuation of sandy sediments varies with frequency. Sesarego et al. [15] measured the sound speed and attenuation of sandy sediments in the 0.5 to 1.3 MHz frequency band in a laboratory setting. Attenuation varies nonlinearly with frequency and sound speed, and attenuation data are inconsistent with the Biot theory, possibly caused by solid particle volumetric scattering. Yu et al. [16] obtained the sound speed and attenuation of fine sand in the 90–170 kHz frequency band in a laboratory water tank. The results showed that the sound speed dispersion of the sand sample is very weak, and consistent with the Biot–Stoll model, and the attenuation is approximately proportional to $f^{0.35}$, but higher than that predicted by the model, possibly due to the additional sound attenuation caused by the internal inhomogeneity of the sediment samples. The above studies focused on the coarse sediments, such as sandy sediment, but few studied on the fine-grained sediments acoustic properties.

In this paper, three fine-grained sediments in the South China Sea (SCS) were statistically analyzed, and their high-frequency acoustic properties were measured, and the high-frequency dependence of acoustic properties of the three sediments in the SCS was analyzed and compared using Biot–Stoll model.

2. Study Area and Method

In this paper, historical data of acoustic properties of seafloor sediments in the SCS are collected. The study area is located in the northern shelf and continental slope of the SCS, with a water depth ranging from 113 m to 1271 m. The northern continental shelf of the SCS is dominated by terrigenous clastic deposits, and there are four main types of sediments. Their distribution and characteristics are as follows: (1) Gravely sands are mainly distributed on the continental shelf south of the Pearl River Estuary, among which bioclasts are more common. (2) Sandy sediments are mainly distributed on the middle and outer continental shelves east of 116° E with a water depth of 50–200 m. This region has the characteristics of gradually thickening from west to east, and the sandy sediments near the 200 m water depth of the outer shelf front east of 113° E are the products of the early high-energy coastal zone. The rest are mainly distributed in the Beibu Gulf–Indochina Peninsula coastal estuary and the western and southwestern coastal shelf areas of Hainan Island. (3) Clay silt sediments are mainly distributed parallel to the coast. (4) The silty clay sediments are mainly distributed on the vast middle and outer continental shelves with a water depth of 50–200 m in the west of the Pearl River Estuary and are distributed in sheets or strips. The types of sediments in this area include silty clay, clay silt, silt, silty sand, sandy silt, and clay sand. From 2016 to 2018, the First Institute of Oceanography of the Ministry of Natural Resources and the South China Sea Institute of Oceanography of the Chinese Academy of Sciences carried out continuous measurement of the acoustic properties of seafloor sediments in the northern of the SCS. In this paper, three fine-grained sediments are selected to carry out high-frequency-dependent characteristic analysis, they are the sediment types with representative physical properties and obvious differences in the study area, including 37 stations of silty clay sediment samples, 31 stations of silty sediment samples, and 12 stations of silty sand sediment samples. All these sediments are collected by gravity sampler and acoustic properties are measured in the top 0.3 m of the sediment cores.

2.1. Laboratory Measurement Method

The whole measurement system consists of an acoustic measuring platform, a power amplifier, a self-developed acoustic transmitter/receiver instrument (ATRI), a prefilter amplifier, and transmitting and planar acoustic transducers with different frequencies. The ATRI is used to drive the transmitting transducer and receive the acoustic wave. The power amplifier is used to excite the transmitting acoustic signals. The prefilter amplifier is used to excite the receiving acoustic signals. The technical parameter of ATRI system is listed as follows:

- Number of acquisition channels: 2 channels;
- Sampling rate: up to 16 MHz, configurable by software;
- Sampling length: 10 ms;
- Sampling rate: 16 MHz;
- Resolution: 16 bit;
- Storage method: computer storage;
- Transmitting channel: 1 channel;
- Transmission frequency: 20 Hz~1 MHz, adjustable;
- Transmission waveform: sine wave, PCW, etc., the period is adjustable.

Before starting the measurement, all equipment was connected as shown in Figure 1 and place the sediment cores on the acoustic measuring platform. The sediment core length was measured with accuracy of ± 0.1 mm by the measuring platform, and the sound wave sampling rate was 16 MHz by the acoustic instrument, so that the accuracy of the sound

speed was estimated to be better than $\pm 0.1\%$ for a typical sample with a length of 30 cm and the sound speed of 1500 m/s. The sound speed and attenuation were measured at the frequencies of 27, 51, 111, 214, and 247 kHz, respectively. The waveforms of sound signals at different frequencies recorded by the acoustic system are shown in Figure 2. The measurement was conducted in the standard condition (standard atmospheric pressure, 23°), and under the standard laboratory conditions the laboratory measurements can be corrected to the in situ condition by using sound speed ratio method [17]. The details of the acoustic measurements can be found in Hou et al. [18] Section 2 and Figure 2.



Figure 1. Laboratory measurement system.

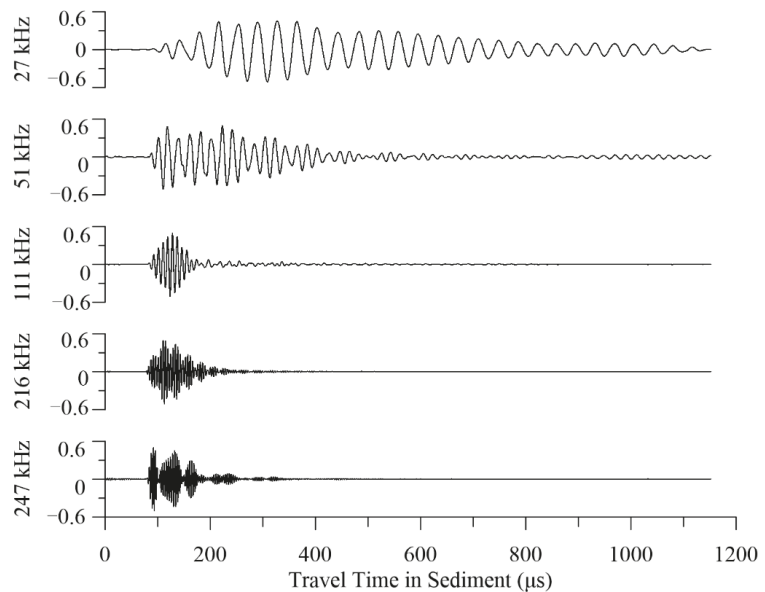


Figure 2. The waveforms of sound signals at different frequencies recorded by the acoustic system.

2.2. Biot–Stoll Model

In Biot–Stoll’s theory, sediment is regarded as a two-phase system composed of solid particles and pore water. Under the action of sound waves, the two displacements are different. Sediment particles are coupled with pore water as an elastic frame, and this coupling generates three types of wave fields from the interactions between the compression wave in the pore water, and the compression and shear wave in the elastic solid frame.

The Biot–Stoll model involves 13 parameters [19]: Porosity n , Grain bulk modulus K_g , Fluid dynamic viscosity η , Grain density ρ_s , Fluid density ρ_f , Fluid bulk modulus K_f , Permeability κ , Tortuosity α , Pore size a , Dissipative Skeletal Bulk Modulus K_0 , Dissipative Skeletal Shear Modulus μ_0 , Bulk dissipation factor δ_k , and Shear dissipation factor δ_μ .

The longitudinal wave equation of Biot–Stoll is:

$$\nabla^2(H\varepsilon - C\zeta) = \frac{\partial^2}{\partial t^2}(\rho\varepsilon - \rho_f\zeta) \tag{1}$$

$$\nabla^2(C\varepsilon - M\zeta) = \frac{\partial^2}{\partial t^2}(\rho_f\varepsilon - m\zeta) - \frac{F\eta}{\kappa} \frac{\partial \zeta}{\partial t} \tag{2}$$

$$\varepsilon = \nabla \bullet \mathbf{u} \tag{3}$$

$$\zeta = n \nabla \bullet (\mathbf{u} - \mathbf{U}) \tag{4}$$

$$\rho = (1 - n)\rho_s + n\rho_f \tag{5}$$

where the \mathbf{u} and \mathbf{U} are the skeleton and pore fluid displacement vectors, respectively. The Biot elastic moduli \mathbf{H} , \mathbf{C} , and \mathbf{M} are expressed as the bulk modulus of the framework, the bulk modulus of the pore fluid, and the bulk modulus of the particles, respectively:

$$\mathbf{H} = \frac{(K_g - K_b)^2}{D - K_b} + K_b + \frac{4\mu}{3} \tag{6}$$

$$\mathbf{C} = K_g \frac{(K_g - K_b)}{D - K_b} \tag{7}$$

$$\mathbf{M} = \frac{K_g^2}{D - K_b} \tag{8}$$

$$D = K_g \left[1 + n \frac{K_g}{K_f - 1} \right] \tag{9}$$

where K_b and μ are Skeletal bulk modulus and shear modulus, which are complex constants:

$$K_b = K_b(1 + i\delta_k) \tag{10}$$

$$\mu = \mu_0(1 + i\delta_\mu) \tag{11}$$

The dispersion relations for the fast and slow waves corresponds to the roots of the following determinant system:

$$\begin{vmatrix} Hl^2 - \rho\omega^2 & \rho_f\omega^2 - Cl^2 \\ Cl^2 - \rho_f\omega^2 & m\omega^2 - Ml^2 - i\frac{\omega F\eta}{\kappa} \end{vmatrix} = 0 \tag{12}$$

$$l = l_r - j\alpha = \frac{\omega}{V} - j\alpha \tag{13}$$

$$\omega = 2\pi f \tag{14}$$

where l is the complex wave number. Once the roots of above equations are found, the compressional wave speed and attenuation can be expressed as:

$$V_p = \frac{1}{Re\sqrt{l_1}} \tag{15}$$

$$\alpha_p = -\text{Im}(l_1) \tag{16}$$

where l_1 is the root with a negative imaginary component and the smaller real component.

3. Results and Discussion

3.1. Measured Data

The average measured sound speed and attenuation at different frequencies for different sediment types including the ones from the three study areas are shown in Table 1. Figure 3 shows the sound speed dispersion of different sediments and the sound speed dispersion empirical formulas. The results show that the sound speed dispersion is a positive linear relation, $V_p = kf + b$, and the slope k changes with the sediment types and sedimentary environment. In SCS, the lowest slope is the silty clay sediment, $k = 0.0658$, and the highest slope is the silty sand, $k = 0.0956$. It is evident that in SCS, the slope k is related with the grain size, and when the grain size increased, the slope k increased. The slope k of clayey silt in Western Pacific (WP) is 0.0614, and the dispersion curve of WP has the similar trend with the SCS.

Table 1. The measured sound speed and attenuation at different frequencies.

Study Area	Sediment Type	Range	Sound Speed (m/s)					Attenuation (dB/m)				
			27 kHz	51 kHz	111 kHz	214 kHz	247 kHz	27 kHz	51 kHz	111 kHz	214 kHz	247 kHz
South China Sea	Silty sand	Maximum	1641.13	1637.64	1643.92	1657.43	1671.05	29.99	42.01	59.24	78.71	112.05
		Minimum	1576.70	1586.23	1591.61	1586.86	1598.36	5.72	17.30	36.46	43.99	59.01
		Mean	1609.17	1616.43	1622.47	1627.38	1634.16	14.42	25.1	42.6	54.12	75.81
	Silt	Maximum	1568.66	1568.77	1574.62	1580.10	1583.05	27.9	35.0	37.14	51.7	75.5
		Minimum	1529.86	1527.96	1537.80	1539.12	1547.14	9.83	14.9	16.9	20.9	26.09
		Mean	1546.16	1550.56	1555.20	1560.32	1565.04	11.13	16.7	22.3	36.04	45.89
Silty clay	Maximum	1461.18	1468.78	1469.51	1475.72	1474.19	6.06	18.5	24.52	40.6	65.87	
	Minimum	1439.92	1442.96	1453.8	1453.74	1458.77	2.97	9.3	8.09	16.05	18.55	
	Mean	1451.19	1454.56	1459.20	1464.30	1466.7	4.25	10.7	13.3	26.22	35.45	
Western Pacific	Clayey silt	Maximum	1511.06	1512.11	1512.89	1515.71	1520.28	26.15	28.58	36.48	58.46	64.11
		Minimum	1495.53	1497.86	1499.06	1501.49	1505.79	18.19	22.58	28.91	34.15	39.19
		Mean	1503.28	1501.76	1504.08	1510.88	1516.96	22.38	24.21	33.57	42.36	49.59

The degree of dispersion is used to describe the frequency dispersion of sound velocity, defined as by subtracting the minimum from the maximum sound speed and then dividing by the minimum sound velocity. The dispersion curves of the SCS and WP sediments are almost parallel, the frequency dispersion degree of the four sediments is 1.0687% (silty clay), 1.0121% (clayey silt), 1.22% (silt), and 1.5529% (silty sand), respectively. From the slope k and dispersion degree, the SCS and WP sediments have little sound speed dispersion in the measured frequencies.

Williams et al. [1] believed that the grain modulus and porosity affect the sound speed dispersion over the frequency range, the permeability affects the sound speed dispersion in the middle frequency range from 10 kHz to 50 kHz, and the tortuosity affects the sound speed dispersion in the high frequency above 50 kHz. For our measurement frequency range, the four factors are all related with our measurement results, and the dispersion degree is a comprehensive reflection of these parameters. Figure 3 also shows that for silty clay, clayey silt, silt, and silty sand, the dispersion characteristics of these four sediments are basically consistent.

The tortuosity is closely related with the grain size, when the mean grain size is between 4 and 8 (ϕ), which is the average particle size of fine-grained sediment, the tortuosity is calculated by $\alpha = -0.3 + 0.412 \phi$; that is to say, the tortuosity changes linearly with grain size. The average porosity of the four sediments (silty clay, clayey silt, silt, and silty sand) is 0.694, 0.663, 0.550, and 0.482, respectively, and the general trend is that

porosity gradually decreases with particle size. Although the mean grain size of silty clay and clayey silt is similar, the permeability of clayey silt is order of magnitude less than silty clay, which may be the reason why the dispersion characteristics of clayey silt are smaller than that of silty clay.

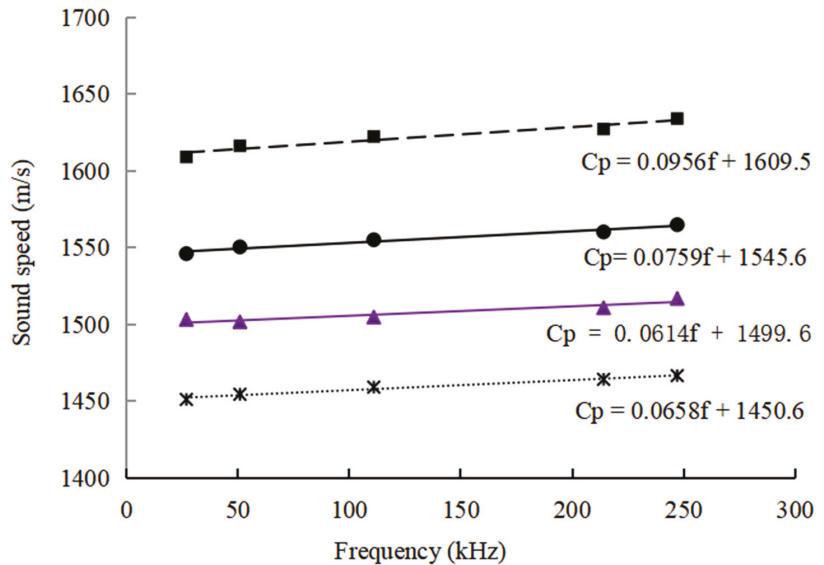


Figure 3. The sound speed dispersion of different sediments. The black ■ dots are silty sand, the black ● dots are silt, the black * dots are silty clay in SCS, and the purple ▲ is clayey silt in WP.

Figure 4 shows the attenuation dispersion of different sediments and the attenuation dispersion empirical formulas. It is shown that the attenuation follows a power-law frequency dependence, $\alpha = kf^n$, and the n value of the four sediments is 0.35 (clayey silt), 0.59 (silt), 0.68 (silty sand), and 0.87 (silty clay), respectively. The attenuation of silty clay is the lowest in the four sediments, but the attenuation dispersion is the highest. Although silty clay in SCS and clayey silt in WP have similar particle size and porosity, their attenuation dispersion characteristics are quite different, the attenuation of clayey silt is the lowest in the four sediments ($n = 0.35$). This phenomenon also shows that attenuation is affected by many factors, and sediment attenuation characteristics in different regions are different. Hamilton (1972) consistently maintained that the frequency dependence of attenuation in sediments obeys an f^1 dependence, while according to the Biot–Stoll model, the attenuation coefficient deviates from a first-power dependence on frequency and varies as the square root of frequency ($f^{1/2}$) at the high frequencies. According to our actual measurement results, attenuation is affected by many factors, such as the sediment types and sedimentary environment, and the attenuation frequency dependency is not strictly following f^1 or $f^{1/2}$ dependence. In this study, the n value of the three sediments in SCS changes from 0.59 to 0.87, while in WP, the n value of clayey silt is only 0.36.

3.2. Biot–Stoll Model Comparison

Seafloor sediments are composed of particles that form a solid skeleton, the voids between the units form pore spaces, and the pores are filled with fluids. This porous structure makes it very different from dense solid matter in many aspects such as mechanical properties and material state. The irregularity of the pore structure of the porous medium and the heterogeneity of the porous medium constitute the inhomogeneity of different types of sediments. This microscopic inhomogeneity causes the macroscopic physical

properties of the sediments to be very sensitive to slight changes in the pore fluid or pore structure. Therefore, when the sound wave propagates in the sediment, under its influence, the pores or fractures of the medium will be closed or opened, and the fluid in the pore spaces is moving relative to the elastic frame, resulting in changes in the macroscopic physical properties of the sediment, and resulting in changes in the speed of sound wave propagation, dissipation of energy, and attenuation of amplitude. The Biot–Stoll model involves 13 input parameters, and the true and accurate description of these parameters is the basis for describing the variation of the acoustic propagation characteristics of sediments and has far-reaching significance and great value for solving the general porous problem in practical applications.

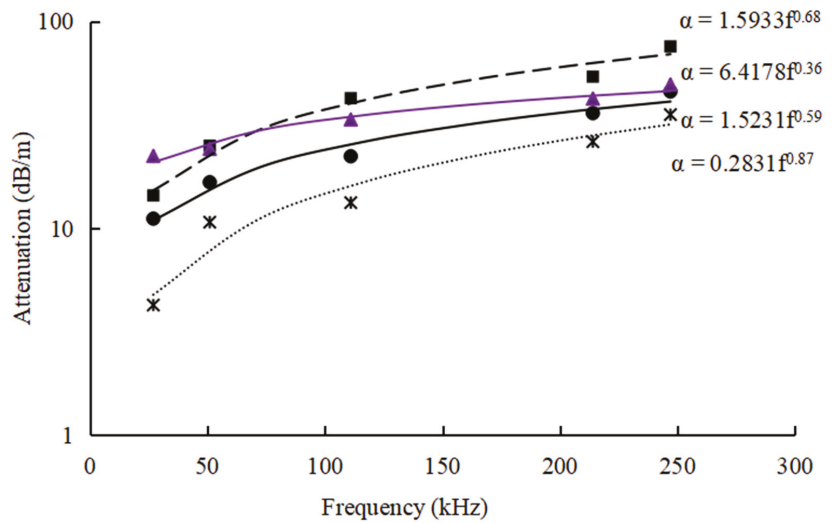


Figure 4. The attenuation dispersion of different sediments. The black ■ dots are silty sand, the black ● dots are silt, the black * dots are silty clay in SCS, and the purple ▲ is clayey silt in WP.

Table 2 list the values of Biot–Stoll model input parameters for different sediment types, including silty sand, silt, silty clay sediment in SCS, and clayey silt sediment in WP. Figure 5 shows the best Biot–Stoll model fit sound speed predictions for different sediments in SCS. The silty sand has highest sound speed and the inflection point from low frequency to high frequency is more obvious. In general, coarse particles have significant sound speed dispersion and the inflection point is located in the low frequency band, while fine particles have weak sound speed dispersion and the inflection point is located in the high-frequency band. Figure 5 shows that the sound speed and attenuation inflection point of coarse grain sediment is obvious and low in frequency (silty sand), while that of fine grain sediment is not obvious and high in frequency (silty clay). Williams et al. [1] studied the uncertainty in model predictions given the uncertainty for the measured physical parameters, and their result shows that the permeability and tortuosity uncertainties result in the largest model attenuation uncertainties, and for sound speed, the permeability affects the sound speed dispersion in the middle-frequency range, and the tortuosity affects the sound speed dispersion in the high-frequency range. For attenuation, the permeability affects the whole frequency range, whereas the tortuosity affects the >1 kHz frequency range. In the Figure 1 of Williams et al. [1], the sound speed dispersion inflection point is influenced by the permeability parameter; in this study, the permeability of silty sand is 2.25×10^{-11} and the silty clay is only 2.14×10^{-12} ; the three sediments in SCS also showed that, the higher permeability is, the lower the frequency of the sound speed and attenuation dispersion inflection point.

Table 2. The values of Biot–Stoll model input parameters for different sediment types.

Physical Parameter	Symbol	Unit	South China Sea Silty Sand	South China Sea Silt	South China Sea Silty Clay	Western Pacific Clayey Silt
Porosity	n	-	0.482	0.550	0.694	0.663
Mean grain size	Mz	ϕ	3.19	5.01	6.58	6.98
Grain bulk modulus *	K_g	Pa	3.6×10^{10}	3.6×10^{10}	3.6×10^{10}	3.6×10^{10}
Fluid dynamic viscosity *	η	$\text{kg}\cdot\text{m}^{-1}\cdot\text{s}^{-1}$	0.00105	0.00105	0.00105	0.00105
Grain density	ρ_g	$\text{kg}\cdot\text{m}^{-3}$	2650	2650	2650	2650
Fluid density *	ρ_f	$\text{kg}\cdot\text{m}^{-3}$	1023	1023	1023	1023
Fluid bulk modulus *	K_f	Pa	2.23×10^9	2.23×10^9	2.23×10^9	2.23×10^9
Permeability +	κ	m^2	2.25×10^{-11}	4.38×10^{-12}	2.14×10^{-12}	8.89×10^{-13}
Tortuosity +	α	—	1.35	1.76	2.41	2.58
Pore size +	a	m	2.49×10^{-5}	1.01×10^{-5}	6.27×10^{-6}	4.13×10^{-6}
Frame shear modulus *	μ	Pa	$(1.178 - i0.18) \times 10^7$	$(0.725 - i0.18) \times 10^7$	$(0.299 - i0.18) \times 10^7$	$(0.368 - i0.18) \times 10^7$
Frame bulk modulus *	K_b	Pa	$(1.532 - i0.24) \times 10^7$	$(0.943 - i0.20) \times 10^7$	$(0.389 - i0.24) \times 10^7$	$(0.479 - i0.20) \times 10^7$

The symbol (*) indicates estimated parameters from the literature. The symbol (+) indicates the calculated parameter using measured parameters. The calculation of permeability, tortuosity, and pore size can be seen in [20], Formulas (3) to (6).

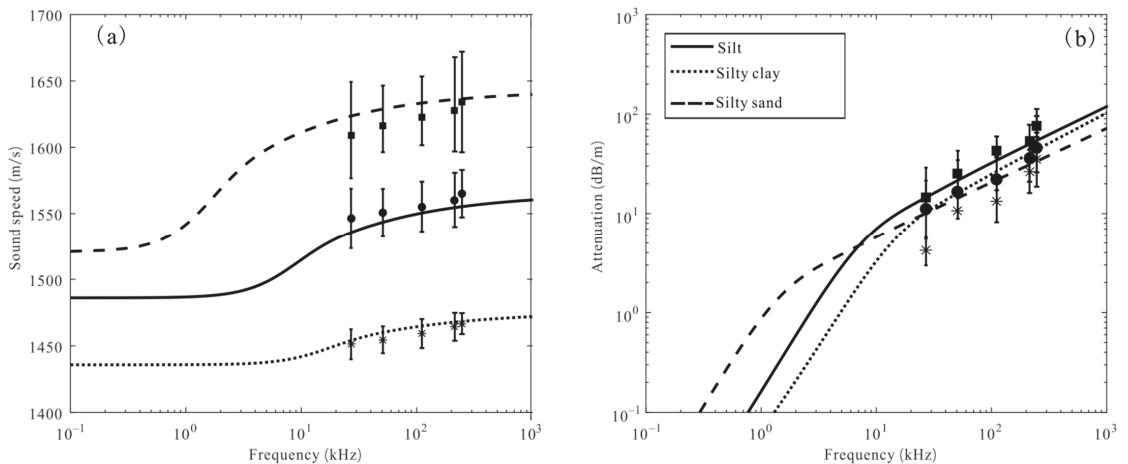


Figure 5. The sound speed (a) and attenuation (b) dispersion of different sediments in SCS.

Figure 6 shows the comparison of different sediments from different areas. The blue line is the coarse sand sediment measured during the sediment acoustics experiment in 1999 (SAX99) by Williams et al. [1], and the measurements span the frequency range of about 125 Hz–400 kHz, and the permeability of the coarse sand is 2.5×10^{-11} . The red line is the fine sand sediment measured in the East China Sea shelf [21], with a frequency range of 30–87 kHz, including the in situ data with the measured frequency of 30 kHz, and the sediment core measurement data with the frequencies range of 47–87 kHz, and the permeability of the fine sand is 3.77×10^{-12} . The green line is the sandy silt sediment measured in Currituck Sound, North Carolina [22], the compressional wave sound speed and attenuation were measured in the frequency band of 5–100 kHz, and the permeability of the sandy silt is 8.5×10^{-12} . The purple line is the clayey silt sediment in WP measured at the frequencies of 27, 51, 111, 214, and 247 kHz, respectively, (unpublished), and the permeability of the clayey silt is 8.9×10^{-13} . In Figure 6, the dispersion inflection point is closely related with the permeability, and it confirmed that the higher permeability is, the lower the frequency of the sound speed and attenuation dispersion inflection point.

In Figure 6, the attenuations of coarse sand and silty sand are the greatest attenuations in the low-frequency band (<10 kHz). However, as the frequency increased, the attenuation of coarse sand and silty sand sediment become lowest in the high-frequency band (>10 kHz).

By contrast, the silty clay and clayey silt sediments have low attenuation in the low-frequency band (<10 kHz) and become high as the frequency increases. In the low-frequency band, the sound speed ratio of silt and clayey silt is similar, while in the high-frequency band, the sound speed ratio of silt and is obviously higher than that of clayey silt, which is because at the high frequency, silt and clayey silt have almost equal sound attenuation, while the sound speed of silt is higher than that of clayey silt.

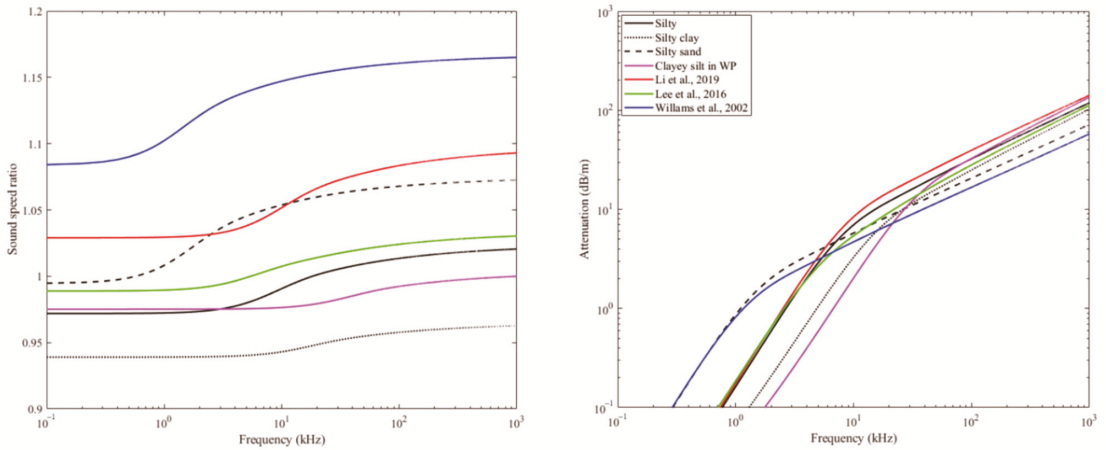


Figure 6. The sound speed and attenuation dispersion for different area and sediment types. The blue line is coarse sand [1], The red line is fine sand [21], the green line is sandy silt [22], and the purple line is clayey silt in WP.

In sound speed dispersion curve, coarse sand [1] and silty sand (SCS) have obvious differences with the other four kinds of sediment; because of their high permeability, the dispersion inflection point of coarse sand and silty sand occurs at lower frequencies than the other four kinds of sediment. As the attenuation of coarse sand and silty sand is the largest at the low-frequency band, the low-frequency dispersion curve of coarse sand and silty sand has a certain radian, while the other four kinds of sediment are basically parallel to the coordinate axis at low frequency, and the variation of the low-frequency dispersion is small.

4. Conclusions

In this paper, historical data of acoustic properties of seafloor sediments in the SCS are collected, and three typical types (silty clay, silt, and silty sand) of sediments are selected to carry out high-frequency-dependence (27, 51, 111, 214, and 247 kHz, respectively) characteristic analysis, and established the relation between sound speed and attenuation dispersion of fine sediment. The frequency dispersion of the three sediments were modeled by the Biot–Stoll model and compared with different sediments from different literatures.

(1) The dispersion curves of the SCS and WP sediments are almost parallel, and the frequency dispersion degree of the four sediments is 1.0687% (silty clay), 1.0121% (clayey silt), 1.22% (silt), and 1.5529% (silty sand), respectively.

(2) The sound speed dispersion of different sediments at the frequency of 27–247 kHz:
 $C_p = 0.0956f + 1609.5$ (silty sand); $C_p = 0.0759f + 1545.6$ (silt); $C_p = 0.0614f + 1499.6$ (clayey silt); $C_p = 0.0658f + 1450.6$ (silty clay).

The attenuation dispersion of different sediments at the frequency of 27–247 kHz:
 $\alpha = 1.5933f^{0.68}$ (silty sand); $\alpha = 1.5231f^{0.59}$ (silt); $\alpha = 6.4178f^{0.35}$ (clayey silt); $\alpha = 0.2831f^{0.87}$ (silty clay).

(3) The inflection point of frequency dispersion is different for different types of sediments. Permeability is the key parameter that determines the inflection point of high frequency to low frequency. In this study, the sound speed dispersion degree of three kinds of sediments in SCS: silty sand > silt > silty clay, and silty sand has the earliest inflection point.

In the low-frequency band, sound attenuation varies greatly, the coarse sand [1] and silty sand (SCS) have the highest attenuation, and clayey silt (WP) has the lowest attenuation. In the high-frequency band, the variation of attenuation is small, and the attenuation coefficients of these sediments are basically parallel. The largest attenuation is fine sand [19], and the smallest attenuation is coarse sand [1].

Author Contributions: Conceptualization, J.W. and Z.H.; methodology, J.W. and Z.H.; validation, G.L., G.K., X.M., B.L. and L.S.; formal analysis, Z.H.; investigation, J.W., G.L., G.K., X.M., Q.H. and L.S.; data curation, J.W. and Z.H.; writing—original draft preparation, Z.H.; writing—review and editing, J.W. and Z.H.; visualization, J.W.; supervision, B.L.; project administration, J.W. and Z.H.; funding acquisition, J.W. and Z.H. All authors have read and agreed to the published version of the manuscript.

Funding: This study was supported by the National Key R&D Program of China (2021YFF0501202), Basic Scientific Fund for National Public Research Institutes of China (2022S01), the National Natural Science Foundation of China under contracts Nos. 42176191, the National Key Laboratory of Science and Technology on Underwater Acoustic Antagonizing, Youth Innovation Promotion Association CAS, the Rising Star Foundation of The Integrated Research Center For Islands And Reefs Sciences, CAS (ZDRW-XH-2021-2-03), the Taishan Scholar Project Funding under contract No. tspd20161007, the CAS Key Laboratory of Science and Technology on Operational Oceanography Open Project Funding No OOST2021-01.

Institutional Review Board Statement: Not applicable.

Informed Consent Statement: Not applicable.

Data Availability Statement: Not applicable.

Acknowledgments: We thank the associate editor and the reviewers for their useful feedback that improved this paper.

Conflicts of Interest: The authors declare no conflict of interest.

References

1. Williams, K.L.; Jackson, D.R.; Thorsos, E.I.; Tang, D.; Schock, S.G. Comparison of sound velocity and attenuation measured in a sandy sediment to predictions based on the Biot theory of porous media. *IEEE J. Ocean. Eng.* **2002**, *27*, 413–428. [[CrossRef](#)]
2. Guo, X.S.; Stoesser, T.; Nian, T.K.; Jia, Y.G.; Liu, X.L. Effect of pipeline surface roughness on peak impact forces caused by submarine mudflow. *Ocea. Eng.* **2022**, *243*, 110184. [[CrossRef](#)]
3. Gassmann, F. Über die Elastizität poroser Medien (Elasticity of porous media. *Vierteljahrsschrift der Naturforschenden. Gesellschaft Zur.* **1951**, *96*, 1–23.
4. Biot, M.A. Theory of propagation of elastic waves in a fluid-saturated porous solid. II. Higher frequency range. *J. Acoust. Soc. Am.* **1956**, *28*, 179–191. [[CrossRef](#)]
5. Hamilton, E.L. Geoacoustic modeling of the sea floor. *J. Acoust. Soc. Am.* **1980**, *68*, 1313–1340. [[CrossRef](#)]
6. Stoll, R.D.; Kan, T.K. Reflection of acoustic waves at a water-sediment interface. *J. Acoust. Soc. Am.* **1981**, *28*, 149–156. [[CrossRef](#)]
7. Williams, K.L. An effective density fluid model for acoustic propagation in sediments derived from Biot theory. *J. Acoust. Soc. Am.* **2001**, *110*, 2276–2281. [[CrossRef](#)] [[PubMed](#)]
8. Jackson, D.R.; Richardson, M.D. *High-frequency Seafloor Acoustics*; Springer Science + Business Media: New York, NY, USA, 2007.
9. Hovem, J.M.; Ingram, G.D. Viscous attenuation of sound in saturated sand. *J. Acoust. Soc. Am.* **1979**, *66*, 1807–1812. [[CrossRef](#)]
10. Simpson, H.J.; Houston, B.H.; Liskey, S.W.; Frank, P.A.; Berdoz, A.R.; Kraus, L.A.; Frederickson, C.K.; Stanic, S. At-sea measurements of sound penetration into sediments using a buried vertical synthetic array. *J. Acoust. Soc. Am.* **2003**, *114*, 1281–1290. [[CrossRef](#)] [[PubMed](#)]
11. Ragione, L.L.; Recchia, G.; Jenkins, J.T. Wave propagation in an unconsolidated granular material: A micro-mechanical approach. *Wave Motion* **2020**, *99*, 102653. [[CrossRef](#)]
12. Buckingham, M.J. On pore-fluid viscosity and the wave properties of saturated granular materials including marine sediments. *J. Acoust. Soc. Am.* **2007**, *122*, 1486. [[CrossRef](#)] [[PubMed](#)]

13. Bonomo, A.L.; Isakson, M.J. A comparison of three geoacoustic models using Bayesian inversion and selection techniques applied to wave speed and attenuation measurements. *J. Acoust. Soc. Am.* **2018**, *143*, 2501–2513. [[CrossRef](#)]
14. Holmes, J.D.; Carey, W.M.; Dediu, S.M.; Siegmann, W.L. Nonlinear frequency-dependent attenuation in sandy sediments. *J. Acoust. Soc. Am.* **2007**, *121*, EL218–EL222. [[CrossRef](#)] [[PubMed](#)]
15. Sessarego, J.P.; Ivakin, A.N.; Ferrand, D. Frequency Dependence of Phase Speed, Group Speed, and Attenuation in Water-Saturated Sand: Laboratory Experiments. *IEEE J. Ocean. Eng.* **2009**, *33*, 359–366. [[CrossRef](#)]
16. Yu, S.; Wang, F.; Zheng, G.; Huang, Y. Progress and discussions in acoustic properties of marine sediments. *J. Harbin Eng. Univ.* **2020**, *41*, 7.
17. Hamilton, E.L. Compressional wave attenuation in marine sediments. *Geophysics.* **1972**, *37*, 620–646. [[CrossRef](#)]
18. Hou, Z.; Chen, Z.; Wang, J.; Zheng, X.; Yan, W.; Tian, Y.; Luo, Y. Acoustic characteristics of seafloor sediments in the abyssal areas of the South China Sea. *Ocea. Eng.* **2018**, *156*, 93–100. [[CrossRef](#)]
19. Stoll, R.D. *Sediment Acoustics*; Springer: Berlin/Heidelberg, Germany, 1989.
20. Wang, J.; Li, G.; Kan, G.; Hou, Z.; Meng, X.; Liu, B.; Liu, C.; Lei, S. High frequency dependence of sound speed and attenuation in coral sand sediments. *Ocea. Eng.* **2021**, *234*, 109215. [[CrossRef](#)]
21. Li, G.; Wang, J.; Liu, B.; Meng, X.; Kan, G.; Pei, Y. Measurement and modeling of high-frequency acoustic properties in fine sandy sediments. *Earth Space Sci.* **2019**, *6*, 2057–2070. [[CrossRef](#)]
22. Lee, K.M.; Ballard, M.S.; Mcneese, A.R.; Muir, T.G.; Wilson, P.S.; Costley, R.D.; Hathaway, K.K. In situ measurements of sediment acoustic properties in Currituck Sound and comparison to models. *J. Acoust. Soc. Am.* **2016**, *140*, 3593. [[CrossRef](#)] [[PubMed](#)]

Article

Normalized Stress–Strain Behavior of Deep-Sea Soft Soils in the Northern South China Sea

Ying Yang ^{1,2}, Hailei Kou ^{1,2}, Zhenghui Li ^{3,*}, Yonggang Jia ^{3,4} and Chaoqi Zhu ^{3,4,*}

¹ College of Engineering, Ocean University of China, Qingdao 266100, China

² Shandong Provincial Key Laboratory of Ocean Engineering, Ocean University of China, Qingdao 266100, China

³ College of Environmental Science and Engineering, Ocean University of China, Qingdao 266100, China

⁴ Shandong Provincial Key Laboratory of Marine Environment and Geological Engineering, Ocean University of China, Qingdao 266100, China

* Correspondence: lizhenghui@stu.ouc.edu.cn (Z.L.); zhuchaoqi@ouc.edu.cn (C.Z.)

Abstract: The study of the physical and mechanical properties of marine soil is of great importance for marine geohazard prediction, submarine energy extraction, and submarine foundation design. In this study, a series of basic geotechnical tests and triaxial compression tests are performed on samples taken from the Shenhu sea area in the South China Sea (SCS). Physical and mechanical properties, particularly normalized stress–strain behavior, are investigated. The microstructural and mineralogical characterization is carried out, through scanning electron microscopy (SEM), and X-ray diffraction (XRD). The results indicated that the sample could be classified as high-plasticity silt (MH) with high water content and high compressibility, that the soil has the highest quartz content in its mineral composition, a loose skeleton composed of flocculent structures under the microscope and is distributed with the remains of marine organisms. Furthermore, a new stress–strain-normalized condition is theoretically derived, based on the hyperbola function. In this condition, the concept of standard normalized factor, which is defined as the ultimate value of principal stress difference, is introduced. Meanwhile, the normalized stress–strain relationship of soft soil from the SCS is established under consolidated undrained conditions and the results of the model are compared with the experimental results, with a good normalization effect. It is believed that the work presented in this paper could contribute to the design and construction of offshore engineering.

Keywords: South China Sea; submarine soft soil; triaxial test; mechanical properties; normalized behavior

Citation: Yang, Y.; Kou, H.; Li, Z.; Jia, Y.; Zhu, C. Normalized Stress–Strain Behavior of Deep-Sea Soft Soils in the Northern South China Sea. *J. Mar. Sci. Eng.* **2022**, *10*, 1142. <https://doi.org/10.3390/jmse10081142>

Academic Editors:

George Kontakiotis, Xiaolei Liu, Thorsten Stoesser and Xingsen Guo

Received: 7 July 2022

Accepted: 11 August 2022

Published: 18 August 2022

Publisher’s Note: MDPI stays neutral with regard to jurisdictional claims in published maps and institutional affiliations.



Copyright: © 2022 by the authors. Licensee MDPI, Basel, Switzerland. This article is an open access article distributed under the terms and conditions of the Creative Commons Attribution (CC BY) license (<https://creativecommons.org/licenses/by/4.0/>).

1. Introduction

Offshore developments for hydrocarbon resources and offshore engineering construction have now developed for use in deep-water areas [1,2]. The geotechnical properties of seabed sediments play a crucial role in the safety and stability of deep-water foundations [3]. The deep-sea sediments, which usually consist of normal consolidated (NC) or lightly over-consolidated (OC) clay [4], are generally characterized by their poor mechanical properties [5–8]. Meanwhile, due to the complex and changeable marine environment, the mechanical properties of seabed sediments are prone to change under the coupling of complex loads such as wind, waves, currents, and hydrate decomposition, resulting in engineering geological disasters such as submarine instability and submarine landslides, which pose serious threats to marine infrastructure and engineering construction [9–11].

However, due to the difficulty of obtaining deep-sea soils, and the specific nature of marine and terrestrial sediments, the presence of natural gas hydrates usually directly or indirectly affects the physical and mechanical properties of the soil. Many scholars have summarized the different characteristics of natural gas hydrates, as well as their formation and decomposition principles [12], and suggested possible effects of hydrate

saturation and pore-scale distribution in sediments on the mechanical properties of sediments [13,14]. Therefore, the study of physical and mechanical properties, as well as the mineral composition of deep-sea soils, is crucial. The basic physical properties of deep-sea soils can be determined by geotechnical tests [15–18]. To better understand the engineering properties of deep-sea soils, many scholars have researched this topic. Through geotechnical property tests on marine soils in the South China Sea, the mechanical properties of submarine soils on the continental slope of the South China Sea were revealed from macroscopic and microscopic perspectives; based on triaxial compression tests, the stress–strain characteristics between in situ soils and remodeled soils were analyzed, and six structural types of submarine sediments on the continental shelf in the northern part of the South China Sea were described [19–21]. Meanwhile, the effect of temperature on the mechanical properties of deep-sea soils can be studied by considering triaxial compression tests at different temperatures [22–24]. The microstructure and undrained shear strengths of deep-sea sediments were analyzed based on critical state lines and different stress paths of isotropy that remodeled deep-sea soils [25,26]. In addition, Silva et al. conducted a comparative study of deep-sea fine-grained sediments and terrestrial clays, considering consolidation undrained triaxial tests under isotropically (CIU) and anisotropically (CAU) conditions, and pointed out that the difference in mineral composition of the soil also affects the mechanical parameters of the material, and the sufficient attention should be paid to the creep properties of clay in deep-sea engineering [27,28]. The deformation and strength properties of soils can be expressed by stress–strain relationships from triaxial tests, while the engineering mechanical properties of soils are complex due to the influence of boundary conditions such as confining pressure and stress paths [29–31]. To express the stress–strain relationship of soft soils in a unified equation, it is crucial to normalize the stress–strain relationship of soft soils. Several scholars have also proposed normalization factors [32,33]. However, due to the harsh normalization conditions of the existing normalization factors, the soft soils in many regions cannot be satisfied, and if the existing normalization factors are used to normalize the stress–strain relationship of soft soils that do not meet these harsh normalization conditions, satisfactory normalization will not be achieved [34–36]. The quality of the normalization factor selection will directly affect the degree of normalization of the stress–strain relationship of soft soil.

In this study, a series of basic geotechnical tests and triaxial compression tests were carried out on deep-sea soft soil taken from the SCS to investigate its physical and mechanical properties. The microstructure and mineral composition of the soil samples are analyzed using SEM and XRD tests. Furthermore, based on the hyperbolic equation of the stress–strain relationship proposed by Konder, the normalization factors and normalization conditions for normalizing the stress–strain relationship in soft soil are discussed, and the normalization factors proposed in this study are applied to the consolidation-undrained test of soft soil in the SCS. Based on this analysis, normalized models are established to predict the stress–strain relationship.

2. Materials and Methods

2.1. Soil Samples

In this study, soil samples were taken from the Shenhu sea area in the north of the SCS based on the 2020 shared voyage of the SCS scientific research, as shown in Figure 1. Using a gravity sampler, the longitude and latitude of the sampling point were found to be 114.57 degrees east longitude and 20.27 degrees north latitude, the water depth of the sampling site was 561 m, and the sampling depth of the soil sampling was 4.85 m.

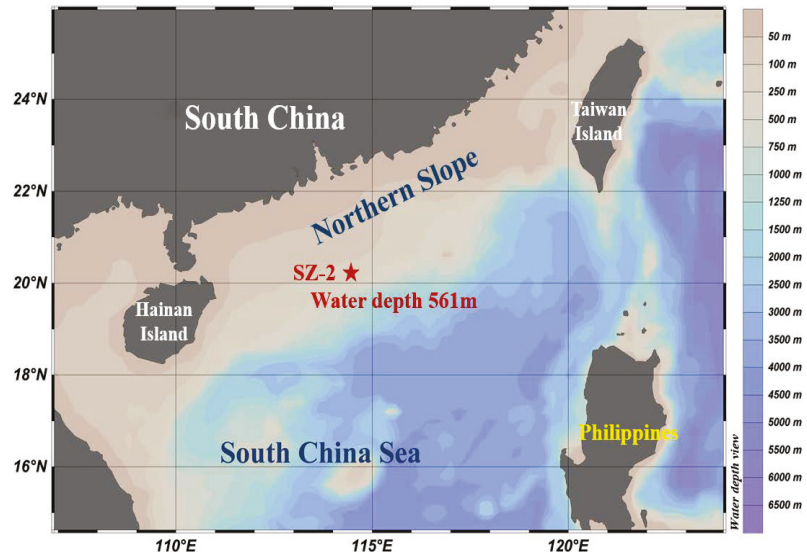


Figure 1. Sampling site (modified from [6]).

2.2. Testing Methods

The basic geotechnical test was carried out by taking the surface column sample (30 cm) of the in situ specimen according to the standard of ASTM D421-85 (2007) [37]; sediment samples were taken from the PVC tube, the grain size distribution of soil samples was determined by the densitometry method, the water content was measured by the drying method, and the liquid limit and plasticity were measured by the GYS-2 digital soil liquid–plastic limit analyzer. All methods were subjected to three parallel tests, and the basic mechanical property parameters of the soil were obtained.

X-ray diffraction (XRD) tests were conducted to determine the mineral composition of the soil samples. These tests were conducted with a Shimadzu XD-D1 X-ray diffractometer. “MDI jade 9.0” software was used to carry out the qualitative analysis. X-ray diffraction patterns were obtained using a continuous-scanning-mode X-ray tube with a scanning range from 2° to 32° (2θ) and a scanning rate of 4° per minute. The diffraction data on crystal plane spacing and diffraction intensity were obtained through sorting and compared with the diffraction data of standard minerals for mineral identification.

Scanning Electron Microscopy (SEM) analyses of in situ soils were performed in an S-4800 Cold Field Emission SEM produced by Hitachi. First, the in situ samples were processed by the vacuum freeze-drying method, and then they were sputtered with a layer of carbon and one or more layers of gold. For each specimen, a set of images were taken at a range of magnifications to provide contact patterns between soil particles and to understand the microscopic properties of the soil sample.

Additionally, consolidated undrained triaxial shear tests were performed to investigate the geotechnical behavior of deep-sea soft clay, the GDS Triaxial testing system (as shown in Figure 2) was used in the tests. In situ samples were taken in the laboratory and solid cylindrical triaxial samples of diameter $\varnothing = 50$ mm and height $h = 100$ mm were cut with soil cutters and wire saws. Before the test, the samples were vacuum pumped and saturated by the vacuum pump. In this test, the specimens were first saturated by the backpressure saturation method, and a strain-controlled method was conducted with a 0.14 mm/min axial shear rate; three triaxial samples were taken and consolidated under the confining pressure of 100 kPa, 200 kPa, and 300 kPa, and then the consolidated undrained (CU) shear test was performed, and, finally, the test was terminated when the axial strain reached 20%.

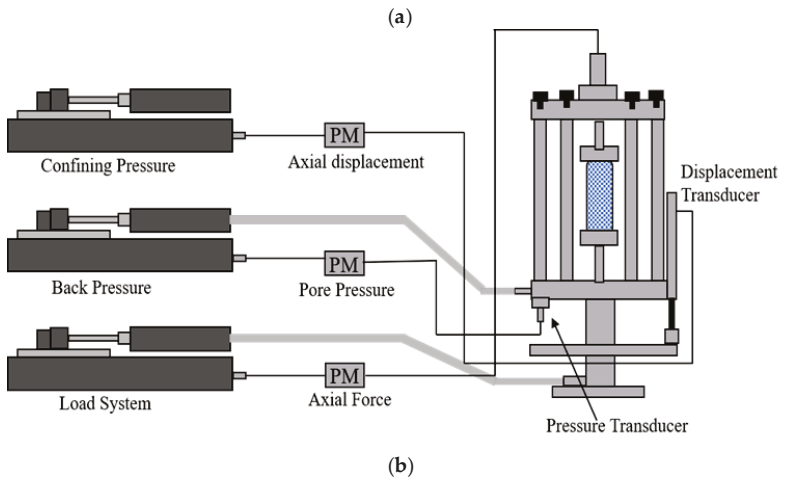
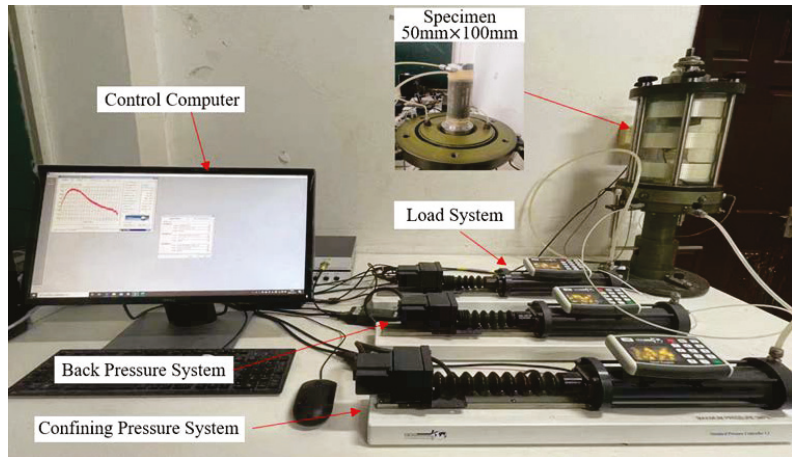


Figure 2. GDS Triaxial testing system. (a) Physical apparatus; (b) Schematic diagram.

3. Results and Discussion

3.1. Basic Physical Properties

A series of laboratory tests were performed to investigate the basic physical properties of the soil samples. The results of the basic physical properties tests of soil samples are shown in Table 1 according to the standard of ASTM D421-85 (2007) [37].

Table 1. Basic properties of soil samples.

Property	Value
Water content, w (%)	46.4
Density, ρ (g/cm^3)	1.517
Initial void ratio, e_0	1.63
Liquid limit, LL (%)	59.8
Plastic limit, PL (%)	34.8
Plasticity index, PI (%)	25
Specific gravity, G_s	2.73

The grain-size distribution of the sample is shown in Figure 3; different particle diameter indices of the soil samples were calculated as shown in Table 2. The coefficient of nonuniformity C_u and coefficient of curvature C_c of the deep-sea soil samples are calculated as follows:

$$C_u = \frac{d_{60}}{d_{10}} = 7.5 \tag{1}$$

$$C_c = \frac{d_{30}^2}{d_{10} \times d_{60}} = 0.53 \tag{2}$$

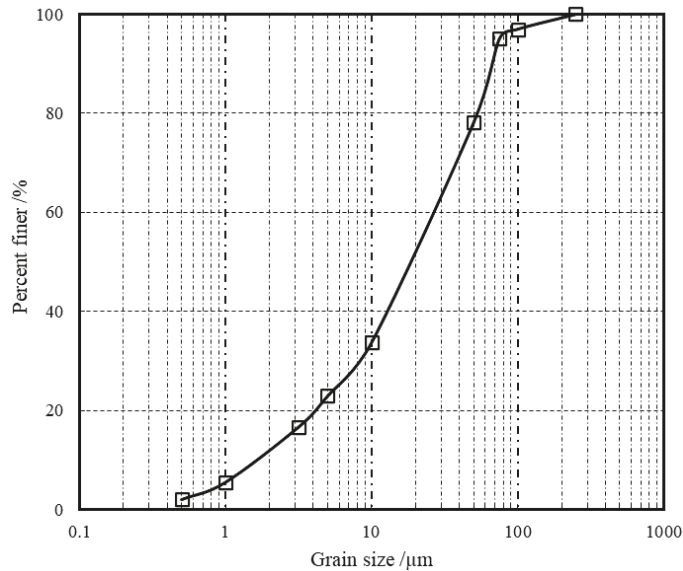


Figure 3. Grain size distribution curve of soil samples.

Table 2. Different particle diameter indices of soil samples.

Particle Diameter Indices	Value
Effective particle diameters, d_{10} (mm)	0.004
Continuous particle diameters, d_{30} (mm)	0.008
The median of particle diameters, d_{50} (mm)	0.021
Control of particle diameters, d_{60} (mm)	0.03

From the test results, it can be concluded that the coefficient of nonuniformity $C_u = 7.5 \geq 5$. This soil was shown to contain particles of different thicknesses, which can be categorized into heterogeneous soils [37]; however, since the coefficient of curvature $C_c = 0.53 < 1$, it can be concluded that the soil is poorly graded [37] and the particle composition of the soil is mainly powder, followed by clay and sand.

The plastic limit (PL), liquid limit (LL), and plasticity index (PI) were 34.8%, 59.8%, and 25%, respectively. Therefore, according to the Unified Soil Classification System (USCS) (ASTM, 2017) [38], the study sample in this area was classified as MH (high-plasticity silt), as shown in Figure 4.

The mineral composition was determined by X-ray (XRD) diffraction tests, the results of which are given in Figure 5, and the mineral content results are shown in Table 3. The XRD pattern shows some high peaks at the 2θ angle of 20.827° , 26.609° , and 29.368° . The clay minerals are mostly powdered, with the highest percentage of quartz SiO_2 , followed by muscovite, calcite, and a small amount of albite and clinocllore. The ionic composition

of the soil sample, in order of content, is Si, Al, Ca, Fe, K, Na, Mg. Compounds mainly include SiO_2 and CaCO_3 , etc.

The in situ samples were processed by the vacuum freeze-drying method and analyzed by scanning electron microscopy (SEM) to obtain the microstructural properties of the soil. The microstructure electron microscope scan photo of the in situ sample is shown in Figure 6. From the figure, it can be seen that the soil particles are more obvious between the large-pore soil skeleton structure, the surface contains more marine biological debris under the sedimentation in the marine environment, contact between particles mostly occurs in the form of edge-surface, and the soil sample as a whole shows an open flocculation structure; this is the main structural characteristic in an all-seawater sedimentary environment.

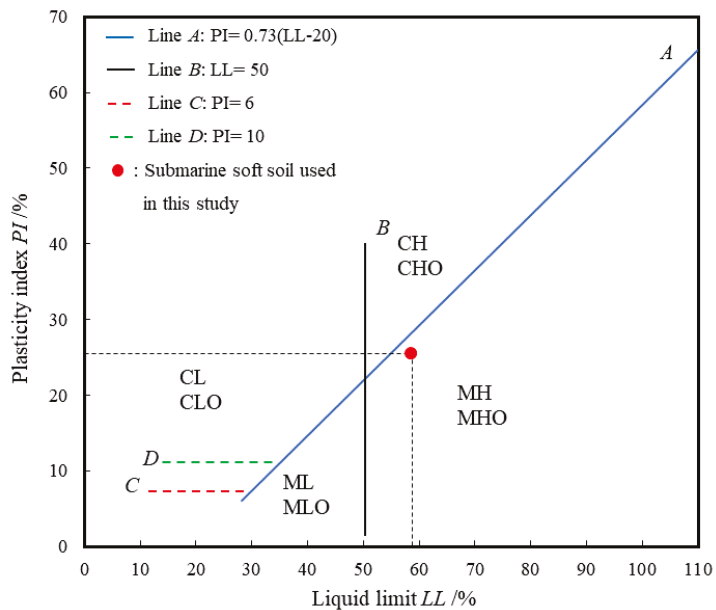


Figure 4. Plasticity diagram (ASTM D2487). Note: CL: Low-plasticity clay; CLO: Low-plasticity organic clay; ML: Low-plasticity silt; MLO: Low-plasticity organic silt; CH: High-plasticity clay; CHO: High-plasticity organic clay; MH: High-plasticity silt; MHO: High-plasticity organic silt.

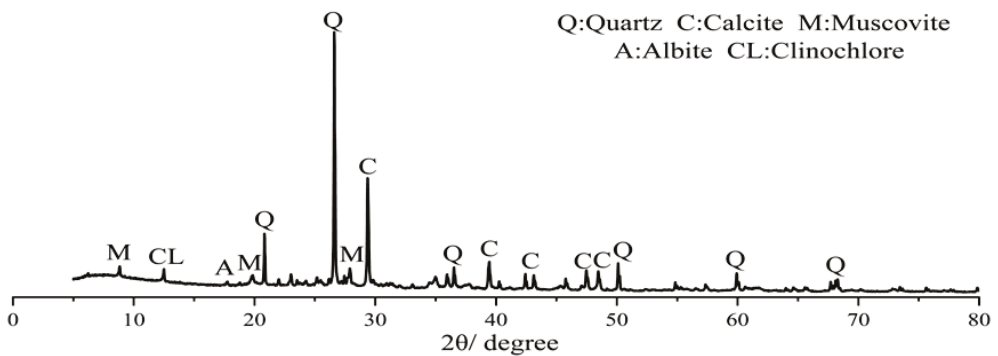


Figure 5. X-ray diffraction curves of soil.

Table 3. Compositions of clay minerals.

Composition	Percentage (%)
Quartz	40.9
Muscovite	29.3
Calcite	22.5
Albite	6.6
Clinochlore	0.623

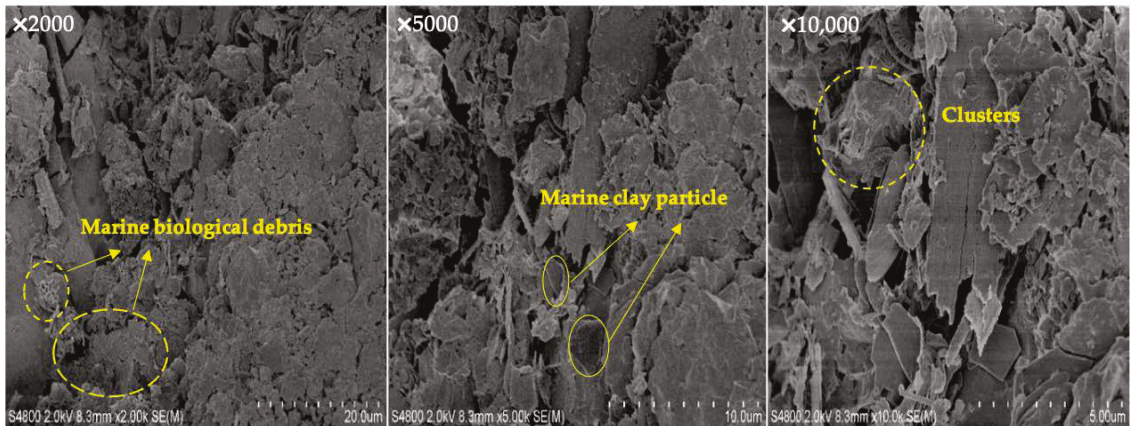


Figure 6. Microstructure of soil by SEM tests.

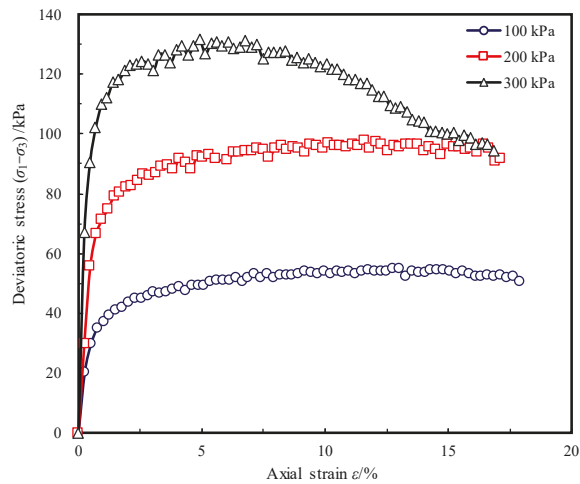
3.2. Mechanical Properties

The stress–strain behavior under different confining pressures is present in Figure 7a. One can note that there is no obvious peak point in each curve at a low confining pressure; the strength at final stability is about 54 kPa and 93 kPa, respectively, the soil shows stable or weaker strain-hardening characteristics, and the stress increases slowly, step by step, with the increase in strain. When the confining pressure reaches 300 kPa, the curve shows a clear peak point, and when the peak strength is 132 kPa, the soil exhibits strain-softening characteristics. It can be concluded that the strength of the soil gradually increases with the increase in the surrounding pressure. This phenomenon is mainly due to the large void space in the soft soil of the seabed. The soil body shows the compression of pore volume under a low perimeter pressure, and the microstructure between the soil skeleton does not change; thus, the soil strength is low. Under a high perimeter pressure, the soil will not only undergo compression of pore volume, but also cause the microstructure between soil particles to change, and the soil skeleton will become more compact and dense, which significantly increases the soil body’s ability to resist external load, and the shear strength also increases as a result. When the load reaches the ultimate bearing capacity, the soil skeleton is damaged and the microstructure of the soil is destroyed; thus, the bearing capacity is reduced and the strain-softening characteristics are exhibited.

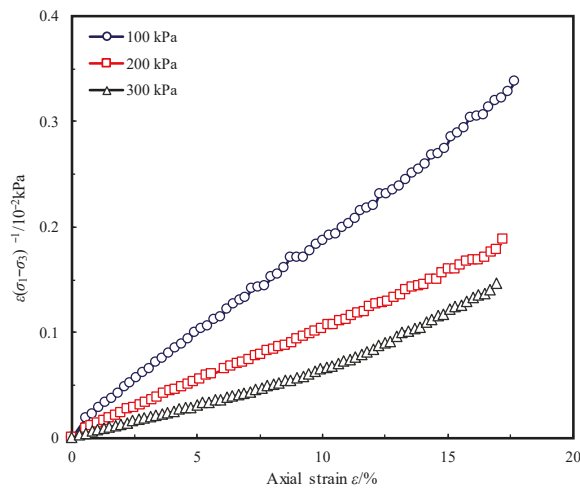
In addition, Figure 8 illustrates the effective stress paths obtained from the consolidated–undrained triaxial test. From the soil samples plotted on the $p'-q$ coordinate plane, it can be observed that the sample generates positive pore-water pressure (the effective stress paths gradually bend to the upper left), passes through a phase-transformation state, and then dilates with the same stress ratio and terminates with the critical state line (CSL). As deep-sea sediments are mainly composed of powder particles and clay particles, the natural sedimentation process of in situ marine sediment can form a high-porosity structure such as honeycomb, velvet, and flocculation by lapping between clay particles, which forms a certain cementation structure between the particles. The higher the clay content, the

more significant the cementation effect, as shown in Figure 9, thus increasing the shear strength of the soil [39,40]. However, with the increase in confining pressure, as shown in Figures 7a and 8, the structure of the marine sediments is gradually destroyed; that is, the clay particles gradually became densely stacked, the sediments were destroyed and strain-softening obviously occurred.

Figure 10 shows the relationship curve between pore water pressure development and axial strain, which shows a two-stage change characteristic. The pore water pressure rapidly increases in the initial stage, and subsequently, when the axial strain is approximately 4%, with the increase in axial strain, the growth rate of pore water pressure gradually decreases and tends toward a critical point, showing the continuous accumulation of pore water pressure.



(a)



(b)

Figure 7. Stress–strain curves in CU test. (a) Deviatoric stress–strain behaviour; (b) Normalized deviator stress–strain behaviour.

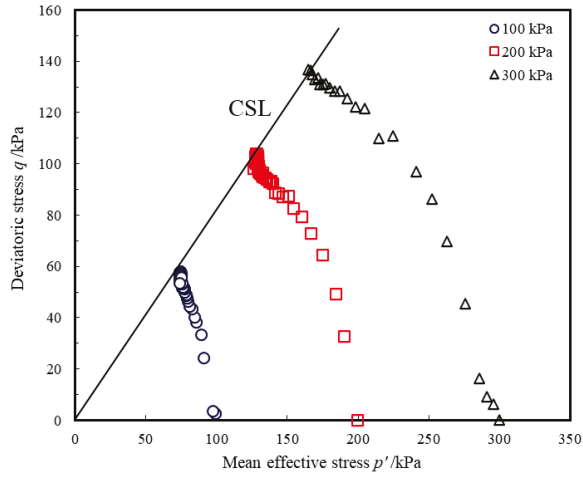


Figure 8. Effective stress paths in CU test.

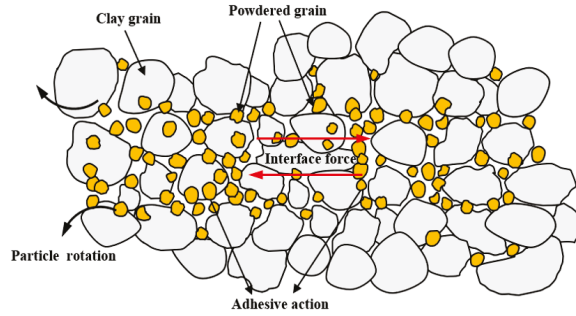


Figure 9. Schematic diagram of the interface mechanical interaction between soil particles.

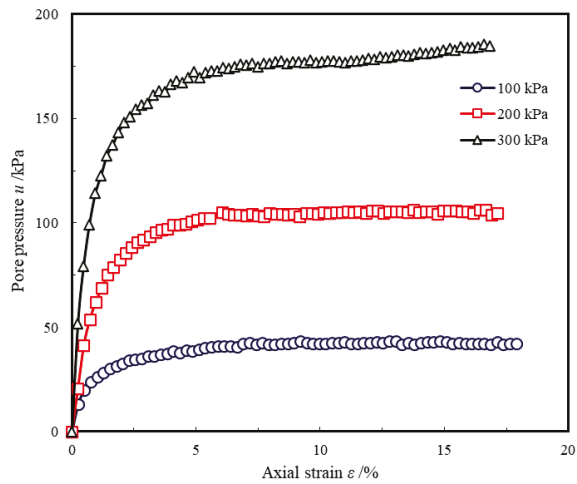


Figure 10. Pore pressure-strain curves in CU test.

3.3. Selection of Normalization Factors

Konder proposed that the $(\sigma_1 - \sigma_3) - \varepsilon$ to determine the conventional static triaxial test relationship can be approximated by the hyperbolic equation [41] as follows:

$$\sigma_1 - \sigma_3 = \frac{\varepsilon}{a_i \varepsilon + b_i} \tag{3}$$

where a_i is the reciprocal of the asymptotic value of the principal stress difference $(\sigma_1 - \sigma_3)_{\text{ulti}}$ under a certain constant consolidation confining pressure; b_i is the reciprocal of the initial tangent modulus E_{0i} under a certain constant consolidation confining pressure.

Equation (3) can be converted to:

$$\frac{\varepsilon}{\sigma_1 - \sigma_3} = a_i \varepsilon + b_i \tag{4}$$

Both sides of Equation (4) are multiplied by A to:

$$\frac{\varepsilon}{\sigma_1 - \sigma_3} A = A a_i \varepsilon + A b_i \tag{5}$$

Since the two parameters of Equation (3) are different under different confining pressures parameters, to obtain the $(\sigma_1 - \sigma_3) - \varepsilon$ relationship normalized equation under different confining pressures, σ_3 , such that:

$$\frac{\varepsilon}{\sigma_1 - \sigma_3} A = M \varepsilon + N \tag{6}$$

where M and N are constants.

From Equations (5) and (6):

$$M = A a_i \tag{7}$$

$$N = A b_i \tag{8}$$

From Equations (7) and (8):

$$A = M(\sigma_1 - \sigma_3)_{\text{ulti}} \tag{9}$$

$$A = N E_{0i} \tag{10}$$

Combining Equations (9) and (10) yields:

$$M(\sigma_1 - \sigma_3)_{\text{ulti}} = N E_{0i} \tag{11}$$

The normalization factor of the normalization curve of the relationship between $(\sigma_1 - \sigma_3) - \varepsilon$ under the different confining σ_3 is desirable $M(\sigma_1 - \sigma_3)_{\text{ulti}}$, and its normalization conditions are:

$$\frac{(\sigma_1 - \sigma_3)_{\text{ulti}}}{E_{0i}} = \frac{N}{M} \tag{12}$$

That is, the asymptotic value of the principal stress difference $(\sigma_1 - \sigma_3)_{\text{ulti}}$ is a positive proportional function of the initial tangent modulus E_{0i} .

The stress-strain relationship curve of the specimen in Figure 7b is fitted with Equation (4), and parameters a_i and b_i are shown in Table 4.

Table 4. Fitting parameters.

σ_3/kPa	a_i	b_i	$(\sigma_1 - \sigma_3)_{\text{ulti}}/\text{kPa}$	R^2
100	0.01815	0.00813	44.39	0.99825
200	0.01026	0.00282	100.57	0.99884
300	0.01026	-0.01091	167.74	0.97516

When the initial tangent modulus $E_{0i} = 0$, this can be inferred from Equation (3), $(\sigma_1 - \sigma_3)_{ult} = 0$. Thus, according to the relevant parameters of Table 4, the relationship between the asymptotic value of the principal stress difference $(\sigma_1 - \sigma_3)_{ult}$ and the confining pressure σ_3 under different confining pressures is shown in Figure 11. The relationship curve in Figure 11 can be fitted with a linear equation:

$$(\sigma_1 - \sigma_3)_{ult} = 0.61675\sigma_3 - 19.11667 \tag{13}$$

correlation coefficient $R^2 = 0.9947$.

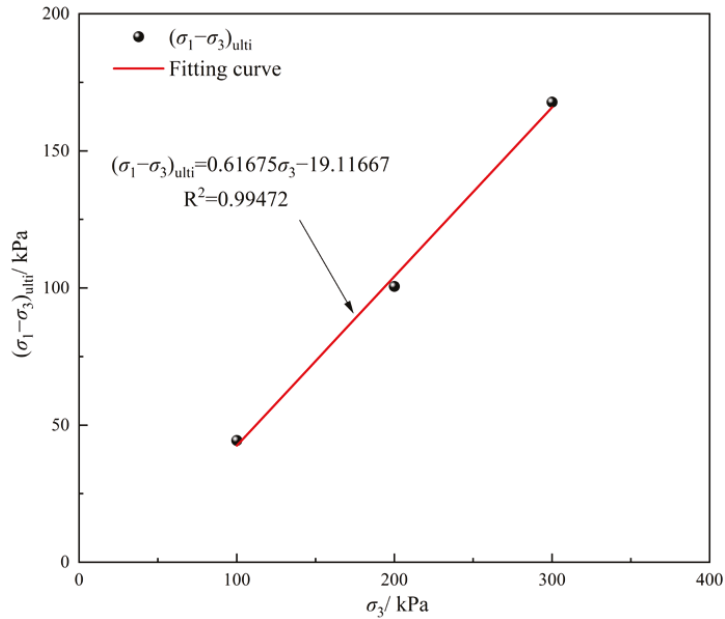


Figure 11. Relationship between $(\sigma_1 - \sigma_3)_{ult}$ and σ_3 .

3.4. Normalized Analysis of Stress–Strain Properties

A normalized analysis of the CU stress–strain characteristics of soft soil in the SCS is presented. Taking the asymptotic value of the principal stress difference $(\sigma_1 - \sigma_3)_{ult}$ as the normalization factor, the normalization analysis of the $\frac{\epsilon}{\sigma_1 - \sigma_3} - \epsilon$ relationship under different confining pressures is shown in Figure 12.

According to Figure 12, the resulting normalization equation is:

$$\frac{\epsilon}{\sigma_1 - \sigma_3} (\sigma_1 - \sigma_3)_{ult} = \epsilon + 0.69004 \tag{14}$$

Its correlation coefficient is $R^2 = 0.9927$, which has good normalization.

Combining Equations (13) and (14) yields:

$$\frac{\sigma_1 - \sigma_3}{\epsilon} = \frac{0.61675\sigma_3 - 19.11667}{\epsilon + 0.69004} \tag{15}$$

Equation (15) is a normalization equation based on the asymptotic value of the principal stress difference, with $(\sigma_1 - \sigma_3)_{ult}$ as the normalization factor.

Equation (15) can predict the $\frac{\epsilon}{\sigma_1 - \sigma_3} - \epsilon$ relationship under different consolidation confining pressures and $(\sigma_1 - \sigma_3) - \epsilon$ relationship curve, as shown in Figure 13.

As can be seen from Figures 12 and 13, the normalization analysis of the stress–strain characteristics of deep-sea soft soils from the SCS was carried out using the principal stress difference asymptote value $(\sigma_1 - \sigma_3)_{ult}$ as the n–ormalization factor. When the soil sample shows strain-hardening or strain-stabilization under different confining pressures, its normalization effect is perfect; when the soil sample exhibits strain-softening under a high confining pressure, there is a certain error in the normalization effect of the softening stage. The stress–strain relationship equation represented in Equation (15) can predict the stress–strain relationship under the low confining pressures of soft soils in the SCS under the consolidated–undrained triaxial test.

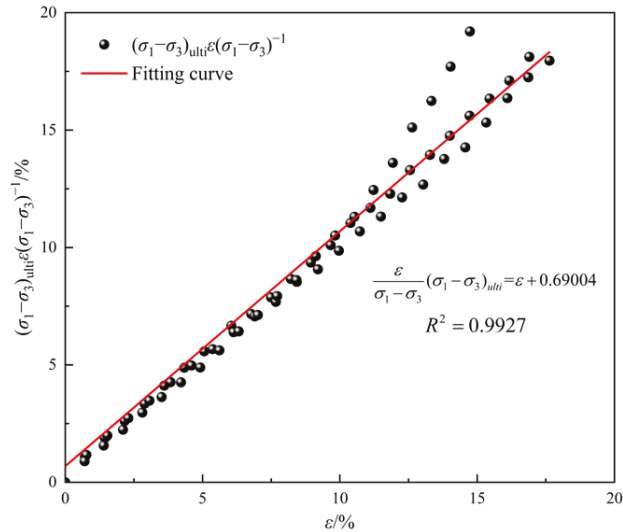


Figure 12. Normalized stress–strain curves with $(\sigma_1 - \sigma_3)_{ult}$ adopted as the normalized factor.

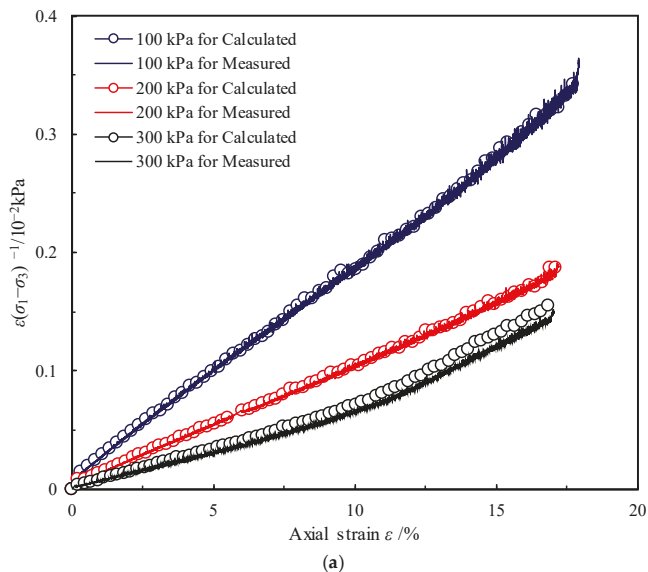


Figure 13. Cont.

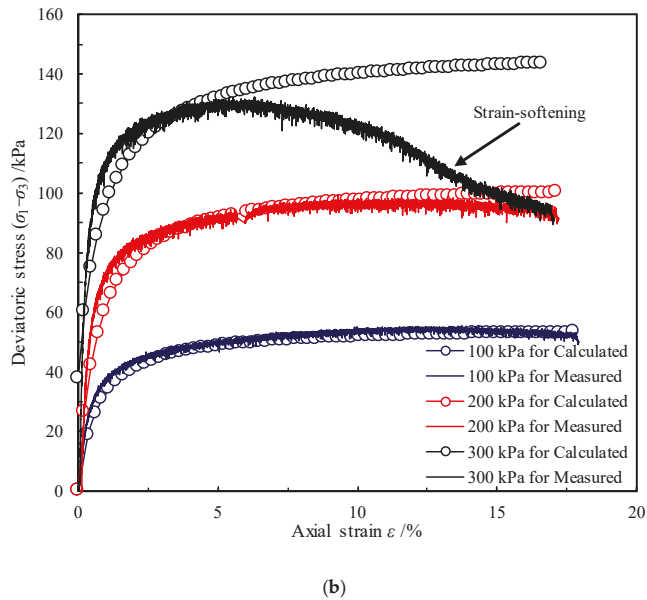


Figure 13. Predicted stress–strain curves with $(\sigma_1 - \sigma_3)_{\text{ulti}}$ adopted as normalized factor. (a) Normalized deviator stress–strain behaviour; (b) Deviatoric stress–strain behaviour.

4. Conclusions

The particle composition of the deep-sea soft soil in this study is mainly powder, followed by clay soil and sand, the soil sample is classified as MH, and the soil particle gradation is poor. The mineral composition of the soil is mainly quartz, muscovite, and calcite, and the soil also contains a small amount of albite and chlorite. Microscopically, the skeleton structure of the soil is very loose, containing more marine biological debris, contact between particles mostly occurs in the form of edge-surface, and the soil sample presents an open flocculation structure overall.

The stress–strain relationship of soft soil from the SCS under consolidation undrained conditions shows a typical hyperbolic relationship. Under a low confining pressure, the soil exhibits a stable or weakly strained hardening type; under a high confining pressure, the soil embodies a strained softening.

According to the stress–strain hyperbolic equation proposed by Konder, the normalization conditions must be met to normalize the stress–strain equation. An asymptotic value of principal stress difference $(\sigma_1 - \sigma_3)_{\text{ulti}}$ is proposed as the standard normalization factor. The stress–strain relationship equation for soft soil from the SCS under consolidated–undrained conditions, established by the standard normalization factor, can predict the stress–strain relationship under different confining pressures using the consolidated–undrained shear test of the soft soil.

The stress–strain relationship normalization equation established in this paper is based on the stress–strain hyperbolic equation proposed by Konder, so the normalization equation is only suitable for strain stabilization and strain-hardening, and is not suitable for the softening stage of strain-softening.

Author Contributions: Conceptualization, Z.L. and H.K.; Data curation, Y.Y.; Formal analysis, Y.Y. and Z.L.; Funding acquisition, H.K. and Y.J.; Writing—original draft, Y.Y.; Writing—review and editing, H.K., Y.Y., C.Z. and Z.L. All authors have read and agreed to the published version of the manuscript.

Funding: This research was funded by the National Natural Science Foundation of China (No. 41831280), and supported by Shandong Provincial Key Laboratory of Ocean Engineering.

Institutional Review Board Statement: Authors have signed the statement.

Informed Consent Statement: Authors have signed the statement.

Data Availability Statement: Authors state that all data are available.

Acknowledgments: Authors are indebted to the 2020 shared voyage of the Northern South China Sea scientific research. We thank the anonymous reviewers for their valuable comments.

Conflicts of Interest: The authors declare no conflict of interest.

References

1. Li, X.; Jiang, X.; Hopman, H. A review on predicting critical collapse pressure of flexible risers for ultra-deep oil and gas production. *Appl. Ocean Res.* **2018**, *80*, 1–10. [[CrossRef](#)]
2. Guo, X.; Stoesser, T.; Nian, T.; Jia, Y.; Liu, X. Effect of pipeline surface roughness on peak impact forces caused by hydrodynamic submarine mudflow. *Ocean Eng.* **2022**, *243*, 110184. [[CrossRef](#)]
3. Peng, J.; Liu, H. Analytical study on comprehensive behaviors of drag anchors in the seabed. *Appl. Ocean. Res.* **2019**, *90*, 101855. [[CrossRef](#)]
4. Ren, Y.; Yang, Q.; Wang, Y.; Zhao, W. Experimental study on the undrained shear strength of deep-sea soft soil using improved T-bar penetrometer. *Mar. Georesour. Geotechnol.* **2020**, *38*, 1199–1208. [[CrossRef](#)]
5. Li, Y.; Wang, G.; Jing, L.; Zhang, L.; Cheng, X. Unified Description of the Mechanical Properties of Typical Marine Soil and Its Application. *Shock. Vib.* **2017**, *2017*, 3892193. [[CrossRef](#)]
6. Ting-Kai, N.; Hou-bin, J.; Ning, F.; Xing-Sen, G.; Yong-gang, J. Experiment on dynamic strain-pore pressure of soft clay in the northern slope of South China Sea. *Rock Soil Mech.* **2018**, *39*, 1564.
7. Nian, T.K.; Jiao, H.B.; Fan, N.; Guo, X.S. Microstructure analysis on the dynamic behavior of marine clay in the South China Sea. *Mar. Georesour. Geotechnol.* **2020**, *38*, 349–362. [[CrossRef](#)]
8. Yang, Q.; Ren, Y.; Niu, J.; Cheng, K.; Hu, Y.; Wang, Y. Characteristics of soft marine clay under cyclic loading: A review. *Bull. Eng. Geol. Environ.* **2018**, *77*, 1027–1046. [[CrossRef](#)]
9. Zhu, C.; Jiao, X.; Cheng, S.; Li, Q.; Liu, K.; Shan, H.; Li, C.; Jia, Y. Visualising fluid migration due to hydrate dissociation: Implications for submarine slides. *Environ. Geotech.* **2020**. [[CrossRef](#)]
10. Guo, X.S.; Zheng, D.F.; Nian, T.K.; Lv, L.T. Large-scale seafloor stability evaluation of the northern continental slope of South China Sea. *Mar. Georesour. Geotechnol.* **2020**, *38*, 804–817. [[CrossRef](#)]
11. Guo, X.S.; Nian, T.K.; Gu, Z.D.; Li, D.Y.; Fan, N.; Zheng, D.F. Evaluation methodology of laminar-turbulent flow state for fluidized material with special reference to submarine landslide. *J. Waterw. Port Coast. Ocean. Eng.* **2021**, *147*, 04020048. [[CrossRef](#)]
12. Zhu, C.; Li, Z.; Chen, D.; Li, S.; Song, X.; Shan, H.; Jia, Y. Seafloor breathing helping forecast hydrate-related geohazards. *Energy Rep.* **2021**, *7*, 8108–8114. [[CrossRef](#)]
13. Farahani, M.V.; Hassanpouryouzband, A.; Yang, J. Development of a coupled geophysical–geothermal scheme for quantification of hydrates in gas hydrate-bearing permafrost sediments. *Phys. Chem. Chem. Phys.* **2021**, *23*, 24249–24264. [[CrossRef](#)] [[PubMed](#)]
14. Farahani, M.V.; Hassanpouryouzband, A.; Yang, J. Insights into the climate-driven evolution of gas hydrate-bearing permafrost sediments: Implications for prediction of environmental impacts and security of energy in cold regions. *RSC Adv.* **2021**, *11*, 14334–14346. [[CrossRef](#)]
15. Huang, W.; Li, J.; Lu, Y.; Li, D.; Mou, Y.; Wu, X.; Li, Z. Mechanical Properties of Soft Soil considering the Influence of Unloading Stress Paths. *Adv. Civ. Eng.* **2021**, *2021*, 8813882. [[CrossRef](#)]
16. Dai, X.; Xu, T.; Chen, J. Physical and Mechanical Properties of Deep Oceanic Sediments Cored from the Bottom of Challenger Deep, Mariana Trench. *Geofluids* **2021**, *2021*, 9109132. [[CrossRef](#)]
17. Guo, X.S.; Nian, T.K.; Wang, Z.T.; Zhao, W.; Fan, N.; Jiao, H.B. Low-temperature rheological behavior of submarine mudflows. *J. Waterw. Port Coast. Ocean. Eng.* **2020**, *146*, 04019043. [[CrossRef](#)]
18. Liu, X.; Zhang, M.; Zhang, H.; Jia, Y.; Zhu, C.; Shan, H. Physical and mechanical properties of loess discharged from the Yellow River into the Bohai Sea, China. *Eng. Geol.* **2017**, *227*, 4–11. [[CrossRef](#)]
19. Lu, B.; Li, G.; Huang, S.; Li, C. Physical properties of sediments on the Northern Continental Shelf of the South China Sea. *Mar. Georesour. Geotechnol.* **2006**, *24*, 47–60. [[CrossRef](#)]
20. Guo, X.; Nian, T.; Zhao, W.; Gu, Z.; Liu, C.; Liu, X.; Jia, Y. Centrifuge experiment on the penetration test for evaluating undrained strength of deep-sea surface soils. *Int. J. Min. Sci. Technol.* **2022**, *32*, 363–373. [[CrossRef](#)]
21. Luo, T.; Song, Y.; Zhu, Y.; Liu, W.; Liu, Y.; Li, Y.; Wu, Z. Triaxial experiments on the mechanical properties of hydrate-bearing marine sediments of South China Sea. *Mar. Pet. Geol.* **2016**, *77*, 507–514. [[CrossRef](#)]
22. Sun, A.; Yang, G.; Yang, Q.; Qi, M.; Wang, N.; Ren, Y. Experimental investigation of thermo-mechanical behaviors of deep-sea clay from the South China Sea. *Appl. Ocean. Res.* **2022**, *119*, 103015. [[CrossRef](#)]
23. Abuel-Naga, H.M.; Bergado, D.T.; Bouazza, A.; Ramana, G.V. Volume change behaviour of saturated clays under drained heating conditions: Experimental results and constitutive modeling. *Can. Geotech. J.* **2007**, *44*, 942–956. [[CrossRef](#)]
24. Delage, P.; Sultan, N.; Cui, Y.J. On the thermal consolidation of Boom clay. *Can. Geotech. J.* **2000**, *37*, 343–354. [[CrossRef](#)]

25. Hattab, M.; Hammad, T.; Fleureau, J.M.; Hicher, P.Y. Behaviour of a sensitive marine sediment: Microstructural investigation. *Géotechnique* **2013**, *63*, 71–84. [[CrossRef](#)]
26. Low, H.E.; Lunne, T.; Andersen, K.H.; Sjørsen, M.A.; Li, X.; Randolph, M.F. Estimation of intact and remoulded undrained shear strengths from penetration tests in soft clays. *Géotechnique* **2010**, *60*, 843–859. [[CrossRef](#)]
27. Silva, A.J.; Moran, K.; Akers, S.A. Stress–strain–time behavior of deep sea clays. *Can. Geotech. J.* **1983**, *20*, 517–531. [[CrossRef](#)]
28. Lee, H.J. The role of laboratory testing in the determination of deep-sea sediment engineering properties. In *Deep-Sea Sediments*; Springer: Boston, MA, USA, 1974; pp. 111–127.
29. Cai, Y.; Hao, B.; Gu, C.; Wang, J.; Pan, L. Effect of anisotropic consolidation stress paths on the undrained shear behavior of reconstituted Wenzhou clay. *Eng. Geol.* **2018**, *242*, 23–33. [[CrossRef](#)]
30. Guo, X.; Nian, T.; Wang, D.; Gu, Z. Evaluation of undrained shear strength of surficial marine clays using ball penetration-based CFD modelling. *Acta Geotech.* **2022**, *17*, 1627–1643. [[CrossRef](#)]
31. Wang, L.; Lei, H.; Bo, Y.; Jiang, M.; Wang, P.; Liu, M. Geotechnical behavior of soft dredger fill and deep sea soft clay. In *IOP Conference Series: Earth and Environmental Science*; IOP Publishing: Bristol, UK, 2020; Volume 570, p. 062036.
32. Puzrin, A.; Frydman, S.; Talesnick, M. Normalized nondegrading behavior of soft clay under cyclic simple shear loading. *J. Geotech. Eng.* **1995**, *121*, 836–843. [[CrossRef](#)]
33. Puzrin, A.M.; Burland, J.B. Non-linear model of small-strain behaviour of soils. *Geotechnique* **1998**, *48*, 217–233. [[CrossRef](#)]
34. Prevost, J.H.; Keane, C.M. Shear stress-strain curve generation from simple material parameters. *J. Geotech. Eng.* **1990**, *116*, 1255–1263. [[CrossRef](#)]
35. Wu, C.S.; Hong, Y.S.; Lin, H.C. Axial stress–strain relation of encapsulated granular column. *Comput. Geotech.* **2009**, *36*, 226–240. [[CrossRef](#)]
36. Liu, J.; Chang, D.; Yu, Q. Influence of freeze-thaw cycles on mechanical properties of a silty sand. *Eng. Geol.* **2016**, *210*, 23–32. [[CrossRef](#)]
37. *ASTM D421-85*; Standard Practice for Dry Preparation of Soil Samples for Particle-Size Analysis and Determination of Soil Constants (Withdrawn 2016). ASTM International: West Conshohocken, PA, USA, 2007.
38. *ASTM D2487-17*; Standard Practice for Classification of Soils for Engineering Purposes (Unified Soil Classification System). ASTM International: West Conshohocken, PA, USA, 2017.
39. Zhang, C.; Pan, Z.; Yin, H.; Ma, C.; Li, X. Influence of clay mineral content on mechanical properties and microfabric of tailings. *Sci. Rep.* **2022**, *12*, 10700. [[CrossRef](#)]
40. Daha, B.K.; Zheng, J.J.; Zhang, R.J.; Song, D.B. Enhancing the mechanical properties of marine clay using cement solidification. *Mar. Georesour. Geotechnol.* **2019**, *37*, 755–764.
41. Duncan, J.M.; Chang, C.Y. Nonlinear analysis of stress and strain in soils. *J. Soil Mech. Found. Div.* **1970**, *96*, 1629–1653. [[CrossRef](#)]

Article

Analysis of Cyclic Shear Stress–Displacement Mechanical Properties of Silt–Steel Interface in the Yellow River Delta

Peng Yu ^{1,2}, Jie Dong ^{1,2}, Haisong Liu ^{1,2}, Rui Xu ^{1,2}, Rujie Wang ^{1,2}, Meijun Xu ^{1,2} and Hongjun Liu ^{3,4,*}

- ¹ Key Laboratory of Geological Safety of Coastal Urban Underground Space, Ministry of Natural Resources, Qingdao 266100, China
² Qingdao Geo-Engineering Surveying Institute, Qingdao Geological Exploration Development Bureau, Qingdao 266100, China
³ Department of Environmental Science and Engineering, Ocean University of China, Qingdao 266100, China
⁴ Key Laboratory of Marine Environmental Science and Ecology, Ministry of Education, Qingdao 266100, China
* Correspondence: hongjun@ouc.edu.cn; Tel.: +86-186-6179-0379

Abstract: Pile foundations of offshore structures are often subjected to cyclic loads under storm loads, thus reducing their vertical bearing capacity. Therefore, studying the cyclic shear behavior of the soil–structure interface is important for maintaining the stability of offshore structures. A series of cyclic shear tests of the silt–steel interface were carried out using a large interface shear apparatus. The effects of various factors (i.e., normal stress, shear displacement amplitude, roughness, and water content) on the shear stress characteristics of the silt–steel interface were investigated. The stress–displacement model of the cyclic shear silt–steel interface was deduced. The results showed that the shear stress at the silt–steel interface was softened, and the type of bulk deformation was shear shrinkage under cyclic shear. With the increase in shear amplitude, the hysteresis curve gradually developed from “parallelogram” to “shuttle” and “hysteresis cake”. With the increase in normal stress and roughness and the decrease in water content, the interfacial shear strength, volume displacements growth rate, and growth rate increased. The stress–displacement mathematical model of the silt–steel interface based on the modified hyperbolic model was in good agreement with the test data.

Keywords: cyclic shear test; silt–steel interface; stress–displacement mechanical properties

Citation: Yu, P.; Dong, J.; Liu, H.; Xu, R.; Wang, R.; Xu, M.; Liu, H. Analysis of Cyclic Shear Stress–Displacement Mechanical Properties of Silt–Steel Interface in the Yellow River Delta. *J. Mar. Sci. Eng.* **2022**, *10*, 1704. <https://doi.org/10.3390/jmse10111704>

Academic Editors: Dong-Sheng Jeng and José António Correia

Received: 21 September 2022

Accepted: 7 November 2022

Published: 9 November 2022

Publisher’s Note: MDPI stays neutral with regard to jurisdictional claims in published maps and institutional affiliations.



Copyright: © 2022 by the authors. Licensee MDPI, Basel, Switzerland. This article is an open access article distributed under the terms and conditions of the Creative Commons Attribution (CC BY) license (<https://creativecommons.org/licenses/by/4.0/>).

1. Introduction

Pile foundations are increasingly widely used in offshore projects, such as offshore wind power and oil and gas platforms. During their service period, they bear the static load generated by the self-weight of the superstructure and the cyclic load generated by waves and winds. Research on the weakening mechanism of the pile–soil interface under cyclic loading is helpful in revealing the mechanical characteristics and load transfer mechanism of the pile–soil interface and is significant for further study of the long-term bearing capacity of pile foundations.

Scholars in the relevant field have carried out cyclic shear tests on soil–structure interfaces. For example, Zhang et al. (2018) [1] designed and developed a new type of 80 ton 3D multi-functional equipment to study the cyclic characteristics of the soil–structure interface under 2D and 3D complex load conditions. Li and Guo (2020) [2] studied the influence of cementitious materials and surface roughness on interfacial shear strength. Jotisankasa et al. (2018) [3] and Li et al. (2020) [4] studied the mechanical properties of sandy soil and the clay pile–soil interface, respectively, and specifically considered the change rule for the shear stiffness and the damping ratio. Wang et al. (2016) [5] used the direct shear after cyclic shear (PCDS) test method to discuss the mechanical properties, including the residual strength, of the interface after re-consolidation under large shear deformation. With regard to the soil–structure interface cyclic shear mechanical model, Liu et al. (2014) [6] proposed a

constitutive interface model based on critical state soil mechanics and generalized plasticity that could simulate the cyclic 3D behavior of the soil–structure interface for wide ranges of soil density, normal pressure, and normal stiffness. Stutz et al. (2016) [7] proposed an enhanced non-plastic interface model. The existing plastic model with a predefined sand limit state surface was converted into an interface model by reducing the stress and tension vectors and redefining the tensor. Saberi et al. (2020) [8] continuously revised and improved a two-sided plastic interface constitutive model by introducing critical state soil mechanics, a particle breakage rate, a new failure surface, a 3D shear coupling load, etc., so that the interface model could simulate the complex cyclic behavior of various soil–structure interfaces. However, there are few studies on the silt–structure interface.

Silt, as a transitional soil between sand and clay, presents dual mechanical behavior related to both and has relatively special engineering properties. However, the Yellow River delta silt is formed from rapid sedimentation. The soil has the characteristics of high water content, high pore water pressure, high compressibility, and low shear strength. In this study, a large-scale cyclic shear test of the silt–steel interface was carried out for the silt in the Yellow River subaqueous delta. Considering normal stress, roughness, water content, number of cycles, and shear amplitude, the mechanical characteristics of the shear stress and the displacement at the pile–soil interface under storm cyclic loading were studied, and the mathematical model of stress and displacement was derived. The results are expected to provide a theoretical reference for the design and evaluation of engineering structures under vertical cyclic loading in the Yellow River delta.

2. Materials and Methods

2.1. Test Instruments and Materials

The cyclic shear test was carried out in the Seismic Research Institute of Dalian University of Technology using the *JAW-500* large shear apparatus (Figure 1). This large-scale shear apparatus includes the following important components: (1) A computer-controlled automatic hydraulic loading system. The system is equipped with cooling equipment so that a constant load can be applied during the test. (2) A large shear box. The size of the shear box is 500 mm × 500 mm × 300 mm. Transparent glass is set on the side to observe the shear behavior, and the larger size also reduces the boundary effect [9]. (3) A shearing box protection device. The upper part of the shear box is provided with a base plate, and the normal stress is transmitted to the contact surface through the base plate to effectively control the normal boundary conditions. The lower part of the shear box is equipped with 20 springs to measure the volume change during the shearing process.

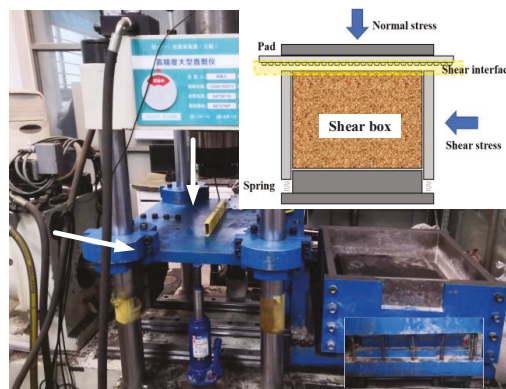


Figure 1. Large-scale shear instrument.

In accordance with the test conditions, the soil used in this test was the remolded silty seabed soil of the Yellow River delta [10]. The mechanical parameters and grading of

the silt are shown in Tables 1 and 2, and the average particle size $d_{50} = 0.03$ mm. Firstly, undisturbed soil with high porosity and poor permeability was remolded through drying, crushing, and screening. Then, the dry density of soil was set to 1.61 g/cm^3 , and soil samples with different water content were prepared by adding water of different quality. The water content was set according to the engineering geological characteristics of soft soil sediments in the modern underwater delta of the Yellow River [11–13] and the optimal water content (19.6%) for soil samples. The relationship between natural water content and void ratio $w = 36.668e - 0.983$ was adopted for calculations. In addition, considering that soil is close to a soft plastic state when the water content is too large, it cannot withstand the normal pressure of 300 kPa, and the conventional direct shear test cannot be carried out. Therefore, the maximum water content was set to 24% (saturation of 95.2%). Finally, remolded soil samples with a water content of 16%, 20%, and 24% (saturation of 63.5%, 79.3%, and 95.2%) were obtained. After the soil samples were fully stirred, the uniformly stirred soil samples were stored for two days (Figure 2).

Table 1. Basic physical properties of silt.

Specific Gravity <i>G_s</i>	Optimum Water Content %	Void Ratio <i>e</i>	Plastic Limit <i>ω_p</i> /%	Liquid Limit <i>ω_L</i> /%
2.7	19.60%	0.69	18.3	30.1

Table 2. Particle size distribution of silt.

Specimen Numbers	0.25–0.075	0.075–0.05	0.05–0.01	0.01–0.005	<0.005
Percentage	6.6%	21.6%	51.8%	5.9%	14.1%



Figure 2. Preparation process for soil samples.

To ensure that the effective contact area between the soil samples and steel plate remained unchanged during shearing, the steel plate size along the shearing direction was 220 mm longer than the lower shear box, and the selected steel plate size was 720 mm × 580 mm × 5 mm (Figure 3). In order to simulate the rusting or erosion of pile foundations under actual sea conditions, three steel plate roughness levels (i.e., R_0 (smooth), R_1 (relatively rough), and R_2 (rough)) were set using the modified sand filling method (Table 3) [14]. The steel plate parameters included valley peak height H , groove cross-section width L_1 , and platform spacing L_2 . The roughness calculation equation used was as follows:

$$R = \frac{HL_1}{2(L_1 + L_2)} \tag{1}$$

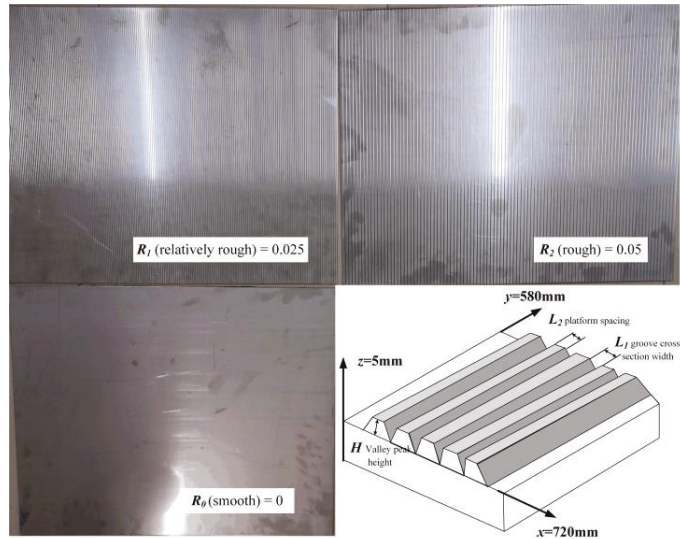


Figure 3. Steel plates with different roughness levels.

Table 3. Different roughness levels of steel plates.

R	N	L ₁ (mm)	L ₂ (mm)	H (mm)
0	\	\	\	\
0.025	200	0.6	3	0.3
0.05	100	1.2	6	0.6

2.2. Test Methods

In order to study the relationship between cyclic shear stress and displacements at the silt–steel interface, five influencing factors—normal stress, cycle times, shear amplitude, roughness, and water content—were selected in this test. Given the problems of the large loading and unloading workload and the long test time needed for the large shear apparatus, nine groups were set up in this test: three normal stresses, three shear amplitudes, three roughness levels, and three levels of moisture content (Table 4). It should be noted that this experiment was carried out under the condition of constant normal load (CNL).

Table 4. Test group.

Group	Roughness	Water Content (%)	Normal Stress (kPa)	Shear Amplitude (mm)
1	0.05	16	200	35
2	0.05	20	100	5
3	0.05	20	200	5
4	0.05	20	300	5
5	0.05	20	200	15
6	0.05	20	200	35
7	0.05	24	200	35
8	0	20	200	35
9	0.025	20	200	35

Ren et al. (2020) [15] found that the underwater delta of the Yellow River consolidated due to rapid sedimentation, wave action, etc., during its formation. Therefore, undrained fast shear was adopted in this test. Due to the lack of experimental research on the silt

interface in the Yellow River subaqueous delta, the test parameters were set according to previous studies on clay and loess interfaces. The normal stress was obtained from the round hole expansion theory, the coefficient of static earth pressure of silt $K_0 = 0.33$, and the horizontal self-weight stress of soil mass $\sigma_{cx} = \sigma_{cy} = K_0\sigma_{cz} = K_0\gamma z$. The maximum normal stress was set as 300 kPa. The shear rate was set as 1 mm/s, as recommended by Wang et al. (2019) [16]. The shear amplitudes were set as 5 mm, 15 mm, and 35 mm, in accordance with the size of the instrument. Each group of tests cycled 30 times with a frequency of 0.01 Hz.

Before the test, the soil sample in the shear box was compacted using an automatic compactor. Each layer was filled with 6 cm of soil and was compacted five times. The surface of the soil sample was roughened after each compaction to ensure that the soil sample was isotropic and uniform. After all soil samples were loaded, the soil samples were consolidated for a short time (15 min) under a vertical pressure of 25 kPa to ensure the full transmission of normal stress and avoid the influence of the over-consolidation ratio.

At the beginning of the test, constant normal pressure was applied first, followed by a tangential waveform force. The tangential force, tangential displacement, normal displacement, and other parameters were collected during the test. After the test, the shear plane failure was observed (Figure 4). A large amount of original data for each group of tests was processed using the average displacement value. Furthermore, 20–25 representative points were counted for drawing and analysis. Therefore, the fluctuation in the data curve caused by volume change was not significant [17].

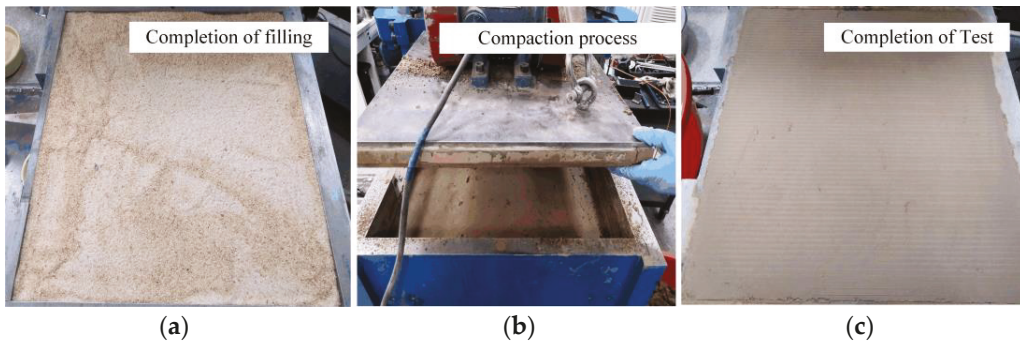


Figure 4. Process of shear test: (a) completion of filling; (b) compaction process; (c) completion of test.

3. Results and Discussion

3.1. Relationship between Shear Stress and Shear Displacement

Isochronous voltage automatic measurement was adopted for data acquisition in the test. There were 1000 data points in each cycle and 30,000 data points in each group of 30 cycles. The data were too extensive to be displayed individually, so the results of the 1st, 5th, 10th, 15th, 20th, 25th, and 30th test cycles were selected as representative data for analysis.

3.1.1. Effect of Normal Stress

Figure 5 shows the shear stress–shear displacement curves under different normal stresses of 100 kPa, 200 kPa, and 300 kPa, with a fixed shear amplitude of 5 mm, steel plate roughness of 0.05, and water content of 20%. The results showed that:

(1) Except for the first cycle, the shear stress–shear displacement hysteresis curve was basically closed. With the increase in the number of cycles, the hysteresis loop shrank inwards, indicating that the interfacial shear stress was softening. This test phenomenon was inconsistent with the test results obtained by Wang et al. (2021) [18] and Rui et al. (2020) [19]. One of the reasons for the inconsistency was the different types of

test soil. The above scholars used coarse sand and rockfill materials with larger particle sizes. With increases in the number of cycles, particles break, which causes hardening. However, silt from the Yellow River delta with a smaller particle size was used in this study. In addition, the softening phenomenon was consistent with the test results for red clay with smaller particle sizes [20] and silt [21] from the Yellow River flood area, while the shear amplitude was different. The shear amplitude of 1–3 mm set by the above scholars was relatively small. However, larger shear amplitudes of 5 mm, 15 mm, and 35 mm were selected for this test. In the first few cycles (total shear displacement < 50 mm), the stage of failure equilibrium was almost reached. Therefore, with the increase in the shear displacement, softening occurred;

(2) Under the condition of small shear amplitude, the shear stress–shear displacement hysteresis curve was a parallelogram, and the slope of the loading section was smaller than that of the unloading section. With the increase in normal stress, the slope of the loading section increased while the slope of the unloading section decreased;

(3) In the same cycle, the mechanical properties along different shear directions showed anisotropy. The maximum shear stress in the positive and negative directions appeared at the maximum shear displacement in the respective directions, but the values were different. The maximum shear stress in each direction increased with the increase in normal stress. Zhang et al. (2018) [1] attributed the anisotropy between the shear mechanical response and the shear direction of this interface to the directional constraint of the roughness of the steel plate on the soil particles, and the reverse shear effect caused the soil particles to become reordered.

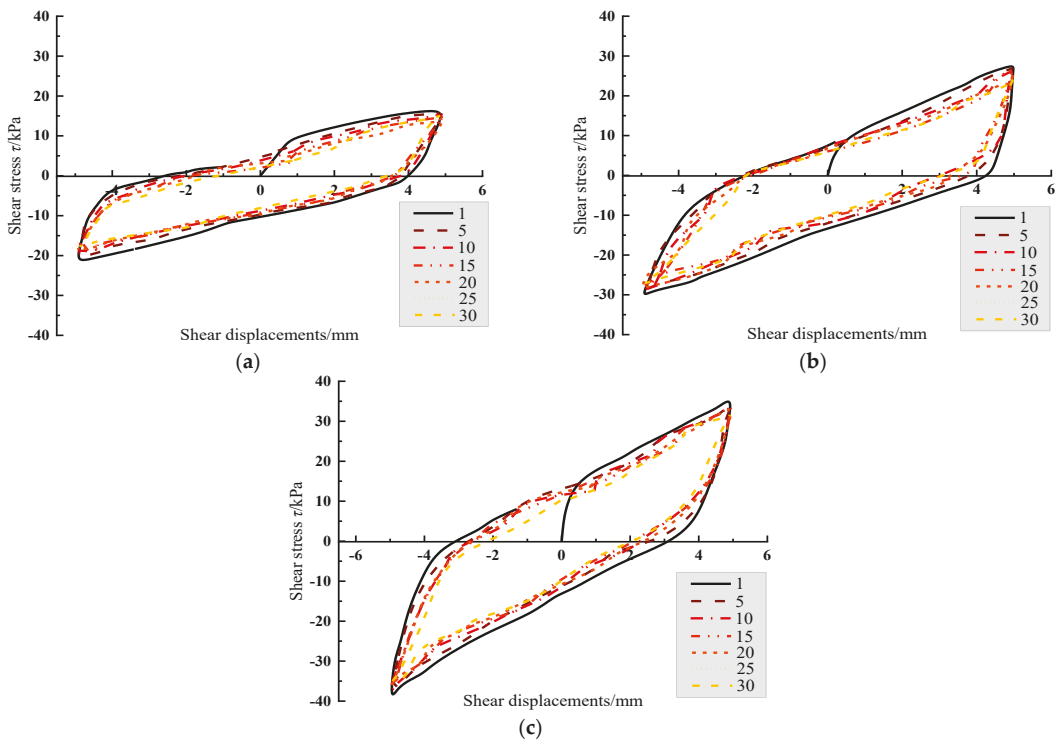


Figure 5. Shear stress–shear displacement curves under different constant normal stresses: (a) 100 kPa; (b) 200 kPa; (c) 300 kPa.

3.1.2. Effect of Shear Amplitude

Figure 6 shows the shear stress–shear displacement curves under different shear amplitudes of 5 mm, 15 mm, and 35 mm with a fixed constant normal stress of 200 kPa, steel plate roughness of 0.05, and water content of 20%. The results showed that:

- (1) A change in the shear amplitude could change the shape of the hysteresis curve. With the increase in the shear amplitude, the hysteresis curve gradually developed from “parallelogram” to “shuttle” and “hysteresis cake”;
- (2) The slope of the loading section increased with the increase in the shear amplitude, while the slope of the unloading section decreased with the increase in the shear amplitude.

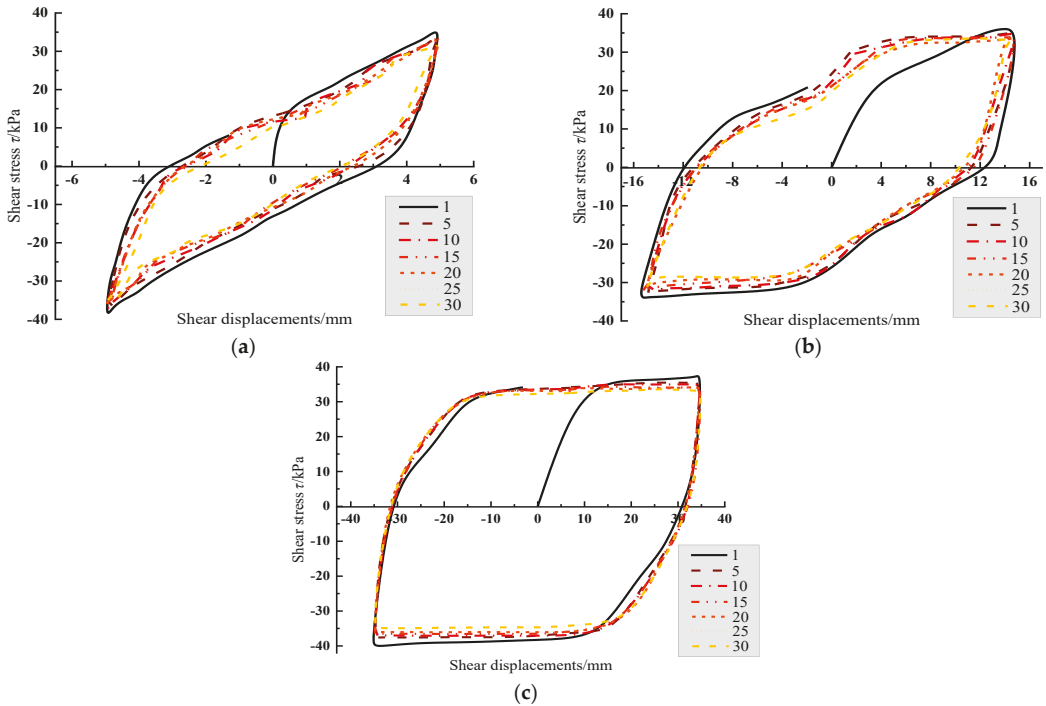


Figure 6. Shear stress–shear displacement curves with different shear amplitudes: (a) 5 mm; (b) 15 mm; (c) 35 mm.

3.1.3. Effect of Roughness

Figure 7 shows the shear stress–shear displacement curve under the conditions of $R = 0, 0.025, \text{ and } 0.05$ with a fixed constant normal stress of 200 kPa, shear amplitude of 35 mm, and water content of 20%. Roughness had little effect on the hysteresis curve. The change in the roughness mainly affected the maximum shear stress. Greater roughness resulted in greater maximum shear stress, which was consistent with the conclusion of the direct shear test [22].

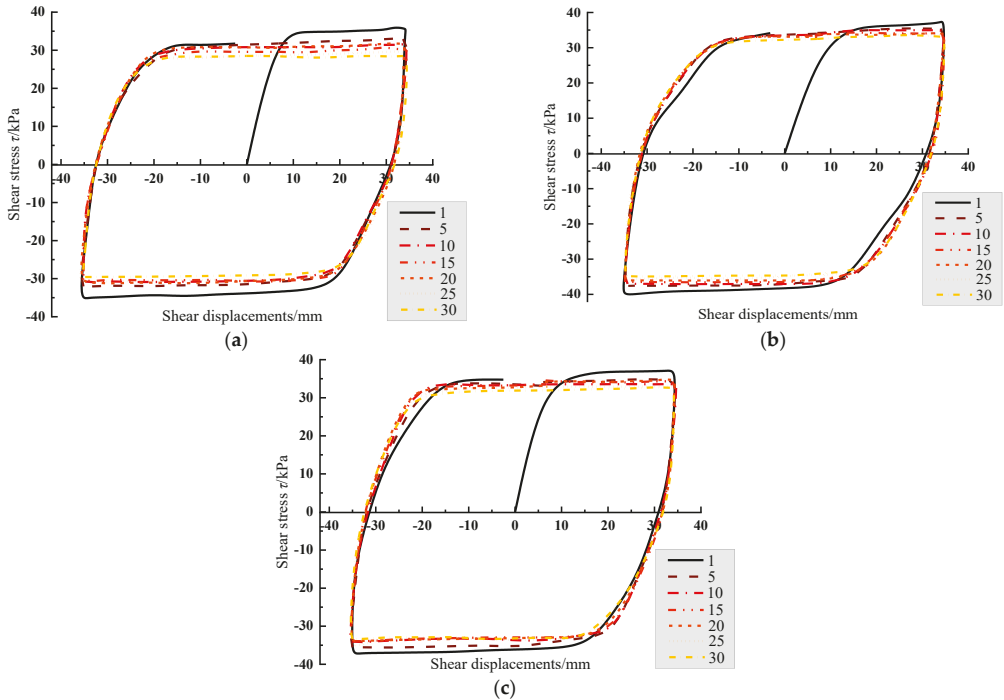


Figure 7. Shear stress-shear displacement curves with different roughness levels: (a) R_0 ; (b) R_1 ; (c) R_2 .

3.1.4. Effect of Water Content

Figure 8 shows the shear stress–shear displacement curves with a fixed constant normal stress of 200 kPa, shear amplitude of 35 mm, and steel plate roughness of 0.05 under different water content conditions of 16%, 20%, and 24%. Water content also had little effect on the hysteresis curve. The change in the water content mainly affected the maximum shear stress. Lower water content resulted in greater maximum shear stress, which was consistent with the conclusion of the direct shear test [22].

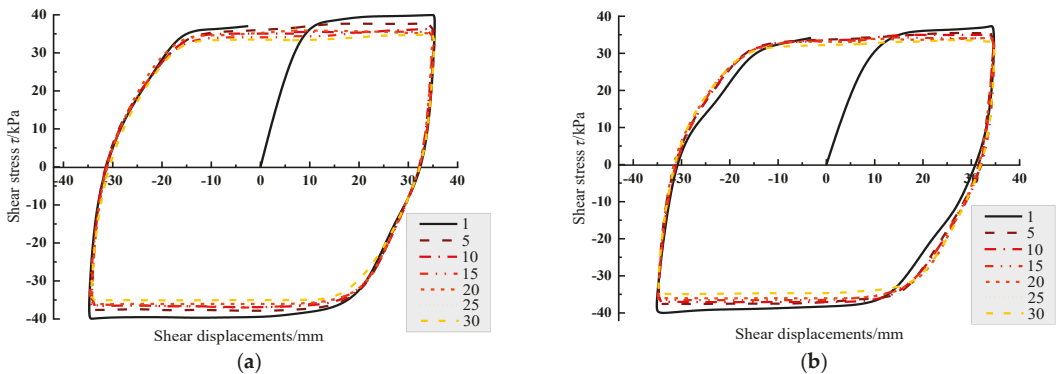


Figure 8. Cont.

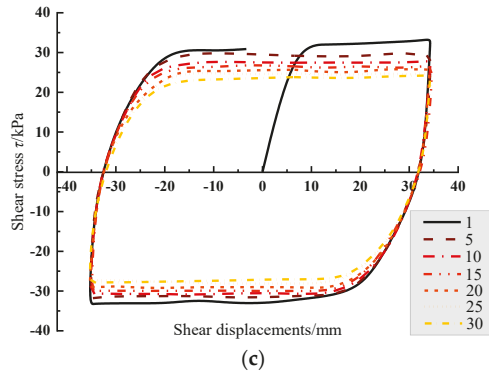


Figure 8. Shear stress-shear displacement curves with different levels of water content: (a) 16%; (b) 20%; (c) 24%.

3.1.5. Shear Strength

The concept of peak shear stress τ^{max} was also introduced, and the influence of various factors on the interface shear strength was calculated. The peak shear stress is calculated as follows:

$$\tau^{max} = \frac{\tau_1 + |\tau_2|}{2} \tag{2}$$

where τ_1 is the maximum shear stress in the positive direction of a cycle and τ_2 is the maximum shear stress in the negative direction of a cycle.

The peak shear stress of the first cycle was defined as the shear strength, and the peak shear stress of the last cycle was defined as the residual shear strength, as shown in Figure 9. The results were as follows:

1. With the increase in the cyclic shear, the interface tended to weaken. The shear strength and residual shear strength increased with the increase in the shear amplitude.
2. With the increase in the normal stress and roughness and the decrease in the water content, the interfacial shear strength and residual shear strength increased. The results were consistent with the direct shear test results for the silt–steel interface [22].

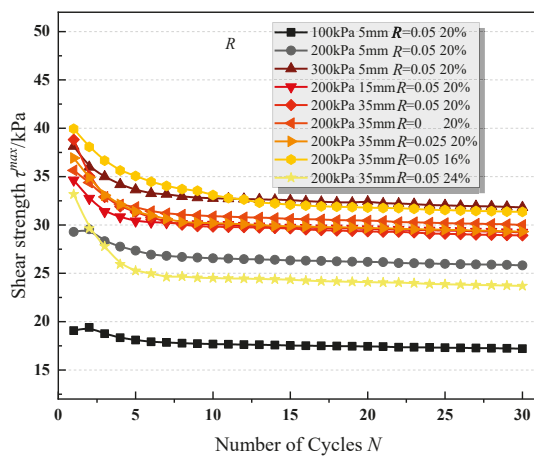


Figure 9. Shear strength of each group.

3.2. Body Change Law

In this experiment, the area of the contact surface remained unchanged during the shearing process. Therefore, the change in the normal displacement of the contact surface reflected the volume change law for the soil during the shearing process.

3.2.1. Typical Curve for Normal Displacement–Shear Displacement

As the volume change laws obtained from each group of tests were approximately similar, the test data curve with the constant normal stress of 200 kPa, shear amplitude of 35 mm, steel plate roughness of 0.05, and water content of 20% was selected as the typical characteristic curve to analyze the influence of cycle times on the volume change laws. The defined shrinkage was positive, the shrinkage of each circle was defined as the shrinkage value at the end of the circle, and the final shrinkage value was defined as the shrinkage value at the end of the last circle. The normal displacement–shear displacement curve in Figure 10 shows that:

1. In the process of cyclic shear, the silt–steel interface generally presented shear shrinkage, and the shear shrinkage in the first five cycles was the largest. With the progress of the cyclic shear, the shear shrinkage increment presented a decreasing trend, but the overall shear shrinkage showed an increasing trend. This phenomenon can be explained according to the test conclusions drawn by Wang et al. [21] and Yu et al. [22]. In the process of loading and compaction, the soil body undertakes part of the compaction work. During the shearing, due to the displacement of soil particles, the accumulated cohesive potential energy and friction potential energy from compaction are released, resulting in an upward force. When the normal stress is high, the pressure difference between the upward force and the normal stress is negative and the soil particle gap is compressed, and the interface thereby shows shear shrinkage;
2. In the same cycle, shear shrinkage and shear expansion occurred alternately. The shear shrinkage occurred in the loading stage, and shear expansion occurred in the unloading stage. The results show that the shear direction affected the development of the normal displacement, leading to an asymmetry in the volume change law. This phenomenon corresponds to the above conclusion on the anisotropy of shear stress. The reasons for the phenomenon are as follows. In the case of positive shear, the soil particles develop from the initial disordered arrangement to the directional arrangement, and the interface produces an apparent shear directional effect. The particle breakage and the space compression between soil particles produce shear shrinkage. In reverse shear, the stress direction of soil particles near the shear surface changes. On the one hand, the soil particles are gradually evacuated from the compaction state until they make contact again and become stable, showing shear expansion. On the other hand, the directional deformation generated during the positive shear impedes the deformation of the soil in the opposite direction, resulting in the shear expansion being less than the shear shrinkage, and a certain amount of residual deformation (shear shrinkage) occurs at the end of each cycle. When the shear direction changes, the soil particle movement is most active, resulting in apparent volume change and leading to the directivity in the macroscopic volume variation;
3. Based on the comprehensive analysis of the causes of the above phenomena, the overall shear deformation in a complete shear cycle can be divided into reversible shear deformation and irreversible shear deformation. Irreversible deformation is mainly caused by stable normal stress and soil particle crushing, while reversible deformation is mainly caused by changes in the shear direction. At the initial stage of cyclic shear, the soil particles are angular and disorderedly arranged, and the irreversible body becomes dominant. However, as the shear continues, the soil particles at the shear interface slowly reach a stable state, and the amount of soil particle breakage decreases. At this time, the reversible shear deformation formed by the change in the shear direction plays a major role. Therefore, the macroscopic performance is defined by the fact that, with the increase in shear times, the volume deformation curves

gradually recombine, which indicates that, during the shear test, the irreversible shear deformation of the sample becomes small, while the reversible shear deformation always exists. Zhao et al. (2019) [23] has reported that this deformation characteristic is related to the shear band.

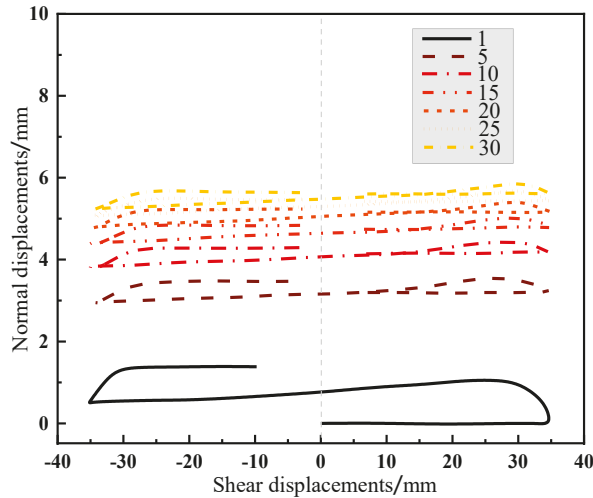


Figure 10. Normal displacement–shear displacement curve with different numbers of cycles.

3.2.2. Effect of Normal Stress

In order to more clearly explore the influence of different factors on the volume change, the number of test cycles in each group was selected as $N = 1, 5, 10, 15, 20, 25,$ and 30 ; the volume variable at the end of each cycle was taken as the volume variable of the cycle; and the curve for the number of normal displacement cycles was drawn.

Figure 11 shows the change curve for the interface body under three different constant normal stress conditions with a fixed shear amplitude of 5 mm, steel plate roughness of 0.05, and water content of 20%. The results were as follows:

1. Under different normal stress conditions, the initial ($N = 1$) cyclic interface showed shear shrinkage. A larger normal stress means larger initial shear shrinkage;
2. Under the action of low normal stress (100 kPa), the shear shrinkage gradually decreased with the increase in the number of cycles, showing a certain shear expansion trend. Under the action of medium-high normal stress (200 kPa and 300 kPa), with the increase in the normal stress, the effect of the steel plate’s constraint on the soil particles on the interface increased, the rate of the increase in the deformation displacement with the number of cycles grew, and the amplitude increased. The results suggest that greater normal stress indicates greater final shear shrinkage, which is consistent with the volume change rule from the direct shear test [22]. The reason for the result was that the cohesive potential energy and friction potential energy between soil particles were fully released under low normal stress and showed dilatancy characteristics. Dejong et al. (2009) [24] also reported that the increase of normal stress inhibited the shear expansion behavior;
3. The volume variable in the first few shear cycles ($N < 5$) accounted for more than 70% of the total variation. As the shear cycle continued, the arrangement of soil particles at the interface and the volume change were also stable.

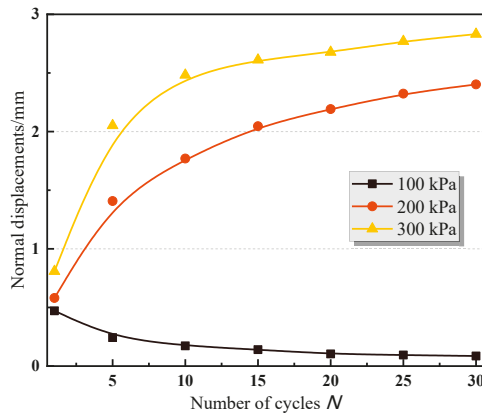


Figure 11. Curve for normal displacement–number of cycles under different constant normal stress.

3.2.3. Effect of Other Factors

Figure 12 shows the development curve for the normal displacement of the interface with the number of cyclic shear cycles under different conditions involving other factors (shear amplitude, roughness, and water content) when the fixed normal stress was 200 kPa. The volume deformation law was consistent with the law determining the influence of the various factors on shear strength, indicating that, with the increase in the shear amplitude, the roughness, water content, and volume deformation speed and increment increased. Under the condition of high water content (24%), the increase in shear shrinkage was far greater than that under the condition of 16–20% water content, which may have been because some water was squeezed out of the soil sample with high water content in the process of cyclic shear under nearly saturated conditions.

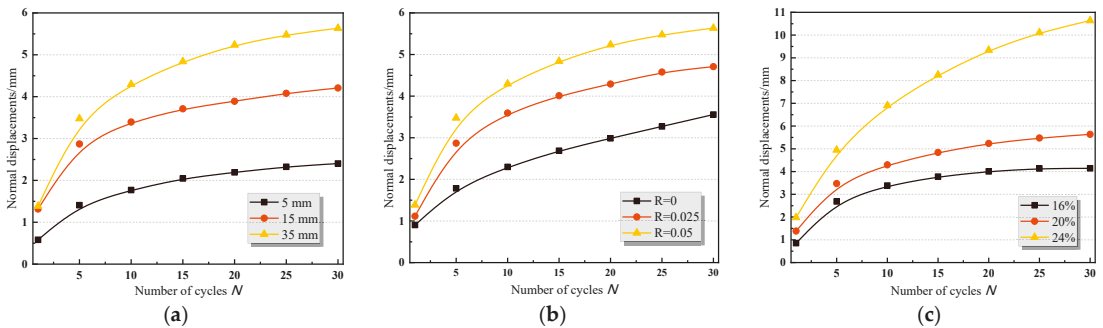


Figure 12. Curve for normal displacement–number of cycles under different conditions: (a) shear amplitude; (b) roughness; (c) water content.

3.3. Stress–Displacement Mathematical Model for Cyclic Shear Silt–Steel interface

3.3.1. Model Derivation

The cyclic test results show that the stress–displacement curve for the silt–steel interface in the Yellow River delta basically presented a “hysteresis loop” shape. Except for the shear amplitude, its different influencing factors, such as normal stress, roughness, water content, and the number of cycles, only affected the extreme values and curve ranges and had little impact on the overall shape of the curve. In order to describe the cyclic shear stress–displacement relationship applicable to the silt–steel interface in the Yellow River delta reasonably and accurately, the stress–displacement curve can be divided into five

stages: (1) forward loading section; (2) forward unloading section; (3) direction-changing shear section; (4) reverse unloading section; (5) reverse loading section. A complete set of cyclic shear stress–displacement mathematical models was constructed by describing the curve characteristics of each stage. The phase division diagram is shown in Figure 13.

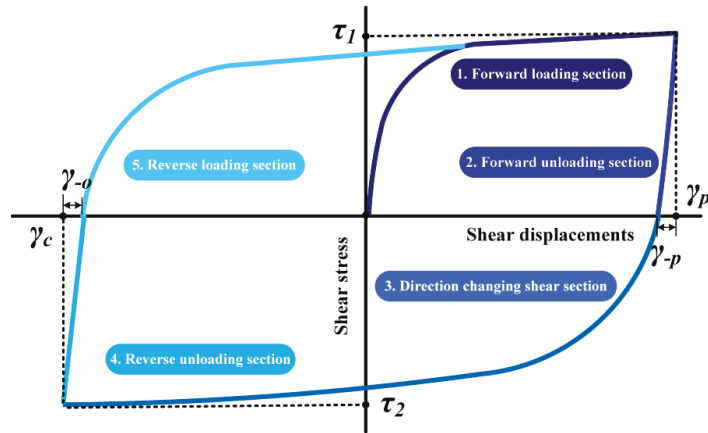


Figure 13. Cyclic shear hysteresis.

Figure 13 shows that the shear stress–shear displacement relationship curves of the positive loading section, variable shear section, and reverse loading section were close to the hyperbola. Lu (2015) [25] proved through tests that the hyperbola model for the cyclic shear test is also applicable to the situation under cyclic stress if it is modified based on the Clough classical hyperbola model. Its simplified form is:

$$\tau = \frac{\gamma}{a + b\gamma} \tag{3}$$

where a and b are test parameters; $1/a$ is the initial shear stiffness coefficient k_{si} of the contact surface, which can be determined from the initial slope of the shear stress–shear displacement curve; and $1/b$ is the ultimate shear stress τ_u of the contact surface, which can be determined from the asymptote of the shear stress–shear displacement curve. Referring to the hyperbola correction model published by He et al. (2019) [26], the basic form can finally be obtained:

$$\tau = \frac{\gamma}{\frac{1}{k_{si}} + \frac{R_f}{\tau_{max}} \gamma} \tag{4}$$

Considering the cohesive force of the silty seabed soil in the Yellow River delta, the shear strength conforms to Mohr Coulomb’s law.

According to Figure 12 and Equation (4), the forward loading section can be expressed as follows:

$$\tau_p = \frac{\gamma}{\frac{1}{k_{sip}} + \frac{R_{fp}}{\tau_{maxp}} \gamma} \quad \gamma \leq \gamma_p \tag{5}$$

The direction-changing shear section can be expressed as follows:

$$\tau_c = \frac{\gamma - (\gamma_p - \gamma_{-p})}{\frac{1}{k_{sic}} + \frac{R_{fc}}{\tau_{maxc}} (-\gamma + (\gamma_p - \gamma_{-p}))} \quad \gamma_c < \gamma \leq \gamma_p - \gamma_{-p} \tag{6}$$

The reverse loading section can be expressed as follows:

$$\tau_o = \frac{\gamma - (\gamma_c + \gamma_{-o})}{\frac{1}{k_{sio}} + \frac{R_{fo}}{\tau_{maxo}}(\gamma - (\gamma_c + \gamma_{-o}))} \quad \gamma_c + \gamma_{-o} < \gamma \tag{7}$$

The parameters in the equation were uniformly characterized. The results are shown in Figure 13. γ_p and γ_c are the displacements at the end of the forward loading and direction-changing shear section, respectively; γ_{-p} and γ_{-o} are the displacements required for the forward unloading section and reverse unloading section, respectively; $K_{si(p,c,o)}$ indicates the initial shear stiffness values for the forward loading section, direction-changing shear section, and reverse loading section, respectively; and $\tau_{max(p,c,o)}$ and $R_{f(p,c,o)}$ are the shear strength and failure ratio corresponding to the three stages.

The forward unloading and reverse unloading sections are represented by straight lines. Furthermore, the forward unloading section can be represented as:

$$\tau_{-p} = \frac{[\gamma - (\gamma_p - \gamma_{-p})]}{\gamma_{-p}} \tau_1 \quad \gamma_p - \gamma_{-p} < \gamma \leq \gamma_p \tag{8}$$

The reverse unloading segment can be expressed as:

$$\tau_{-o} = \frac{[-\gamma + (\gamma_c + \gamma_{-o})]}{\gamma_{-o}} \tau_2 \quad \gamma_c < \gamma \leq \gamma_c + \gamma_{-o} \tag{9}$$

The parameters are shown in Figure 12, where τ_1 and τ_2 are the shear stress at the end of the forward loading and direction-changing shear sections, respectively.

The simultaneous Equations (4)–(9) were used to obtain the cyclic shear stress–displacement mathematical model of the silt–steel interface in the Yellow River delta.

3.3.2. Parameter Determination and Model Verification

For the above stress–displacement mathematical model, the displacement parameters γ_p , γ_c , γ_{-p} , and γ_{-o} and the stress parameters τ_1 , τ_2 , and $\tau_{max(p,c,o)}$ were statistically obtained from shear test data. The shear stiffness $k_{si(p,c,o)}$ and failure ratio $R_{f(p,c,o)}$ for the model parameters were obtained by fitting the shear test data. The damage ratio was $R_f = \tau_{max} / \tau_u$. By fitting the asymptote of the test data curve, the value range was found to be 0.91–0.96. The initial shear stiffness k_{si} was the slope of the stress–displacement relationship curve at the tangent line of the origin. The concept of ultimate relative displacement Δ_{cr} can be introduced:

$$k_{si} = \frac{\tau_{max}}{R_f \Delta_{cr}} \tag{10}$$

In accordance with the suggestion by Fellenius (2006) [27], the ultimate relative displacement Δ_{cr} was taken as 2 mm.

The displacement parameters and stress parameters obtained from the test are shown in Table 5. The cyclic shear test data from the first cycle of group 6 with the constant normal stress of 200 kPa, roughness of $R = 0.05$, water content of 20%, and shear amplitude of 35 mm are selected for comparison verification. According to these cyclic shear test data, the displacement required for the forward unloading section γ_{-p} was 2.1 mm; the failure ratio R_{fc} of the direction-changing shear section was 0.93; the displacement required for the reverse unloading section γ_{-o} was approximately 2 mm; and the value of the failure ratio R_{fo} for the reverse loading section was 0.95. In addition, the shear strengths of the forward loading section, direction-changing shear section, and reverse loading section were 34.21 kPa, 36.05 kPa, and 33.02 kPa, respectively, and the unified value of ultimate relative displacement Δ_{cr} is 2 mm. Therefore, the initial shear stiffness values k_{sip} , k_{sicr} , and k_{sio} of the three stages were 18.39 kPa/mm, 20.03 kPa/mm, and 17.38 kPa/mm, respectively. Figure 14 shows that the stress–displacement mathematical model had a high degree of coincidence with the test curve. Furthermore, the shear strengths of the forward

loading section, direction-changing shear section, and reverse loading section showed little difference from the test data. The results prove that the model has good applicability.

Table 5. The displacement parameters and stress parameters.

Group	γ_p (mm)	γ_c (mm)	γ_p (mm)	γ_o (mm)	τ_{maxp} (kPa)	τ_{maxc} (kPa)	τ_{maxo} (kPa)	k_{sip} (kPa/mm)	k_{sic} (kPa/mm)	k_{sio} (kPa/mm)	Others
1	35.63	35.06	3.13	3.84	39.97	39.96	39.14	21.26	21.25	20.81	
2	5.00	5.00	0.98	1.07	16.47	21.71	9.57	8.76	11.54	5.09	
3	4.98	5.00	0.66	1.13	27.92	30.69	12.37	14.85	16.32	6.57	
4	5.07	4.95	0.91	1.10	36.52	39.87	15.10	19.42	21.20	8.03	
5	15.00	14.97	1.91	2.51	36.05	34.08	25.31	19.17	18.12	13.46	
6	35.00	35.00	2.10	2.00	34.21	36.05	33.02	18.39	20.03	17.38	$\Delta_{\tau} = 2 \text{ mm}$
7	34.45	35.60	2.43	3.21	33.39	33.37	31.90	17.76	17.75	16.96	$R_p = 0.91\sim 0.96$
8	34.50	36.21	3.09	3.71	36.15	35.20	34.57	19.23	18.72	18.38	
9	34.51	35.21	2.59	3.43	37.23	37.40	35.21	19.80	19.89	18.72	

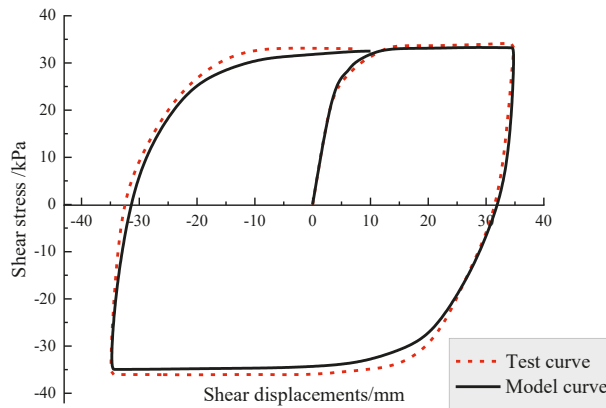


Figure 14. Comparison of theoretical and experimental results.

4. Conclusions

Using a large-scale shear apparatus, a series of cyclic shear tests were performed on a silt–steel interface in this study. The results can provide a reference for engineering design and safety evaluation in the Yellow River delta. The specific conclusions are as follows:

1. With the increase in the the number of cycles, the hysteresis loop shrank inwards, indicating that the interfacial shear stress was softened and that the type of bulk deformation was shear shrinkage. The mechanical properties along different shear directions showed anisotropy in the same cycle;
2. The change in the shear amplitude could change the shape of the hysteresis curve. With the increase in the shear amplitude, the hysteresis curve gradually developed from “parallelogram” to “shuttle” and “hysteresis cake”. At the same time, the shear strength and the volumetric displacements increased;
3. The effects of normal stress, roughness, and water content on shear strength and volume change were similar to those found in the direct shear test. With the increase in the normal stress and roughness and the decrease in the water content, the shear strength, volume displacement growth rate, and growth rate increased;
4. Based on the modified hyperbolic model, the cyclic shear stress–displacement relationship for the silt–steel interface in the Yellow River Delta was described. The model results were in good agreement with the test results.

Author Contributions: Conceptualization, H.L. (Hongjun Liu) and P.Y.; formal analysis, H.L. (Haisong Liu) and R.X.; data curation, R.W. and P.Y.; writing—original draft preparation, P.Y. and H.L. (Haisong Liu); writing—review and editing, H.L. (Hongjun Liu) and P.Y.; visualization, M.X. and P.Y.; project administration, J.D.; funding acquisition, J.D. The final manuscript has been approved by all the authors. All authors have read and agreed to the published version of the manuscript.

Funding: This research was funded by the Shandong Provincial Bureau of Geology and Mineral Resources (grant number KY202223) and the Key Laboratory of Geological Safety of Coastal Urban Underground Space, Ministry of Natural Resources (grant number BHKF2021Z11).

Institutional Review Board Statement: Not applicable.

Informed Consent Statement: Not applicable.

Data Availability Statement: The data presented in this study are available on request from the corresponding author.

Conflicts of Interest: The authors declare no conflict of interest.

References

1. Zhang, J.M.; Feng, D.K.; Hou, W.J. An automated large-scale apparatus for 3-D cyclic testing of soil-structure interfaces. *Geotech. Test. J.* **2018**, *41*, 20170129. [[CrossRef](#)]
2. Li, Y.J.; Guo, Z.; Wang, L.Z.; Li, Y.L.; Liu, Z.Y. Shear resistance of MICP cementing material at the interface between calcareous sand and steel. *Mater. Lett.* **2020**, *274*, 128009. [[CrossRef](#)]
3. Jotisankasa, A.; Rurgchaisri, N. Shear strength of interfaces between unsaturated soils and composite geotextile with polyester yarn reinforcement. *Geotext. Geomembr.* **2018**, *46*, 338–353. [[CrossRef](#)]
4. Li, M.J.; Fang, H.Y.; Du, M.R.; Zhang, C.; Su, Z.; Wang, F. The behavior of polymer-bentonite interface under shear stress. *Constr. Build. Mater.* **2020**, *248*, 118680. [[CrossRef](#)]
5. Wang, S.J.; Liu, F.Y.; Wang, P.; Cai, Y.Q. Particle size effects on coarse soil-geogrid interface response in cyclic and post-cyclic direct shear tests. *Geotext. Geomembr.* **2016**, *44*, 854–861. [[CrossRef](#)]
6. Liu, J.M.; Zou, D.K.; Kong, X.J. A three-dimensional state-dependent model of soil–structure interface for monotonic and cyclic loadings. *Comput. Geotech.* **2014**, *61*, 166–177. [[CrossRef](#)]
7. Stutz, H.; Mašin, D.; Wuttke, F. Enhancement of a hypoplastic model for granular soil-structure interface behaviour. *Acta Geotech.* **2016**, *11*, 1249–1261. [[CrossRef](#)]
8. Saberi, M.; Annan, C.; Konrad, J. Three-dimensional constitutive model for cyclic behavior of soil-structure interfaces. *Soil Dyn. Earthq. Eng.* **2020**, *134*, 106162. [[CrossRef](#)]
9. Feng, X.L.; Wang, F.Y.; Tang, X.; Xiong, Z.H. Effects of shear box size and mean grain size on sandy soil shearing strength. *Sci. Technol. Eng.* **2017**, *17*, 1671–1815. (In Chinese)
10. Jia, Y.G.; Zhang, L.P.; Zheng, J.W. Effects of wave-induced seabed liquefaction on sediment re-suspension in the Yellow River Delta. *Ocean. Eng.* **2014**, *89*, 146–156. [[CrossRef](#)]
11. Zhang, Y.; Feng, X.L.; Ding, C.H.; Liu, Y.N.; Liu, T. Study of cone penetration rate effects in the Yellow River Delta silty soils with different clay contents and state parameters. *Ocean. Eng.* **2022**, *250*, 110982. [[CrossRef](#)]
12. Liu, X.; Lu, Y.; Yu, H.; Ma, L.; Li, X.; Li, W.; Zhang, H.; Bian, C. In-situ observation of storm-induced wave-supported fluid mud occurrence in the subaqueous Yellow River delta. *J. Geophys. Res. Ocean.* **2022**, *127*, e2021JC018190. [[CrossRef](#)]
13. Yu, H.; Liu, X.; Lu, Y.; Li, W.; Gao, H.; Wu, R.; Li, X. Characteristics of the sediment gravity flow triggered by wave-induced liquefaction on a sloping silty seabed: An experimental investigation. *Front. Earth Sci.* **2022**, *10*, 909605. [[CrossRef](#)]
14. Liu, J.W.; Cui, L.; Zhu, N.; Han, B.; Liu, J. Investigation of cyclic pile-sand interface weakening mechanism based on large-scale CNS cyclic direct shear tests. *Ocean. Eng.* **2019**, *194*, 106650. [[CrossRef](#)]
15. Ren, Y.; Xu, G.; Xu, X.; Zhao, T.; Wang, X. The initial wave induced failure of silty seabed: Liquefaction or shear failure. *Ocean. Eng.* **2020**, *200*, 106990. [[CrossRef](#)]
16. Wang, Y.; Zhang, M.; Bai, X.; Liu, J. Experimental research on effect of shear rate on shear strength of clayey soil-concrete interface. *J. Civ. Environ. Eng.* **2019**, *41*, 48–54. (In Chinese)
17. Zeghal, M.; Edil, T.B.; Plesha, M.E. Discrete element method for sand-structure interaction. In Proceedings of the 3rd International Conference on Discrete Element Methods, Santa Fe, NM, USA, 23–25 September 2010; pp. 317–322.
18. Wang, J.; Ying, M.; Liu, F.; Yuan, G.; Fu, H. Experimental investigation on the stress-dilatancy response of aggregate-geogrid interface using parameterized shapes. *Constr. Build. Mater.* **2021**, *289*, 123170. [[CrossRef](#)]
19. Rui, S.J.; Zhen, G.; Wang, L.Z.; Zhou, W.J.; Li, Y.J. Experimental study on cyclic shear stiffness and damping ratio of carbonate sand-steel interface. *Rock Soil Mech.* **2020**, *41*, 78–86. (In Chinese)
20. Chen, H.; Wang, H.; Zhang, J.S.; Wang, Q.Y. Effects of Roughness on Cyclic Shear Behavior of Red Clay-Concrete Interface. *J. South China Univ. Technol.* **2018**, *46*, 146–152. (In Chinese)

21. Wang, T.; Zhang, Z. Experimental studies of cyclic shear behavior of steel—Silt interface under constant normal stiffness condition. *Chin. J. Geotech. Eng.* **2019**, *41*, 1921–1927. (In Chinese)
22. Yu, P.; Liu, C.; Liu, H.J. Large—Scale direct shear test study on the silt—Steel interface in the Yellow River Dlta. *Period. Ocean. Univ. China* **2021**, *51*, 71–79. (In Chinese)
23. Zhao, C.; Xie, J.F.; Wang, W.D.; Zhou, M. Experimental Study on Shear Behavior of Interface Between Coarse Sand and Structure. *J. Tongji Univ.* **2019**, *47*, 1406–1413. (In Chinese)
24. Dejong, J.T.; Westgate, Z.J. Role of initial state material properties and confinement condition on local and global soil-structure interface behavior. *J. Geotech. Geoenviron. Eng.* **2009**, *13*, 1646–1660. [[CrossRef](#)]
25. Lu, X.Z. Constitutive Model of Steel-Soil Contact Interface and Its Application in the Bearing Behavior Study of Rock-Socketed Filling Pile with Steel Tube. Master’s Thesis, Chongqing Jiaotong University, Chongqing, China, 2015. (In Chinese).
26. He, Z.J.; Mo, H.Q.; Zou, J.F. Research on the parameters of nonlinear hyperbolic model for clay-geogrid interfaces based on large scale direct shear tests. *Transp. Geotech.* **2019**, *18*, 39–45. [[CrossRef](#)]
27. Fellenius, B.H. Results from long-term measurement in piles of drag load and downdrag. *Can. Geotech. J.* **2006**, *43*, 409–430. [[CrossRef](#)]

Article

Study on the Rheology of CO₂ Hydrate Slurry by Using the Capillary Method

WeiQi Fu ¹, Wei Wei ², Hao Wang ¹, Bingxiang Huang ^{1,*} and Zhiyuan Wang ³

¹ State Key Laboratory of Coal Resources and Safe Mining, China University of Mining and Technology, Xuzhou 221116, China

² CNPC Research Institute of Exploration and Development (Langfang), Langfang 065000, China

³ School of Petroleum Engineering, China University of Petroleum (East China), Qingdao 266580, China

* Correspondence: huangbingxiang@cumt.edu.cn

Abstract: The rheological properties of the CO₂ hydrate slurry are experimentally investigated by using a new flow loop with an inner diameter of 50 mm. The pressure drops of the CO₂ hydrate slurry are measured experimentally under the volumetric hydrate fraction, ranging from 1.4 to 17.2 vol%, and the shear rate ranging from 40 to 590 s⁻¹. Using the capillary method, the rheology of the CO₂ hydrate slurry is analyzed based on pressure drop. The CO₂ hydrate slurry is identified as a power-law fluid and exhibits strong shear-thickening behavior. The increase in the volumetric hydrate concentration not only ascends the apparent viscosity, but also makes the non-Newtonian behavior of the hydrate slurry become more obvious. The non-Newtonian index and the consistence factor of fluid increase exponentially with the volumetric hydrate concentration increasing. A Herschel–Bulkley-type rheological model of the CO₂ hydrate slurry is correlated from experimental data. The developed model performs the average discrepancy of less than 16.3% within the range of the experiment.

Keywords: CO₂ hydrate slurry; rheology; shear-thickening; Herschel–Bulkley-type model

Citation: Fu, W.; Wei, W.; Wang, H.; Huang, B.; Wang, Z. Study on the Rheology of CO₂ Hydrate Slurry by Using the Capillary Method. *J. Mar. Sci. Eng.* **2022**, *10*, 1224. <https://doi.org/10.3390/jmse10091224>

Academic Editors: Timothy S. Collett and Alberto Ribotti

Received: 7 July 2022

Accepted: 30 August 2022

Published: 1 September 2022

Publisher's Note: MDPI stays neutral with regard to jurisdictional claims in published maps and institutional affiliations.



Copyright: © 2022 by the authors. Licensee MDPI, Basel, Switzerland. This article is an open access article distributed under the terms and conditions of the Creative Commons Attribution (CC BY) license (<https://creativecommons.org/licenses/by/4.0/>).

1. Introduction

Initially, the CO₂ hydrate is a secondary refrigerant used to reduce the usage of the primary refrigerants and to improve the efficiency of the secondary system [1]. Understanding the rheology of the CO₂ hydrate slurry can predict the pressure drop of refrigerating pipes accurately and help to optimize the efficiency of the refrigerating system. In recent years, as the development of oil and gas in deep-water regions progresses [1], the reservoir gases become compounds, including methane, ethane, propane, butane, CO₂ and H₂S [2,3]. The acid gas (CO₂ and H₂S) can form gas hydrates in the wellbore much more easily than methane. Thus, the hydrate flow assurance problem in the wellbore and pipe becomes more complicated when natural gas contains CO₂.

Currently, the rheology of the hydrate slurry is a fundamental issue in calculating the pressure drop along the pipe length and time, and plays an important role in predicting hydrate plugging in the wellbore. However, CO₂ hydrate accelerates the process of gas hydrate formation and amplifies the pressure drop induced by hydrate slurry flowing. Thus, the current prevention method for gas hydrate underestimates the risk of gas hydrate containing acid gas. The current hydrate management plan becomes improper. Studies focusing on the rheology of the rCO₂ hydrate slurry contributes to the development of a high-efficiency hydrate management plan. Moreover, the rheology of the CO₂ hydrate slurry participates in a number of industrial applications as an important fundamental concept, such as CO₂ secondary refrigeration and CO₂ storage in deep-water stratum.

Generally, the rheology of the hydrate slurry is influenced by multiple factors, including mesoscopic structure between hydrate particles, hydrate concentration, rheology

of the carry fluid, additive concentrations, etc. [4–6]. Since the hydrate slurry only keeps stable under the high-pressure and low-temperature environment, only two kinds of viscosimeters can satisfy the experimental requirement after a customizing upgrade, which are the Ostwald viscosimeter and rotatory viscosimeter [4–11]. Based on the kinds of carry fluid, the studies of hydrate slurry rheology can be divided into two parts [11]. The first part is the hydrate slurry formed from the water-in-oil emulsion system [5,7–10]. The other is the hydrate slurry formed from the aqueous solution [12–21]. In the water-in-oil emulsion system, Sinquin et al. (2004) pointed out that the increase in pressure drop by the hydrate slurry is dominated by the friction factor under turbulent flow and the apparent viscosity under laminar flow [7]. In the most of their experiments, the hydrate slurry exhibits Newtonian behavior, and the relative viscosity of the hydrate slurry increases with the volume fraction of hydrate [7]. In some specific cases, the hydrate slurry exhibits shear-thinning behavior due to high enough interparticle forces between hydrate particles [7]. Peng et al. (2012) and Yan et al. (2014) conducted a series of experiments to investigate rheological properties of natural gas hydrate slurries with varied anti-agglomerants [5,8]. They also used the flow loop to test flow performance of the hydrate slurry under the shut-down and the restarting condition [5,8]. The hydrate slurry in a water-in-diesel oil emulsion exhibits obvious shear-thinning behavior and the increase in hydrate volume fraction makes the hydrate slurry become more shear-thinning. An empirical Herschel–Bulkley-type equation is developed, considering the hydrate volume fraction to describe the rheological property of the hydrate slurry [5,8]. Webb et al. (2012, 2014) experimentally investigated the rheology of the hydrate slurry in the water-in-crude oil emulsion, which varied in time, shear rate ($1\sim 500\text{ s}^{-1}$), water cut (0~50%), temperature (0~6 °C) and initial pressure of methane (750~1500 psig) [22,23]. The yield stress of the hydrate slurry was found to increase with an annealing time of up to 8 h, and then remain constant. The hydrate slurry performed shear-thinning behavior and the increase in water cut resulted in an increase in the apparent viscosity and the yield stress [22,23]. Qin et al. (2017) used a control-stress rheometer to study the rheology of hydrate slurries in water-in-oil emulsion, which found that the hydrate formation induced the significant increase in apparent viscosity [9]. The yield stress of the hydrate slurry in oil varied between 3 and 25 Pa at the water cut, ranging from 0.05 to 0.3 [9]. Liu et al. (2020) experimentally analyzed the influence of the surfactant's concentration on the rheology of the hydrate slurry. The surfactant had a positive contribution to the stability of the hydrate slurry [24]. When the surfactant concentration was beyond 5 wt%, the viscosity of the slurry decreased significantly [24]. The yield stress of the hydrate slurry was related to the shut-in time. In the first 10 min of shut-in, the yield stress was constant. When the shut-in time is beyond 20 min, the yield stress increased greatly. Liu et al. (2021) studied the rheology of the hydrate slurry containing wax and defined the three stages of apparent profile, which are the initial growth and aggregation, dynamic recovery and the balanced stage [10]. Wax can increase the viscosity of the hydrate slurry but weaken the thixotropy of the hydrate slurry [10]. The most proper reason that wax can induce an extra increment of viscosity for the hydrate slurry is due to the emergence of wax-hydrate coupling aggregates [10].

In the aqueous solution, Andersson and Gudmundsson (2000) firstly used the flow loop to text the rheology of hydrate-in-water and pointed out that the hydrate-in-water exhibits Bingham behavior [12]. Darbouret et al. (2005) experimentally investigated the rheology of TBAB hydrate slurries as the requirement from the secondary refrigeration field [25]. The Bingham behavior of TBAB hydrate slurries was found in experiments of the ranges of particle contents and shear rates, and a corresponding method was proposed to decide its apparent viscosity and yield stress [25]. Delahaye et al. (2008, 2011) conducted research on the rheology of the CO₂ hydrate slurry with additives [1,15]. The rheology of the CO₂ hydrate slurry is highly dependent on the volumetric hydrate fraction [1,15]. Without the effect of additives, the CO₂ hydrate slurry exhibits shear-thickening behavior with a volumetric hydrate fraction ranging

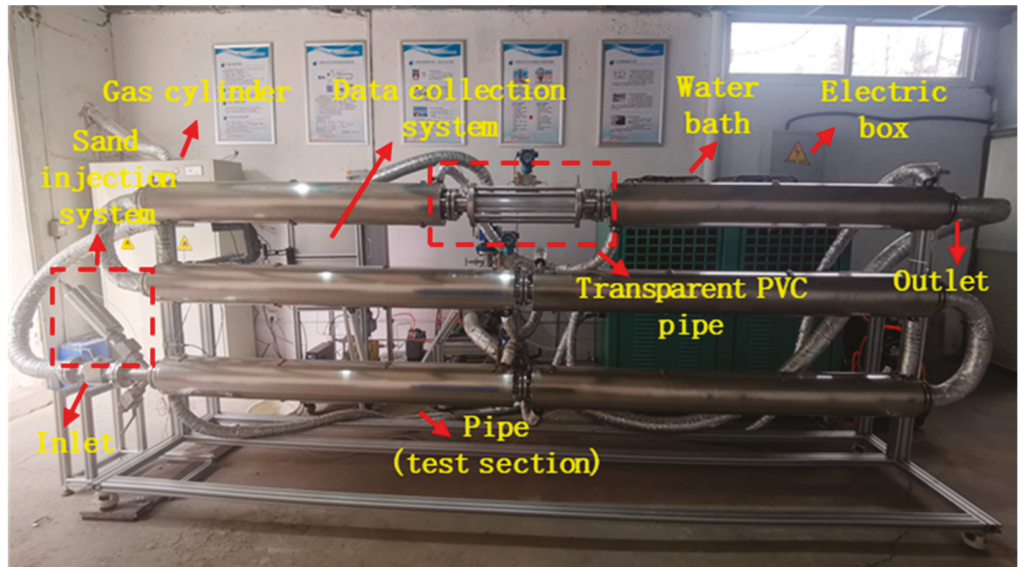
from 4 to 10 vol%, and shear-thinning behavior with volumetric hydrate fraction ranging from 11 to 20 vol% [1,15]. Hashimoto et al. (2011) used a stress-control-type rheometer to study the rheology of TBAB and TBAF hydrate slurries, and pointed out their rheology exhibits pseudoplastic [16]. Clain et al. (2012, 2015) experimentally verified the shear-thinning behavior of the TBPB hydrate slurry with a volumetric hydrate concentration ranging from 0 to 28.2 vol% [4,25]. Meanwhile, the particle size of the TBPB hydrate slurry was confirmed at range between 75 to 160 μm by focused-beam reflectance measurement (FBRM) [25]. The hydrate particle growth and agglomeration were indicated to have a potential relation with the rheological properties of the hydrate slurry. Jerbi et al. (2013) used the capillary viscometer method to reveal the rheological properties of the CO_2 hydrate slurry by using a flow loop with an inner diameter of 7.74 mm [17]. The CO_2 hydrate slurry is a power fluid and the non-Newtonian index decreased from 1 to 0.6 as the volumetric hydrate concentration increased from 0 to 22 vol% [17]. Sun et al. (2020) experimentally revealed the rheology of the methane hydrate slurry in the bubbly flow and pointed out that the methane hydrate slurry with bubbly exhibited shear-thinning under low-shear-rate conditions and shear-thickening under high shear rate condition [18]. Fu et al. (2020a,b, 2022) used the same method as Sun et al., to investigate the influence of hydrate formation on water-based drilling fluid [6,19,21]. The hydrate has an obvious effect on the rheology of the drilling fluid. The increase in volumetric hydrate concentration enhances the non-Newtonian behavior of the drilling fluid. Under the high shear rate condition, the water-based drilling fluid with hydrate also tends to the shear-thickening behavior [6,19,21]. Muhlstedt et al. (2021) used a stress-control rotational rheometer to study the rheology of water-based drilling fluid with THF hydrate. The influence of hydrate formation on the shear-stress and shear rate were analyzed [26]. Based on Fu et al., and Muhlstedt et al.'s work, although the effect of the hydrate on the rheology of the drilling fluid is negligible, the rheology of water-based drilling fluid is highly dependent on the additives of drilling fluid. Sakurai et al. (2021) revealed the hydrate formation process in the water-dominated bubbly flow and verified Sun et al.'s result in which the hydrate formation in the bubbly flow can increase the shear stress of the bubbly flow [27].

Although previous researchers have conducted experiments to reveal the rheology of the CO_2 hydrate slurry, a consistent conclusion has not been reached. In Delahaye et al.'s work, the rheology of the CO_2 hydrate slurry could be shear-thinning and shear-thickening depending on volumetric hydrate concentration [1,15]. In Jerbi et al., and Lv et al.'s work, the CO_2 hydrate slurry was found to be shear-thinning fluid [27,28]. In this work, a new flow loop with an inner diameter of 50 mm is built up to study the rheology of the CO_2 hydrate slurry by using the capillary method, where the 50 mm inner diameter of the flow loop is quietly closed to the industrial conditions and the experiments are designed based on the Reynolds number similar criterion. Different from previous works, the CO_2 hydrate slurry exhibits an apparent shear-thickening behavior in the whole experiment. An empirical Herschel-Bulkley-type equation is developed to predict the shear stress and the apparent viscosity of the CO_2 hydrate slurry.

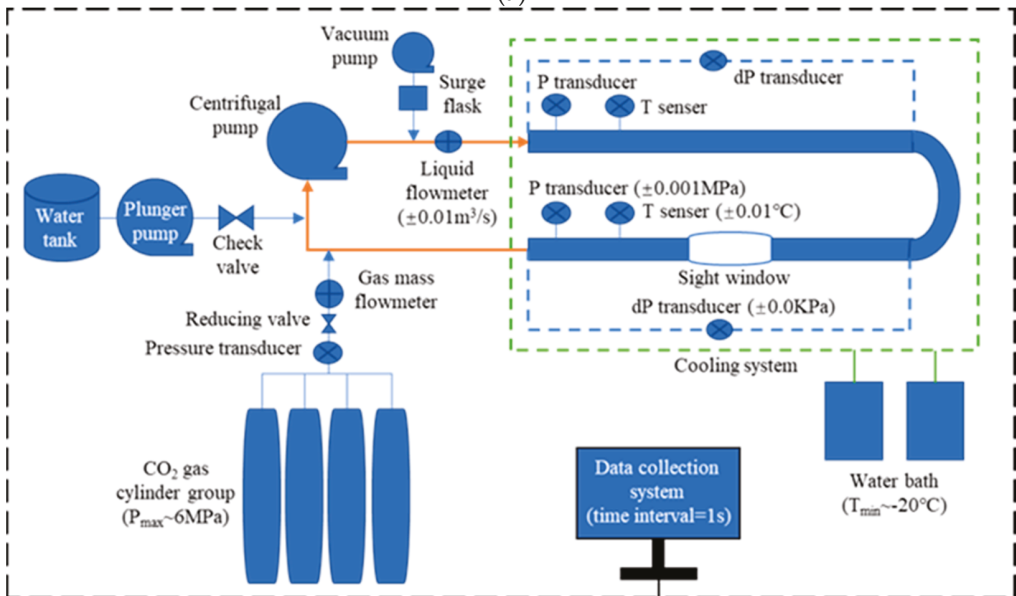
2. Experiment

In this work, a new flow loop was built up to study the rheology of the CO_2 hydrate slurry. Compared to our previous flow loop, the new loop had a larger inner diameter and longer test section, which were 50 mm and 15 m, respectively. The large diameter of test section pipe provided a flow condition closed to the industrial condition, where the drainage line in deep-water well had a diameter of 80 to 100 mm. The centrifugal pump equipped in the flow loop could tolerate 10 vol% volumetric gas fraction which enabled the void fraction and hydrate fraction inside the flow loop to be up to 10 vol% and beyond 12 vol%, correspondingly. The accuracies of temperature, pressure, pressure drop and flow rate were 0.01 $^\circ\text{C}$, 0.001 MPa, 0.01 Kpa and 0.01 m^3/s . The tolerances of pressure and temperature were 5 Mpa and 0 $^\circ\text{C}$. The interval of data collection was 1 s. The transparent

PVC pipe enabled the observation of flow pattern and morphology of the hydrate slurry but limited the maximum pressure of the flow loop. The total volume of the flow loop was 43,000 mL. The image and schematic of the new flow loop are given in Figure 1a,b.



(a)



(b)

Figure 1. Introduction of high-pressure and low-pressure multiphase flow loop. (a) Image of flow loop. (b) Schematic of flow loop.

The experiments were designed based on the Reynolds number similar criterion, where the CO₂ hydrate slurry had the same Reynolds number with fluid in the drainage

line of a deep-water natural-gas hydrate well. The rheology of the CO₂ hydrate slurry was tested by the capillary method. The capillary method uses the pressure drop of the hydrate slurry in the horizontal pipe to evaluate its rheology. Since the rheology is measured in the pipe, the flow condition in the experiment was the same as the deep-water well. Thus, the rheological model developed based on the capillary method is more reliable for the petroleum engineers. The experiments had void fractions ranging from 0 to 7.09 vol%, flow velocity ranging from 0 to 4 m/s, volumetric hydrate concentration ranging from 1.4 to 17.2 vol% and pressure ranging from 0 to 4 Mpa. The experimental procedure is illustrated as follows:

- (1) In the preparation stage, the flow loop is cleaned up by the deionized water and vacuumed by the vacuum pump. When the pressure of the flow loop drops to 0.1 MPa, the flow loop is vacuumed. Then, the plunger pump is used to pump water inside the flow loop until the expected volume of water and an electric weight can weigh the pumped water in real time. At this stage, the data collection system starts to record experimental data, such temperature, pressure, pressure drop, flow rate, etc.
- (2) Then, the valve of the gas cylinder opens and CO₂ is injected inside the flow loop. At the same time, the cooling system starts to cool down the test section and the pressure of the flow loop is kept under 1.2 MPa. In this stage, the temperature of the flow loop decreases and CO₂ dissolves into water. When the temperature drops to the target and the pressure is kept the constant, the water is saturated with CO₂.
- (3) CO₂ is injected into the flow loop until the pressure reaches the target and the valve of the gas cylinder closes. CO₂ hydrate starts to crystalline in the flow loop, and the pressure of the flow loop decreases correspondingly.
- (4) When the pressure keeps the constant, the hydrate formation stops in the flow loop. Thus, the flow loop varies from 37 Hz to 7 Hz and records the flow velocity and pressure drop of the hydrate slurry at the same time.
- (5) CO₂ is injected into the flow loop again and the second hydrate formation experiment is conducted to increase the volumetric hydrate concentration in the flow loop. When the void fraction decreases to be negligible, and the volumetric hydrate concentration becomes hard to increase, the experiment stops.

The rheological experiments of the CO₂ hydrate slurry consist of a CO₂ hydrate formation experiment and rheological examination experiment. The CO₂ hydrate formation experiment increases the volumetric concentration in the flow loop. The rheological examination experiment tests the pressure drop of the hydrate slurry under a different flow velocity, where such pressure drops can evaluate the rheology of the hydrate slurry by the capillary method. The whole procedure of the rheological experiment is given in Figure 2a,b.

In Figure 2a, the experiment consists of 20 times of CO₂ injections, which means 20 times of CO₂ hydrate formation experiments. The volumetric hydrate concentration is increased after each hydrate formation experiment and gradually ascends from 1.4 to 17.2 vol%. After hydrate formation, the pump frequency (f_{pump}) decreases from 37 Hz to 7 Hz and the flow velocity of the hydrate slurry also decreases correspondingly. In Figure 2a, as the volumetric hydrate fraction increases, the range of flow velocity shrinks at the same time. This is because the increased viscosity of the hydrate slurry induces higher friction force with the pipe wall, and the centrifugal pump needs more frequency to maintain the velocity of the hydrate slurry. At 37 Hz, the velocity of the hydrate slurry decreases from 4 to 2.16 m/s, which is about a half, as the volumetric hydrate concentration increases from 1.4 to 17.2 vol%. Figure 2b exhibits the effect of volumetric hydrate concentration on the pressure drop of the hydrate slurry, where first and third hydrate formation experiments are marked. The pressure drop of the hydrate slurry increases greatly as the volumetric hydrate concentration increases. For instance, under the hydrate slurry velocity of 15.5 m/s, the pressure drops are 6 and 65.8 kPa at the volumetric hydrate concentration of 1.4 and 17.2 vol%. The pressure drops increase by about 11 times.

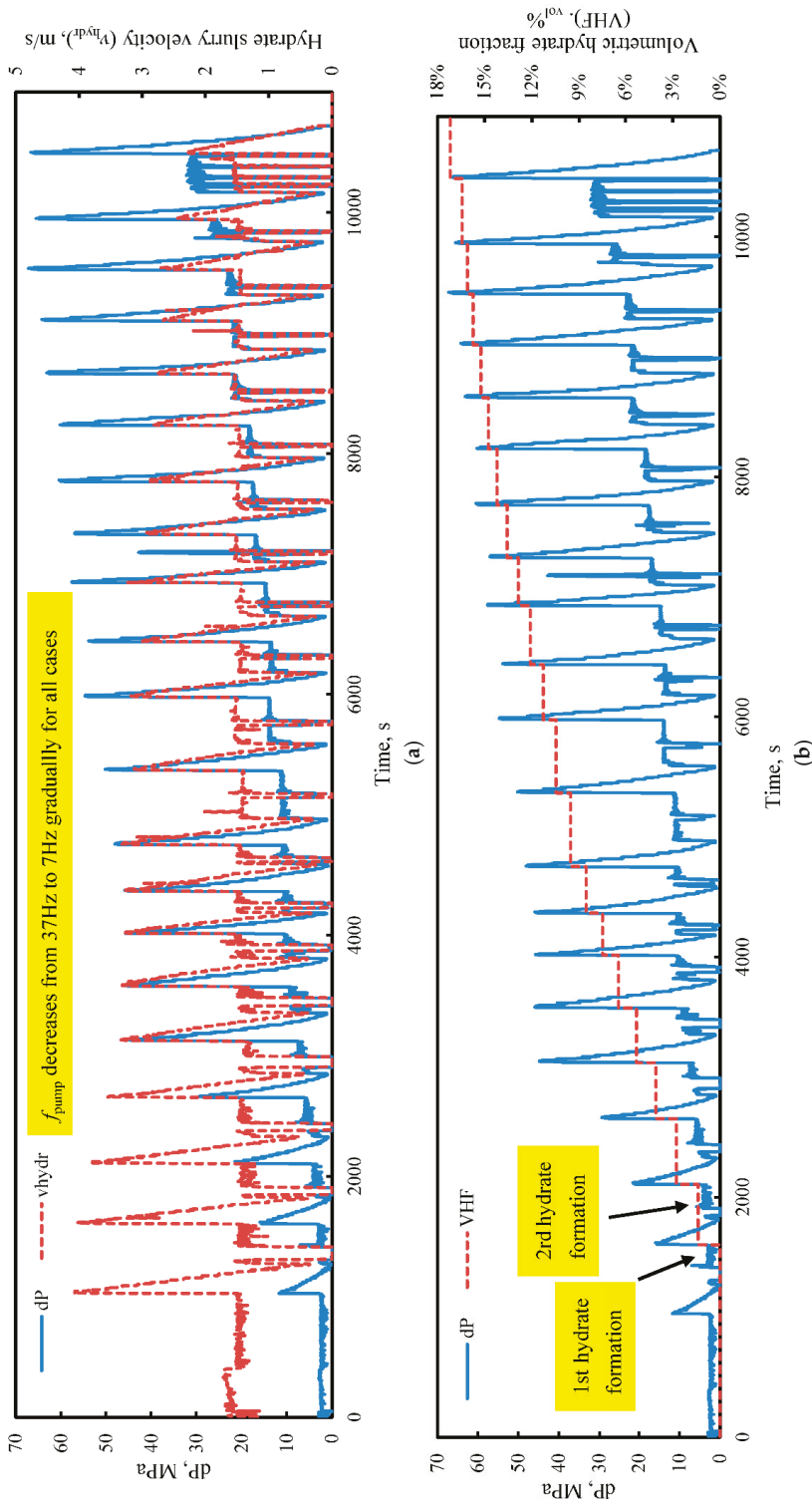


Figure 2. Variations of key flow parameters in the experiment. (a) Variations of pressure drop and hydrate slurry velocity in the experiment. (b) Variations of pressure drop and volumetric hydrate fraction in the experiment.

3. Rheological Model

Previous researchers have performed numbers of experiments to study the rheology of hydrate slurries in aqueous solutions, as shown in Table 1 [1,4,6,12–15,18,19,21]. All those works use the capillary method (Ostwald viscosimeter) to investigate the rheology of the hydrate slurry. However, their rheology does not meet a unique conclusion which exhibits Bingham, shear-thinning and shear-thickening in different aqueous solutions. If the aqueous solution contained additives, the hydrate slurry would be highly related to the physical and chemical properties of additives. Compared with Delahaye et al.'s work, we used the flow loop with a larger inner diameter to research the rheology of the CO₂ hydrate slurry and a wider range of apparent viscosities. The flow loop with a larger diameter enables the flow condition of the hydrate slurry in experiments to be closed to the industrial condition and the experimental results become reliable.

Although no clear agreement for the CO₂ hydrate slurry rheology is reached, the hydrate slurry is recognized as a power-law fluid which is a non-Newtonian fluid. In this model, the rheology of the CO₂ hydrate slurry is assumed to be a laminar flow regime in the cylindrical pipe under most of the experimental conditions. Since the wall slip is widely considered in the multiphase flow in porous media or in the micro-tube, the flow behavior of the hydrate slurry in the pipeline is a macroscopic problem, and the other influencing factors are more important than the wall slip, such as hydrate concentrations and flow velocity [18]. Therefore, we ignore the wall slip in this work. The Metzner and Reed model (1955) is a theoretical and fundamental base to describe the rheology of the hydrate slurry which revealed the relationship between flow rate, shear rate and shear stress, as shown in Equation (1) [29]:

$$\frac{Q}{\pi R^3} = \frac{1}{\pi^3} \int_0^{\tau_w} \tau^2 \dot{\gamma} d\tau \tag{1}$$

where Q is the flow rate of the hydrate slurry, m³/s, R is the inner diameter of the pipe, m, τ is the shear stress, Pa, $\dot{\gamma}$ is the shear rate, s⁻¹.

The shear stress of the hydrate slurry is formulated by the pressure drop of the hydrate slurry, test section length and the diameter of the pipe [30], as shown in Equation (2):

$$\tau_{HS} = \frac{D \Delta P}{4 L} \tag{2}$$

where τ_{HS} is the shear stress of the hydrate slurry, Pa, ΔP is the pressure drop of the hydrate slurry, Pa, D is the diameter of the pipe, m, L is the length of the test section pipe, m.

Moreover, the Herschel–Bulkley equation is a classical expression for the non-Newtonian fluid to illustrate the relationship between shear rate and shea stress [30], as shown in Equation (3):

$$\tau_{HS} = \tau_0 + K \gamma_{HS}^n \tag{3}$$

where τ_0 is the yield stress of the hydrate slurry, Pa, γ_{HS} is the shear rate of the hydrate slurry, s⁻¹, n is the non-Newtonian fluid index, K is the consistency factor. Equation (4) defines the n index [30]:

$$n = n' = \frac{d \ln \left(\frac{D \Delta P}{4 L} \right)}{d \ln \left(\frac{8v_{HS}}{D} \right)} \tag{4}$$

In our previous works, the apparent viscosity of the hydrate slurry was defined as the ratio of shear stress and shear rate of the hydrate slurry [6], as shown in Equation (5):

$$\mu_{app} = \frac{\tau_{HS}}{\gamma_{HS}} = \frac{\tau_0}{\gamma_{HS}} + K \gamma_{HS}^{n-1} \tag{5}$$

where μ_{app} is the apparent viscosity of the hydrate slurry, mPa s.

Table 1. Rheology of hydrate slurries in aqueous phase [1,4,6,12–15,18,19,21].

References	Hydrate Slurry Types	Experimental Method	Hydrate Fraction (vol%)	Rheological Behavior	Apparent Viscosity (mPa s)	Shear Rate (s ⁻¹)			
Andersson and Gudmundsson [12]	NG hydrate	Ostwald viscosimeter (D _i = 8 mm and 20 mm)	1~11	Bingham plastic	1~3.5	0~800			
Darbour et al. [13]	TBAB hydrate	Ostwald viscosimeter (D _i = 8 mm and 20 mm)	4~53	Bingham plastic	8~170	5~270			
Fukushima et al. [15]	TBAB hydrate	Ostwald viscosimeter	26~35	Pseudoplastic	50~148	/			
Delahaye et al. [1]	CO ₂ hydrate	Ostwald viscosimeter (D _i = 16 mm)	4~20	$\alpha_{hydr} < 5 \text{ vol\%}$: Dilatant $5 \text{ vol\%} \leq \alpha_{hydr} < 10 \text{ vol\%}$: HB-type (dilatant trend) $\alpha_{hydr} = 10 \text{ vol\%}$: Bingham plastic $10 \text{ vol\%} < \alpha_{hydr}$: HB-type (pseudoplastic trend)	3.8~42.2	500~1000			
Delahaye et al. [15]	CO ₂ hydrate with additives	Ostwald viscosimeter (D _i = 5 mm)	4~10	4 vol% ≤ α_{hydr} < 10 vol%: Newtonian (Cafion)	7~15 at 600 s ⁻¹	500~750			
Wang et al. [14]	CH ₃ CCl ₂ F hydrate	Ostwald viscosimeter (D _i = 42 mm)	10~68				Dilatant	1.1~1.7	/
Clain et al. [4]	TBPB hydrate	Ostwald viscosimeter (D _i = 8 mm)	0~28.2				Pseudoplastic	4~41	130~700
Sun et al. [18]	CH ₄ hydrate	Ostwald viscosimeter (D _i = 25.4 mm)	6~11	$20 \leq \gamma_{HS} < 180 \text{ s}^{-1}$: Pseudoplastic $180 \text{ s}^{-1} \leq \gamma_{HS} < 300 \text{ s}^{-1}$: HB-type (transient region) $300 \text{ s}^{-1} \leq \gamma_{HS}$: Dilatant	3~50	20~700			
Fu et al. [6,19,21]	CH ₄ hydrate with XG and CMC	Ostwald viscosimeter (D _i = 25.4 mm)	1~9	Both pseudoplastic and dilatant depending on shear rate and additive concentration	12~500	10~750			
Fu et al. (present work)	CO ₂ hydrate	Ostwald viscosimeter (D _i = 50 mm)	1.4~17.2				Dilatant	12~520	40~590

4. Experimental Results and Discussion

The rheology of the CO₂ hydrate slurry in current experiments are studies within volumetric hydrate concentrations from 1.4 to 17.2 vol%, shear rates from 40 to 590 s⁻¹ and void fractions from 7.09 to 2.32 vol%. The rheology model of the CO₂ hydrate slurry is developed based on the Herschel–Bulkley equation (power-law model). The volumetric hydrate concentration is taken into account when describing the non-Newtonian index (*n* factor) and the consistency factor (*K* factor).

The *n* index is obtained from the differential ratio of Ln(DΔP/(4L)) and Ln(8v_{HS}/D) which is the slope of the curve in Ln(DΔP/(4L)) verse Ln(8v_{HS}/D) as an expression of Equation (4). The pressure drop is directly measured in experiments and the flow velocity of the hydrate slurry is calculated based on the flow rate measured in experiments. As shown in Figure 3, under each volumetric hydrate concentration condition, Ln(DΔP/(4L)) and Ln(8v_{HS}/D) have a linear relationship between them, indicating that they have a unique *n* index under a certain hydrate concentration condition. When CO₂ hydrate starts to form in the flow and the volumetric hydrate concentration increases from 1.4 to 17.2 vol%, the *n* index varies from 1.53 to 1.79. The *n* index is always above 1, which indicates that the CO₂ hydrate slurry performs shear-thickening behavior.

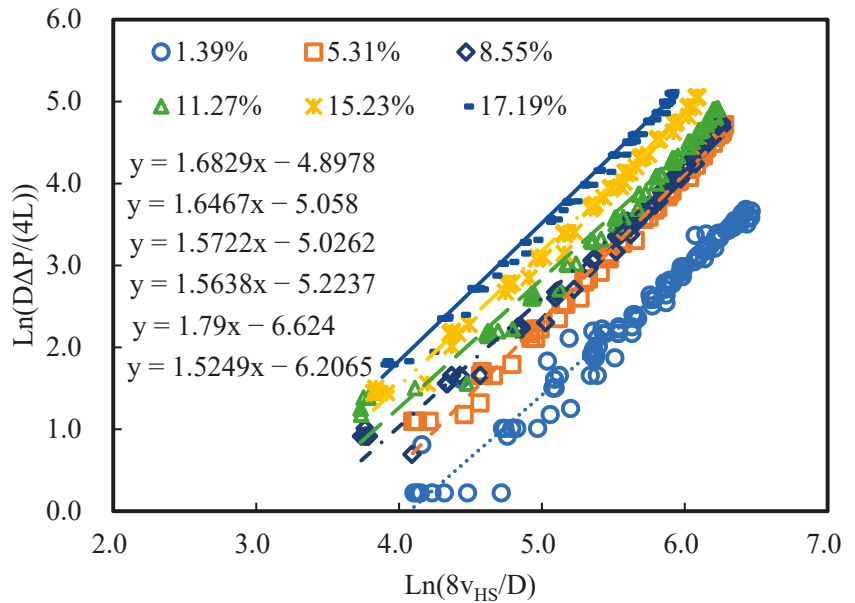


Figure 3. Representation of Ln(DΔP/(4 L)) and Ln(8v_{HS}/D) for CO₂ hydrate concentrations from 1.39 to 17.19 vol%.

In Figure 4, the relationship between shear stress and shear rate is exhibited. The shear stress increases exponentially while the shear rate increases, which identifies that the CO₂ hydrate slurry is a typical power-law model. Compared with Equation (3), the coefficient of the regression equation for shear stress and shear rate is the consistency factor of the CO₂ hydrate slurry. As the volumetric hydrate concentration ranges from 1.4 to 17.2 vol%, the *K* factor varies from 0.0016 to 0.0095. Moreover, the regression equation has no intercept with shear stress. The yield stress of the CO₂ hydrate slurry is zero, and Equation (5) is simplified as $\mu_{app} = K\gamma_{HS}^{n-1}$.

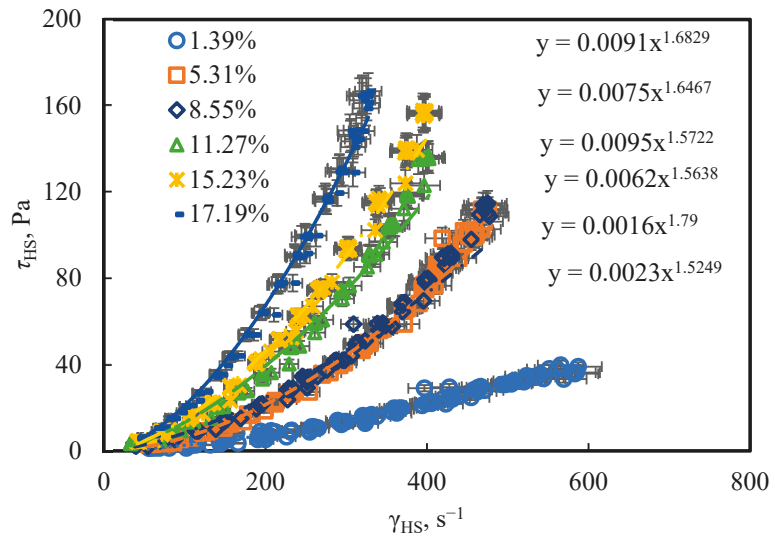


Figure 4. Representation of shear stress and shear stress for CO₂ hydrate concentrations from 1.39 to 17.19 vol%.

Based on the simplified Equation (5), Figure 5 is plotted to present the relationship between shear rate and the apparent viscosity of the CO₂ hydrate slurry. The apparent viscosity increases exponentially with the shear rate increasing, where the CO₂ hydrate slurry is demonstrated by shear-thickening behavior. As the volumetric hydrate concentration increases from 1.4 to 17.2 vol%, the ascending trend of the apparent viscosities along the shear rate become more obvious. Generally, the increase in the volumetric hydrate concentration enhances the non-Newtonian behavior of the CO₂ hydrate slurry. This result reaches an agreement with our previous works.

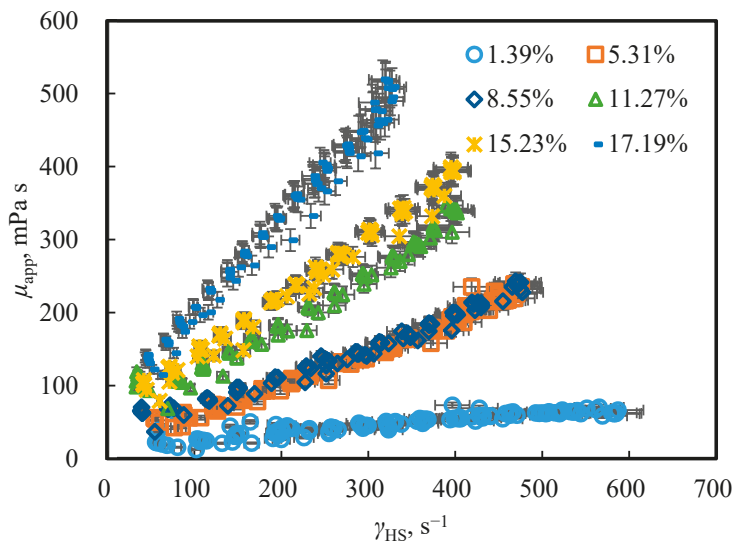


Figure 5. Representation of shear rate and apparent viscosity for CO₂ hydrate concentrations from 1.39 to 17.19 vol%.

In this work, the formation of CO₂ hydrate in the flow loop induces a CO₂–water two-phase flow transits to become a CO₂–water–CO₂ hydrate three-phase flow. CO₂ hydrates result in the non-Newtonian behavior of the hydrate slurry and the increase in the apparent viscosity. The CO₂ hydrate slurry exhibits obvious shear-thickening behavior throughout both the low-shear-rate region and high-shear-rate region. This result shows an apparent difference to our previous work [18,19] and Delahaye et al.’s work [1,15]. In the previous work, the rheology of the hydrate slurry would transit between the shear-thinning behavior and the shear-thickening behavior according to the variations of the volumetric hydrate concentration or the shear rates [15,18]. Generally, the shear-thinning behavior of the hydrate slurry depends on the inner structure between hydrate particles. If hydrate particles have agglomerated structure between each other, the increase in flow velocity and shear rate can break up the agglomerate of hydrate particles and make the hydrate slurry flow more easily [5,8,11]. Thus, the hydrate slurry would exhibit shear-thinning behavior. The shear-thickening behavior of the hydrate slurry depends on the friction and collision between hydrate particles [31,32]. If hydrate particles are suspended in the hydrate slurry as individual particles or small agglomerates, the flow of the hydrate slurry would induce frictions and collisions between hydrate particles and cause additional energy dissipations and pressure drops [33,34]. Thus, the higher flow velocity of the hydrate slurry causes the higher intensity of frictions and collisions between hydrate particles. The increase in flow velocity results in more increments of pressure drop, and the hydrate slurry starts to exhibit shear-thickening behavior. In this work, since the hydrate slurry is always under high circulation condition, the hydrate particles suspended in the flow loop are fully dispersed. Thus, the CO₂ hydrate slurry in the current experiment performs shear-thickening behavior.

The effect of volumetric hydrate concentration and shear rate on the apparent viscosity of the CO₂ hydrate slurry is revealed in Figure 6. Because of the shear-thickening behavior of the hydrate slurry, the increase in shear rate results in the apparent viscosity increasing for all hydrate concentration conditions. Moreover, the ascent of volumetric hydrate concentration also induces the apparent increase in viscosity. The increase in volumetric hydrate concentration means the quantity of suspended hydrate particles in the hydrate slurry increases. The probability of frictions and collisions between hydrate particles is improved and the increment of pressure drops induced by the hydrate slurry flowing is enhanced. Thus, the increase in volumetric hydrate concentration drives the hydrate slurry performing more non-Newtonian.

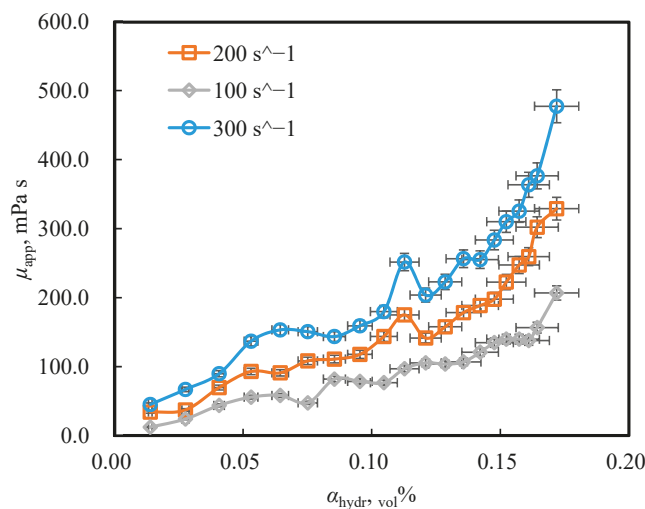


Figure 6. Evolution of apparent viscosity of CO₂ hydrate slurry along with hydrate concentration increasing under shear rate at 100, 200 and 300 s⁻¹.

From Equation (4) and Figure 3, the non-Newtonian fluid index (n index) under varied volumetric hydrate concentration condition can be obtained. Figure 7 exhibits variations of the n index of the CO₂ hydrate slurry along the volumetric hydrate concentration. The n index increases exponentially with the increase in volumetric hydrate concentration. Different from our previous work, the trend in the n index is discontinuity along the volumetric hydrate concentration, increasing from 1.4 to 17.2 vol%. The regressed correlations of the n index are given in Equation (6):

$$\begin{cases} n = 1.9239\alpha_{hydr}^{0.048} & (\alpha_{hydr} < 8.6\text{vol}\%) \\ n = 2.0753\alpha_{hydr}^{0.1224} & (8.6\text{vol}\% \leq \alpha_{hydr}) \end{cases} \quad (6)$$

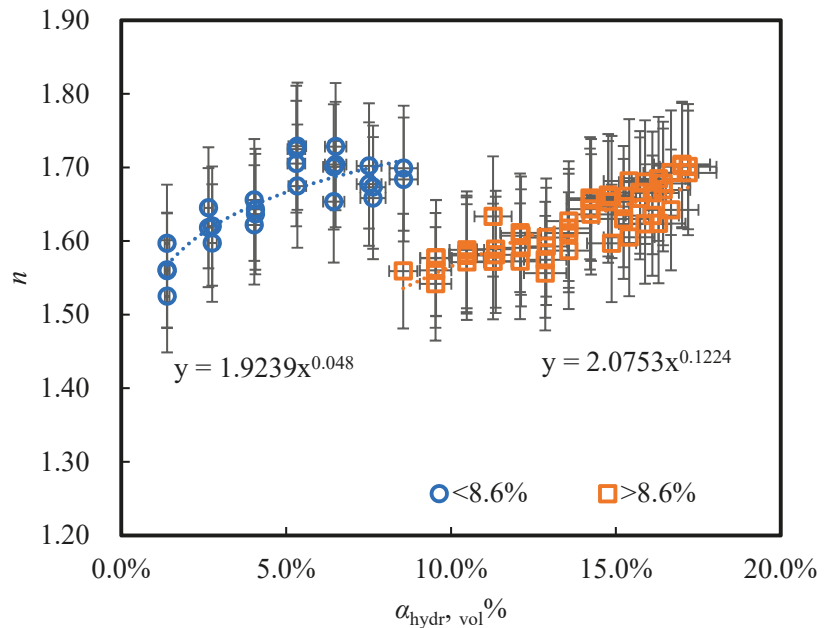


Figure 7. Evolution of the non-Newtonian index n of a function of volumetric hydrate fraction for CO₂ hydrate slurry.

The discontinuity of the n index of the CO₂ hydrate slurry indicates the change of rheological property of the hydrate slurry. The critical volumetric hydrate concentration is 8.6 vol% in Figure 7. Although no solid evidence was found in the experiment to explain this discontinuity, the existing theory does. The main reason for this is that the CO₂ hydrate slurry is not fully converted to the non-Newtonian fluid when the volumetric hydrate concentration is less than 8.6 vol%. A similar conclusion is received in the CH₄ hydrate slurry [18]. Under 8.6 vol%, the CO₂ hydrate slurry starts to exhibit non-Newtonian fluid behavior due to hydrate particles but is still not fully converted where the flow pattern is located in the transient zone. At this stage, the pressure drop of the hydrate slurry is mainly contributed by turbulent flow and its rheology. Above 8.6 vol%, the CO₂ hydrate slurry is fully converted to the non-Newtonian fluid, where flow pattern is a normally laminar flow. At this stage, the pressure drop of hydrate slurry is dominated by the rheology. However, in this work, once the hydrate forms in the flow loop, the CO₂ hydrate slurry is considered a non-Newtonian fluid, and the same assumption is made in previous work. This assumption takes an advantage for modeling the rheology of the hydrate slurry easily

and has good accuracy within the experimental range. Local engineers can utilize this model easily and conveniently.

From Equation (3) and Figure 4, the consistency factor (K) factor under varied volumetric hydrate concentration condition can be plotted in Figure 8. Based on the critical volumetric hydrate concentration, the correlations of the K factor are also regressed differently as shown in Figure 7. The K factor increases exponentially as the volumetric hydrate concentration increases. Moreover, by substituting Equations (6) and (7) into simplified Equation (5), the expression of the apparent viscosity of the CO_2 hydrate slurry is obtained, as shown in Equation (8).

$$\begin{cases} K = 0.0034\alpha_{hydr}^{0.1763} & (\alpha_{hydr} < 8.6_{vol}\%) \\ K = 0.0144\alpha_{hydr}^{0.4381} & (8.6_{vol}\% \leq \alpha_{hydr}) \end{cases} \quad (7)$$

$$\begin{cases} \mu_{app} = 0.0034\alpha_{hydr}^{0.1763} \gamma_{HS}^{1.9239\alpha_{hydr}^{0.048}-1} & (\alpha_{hydr} < 8.6_{vol}\%) \\ \mu_{app} = 0.0144\alpha_{hydr}^{0.4381} \gamma_{HS}^{2.0753\alpha_{hydr}^{0.1224}-1} & (8.6_{vol}\% \leq \alpha_{hydr}) \end{cases} \quad (8)$$

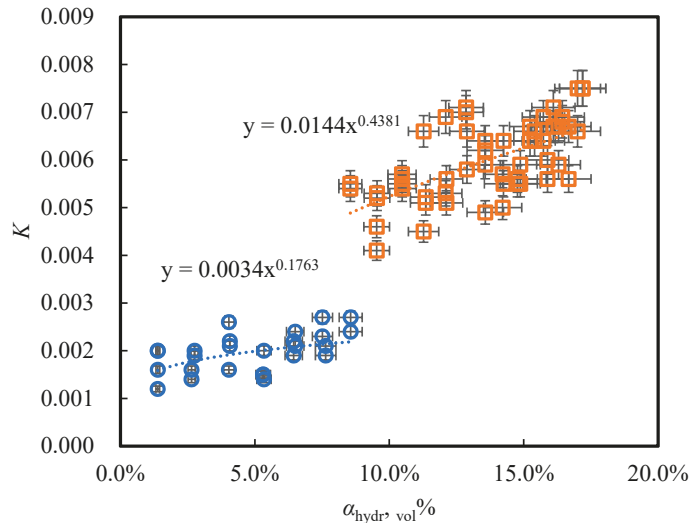


Figure 8. Evolution of the consistency factor K of a function of volumetric hydrate fraction for CO_2 hydrate slurry.

5. Validation

With Equation (8), the apparent viscosities of the CO_2 hydrate slurry are well predicted. Comparisons between experimental data and predicted values are shown in Figure 9. Most of the predicted apparent viscosities exhibit good accuracies and have discrepancies within $\pm 20\%$. The average discrepancies of the predicted values are within 16.3%. The developed correlation of the apparent viscosity satisfies the application in the industrial condition.

Generally, the developed model shows a good performance at the low apparent viscosity condition, but the absolute discrepancy between the predicted value and the experimental value is higher at the high apparent viscosity condition. The high apparent viscosity means a high shear rate and flow velocity of the hydrate slurry, where the flow regime tends to transit from the laminar to the turbulent. The reliability of the developed model decreases gradually.

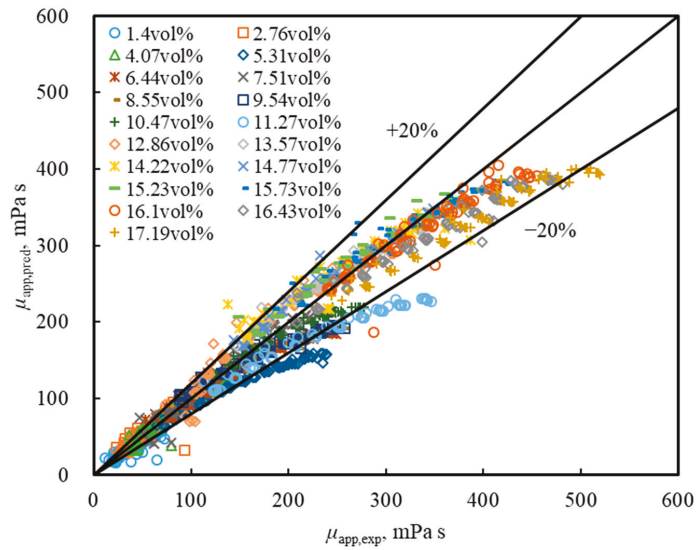


Figure 9. Comparison between experimental data and predicted apparent viscosity.

Moreover, the developed correlation is empirical and correlated from experimental data. The accuracy of the correlation will have good performance within the range of the experiment. However, the experimental range in the current work covers most parts of industrial conditions in the aspects of flow velocity, void fraction and volumetric concentration. Additionally, Figure 10 gives the distribution of Reynolds numbers along the shear rate of the hydrate slurry under different hydrate concentration conditions. It shows that all Reynolds number are less than 4500 and the most of them are less than 2100, where the hydrate slurry is under laminar flow condition. The increase in hydrate concentrations results in the reduction of Reynolds numbers. In the future, the inner mechanism is studied necessarily, where the CO₂ hydrate slurry exhibits shear-thickening behavior. The application scope of the rheology model needs to improve by developing a mechanistic rheological model.

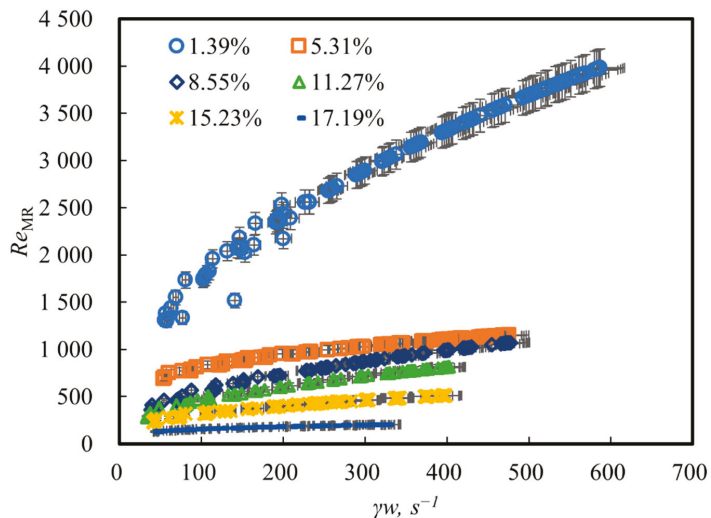


Figure 10. Reynold numbers along shear rate under different hydrate concentration conditions.

6. Conclusions

Considering that CO₂ is one of reservoir fluid components, CO₂ can amplify the risk of hydrate plugging in the production line of deep-water oil and gas wellbore under a low-temperature and high-pressure environment. The rheology of the CO₂ hydrate slurry is experimentally studied by a new flow loop with an inner diameter of 50 mm. The CO₂ hydrate slurry is a power-law fluid and performs obvious shear-thickening behavior for the shear rate ranging from 40 to 590 s⁻¹, and volumetric hydrate concentration ranging from 1.4 to 17.2 vol%. The increases in shear rate and volumetric hydrate concentration both result in the apparent viscosity of the hydrate slurry increasing. The n index and the K factor of the hydrate slurry increase exponentially as the volumetric hydrate concentration increases, where their empirical correlations are obtained from experimental data. An empirical correlation for the rheology of the CO₂ hydrate slurry is developed based on the power-law model, with an average discrepancy of 16.3%. This work provides a fundamental theoretical base and a new sight for deep-water oil and gas production, CO₂ storage in the deep-water environment and secondary refrigeration.

Author Contributions: Conceptualization, W.F. and W.W.; methodology, W.F. and Z.W.; formal analysis, W.F., B.H. and Z.W.; investigation, W.F. and W.W.; data curation, H.W.; writing—original draft preparation, W.F.; writing—review and editing, W.F., W.W. and H.W.; supervision, B.H.; funding acquisition, W.W. All authors have read and agreed to the published version of the manuscript.

Funding: This research was funded by the National Natural Science Foundation of China (NSFC) Youth Fund (52104047), CNPC Innovation Fund (2021DQ02—1005), the Natural Science Foundation of Jiangsu Province Youth Fund (BK20210507), and the Independent Research Project of State Key Laboratory of Coal Resources and Safe Mining, CUMT (SKLRCRSM22X002).

Institutional Review Board Statement: Not applicable.

Informed Consent Statement: Not applicable.

Data Availability Statement: Data is from the experiments we conducted in this work.

Conflicts of Interest: The authors declare no conflict of interest.

References

- Delahaye, A.; Fournaison, L.; Marinhas, S.; Martínez, M.C. Rheological study of CO₂ hydrate slurry in a dynamic loop applied to secondary refrigeration. *Chem. Eng. Sci.* **2008**, *63*, 3551–3559.
- Sun, B.; Song, R.; Wang, Z. Overflow behaviors of natural gas kick well with high content of H₂S gas. *China Univ. Pet.* **2012**, *36*, 73–79.
- Sun, B.; Sun, X.; Wang, Z.; Chen, Y. Effects of phase transition on gas kick migration in deepwater horizontal drilling. *J. Nat. Gas Sci. Eng.* **2017**, *46*, 710–729.
- Clain, P.; Delahaye, A.; Fournaison, L.; Mayoufi, N.; Dalmazzone, D.; Fürst, W. Rheological properties of tetra-n-butylphosphonium bromide hydrate slurry flow. *Chem. Eng. J.* **2012**, *193–194*, 112–122. [[CrossRef](#)]
- Peng, B.Z.; Chen, J.; Sun, C.Y.; Dandekar, A.; Guo, S.H.; Liu, B.; Mu, L.; Yang, L.A.; Li, W.Z.; Chen, G.J. Flow characteristics and morphology of hydrate slurry formed from (natural gas+diesel oil/condensate oil+water) system containing anti-agglomerant. *Chem. Eng. Sci.* **2012**, *84*, 333–344.
- Fu, W.; Wang, Z.; Zhang, J.; Cao, Y.; Sun, B. Investigation of rheological properties of methane hydrate slurry with carboxmethyl-cellulose. *J. Pet. Sci. Eng.* **2020**, *184*, 106504.
- Sinquin, A.; Palermo, T.; Peysson, Y. Rheological and Flow Properties of Gas Hydrate Suspensions. *Oil Gas Sci. Technol.* **2004**, *59*, 41–57. [[CrossRef](#)]
- Yan, K.-L.; Sun, C.-Y.; Chen, J.; Chen, L.-T.; Shen, D.-J.; Liu, B.; Jia, M.-L.; Niu, M.; Lv, Y.-N.; Li, N.; et al., Flow characteristics and rheological properties of natural gas hydrate slurry in the presence of anti-agglomerant in a flow loop apparatus. *Chem. Eng. Sci.* **2014**, *106*, 99–108.
- Qin, Y.; Zachary, M.A.; Paul, F.P.; Michael, L.J.; Eric, F.M. High Pressure Rheological Measurements of Gas Hydrate-in-Oil Slurries. *J. Non-Newton. Fluid Mech.* **2017**, *248*, 40–49.
- Liu, Y.; Lv, X.; Shi, B.; Zhou, S.; Lei, Y.; Yu, P.; Chen, Y.; Song, S.; Ma, Q.; Gong, J.; et al., Rheological study of low wax content hydrate slurries considering phase interactions. *J. Nat. Gas Sci. Eng.* **2021**, *94*, 104106.
- Bohui, S.; Shangfei, S.; Yuchuan, C.; Xu, D.; Qingyun, L.; Shunkang, F.; Lihao, L.; Jinhao, S.; Junpeng, J.; Haotian, L.; et al., Status of Natural Gas Hydrate Flow Assurance Research in China: A Review. *Energy Fuels* **2021**, *35*, 3611–3658.

12. Andersson, V.; Gudmundsson, J.S. Flow Properties of Hydrate-in-Water Slurries. *Ann. N. Y. Acad. Sci.* **2000**, *912*, 322–329. [[CrossRef](#)]
13. Darbouret, M.; Cournil, M.; Herri, J.-M. Rheological study of TBAB hydrate slurries as secondary two-phase refrigerants. *Int. J. Refrig.* **2005**, *28*, 663–671. [[CrossRef](#)]
14. Wang, W.; Fan, S.; Liang, D.; Yang, X. Experimental study on flow characters of CH₃CCl₂F hydrate slurry. *Int. J. Refrig.* **2008**, *31*, 371–378. [[CrossRef](#)]
15. Fournaison, L.; Jerbi, S.; Delahaye, A. Rheological Properties of CO₂ Hydrate Slurry Flow in the Presence of Additives. *Ind. Eng. Chem. Res.* **2011**, *50*, 8344–8353.
16. Hashimoto, S.; Kawamura, K.; Ito, H.; Nobeoka, M.; Ohgaki, K.; Inoue, Y. Rheological Study of TNBA Slaly Semi-Clathrate Hydrate Slurries. In Proceedings of the 7th International Conference on Gas Hydrates (ICGH 2011), Edinburgh, Scotland, UK, 17–21 July 2011.
17. Jerbi, S.; Delahaye, A.; Oignet, J.; Fournaison, L.; Haberschill, P. Rheological properties of CO₂ hydrate slurry produced in a stirred tank reactor and a secondary refrigeration loop. *Int. J. Refrig.* **2013**, *36*, 1294–1301. [[CrossRef](#)]
18. Baojiang, S.; Weiqi, F.; Zhiyuan, W.; Jianchun, X.; Litao, C.; Jintang, W.; Jianbo, Z. Characterizing the Rheology of Methane Hydrate Slurry in a Horizontal Water-Continuous System. *SPE J.* **2020**, *25*, 1026–1041.
19. Weiqi, F.; Zhiyuan, W.; Baojiang, S.; Jianchun, X.; Litao, C.; Xuerui, W. Rheological Properties of Methane Hydrate Slurry in the Presence of Xanthan Gum. *SPE J.* **2020**, *25*, 2341–2352.
20. Cao, X.; Yang, K.; Bian, J. Investigation of CO₂ hydrate slurry flow characteristics with particle dissociation for carbon storage and transportation. *Process Saf. Environ. Prot.* **2021**, *152*, 427–440.
21. Fu, W.; Chen, B.; Zhang, K.; Liu, J.; Sun, X.; Huang, B.; Sun, B. Rheological Behavior of Hydrate Slurry with Xanthan Gum and Carboxymethylcellulose under High Shear Rate Conditions. *Energy Fuels* **2022**, *36*, 3169–3183. [[CrossRef](#)]
22. Webb, E.B.; Rensing, P.J.; Koh, C.A.; Sloan, E.D.; Sum, A.K.; Liberatore, M.W. High-Pressure Rheology of Hydrate Slurries Formed from Water-in-Oil Emulsions. *Energy Fuels* **2012**, *26*, 3504–3509.
23. Webb, E.B.; Koh, C.A.; Liberatore, M.W. High Pressure Rheology of Hydrate Slurries Formed from Water-in-Mineral Oil Emulsions. *Ind. Eng. Chem. Res.* **2014**, *53*, 6998–7007.
24. Liu, Z.; Song, Y.; Liu, W.; Liu, R.; Lang, C.; Li, Y. Rheology of methane hydrate slurries formed from water-in-oil emulsion with different surfactants concentrations. *Fuel* **2020**, *275*, 117961.
25. Clain, P.; Ndoye, F.T.; Delahaye, A.; Fournaison, L.; Lin, W.; Dalmazzone, D. Particle size distribution of TBPB hydrates by focused beam reflectance measurement (FBRM) for secondary refrigeration application. *Int. J. Refrig.* **2015**, *50*, 19–31. [[CrossRef](#)]
26. Muhlstedt, G.; Galdino, J.F.; Andrade, D.E.V.; Negrao, C.O.R. Rheological Properties of Hydrate Slurry in the Water-Based Drilling Fluid. *Energy Fuels* **2021**, *35*, 10488–10497.
27. Sakurai, S.; Hoskin, B.; Choi, J.; Nonoue, T.; May, E.F.; Kumar, A.; Norris, B.W.E.; Aman, Z.M. Investigating hydrate formation rate and the viscosity of hydrate slurries in water-dominant flow: Flowloop experiments and modelling. *Fuel* **2021**, *292*, 120193.
28. Lv, X.; Zhang, J.; Zuo, J.; Zhao, D.; Liu, Y.; Zhou, S.; Du, H.; Song, S. Study on the Formation Characteristics of CO₂ Hydrate and the Rheological Properties of Slurry in a Flow System Containing Surfactants. *ACS Omega* **2022**, *7*, 2444–2457. [[CrossRef](#)]
29. Metzner, A.B.; Reed, J.C. Flow of non-newtonian fluids—correlation of the laminar, transition, and turbulent-flow regions. *Aiche J.* **1955**, *1*, 434–440. [[CrossRef](#)]
30. Dodge, D.W.; Metzner, A.B. Turbulent flow of non-newtonian systems. *Aiche J.* **1959**, *5*, 189–204. [[CrossRef](#)]
31. Metzner, A.B.; Whitlock, M. Flow Behavior of Concentrated (Dilatant) Suspensions. *Trans. Soc. Rheol.* **1958**, *2*, 239. [[CrossRef](#)]
32. Griskey, R.G.; Green, R.G. Flow of dilatant (shear-thickening) fluids. *Aiche J.* **1971**, *17*, 725–728. [[CrossRef](#)]
33. Fu, W.; Yu, J.; Xu, Y.; Wang, C.; Huang, B.; Sun, B. A Pressure Drop Prediction Model for Hydrate Slurry Based on Energy Dissipation under Laminar Flow Condition. *SPE J.* **2022**, *27*, 209586.
34. Fu, W.; Yu, J.; Xiao, Y.; Wang, C.; Huang, B.; Sun, B. A pressure drop prediction model for hydrate slurry based on energy dissipation under turbulent flow condition. *Fuel* **2022**, *311*, 122188. [[CrossRef](#)]

MDPI
St. Alban-Anlage 66
4052 Basel
Switzerland
Tel. +41 61 683 77 34
Fax +41 61 302 89 18
www.mdpi.com

Journal of Marine Science and Engineering Editorial Office
E-mail: jmse@mdpi.com
www.mdpi.com/journal/jmse



MDPI
St. Alban-Anlage 66
4052 Basel
Switzerland

Tel: +41 61 683 77 34

www.mdpi.com



ISBN 978-3-0365-7057-0